

# Robust linear and nonlinear modelling and analysis approaches for uncertain aeroelastic systems



ANDREA IANNELLI

Department of Aerospace Engineering

School of Civil, Aerospace and Mechanical Engineering

University of Bristol

A dissertation submitted to the University of Bristol  
in accordance with the requirements of the degree of  
DOCTOR OF PHILOSOPHY in the Faculty of Engineering.

MARCH 2019



## ABSTRACT

The goal to mitigate the increasing environmental impact of aviation has prompted research into advanced solutions which enable noxious and harmful emissions to be reduced. One of these is represented by aircraft design layouts able to achieve a decrease in aerodynamic drag and aircraft weight, with a tremendous benefit in terms of fuel saving.

An important drawback of these configurations (e.g. high aspect ratio and lightweight wings) is their increased flexibility and resulting large deformations, which in turn can drive the aircraft into dangerous instabilities featuring coupling among aerodynamics, structural dynamics and flight dynamics. The discipline addressing the interplay among these different physical mechanisms is called aeroelasticity. Flutter is a dynamic instability in which the aeroelastic coupling is able to produce self-sustained oscillatory motion, and is recognised as a very dangerous and safety-critical phenomenon.

The main issues with the established approaches for predicting flutter are the sensitivity to model uncertainties and the difficulty to reliably interpret the effect of nonlinearities on the response of the system. In order to address these challenging aspects, in this thesis techniques from robust control have been explored since this represents a natural setting for providing stability guarantees in the face of uncertainties and nonlinearities, and for constructing models featuring a good trade-off between complexity and reliability. In addition, dynamical systems approaches are investigated because they offer a powerful framework to understand the complex dynamics arising in aeroelastic systems and also observed experimentally.

The high-level objective of the thesis is therefore to explore novel approaches to model and analyse aeroelastic systems subject to generic uncertainty and nonlinearities by leveraging the advantages of the above frameworks. Linear methods are first investigated, and original contributions are provided for: construction of Linear Fractional Transformation models; efficient application of  $\mu$  analysis to the flutter problem; and worst-case performance analysis of Linear Time-Varying systems. In the second part of the thesis, the nonlinear response known as Limit Cycle Oscillation and the closely related problem of determining Region of Attraction have been addressed by proposing novel analysis methodologies which contribute to the state-of-the-art by allowing the effect of uncertainties to be studied. The pursued reconciliation between robust control and dynamic system approaches finally culminates in the proposal of the concept of robust bifurcation margins, which has the potential to extend the use of  $\mu$  analysis technique to the nonlinear context.



*To Mama and Dad*



Ἐν οἴδα ὅτι οὐδὲν οἴδα  
*I neither know nor think that I know*

*Plato, Apology of Socrates*

“But I don’t want to go among mad people” Alice remarked.

“Oh, you can’t help that,” said the Cat: “we’re all mad here. I’m mad. You’re mad.”

“How do you know I’m mad?” said Alice.

“You must be,” said the Cat, “or you wouldn’t have come here”

*Lewis Carroll, Alice in Wonderland*

Vien dietro a me, e lascia dir le genti:  
sta come torre ferma, che non crolla  
già mai la cima per soffiar di venti

*Dante, Purgatorio, Canto V*

E quando lui chiese “Perché “  
lui gli rispose “Questo è niente  
e adesso è ora che io vada”

*Fabrizio De André, La cattiva strada*



## ACKNOWLEDGEMENTS

The first big thank you goes undoubtedly to my supervisor Andrés Marcos, for his guidance and trust during the doctoral studies. Your continuous support and enthusiasm have created an ideal environment to work at the ideas presented in this thesis. I have also greatly appreciated the very inclusive attitude you have always had with your students, which has resulted invariably in thought-provoking conversations, enjoyable socials, and numerous tastings. I am also grateful to my co-supervisor Mark Lowenberg, for our valuable discussions on bifurcation and other (not least important) matters, including job interviews and southern hemisphere rugby. Your calm and joviality in all kinds of circumstances have always impressed me.

I am indebted to Pete Seiler for all that I have learned during our short but very fruitful collaboration. Thank you also for the insightful conversations and the kind words on the work. I would like to thank my friends and colleagues Rauno Cavallaro and Rocco Bombardieri for making the solver CHSELL available and for the time spent working on our joint activity. Thanks also to all the collaborators from the project FLEXOP for the many interesting discussions.

Doing a PhD is a long journey, and for that you need good travel buddies. I have had the luck to share my work space with great colleagues. A big thank you to all the Cavemen and Farmers that have filled our (various) offices with enthusiasm and laughs, and by doing so have made them a better place to work. From strenuous walks around Bristol (Pedro and Tim) to legendary trips across the ocean (Diego and Erwin), it is undeniable that we have had some good fun together. A deserved mention also to: Kaiqiang for his wisdom; Sérgio for his irony; Robert for his memorable Christmas cards; Henri for being an excellent ambassador of the British traditions; Dave for being a model of athleticism.

My experience in Bristol would have not been the same without my Geezers friends Gary and Honza. Thank you for having explored with me every corner of this exciting city, as well as many other places around UK. Your positive attitude and curiosity for many common interests has been a perfect mix. I am also grateful to the Ramblers and Brunel walking groups for the many hikes with sun, rain, wind, and hail. After all, there is no such thing as bad weather, only bad clothing. I will bring with me also the energy and passion of the volunteers at Amnesty International and Global Justice Now, your values and dedication have been empowering.

Thank you Dimitra for having shared with me the last part of this adventure. Your strength and determination have been inspiring, and our complicity have pushed us both towards our great achievements. My gratitude goes finally to my parents, for having been always by my side in a roller-coaster ride started many years ago. Who'd have thought? This is for you. Grazie.



## AUTHOR'S DECLARATION

I declare that the work in this dissertation was carried out in accordance with the requirements of the University's Regulations and Code of Practice for Research Degree Programmes and that it has not been submitted for any other academic award. Except where indicated by specific reference in the text, the work is the candidate's own work. Work done in collaboration with, or with the assistance of, others, is indicated as such in the introductions of Chapters 4, 5, and 7. Any views expressed in the dissertation are those of the author.

SIGNED: ..... DATE: .....



## TABLE OF CONTENTS

	<b>Page</b>
<b>List of Tables</b>	<b>xv</b>
<b>List of Figures</b>	<b>xvii</b>
<b>Nomenclature</b>	<b>xxi</b>
<b>Acronyms</b>	<b>xxvii</b>
<b>1 Introduction</b>	<b>1</b>
1.1 Motivation and objectives . . . . .	2
1.2 Contributions . . . . .	4
1.3 Organisation of the thesis . . . . .	7
1.4 Publications . . . . .	7
1.5 Flexop H2020 project . . . . .	10
<b>2 Preliminaries</b>	<b>11</b>
2.1 Literature review . . . . .	11
2.1.1 Flutter analysis . . . . .	11
2.1.2 Robust control theory . . . . .	14
2.1.3 Dynamical systems approaches . . . . .	20
2.2 Fundamental aeroelastic models . . . . .	24
2.3 Physical systems . . . . .	27
2.3.1 Typical section . . . . .	27
2.3.2 Simplified aircraft . . . . .	30
2.3.3 Joined-wing configuration . . . . .	33
2.3.4 FLEXOP demonstrator . . . . .	36
<b>3 Linear Fractional Transformation modelling for robust flutter analysis</b>	<b>39</b>
3.1 Mathematical background . . . . .	40
3.1.1 Linear Fractional Transformation . . . . .	40
3.1.2 $\mu$ analysis . . . . .	43

---

**TABLE OF CONTENTS**

---

3.2	LFT modelling of aeroelastic systems . . . . .	45
3.2.1	Model development path . . . . .	45
3.2.2	Uncertainty description of aerodynamic operators . . . . .	48
3.2.3	A unified LFT modelling approach . . . . .	53
3.3	Coupling LFT modelling with Fluid-structure interaction solvers . . . . .	56
3.3.1	Standard numerical LFT modelling approaches and possible improvements	56
3.3.2	A symbolic LFT-FSI modelling approach . . . . .	58
3.4	Chapter summary . . . . .	67
<b>4</b>	<b>Nominal and robust flutter analysis of linear systems</b>	<b>69</b>
4.1	Nominal flutter analysis . . . . .	70
4.1.1	Flutter algorithms . . . . .	70
4.1.2	Application to the typical section . . . . .	72
4.1.3	Parametric study of body freedom flutter . . . . .	73
4.2	Robust flutter analysis with $\mu$ . . . . .	77
4.2.1	Typical section . . . . .	78
4.2.2	Body freedom flutter . . . . .	83
4.3	Application of $\mu$ to uncertain high-order models . . . . .	89
4.3.1	Nominal analysis of the joined-wing case study . . . . .	89
4.3.2	Robust flutter analysis with the symbolic LFT-FSI approach . . . . .	91
4.3.3	Optimality analysis of the worst-case perturbation . . . . .	94
4.3.4	Reconciliation with previous results . . . . .	96
4.4	Chapter summary . . . . .	98
<b>5</b>	<b>Worst-case analysis of finite horizon Linear Time-Varying systems</b>	<b>101</b>
5.1	Mathematical background . . . . .	102
5.1.1	Generalities on LTV performance . . . . .	102
5.1.2	Hamiltonian dynamics . . . . .	105
5.2	An algorithm for constructing worst-case disturbances on finite horizons . . . . .	106
5.2.1	Theoretical construction . . . . .	107
5.2.2	A numerically robust construction of worst-case disturbance . . . . .	109
5.3	Gust analysis of the FLEXOP demonstrator . . . . .	113
5.3.1	Manoeuvre definition . . . . .	113
5.3.2	Finite horizon LTI vs LTV . . . . .	114
5.3.3	Open-loop vs. Closed-loop manoeuvres . . . . .	116
5.3.4	Comparison with standard gust performance analysis . . . . .	119
5.4	Chapter summary . . . . .	122
<b>6</b>	<b>Limit Cycle Oscillations in systems with uncertainties</b>	<b>123</b>

6.1	Mathematical background . . . . .	124
6.1.1	Describing Functions . . . . .	124
6.1.2	Integral Quadratic Constraints . . . . .	126
6.2	Robust LCO analysis with Describing Functions and $\mu$ . . . . .	130
6.2.1	Limit Cycle Oscillations in nominal systems . . . . .	130
6.2.2	Worst-case LCO curve with $\mu$ . . . . .	137
6.2.3	LCO amplitude tailoring . . . . .	140
6.3	LCO analysis with IQC . . . . .	145
6.3.1	Posing of the problem . . . . .	145
6.3.2	Sensitivity of results to the multipliers . . . . .	147
6.3.3	Post-critical analysis with IQC . . . . .	150
6.4	Chapter summary . . . . .	155
<b>7</b>	<b>Approaches for the estimation of the Region of Attraction</b>	<b>157</b>
7.1	Mathematical background . . . . .	158
7.1.1	Problem statement . . . . .	158
7.1.2	State-of-practice in nominal ROA analysis . . . . .	159
7.2	Invariant sets approach . . . . .	162
7.2.1	Computation of nominal ERAs using invariant sets . . . . .	163
7.2.2	Robust ROA with invariant sets . . . . .	171
7.3	IQC approach . . . . .	178
7.3.1	Region of attraction certificates . . . . .	178
7.3.2	Numerical examples . . . . .	188
7.4	Chapter summary . . . . .	193
<b>8</b>	<b>Robustness from a dynamical systems perspective</b>	<b>195</b>
8.1	Mathematical background . . . . .	196
8.1.1	Bifurcation theory . . . . .	196
8.1.2	Numerical continuation . . . . .	198
8.2	Computation of robust bifurcation margins based on LFT and $\mu$ . . . . .	199
8.2.1	Problem statement . . . . .	200
8.2.2	Solution via nonlinear optimisation . . . . .	201
8.2.3	Continuation-based multi-start strategy . . . . .	207
8.3	Application to the typical section case study . . . . .	211
8.3.1	Nonlinear problem definition and bifurcation analysis . . . . .	212
8.3.2	Robust margins to nonlinear flutter . . . . .	215
8.3.3	Effect of control surface stiffness uncertainty . . . . .	224
8.4	Chapter summary . . . . .	229

---

**TABLE OF CONTENTS**

---

<b>9 Conclusions</b>	<b>231</b>
9.1 Contributions . . . . .	231
9.2 Recommendations for future research . . . . .	234
<b>A Case studies data</b>	<b>237</b>
A.1 Chapter 3 . . . . .	237
A.2 Chapter 4 . . . . .	237
A.2.1 Linear typical section . . . . .	237
A.2.2 Aircraft model . . . . .	239
A.2.3 Joined Wings . . . . .	240
A.3 Chapter 5 . . . . .	242
A.4 Chapter 6 . . . . .	242
A.5 Chapter 7 . . . . .	243
A.6 Chapter 8 . . . . .	243
<b>B Equilibrium-independent ROA</b>	<b>245</b>
B.1 Equilibrium-independent region of attraction certificate . . . . .	246
B.1.1 Problem formulation . . . . .	246
B.1.2 Equilibria identification and computation of inner estimates of Equilibrium-Independent Region of attraction (EIR) . . . . .	248
B.2 Numerical example . . . . .	250
B.2.1 System description . . . . .	250
B.2.2 EIR of the sinks . . . . .	252
<b>Bibliography</b>	<b>255</b>

## LIST OF TABLES

TABLE	Page
2.1 FLEXOP demonstrator main design features [155, 226]. . . . .	36
4.1 Comparison of flutter results with different algorithms. . . . .	72
4.2 Comparison of flutter analysis of the Goland wing with literature results. . . . .	74
4.3 Worst-case perturbations for LFT-1 (with uncertainty levels $\lambda_{EI} = 0.3$ , $\lambda_D = 0.1$ ) at the two frequency peaks. . . . .	87
4.4 Worst-case perturbations for LFT-2 (with uncertainty levels $\lambda_{m_w} = 0.2$ , $\lambda_{EI} = 0.1$ , $\lambda_D = 0.1$ ) at the two frequency peaks. . . . .	88
4.5 Flutter speed and corresponding perturbation matrix's norm at each iteration of Algorithm 3.3. . . . .	93
4.6 Tested worst-case perturbations in the optimality check. . . . .	95
5.1 Comparison of finite horizons LTI and LTV performance based on $\mathcal{L}_2$ and Euclidean gains. . . . .	115
5.2 Comparison of OL and CL performance of $G_{LTV}$ based on $\mathcal{L}_2$ and Euclidean gains. . . . .	116
6.1 Change in the tailoring variables to achieve the amplitude reduction goal. . . . .	144
6.2 LFT models employed in the IQC analyses. . . . .	148
6.3 IQC analysis of LFT 1 (only freeplay). . . . .	148
6.4 IQC analysis of LFT 2 (only uncertainties). . . . .	149
6.5 IQC analysis of LFT 3 (nonlinear uncertain). . . . .	149
6.6 Local IQC analysis of LFT 1 and LFT 3. . . . .	151
7.1 Computational statistics for the invariant sets ROA analyses. . . . .	169
7.2 Computational statistics for the invariant sets robust ROA analyses. . . . .	176
7.3 Computational statistics for the hard and soft IQCs . . . . .	193
8.1 Hopf bifurcations of the nominal system for different combinations of nonlinearities and trim states. . . . .	213
8.2 Robust bifurcation margins at $\bar{V}_0 = 270 \frac{m}{s}$ for different combinations of nonlinearities and trim states. . . . .	216

8.3	Worst-case perturbations and margins to the onset of supercritical and subcritical Hopf bifurcations for $s_5$ and $s_6$ (structural and aerodynamic uncertainties). . . . .	218
8.4	Worst-case perturbations and margins to the onset of supercritical and subcritical Hopf bifurcations for $s_5$ and $s_6$ (uncertainty also in the nonlinear coefficients). . . . .	222
8.5	Worst-case perturbations for the onset of a subcritical Hopf bifurcation with uncertainty also in $K_\beta$ . . . . .	226
A.1	Parameters of the linear typical section case study. . . . .	238
A.2	Parameters for the aircraft model used in the BFF analyses. . . . .	240
A.3	Perturbation matrix $\Delta_{ITER\#}^{cr}$ and corresponding speed $V_{f\mu}$ at each iteration. . . . .	241
A.4	Perturbation matrix $\Delta_{ITER3-new}^{cr}$ and corresponding $V_{f\mu}$ at the final iteration of the re-initialised cycle. . . . .	242
A.5	Parameters of the nonlinear (with freeplay) typical section case study. . . . .	242

## LIST OF FIGURES

<b>FIGURE</b>	<b>Page</b>
1.1 Thematic triangle of the thesis. . . . .	3
1.2 Concept map of the thesis. . . . .	6
1.3 FLEXOP consortium. . . . .	10
2.1 Literature review chart and connections explored in the research. . . . .	12
2.2 Standard feedback configuration in robust control. . . . .	14
2.3 Typical section. . . . .	28
2.4 Straight wing. . . . .	30
2.5 Simplified aircraft. . . . .	31
2.6 Structural model for flutter analysis of <i>PrP250</i> (from [55]). . . . .	34
2.7 Schematic view of the FLEXOP demonstrator (from [155]). . . . .	36
2.8 FLEXOP demonstrator's rendering picture. . . . .	37
3.1 Feedback interpretation of an LFT. . . . .	42
3.2 Realisation technique interpretation of an LFT. . . . .	43
3.3 LFT coverage of the transfer function from $\alpha$ to $L_\alpha$ for $Q_{hh}$ , $Q_{Rg}$ and $Q_{MS}$ . . . . .	50
3.4 Schematic uncertainty description of a notional aircraft wing. . . . .	59
3.5 Block diagram of the symbolic modelling algorithm. . . . .	61
3.6 Block diagram of the iterative scheme. . . . .	64
3.7 Block diagram of the worst-case optimality check algorithm. . . . .	66
4.1 Poles location of the flap, pitch, and plunge modes as speed increases obtained with the $p$ method. . . . .	73
4.2 Flutter analysis of the typical section with the $p$ - $k$ method. . . . .	74
4.3 Parametric flutter analysis for discrete values of $\sigma_s$ (i.e. EI) and $D$ . . . . .	75
4.4 Poles location for two aircraft configurations. . . . .	76
4.5 Comparison of the $\mu$ analysis based on the state-space (SS) and frequency-domain (FD) formulations for the case of structural uncertainties. . . . .	79
4.6 Comparison of $\mu$ algorithms for the case of structural uncertainties. . . . .	80

4.7	Comparison of $\mu$ analysis for the case of uncertainties only in the lag roots of the two approximated aerodynamic operators. . . . .	82
4.8	Comparison of the $\mu$ analysis for the unified ( <i>uni</i> ) and frequency-domain (FD) formulations for the case of aerodynamics and structural uncertainties. . . . .	83
4.9	Poles location for the nominal aircraft model. . . . .	84
4.10	$\mu$ -based sensitivity to EI and D using LFT-1. . . . .	86
4.11	$\mu$ -based sensitivity to EI, D, and $m_w$ using LFT-2. . . . .	87
4.12	Flutter analysis of <i>PrP250</i> (real and imaginary part of the first 5 modes shown). . . . .	89
4.13	Layout of the <i>PrP250</i> featuring a clamped flexible fuselage. . . . .	90
4.14	Flutter analysis of <i>PrP250</i> with elastic fuselage. . . . .	90
4.15	Uncertainty description for the joined-wing configuration. . . . .	91
4.16	Results of the $\mu$ -based iterative algorithm (convergence attained at the 4 <sup>th</sup> iteration). . . . .	93
4.17	$\mu$ analysis of LFTs featuring different nominal plants. The value of the peak is a measure of the proximity of the nominal plant to the actual worst-case. . . . .	95
4.18	$\mu$ -based sensitivity to the mass and stiffness parameters. . . . .	97
5.1	Spectral radius of Y for the upper and lower bound cases. . . . .	105
5.2	Worst-case $\mathcal{L}_2$ gain from Algorithm 5.1 vs. guaranteed $\gamma_{LB}$ for different horizons $T$ . . . . .	109
5.3	Worst-case $\mathcal{L}_2$ gain from Algorithm 5.2 vs. guaranteed $\gamma_{LB}$ for different horizons $T$ . . . . .	112
5.4	Detail of the analysed manoeuvre. . . . .	113
5.5	$\mathcal{L}_2$ gain worst-case disturbances for $a_{z-CG}$ (LTI vs. LTV). . . . .	115
5.6	$\mathcal{L}_2$ -to-Euclidean gain worst-case disturbances for $a_{z-tR}$ (LTI vs. LTV). . . . .	116
5.7	$\mathcal{L}_2$ gain worst-case disturbances for $a_{z-CG}$ (OL vs CL). . . . .	117
5.8	$\mathcal{L}_2$ gain worst-case disturbances for $a_{z-CG}$ (OL vs CL). Deceleration from $V_2$ to $V_1$ . . . . .	118
5.9	Effect of $T$ on the $\mathcal{L}_2$ gain worst-case disturbances for the CL system. . . . .	119
5.10	Set of 1-cosine gust signals for different gust length $L_g$ . . . . .	120
5.11	$\mathcal{L}_2$ and $\mathcal{L}_2$ -to-Euclidean gains as a function of the gust length. . . . .	121
6.1	Feedback representation of a nonlinear system for DF analysis. . . . .	124
6.2	Feedback $G - \Delta$ studied in IQC. . . . .	126
6.3	Augmented plant for the time-domain interpretation of IQC. . . . .	129
6.4	Freeplay nonlinearity. . . . .	131
6.5	Freeplay describing function. . . . .	132
6.6	Flutter speed $V_f$ and frequency $\omega_f$ vs. quasi-linear flap stiffness $K_\beta^{QL}$ . . . . .	135
6.7	LCO amplitude $\frac{\beta_s}{\delta}$ vs. speed $V$ . . . . .	136
6.8	$\mu$ analysis at $V = 10.3 \frac{m}{s}$ and $\frac{\beta_s}{\delta} = 1.9$ . . . . .	138
6.9	Robustness analysis of the LCO for scattered operating point. . . . .	138
6.10	Worst-case LCO curve. . . . .	140
6.11	Objective definition for the DF and $\mu$ -based tailoring. . . . .	141

6.12	$\mu$ analysis for the nominal plant identified by the square marker.	142
6.13	LCO amplitudes $\frac{\beta_s}{\delta}$ obtained with the proposed tailoring strategy (3 possible designs are considered).	144
6.14	Standard sector constraint.	148
6.15	Local sector constraint for LCO analyses.	150
6.16	Validation via simulation of the worst-case LCO curve.	153
6.17	Simulated responses at two different speeds.	154
7.1	Comparison of the ERA of the short-period model with different algorithms.	169
7.2	Upper bounds of the ERA.	171
7.3	Comparison of the rERA of the short-period model with different algorithms.	177
7.4	Upper bounds of the rERA.	177
7.5	Augmented plant for IQC-based ROA analysis.	179
7.6	Relaxed sector constraint exploiting bounds on $q_{max}$ .	189
7.7	Estimates of the region of attraction for different saturation levels.	191
7.8	Estimates of the region of attraction for the uncertain Van der Pol oscillator.	192
8.1	Concept of robust bifurcation margins.	201
8.2	Bifurcation diagram of the nominal system for different combinations of nonlinearities and trim states.	214
8.3	Zoom on the plunge (solid) and pitch (dashed) frequencies around the linear nominal flutter speed.	215
8.4	Bifurcation diagram of the perturbed system $s5$ : supercritical and subcritical LCOs.	220
8.5	Linearised pitch (solid) and plunge (dashed) mode frequencies of the perturbed systems as $V$ is increased.	221
8.6	Effect of uncertainty in the nonlinear coefficients on the onset of a subcritical Hopf bifurcation.	223
8.7	Frequency representation of the reciprocal of the robust bifurcation margin.	224
8.8	Comparison of $k_m$ for the cases with and without uncertainty in $K_\beta$ .	225
8.9	Linearised frequencies and MAC around the branch of equilibria for nominal (red) and perturbed (black) case $s6$ .	227
8.10	Periodic behaviour of the perturbed system $s6$ at $\tilde{V}_0$ .	228
8.11	Bifurcation diagram of the perturbed $s6$ for the DOFs $\frac{h}{b}$ (red) and $\alpha$ (black).	228
B.1	Characterisation of the set of sinks via level sets.	251
B.2	EIR for $\partial(\tilde{V}) = 2$ and $\partial(\tilde{V}) = 4$ .	252
B.3	Level sets $\Omega_{V,\gamma}$ and $\Omega_{V,\gamma_f}$ associated with $\delta = 0.9$ .	253
B.4	Degradation of the local stability in the face of uncertainties.	254



## NOMENCLATURE

### Notation

$\mathbb{R}_+$	Set of positive real numbers
$\mathbb{R}^{n \times m}, \mathbb{C}^{n \times m}$	Real and complex valued matrices with $n$ rows and $m$ columns
$\mathbb{S}^n$	Real symmetric matrix of size $n$
$\mathbb{RL}_\infty$	Set of rational functions with real coefficients that are proper and have no poles on the imaginary axis
$\mathbb{RH}_\infty$	Subset of functions in $\mathbb{RL}_\infty$ that are analytic in the closed right half of the complex plane
$\mathbb{RL}_\infty^{m \times n}, \mathbb{RH}_\infty^{m \times n}$	Sets of $m \times n$ matrices whose elements are in $\mathbb{RL}_\infty$ and $\mathbb{RH}_\infty$ , respectively
$\mathbb{R}[x], \Sigma[x]$	Set of polynomials and SOS polynomials with variables $x$
$\Re, \Im$	Real and Imaginary part of a complex number
$\langle r, q \rangle$	Given $r, q \in \mathbb{C}^n$ , $\langle r, q \rangle = \bar{r}^\top q$
$[x; y]$	Vertical concatenation of two vectors $x \in \mathbb{C}^n$ and $y \in \mathbb{C}^m$
$\text{diag}(\cdot)$	Block diagonal matrix made up of elements in $(\cdot)$
$\bar{\sigma}(P)$	Maximum singular value of a matrix $P$ (or induced 2-norm)
$\rho(P)$	Spectral radius of $P$
$\mathcal{L}_2^n[0, \infty)$	Space of all square integrable functions $v : [0, \infty) \rightarrow \mathbb{R}^n$ , i.e. satisfying $\ v\ _2 < \infty$
$\mathcal{L}_2^n[0, T]$	Space of all functions $v : [0, T] \rightarrow \mathbb{R}^n$ satisfying $\ v\ _{2,[0,T]} < \infty$
$\ G\ _\infty$	$\mathcal{H}_\infty$ norm of the transfer matrix $G$ , i.e. $\sup_{\omega \in \mathbb{R}} \bar{\sigma}(G(i\omega))$
$\ G\ _{2,[0,T]}$	Finite-horizon induced $\mathcal{L}_2$ -gain of $G$

---

$\ G\ _{E,[0,T]}$	Finite-horizon induced $\mathcal{L}_2$ -to-Euclidean gain of $G$
$\ v\ _2$	$\mathcal{L}_2$ norm of the time-domain signal $v$ , i.e. $\sqrt{\int_0^\infty v(t)^\top v(t) dt}$
$\ v\ _{2,[0,T]}$	Finite-horizon $\mathcal{L}_2$ norm of $v$ , i.e. $\sqrt{\int_0^T v(t)^\top v(t) dt}$
$\ w\ $	Euclidean norm of a vector $w$
$G^\sim$	Para-Hermitian conjugate of $G \in \mathbb{RL}_\infty^{m \times n}$ , i.e. $G^\sim(s) := G(-s)^\top$
$I_n$	Identity matrix of size $n$
$M^\top, M^*$	Transpose and complex conjugate transpose of $M \in \mathbb{C}^{n \times m}$
$M_{x,11}$	Coefficient 11 of the matrix $M_x$
$\bar{r}$	Complex conjugate of $r \in \mathbb{C}^n$

## Symbols

$\Delta^{cr}$	Worst-case perturbation matrix determining singularity of the LFT
$\Delta^{y,R-z,C}$	Structured uncertainty set with repeated $y$ real and $z$ complex uncertainties
$\hat{\Delta}^{cr}$	Worst-case matrix provided by the iterative $\mu$ algorithm which determines a flutter speed $V_{f\mu} \approx V_\mu$ in the perturbed system.
$\delta_d, \lambda_d$	Normalised uncertainty parameter $d$ and corresponding level of uncertainty
$\omega$	Frequency of oscillation
$\Pi$	IQC frequency-domain multiplier
$\Psi, M$	$\Psi \in \mathbb{RH}_\infty^{n_z \times (n_v + n_w)}$ and $M = M^\top \in \mathbb{R}^{n \times n}$ defining a possible state-space factorisation of $\Pi$
$\Omega_{r,c}$	Level set associated with a scalar $c > 0$ and polynomial $r \in \mathbb{R}[x]$ , i.e. $\{x \in \mathbb{R}^n : r(x) \leq c\}$
$\partial\Omega_{r,c}$	Boundary of $\Omega_{r,c}$ , i.e. $\{x \in \mathbb{R}^n : r(x) = c\}$
$\partial(r)$	Degree of the polynomial $r \in \mathbb{R}[x]$
$\bar{\Phi}, \bar{\Psi}$	Zero problem and monitor functions of the extended continuation problem
$\mathcal{A}, \mathcal{B}, \mathcal{C}, \mathcal{D}$	State matrices of an LTI system

$\mathcal{F}_u(M, \Delta)$	Linear Fractional Transformation of $M$ with uncertainty set $\Delta$
$f, J$	Vector field and associated Jacobian
$\tilde{f}, \tilde{J}$	Uncertain vector field and associated Jacobian
$\mathcal{H}$	Manifold of Hopf bifurcation points connected to $\hat{X}$
$\mathcal{H}_g$	Restriction of $\mathcal{H}$ through parameterisation of the uncertainty set via $g$
$k_m$	Robust bifurcation margin
$l_1$	First Lyapunov coefficient
$N$	Describing function
$N^F$	Freeplay describing function
$n_\delta$	Number of uncertain parameters
$p_H$	Value of the continuation parameter $p$ at the Hopf bifurcation
$\bar{p}_0$	Value of the continuation parameter $p$ for which the robust bifurcation margin is computed
$\mathcal{R}$	Region of attraction
$\mathcal{R}_\delta$	Robust region of attraction
$s, \bar{s}$	Laplace variable and its dimensionless counterpart
$V_{lin}$	Quadratic Lyapunov function proving asymptotic stability of a linear (or linearised) system
$\hat{X}$	Solution of the robust bifurcation optimisation problem
$x$	Vector of states of dimension $n_x$

## Aeroelastic variables

$\gamma_i$	Lag roots of the rational function approximation
$\Gamma_{QS}, \Gamma_{lag}$	Quasi-steady and lag part of the rational function approximation
$\omega_n$	Natural frequency
$\omega_b, \omega_\alpha$	Lowest bending and torsional natural frequencies

## NOMENCLATURE

---

$\eta$	Vector of generalised coordinates
$\Phi$	Modal matrix
$\sigma_s$	Bending stiffness factor ( $EI = \sigma_s EI_G$ , with $EI_G$ Goland wing bending stiffness)
$\bar{\delta}$	Freeplay size
$\omega_f$	Flutter frequency
$b$	Typical section half chord
$D$	Tail leading edge distance from the nose
$EI, GJ$	Bending and torsional stiffness of the uniform wing
$F_e, F_r$	Loads on the wing due to elastic deformation and rigid-body motion, respectively
$h, \alpha, \beta$	Typical section DOFs: plunge, pitch, and control surface rotation
$K_h, K_\alpha, K_\beta$	Bending, torsional and control surface stiffness parameters
$K_h^L, K_\alpha^L$	Linear bending and torsional stiffness parameters
$K_h^{NL}, K_\alpha^{NL}$	Proportional coefficients between nonlinear and linear stiffness parameters
$K_s^L, K_s^{NL}$	Linear and nonlinear structural stiffness matrix
$k$	Reduced frequency
$L_r$	Reference length
$L$	Wing span
$\bar{M}_s, \bar{C}_s, \bar{K}_s$	Generalised structural mass, damping and stiffness matrices
$M_s, C_s, K_s$	Physical structural mass, damping and stiffness matrices
$m$	Aircraft total mass
$m_w$	Wing mass per unit span
$n_s$	Number of aeroelastic modes after modal truncation
$Q_{hh}$	Generalised aerodynamic force matrix
$Q_{Rg}, Q_{MS}$	Rational approximations of $Q_{hh}$ obtained with Roger and Minimum State method respectively
$q_\infty$	Dynamic pressure

$T$	Aeroelastic frequency response matrix
$V$	Speed
$V_f$	Flutter speed
$\bar{V}_0$	Speed (associated with a stable equilibrium) for which the robust bifurcation margin is computed
$V_H$	Hopf bifurcation speed
$V_{HT}$	Tail volume
$x_r, x_s, x_a$	Vector of rigid, structural, and aerodynamic states
$x_t$	Trim state
$Z_\bullet^e, M_\bullet^e$	Aerodynamic and aeroelastic stability derivatives for the elastic equilibrium
$Z_\bullet^r, M_\bullet^r$	Aerodynamic and aeroelastic stability derivatives for the rigid-body equilibrium
.	.



## ACRONYMS

- BFF** Body Freedom Flutter
- DOF** Degree of Freedom
- DF** Describing Functions
- DLM** Doublet Lattice Method
- EIR** Equilibrium-Independent Region of attraction
- ERA** inner Estimates of the ROA
- FEM** Finite Element Method
- FSI** Fluid-structure interaction
- GAF** Generalised Aerodynamic Force
- IQC** Integral Quadratic Constraints
- KYP** Kalman-Popov-Yakubovich
- LCO** Limit Cycle Oscillation
- LF** Lyapunov Functions
- LFT** Linear Fractional Transformation
- LMI** Linear Matrix Inequalities
- LTI** Linear Time-Invariant
- LTV** Linear Time-Varying
- MAC** Modal assurance criteria
- RCT** Robust Control Toolbox
- RDE** Riccati Differential Equation

## ACRONYMS

---

**rERA** Robust inner Estimates of the ROA

**RFA** Rational function approximation

**ROA** Region of attraction

**RS** Robust Stability

**SDP** Semidefinite Program

**SOS** Sum of Squares

## INTRODUCTION

A major challenge faced today by a more environmentally friendly aeronautical industry is the need to sensibly reduce fuel consumption ensuring at the same time that all the safety constraints are fulfilled. Two design solutions to pursue this goal are represented by lightweight aircraft configurations and wing layouts featuring high aspect ratios. Indeed, the former allows the total weight of the aircraft to be reduced and therefore save on fuel burn, whereas the latter has the advantage of determining a smaller aerodynamic drag with a similar benefit. The adoption of this design paradigm shift has been hindered thus far by the consequent increase in deformation experienced by the structural parts. Among the most dangerous phenomena associated with a greater flexibility, the so-called *Fluid-structure interaction* (FSI) problem have received increasing attention in the aerospace community in recent years.

Aeroelasticity addresses the FSI problem by providing models and analysis methods to study the coupling between a flexible structure and a fluid flow generating a pressure depending on its geometry. An important phenomenon which can be investigated within the aeroelastic framework is flutter, a self-excited dynamic instability in which aerodynamic forces acting on a flexible body couple with its natural modes of vibration producing oscillatory motion. The level of vibration may result in sufficiently large amplitudes to provoke failure and often it enforces strict constraints on the design of the entire system.

Due to the complexity of flutter, a large amount of effort has been spent with the aim to provide numerical techniques to study it. However, it is acknowledged at present that predictions based only on the available computational approaches are not totally reliable, largely due to the effects of nonlinearity and uncertainty not adequately captured in the analyses. Currently, this is compensated with the requirement to satisfy conservative safety margins by design, and to perform expensive flights test campaigns before certification. This state-of-practice guarantees

the avoidance of flutter in commercial aircraft, but results in a process that is costly and lengthy, let alone inefficient from a structural design perspective. In a scenario marked by increased flexibility, the difficulties in predicting and characterising this phenomenon are further accentuated. Therefore, flutter represents a potential showstopper for the development of the next generation greener aircraft, and the investigation and proposal of novel methods for more systematic and reliable studies are highly welcome in the community.

## 1.1 Motivation and objectives

Based on the research done on the topic in the last two decades, two aspects are identified as critical for the current limitations discussed above.

The first is the sensitivity of flutter to *uncertainties*, which are caused for example by variations in system's parameters or simplifying modelling hypotheses. In other words, predictions of the conditions at which the instability takes place can substantially change depending on the level of fidelity with which the system is modelled and its subparts are defined. Mismatches among the predictions originate not only from lack of knowledge or simplifying assumptions, but also from the numerous layout changes inherent to the complex and multi-objective aircraft design process. As a result, it is desirable to develop modelling frameworks that: are able to describe the system as a *family* (or collection) of several realisations; and allow analysis techniques capable of providing guaranteed results (*robust* to a given dispersion of the *nominal* data) to be performed. In fact, the availability of these tools provides more confidence on the validity of the results, and thus they have the potential to relax the tight safety margins and the amount of test flights required for flutter clearance, both helping to reduce time and cost.

The second factor is the presence of *nonlinearities*, in different forms (geometric, aerodynamic, structural, and potentially also in automatic control systems in the case of aeroservoelastic studies), in fluid-structure interaction problems. While flutter analysis commonly relies on linear hypotheses, nonlinear aeroelasticity has received increasing attention from research and industry. However, a clear understanding of the responses exhibited when nonlinear features are retained in the model (and also observed experimentally) and the physical mechanisms prompting them is far from being reached. Enhanced comprehension of the role played by nonlinearities is indeed another fundamental step towards building confidence in the ability to predict flutter. In addition, the interplay between uncertainties and nonlinearities in the aeroelastic scenario deserves special focus. Their combined effect can indeed give rise to unexpected behaviours, not captured by applying analysis approaches which address them separately.

A number of advanced modelling and analysis tools are considered in this thesis to address the challenges discussed above. Techniques from the *robust control* community provide a natural framework to investigate systems subject to generic uncertainties. For example, Linear Fractional Transformation (LFT) models and  $\mu$  (or structured singular value) analysis are well established

for studying stability and performance of linear time-invariant systems. Another instrumental technique for this work is represented by Integral Quadratic Constraints (IQC), which is able to handle uncertainties and nonlinearities in a unified framework, and presents connections with another powerful paradigm in control, namely dissipativity. Building on different theoretical foundations, *dynamical systems* approaches, for example bifurcation theory and numerical continuation, can help tackling similar problems. As the study of aeroelastic phenomena, particularly with respect to novel aircraft configurations, is a multi-faceted problem, the high-level objective of this PhD is to investigate novel approaches by leveraging the advantages of these different frameworks and unexplored connections. An outcome of this effort would then also be the creation of bridges among the different communities which have the potential to take part in the solution, namely the aeroelastic, robust control and dynamical systems ones. A diagrammatic illustration of this idea is given in Fig. 1.1, where the distinctive features of each discipline are highlighted.

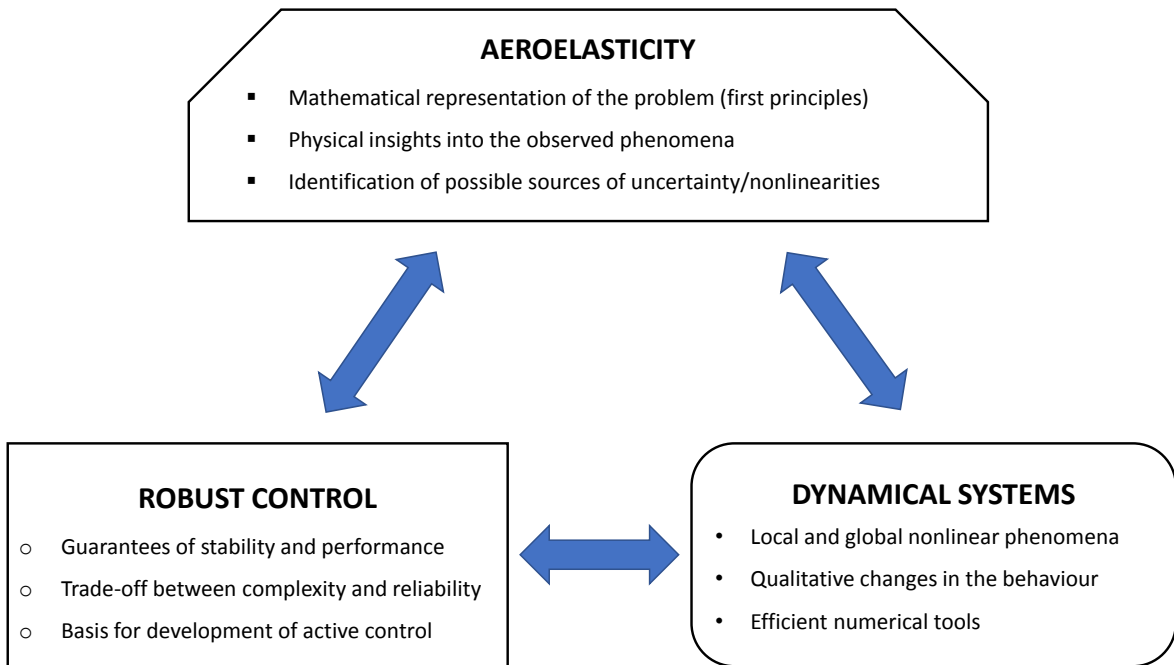


Figure 1.1: Thematic triangle of the thesis.

The main objectives of this thesis are laid down next.

- Investigate the application of Linear Fractional Transformation and  $\mu$  analysis to the study of flutter for linear models featuring uncertainties. Previous works have partially tackled this problem, but relevant tasks which still need consideration and are covered in this thesis are: address modelling aspects specific to aeroelastic systems; emphasizing the different types of information that can be inferred from the analyses; and reconciling the results with a physical-based aeroelastic perspective.

- Address *quantitatively* the effect of uncertainties on nonlinear phenomena to which aeroelastic systems are typically prone. New connections between different techniques from the robust control theory (e.g. Integral Quadratic Constraints and dissipativity) are sought in order to reduce conservatism and extend their range of application. At the same time, the proposed approaches should be presented in a methodological manner, and their rationale discussed critically, in order to favour their reception in the other communities.
- Highlight complementarities and possible connections between robust control and dynamical systems-based approaches for uncertain and nonlinear flutter problems. Despite sharing similar features (e.g. focus on the effect of parameters on the dynamics; rigorous mathematical foundations), there have not been many attempts yet to combine them, thus new results on this can spark further theoretical developments and applications. Specifically, an interesting research question tackled in this thesis is whether the tools for robustness analysis used in the context of linear systems could be extended to the analysis of bifurcations of uncertain vector fields.

## 1.2 Contributions

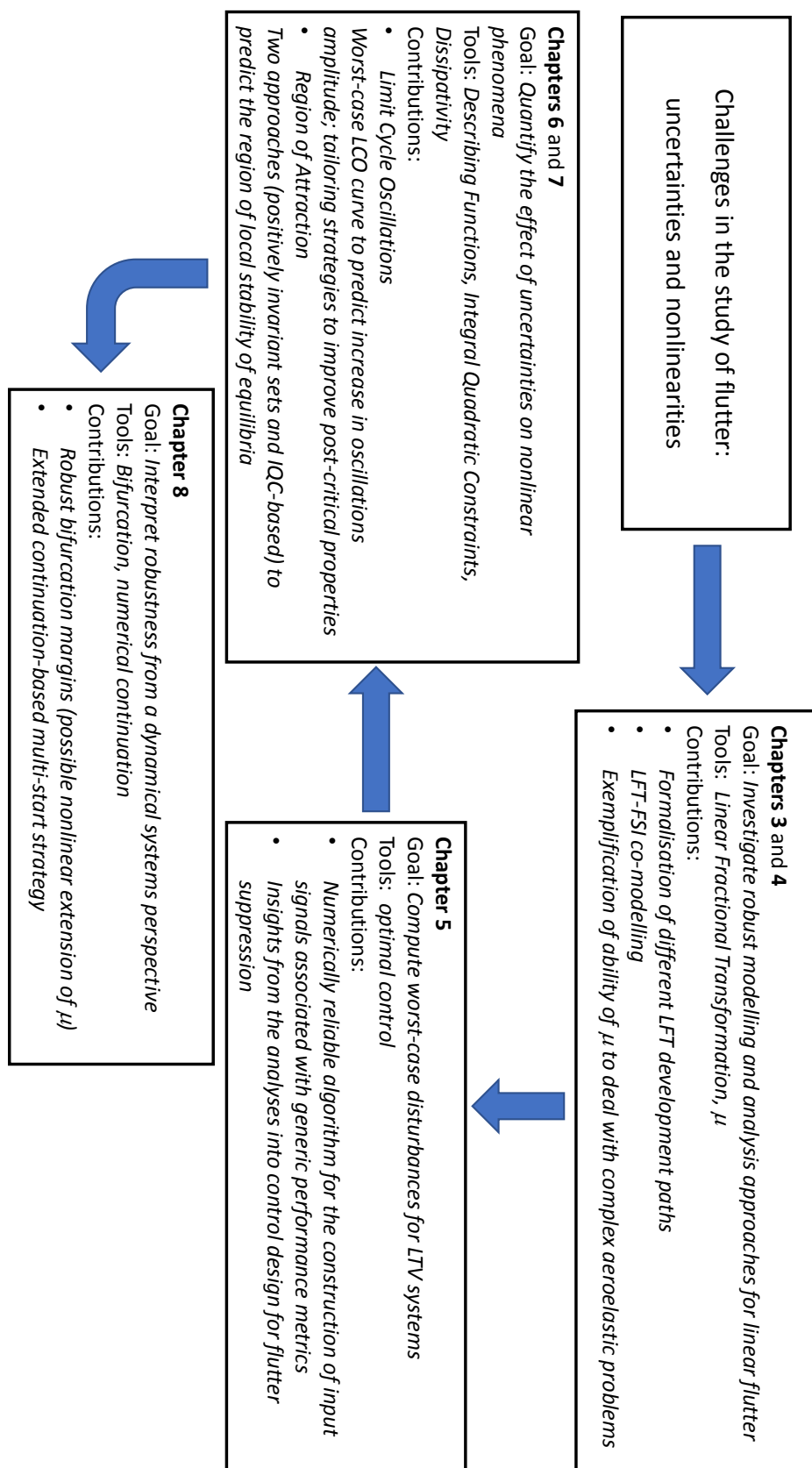
The main contributions of this thesis are the following.

- The construction of Linear Fractional Transformation models of uncertain aeroelastic systems is studied in Chapter 3. Two possible modelling processes are presented in detail and their distinctive features discussed. In this way, the challenges of providing a physical-based definition of the uncertainties, which is addressed in the remainder of the chapter, are clearly pointed out. The proposed approaches represent the basis for development of the models used throughout the work. Highlights of this chapter include a detailed evaluation of aerodynamic uncertainty description strategies and a novel method to build up uncertainty models for systems described by means of state-of-practice fluid-structure interaction solvers, typically leading to high order models.
- The benefits of employing  $\mu$  analysis to study the robust flutter problem are demonstrated in Chapter 4. The results show that this framework provides something more than a binomial-type of test on robust stability, with emphasis on: sensitivity of the instability to parameters; insights gained from the worst-case perturbations; and frequency interpretation of the results. These aspects are showcased with the investigations of: body freedom flutter, a particular dynamic instability featuring the interaction between rigid-body and elastic modes; and an unconventional aircraft layout, whose aeroelastic behaviour currently poses challenges to their design.
- The construction of worst-case input signals verifying that a given performance is not achieved is developed in Chapter 5 for Linear Time-Varying (LTV) systems. Capturing the

presence of time-varying properties provides a more realistic description for aircraft (where properties of the system might change during a manoeuvre), and crucially represents a stepping stone to the nonlinear descriptions used later on. The technical result builds on known optimal control facts (e.g. strict bounded real lemma) but provides an original solution to the problem of simulating Hamiltonian dynamics. The proposed algorithm is a powerful tool for the analysis of very flexible aircraft and an example is provided with analyses in support of a realistic flight test scenario.

- Methodologies to study Limit Cycle Oscillation (LCO) and Region of attraction (ROA) are developed in Chapter 6 and Chapter 7, respectively. IQC are pivotal to enable the study of these inherently nonlinear phenomena in the presence of uncertainties, but extensions with respect to its common use are proposed in order to overcome known limitations. Specifically, Describing Functions are employed to provide a relaxation of standard IQC multipliers and allow the study of post-critical behaviour (other than just stability) as well as the formulation of the concept of *worst-case LCO curve*. Connections between dissipativity and multiplier theory, recently proposed in the literature, are leveraged to develop a framework for ROA analysis which allows generic nonlinear uncertain vector fields to be analysed.
- A possible interpretation of robustness from a dynamical systems perspective is proposed in Chapter 8. The investigated problem consists of studying robustness to the onset of Hopf bifurcations for polynomial vector fields, and it is solved by introducing the concept of *robust bifurcation margin*  $k_m$ . Its definition and the underlying mathematical problem has formal similarities with  $\mu$ , thus it can be considered as a possible extension of the structured singular value to the nonlinear context. Another contribution of this chapter is the development of a numerical method to determine manifolds of Hopf bifurcation points in the uncertain parameters space, which leverages the extended continuation framework and allows more accurate estimations of  $k_m$  to be computed.

A concept map of the thesis is depicted in Fig. 1.2. The chapters are grouped based on the goals and contributions, and for each block the main mathematical tools adopted are also reported. The arrows signify the logic relationships among the research tasks with respect to the objectives stated in Section 1.1.



### 1.3 Organisation of the thesis

The thesis is organised as follows. Chapter 2 presents the literature review, an overview of the fundamental mathematical description used in aeroelasticity and the physical systems analysed in the work. Chapter 3 is devoted to the problem of constructing Linear Fractional Transformation models for aeroelastic systems. Chapter 4 investigates application of robust flutter analysis with  $\mu$ . Chapter 5 develops the numerical algorithms for the computation of worst-case signals for LTV systems on finite horizons. Chapter 6 proposes two different strategies to study Limit Cycle Oscillations in systems subject to uncertainties. Chapter 7 is dedicated to the problem of computing the Region of Attraction for generic nonlinear uncertain systems. Chapter 8 proposes a framework for the computation of robustness of stable equilibria to the onset of Hopf bifurcations. And finally, Chapter 9 concludes the thesis by summarising the main contributions and pointing to directions for future research. In Appendix A the data for the analysed case studies are presented in order to allow reproducibility of the results, while Appendix B provides a self-contained technical result on the determination of the region of attraction of uncertainty-dependent equilibria.

### 1.4 Publications

The work presented in this thesis has been published by the time of submission in journals (J), peer-reviewed conferences (C) and a book chapter (B), as listed below.

#### Chapter 3

- [J1] **Iannelli A.**, Marcos A., Lowenberg M. *Aeroelastic modeling and stability analysis: A robust approach to the flutter problem*. International Journal of Robust and Nonlinear Control, 28, 342–364, 2017.
- [C1] **Iannelli A.**, Marcos A., Lowenberg, M. *Comparison of Aeroelastic Modeling and Robust Flutter Analysis of a Typical Section*. IFAC Symposium on Automatic Control in Aerospace - ACA 2016.

#### Chapter 4

- [J2] **Iannelli A.**, Marcos A., Lowenberg M. *Study of Flexible Aircraft Body Freedom Flutter with Robustness Tools*. Journal of Guidance, Control, and Dynamics, 41, 1083-1094, 2017.
- [C2] **Iannelli A.**, Marcos A., Lowenberg, M. *Modeling and Robust Body Freedom Flutter Analysis of Flexible Aircraft Configurations*. IEEE Multi-Conference on Systems and Control - MSC 2016.

- [C3] **Iannelli A.**, Marcos A., Bombardieri R., Cavallaro R. *A symbolic LFT approach for robust flutter analysis of high-order models*. IEEE European Control Conference - ECC 2019.

## Chapter 5

- [J3] **Iannelli A.**, Seiler P., Marcos A. *Worst-case disturbances for Time-Varying systems with application to flexible aircraft*. Journal of Guidance, Control, and Dynamics (accepted December 2018).
- [C4] Luspay T., Ossmann D., Wuestenhagen M., Teubl D., Baár T., Pusch M., Kier T.M., Waitman S., **Iannelli A.**, Marcos A., Vanek B., Lowenberg M. *Flight control design for a highly flexible flutter demonstrator*. AIAA Scitech 2019.

## Chapter 6

- [J4] **Iannelli A.**, Marcos A., Lowenberg M. *Nonlinear robust approaches to study stability and post-critical behaviour of an aeroelastic plant*. IEEE Transactions on Control Systems Technology, 27, 703–716, 2019.
- [B1] **Iannelli A.**, Marcos A., Lowenberg M. *Limit Cycle Oscillation amplitude tailoring based on Describing Functions and  $\mu$  Analysis*. Advances in Aerospace Guidance, Navigation and Control - Springer-Verlag - 2017.
- [C5] **Iannelli A.**, Marcos A., Lowenberg M. *Nonlinear flutter analysis with uncertainties based on Describing Function and Structured Singular Value with an IQC validation*. European Conference for Aeronautics and AeroSpace Sciences - EUCASS 2017.
- [C6] **Iannelli A.**, Marcos A., Lowenberg M. *Nonlinear stability and post-critical analysis of an uncertain plant with Describing Functions and Integral Quadratic Constraints*. IEEE Conference on Decision and Control - CDC 2017.

## Chapter 7

- [J5] **Iannelli A.**, Marcos A., Lowenberg M. *Robust estimations of the region of attraction using invariant sets*. Journal of The Franklin Institute, 356, 4622-4647, 2019.
- [C7] **Iannelli A.**, Seiler P., Marcos A. *Estimating the region of attraction of uncertain systems with Integral Quadratic Constraints*. IEEE Conference on Decision and Control - CDC 2018.
- [C8] **Iannelli A.**, Marcos A., Lowenberg M. *Estimating the region of attraction of uncertain systems with invariant sets*. IFAC Symposium on Robust Control Design - ROCOND 2018.

- [C9] **Iannelli A.**, Marcos A., Lowenberg M. *Algorithms for the estimation of the region of attraction with positively invariant sets*. International Conference on Systems and Control - ICSC 2018.

## Chapter 8

- [C10] **Iannelli A.**, Lowenberg M., Marcos A. *An extension of the structured singular value to nonlinear systems with application to robust flutter analysis*. CEAS Specialist Conference on Guidance, Navigation & Control - EGNC 2019.

## Appendix B

- [C11] **Iannelli A.**, Seiler P., Marcos A. *An equilibrium-independent region of attraction formulation for systems with uncertainty-dependent equilibria*. IEEE Conference on Decision and Control - CDC 2018.

The following papers are currently under review.

- [J] **Iannelli A.**, Seiler P., Marcos A. *Region of attraction analysis with Integral Quadratic Constraints*. Automatica.
- [J] **Iannelli, A.**, Lowenberg M., Marcos A. *Computation of bifurcation margins based on robust control concepts*. SIAM Journal on Applied Dynamical Systems.

The following articles were published during the doctoral studies but are not featured in this dissertation.

- [C12] **Iannelli A.**, Simplicio P., Navarro-Tapia, D., Marcos A. *LFT Modeling and  $\mu$  Analysis of the Aircraft Landing Benchmark*. IFAC World Congress 2017.
- [C13] Navarro-Tapia D., Simplicio P., **Iannelli A.**, Marcos A. *Robust Flare Control Design Using Structured  $\mathcal{H}$  Synthesis: a Civilian Aircraft Landing Challenge*. IFAC World Congress 2017.
- [C14] Simplicio P., Navarro-Tapia, D., **Iannelli A.**, Marcos A. *From Standard to Structured Robust Control Design: Application to Aircraft Automatic Glide-slope Approach*. IFAC Symposium on Robust Control Design - ROCOND 2018.

## 1.5 Flexop H2020 project

This PhD study is part of the FLEXOP (Flutter Free FLight Envelope eXpansion for ecOnomical Performance improvement –[www.flexop.eu](http://www.flexop.eu)) European Horizon 2020 project. The aim of the project is to develop multidisciplinary flexible aircraft design capabilities that will increase competitiveness in terms of aircraft development costs. This will be achieved by:

- developing aeroelastic tailoring methods and tools;
  - advancing the state-of-the-art in flutter modelling, analysis and control;
  - demonstrating the effectiveness of the developed methodologies with flights tests of an affordable demonstrator.

One of the main expected outcomes is to prove in flight the successful deployment of active flutter suppression strategies to extend the flutter-free envelope and foster the adoption of this solution at industrial level. The consortium consists of two research centres, three universities and three industrial partners (Fig. 1.3).

The work done during this PhD was in support of the activity in Work Package 2, dedicated to flutter prediction and control design methods.

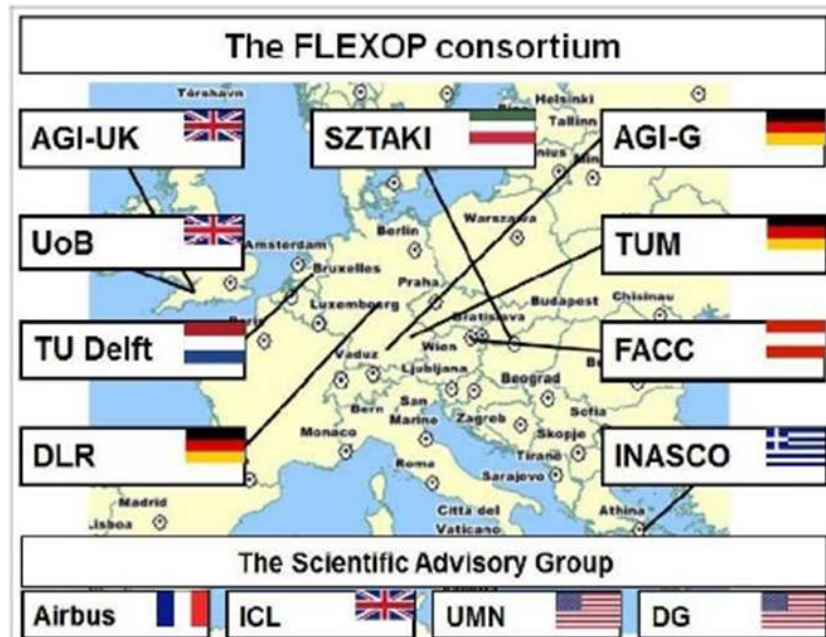


Figure 1.3: FLEXOP consortium.

## PRELIMINARIES

This chapter provides a fundamental overview of topics and models featuring the thesis. Section 2.1 is dedicated to the literature review, while Section 2.2 presents the basic mathematical formulation of the aeroelastic problem, serving as basis for all the analysed models. Section 2.3 illustrates the physical systems used throughout the thesis to exemplify the developed modelling and analysis algorithms, and it highlights their essential features.

### 2.1 Literature review

The literature review follows the flow of the work illustrated in Chapter 1, and aims at highlighting important aspects of the different subjects dealt with in this thesis: flutter analysis (Section 2.1.1), robust control (Section 2.1.2) and dynamical systems (Section 2.1.3). In order to facilitate readability, Fig. 2.1 sketches the main topics and shows the connections investigated in this research.

#### 2.1.1 Flutter analysis

The interaction among inertial, damping and elastic forces in a mechanical system is the subject of structural dynamics. For systems such as wings, the external loading is represented by aerodynamic forces, which depend on the geometry of the body. The study of these systems is addressed by aeroelasticity [30], which investigates the coupled problem of a flexible structure surrounded by a fluid flow. The analysis results provided by structural dynamics (e.g. mode shapes, natural frequencies, response to initial conditions) change due to this coupling [111]. The same situation arises with the load estimation [256], which is only approximately captured with a purely aerodynamics-based approach, i.e. by considering an infinitely stiff body surrounded

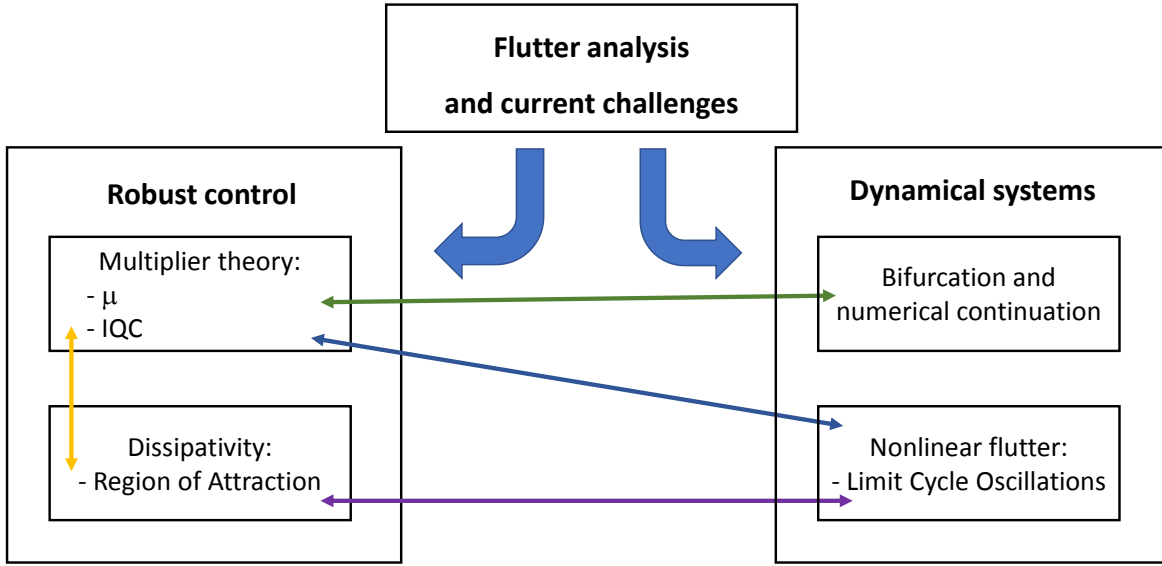


Figure 2.1: Literature review chart and connections explored in the research.

by the flow. Due to the significant effects of their coupled behaviour, it is then compulsory, when discussing stability and performance, to consider a description of the system capturing these close interactions.

Flutter consists of a self-sustained instability and is one of the most important phenomena which can be investigated within the aeroelastic framework. Computational methods to predict its occurrence have been widely investigated in the community [111, 202, 256], and to this end it is common practice to use dedicated Fluid-structure interaction (FSI) solvers. These typically consist of a structural solver (e.g. based on the Finite Element method) coupled with an unsteady aerodynamic solver. The level of accuracy can vary from beam to shell models for the former [21] and from Doublet Lattice Method (DLM) [3] to Computational Fluid Dynamics (CFD) [80] algorithms for the latter (see [213] for a review on computational aeroelasticity).

In aeronautical industry most of the flutter analysis work relies on linear models, and among the most established algorithms there can be listed:  $p$  method [111],  $k$  method [63],  $p-k$  method [102], and  $g$  method [46]. The common goal is to solve a parametric eigenvalue problem that yields the flight speed  $V_f$  and frequency  $\omega_f$  at which flutter occurs. These methods are efficiently implemented in aeroelastic solvers such as Nastran [203] and ZAEROS [270]. The  $p$  method solves the problem in the Laplace transform domain (or equivalently in the state-space form). However, the Generalised Aerodynamic Force (GAF) matrix is typically provided for flutter analysis purposes at discrete frequencies (e.g. by the panel method solver DLM) and thus Rational function approximation (RFA) techniques are employed. These techniques, which include the Roger [204] and the Minimum State [134] methods, allow the frequency-domain GAF to be transformed into state-space models, particularly suited for aeroservoelastic applications.

Aeroservoelasticity studies the interplay of aeroelastic and control design aspects, see the dedicate survey papers [153, 176, 177] and examples of applications in [57, 175]. The other listed flutter methods solve instead the problem directly in the frequency-domain, and thus do not require approximations of the aerodynamic operator.

In aircraft design, the modelling and analysis of the dynamics of a vehicle are generally addressed, at least for preliminary evaluations, considering the rigid-body and elastic dynamics separately, on account of a wide frequency separation between the two sets of natural modes. As a result, preliminary flutter predictions are based on restrained body models (e.g. cantilever wing), which assume the occurrence of dynamic instabilities in a lifting surface as unrelated to the rigid-body motion of the vehicle where it is mounted. However, this hypothesis is being questioned by the increased trend towards an optimal structural sizing and lightweight material selection, as well as by the conception of aircraft geometric layouts with low static stability (or statically unstable) but compensated with full-authority control systems. The increasing coupling between the rigid and flexible dynamics thus compels consideration of a model retaining both aeroelastic and flight mechanics physical effects [212]. Among the first studies on the interaction between aircraft motion and structural flexibility, the work presented in [253], which focused on high-speed forward swept wing aircraft, is foundational. The observed detrimental coupling between the rigid-body and the elastic dynamics of the vehicle, termed Body Freedom Flutter (BFF), was exemplified by means of a simple low-order model and a wealth of references where a similar problem had been investigated was provided. Recent studies [40, 154] have confirmed, using more sophisticated models, that structural sizing aimed at achieving very light weight structures, and thus a significant degree of flexibility, could lead to multiple flutter mechanisms. Design features which are responsible for amplifying the interaction between rigid and elastic dynamics have also been investigated in references [25, 190].

Despite the large amount of effort spent in understanding and modelling flutter, two important factors make it still a very challenging phenomenon to comprehend for the designer. On the one hand, the sensitivity of flutter to perturbations in parameter and modelling assumptions [192] represent a critical limitation of the established techniques. Due to the consequent risk of overestimating the stability margins of the system, this is currently compensated by the addition of conservative safety margins to the analysis results followed by expensive flutter test campaigns. On the other hand, the increase in the aircraft structure flexibility and the demand for a more realistic description of the system compel to consider cases where the linear hypothesis no longer holds [74]. In fact, the presence of nonlinearities might not only alter the predictions obtained with linear models, but also determine inherently nonlinear phenomena. Examples of these are the existence of limited amplitude flutter responses before the linear flutter speed and local (instead of global) stability of the equilibrium configuration.

While existing techniques have been applied to tackle individually these two issues (see the two references above [74, 192] and [59], where an industry oriented review on nonlinear

methods for aircraft applications is discussed), there is interest in the aerospace community for methodologies able to handle uncertainties and nonlinearities in a unified framework. This motivates a deeper research in the available techniques from the robust control theory community which has developed in the last decades different approaches to tackle these problems.

### 2.1.2 Robust control theory

The birth of modern robust control dates back to the late 70s, which saw the confluence of interest in uncertainty and multivariable systems [73, 208]. The common feature of the approaches developed within this field is to represent the system as the feedback interconnection of a nominal (usually, but not necessarily, Linear Time-Invariant (LTI)) system (or plant)  $G$  with an unknown operator, typically denoted by  $\Delta$  (Fig. 2.2). When the latter is set to zero, this setting is equivalent to the standard representation in classic control of a fixed *nominal* system with transfer matrix  $G$ . In general,  $\Delta$  may include uncertain linear dynamics systems, linear-time-varying parameters, complex systems and even nonlinearities. The underlying idea is to decouple the known (linear) and unknown (uncertain and/or nonlinear) parts, and formulate conditions for stability or performance objectives with respect to  $G$  only. This feedback representation is usually referred to as Linear Fractional Transformation (LFT), originally studied in [200] and representing a cornerstone modelling paradigm for modern robust control. Its prowess in addressing the modelling of complex aerospace uncertain systems has been demonstrated in the last decades providing: models for the analysis of the flight control system for the X-38 crew return vehicle [222]; Linear Parameter-Varying models for the Boeing 747 [158]; and reduced order models for flexible aircraft [197]. In this study the LFR toolbox [156], which implements efficient algorithms for the manipulation of LFT objects, will be employed.

Given this setting, robust control generalised results from classic control to the multivariable case. This was, for example, the case of  $\mathcal{H}_\infty$  control [76], which extended loop shape synthesis, and of structured singular value (or  $\mu$ ) [75], which provided a stability and performance robustness indicator by extending the concept of singular value. An overview of contributions of robust control relating to this work are discussed next.

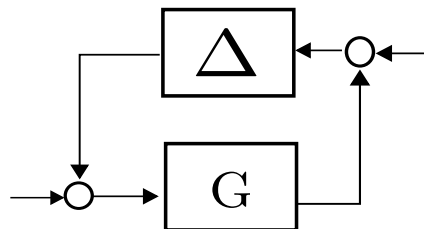


Figure 2.2: Standard feedback configuration in robust control.

### 2.1.2.1 Multipliers theory

The concept of *multiplier* plays an important role in robust control and allows the stability problem of the interconnection  $G-\Delta$  to be studied [264–266]. In fact, known results such as the structured singular value [75] and Popov criterion [195] can be derived from this framework by specializing the nature of  $\Delta$  (a structured uncertainty set in the former case and a sector bounded nonlinearity in the latter). The multiplier is a fictitious system which is introduced in the feedback loop with its inverse, and can thus be thought of as a loop transformation. The reasoning behind this is that the study of the interconnection  $G-\Delta$  is formulated via conditions on the known part  $G$  of the loop only. The idea is that, by introducing multipliers in the loop, these conditions are relaxed compared to the original  $G-\Delta$  setup, and thus less conservative results can be generally obtained. The distinctive feature of the multiplier approach is to associate a class of uncertain operators  $\mathcal{D}$  (e.g. sector nonlinearities) with the corresponding class of multipliers  $\mathcal{M}$ , based on some properties of  $\mathcal{D}$ . Then stability is guaranteed for *any* uncertainty belonging to  $\mathcal{D}$ . The *rule* by which the classes  $\mathcal{M}$  and  $\mathcal{D}$  are associated depends on the theory used in conjunction with the multiplier approach. For example, in passivity [64] the class of positive nonlinearities  $\Phi \in \mathcal{D}$  is considered [137]. Then, the search is on multipliers  $M \in \mathcal{M}$  such that  $M^* \Phi$  is also positive. In passivity the use of multipliers can be qualitatively interpreted as the exchange of a positive and negative amount of passivity between the two paths of the feedback loop.

Another example is represented by the Integral Quadratic Constraints (IQC) theory [170], which build on the original work [259]. IQC allows a broad spectrum of problems concerned with robustness of uncertain nonlinear systems to be described within a unifying framework. Even though similar conditions to passivity are derived to solve the problem when using IQC, technical differences in the properties required for the multipliers (e.g. causality) hold [39]. The rule in IQC is to characterise the operator  $\Delta$  by means of frequency-domain multipliers  $\Pi$  which satisfy integral quadratic constraints on the Fourier transforms of its input and output. A library of multipliers exists for various types of operators as summarised in [251], and the original IQC theorem [170] involves frequency-domain inequalities to test stability. However, in order to allow the search for stability certificates to be recast into a Linear Matrix Inequalities (LMI) problem [34, 210], state-space factorisations  $(\Psi, M)$  of  $\Pi$  are typically employed and a fundamental result known as Kalman-Popov-Yakubovich (KYP) Lemma [260] is exploited. These factorisations allow to translate the standard frequency-domain constraints into time-domain ones, and thus open up the possibility of interpreting IQC from a time-domain perspective [211, 215].

The versatility of the framework, and its numerical formulation as an LMI favouring the adoption of efficient convex Semidefinite Program (SDP) solvers [173], motivates the interest on IQC from an application perspective. Indeed, IQC have been recently applied in the aerospace community to study: stability of nonlinear uncertain aeroelastic systems [61]; worst-case performance of saturated aeroelastic systems [140]; performance of re-entry vehicles [163].

**Structured singular value or  $\mu$** 

One of the main contribution of the family of approaches belonging to multipliers theory is the structured singular value or  $\mu$  analysis. While there is consensus on the fact that  $\mu$  was first proposed in [75], robustness tests based on singular values and diagonal scalings were investigated in those exciting years also in [196, 209]. An important pre-existing result is the small gain theorem [264], which gives conditions for the stability of the interconnection  $G-\Delta$  in terms of an inequality constraint involving the  $\mathcal{H}_\infty$  norms of  $G$  and  $\Delta$ , where  $\Delta$  is an unstructured uncertainty set. This result served as starting point for the development of advanced analysis techniques that exploit further properties of  $\Delta$ . Specifically, in  $\mu$  analysis  $\Delta$  is a structured uncertainty set made up of constant real and complex parameters as well as unmodelled dynamics (full blocks). The problem is formulated as the search for the smallest perturbation matrix belonging to  $\Delta$  such that the feedback  $G-\Delta$  loses stability, or, equivalently, the associated LFT becomes singular. By using a result known as Main Loop theorem [269], performance of the closed loop can also be studied within this setting. A known issue with  $\mu$  is that its computation is NP (nondeterministic polynomial time)-hard with either pure real or mixed real-complex uncertainties [35], thus all  $\mu$  algorithms work by searching for upper and lower bounds. The difficulty in calculating accurate bounds is mainly related to the size of the  $\Delta$  matrix and whether it is complex, real or mixed [81]. An overview of the computational aspects is given next.

Lower bound algorithms, which also provide the perturbation matrix capable of violating stability (or performance) of the system, can be categorised based on the type of uncertainty set. For pure complex problem, the standard power iteration [180], derived from the well known algorithm to find the largest eigenvalue and associated eigenvector of a matrix, has proved to be accurate and fast. Extensions to the mixed real/complex problem have also been proposed [262], but they may not provide accurate results, especially in the case of purely real uncertainties. Lower bounds for the latter have proven to be challenging both from accuracy (real  $\mu$  can be a discontinuous function of the problem data [183]) and run time perspective (many available algorithms have a computational cost that grows exponentially with the problem size [54]). Sometimes this is overcome by artificially introducing a small amount of complex uncertainty to some of the uncertain real parameters [183] in order to regularise the problem and use the power iteration efficiently, but inaccuracies may arise if a large magnitude of fictitious complexity is needed to achieve convergence. In the last decade improvements have been achieved with different approaches: gain-based algorithm [219]; pole migration techniques [132]; direct optimisation-based techniques [103, 261]. A comprehensive review on  $\mu$  lower bounds can be found in [206].

The computation of the upper bound is typically more reliable. The standard upper bound from complex  $\mu$  theory consists of finding scaling matrices  $D$  (named  $D$  scalings in the literature) which minimise the maximal singular value of a given matrix [180]. This problem is convex and can be solved in different efficient ways, but it does not distinguish between real and complex

parameters (i.e. they are treated in the same way), thus the outcome is often poor for mixed or real  $\mu$  problems. An established algorithm to overcome this issue is based on the search of scaling matrices  $D$  and  $G$  (named  $D$ - $G$  scalings) satisfying the minimisation of a maximal singular value [78]. This formulation loses convexity, but keeps favourable features: minimizing the norm of a given matrix generally offers numerical advantages; the  $D$  scalings enter the problem as in the standard complex upper bound; the  $G$  scalings enter in a symmetric balanced fashion (from which derives the name of the algorithm as Balanced form). An alternative is to recast the computation as the minimisation of a maximal generalised eigenvalue [263]. The advantage of this alternative approach is that, since  $D$  and  $G$  enter linearly, it can be solved as a LMI and thus it retains convexity, at the cost of a higher run time. The results presented in this thesis use the algorithms as implemented in the Robust Control Toolbox (RCT) in MATLAB R2015b [14], which includes all the algorithms reviewed in this section.

In the last two decades,  $\mu$ -analysis has been used in aeroelasticity to quantify the sensitivity of flutter to modelling uncertainties. The so-called robust flutter analysis aims to quantify the gap between the prediction of the nominal stability analysis (model without uncertainties) and the worst-case scenario when the whole set of uncertainty is contemplated. Cornerstone works are [150] and [33], based on which applications to realistic aircraft configurations have successfully been proposed. In [148], F/A-18 SRA aircraft robust flutter margins, with the uncertainty set informed by extensive flight data, were computed. The outcome indicated that the envelope was safe from aeroelastic instabilities, although the margins laid distinctly closer to the flight envelope than previously estimated by classic (nominal) techniques. The capability of  $\mu$  to predict behaviours exhibited in flight was showcased in [22], where aeroelastic instabilities of F-16A/B in heavy store configuration were investigated. In particular, nonlinear responses measured in flight-test runs were predicted numerically considering parameter-dependent  $\mu$  analyses with variable mass, stiffness, damping, and Mach. In [175] an example of application to aeroservoelastic design of an uncertain fighter aircraft with the aim to achieve robust stability and robust closed-loop performance requirements was proposed.

### 2.1.2.2 Dissipativity

The notion of dissipativity [254] is paramount in systems theory and formalises the intuitive idea that at any time the amount of energy that a stable system can supply to its environment can not be greater than what has been absorbed. That is, a fraction of the exchanged energy will be dissipated by the system. In the theory of dissipative systems the *storage* and *supply rate* scalar functions are introduced. The former depends only on the states and represents an energy function of the system, while the latter depends on the inputs and outputs and represents the rate at which energy is absorbed by the system. A system is said dissipative if the rate of change of the storage function along any trajectory of the system will never exceed the supply rate for any input. The dissipativity property can be expressed as a time-domain integral

constraint or, equivalently, as a differential (dissipation) inequality. The search for quadratic storage functions is particularly attractive because it can be performed, in the case of (given) quadratic supply rates, by solving an LMI [210]. An interesting feature of dissipativity is that it generalises and allows to reinterpret important properties of linear and nonlinear systems in a more general context by defining appropriate supply rates. This is for example the case of Lyapunov stability, where the storage function satisfying the dissipation inequality is a possible Lyapunov Functions (LF). The connection with Lyapunov function methods is important since the latter have several applications in the study of nonlinear systems. Other notions that can be retrieved from dissipativity are passivity (positive real lemma) and performance objectives classically used in  $\mathcal{H}_\infty$  and Linear Parameter-Varying problems (bounded real lemma).

Despite their prime significance in robust control, the reconciliation between Integral Quadratic Constraints and dissipation theory was not fully explored until recently. They feature indeed important differences such as the formulation of the problem in frequency-domain for the former and time-domain for the latter, and the use of distinct artificial operators (respectively, multipliers and storage/supply functions). The crucial common ground is that in both cases the problem is recast for computational purposes as the solution of a *similar* LMI (via the KYP lemma). However, two important issues arise: first, the dissipation inequality framework requires a positive definite storage function, which translates into an additional constraint (positive semi-definiteness of a matrix, e.g.  $P \succeq 0$ ) not required by the IQC formulation; second, the state-space factorisation of the IQC multipliers holds in general only for infinite-horizon time integrals (soft IQCs), whereas the dissipativity framework requires finite-horizon time integrals (hard IQCs). These aspects were dealt with for the first time in full generality in [215], where a particular factorisation for the multiplier, named  $J$ -spectral, was proposed to address the aforementioned issues and by doing so guarantee the equivalence. However, it is not always possible or practical to compute a  $J$ -spectral factorisation, hence in [82, 193, 216] finite horizon bounds for hard IQCs were presented. This enables the use of IQC-based descriptions of nonlinear uncertain operators in the dissipativity framework. The link between dissipativity and IQC has been recently formalised also in [211] by virtue of a novel (time-domain) IQC theorem.

The possibility to use multiplier approaches to study problems inherently formulated within a dissipative setting has great potential. The former indeed is well suited to reduce the conservatism of the analyses (in IQC this is exemplified by the possibility to enrich the description of  $\Delta$  by considering several multipliers  $\Pi$ ), while the latter allows to formulate a larger variety of problems (e.g. inclusion of constraints for regional, or local, analysis). This is demonstrated by previous works that have tried to bridge these two frameworks by focusing on specific problems: region of attraction of saturated systems based on Integral Quadratic Separation (a concept closely related to IQC) [191]; local performance analysis of saturated nonlinear systems with hard IQCs [44]; robust performance for the case of structured LTI uncertainties [13].

### Region of Attraction

An important example of analysis that can greatly benefit from the aforementioned reconciliation is the study of the Region of attraction (ROA) for locally stable equilibria. While stability for linear systems ensures convergence to the equilibrium regardless of the initial condition, for nonlinear systems this property holds only locally and thus its knowledge is of practical interest to guarantee their safe operation. Finding analytically the exact region of attraction might be difficult or, depending on the complexity of the system, even impossible [88]. Several algorithms have thus been proposed to numerically calculate inner Estimates of the ROA (ERA), which can be broadly classified into two categories: Lyapunov methods and non-Lyapunov methods. The former build on the invariance and contractiveness properties held by Lyapunov functions level sets [137]. When the LF space is restricted to quadratic functions, an ERA for polynomial (or even rational) systems is the largest ellipsoid obtained by computing the Lyapunov matrix [247], whose calculation can be posed as a line search involving the solution of a series of LMIs. In the general case of higher order LF, Sum of Squares (SOS) optimisation is typically employed [7]. SOS are a well established technique concerned with the problem of finding a sum of squares decomposition for a polynomial (hence guaranteeing that this is positive) possibly subject to semialgebraic set constraints and objective functions. Their appeal derive from the connection with convex optimisation [187], which allows their computation to be fully automated. This is implemented in dedicated toolboxes [15, 185], which provide an helpful interface between the user and SDP solvers [229] and by doing so has fostered the use of this optimisation technique in various applications [48, 50, 107]. The inner estimation of ROA typically consists of enforcing set containment conditions, which result in bilinear terms that can not be handled by the aforementioned solvers. The ensuing non-convex optimisation problem can be handled with bilinear matrix inequalities solvers [142], as shown by the authors in [233]. The most common approach, however, consists of alternatively fixing one set of parameters and optimizing the other with convex programs. An example is the work in [43], which analysed the complex nonlinear behaviour of an aircraft fighter. Another approximate method to solve bilinear matrix inequalities is the path-following approach presented in [101].

Non-Lyapunov methods have also been studied to reduce the conservatism typically associated with the characterisation of ROA as contractive level sets. In [108] it is shown that the problem can be theoretically formulated as an infinite-dimensional linear program, which is solved with a hierarchy of convex finite-dimensional LMIs with asymptotically vanishing conservatism by making use of the concept of occupation measures. In recently published works [100, 246], the recipes for calculating ERA are expressed in terms of positively invariant sets. These approaches, prompted by LaSalle's theorem [137], still use Lyapunov stability concepts but relax the conditions that must be fulfilled by the function used to define the ERA.

All the approaches above share the common feature that are either only applicable to polynomial vector fields or rely on SOS techniques. As a result, a limitation holds on the types of

nonlinearities that can be considered. An example of a more general approach is the so-called Zubov's method [271], which is based on a converse Lyapunov theorem and requires to solve a partial differential equation, but this makes it difficult to be employed for practical cases. Relaxed versions of this result have also been proposed, for example in [248] where the concept of maximal Lyapunov function was introduced.

The case when the system is subject to uncertainties has received far less attention, with most of the research carried out within the Lyapunov method class of approaches. A first important distinction concerns the dependence of the sought LF on the uncertain parameters. In [241] an algorithm restricted to systems with a specific (i.e. affine) dependence on the uncertainties is proposed, based on parameter-independent LF. That is, a single Lyapunov function is used to certify the local stability of a system over its entire parameter uncertainty set. In [243] improvements based on a branch-and-bound algorithm were discussed to alleviate the conservatism associated with the parameter-independent LF. Other studies considered parameter-dependent LFs [49, 233], with the ensuing SOS-based optimisation problem featuring a substantial increase in computational burden. Recent works [194, 245] addressed this problem by computing rational Lyapunov functions of the states and uncertain parameters without recurring to SOS relaxations. In [245] Finsler's Lemma and the notion of annihilators are employed to formulate affine parameter dependent LMIs conditions for systems with rational vector fields. A further improvement of this algorithm is proposed in [194] where a method based on Linear Fractional Transformations is developed to inform the selection of the rational terms and thus allowing a more efficient computation of the LF.

A major drawback of the approaches employed to deal with uncertain systems is that in general they do not exploit specific properties of the uncertainties (e.g. linear time-invariant, real constant, time-varying), hence they inherently provide conservative outcomes because the results must hold for a larger set of uncertainties than the one actually affecting the system. This is one of the aspects where the combined use of techniques from the robust control theory could be invaluable.

### 2.1.3 Dynamical systems approaches

A well established framework to study nonlinear systems depending on parameters is represented by bifurcation theory. The term bifurcation was originally introduced by Poincaré to describe branching of equilibria in a family of differential equations, and is used to denote *qualitative changes* (e.g. loss of stability, onset of new branches) of the steady-state solutions (e.g. fixed points, periodic orbits) when one or more parameters on which the dynamics depend are varied [99, 145]. The advantage of this approach is that complex nonlinear behaviours can be characterised, tracked and quantitatively assessed without the need for exhaustive numerical integration. The latter does not only feature a clear computational burden, but offers poor guarantees of capturing all the possible responses due to the sensitivity to initial conditions, and does not provide a comprehensive picture of the response. The main computational tool of bifurcation

theory is numerical continuation, providing path-following algorithms allowing implicitly defined manifolds to be computed as one or more continuation parameters are varied [27, 96]. Examples of these algorithms are Newton-Raphson, arclength, and pseudo-arclength continuation, efficiently implemented in freely available software, e.g., AUTO [72] and COCO [56].

Due to these appealing features, bifurcation has been extensively applied in nonlinear aeroelasticity, as discussed in the dedicated monograph [69]. Note that bifurcation theory can also cope with non-smooth vector fields [66], which is an advantageous feature considering that many nonlinearities in this field are discontinuous (e.g. saturation, friction). See for example the work in [68] where a method to analyse the effect of freeplay was proposed. From a dynamical systems perspective, the flutter point coincides with a Hopf bifurcation, which arises when branches of fixed points and periodic solutions meet. Analogously to the case of linear flutter, the analysis is typically carried out starting from a stable equilibrium point at low speeds and increasing the speed (used as continuation parameter) until the flutter boundary is found. At this speed, denoted by  $V_H$ , two scenarios can take place [69]. If the Hopf bifurcation is supercritical, than for  $V > V_H$  a stable Limit Cycle Oscillation (LCO) exists. Limit cycles, broadly defined as initial condition-independent isolated periodic orbits which occur in unforced systems, can be tracked by applying continuation. This reveals important properties of the LCO such as amplitude, period and stability. When the bifurcation is supercritical, the phenomenon is reversible and by reducing the speed below  $V_H$  the stable branch of equilibria is recovered (benign LCO). Vice versa, if the bifurcation is subcritical, for  $V < V_H$  an unstable LCO exists which typically undergoes a periodic fold bifurcation and thus transitions to a stable one featured by higher amplitudes. This is a far more dangerous scenario since the system will suddenly jump to this LCO branch for  $V$  slightly larger than  $V_H$ , and the absence of oscillations cannot be recovered by simply decreasing  $V$ , because of hysteresis. Moreover, for a range of subcritical speeds multiple stable steady-solutions exist and thus the branch of equilibria associated with the operational envelope of the aircraft is only locally stable.

### **Limit Cycle Oscillations**

The complex behaviour associated with the onset of Limit Cycle Oscillations have been observed numerically [147, 189] and confirmed experimentally [235] in aeroelastic systems. Therefore, effort has been put to gain a better understanding, especially with regard to the effect of design parameters on the criticality of the Hopf bifurcation and the features of the emanating LCO. It is indeed deemed important to take into considerations these aspects from the preliminary design stage. The two most common approaches are represented by [59]: (i) numerical continuation for detection of onset of Hopf bifurcations and tracking of periodic solutions (e.g. revealing changes in period and amplitude with the bifurcation parameter); and (ii) time-integration simulations. Alternative approaches have also been developed. The *direct* method exploits the results of bifurcation analysis and provides estimates of LCO onset, amplitude and period at a computational cost amenable to real aircraft applications [228]. The

idea is to solve a nonlinear set of algebraic equations derived from the Hopf bifurcation conditions to detect the flutter onset, and then a nonlinear perturbation analysis around this point is performed to estimate properties of the LCO. The latter step can be performed in different ways, e.g. method of multiple scales [23], centre manifold theory [255]. The advantage of these methods is that they reduce the problem to a two-degree-of-freedom system capturing the dynamics of the critical mode shape only, but neglects higher order nonlinear terms and thus the accuracy tends to deteriorate far from the flutter point in the presence of strong nonlinearities. Frequency-domain methods, of which the harmonic balance is the most established [143], are established, too. In the harmonic balance method, the response of the nonlinear system is approximated as a Fourier series featuring  $n$  components (where  $n$  is the order of the method), and then the coefficients of the expansions are balanced. This leads to a set of nonlinear algebraic equations which has also the fundamental frequency as unknown. Even though in a few cases it has been found that a large number of harmonics were needed to correctly describe the LCO [151], often the oscillations in the system have a dominant frequency and hence it suffices to retain only the first harmonic in the expansion. A particular instance of first-order harmonic balance method is the Describing Functions (DF) approach [87], which is a quasi-linearisation technique providing an equivalent definition of frequency response for nonlinear systems. The equivalence is established by fixing the form of the response of the system and then minimizing the mean squared error between approximation and true output [26]. If the assumed form is a sinusoid (with unknown amplitude and frequency), the first-order harmonic balance method is retrieved with the additional advantage of having libraries of frequency response functions for different nonlinearities. The DF method has been applied to nonlinear aeroelastic problems [234] and its effectiveness supported by experimental validations of the results [52]. DF was also used to analyse and inform redesign strategies to tackle large LCO responses of the Tornado aircraft provoked by actuator rate limits [83].

The effect of uncertainties on LCO, as it was the case for ROA, has not received as much attention. Most of the works have focused on the application of stochastic methods, of which [24] presents a detailed review. A particular class of these, namely polynomial chaos expansion methods, is used in [90] to calculate the sensitivity of the flutter speed to variations in the linear and nonlinear coefficients of stiffness parameters of a rigid aerofoil. The method however fails to accurately predict the post-critical behaviour and the effect on the type of Hopf bifurcation. In the same work a strategy based on normal form [178] is also proposed, but its application to the uncertainty case is not fully explored and only qualitative inferences are derived. In [240] instead it is shown by means of a parametric study based on the harmonic-balance approach that uncertainties in the natural frequencies and aerodynamic parameters have an important effect on the LCO amplitude. In [16] the idea of using the DF method in conjunction with  $\mu$  analysis to study LCO of an uncertain aeroelastic system was discussed. This work built on [136], where the combination of  $\mu$  and DF was originally presented, and [81], where this idea was furthered.

### Robustness of bifurcations

It can be noted from the previous discussion that the most common approaches to study robustness of the LCO do not frame the problem into the setting of bifurcation theory, unlike the methods reviewed for the nominal case. In fact, bifurcation inherently studies the effect on the response of changes in the system's parameters. However, the *continuation* (or bifurcation) *parameters* are usually equal in number to the codimension of the studied bifurcation, defined as the smallest number of independent parameters required for its occurrence. Since the Hopf bifurcation is of codimension-1, analyses aimed to detect its occurrence in a branch of equilibria (and thus the onset of LCO) make use of one parameter. If a larger number of parameters is investigated, this is typically handled by continuing one parameter at a time, while keeping the others fixed. In other words, bifurcation allows to characterise the effect of distinct parameters (usually known *a priori* to be relevant for the studied dynamics, e.g. speed in flutter analysis), but is not particularly suited to assess robustness in the face of *uncertain parameters*, which generally are not restricted in number, may vary simultaneously and have an influence on the dynamics not known *a priori*. The study of robustness within a dynamical systems perspective can be attempted by adopting singularity theory techniques (e.g. Lyapunov-Schmidt reduction) [94], as shown by recently published research [51, 97]. The central idea is to perform a reduction of the original dynamics to a lower dimension map, whose singularities represent transitions between qualitatively different bifurcation diagrams. Even though it is theoretically possible to track these singularities without computing explicitly the reduction [51], application of these techniques to systems with a moderately complex mathematical description and with generic number of uncertainties is not straightforward and has not been presented in the literature yet. Moreover, this approach does not directly provide information on the distance from a given (nominally stable) operating point to the closest bifurcation, that is, it does not provide a margin to bifurcation. Previous works have attempted to tackle this aspect. In [71] an extension to multidimensional parameter spaces of standard methods for codimension-1 bifurcations is proposed. The problem of determining locally closest bifurcations is solved by introducing a normal vector to hypersurfaces of bifurcation points, and makes use of both direct and iterative methods. While the latter is limited to static bifurcations (i.e., saddle node, transcritical, and pitchfork), the former is in principle applicable also to the Hopf case even if the work focuses mostly on static bifurcations. The direct method consists of solving the full set of equations defining the bifurcation (plus additional equations to close the problem which derives from conditions on the normal vector) and, as also pointed out by the authors, may be too onerous from a computational viewpoint. This approach was applied in [166] to the analysis of static bifurcations in flexible satellites, making a number of simplifying assumptions, e.g., no dependence of the equilibrium on the uncertainties, system with Hamiltonian dynamics. A closely related approach, which according to the authors generalises the method from [71], is discussed in [37]. The work considers saddle-node bifurcations only, and the computation of the smallest perturbation to bifurcation is done

by applying the generalised reduced-gradient method. In essence, this consists of a nonlinear optimisation strategy making use of corrector and predictor steps and solving the system of equations defining the bifurcation. However, the issue of local minima is not addressed and the same objection regarding the total dimension of the problem is envisaged for the Hopf bifurcation case (not discussed in the work). The idea of using normal vectors to manifold of bifurcation points is also present in [89] and other works from the same group [174], where the design of robustly stable and feasible (chemical) processes is pursued.

## 2.2 Fundamental aeroelastic models

In the previous section, a state-of-the-art review was presented for the different topics that will be covered in this thesis. Now, a cursory presentation of the fundamental aeroelastic models is given as they underline the physical systems that will be studied.

The basic representation of a fluid-structure interaction problem describing the coupling between structural deformation and aerodynamic forces in the Laplace domain is:

$$[s^2 \bar{M}_s + s \bar{C}_s + \bar{K}_s - q_\infty Q_{hh}(s)] \eta = 0, \quad (2.1)$$

where  $q_\infty = \frac{1}{2} \rho_\infty V^2$  is the dynamic pressure,  $\rho_\infty$  is the air density,  $V$  is the speed, and  $s$  is the Laplace variable.  $\bar{M}_s, \bar{C}_s, \bar{K}_s \in \mathbb{R}^{n_s \times n_s}$  represent respectively the generalised structural mass, damping and stiffness matrices,  $Q_{hh} \in \mathbb{C}^{n_s \times n_s}$  is the generalised aerodynamic force (GAF) coefficient matrix, and  $\eta \in \mathbb{R}^{n_s}$  is the generalised coordinates vector. The system exhibits self-sustained oscillations when (2.1) has a solution  $s = i\omega$  for non-trivial  $\eta$ , with  $\omega$  denoting the frequency. In general, the objective of flutter analysis is the determination of the smallest speed such that this occurs, i.e. the flutter speed  $V_f$ . By introducing a reference length  $L_r$ , it is customary in aeroelasticity to work with the dimensionless counterparts of  $s$  and  $\omega$ , respectively  $\bar{s} = \frac{s L_r}{V}$  and  $k = \frac{\omega L_r}{V}$  (also named reduced frequency).

The generalised structural matrices are usually obtained with the modal decomposition approach from their *physical* counterparts  $M_s, C_s, K_s \in \mathbb{R}^{N_s \times N_s}$ , with  $N_s$  indicating the number of structural degrees of freedom:

$$\begin{aligned} \bar{M}_s &= \Phi^T M_s \Phi, \\ \bar{C}_s &= \Phi^T C_s \Phi, \\ \bar{K}_s &= \Phi^T K_s \Phi, \end{aligned} \quad (2.2)$$

where  $\Phi \in \mathbb{R}^{N_s \times n_s}$  is the matrix of  $n_s$  normal modes. This matrix is obtained from the solution of the classic eigenvalue-eigenvector free vibration problem of the structure and thus depends on  $M_s$  and  $K_s$ . For flutter analysis purposes, it typically holds  $n_s \approx 20 \ll N_s$  [202].

The physical matrices  $M_s, C_s, K_s$  are available analytically for simple systems (examples will be given in Sec. 2.3.1), but for most systems the state-of-practice is to derive them via Finite Element Method (FEM) [21], as will be commented on in Sec. 2.3.3.1.

The aerodynamic forces are typically obtained for flutter analysis purposes with panel method solvers (e.g. based on the Double Lattice Method) [3]. Given a reduced frequency  $k$  and a set of  $n_s$  normal modes, the DLM provides the GAF matrix  $Q_{hh}(ik)$  gathering the transfer functions from generalised displacements  $\eta$  to generalised aerodynamic forces.  $Q_{hh}$  does not have an analytical dependence on  $k$  (this is an effect of the unsteady part of the aerodynamic loads) and is only available at discrete values. Further details on the DLM will be provided in Sec. 2.3.3.2.

To set up a state-space formulation of (2.1), which is generally required for aeroservoelastic applications, an analytical dependency of  $Q_{hh}$  on the Laplace variable  $s$  is needed. Standard rational function approximation strategies propose a general two-part approximation model based on the distinction between quasi-steady and unsteady (or lag) contributions [202]:

$$Q_{hh}(ik) \approx \Gamma_{QS}(\bar{s}) + \Gamma_{lag}(\bar{s}). \quad (2.3)$$

Crucially,  $\Gamma_{lag}$  captures the memory effect of the wake, which results in a phase shift and magnitude change with respect to the instantaneous aerodynamic loads (given by  $\Gamma_{QS}$ ). This is also referred to as time lag effect.

In this thesis two of the most established algorithms are considered: the Roger [204] and the Minimum State [134] methods, which provide respectively the approximate operators  $Q_{Rg}$  and  $Q_{MS}$ . They propose an identical expression for  $\Gamma_{QS}$ :

$$\Gamma_{QS}(\bar{s}) = A_2\bar{s}^2 + A_1\bar{s} + A_0, \quad (2.4)$$

where  $A_2$ ,  $A_1$  and  $A_0$  are real coefficient matrices modelling respectively the acceleration, speed and displacement contributions to the instantaneous force.

Roger proposed the following expression for the unsteady part:

$$\Gamma_{lag-Rg}(\bar{s}) = \sum_{L=1}^{N_l} \frac{\bar{s}}{\bar{s} + \gamma_L} A_{L+2}, \quad (2.5)$$

where  $N_l$  is the number of lag terms. The partial fractions inside the summation are the so-called *lag terms* and represent high-pass filters with the lag roots  $\gamma_i$ , selected by the user, as cross-over frequencies. These are usually taken in the range  $[0.1, 1]$  which, due to the normalisation, is a valid choice irrespective of the particular system considered. The selection of the range can then be improved after a first flutter calculation by placing some of the lags around the reduced flutter frequency. The real coefficient matrices  $A_i$ , with  $i = 0, \dots, N_l + 2$ , are found using a linear least-square technique for a term-by-term fitting of the aerodynamic operator. The resulting state-space equation includes aerodynamic lag states  $x_a$  equal in number to  $N_l$  multiplied by the number of generalised coordinates, i.e.  $n_a = N_l n_s$ .

The Minimum State (MS) method tries to improve the efficiency with respect to Roger method in terms of number of augmented states per given accuracy of the approximation. There is no clear quantification of this advantage, but it has been stated [131] that the number of aerodynamic states required by MS is usually, in realistic aircraft application, 6-8 times smaller than with the

application of the Roger method for the same level of model accuracy. The proposed expression for the unsteady part is:

$$\Gamma_{lag-MS} = \bar{D} \begin{bmatrix} \frac{1}{\bar{s} + \gamma_1} & \dots & 0 \\ \vdots & \ddots & \vdots \\ 0 & \dots & \frac{1}{\bar{s} + \gamma_{N_l}} \end{bmatrix} \bar{E} \bar{s}. \quad (2.6)$$

The coefficients of the matrices  $\bar{D}$  and  $\bar{E}$  are iteratively determined through a nonlinear least square since (2.6) is bilinear in these two unknowns, while the matrices defining  $\Gamma_{QS}$  (see Eq. 2.4) are obtained imposing the constraint of matching the aerodynamic operator at  $k=0$  as well as at another reduced frequency (typically chosen in the range of expected reduced flutter frequencies). Note that the number of augmented states  $n_a$  is now equal to the number of roots, i.e.  $n_a = N_l$ .

Equations (2.5)-(2.6) show the difference in the expression of  $\Gamma_{lag}$  for these approximations, and in particular in the role played by the lag roots  $\gamma_i$ . In Roger method there is a one-to-one correspondence between the  $N_l$  gains of the high-pass filters (i.e. the coefficients of  $A_{L+2}$  for  $L = 1, \dots, N_l$ ) and their cross-over frequencies  $\gamma_L$ , whereas in the MS method there is a coupling between the various gains and roots as a consequence of the compact expression of  $\Gamma_{lag-MS}$ . The impact that the differences in the expression of  $\Gamma_{lag}$  have on uncertainty modelling and robust flutter analysis will be investigated respectively in Sec. 3.2.2 and Sec. 4.2.1.

Both RFA methods lead formally to the same shorthand state matrix:

$$\dot{x} = \begin{bmatrix} \dot{x}_s \\ \dot{x}_a \end{bmatrix} = \mathcal{A}x = \begin{bmatrix} \chi_{ss} & \chi_{sa} \\ \chi_{as} & \chi_{aa} \end{bmatrix} \begin{bmatrix} x_s \\ x_a \end{bmatrix}, \quad (2.7)$$

where the vector of system's states  $x = [x_s; x_a]$  is composed of the structural states  $x_s = [\eta; \dot{\eta}]$  and the aerodynamic lag states  $x_a$ . The state-matrix  $\mathcal{A}$  has been partitioned as:  $\chi_{ss}$  quasi-steady aeroelastic matrix,  $\chi_{sa}$  coupling term of lag terms on quasi-steady equilibrium,  $\chi_{as}$  coupling term of structural states on lag terms dynamics, and  $\chi_{aa}$  pure lag terms dynamics matrix. Their specific expressions depend on the RFA method adopted and are reported next for both methods:

$$\begin{aligned} \chi_{ss-Rg} = \chi_{ss-MS} &= \begin{bmatrix} 0 & I \\ -M^{-1}K & -M^{-1}C \end{bmatrix}, \\ \chi_{sa-Rg} &= \begin{bmatrix} 0 & \dots & 0 \\ q_\infty M^{-1}A_3 & \dots & q_\infty M^{-1}A_{N_l+2} \end{bmatrix}, \quad \chi_{sa-MS} = \begin{bmatrix} 0 \\ q_\infty M^{-1}\bar{D} \end{bmatrix}, \\ \chi_{as-Rg} &= \begin{bmatrix} 0 & I \end{bmatrix}, \quad \chi_{as-MS} = \begin{bmatrix} 0 & \bar{E} \end{bmatrix}, \\ \chi_{aa-Rg} &= \begin{bmatrix} -\frac{V}{L_r}\gamma_1 I_{n_s} & 0 & 0 \\ 0 & \ddots & 0 \\ 0 & 0 & -\frac{V}{L_r}\gamma_{N_l} I_{n_s} \end{bmatrix}, \quad \chi_{aa-MS} = \begin{bmatrix} -\frac{V}{L_r}\gamma_1 & 0 & 0 \\ 0 & \ddots & 0 \\ 0 & 0 & -\frac{V}{L_r}\gamma_{N_l} \end{bmatrix}, \end{aligned} \quad (2.8)$$

where  $M$ ,  $C$ , and  $K$  are respectively the aeroelastic inertial, damping, and stiffness matrices:

$$\begin{aligned} M &= \bar{M}_s - \frac{1}{2}\rho_\infty L_r^2 A_2, \\ C &= \bar{C}_s - \frac{1}{2}\rho_\infty L_r V A_1, \\ K &= \bar{K}_s - \frac{1}{2}\rho_\infty V^2 A_0. \end{aligned} \quad (2.9)$$

The difference in number of states between the two RFA methods can be appreciated from Eq. (2.8) by observing the two expressions for  $\chi_{aa}$ , which show that, for each lag term, the Roger method increases the size of  $\mathcal{A}$  of  $n_s$  states (number of generalised coordinates).

## 2.3 Physical systems

The previous section has provided a background on the essential aspects of generic aeroelastic models, while here this description is specialised to the physical systems considered throughout the thesis.

A good comprehension of the physical mechanisms underlying flutter, and of the role of the main parameters in prompting it, is deemed important in order to efficiently develop robust modelling and analysis techniques. For this reason, an incremental approach has been taken in this work and different aeroelastic systems, distinguished by an increasing level of sophistication but all featuring various degrees of similarities with state-of-practice models, will be considered and are listed in the following:

- Typical section (Section 2.3.1): rigid aerofoil with lumped springs and unsteady aerodynamics.
- Simplified aircraft (Section 2.3.2): aircraft model with the aim to investigate interaction between rigid-body and structural dynamics.
- Joined-wing aircraft configuration (Section 2.3.3): unconventional system layout described by a state-of-practice fluid-structure interaction solver.
- FLEXOP demonstrator (Section 2.3.4): family of reduced order LTI models obtained linearising the original high-fidelity model at different flight speeds.

Essential features are discussed below.

### 2.3.1 Typical section

The typical section model was introduced in the early stages of aeroelasticity to investigate phenomena such as flutter [30]. Its validity was assessed to quantitatively study the dynamics of an unswept wing when the properties are taken at a station 70-75% from the centreline.

Despite its simplicity, see Fig. 2.3, it captures essential aeroelastic effects in a simple model representation.

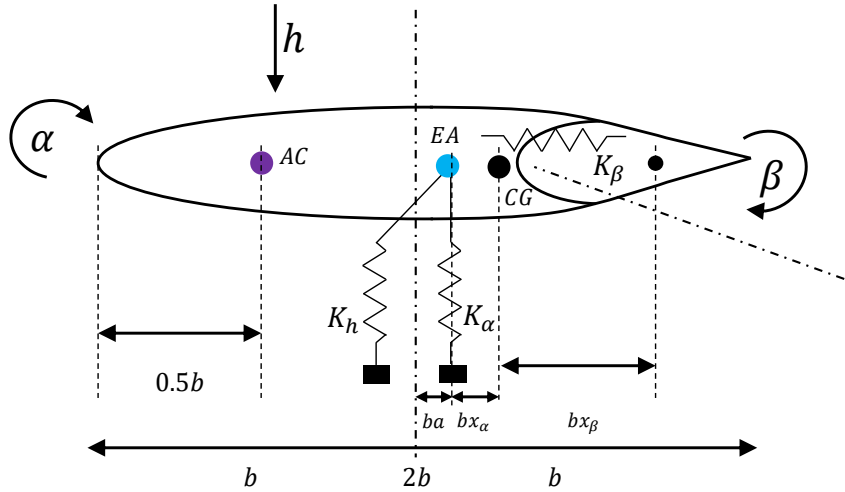


Figure 2.3: Typical section.

From the structural side, it basically consists of a rigid aerofoil with lumped springs simulating the 3 degrees of freedom (DOFs) of the section: plunge  $h$ , pitch  $\alpha$  and control surface rotation (or flap)  $\beta$  –there are simpler typical section modes that remove the latter DOF. The positions of the elastic axis (EA), centre of gravity (CG) and aerodynamic centre (AC) are also marked. The main parameters in the model are:  $K_h$ ,  $K_\alpha$  and  $K_\beta$  –respectively the bending, torsional and control surface stiffnesses; half chord distance  $b$  (used as reference length  $L_r$ ); dimensionless distances  $a$ ,  $c$  from the mid-chord to respectively the elastic axis and the hinge location, and  $x_\alpha$  and  $x_\beta$ , which are dimensionless distances from flexural axis to aerofoil centre of gravity and from hinge location to control surface centre of gravity ( $S_\alpha$  and  $S_\beta$  are the counterparts with dimension). The inertial characteristics of the system are given by: the wing mass per unit span  $m_w$ , the moment of inertia of the section about the elastic axis  $I_\alpha$ , and the moment of inertia of the control surface about the hinge  $I_\beta$ . If structural damping is considered, this can be expressed specifying the damping ratios for each DOF, which are then applied as modal damping (see Sec. 2.3.3.1 for more details).

Based on these parameters, the physical structural mass  $M_s$  and stiffness  $K_s$  matrices are defined as:

$$M_s = m_w b^2 \begin{bmatrix} 1 & x_\alpha & x_\beta \\ x_\alpha & r_\alpha^2 & r_\beta^2 + x_\beta(c-a) \\ x_\beta & r_\beta^2 + x_\beta(c-a) & r_\beta^2 \end{bmatrix}, \quad K_s = \begin{bmatrix} K_h & 0 & 0 \\ 0 & K_\alpha & 0 \\ 0 & 0 & K_\beta \end{bmatrix}, \quad (2.10)$$

where  $r_\alpha = \sqrt{\frac{I_\alpha}{m_w b^2}}$  and  $r_\beta = \sqrt{\frac{I_\beta}{m_w b^2}}$  are respectively the dimensionless radius of gyration of the section and of the control surface. Due to the low dimension of the problem, no modal decomposition is applied and (2.1) can be directly expressed in terms of physical coordinates (rather than generalised).

The adopted unsteady aerodynamic model is the one from Theodorsen [239], based on the assumption of a thin aerofoil moving with small harmonic oscillations in a potential and incompressible flow. The expression for the GAF  $Q_{hh}$  is:

$$Q_{hh} = \left( M_{nc} \bar{s}^2 + (B_{nc} + C(\bar{s}) R_1 \cdot S_2) \bar{s} + K_{nc} + C(\bar{s}) R_1 \cdot S_1 \right), \quad (2.11)$$

where  $M_{nc}, B_{nc}, K_{nc}, R_1, S_1$  and  $S_2$  are real coefficients matrices. The first three are respectively inertial, damping and stiffness noncirculatory terms while the others are damping and stiffness circulatory terms, all depending on the dimensionless distances  $a$  and  $c$ . See Appendix A.2.1 for the expression of all the operators in (2.11). The complex scalar  $C(\bar{s})$  is the Theodorsen function, originated by the ratio of modified Bessel functions of order 0 and 1, and thus an analytical dependence on  $\bar{s}$  is not available.

Note that  $Q_{hh}$  in (2.11) is the transfer matrix from the physical DOFs to the aerodynamic forces as shown next:

$$F_e = \begin{bmatrix} L_h \\ L_\alpha \\ L_\beta \end{bmatrix} = q_\infty Q_{hh} \begin{bmatrix} \frac{h}{b} \\ \alpha \\ \beta \end{bmatrix}, \quad (2.12)$$

where  $F_e$  is the vector of aerodynamic loads acting on the typical section's DOF caused by the elastic deformation. Due to the motion assumptions underlying Theodorsen theory, the expression in (2.11) has to be evaluated at  $\bar{s}=ik$ . Note that such a description of the aerodynamic forces is pertinent to analyse flutter, which is defined as a condition of neutral stability of the system, i.e. pure harmonic motion. This explains why this theory, despite being generalised to an arbitrary aerofoil motion in [214], has represented a paradigm for more improved models aimed at flutter analysis. For example the DLM always works in the framework of potential theory and harmonic motion of the body and provides an expression of the GAF at discrete frequencies, as it is the case in (2.11).

In view of the formal similarities with the template of generic aeroelastic model evaluated in Sec. 2.3, the typical section is deemed a valid starting point for investigations on modelling of uncertainties in the aeroelastic operators. Moreover, different sources of nonlinearities can be easily added and thus this system will be employed for both linear and nonlinear analyses throughout the thesis. Specifically, two different case studies from the literature will be considered:

- the linear case study from [134] will be used for the nominal and robust flutter analyses in Chapter 4; this will also form the basis for an augmented system including polynomial nonlinearities in the stiffness terms which will serve as an example for the robust bifurcation margins in Chapter 8;

- the case study from [234], featuring freeplay nonlinearity in the control surface degree of freedom, will be used for the nominal and robust LCO analyses in Chapter 6.

### 2.3.2 Simplified aircraft

The premise of the so-called restrained body models (e.g. cantilever wing) is the assumption that the occurrence of flutter in a lifting surface is unrelated to the rigid-body motion of the aircraft where it is mounted, but this hypothesis has been challenged by modern trends in aircraft design [25, 253].

With the aim to capture the basic features of the interaction of the wing flexibility with the motion of the aircraft, a modelling strategy to augment the typical section with rigid-body effects was developed during this research and is briefly presented here. This was published in [118, 125], and took reference [212], which provides a comprehensive study on the subject, as inspiration.

First, a simplified wing configuration (see Fig. 2.4) with mean aerodynamic chord  $\bar{c}$  (used as reference length  $L_r$ ) and span  $L$ , featuring large aspect ratio, small sweep angle and spanwise characteristics varying smoothly, is considered. Experimental studies (see [30] and references therein) have confirmed that the dynamics of such a wing can be described as an equivalent typical section by properly choosing structural and aerodynamic properties. The geometry and inertial characteristics used to define the structural mass matrix  $M_s$  in (2.10) are selected to match the corresponding properties of the wing at a span station about 70% distant from the aircraft centreline. A similar rationale is adopted for the aerodynamics, with the GAF matrix defined in (2.11) specialised to the geometry at the prescribed wing station. Note that the 2D flow assumption is in line with the aforementioned properties assumed for the wing (which allow 3D effects to be neglected).

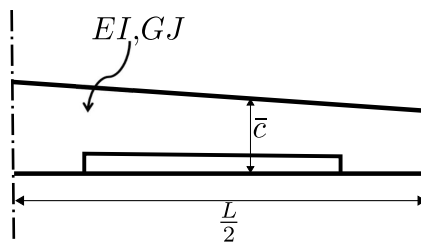


Figure 2.4: Straight wing.

As for the structural stiffness matrix  $K_s$ , an equivalence in terms of the first bending  $\omega_h$  and torsional  $\omega_a$  natural frequencies of a cantilever beam (at zero speed, i.e.  $V = 0$ ) is imposed. To this end, structural properties commonly used to characterise the wing elasticity, such as bending stiffness  $EI$  and torsional stiffness  $GJ$ , are introduced. Then, an equivalence [18] between the

typical section ( $K_h, K_\alpha$ ) and the wing stiffness parameters ( $EI, GJ$ ) is established:

$$\begin{aligned}\omega_h &= \left(0.597 \frac{2\pi}{L}\right)^2 \sqrt{\frac{EI}{m_w}} = \sqrt{\frac{K_h}{m_w}}, \\ \omega_\alpha &= \frac{\pi}{L} \sqrt{\frac{GJ}{I_\alpha}} = \sqrt{\frac{K_\alpha}{I_\alpha}}.\end{aligned}\quad (2.13)$$

The considered aircraft geometry is a conventional wing-fuselage-tail configuration, with new parameters introduced for the aircraft properties. Geometry parameters include the tail's leading-edge distance from the nose  $D$ , span  $L_t$  and mean chord  $c_t$  ( $S_t=L_t c_t$  is the resulting tail surface). The inertia quantities considered are: tail  $m_t$  and wing  $m_w$  mass ratios, payload mass  $m_p$ , total aircraft mass  $m$ , and the aircraft pitch moment of inertia  $I_{yy}$  (similarly composed of tail inertia  $I_{yy_t}$ , wing inertia  $I_{yy_w}$ , and payload inertia  $I_{yyp}$ ). A proposed simplification, commonly accepted for studies concerned with aeroelastic stability only [190], is to consider the fuselage and tail as rigid, which means that all the elasticity is assumed concentrated in the wing. Finally, aerodynamic properties such as wing and tail lift effectiveness coefficients  $C_{L_\alpha}^w$  and  $C_{L_\alpha}^t$  are also specified. The sketch of a notional aircraft is depicted in Fig. 2.5.

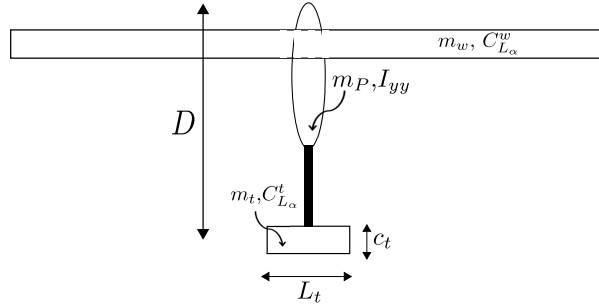


Figure 2.5: Simplified aircraft.

Only the longitudinal dynamics is retained for the aircraft motion, resulting in three additional states: the vehicle angle of attack  $\bar{\alpha}$ , the pitch angle  $\bar{\theta}$  and its pitch rate  $\bar{q}$ . This is the short period approximation, which for conventional aircraft involves rapid heave and pitch oscillations at almost constant translational speed. Surge velocity is neglected since, as discussed in [212], the phugoid mode does not typically experience coupling with the elastic modes of the wing. The shorthand description of the longitudinal dynamics for level flight is given in the frequency-domain by:

$$\begin{bmatrix} (mV - Z_{\dot{\alpha}}^r)s - Z_{\ddot{\alpha}}^r & -(Z_{\dot{q}}^r + mV) & 0 \\ -(M_{\dot{\alpha}}^r s + M_{\ddot{\alpha}}^r) & I_{yy}s - M_{\dot{q}}^r & 0 \\ 0 & 1 & -s \end{bmatrix} \begin{bmatrix} \bar{\alpha}(s) \\ \bar{q}(s) \\ \bar{\theta}(s) \end{bmatrix} = \begin{bmatrix} 0 \\ 0 \\ 0 \end{bmatrix}. \quad (2.14)$$

where the aerodynamic stability derivatives  $Z_{\dot{\alpha}}^r, Z_{\ddot{\alpha}}^r, Z_{\dot{q}}^r, M_{\dot{\alpha}}^r, M_{\ddot{\alpha}}^r, M_{\dot{q}}^r$  have been introduced (see Appendix A.2.2 for details). The characteristic equation associated with (2.14) is a third order

polynomial with one pole at the origin and the remaining second-order polynomial expressing the short-period approximation properties:

$$\begin{aligned} \omega_{SP}^2 &\approx \frac{M_{\bar{\alpha}}^r}{I_{yy}} \frac{Z_{\bar{\alpha}}^r}{mV - Z_{\bar{\alpha}}^r} - \frac{M_{\bar{\alpha}}^r}{I_{yy}} \frac{mV + Z_{\bar{\alpha}}^r}{mV - Z_{\bar{\alpha}}^r}, \\ 2\zeta_{SP}\omega_{SP} &\approx - \left( \frac{M_{\bar{\alpha}}^r}{I_{yy}} + \frac{Z_{\bar{\alpha}}^r}{mV - Z_{\bar{\alpha}}^r} + \frac{M_{\bar{\alpha}}^r}{I_{yy}} \frac{mV + Z_{\bar{\alpha}}^r}{mV - Z_{\bar{\alpha}}^r} \right). \end{aligned} \quad (2.15)$$

The evaluation of the aerodynamic stability derivatives is standard and can be performed (Appendix A.2.2) using a first-order approximation and the assumption of quasi-steady flow [212]. Important quantities that influence the flight mechanics properties are  $\bar{X}_{AC}^t$ ,  $\bar{X}_{AC}^w$ ,  $\bar{X}_{AC}$ , and  $\bar{X}_{CG}$ , the dimensionless distances from the aircraft nose to respectively the tail, wing, and aircraft aerodynamic centre and the aircraft centre of gravity.

The final task is to determine the coupling terms between elastic and rigid states. Crucial aspects to address are: how the wing deformation affects the aerodynamic forces generated by the vehicle, and how the motion of the vehicle contributes to change the loads acting on the structure. To this purpose, the expression of the local angle of attack is written as  $\alpha_{loc} = \alpha_0 + \alpha + \frac{h}{V}$ , where  $\alpha_0$  is the rigid-body angle of attack of the section, related through the twist to  $\bar{\alpha}$ . The dependence of the wing lift coefficient  $C_L^w$  on the wing deformation can be derived as follows:

$$\left\{ \begin{array}{l} C_L^w = C_{L_a}^w (\alpha_0 + \alpha + \frac{h}{V}) \\ C_L^w = C_L^{w,R} + C_L^{w,E} \end{array} \right. \Rightarrow \begin{array}{l} C_L^{w,R} = C_{L_a}^w \alpha_0, \\ C_L^{w,E} = C_{L_a}^w \left( \alpha + \frac{h}{V} \right), \end{array} \quad (2.16)$$

where  $C_{L_a}^w$  is the wing lift effectiveness,  $C_L^{w,R}$  is the rigid wing lift coefficient (accounted for in the aerodynamic derivatives, see Eq. A.4) and  $C_L^{w,E}$  its elastic counterpart. This leads to the definition of the aeroelastic stability derivatives  $Z_{\alpha}^r$  and  $Z_{\bar{\alpha}}^r$ , and, following the same line of reasoning,  $M_{\alpha}^r$  and  $M_{\bar{\alpha}}^r$  are obtained given the geometry of the wing and the relative position of centre of gravity and aerodynamic centres.

The aircraft motion in turn influences the loads acting on the wing and thus its dynamics. Specifically, a change in angle of attack  $\bar{\alpha}$  and pitch rate  $\bar{q}$  causes elastic terms containing  $\frac{h}{b}$  and  $\alpha$  to generate further loads on the structure. If a quasi-steady flow is considered, then the procedure follows the one outlined in (2.16). More interestingly, when unsteadiness is retained (and this would be consistent with the other aerodynamic terms featuring the elastic equilibrium), the relation between displacements and forces can be represented with the Theodorsen model. In particular, it is possible to write the loads on the wing due to the rigid motion  $F_r$  as:

$$F_r = q_\infty Q_{hh} R x_r, \quad (2.17)$$

where  $x_r = [\bar{\alpha}; \bar{\theta}; \bar{q}]$  and the formal similarity with Eq. (2.12) is apparent. In fact, the difference is given by the transformation matrix  $R$  which allows the typical section DOFs to be expressed in terms of  $x_r$ . This defines the remaining aeroelastic stability derivatives  $Z_{\bar{\alpha}}^e$ ,  $Z_{\bar{q}}^e$ ,  $M_{\bar{\alpha}}^e$ ,  $M_{\bar{q}}^e$ .

A shorthand expression for the coupled system in the frequency-domain is given by:

$$\begin{bmatrix} s^2 & \begin{bmatrix} M_{rr} & M_{rs} \\ M_{sr} & M_{ss} \end{bmatrix} \\ & + s \begin{bmatrix} C_{rr} & C_{rs} \\ C_{sr} & C_{ss} \end{bmatrix} + \begin{bmatrix} K_{rr} & K_{rs} \\ K_{sr}(\bar{s}) & K_{ss}(\bar{s}) \end{bmatrix} \end{bmatrix} \begin{bmatrix} x_r(s) \\ \eta(s) \end{bmatrix} = \begin{bmatrix} 0 \\ 0 \end{bmatrix}, \quad (2.18)$$

where the subscripts  $r$  and  $s$  refer to the rigid-body and structural DOFs. Note that setting the cross-coupling terms ( $rs$  and  $sr$ ) to zero amounts to consider separately the short-period approximation of the aircraft (governed by the  $rr$  terms) and the restrained wing aeroelastic problem (described by the  $ss$  terms). A state-space description akin to Eq. (2.7) is also available when an RFA for the matrices  $K_{sr}$  and  $K_{ss}$  is computed:

$$\begin{bmatrix} \dot{x}_r \\ \dot{x}_s \\ \dot{x}_a \end{bmatrix} = \begin{bmatrix} \chi_{rr} & \chi_{rs} & \chi_{ra} \\ \chi_{sr} & \chi_{ss} & \chi_{sa} \\ \chi_{ar} & \chi_{as} & \chi_{aa} \end{bmatrix} \begin{bmatrix} x_r \\ x_s \\ x_a \end{bmatrix}. \quad (2.19)$$

The proposed simplified aircraft model provides an analytical description of the interaction between elastic and rigid modes. This will enable on the one hand a better understanding of the dynamics arising because of the coupling, and on the other a profitable application of robust flutter analysis since the meaningful physical parameters are all clearly identifiable. The considered case study, analysed in Chapter 4, will consist of the Goland wing [93] for the wing properties and a scaled version of the benchmark aircraft in [190] for the flight mechanics properties.

### 2.3.3 Joined-wing configuration

In order to exemplify the application of robust modelling and analysis strategies to systems described with state-of-practice FSI solvers, a joined-wing aircraft configuration is considered. Among unconventional configurations, Joined Wings have prospective advantages in terms for example of increased efficiency and reduction noise and emissions [41]. These unconventional aircraft configurations are known to exhibit complex aeroelastic behaviours, thus they represent a challenging test bed for the presented strategies. The general concept behind joined-wings configurations is to have two interconnected wings which form an overconstrained system. Among these, *PrandtlPlanes* [41] are layouts characterised by two wings having approximately the same wingspan, joined at their tips through a vertical wing. The driving reason for arranging the lifting system in such a way is the reduction of induced drag, as first shown by Prandtl. However, according to the literature, other relevant benefits (in terms of structures, flight mechanics and engine integration) may be gained [85].

The PrandtlPlane selected as case study was originally analysed in [55]. The configuration, denominated PrandtlPlane 250 (*PrP250*), is a 250 passenger mid-long range aircraft with a maximum take off weight of 230 tons, and was designed by considering a multidisciplinary approach. A view of the finite element structural model is given in Fig. 2.6.

The mathematical model used to study flutter of the wing in Fig. 2.6 is formally identical to that in Eqs. (2.1)-(2.7). The structural and aerodynamics operators are obtained in this

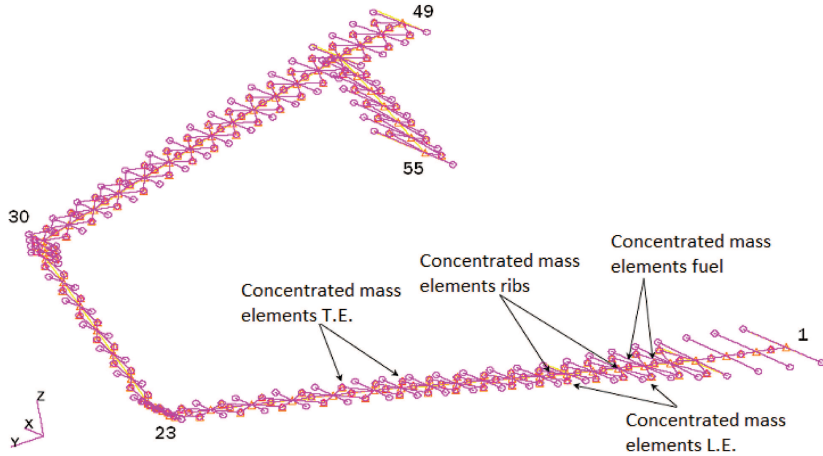


Figure 2.6: Structural model for flutter analysis of *PrP250* (from [55]).

case through a dedicated fluid-structure interaction solver, namely CSHELL, a proprietary software developed by the authors of references [40, 60]. The modules used in the work are the computational solid dynamics one, relying on the FEM approach, and the aerodynamic one, using the DLM [3]. These are briefly described next.

### 2.3.3.1 Structural matrices with Finite Element methods

The elasticity of the wing is modelled with beam finite elements derived by the Euler-Bernoulli formulation [21]. The FEM matrices  $M_s$  and  $K_s$  are obtained through the procedure of matrix assembly starting from the structural operators at element level (i.e. single beam) and connecting them based on the geometry and properties of the system. As an example of this procedure, the elastic stiffness matrix is considered next. The matrix  $K_s$  is obtained from the corresponding beam element matrices  $K_e$  as follows:

$$K_s = \sum_e R_e^T K_e R_e, \quad (2.20)$$

where  $R_e$  is the rotation matrix relating the local nodal displacements (element's level) and the global ones (expressed in the global reference system), and the  $\sum_e$  operation is adopted in its general meaning of assembly over all the finite elements [21].

The stiffness element matrix  $K_e$  is specific to the finite element and physical contributions considered. For example, in a beam element the bending contribution  $K_{eB}$  to  $K_e$  is obtained evaluating the integral:

$$K_{eB} = \int_0^l EI(x) B_k^T B_k dx, \quad (2.21)$$

where the integrand is a function of the local properties of the beam, namely:  $E$  the material Young's modulus of the beam,  $I$  its moment of inertia,  $l$  the beam length and  $B_k$  a kinematic matrix relating the element strain to the nodal displacements. The adopted shape functions and

kinematic assumptions specialise the above integral to the selected beam formulation. Other contributions to  $K_e$  such as axial stiffness can be similarly taken into account starting from a characterisation of the local beam properties.

Note finally that in [55] no structural damping was considered, thus it will be assumed null here. However, the physical and generalised damping matrices can be easily obtained from the damping ratios  $\zeta$  associated with each structural mode, e.g. derived from logarithmic decrement calculations after dedicated ground vibration tests. The damping matrix in the generalised coordinates space is thus given by:

$$\tilde{C}_s = \text{diag}(2m_{g,1}\omega_{n,1}\zeta_1, \dots, 2m_{g,i}\omega_{n,i}\zeta_i, \dots, 2m_{g,n_s}\omega_{n,n_s}\zeta_{n_s}), \quad (2.22)$$

where  $m_{g,i}$  and  $\omega_{n,i}$  are respectively modal mass and natural frequency of mode  $i$  obtained by the free vibration problem of the structure. The transformation from generalised to physical coordinates enables finally to obtain the physical damping matrix  $C_s$ :

$$C_s = \Phi^{-T} \tilde{C}_s \Phi^{-1}. \quad (2.23)$$

### 2.3.3.2 Aerodynamic operator with DLM

The evaluation of unsteady aerodynamic forces is performed using a DLM solver developed by the authors of reference [60]. This provides, at a fixed reduced frequency  $k$ , the transfer matrix from generalised displacements to generalised aerodynamic forces. The fundament for its derivation is the linearised formulation of the oscillatory lifting surface theory, relating the normal velocity (downwash)  $\bar{w}$  at the surface to the pressure difference  $\bar{p}$  across the surface. The singular integral equation providing this relationship is:

$$\bar{w}(s_1, s_2) = \frac{1}{8\pi} \int_S \tilde{K}(s_1, \xi, s_2, \sigma; k, M) \bar{p}(\xi, \sigma) d\xi d\sigma, \quad (2.24)$$

where  $s_1$  and  $s_2$  are orthogonal coordinates on the surface  $S$ ,  $M$  is the Mach number and  $\tilde{K}$  is the Kernel expression which, for an aerodynamic surface discretised with rectangular panels, is provided by the DLM. Since the GAF represents a transfer matrix between generalised quantities,  $\tilde{K}$  depends on the structural modes  $\Phi$ , which are provided as input to the DLM code. As a result, variations in the structural parameters do have an effect on the calculation of  $Q_{hh}$ .

The numerical solution of (2.24) leads to the following expression for the downwash (at the aerodynamic collocation points):

$$\bar{w}_i = \sum_{j=1}^{n_p} \bar{D}_{ij} \bar{p}_j, \quad (2.25)$$

where  $n_p$  is the number of aerodynamic panels and  $\bar{D}_{ij}$  comes from the discretisation of the integral in (2.24). The generic coefficient  $ij$  of the GAF matrix, representing the aerodynamic force generated by the structural mode  $j$  and projected onto mode  $i$ , is given by:

$$Q_{hh,ij} = \frac{1}{q_\infty} \sum_{k=1}^{n_p} \Delta S_k \bar{w}_k^{(i)} \bar{p}_k^{(j)}; \quad i, j = 1, \dots, n_s, \quad (2.26)$$

where  $\Delta S_k$  is the surface of the  $k^{th}$  considered panel.

### 2.3.4 FLEXOP demonstrator

The demonstrator designed within the FLEXOP project is briefly described in this section. The goal of the demonstrator is to validate through flight tests the modelling, analysis, and design strategies developed within the project [155, 226, 257] to achieve active flutter suppression solutions. Fig. 2.7 shows a schematic representation of the demonstrator developed by the consortium, where the control effectors and sensors for closed-loop control are highlighted. Specifically, 8 control surfaces, 4 for each wing (*R* right and *L* left), are available. As for the sensors, accelerometers at 3 stations across each wing and one in the centre of gravity of the aircraft are also indicated with black rectangles. Table 2.1 reports the main design features of the aircraft and open loop flutter properties.

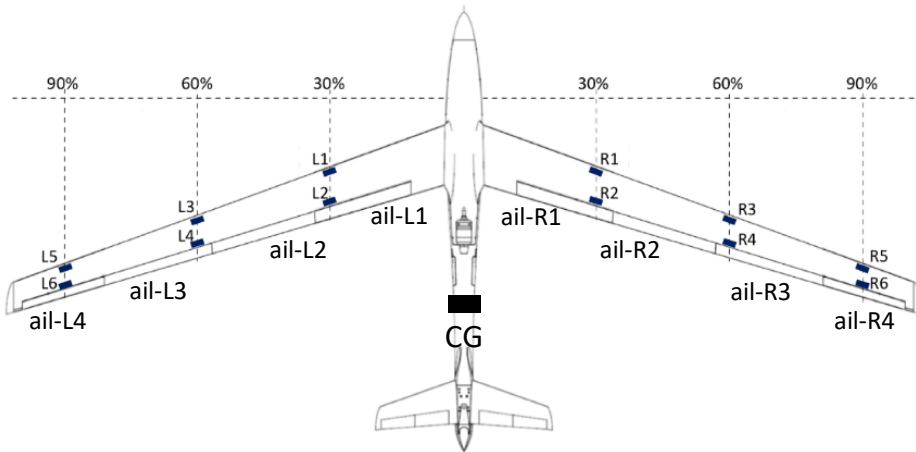


Figure 2.7: Schematic view of the FLEXOP demonstrator (from [155]).

Table 2.1: FLEXOP demonstrator main design features [155, 226].

Wingspan	$7m$
Aspect ratio	20
Takeoff Mass	$55\ kg$
Flutter speed	$52\ \frac{m}{s}$
Flutter frequency	$38\ \frac{rad}{s}$

The aircraft was modelled by other partners of the project (specifically, the authors of [167, 257]) with an FSI solver featuring a linear aeroelastic module (based on beam FEM and DLM solvers) coupled with the nonlinear rigid-body dynamics. Roger approach was employed to build

up an RFA of the aerodynamic operator and provide a nonlinear high-fidelity Simulink model of the system for time-domain simulations.

Starting from this input from the partners, the model has been trimmed and linearised at different speeds leading to a family of high-order (1000+ states) LTI systems. This set was initially reduced to approximately 500 states with modal truncation and further reduced to a size of 38 states with balanced truncation to preserve a certain degree of fidelity in the input/output channels (the MATLAB function *balred* was used for this purpose) [92]. Accuracy among the various reduced order models was finally checked by means of standard indicators, e.g. spectrum of the state-matrices, Bode plots.

This case study will be used in Chapter 5 to exemplify the application of the worst-case LTV analysis framework to a notional flight test manoeuvre.



Figure 2.8: FLEXOP demonstrator's rendering picture.



## LINEAR FRACTIONAL TRANSFORMATION MODELLING FOR ROBUST FLUTTER ANALYSIS

This chapter deals with the construction of Linear Fractional Transformation (LFT) models of uncertain aeroelastic systems, a paramount step in order to obtain accurate and reliable results when robust control analysis and design techniques are applied to the flutter problem. Previous works have partially investigated this problem [22, 33, 150, 197], but specific features of aeroelastic systems and inherent complexities associated with their modelling within the LFT framework have still to be addressed. Specifically, a physical based rationale to select the uncertainties and systematic methods to represent them as LFTs which are effective regardless of the fidelity used to model the system, are still lacking in the community and have driven the research presented here.

After reviewing the fundamental background, the two contributions of the chapter are presented. Section 3.2 examines LFT features peculiar to aeroelastic problems (such as the possibility to employ either a frequency-domain or a state-space formulation) and the modelling of aerodynamic uncertainties. Section 3.3 discusses common issues connected with the application of the LFT paradigm to high-order models and will propose an original solution. The reasoning behind the developed modelling and analysis methodology is to merge fluid-structure interaction and LFT modelling steps, reconciling by doing so the state-of-practice and the state-of-art in flutter analysis.

Note that most of the analysis approaches featured in the thesis leverage a description of the uncertain system as LFT, hence the modelling approaches discussed in this chapter are not only relevant to  $\mu$  analysis. The latter is however introduced here because on the one hand, it provides the reader with a tangible application of the LFT paradigm; on the other,  $\mu$  analysis will be employed in some of the algorithms discussed in Section 3.3, and its presentation will make

easier their understanding.

**Publications**<sup>1</sup>: [117, 122] Section 3.2; [116] Section 3.3.

## 3.1 Mathematical background

### 3.1.1 Linear Fractional Transformation

Linear Fractional Transformation is an instrumental tool in robust control theory for analysis and design of uncertain system [156, 269]. The central idea is to represent the original system in terms of nominal and uncertain components given by matrices. To this end, the unknown part (represented by  $\Delta$ ) is pulled out of the system, so that the problem appears as a nominal system, also referred to as *plant*, subject to an artificial feedback (recall the standard starting point in robust control, Fig. 2.2).

Let  $M \in \mathbb{C}^{(p_1+p_2) \times (q_1+q_2)}$  be a complex matrix partitioned as:

$$M = \begin{bmatrix} M_{11} & M_{12} \\ M_{21} & M_{22} \end{bmatrix}, \quad (3.1)$$

and let  $\Delta \in \mathbb{C}^{q_1 \times p_1}$ . The upper LFT of  $M$  with respect to  $\Delta$  (there is an equivalent lower LFT representation) is defined as the map:

$$\begin{aligned} \mathcal{F}_u : \mathbb{C}^{q_1 \times p_1} &\longrightarrow \mathbb{C}^{p_2 \times q_2}, \\ \mathcal{F}_u(M, \Delta) &= M_{22} + M_{21}\Delta(I - M_{11}\Delta)^{-1}M_{12}. \end{aligned} \quad (3.2)$$

A crucial feature apparent in (3.2) is that the LFT is well posed if and only if the inverse of  $(I - M_{11}\Delta)$  exists. Otherwise,  $\mathcal{F}_u(M, \Delta)$  is said to be singular.

The set  $\Delta$  is used in robust control to isolate the unknown components from the nominal (typically linear) part. An example is the *structured* uncertainty set, here denoted by  $\Delta_u$ , gathering parametric ( $\delta_i$  and  $\delta_j$ ) and dynamic ( $\Delta_{D_k}$ ) uncertainties:

$$\begin{aligned} \Delta_u &= \text{diag}(\delta_i I_{d_i}, \delta_j I_{d_j}, \Delta_{D_k}), \\ i &= 1, \dots, n_R; \quad j = 1, \dots, n_C; \quad k = 1, \dots, n_D. \end{aligned} \quad (3.3)$$

The uncertainties associated with the  $n_R$  real scalars  $\delta_i$ ,  $n_C$  complex scalars  $\delta_j$  and  $n_D$  unstructured (or full) complex blocks  $\Delta_{D_k}$  are listed in diagonal format. The identity matrices of dimension  $d_i$  and  $d_j$  take into account the fact that scalar uncertainties are generally repeated in  $\Delta_u$  when the LFT of the system is built up. Typically the uncertainties are normalised by scaling  $M$  such that  $\mathcal{F}_u(M, 0) = M_{22}$  coincides with the nominal system (i.e. the uncertain parameters are set at their nominal values) and the bound on the maximum singular value of  $\Delta_u$ , namely  $\bar{\sigma}(\Delta_u) \leq 1$ , holds when uncertainties take values in the allowed interval.

---

<sup>1</sup>Material published during the PhD which relates to the content of this chapter.

To exemplify how the expression in (3.2) can be derived from a given uncertainty description, consider two general representations for an uncertain parameter  $d$ :

$$d = d_0 + \lambda_d \delta_d, \quad (3.4a)$$

$$d = d_0(1 + \lambda_d \delta_d), \quad (3.4b)$$

with  $\lambda_d$  indicating the uncertainty level with respect to a nominal value  $d_0$  and  $\delta_d \in [-1, 1]$  representing the normalised uncertain parameter. Eqs. (3.4a)-(3.4b) are referred to as additive and multiplicative uncertainty, respectively. In both cases,  $\delta_d = 0$  corresponds to the nominal value of  $d$ , while  $\delta_d = \pm 1$  are perturbations at the extreme of the uncertainty range. At a matrix level, the operator  $D$  affected by additive uncertainties can thus be expressed as (note that an analogous representation holds for multiplicative uncertainties):

$$D = D_0 + V_D \Delta_D W_D, \quad (3.5)$$

where  $D_0$  is the nominal operator and  $V_D$  and  $W_D$  are scaling matrices. Eq. (3.5) is a particular instance of LFT map in the case when there is no rational dependence on the uncertainty set (recall Eq. 3.2 with  $M_{11}=0$ ). In the general case when the dependence of  $D$  on the uncertain parameters is rational, (3.5) assumes an equivalent expression to (3.2). Therefore, operators subject to parametric uncertainties are LFTs themselves. This feature is helpful in the LFT building process since a fundamental property [269] is that interconnections of LFTs are again LFTs, thus for example it is possible to cascade, add, and invert them resulting always in an LFT. In addition to helping in the construction of LFT models, this property also helps to separate modelling specific details of the system under consideration and to ease the algebraic manipulations [146]. An example will be provided later in this section.

The construction of LFT models can be efficiently performed by means of available toolboxes which directly provide the partitioned matrix  $M$  for the defined set  $\Delta$ . In this thesis the LFR toolbox developed by ONERA [156] will be employed, which allows the uncertainty set to be defined by writing the uncertain parameters in symbolic form. In order to minimise the number of repetitions in  $\Delta$ , different reduction techniques can be adopted such as Horner factorisation or tree decomposition [20, 160, 249].

The LFT representation of an uncertain system can be interpreted in terms of the feedback interconnection in Fig. 3.1. If  $M$  is taken as a transfer matrix,  $\mathcal{F}_u(M, \Delta_u)$  represents the closed-loop transfer matrix from input  $u$  to output  $y$  when the nominal system  $M_{22}$  is subject to the structured perturbation  $\Delta_u$ . The signals  $w$  and  $v$  close the feedback loop with the uncertain block, and the matrices  $M_{11}$ ,  $M_{12}$  and  $M_{21}$  define how the perturbation affects the nominal system. Note that  $M_{11}$  determines the well-posedness of the LFT (3.2), and it is, within this analogy, the transfer matrix seen by the perturbation block  $\Delta_u$ .

Another way of looking at the LFT paradigm is as realisation technique [156, 269]. This viewpoint is discussed here since it will be beneficial for a deeper understanding of the LFT

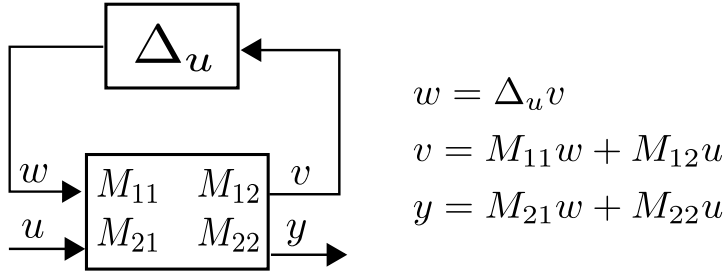


Figure 3.1: Feedback interpretation of an LFT.

framework and for its usage in Chapter 8 in the context of robust bifurcation margins.

Let us consider a nominal Linear Time-Invariant (LTI) system defined by its state-space representation  $(\mathcal{A}, \mathcal{B}, \mathcal{C}, \mathcal{D})$  or equivalently by its transfer matrix  $G$ :

$$\begin{cases} \dot{x} = \mathcal{A}x + \mathcal{B}v, \\ y = \mathcal{C}x + \mathcal{D}v, \end{cases} \quad (3.6a)$$

$$G(s) = \mathcal{D} + \mathcal{C}(sI_{n_x} - \mathcal{A})^{-1}\mathcal{B}. \quad (3.6b)$$

Given the formal equivalence between (3.6b) and (3.2), it can be inferred that LFT generalises the realisation of transfer matrices into state-space representations to the case of rational multivariate matrices. An important fact can then be highlighted. The poles of the LTI (3.6) are typically found with eigenvalue analysis of  $\mathcal{A}$ . Equivalently, the system has a given pole  $v$  if  $(sI_{n_x} - \mathcal{A})^{-1}$  is singular for  $s = v$ . Note that this latter condition can be formulated as the singularity of the LFT  $\mathcal{F}_u(M_v, \Delta_v)$  with:

$$M_v = \begin{bmatrix} \mathcal{A} & \mathcal{B} \\ \mathcal{C} & \mathcal{D} \end{bmatrix}; \quad \Delta_v = \frac{1}{s}I_{n_x}. \quad (3.7)$$

This follows immediately from the fact that:

$$\mathcal{F}_u(M_v, \Delta_v) = \mathcal{D} + \mathcal{C}\frac{1}{s}I_{n_x}(I_{n_x} - \frac{1}{s}\mathcal{A})^{-1}\mathcal{B} = \mathcal{D} + \mathcal{C}(sI_{n_x} - \mathcal{A})^{-1}\mathcal{B}, \quad (3.8)$$

where the diagonal structure of  $\Delta_v$  and the fact that  $\frac{1}{s} \neq 0$  have been exploited. Here  $\Delta_v$  can be seen as an instance of the set  $\Delta$  associated with the realisation of  $(\mathcal{A}, \mathcal{B}, \mathcal{C}, \mathcal{D})$ . The subscript  $v$  is used to emphasise this particular interpretation of LFT (connected with the fact that the underlying linear system features a certain pole  $v$ ).

Consider now the case when the LTI system is subject to uncertainties. The set  $\Delta$  will then consist of two blocks:  $\Delta_u$  containing the structured perturbations, and  $\Delta_v = \frac{1}{s}I_{n_x}$ . The coefficient matrix  $M$  is partitioned correspondingly, as depicted in Fig. 3.2 and reported below:

$$M = \begin{bmatrix} \mathcal{A} & \mathcal{A}_{12} & \mathcal{B} \\ \mathcal{A}_{21} & \mathcal{A}_{22} & \mathcal{B}_1 \\ \mathcal{C} & \mathcal{C}_1 & \mathcal{D} \end{bmatrix}, \quad \Delta = \text{diag}(\Delta_v, \Delta_u). \quad (3.9)$$

$M$  now features the blocks from  $M_v$  and other matrices describing the effect of the uncertainties on the state-matrices. Crucially, neutral stability of the uncertain system is equivalent to the singularity of  $\mathcal{F}_u(M, \Delta)$  for  $s = i\omega$  and uncertainties in the set  $\Delta_u$ .

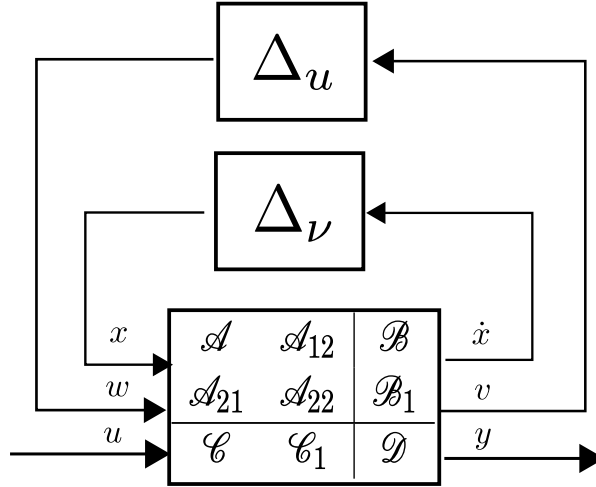


Figure 3.2: Realisation technique interpretation of an LFT.

Finally, it is helpful, by virtue of the interconnection property pointed out before, to visualise an LFT featured by distinct  $\Delta$ -blocks as an interconnections of LFTs. For the LFT in (3.9) it thus holds:

$$\mathcal{F}_u(M, \Delta) = \mathcal{F}_u(\mathcal{F}_u(M, \Delta_v), \Delta_u). \quad (3.10)$$

### 3.1.2 $\mu$ analysis

The  $\mu$  analysis technique leverages the key features of LFT modelling to address the Robust Stability (RS) analysis of LTI systems in the face of structured uncertainties. The structured singular value is a matrix function denoted by  $\mu_\Delta(M)$  and several equivalent definitions are available in the literature [75, 180, 269]. Let us start with a definition that encompasses the aspects discussed in the end of the previous section. Specifically, the LFT defined in (3.10) featuring the block  $\Delta = \text{diag}(\Delta_u, \Delta_v)$  is considered and a first definition follows:

$$\mu_\Delta(M) = \left[ \min_{\Delta_u, \Delta_v} (\kappa : \mathcal{F}_u(\mathcal{F}_u(M, \Delta_v), \kappa \Delta_u) \text{ is singular; } \bar{\sigma}(\Delta_u) \leq 1) \right]^{-1}, \quad (3.11)$$

where  $\kappa$  is a real positive scalar, and  $\mu_\Delta(M) = 0$  if the minimisation problem has no solution. The subscript remarks the dependence on the uncertainty set, in addition to the matrix  $M$ , and will be omitted in the following when clear from the context. Let us assume, as often done in practice, that  $\Delta_v$  is realised by fixing  $s$  (typically  $s = i\omega$  for a given frequency  $\omega$ ), and thus  $\Delta = \Delta_u$ . Then, the problem defined in (3.11) consists of finding the structured uncertainty matrix with the smallest maximum singular value such that the uncertain LTI system has a pair of purely

imaginary eigenvalues  $\pm i\omega$ . This reasoning leads to the standard definition of structured singular value  $\mu$ :

$$\mu(M_{11}) = \left[ \min_{\Delta_u} (\kappa : \det(I - \kappa M_{11} \Delta_u) = 0; \bar{\sigma}(\Delta_u) \leq 1) \right]^{-1}, \quad (3.12)$$

where  $M_{11}$ , which is a function of  $\omega$ , is the submatrix of  $M$  (3.2) involved in the well-posedness condition.  $\mu(M_{11})$  provides a robust stability test for an uncertain LTI. For each frequency  $\omega$ , if  $\mu(M_{11}) \geq 1$  a candidate perturbation matrix (i.e. within the allowed range) exists that violates the well-posedness of  $\mathcal{F}_u(M, \Delta)$ . In essence, the uncertain state-matrix  $\mathcal{A}$  has the eigenvalues  $s = \pm i\omega$  for a combination of the uncertainties. On the contrary, if  $\mu(M_{11}) < 1$  then there is no perturbation matrix inside the set  $\Delta$  such that the  $\mathcal{F}_u(M, \Delta)$  is ill-posed and thus the system is robust stable within the range of uncertainties considered.

For numerical reasons,  $\mu$  is typically evaluated on a discretised frequency range, that is, the  $\Delta_v$  block is fixed as discussed before on a grid of given frequencies  $\omega$  and (3.12) is solved. This has the drawback of possibly missing critical frequencies and thus underestimating the value of  $\mu$ . However, newly developed algorithms using Hamiltonian-based techniques (i.e. SMART library [205] and Robust Control Toolbox from MATLAB R2016b) can also guarantee the validity of results over a continuum range of frequencies.

It is known that  $\mu$  is an NP-hard problem with either pure real or mixed real-complex uncertainties [35], thus upper and lower bounds are computed. The upper bound  $\mu_{UB}$  gives the maximum size perturbation  $\bar{\sigma}(\Delta^{UB}) = \frac{1}{\mu_{UB}}$  for which RS is guaranteed, whereas the lower bound  $\mu_{LB}$  defines a minimum size perturbation  $\bar{\sigma}(\Delta^{LB}) = \frac{1}{\mu_{LB}}$  for which RS is guaranteed to be violated. Along with this information, the lower bound also provides the matrix  $\Delta^{LB} = \Delta^{cr}$  determining singularity of the LFT. If the bounds are close in magnitude, then  $\Delta^{LB}$  is the worst-case matrix, that is, the perturbation with the smallest magnitude leading to neutral stability.

It is remarked finally that  $\mu$  analysis can also be used to analyse robust performance. Achieving a desired nominal performance is typically formulated as the requirement that the  $\mathcal{H}_\infty$  norm of a certain transfer matrix  $G$  fulfils a given frequency domain template  $\Psi(\omega)$ . That is, the following inequality is satisfied:

$$\bar{\sigma}(G(j\omega)) < \Psi(\omega), \quad \forall \omega. \quad (3.13)$$

By scaling of  $G$ , this is expressed without loss of generality as:

$$\bar{\sigma}(G(j\omega)) < 1, \quad \forall \omega. \quad (3.14)$$

If the system represented by  $G$  is subject to uncertainty described in  $\Delta_u$ , robust performance can be tested by considering  $\Delta = \text{diag}(\Delta_u, \Delta_p)$ . The block  $\Delta_p \in \mathbb{C}^{q_2 \times p_2}$  is a full-complex (i.e. unstructured) perturbation matrix closing the lower loop in Fig. 3.1 by connecting the signals  $y$  and  $u$ . This fictitious block doesn't reflect any physical perturbation of the plant and is introduced in order to apply a result known as Main Loop theorem [269]. Let us denote by  $\mathcal{F}_u(M, \Delta)$  the LFT

representation of the uncertain transfer matrix  $G$  and by  $\mu(M)$  the following:

$$\mu(M) = \left[ \min_{\Delta=diag(\Delta_u; \Delta_p)} (\kappa : \det(I - \kappa M \Delta) = 0; \bar{\sigma}(\Delta) \leq 1) \right]^{-1}. \quad (3.15)$$

The Main Loop theorem then ensures that the condition  $\mu_\Delta(M) < 1$  is a test for robust performance. More precisely, for all the perturbation matrices  $\Delta_u$  with  $\|\Delta_u\|_\infty \leq \frac{1}{\beta}$  it holds [269]:

$$\|\mathcal{F}_u(M, \Delta)\|_\infty < \beta \quad \text{if and only if} \quad \mu(M) < \beta. \quad (3.16)$$

Note that  $M$  is now employed in the test (3.15) instead of the submatrix  $M_{11}$  used for RS (3.12).

## 3.2 LFT modelling of aeroelastic systems

The aim of this section is to address specific aspects of the application of LFT modelling to aeroelastic systems. The starting point is the mathematical model describing the interaction of elastic and aerodynamic forces, which was discussed for a generic system in Sec. 2.2. In that section two formulations for the dynamic equilibrium of the system were presented: Eq. (2.1) in the frequency-domain and Eq. (2.7) in state-space (and their relation with the adopted aerodynamic operator was also discussed). While nominal flutter analysis with either of them typically leads to similar predictions (see results in Sec. 4.1), for robust analysis purposes the different formulations have two important consequences. Firstly, the LFT model development path, interpreted here as the process followed to build up LFT models starting from the definition of the nominal system and the uncertainty set, changes. Secondly, the aerodynamic uncertainty captured by the LFT depends on the expression adopted for the Generalised Aerodynamic Force (GAF) matrix, whether the original frequency-dependent or its approximation, and thus on the starting point. These elements have prompted the investigations presented next.

### 3.2.1 Model development path

#### 3.2.1.1 Frequency-domain approach

The construction of the LFT associated with a frequency-domain representation follows the strategy originally presented in [33]. The objective is to recast the aeroelastic system as in Fig. 3.1, where the interpretation of LFT as a transfer matrix was discussed. If a fictitious input force  $u \in \mathbb{C}^{n_s}$  acting on the system is introduced, Eq. (2.1) can be rewritten at  $s = i\omega$  as:

$$[-\omega^2 \bar{M}_s + i\omega \bar{C}_s + \bar{K}_s - q_\infty Q_{hh}(ik)] \eta = u. \quad (3.17)$$

When the operators in the equation above are subject to uncertainties in the set  $\Delta_u$ , the dynamics can be conveniently described in terms of the transfer matrix from input  $u$  to output  $y = \eta$ . In

other words, the objective is to recast (3.17) in the format:

$$\begin{aligned} w &= \Delta_u v, \\ v &= M_{11}w + M_{12}u, \\ \eta &= M_{21}w + M_{22}u. \end{aligned} \quad (3.18)$$

This allows to retrieve the feedback equations in Fig. 3.1, and in turn provides the partitioned matrix  $M$ , which completely defines the LFT together with the associated uncertainty set. The first step of this modelling process consists of explicitly defining the uncertainties in the operators  $\bar{M}_s$ ,  $\bar{C}_s$ ,  $\bar{K}_s$ , and  $Q_{hh}$ . This can be achieved by applying at operator level the additive description in (3.5):

$$\bar{M}_s = \bar{M}_{s0} + V_M \Delta_M W_M, \quad (3.19a)$$

$$\bar{C}_s = \bar{C}_{s0} + V_C \Delta_C W_C, \quad (3.19b)$$

$$\bar{K}_s = \bar{K}_{s0} + V_K \Delta_K W_K, \quad (3.19c)$$

$$Q_{hh} = Q_{hh0} + V_Q \Delta_Q W_Q. \quad (3.19d)$$

Eq. (3.19) can be substituted back in (3.17) leading to:

$$M_{22}(\omega)^{-1} \eta = V \Delta_u W \eta + u, \quad (3.20)$$

where  $\Delta$ ,  $V$  and  $W$  gather the corresponding matrices in (3.19), that is  $\Delta_u = \text{diag}(\Delta_M, \Delta_C, \Delta_K, \Delta_Q)$ ,  $V = [V_M \ V_C \ V_K \ V_Q]$ , and  $W = [W_M; W_C; W_K; W_Q]$ , and:

$$M_{22}(\omega) = \left[ -\omega^2 \bar{M}_{s0} + i\omega \bar{C}_{s0} + \bar{K}_{s0} - q_\infty Q_{hh0}(ik) \right]^{-1}. \quad (3.21)$$

Note that  $M_{22}$  is the frequency response of the nominal system (as expected by definition of LFT). The frequency dependency of  $M_{22}$  is dropped from now on for ease of notation, unless unclear from the context.

Eq. (3.20) can be finally recast in the sought template of Fig. 3.1 by defining  $v = W\eta$  and exploiting the fact that by definition  $w = \Delta_u v$ :

$$\begin{aligned} v &= WM_{22}Vw + WM_{22}u, \\ \eta &= M_{22}Vw + M_{22}u. \end{aligned} \quad (3.22)$$

The last equation provides the desired partition of  $M$ . Indeed, given a frequency  $\omega$ , it holds:

$$M_{11} = WM_{22}V, \quad (3.23a)$$

$$M_{12} = WM_{22}, \quad (3.23b)$$

$$M_{21} = M_{22}V, \quad (3.23c)$$

$$M_{22} = \left[ -\omega^2 \bar{M}_{s0} + i\omega \bar{C}_{s0} + \bar{K}_{s0} - q_\infty Q_{hh0}(ik) \right]^{-1}. \quad (3.23d)$$

The partitioned matrix  $M$  is thus available as a function of  $\omega$ . In particular  $M_{11}$  (3.23a), which is by definition the transfer matrix seen by the perturbation block, can be employed in (3.12) to assess the robust stability of the system.

It is stressed that usually the dependence on  $\omega$  is confined to  $M_{22}$ . However, this formulation allows to employ generic (i.e. not necessarily analytic) frequency-dependent uncertainty descriptions by defining the matrices  $V$  and  $W$  at each (discrete)  $\omega$ . This can be particularly useful for the GAF matrix, which is inherently frequency-dependent, but can be advantageously used also for other purposes (e.g. neglected dynamics at higher frequencies due to modal truncation).

### 3.2.1.2 State-space approach

The construction of the LFT associated with a state-space representation takes its clue from the other interpretation of LFT discussed in Sec. 3.1.1, and its features are assessed next. Recall the LFT of a generic uncertain state-space model  $\mathcal{F}_u(M, \Delta)$  defined in (3.9) and pictorially depicted in Fig. 3.2. The expression for the partitioned matrix  $M$  can be derived starting from the aeroelastic state-space model in Eq. (2.7) by defining the dependence of the matrices  $\chi_{ss}$ ,  $\chi_{sa}$ ,  $\chi_{as}$ , and  $\chi_{aa}$  on the uncertainties. This can be done, for example, by applying the uncertainty additive description to the operators in (2.8). Crucially, while for the structural operators this leads to the same uncertainty description used for the frequency-domain approach (that is, Eqs. 3.19a-3.19c), the aerodynamic operator is now described by the Rational function approximation (RFA) matrices (Eq. 2.3). Therefore, only uncertainties in  $\Gamma_{QS}$  and  $\Gamma_{lag}$  can be considered. This is a first important difference that will be further discussed in Sec. 3.2.2.

Once the dependence of the matrices in (2.8) on the uncertainties is defined,  $M$  can be obtained from standard LFT toolboxes and thus  $\mathcal{F}_u(M, \Delta)$ , which in this formulation has an equivalent representation as  $\mathcal{F}_u(\mathcal{F}_u(M, \Delta_v), \Delta_u)$  through the interconnection property, becomes available. If the goal is to obtain the frequency response of  $\mathcal{F}_u(\mathcal{F}_u(M, \Delta_v), \Delta_u)$  on a grid of frequencies, this can be achieved by realizing the block  $\Delta_v$  (between the channels  $\dot{x}$  and  $x$  in Fig. 3.2) at  $s = i\omega$ . At this point, the LFT recovers the standard transfer matrix form and, since the  $\mu$  analysis technique is typically computed on a grid of frequencies, this is the standard modelling process for linear robust analysis purposes. However, the availability of *state-space LFT* models (that is, in the form  $\mathcal{F}_u(\mathcal{F}_u(M, \Delta_v), \Delta_u)$ ) has the advantage of allowing for other robust control applications. Examples are:  $\mu$  analysis over a continuous range of frequencies using Hamiltonian-based techniques [205]; Integral Quadratic Constraints analysis [170]; and advanced robust synthesis techniques (e.g. structured  $\mathcal{H}_\infty$  control [9]).

To better emphasise this aspect, let us consider the transfer matrix  $M_{11}$  (employed to assess the robust stability of the system). In this formulation,  $M_{11}$  is an LFT formed by the terms in the

upper left block of the coefficient matrix (3.9), that is:

$$\begin{aligned} M_{11}(s) &= \mathcal{A}_{22} + \frac{1}{s}\mathcal{A}_{21}(I_{n_x} - \frac{1}{s}\mathcal{A})^{-1}\mathcal{A}_{12} = \mathcal{A}_{22} + \mathcal{A}_{21}(sI_{n_x} - \mathcal{A})^{-1}\mathcal{A}_{12}, \\ &= \mathcal{F}_u(M_{11v}, \Delta_v), \quad M_{11v} = \begin{bmatrix} \mathcal{A} & \mathcal{A}_{12} \\ \mathcal{A}_{21} & \mathcal{A}_{22} \end{bmatrix}, \quad \Delta_v = \frac{1}{s}I_{n_x}. \end{aligned} \quad (3.24)$$

The partitioned matrix  $M_{11v}$  consists of the nominal state-matrix  $\mathcal{A}$  and the blocks  $\mathcal{A}_{12}$ ,  $\mathcal{A}_{21}$ , and  $\mathcal{A}_{22}$  which arise from the uncertainty modelling of the state-space operators. As pointed out before, the matrix  $M_{11}$  is pivotal in the application of  $\mu$  for robust analysis, and (3.24) provides its analytical dependence on  $s$ . It is interesting to draw a comparison between the expression of  $M_{11}$  in the two formulations, namely Eqs. (3.23a) and (3.24). They both feature a dependence on the frequency response of the nominal plant, which is  $(sI_{n_x} - \mathcal{A})^{-1}$  for the latter and  $M_{22}$  for the former case. The frequency responses are then pre-post multiplied by non-square scaling matrices,  $V$  and  $W$  in Eq. (3.23) and  $\mathcal{A}_{12}$ ,  $\mathcal{A}_{21}$  and  $\mathcal{A}_{22}$  in Eq. (3.24), describing the effect of the perturbations on the system. Note however that the processes by which the two sets of scaling matrices are obtained, and their resulting meaning, are different. Firstly, in the state-space approach these must have a rational dependence on the frequency, whereas in the frequency-domain one they were allowed to be defined independently at each discrete frequency. Secondly, if aerodynamics uncertainties are considered, the scaling matrices describe perturbations in inherently different operators. These aspects, formally demonstrated in this section by explicitly showing the derivation of the LFT models starting from the two possible mathematical descriptions, are preparatory for the discussion in the next section.

### 3.2.2 Uncertainty description of aerodynamic operators

The aerodynamic operator, giving a relation between (generalised) elastic displacements and the corresponding generated loads, is one of the most relevant features of aeroelastic modelling, and standard expressions were discussed in Sec. 2.3. The original GAF matrix  $Q_{hh}$  is typically provided for flutter analysis purposes by a panel method-based solver and is available at discrete (reduced) frequencies. When the problem needs to be recast in state-space, approximate operators are used. In this work, Roger  $Q_{Rg}$  and Minimum State  $Q_{MS}$  approximations are employed, which were both shown to feature a general two-part approximation model based on quasi-steady and lag physical contributions (Eq. 2.3).

Uncertainty in the aerodynamic operator can be ascribed to different causes: limits of validity of the physical assumptions underlying the model (e.g. potential flow for panel method solvers); mismatch of the analytical results with experimental results or other more sophisticated computational tools (e.g. computational fluid dynamics); numerical approximations inherent to the adopted method (e.g. calculation of  $Q_{hh}$  on a discrete set of frequencies); and rational fitting of the approximate operators to name but a few. The objective of this section is to investigate

methodologies to capture these sources of uncertainties within the LFT development paths discussed in Sec. 3.2.1.

In order to provide numerical examples, the  $Q_{hh}$  matrix is based on the Theodorsen theory applied to the typical section system described in Sec. 2.3.1 with the geometrical properties from the case study in [134] (Appendix A.2.1). RFA approximations are performed in the range of reduced frequency  $k \in [0.01; 1]$  by selecting for Roger and Minimum State methods respectively 4 and 6 lag terms equally spaced between 0.1 and 0.7.

### 3.2.2.1 Reconciliation of different aerodynamic LFT descriptions

Let us denote by  $\mathcal{F}_u(Q_\bullet, \Delta_a)$  (where  $\bullet$  is any of  $\{hh, Rg, Ms\}$ ) the *aerodynamic LFT* capturing uncertainty in one of the available aerodynamic operators. For example, the LFT  $\mathcal{F}_u(Q_{hh}, \Delta_{hh})$ , with  $\Delta_{hh} = \text{diag}(\delta_{Q_{hh,12}}, \delta_{Q_{hh,21}}, \delta_{Q_{hh,22}})$ , describes the effect of uncertainties in the coefficients  $Q_{hh,12}$ ,  $Q_{hh,21}$  and  $Q_{hh,22}$  of the original GAF matrix. These are, recall (2.12), the three transfer functions between pitch  $\alpha$  and lift  $L_h$ , plunge  $h$  and pitching moment  $L_\alpha$ , and pitch  $\alpha$  and pitching moment  $L_\alpha$ . The uncertainty is defined such that the value of each uncertain transfer function ranges in the disc of the complex plane centred at the nominal value with uncertainty radius equal to 10% of its magnitude. This can be expressed with the additive uncertainty description for complex uncertainties, as exemplified next by the case for  $Q_{hh,12}$ :

$$Q_{hh,12} = Q_{hh0,12} + Q_{hh0,12} \lambda_{Q_{hh,12}} \delta_{Q_{hh,12}}, \quad (3.25)$$

$$\delta_{Q_{hh,12}} \in \mathbb{C}, \quad |\delta_{Q_{hh,12}}| \leq 1, \quad \lambda_{Q_{hh,12}} = 0.1.$$

The application of (3.25) to all the uncertain transfer functions lead to the definition of the weighting matrices  $V_Q$  and  $W_Q$  in (3.19d). Note that these weights have an arbitrary, that is not necessarily rational, dependence on frequency since they are a function of the nominal GAF  $Q_{hh0}$  (whose dependence on  $k$  was commented on earlier).

The LFTs  $\mathcal{F}_u(Q_{Rg}, \Delta_{Rg})$  and  $\mathcal{F}_u(Q_{Ms}, \Delta_{Ms})$  describe respectively the transfer matrices  $Q_{Rg}$  and  $Q_{Ms}$  when uncertainties in the quasi-steady part of the approximation  $\Gamma_{QS}$  are considered, whereas  $\Gamma_{lag}$  is for now kept at the nominal value. Recalling the definition from (2.4), this means that the matrices  $A_2$ ,  $A_1$  and  $A_0$  are perturbed. Specifically, the same three transfer functions and uncertainty range as above will be considered (note however that  $A_{0,21}$  is always null for physical reasons, since it represents the steady contribution of  $h$ ).

The resulting LFTs are defined by the uncertain blocks below:

$$\Delta_{hh}^{3,C} = \text{diag}(\delta_{Q_{hh,12}}, \delta_{Q_{hh,21}}, \delta_{Q_{hh,22}}), \quad (3.26a)$$

$$\Delta_{Rg}^{8,R} = \Delta_{Ms}^{8,R} = \text{diag}(\delta_{A_{0,12}}, \delta_{A_{0,21}}, \delta_{A_{0,22}}, \delta_{A_{1,12}}, \delta_{A_{1,21}}, \delta_{A_{1,22}}, \delta_{A_{2,12}}, \delta_{A_{2,21}}, \delta_{A_{2,22}}), \quad (3.26b)$$

where the size of the  $\Delta$  blocks and the type of uncertainties (real  $R$  or complex  $C$ ) is recalled in the superscripts. Fig. 3.3 shows the comparison of the LFT coverage for the transfer function between pitch  $\alpha$  and pitching moment  $L_\alpha$ . This is obtained by evaluating the aerodynamic LFTs

at random values of the uncertainty block. Magnitude and phase Bode plots are then presented for the three cases ( $hh$ ,  $Rg$  and  $MS$ ) as a function of  $k$ . The coloured area can be interpreted as the family of transfer functions originated by the provided uncertainty description. In the case of the approximated operators  $\mathcal{F}_u(Q_{Rg}, \Delta_{Rg})$  and  $\mathcal{F}_u(Q_{MS}, \Delta_{MS})$ , i.e. centre and right plot-columns, the families are almost identical, while the phase plot of  $\mathcal{F}_u(Q_{hh}, \Delta_{hh})$  in the left plot-column appears to cover a larger area.

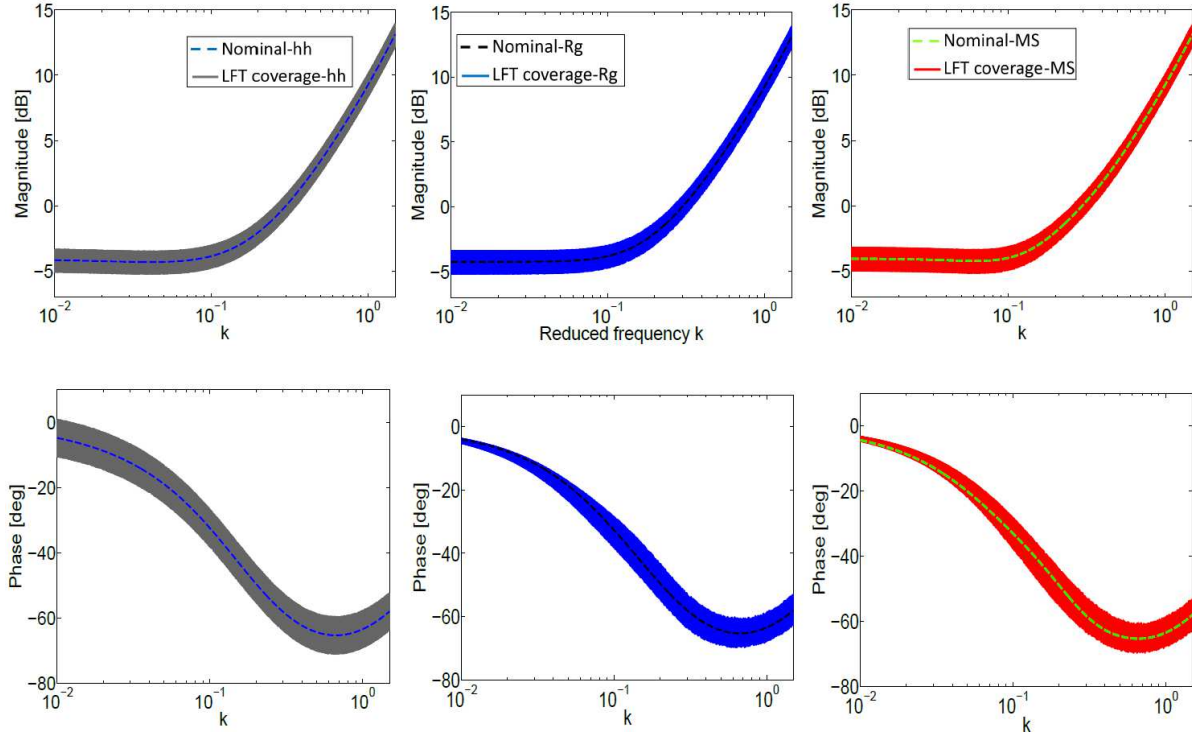


Figure 3.3: LFT coverage of the transfer function from  $\alpha$  to  $L_\alpha$  for  $Q_{hh}$ ,  $Q_{Rg}$  and  $Q_{MS}$ .

It is important to reflect on the fact that a comparison between the LFT associated with the frequency-domain operator ( $Q_{hh}$ ) and the two LFTs originating from the rational approximations ( $Q_{Rg}$  and  $Q_{MS}$ ) is not straightforward. Even when the same transfer functions are perturbed, the uncertainty description is different both in terms of captured features (for  $Q_{hh}$  the whole transfer function is involved, while in the latter two only the quasi-steady part) and in terms of number of uncertainties (see Eq. 3.26). Thus, no clear correspondence from one description to another exists in general. However, Fig. 3.3 provides physical insight into the variability captured by the LFTs. For instance, it suggests that taking into account perturbations in the quasi-steady contribution via  $\mathcal{F}_u(Q_{Rg}, \Delta_{Rg})$  and  $\mathcal{F}_u(Q_{MS}, \Delta_{MS})$  provides similar results to  $\mathcal{F}_u(Q_{hh}, \Delta_{hh})$  for the magnitude, whereas a narrower coverage of the phase diagram is registered. This is in accordance with physical understanding, since uncertainties in  $Q_{hh}$  will capture the whole mechanism underlying the generation of aerodynamic loads, whereas those in the quasi-steady part of the approximate operators only account for specific effects. Notably, the mismatch is mostly confined to the phase

response and this can be explained by noticing that only the quasi-steady part  $\Gamma_{QS}$  of  $Q_{Rg}$  and  $Q_{MS}$  is subject to uncertainties. Recall indeed that  $\Gamma_{lag}$  is used in RFA operators to reproduce, by means of high-pass filters, the unsteady effect consisting of a magnitude decrease and, most importantly, a phase shift with respect to the quasi-steady aerodynamic loads. Note also that the phase shift generated by a high-pass filter at a fixed frequency is dependent only on its cross-over frequency and is unrelated to the gain  $a$ :

$$\begin{aligned} H(\bar{s}) &= \frac{a\bar{s}}{\bar{s} + \gamma}, \quad \bar{s} = ik, \\ H(ik) &= \frac{a ik}{ik + \gamma} = \frac{ak^2 + iak\gamma}{k^2 + \gamma^2}, \quad \arg(H) = \tan^{-1}\left(\frac{\gamma}{k}\right). \end{aligned} \tag{3.27}$$

This shows that perturbations in  $\Gamma_{lag}$ , and in particular in the lag roots  $\gamma_i$ , allow variations in the phase response to be taken into account, and thus inaccuracies in the estimation of the unsteady part of the loads to be captured. Moreover, (3.27) provides a quantitative indication of the effect on the frequency response of uncertain lag roots, and thus, it can be used to calibrate the amount of uncertainty in them based on experimental or numerical data describing the expected aerodynamic behaviour in terms of load generation. It is interesting to observe for example that the lag root effect in phase shifting highly depends on the reduced frequency  $k$ , and thus a weight function of the frequency is envisaged to properly model this uncertainty. In conclusion, the scenario in Fig. 3.3 is ascribed to the fact that only uncertainties in  $\Gamma_{QS}$  were considered and thus the observed mismatch would be reduced by introducing perturbations in  $\Gamma_{lag}$  in accordance with the rationale discussed above.

Motivated by this, in [122] further analyses of the type shown in Fig. 3.3 were performed considering lag uncertainty. Firstly, it was concluded that the two LFTs  $\mathcal{F}_u(Q_{Rg}, \Delta_{Rg})$  and  $\mathcal{F}_u(Q_{MS}, \Delta_{MS})$  with the same uncertainty level in the lag roots lead to considerably different coverage. This was somehow expected since the definition of  $\Gamma_{lag-Rg}$  and  $\Gamma_{lag-MS}$  is different, as stressed in the comments below Eq. (2.6). Secondly, all the aerodynamic transfer functions are perturbed as a result of introducing uncertainty in  $\Gamma_{lag}$ . In fact, by looking at the approximation formula (Eqs. 2.5-2.6) it can be inferred that each high-pass filter influences all the terms in the transfer matrix. This is in contrast to what happens for  $\mathcal{F}_u(Q_{hh}, \Delta_{hh})$ , where the uncertainty is specified directly in each term of the transfer function and thus only the corresponding frequency responses are affected. In summary, when adopting RFA operators the introduction of uncertainty in the lag terms can be physically motivated by the interest in capturing particular features (e.g. phase shift), but this automatically implies perturbing all the transfer functions. Moreover, it is not clear in principle how to define the range of variations of the cross-over frequencies since this might depend, for example, on the approximation algorithm.

Prompted by these findings, a general approach is proposed to correlate LFTs of different aerodynamic operators (possibly affecting different transfer functions). The worst-case  $\mathcal{H}_\infty$  norm of the aerodynamic operator in the face of the allowed perturbations is assumed as metric. Then, the *aerodynamic worst-case gain*  $\gamma^Q$  associated with an aerodynamic LFT  $\mathcal{F}_u(Q, \Delta_Q)$  for a given

bound on the  $\mathcal{H}_\infty$  norm  $\omega$  of the uncertainty matrix  $\Delta_Q$  is defined:

$$\gamma^Q(\mathcal{F}_u(Q, \Delta_Q), \omega) = \max_{\|\Delta_Q\|_\infty \leq \omega} \|\mathcal{F}_u(Q, \Delta_Q)\|_\infty. \quad (3.28)$$

Once  $\omega$  is fixed,  $\gamma^Q$  is a term of comparison among different uncertainty descriptions. The problem in (3.28) is in the form of a worst-case performance test and there exist available algorithms to solve it [179], which frame the numerical problem as a  $\mu$  calculation. In practice,  $\gamma^Q$  can be easily computed with the command *wcgain* of the Robust Control Toolbox in MATLAB [14] once  $\mathcal{F}_u(Q, \Delta_Q)$  and  $\omega$  are provided. Note that there is a crucial difference between the *normalisation* of the set associated with the LFT (typically  $\bar{\sigma}(\Delta_Q) \leq 1$ ) and the *constraint* involving  $\omega$ . The former is performed in the LFT construction stage by scaling the partitioned matrix  $Q$  and is without loss of generality, while the latter defines the allowed variation in the worst-case problem and has a direct impact on the achieved performance (larger  $\omega$  will determine worse performance).

Let us consider a given *reference* aerodynamic LFT  $\mathcal{F}_u(Q_r, \Delta_r)$  and a *tested* LFT  $\mathcal{F}_u(Q_t, \Delta_t)$ . The objective is to determine an uncertainty level for the parameters of the tested LFT such that  $\Delta_t$  maps  $Q_t$  in a similar family to  $\mathcal{F}_u(Q_r, \Delta_r)$ . An algorithm is proposed next to address this task.

**Algorithm 3.1.** *Mapping tested LFT into reference LFT*

**Outputs:** The uncertainty levels vector  $\Lambda = [\lambda_1; \dots; \lambda_i; \dots; \lambda_{n_p}]$  associated with the additive uncertainty description of the  $n_p$  parameters of  $\Delta_t$ .

**Inputs:**  $\mathcal{F}_u(Q_r, \Delta_r)$  (normalised such that  $\bar{\sigma}(\Delta_r) \leq 1$ ) and  $\mathcal{F}_u(Q_t, \Delta_t)$ ; a first guess  $\Lambda_0$ ; positive tolerance parameter  $\epsilon$ ;  $\omega$  (default value 1).

0. Compute  $\gamma_r^Q$  using (3.28),  $\mathcal{F}_u(Q_r, \Delta_r)$ , and  $\omega$ ; set  $\delta_\gamma = 2\epsilon$  and Set  $\Lambda = \Lambda_0$ .

**While**  $|\delta_\gamma| > \epsilon$  **do**

1. Normalise  $\mathcal{F}_u(Q_t, \Delta_t)$  such that  $\bar{\sigma}(\Delta_t) \leq 1$  using  $\Lambda$ .

2. Compute  $\gamma_t^Q$  using (3.28),  $\mathcal{F}_u(Q_t, \Delta_t)$ , and  $\omega$ .

3. Evaluate  $\delta_\gamma = \left( \frac{\gamma_r^Q - \gamma_t^Q}{\gamma_r^Q} \right)$ .

4. Update the uncertainty vector  $\Lambda \leftarrow (1 + \delta_\gamma) \Lambda$ .

**return**  $\Lambda$

**Remark 3.1.** Algorithm 3.1 is iterative, and different options can be tuned to improve the accuracy of the outcome. For example, the proposed rule in Step 4 does simply update the vector of uncertainty levels  $\Lambda$  by uniform scaling. Alternatively, based on the understanding of the role of the uncertain parameters, a vector of weights  $\Lambda_w \in \mathbb{R}^{n_p}$  can be selected and the update rule defined as  $\Lambda_0 \leftarrow (1 + \delta_\gamma \Lambda_w) * \Lambda$ , with  $*$  indicating the component-wise product.

*Note also that different values for  $\omega$  can be used. Based on the analyses performed in support of the work, this option has a very small influence on the final  $\Lambda$ . Certainly, the algorithm will provide different values of  $\gamma^Q$  depending on  $\omega$  (because the worst-case performance depends on the allowed variation of the uncertainties), but the same vector of uncertainty levels  $\Lambda$  is obtained.*

The objective of Algorithm 3.1 is to inform the selection of the number and/or type of uncertain parameters and their uncertainty range in order to cover a family of given (reference) frequency responses. Even though the method has been originally devised to calibrate the amount of uncertainty in a tested LFT such that it generates a similar coverage (in the sense described in Fig. 3.3) to a reference one, its application is quite general.

For example, it could be applied to address the problem of defining the uncertainty in the lag terms of two LFTs derived by different rational approximations. This latter goal was pursued in [122] where a satisfactory overlapping between the two families of transfer functions was achieved by applying Algorithm 3.1 to redefine the uncertainty levels of the lag terms in the LFT relative to the Minimum State method based on the given LFT corresponding to the Roger method. A comparison in terms of robust flutter predictions will be discussed in Sec. 4.2.1.

Alternatively, the reference family can consist of experimental data or high fidelity numerical simulations for which a frequency-domain characterisation is available. In case of nonlinear simulations, this characterisation can be obtained by linearising the response about the studied operating points [162]. The objective would be then to tailor the uncertainty description (in terms of uncertain parameters and corresponding ranges defined in  $\Lambda$ ) such that the reference results lie within the uncertainty set defined by the tested LFT. In this case,  $\gamma_r^Q$  is provided in Step 0 by the supremum over the frequencies of the maximum singular value of the reference frequency responses.

**Remark 3.2.** *Algorithm 3.1 belongs to the class of control-oriented model validation schemes [225], where the goal is to assess whether the proposed model can generate a given set of input/output data. Relevant to this work, in [144] a frequency-domain test was developed to validate (or invalidate) the description provided by an LFT model. The problem is recast, through the inverse LFT theorem, as a  $\mu$ -test associated with a conveniently derived LFT function of the tested model and the input/output data. The difference here is that the worst-case  $\mathcal{H}_\infty$  norm is used as metric, based on the assumption that it is relevant to characterise uncertainty in the aeroelastic operators used for robust flutter analysis (the adoption of  $\mathcal{H}_\infty$  control strategies to tackle the active flutter suppression problem [238] is another example of this reasoning).*

### 3.2.3 A unified LFT modelling approach

In the previous subsection qualitative (based on the visualisation of the LFT coverage) and quantitative (Algorithm 3.1) strategies have been proposed to relate LFT models of different aerodynamic operators. However, as emphasised therein, there are intrinsic difficulties in reconciling

the aerodynamic uncertainty description made within the frequency-domain framework with the one derived from a state-space formulation. In fact, the latter only allows uncertainties to be applied to the building blocks of the approximated operators. This means that the uncertainties can be introduced in the quasi-steady part (not capturing the phase frequency response variability) or in the lag terms of the unsteady part (but this affects the full transfer matrix and not only specific transfer functions as it is often desired).

In addition to that, it is not clear which of the two development paths discussed in Sec. 3.2.1 is preferable, since each has different advantages. For example, adopting the uncertainty description allowed by the frequency-domain framework can help taking into account physical considerations in the aerodynamic uncertainty definition. For instance, if a lack of accuracy, based on the evidence of experimental results or high-fidelity simulations, is detected in specific loads generation mechanisms (e.g. from control surface rotation to pitch moment on the section), this could be captured directly with the additive description in (3.19d). Also, the coefficients of  $Q_{hh}$  are complex and so are the associated uncertainties, with notable improvement on the accuracy and computation time of the  $\mu$  analysis. It is indeed often desired to recast the problem such that it consists of a mixed-perturbation matrix formed by real and complex uncertainties with physical meaning to regularise the  $\mu$  lower bound computation [183]. Another aspect is that in this case the weighting matrices defining the range of variation of the uncertainties can have any type of dependence on the frequency (recall the discussion on  $V$  and  $W$ ), which enhances the uncertainty description options available to the analyst.

While these aspects would tend to favour the frequency-domain formulation, a clear advantage of the state-space approach is that this is the setting where other tasks in addition to linear robust flutter analysis are framed. For example, robust control design for flutter suppression and/or on-line robust predictions during flight tests. Indeed, these tasks have only been demonstrated using the state-space approach [149, 238], since well-consolidated algorithms dictated which framework had to be employed. Advanced robust analysis techniques such as Integral Quadratic Constraints also relies on state-space models [133], even though frequency-domain formulations have also started to emerge [61]. It would then be preferable, and more practical, to apply  $\mu$  analysis directly to the same models used for the aforementioned tasks (e.g. investigating robustness of the closed-loop synthesised with state-space models).

The interest for a unified framework which keeps the advantages of both the approaches is hence natural, and its formulation is the goal of this section. To this end, recall the definitions of the sub-matrix  $M_{11}$ , given for each of the two formulations in respectively (3.23a) and (3.24). Their formal equivalence, already noted, suggests that the only restriction in providing an aerodynamic uncertainty description for the state-space formulation akin to what is done in the frequency-domain lies in the scaling matrices. In particular, they must have a rational dependence on the frequency in the state-space approach, leading to the analytic expression in (3.24), whereas they are built at each frequency point in (3.23), and so are allowed to freely vary with  $\omega$ , in the

frequency-domain approach. To provide a unified formulation, it is leveraged the fact that, due to the algorithmic implementation, the  $\mu$  test (3.12) considers a grid of the analysed frequency range. As a result, the proposed expression for  $M_{11}$  is:

$$M_{11}(s, \bar{s}) = \mathcal{A}_{22}(\bar{s}) + \mathcal{A}_{21}(\bar{s})(sI_{n_x} - \mathcal{A})^{-1}\mathcal{A}_{12}(\bar{s}). \quad (3.29)$$

Note the formal similarity with (3.24), with the important difference that  $\mathcal{A}_{22}$ ,  $\mathcal{A}_{21}$ , and  $\mathcal{A}_{12}$  depend on the dimensionless Laplace variable  $\bar{s}$ , and thus  $M_{11}$  does not have anymore an LFT representation. However, the nominal plant is represented as in (3.24) by  $\mathcal{A}$ , i.e. the state-space model is used as basis for modelling.

The task of obtaining the scaling matrices in (3.29) is illustrated next. The uncertainty description associated with the structural parameters is unaffected and follows either of the approaches outlined in Sec. 3.2.1. For the aerodynamic uncertainties, it is observed that only the aeroelastic stiffness matrix  $K$ , defined in (2.9), is involved. Recall from Sec. 2.3 indeed that the GAF matrix provides a relation between displacements (but not speeds or accelerations) and loads. This matrix can thus be written as:

$$K = K_s - \frac{1}{2}\rho_\infty V^2 A_0 - V_Q(\bar{s})\Delta_Q W_Q(\bar{s}). \quad (3.30)$$

The nominal part of the aeroelastic stiffness matrix (i.e. the first two terms in the right hand side) is given by the state-space model, while the uncertainty part follows the frequency-domain formulation in (3.19d). This representation at operator level provides, at LFT level, the expression for  $M_{11}$  in (3.29).

Summing up, at each frequency of the chosen grid the expression of the uncertain state-matrix is defined by making use of (3.30) for the aerodynamic part and the standard procedures for the other contributions. The calculation of  $M_{11}$  can then be performed and, by sweeping the analysed frequency range, the frequency-response input for the  $\mu$  calculation is provided. The proposed strategy, which will be validated with the analyses shown in Sec. 4.2.1, can be interpreted as a particular application of unmodelled dynamics uncertainty [269].

**Remark 3.3.** Once  $M_{11}(s, \bar{s})$  has been computed at discrete frequencies using Eqs. (3.29)-(3.30), a rational approximation can be performed if an expression of  $M_{11}$  as LFT is sought (this is not strictly necessary for the application of  $\mu$  analysis but it has other benefits already discussed). This is a common task in robust control, and could be addressed for example with the curve fitting techniques used in  $\mu$ -synthesis to realise minimum phase  $D(s)$  and  $G(s)$  scalings from frequency-domain data  $D(i\omega)$  and  $G(i\omega)$  [181]. This aspect has not been tested in detail in this work, but it represents a potential direction to develop in future applications.

### 3.3 Coupling LFT modelling with Fluid-structure interaction solvers

Section 3.2 has investigated the main steps required to build LFT models of aeroelastic systems from the two standard starting points, namely frequency-domain and state-space. Since this distinction mainly lies in the choice for the aerodynamic operator, the relative issues were amply discussed, whereas no emphasis was put on the modelling of the structural operators. That is, an uncertainty description in the form of Eqs. (3.19a-3.19c) was assumed to be available. Recall from the discussion in Sec. 2.3.3 that for real aeronautical applications these operators are typically obtained with high-fidelity Finite Element Method (FEM) solvers and thus practical issues might arise. Among these, the increase in the size of the problem can be identified as one of the most compelling. A solution consists of applying a modal decomposition to the original high dimensional problem and considering only a reduced set of modes for robust modelling and analysis (modal truncation). Unfortunately, with this approach the connection between the uncertain parameters defined in the reduced model and the physical sources of uncertainties is lost. In fact, the latter are well detectable in the fluid-structure interaction solver where the high-order matrices are assembled, but their reconciliation with the uncertain parameters in the LFTs is not straightforward. Even though this is a paramount aspect to profitably make use of the uncertain models, it has not received yet full consideration by the community. This section will address these aspects by reviewing standard approaches in the literature, based on numerical interpolation of LFT models, and proposing possible improvements to them (Section 3.3.1). These considerations pave the way for the proposal of a novel symbolic approach directly integrating the LFT step into the Fluid-structure interaction (FSI) solver, so called LFT-FSI modelling strategy (Section 3.3.2).

#### 3.3.1 Standard numerical LFT modelling approaches and possible improvements

The LFT modelling of high-order systems is typically accomplished via numerical approaches. They are based on evaluating the model at scattered values of the parameters in the uncertainty set, followed by a model-order reduction (possibly after having linearised it, if the system is non-linear) to obtain lower-size LTI representations. The family of LTI systems is then interpolated so that a polynomial description is obtained. Finally, algorithms which allow polynomial expressions to be recast into LFTs are applied [20, 156, 160].

This approach has been applied already to aeroelastic systems in the last two decades, with examples discussed next. In [244] a systematic approach to perform these sequential operations was presented. It was claimed that standard modal truncation cannot be employed as reduction technique because numerical and modal consistency problems can be encountered. Consistency among the reduced LTIs is highly desirable for the accuracy of the resulting interpolation (e.g.

it guarantees regular modal trajectories and frequency responses with respect to the uncertain parameters), but it is no straightforward to achieve with the standard procedure. A possible remedy was discussed in [197], where advanced model reduction strategies, specifically tailored to allow the LFT nature of the final representation to be exploited in the interpolation step, were employed. In both cases [197, 244], the accuracy of the LFT was only validated by comparing eigenvalues and frequency-domain indicators (e.g. Bode plots), but no  $\mu$  flutter analysis was pursued. Thus, there was no validation of the results in terms of worst-case perturbations and resulting flutter speeds with respect to the original high-order system.

This type of validation was addressed in [22], which showed that the robust predictions were able to aid in the comprehension of phenomena observed during flight. However, only a small number of uncertainties was considered and there was no mention of systematic approaches to deal with broader uncertainty sets. Thus, it is deemed relevant to propose improvements on the existing numerical LFT-modelling methodologies in order to tackle the restrictions and limitations noted above.

Let us start by considering the case of perturbations in the structural operators only, since this is the main focus here. Once the corresponding uncertainty set is defined (for conciseness, this will be denoted simply by  $\Delta$  henceforth), an appropriate number of samples  $n_{pts}$  must be selected. A good initial guess is represented by the vertices of the set, i.e. all the possible combinations of the extreme values of the uncertainties. For cases with a large number of uncertainties this will be prohibitively large, i.e.  $n_{pts}=2^{n_\delta}$  where  $n_\delta$  is the number of independent parameters in  $\Delta$ . In these cases it might be necessary to perform a sensitivity analysis and apply as well engineering judgement to reduce the number of samples.

For each sample, the FEM solver is run and the generalised modal operators  $\bar{M}_s$ ,  $\bar{C}_s$ , and  $\bar{K}_s$  are evaluated. This leads to a family of matrices  $\bar{M}_s(\Delta)$ ,  $\bar{C}_s(\Delta)$ , and  $\bar{K}_s(\Delta)$  which are interpolated to find polynomial approximations. This step can be performed, for example, by means of the APRICOT library [207] of the SMAC toolbox [28]. This library offers a wealth of routines to perform the polynomial interpolation more efficiently than the classically employed least-square method, e.g. the routine *olsapprox* implements an orthogonal least-square method that allows obtaining a multivariate sparse polynomial approximation for the coefficients of the matrices. Sparsity is a highly advantageous feature since it alleviates the issue of data overfitting and it has the benefit to minimise the size of the resulting LFT. Finally, the polynomial modal matrices are converted into LFTs, hence an uncertainty description akin to Eqs. (3.19a-3.19c) is available, and either of the LFT development paths discussed in Sec. 3.2.1 can be followed to build up the aeroelastic LFT model.

An important feature of the proposed improvement is the application of the interpolation separately to the modal operators (i.e.  $\bar{M}_s$ ,  $\bar{C}_s$ , and  $\bar{K}_s$ ) instead of directly to the state-matrix  $\mathcal{A}$ . This is referred here as *modal-oriented* approach, to stress that the LFT transformation is applied to the distinct modal operators, rather than to the final state-matrix [197]. This helps

reducing the size of the final LFT, as well as achieving the other benefits enumerated next.

First, it is apparent that this strategy holds for both the frequency-domain and state-space formulations, whereas the standard approach would only apply to the latter. Since it interpolates directly modal quantities, this algorithm automatically provides state vector consistency among the different interpolated operators, which in previous applications proved to require an additional step [244]. Indeed the modal content is discerned with this approach at the structural operator level and not at the aeroelastic one (Eq. 2.7) where the coupling with aerodynamics makes it more difficult. A further advantage is that it is possible to generate different LFTs, each characterised by a fixed number of modes  $n_{s,u}$  affected by uncertainties (with  $n_{s,u} \leq n_s$ , where  $n_s$  is the number of modes retained in the modal decomposition). This allows the minimum number of modes where uncertainties have to be introduced to obtain a valid flutter analysis result to be identified. By doing so, a lower size aeroelastic LFT model to be employed in subsequent extensive robust analyses can be provided. Moreover, by considering cases featuring different  $n_{s,u}$ , the analyst can gain insights into the instabilities affecting the system.

With respect to the case of aerodynamic uncertainties, the aspects discussed in Sec. 3.2.2 can be adopted in this context, too. It is important to note that an additional source of uncertainty, distinctive of high-fidelity models, is the variation in structural parameters. Indeed, recall from Sec. 2.3.3.2 that the GAF matrix  $Q_{hh}$  depends, through the Kernel  $\tilde{K}$  (Eq. 2.24), on the structural modes  $\Phi$ . In principle, this can be taken into account similarly to what is done for the structural operators, i.e. generating a polynomial interpolation of  $Q_{hh}$  at a fixed reduced frequency. However, this could be computationally demanding depending on the number of frequencies analysed. Alternative solutions exist. A frequency-domain characterisation of the uncertainty can be estimated and captured as unmodelled dynamics [135]. This characterisation could also be used to inform a more refined uncertainty description of the affected transfer functions in  $Q_{hh}$ , which could then be implemented with the unified approach from Sec. 3.2.3. Algorithm 3.1 can also be employed with the goal to define uncertainties in the aerodynamic LFT able to map a set of aerodynamic data obtained perturbing the structural parameters.

### 3.3.2 A symbolic LFT-FSI modelling approach

The uncertainty modelling approach discussed in Sec. 3.3.1 is regarded as the state-of-practice when analysing complex systems with the LFT paradigm, but some drawbacks can be observed in relation with: i) accuracy of the LFT as a result of the polynomial interpolation, ii) uncertainty descriptions allowed, and iii) computational efficiency.

Because it relies on a polynomial interpolation, the accuracy of the numerical LFT depends on the uncertainty set considered. To exemplify this aspect, consider Fig. 3.4 where the subdivision in  $N$  stations of a notional aircraft wing is depicted. These can be interpreted as the areas of the wing where perturbations on the mass and stiffness parameters' nominal values are expected, and so their influence on flutter must be ascertained. Alternatively, each of these regions can be

thought of as the variable space of the structural parameters that can be exploited to obtain by design an improved aeroelastic behaviour, and thus a better understanding of their influence on flutter is valued. From both perspectives, it is then natural to aim at considering a description characterised by, with reference to Fig. 3.4, large  $N$  (i.e. refined stations grid) and localised parameters (e.g. a small concentrated mass  $\delta_{M_i}$  in a wing station).

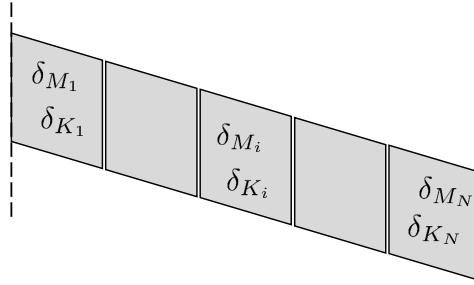


Figure 3.4: Schematic uncertainty description of a notional aircraft wing.

This uncertainty description might prove to be challenging when the numerical LFT approach is pursued. The selection of a large number of uncertain parameters as well as of very localised uncertainties (e.g. small nominal values and/or uncertainty ranges) might hamper the effectiveness of the LFT modelling and the  $\mu$  analysis algorithms. The ensuing interpolation can indeed: be inaccurate (e.g. small variations in localised uncertainties might not be well captured; or a large number of uncertainties might force to consider a coarse parametric grid); lead to intractable LFTs (due to the  $\Delta$ -block size); or be computationally intensive (due to the large number of samples to be computed with the FSI solver). This is indirectly confirmed by examples from the literature [22, 197, 244], where a maximum of three parameters were considered, all representing large quantities (e.g. extreme filling levels of the fuel tanks). As for the computational aspects, in addition to what was said before, note that the numerical LFT approach must be performed anew for any change in the model, and this could be costly depending on the density of the parametric grid and the algorithm employed to perform the polynomial interpolation. The aforementioned aspects prompted the research for alternative LFT modelling strategies, driven by the aim to preserve a close connection between physical source of uncertainties and LFT parameters.

### 3.3.2.1 Symbolic modelling algorithm

The fundamental idea behind the proposed strategy is to perform the LFT modelling task at FSI solver level. By this, it is meant that the uncertain parameters are introduced in the solver when the high-fidelity operators are assembled as described in Sec. 2.3.3.1. The approach proposed here is tailored to structural operators obtained via FEM solvers, but the acronym FSI is used to emphasise the general idea underlying the approach and the fact that other modules (e.g. Doublet Lattice Method) are also indirectly involved.

The steps entailed by this algorithm are listed in Algorithm 3.2, and illustrated in the flow chart of Fig. 3.5.

**Algorithm 3.2.** *Symbolic LFT-FSI modelling algorithm's pseudocode*

**Outputs:** aeroelastic LFT  $\mathcal{F}_u(M, \Delta)$ .

**Inputs:** nominal model, uncertainty set  $\Delta$ , modal matrix  $\Phi$ , aerodynamic operator (based on  $\Phi$ ).

1. Step-S1. Define symbolic parameters associated with the elements in  $\Delta$ .
2. Step-S2. Assemble the symbolic physical matrix inside the structural solver.
3. Step-S3. Compute the symbolic modal matrices via modal truncation using  $\Phi$ .
4. Step-S4. Build an LFT representation of the symbolic modal matrices.
5. Step-S5. Build the aeroelastic LFT with either the state-space or frequency-domain formulations.

To exemplify the main features of the approach, let us consider the structural mass matrix  $M_{B_j}$  of the beam  $j$  which will contribute to the structural matrix  $M_s$  (see also the *Example* box in Fig. 3.5):

$$M_{B_j} = \begin{bmatrix} M_{tt} & M_{tr} \\ M_{tr} & M_{rr} \end{bmatrix}, \quad \begin{aligned} M_{tt} &= F_1(L_j, m_j, I_{z_j}, I_{y_j}), \\ M_{tr} &= F_2(L_j, m_j, I_{z_j}, I_{y_j}), \\ M_{rr} &= F_3(L_j, m_j, I_{z_j}, I_{y_j}), \end{aligned} \quad (3.31)$$

where the subscripts  $t$  and  $r$  refer to translational and rotational DOFs. The parameters  $L_j$ ,  $m_j$ ,  $I_{z_j}$  and  $I_{y_j}$  are respectively the beam length, mass and moments of inertia, while  $F_1$ ,  $F_2$  and  $F_3$  are generic matrix functions. When some of these properties are considered uncertain and thus the functions are not evaluated at the corresponding nominal values, the local physical operator  $M_{B_j}$  is a matrix function of the uncertainties. If the parameters are defined as symbolic objects (Step-S1), then  $M_{B_j}(\Delta(\delta_{j-\bullet}))$  where  $\bullet = L, m, I_z, I_y$ , is a symbolic operator that will contribute to the physical mass matrix, itself a symbolic operator  $M_s(\Delta)$  (Step-S2). This step is general and can be applied to other contributions to the mass operator (e.g. concentrated masses) and to other operators (e.g. stiffness).

Once the *symbolic* physical matrices are obtained with the procedure outlined before, a modal truncation is performed (Step-S3):

$$\begin{aligned} \bar{M}_s(\Delta) &= \Phi^\top M_s(\Delta)\Phi, \\ \bar{C}_s(\Delta) &= \Phi^\top C_s(\Delta)\Phi, \\ \bar{K}_s(\Delta) &= \Phi^\top K_s(\Delta)\Phi, \end{aligned} \quad (3.32)$$

where  $\Delta$  indicates the uncertainty set gathering the symbolic parameters. Note that this relationship is formally identical to the standard modal truncation used in aeroelastic analysis (Eq. 2.2), with the notable difference that the physical matrices are now expressed as symbolic objects.

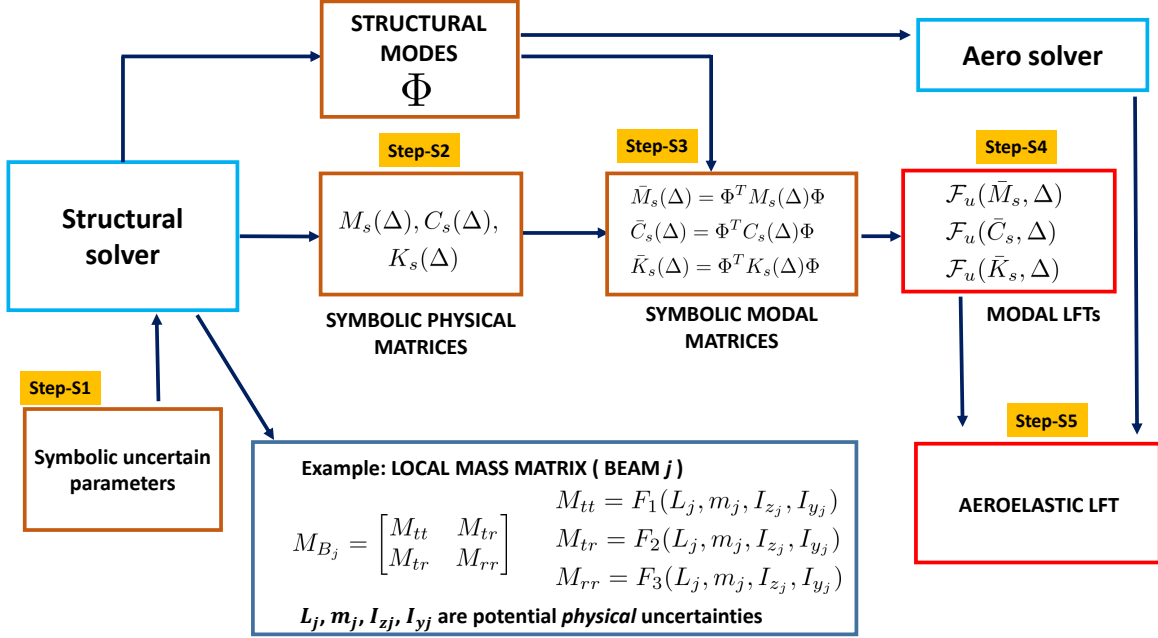


Figure 3.5: Block diagram of the symbolic modelling algorithm.

Given the symbolic modal matrices  $\bar{M}_s$ ,  $\bar{C}_s$  and  $\bar{K}_s$  obtained from Eq. (3.32), it is possible to apply standard LFT algorithms [156] which allow polynomial matrices to be recast as an LFT. In this way, the modal LFTs  $\mathcal{F}_u(\bar{M}_s, \Delta)$ ,  $\mathcal{F}_u(\bar{C}_s, \Delta)$ ,  $\mathcal{F}_u(\bar{K}_s, \Delta)$  are obtained (Step-S4). The final step consists of building up the aeroelastic LFT (Step-S5), which can be done by following either the state-space or frequency-domain development path.

The implementation of the LFT modelling *inside* the FSI solver deserves mention. If the FSI solver is available in MATLAB, as it was the case in the research carried out here, the uncertain physical parameters can be defined as symbolic objects in Step-S1 by means of the Symbolic Math toolbox [164]. This allows to work in Step-S2 and Step-S3 with symbolic objects and then, by means of the LFR toolbox [156], convert them into LFTs (Step-S4) which can then be efficiently handled as LFR objects throughout Step-S5. However, the method discussed in this section can in principle be applied also when the FSI solvers are implemented using other coding languages, thus the implementation aspects should not be regarded as a limitation. For example, in [105] the FORTRAN-based library SLICOT has been interfaced with the symbolic computational language MAPLE to provide computationally efficient framework for LFT modelling.

### 3.3.2.2 Modal bases selection

A crucial aspect to be captured is the effect of the uncertainties on the modal matrix  $\Phi$ . Indeed, the latter in turn modifies both structural and aerodynamic operators, as marked by the two arrows in Fig. 3.5. First, it should be noted that many of the approaches to structural uncertainty

descriptions assume for the robust analyses a fixed modal base (typically the one corresponding to the nominal system) [22, 33, 150, 175]. This is an approximation and potentially a source of error in the predictions since  $\Phi$  is altered when there are structural uncertainties in  $\Delta$ , and different possible solutions have been investigated in the community. In [45] a first-order dependence of the structural modes on the uncertain parameters based on the application of perturbation theory [201] was proposed. This strategy is appealing since it allows the modal matrix to be expressed analytically as a function of the uncertainties, i.e.  $\Phi(\Delta)$ . However, it also presents important drawbacks as observed in [106], where different approaches to tackle the modal bases selection were discussed. The perturbed modal base approach is deemed therein the most computationally expensive among them due to the resulting LFT size, and the linear modal shapes variation hypothesis is shown to be erroneous, even for relatively simple wing geometry layouts, as the structural uncertainties ranges increase. Higher order Taylor expansions can be considered [86], but the overall LFT size grows significantly, making the ensuing analyses numerically intractable or compromising their accuracy. An interesting idea discussed in [106] consists of updating the modal base with the worst-case perturbations obtained by  $\mu$ . This represents the premise of the approach taken in this work.

Note first that, when the operation in Eq. (3.32) is performed, the symbolic modal matrices are generally full. This is a source of error related to the fixed modal base assumption, because due to eigenvectors properties, the modal mass and stiffness matrices are always diagonal. That is, regardless of the specific perturbation matrix affecting the system, the perturbed modal matrices will be diagonal. By exploiting the embedding of the LFT modelling in the FSI solver and the adoption of a modal-oriented approach, this inaccuracy can be eliminated a priori by retaining only the diagonal terms of the matrices (Step S-3 in Fig. 3.5):

$$\begin{aligned}
 \bar{M}_s(\Delta) &\equiv \text{diag}(\Phi^\top M_s(\Delta)\Phi), \\
 \bar{C}_s(\Delta) &\equiv \text{diag}(\Phi^\top C_s(\Delta)\Phi), \\
 \bar{K}_s(\Delta) &\equiv \text{diag}(\Phi^\top K_s(\Delta)\Phi).
 \end{aligned} \tag{3.33}$$

While this modification of Step-S3 allows to mitigate and confine the error in the symbolic modal matrices to the diagonal terms, the fixed modal base assumption can still lead to wrong predictions. For example, the effect of perturbations in  $\Phi$  on the aerodynamic operator must still be addressed.

Prompted by these observations, an iterative algorithm is formulated with the aim to determine (if it exists) a worst-case perturbation  $\hat{\Delta}^{cr}$ , associated with the LFT built with Algorithm 3.2. The attribute *worst-case* is used to emphasise that the matrix  $\hat{\Delta}^{cr}$  represents the smallest combination of uncertain parameters that makes the system flutter at a user-provided speed  $V_\mu$  (smaller than the nominal flutter speed  $V_f$ ). However, it will be discussed later (Sec. 3.3.2.3) that, due to the non-convexity of the underlying optimisation problem, it cannot be mathematically guaranteed that smaller perturbations such that  $V_\mu$  becomes the flutter speed do not exist. It is important to note that Algorithm 3.2 is tailored for LFT models employed for  $\mu$  analysis purposes,

because it requires the availability of a worst-case perturbation matrix. When the LFT models are built up for other applications than linear robust stability analysis, Algorithm 3.2 can still be applied together with the improvements obtained with Eq. (3.33). The following pseudocode details the steps of the iterative scheme, which is schematically illustrated in Fig. 3.6.

**Algorithm 3.3.** *Iterative algorithm for finding a worst-case perturbation*

**Outputs:** a worst-case perturbation  $\hat{\Delta}^{cr}$  such that  $V_\mu$  is the flutter speed.

**Inputs:** speed  $V_\mu$  smaller than the nominal flutter speed  $V_f$ , symbolic physical matrices  $(M_s(\Delta), C_s(\Delta), K_s(\Delta))$ , nominal modal matrix  $\Phi_0$ , tolerance  $\epsilon_V$ ,  $V_{f\mu} = 0$ .

**While**  $|V_\mu - V_{f\mu}| \geq \epsilon_V$  **do**

1.  $\Phi \leftarrow \Phi_0$ .

2. Step-A1. Using  $\Phi$ , update the aerodynamic operator and apply Algorithm 3.2 from Step-S3 to generate an aeroelastic LFT.

3. Step-A2. Compute  $\mu$  using the aeroelastic LFT from Step-A1.

4. Step-A3. Extract  $\Delta^{cr}$  (associated with the highest peak of  $\mu$ ) and compute  $V_{f\mu}$  (flutter speed of the perturbed system) in the FSI solver.

5. (optional) Check optimality of the worst-case perturbation.

6. Step-A4. Compute  $\Phi^{cr}$  from  $\Delta^{cr}$ .

7.  $\Phi_0 \leftarrow \Phi^{cr}$ ,

**return**  $\hat{\Delta}^{cr}$

The algorithm requires as input the symbolic physical matrices  $M_s(\Delta)$ ,  $C_s(\Delta)$ , and  $K_s(\Delta)$  from Step-S2 of Algorithm 3.2, which are held fixed throughout the iterations. The process is then started by initializing  $\Phi$  with the nominal modal matrix  $\Phi_0$ . This allows the aeroelastic LFT to be built (Step-A1) and a standard  $\mu$  analysis to be performed (Step-A2). The perturbation matrix  $\Delta^{cr}$  corresponding to the highest peak of the lower bound  $\mu_{LB}$  is extracted, and the associated flutter speed  $V_{f\mu}$  can be calculated with the FSI solver once the predicted perturbations in the uncertain parameters have been applied (Step-A3). The evaluation of  $V_{f\mu}$  in Step-A3 is standard and can be performed for example with one of the algorithms for nominal flutter analysis discussed in Sec. 4.1. If the difference between  $V_{f\mu}$  and the expected perturbed flutter speed  $V_\mu$  is greater than a given tolerance  $\epsilon_V$ , the modal base is updated with the matrix  $\Phi^{cr}$  corresponding to  $\Delta^{cr}$  (Step-A4) and a new iteration is performed until convergence. It is stressed the difference between  $\Delta^{cr}$  and  $\hat{\Delta}^{cr}$ . The former is provided by the  $\mu$ -lower bound computation at a generic iteration and, due to the modal base error, will not correspond in general to a flutter speed equal to  $V_\mu$  in the FSI

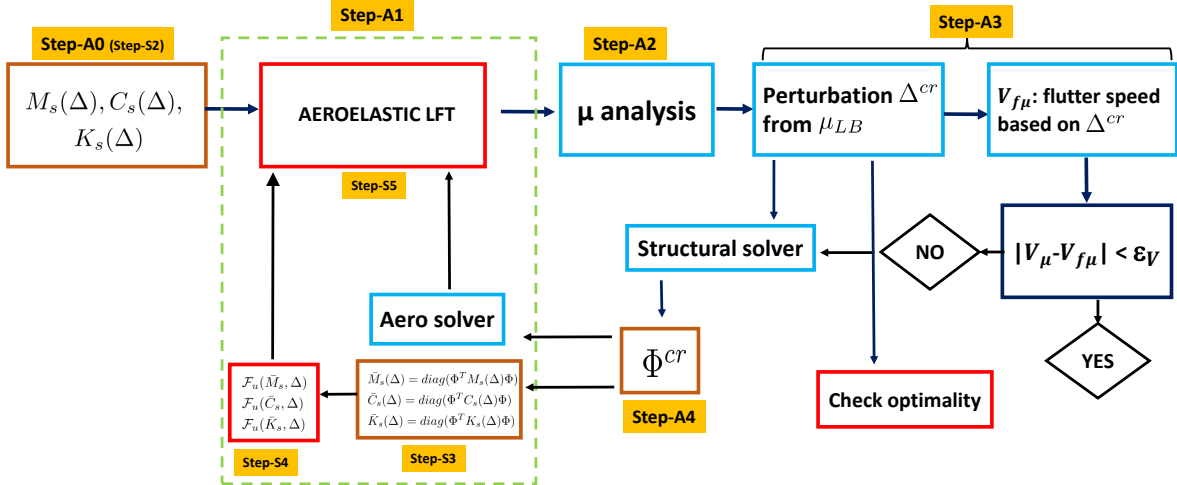


Figure 3.6: Block diagram of the iterative scheme.

solver. The latter instead determines a flutter speed  $V_{f\mu} \approx V_\mu$  within given tolerance and thus is a worst-case perturbation.

To interpret the rationale underlying the analysis algorithm from an LFT perspective, let us indicate the uncertain aeroelastic description achieved at Step-S5 of the modelling algorithm as:

$$\mathcal{F}_u(M, \Delta) = M_{22}(\Delta) + M_{21}(\Delta)\Delta(I - M_{11}(\Delta)\Delta)^{-1}M_{12}(\Delta). \quad (3.34)$$

Eq. (3.34) reflects the fact that it is not possible to express the effect of the uncertainties on  $\Phi$  in the standard linear fractional fashion. Crucially, when compared to the definition of LFT given in Eq. (3.2), the  $\Delta$  block affects here also the partitioned matrix  $M$ . In order to find the worst-case perturbation such that  $(I - M_{11}(\Delta)\Delta)$  is singular, the iterative scheme outlined in Fig. 3.6 proceeds by updating the matrix  $M$  with the value of  $\Delta$  given at the last iteration, that is:

$$\mathcal{F}_u(M, \Delta) \approx M_{22}(\Delta^{cr}) + M_{21}(\Delta^{cr})\Delta(I - M_{11}(\Delta^{cr})\Delta)^{-1}M_{12}(\Delta^{cr}), \quad (3.35)$$

where in the first iteration  $\Delta^{cr} = 0$  (corresponding to the nominal modal matrix  $\Phi_0$ ) is employed.

### 3.3.2.3 Global optimum checks

It is important to stress that Algorithm 3.3 is based on the calculation of the lower bound of  $\mu$ , which is the result of a non-convex optimisation problem [206]. It is also well known that for LFTs of large dimension and/or many parameters, the  $\mu_{LB}$  might be conservative (i.e. distant from the upper bound). This trend can be ameliorated with recently developed  $\mu$  solvers [205] which compute the upper  $\mu_{UB}$  and lower  $\mu_{LB}$  bounds together, ensuring they hold values within a certain tolerance. The algorithms provided in [205] have been used in this work to assess the accuracy of the bounds, but they are computationally demanding and thus, at least for the LFTs used here, it is not practical to embed them in the proposed iterative cycle. In addition, the

schematisation of the problem in Eqs. (3.34)-(3.35) clearly shows that the solved optimisation problem is highly non-convex.

For all these reasons, convergence to the global optimum of the solution found with the iterative algorithm cannot be mathematically guaranteed (hence  $\hat{\Delta}^{cr}$  has been termed a worst-case perturbation matrix). In other words, even if the converged  $\hat{\Delta}^{cr}$  leads to a flutter speed equal (within the prescribed tolerance) to  $V_\mu$ , there could be another one  $\hat{\Delta}_{glob}^{cr}$  with  $\bar{\sigma}(\hat{\Delta}_{glob}^{cr}) < \bar{\sigma}(\hat{\Delta}^{cr})$ . Therefore, strategies to qualitatively check the optimality of the lower bound at each iteration (namely, between Step-A3 and Step-A4) are beneficial.

First, the *directionality* of the worst-case at each iteration is monitored. This entails observing the sign change for each of the uncertain parameters between two consecutive iterations. If this remains the same, it is reasonable even though not rigorous, to argue that the worst-case perturbation for that parameter is detected. For those parameters whose sign (or magnitude) changes, it is advisable to perform a flutter sensitivity analysis, since the sign's discontinuity could be ascribed to the small importance of that parameter for the instability. Examples of  $\mu$ -based sensitivity analysis will be illustrated in Sec. 4.2.2.

A second strategy, which complements the previous assessments, is represented by Algorithm 3.4, schematically depicted in Fig. 3.7. This builds on the idea of testing with  $\mu$  multiple LFTs having different nominal systems, and it can be applied in principle at each iteration (in practice, a trade-off with computational efficiency will arise).

**Algorithm 3.4.** *Check on the optimality of the predicted worst-case*

**Outputs:**  $\mu_{UB}$ -based assessment of the optimality of the worst-case.

**Inputs:** critical perturbation  $\Delta^{cr}$  (from Step-A3 of Algorithm 3.3).

1. Step-C1. Define  $N_c$  tested perturbation matrices  $\Delta_i^t$  ( $i = 1, \dots, N_c$ ).
2. Step-C2. Compute the modal matrices  $\Phi_i^t$  associated with  $\Delta_i^t$ .
3. Step-C3. Use  $\Phi_i^t$  to build  $N_c$  tested aeroelastic LFTs, each centred at  $\Delta_i^t$  (i.e. the parameters in  $\Delta_i^t$  are the nominal values for the uncertainties).
4. Step-C4. Compute  $\mu_{UB}$  for each LFT generated at the previous step.
5. Step-C5. Compare the peaks  $\mu_{UB}^i$  of the curves and assess the optimality of  $\Delta^{cr}$ .

The algorithm takes as input the perturbation matrix  $\Delta^{cr}$  computed at Step-A3 of a generic iteration of Algorithm 3.3 and aims at assessing its optimality (meant here as proximity to the actual worst-case). First,  $N_c$  potential worst-case perturbations  $\Delta_i^t$  (with  $i = 1, \dots, N_c$ ) having all the same magnitude, as measured by  $\bar{\sigma}(\Delta^t)$ , are defined (Step-C1). These definitions can be informed: by the previously discussed tests on the  $\Delta^{cr}$  at different iterations (e.g. modifying the values of those parameters that have shown sign change behaviour), by available insights into certain critical parameters (e.g. from sensitivity analysis) or by considering opposite perturbations

for some of the parameters, e.g.  $\Delta_i^t = -\Delta^{cr}$  if the sign of all parameters is changed. Note that the idea of testing far away from the *current best* is a known strategy in applied optimisation. For example, in [171] a hybrid algorithm was proposed which crosses an evolutionary (global) optimiser with a local one, initialising the latter with either the best candidate in the population or those far away from the current best, depending on the improvement of the cost function. In this thesis, the population is represented by the set of selected  $\Delta_i^t$  and the same idea of exploiting domain knowledge is employed to define it.

In Step-C2 the modal matrices  $\Phi_i^t$  corresponding to each  $\Delta_i^t$  are computed in the FSI solver, and subsequently  $N_c$  aeroelastic LFTs centred at each of the worst-case candidates are constructed (Step-C3). It is stressed that each LFT is computed using the modal basis relative to  $\Phi_i^t$ , and not the modal basis used in the  $\mu$  analysis at Step-A2 of the considered iteration. Then,  $\mu$  analysis is applied to each of these *ad-hoc* created LFTs (Step-C4). It is recommended to focus on the upper bounds  $\mu_{UB}$  since this can be computed with convex programs. The peaks  $\mu_{UB}^i$  of each curve are employed as a measure of the proximity of the perturbed system  $i$  to the actual worst-case of the problem (Step-C5). Specifically, perturbations associated with larger  $\mu_{UB}^i$  point at *worse-case* directions.

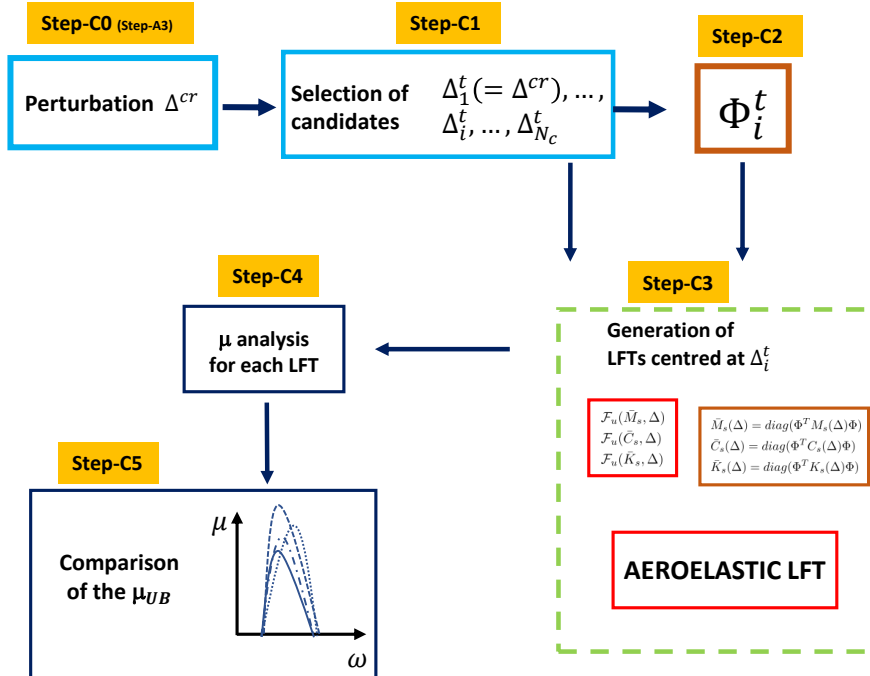


Figure 3.7: Block diagram of the worst-case optimality check algorithm.

Application of all the algorithms discussed in this section will be presented in Section 4.3.

### 3.4 Chapter summary

In this chapter the construction of LFT models of uncertain aeroelastic systems has been investigated.

The two possible LFT modelling processes for aeroelastic plants (one based on a frequency-domain formulation and the other on a state-space one) were presented, together with a discussion on their advantages and limitations, in Section 3.2. Since the main differences between them arise due to the aerodynamic operator, its uncertainty definition has been discussed by focusing on the different options available, i.e. the original frequency-dependent or its state-space approximations. Intrinsic difficulties in reconciling the aerodynamic uncertainty descriptions have been exemplified and motivated in terms of the different physical mechanisms that are captured. Contributions of these investigations are: an algorithm reconciling LFTs capturing different uncertainties; a unified modelling approach retaining most of the advantages of the existing ones.

Following on this discussion, focus was put in Section 3.3 on the development of LFT for aeroelastic systems described by means of state-of-practice fluid-structure interaction solvers, typically leading to high order models. After reviewing the current strategies and highlighting some of their limitations, a novel symbolic LFT-FSI algorithm was presented, which allows the uncertainty modelling to be performed in parallel with the assembly of the structural operators within the FSI solvers. The advantages of this approach range from an enhanced flexibility in the parameters selection (very localized uncertainties can be captured) to a direct connection between uncertainties in the LFT model and physical quantities in the high-order model. The main critical aspect is the handling of the modal matrix, whose dependency on the uncertainties is not easy to capture. For general purpose LFTs, mitigating strategies are proposed based on the modal-oriented approach taken to introduce uncertainties. For LFT models employed for  $\mu$  analysis only, an iterative algorithm is devised to inform the update of the modal matrix based on the worst-case uncertainties and to allow robustness at a fixed (nominally stable) speed to be assessed. Aspects concerning global optimality of the results are also addressed.

This chapter has also two other goals. First, the whole discussion aims to provide better insight into the robust-oriented aeroelastic modelling problem, and thus a detailed presentation has been favoured in pursuit of establishing a common ground between the robust control and the aeroelastic communities. Second, the LFT paradigm is the *modelling pillar* of this thesis and thus the chapter is preparatory for the analysis approaches developed in the remainder of the thesis in that it establishes the framework where they will be formulated.

The application of the methods and algorithms is presented in Chapter 4. This is done to facilitate comprehension by decoupling the research and development activity from the application one.



## NOMINAL AND ROBUST FLUTTER ANALYSIS OF LINEAR SYSTEMS

Flutter is a parameter-dependent problem, since as a parameter of the model is varied the stability properties of the system change. In this chapter the focus will be on linear (time-invariant) analysis methods for predicting this dynamic aeroelastic instability. In nominal approaches the model is specified at a *known* condition and thus the analysis does not assess the effects of perturbations. The problem is typically solved in this case by tracking the eigenvalues at different speeds  $V$ . The result is the definition of a speed  $V_f$ , called flutter speed, such that for all the speeds below it the system is stable. This choice has practical reasons, since typically the speed is representative of the operational conditions of the system, but, in order to gain further insights into its aeroelastic behaviour, parametric analyses can also be performed. Nominal analyses are the focus of Section 4.1, where a background on this subject will be provided and exemplification with two case studies will be discussed.

Robust flutter analysis deals instead with predictions when the aeroelastic system is subject to uncertainties. An important question is whether at a fixed subcritical speed (i.e. lower than the nominal flutter speed  $V_f$ ) the system is stable in the face of the modelled perturbations. The remaining two sections of the chapter will address this task by employing the LFT-based modelling framework described in Chapter 3 in conjunction with the  $\mu$  analysis technique. In particular, Section 4.2 considers how the nominal analyses performed in Section 4.1 are altered by the presence of uncertainties and what type of insight into the unstable mechanisms can be provided by the  $\mu$ -LFT framework. Section 4.3 applies the latter to a joined-wing aircraft configuration and will show the application of the modelling strategies tailored to high-order models and developed in Section 3.3. The latter activity was performed during a research collaboration with Dr. Rauno Cavallaro and Rocco Bombardieri from Universidad Carlos III de Madrid, who shared their aeroelastic expertise and made available the FSI solver. Specifically,

the author devised and carried out autonomously all the analyses presented in Section 4.3.2.

**Publications**<sup>1</sup>: [118, 125] Section 4.2; [116] Section 4.3.

## 4.1 Nominal flutter analysis

### 4.1.1 Flutter algorithms

#### State-space analysis (*p* method)

This approach consists of evaluating the spectrum of the state-matrix  $\mathcal{A}$  (given by Eq. 2.7 for a generic aeroelastic system) starting from a very low value of the speed  $V$  where the system is known to be stable. A crossing of the imaginary axis by one of the eigenvalues detects the occurrence of flutter instability. This methodology is essentially equivalent to what is known in the literature as *p* method [111], although here the adopted mathematical framework is the state-space domain (and not the Laplace domain). If the aerodynamic forces, as it is typical for flutter analysis purposes, are modelled with an unsteady formulation, an RFA method must be adopted. In this thesis Roger and Minimum State methods, introduced in Sec. 2.2, will be employed.

In flutter analysis it is often desirable to associate the eigenpair (eigenvalue and eigenvector) with the corresponding aeroelastic mode (e.g. torsion) in order to get insight into the dynamics underlying flutter and possibly devise solutions to postpone its onset. However, this is not a straightforward task since: the eigenmodes of the state-matrix can drastically change from one speed to another; the presence of augmented states  $x_a$  (due to the RFA) complicate the system spectrum; and often a merging of the frequencies is observed close to the instability, thus using the eigenvalues magnitude as metric to establish the correspondence eigenpair-mode could be inconclusive.

The Modal assurance criteria (MAC) [4] addresses the modes tracking problem by quantifying the linearity between two mode shapes, and is for this reason a very useful tool in flutter analysis [62]. Very briefly, a reference mode  $\phi_r$  and a tested mode  $\phi_t$  are compared in order to assess their similarity (in a linear combination sense). The mathematical definition of MAC follows:

$$MAC(\phi_r, \phi_t) = \frac{|\phi_r^* \phi_t|^2}{(\phi_r^* \phi_r)(\phi_t^* \phi_t)}. \quad (4.1)$$

The output of this comparison is a scalar number between 0 and 1: two identical modal vectors yield a unity value, two orthogonal modal vectors yield a zero value and in between there is a certain degree of similarity between the reference and the tested modes.

The procedure adopted in this work consists of starting the analysis at a low speed such that the aeroelastic modes to be tracked are distinct and well detectable, e.g. based on a comparison

---

<sup>1</sup>Material published during the PhD which relates to the content of this chapter.

with the free-vibration analysis of the system. These modes are then numbered and will represent the basis of reference modes for the first speed. At this speed an eigenvalue analysis is performed and the tested eigenpairs are associated with the physical modes using (4.1) and the aforementioned reference modes. The latter is then updated accordingly and a new eigenvalue analysis, together with the associated tracking of the modes, can be performed at the next speed.

#### Frequency-domain analysis ( $p$ - $k$ method)

The starting point for the  $p$ - $k$  method, originally proposed in [102], is (2.1). The problem is first recast as follows:

$$\left[ p^2 \frac{V^2}{L^2} \bar{M}_s + p \frac{V}{L} \bar{C}_s + \bar{K}_s - q_\infty Q_{hh}(ik) \right] \eta = T(p)\eta = 0, \quad (4.2)$$

where  $p$  is traditionally used in this method to denote the dimensionless Laplace variable  $\bar{s}$ ,  $L$  is a reference length and  $T$  is the aeroelastic frequency response matrix. The objective is to determine, at a given  $V$ , the values of the flutter roots  $p$  such that (4.2) has a solution with non-trivial  $\eta$ , i.e. the determinant of  $T$  is null. The complexity arises due to  $Q_{hh}$ , which is provided by the Doublet Lattice Method (DLM) solver at discrete values of the reduced frequency  $k$  (equal to  $\Im(p)$ ). Therefore, solutions are found iteratively in the form of:

$$p = \gamma k \pm ik = \frac{L_r}{V} s, \quad (4.3)$$

where  $\gamma$  is the rate of decay of the particular mode, i.e. a measure of its damping. An important feature of the formulation can be noticed: structural contributions are not treated as harmonic ( $p$  is not purely imaginary) as it is done for the aerodynamic term. The rationale for this approach is that for sinusoidal motions with slowly increasing or decreasing amplitude (i.e. small rate of decay  $\gamma$ ), aerodynamics based on harmonic motion with constant amplitude are a good approximation. Note that in the  $k$  method, which is an alternative flutter algorithm based also on the solution of (4.2), the real part of  $p$  is assumed null and an artificial unknown damping term proportional to  $\bar{K}_s$  through a coefficient  $g$  is added. This term can be interpreted as the damping required for the existence of harmonic motion, hence flutter occurs for solutions with  $g = 0$ . This means that at  $V_f$  the  $k$  and  $p$ - $k$  methods usually converge to the same value, whereas for  $V < V_f$  the  $p$ - $k$  method is claimed to provide a better estimation of the true damping of the system (as the damping in the  $k$  method is purely a numerical artifice with no physical meaning). This is one of the advantages of the  $p$ - $k$  method and the reason why it is employed in this thesis.

A possible iteration algorithm for computing the flutter roots of (4.2) is the Regula Falsi method [102], which provides the iterate  $p_2$  given two initial guesses  $p_0$  and  $p_1$ :

$$p_2 = \frac{(p_1 \det(T_0) - p_0 \det(T_1))}{\det(T_0) - \det(T_1)}, \quad (4.4)$$

where  $\det(T_0)$  and  $\det(T_1)$  are respectively the determinant of  $T(p_0)$  and  $T(p_1)$ .

In order to initialise the algorithm, one approach is to select the natural frequency  $\omega_n$  corresponding to the mode of interest. Two possible guesses for the roots are then:

$$\begin{aligned} p_0^j &= 0 + i \frac{\omega_n L_r}{V} = ik_0^j, \\ p_1^j &= -0.01k_0^j + ik_0^j. \end{aligned} \quad (4.5)$$

The first analysed speed should be sufficiently small such that  $\omega_n$  is reasonably close to the frequency of the aeroelastic mode at that speed. Eq. (4.4) is then iterated until a specified degree of convergence is attained. This procedure can be repeated for all the speeds in the considered range by initializing  $p_0$  and  $p_1$  with the result at the previous speed. The calculation can then be performed for all the aeroelastic modes of interest providing the sought frequency-damping-velocity diagram.

Note that in the  $p$ - $k$  method the task of tracking modes is made easier by the fact that the algorithm inherently focuses on distinct eigenvalues (across all the speeds), and is initialised with the frequencies associated with the different modes. However, the merging of the frequencies across flutter can still prevent from clearly associating each eigenvalue  $p$  with a physical mode, and in these cases MAC can be advantageously employed.

#### 4.1.2 Application to the typical section

The typical section case study from [134] is considered here to provide a first example of application of nominal flutter analysis. The system was described in Sec. 2.3.1, and its structural and aerodynamic properties are reported in Appendix A.2.1.

In Table 4.1 the results obtained with the different approaches are summarised. No substantial mismatches are found in the nominal flutter speeds and frequencies predicted.

Table 4.1: Comparison of flutter results with different algorithms.

Model	Flutter velocity [ $\frac{m}{s}$ ]	Flutter frequency [ $\frac{rad}{s}$ ]
State Space - Roger	302.7	70.06
State Space - Minimum State	302.5	70.37
Frequency-domain $p$ - $k$	301.8	70.37
Baseline [134]	303.3	70.69

For the  $p$  method, the terms  $\Gamma_{lag-Rg}$  and  $\Gamma_{lag-MS}$  of the RFA approximations used 4 and 6 lag roots equally spaced between 0.1 and 0.7, respectively. Since they provided almost indistinguishable results, in Fig. 4.1 only the case relative to the Minimum State approximation is displayed. The analysis starts at a low speed ( $V=60 \frac{m}{s}$  identified in the figure with a square marker) and tracks the eigenvalues of the three elastic modes (plunge, pitch, and flap) employing

the MAC criterion. Similarly to what was also reported in [134], the system exhibits a violent plunge-pitch flutter at  $V_f \approx 303 \frac{m}{s}$ , featured by a merging of the frequencies just before the instability occurs (this is also confirmed by Fig. 4.2(b) which shows the frequency plot obtained with the  $p$ - $k$  method). The location of the poles at the subcritical speed  $V = 270 \frac{m}{s}$  is highlighted with an asterisk, and  $\omega_f$  indicates the frequency at flutter speed for the unstable mode. This flutter, due to the close interaction of the first two modes, is often referred to as *binary flutter*.

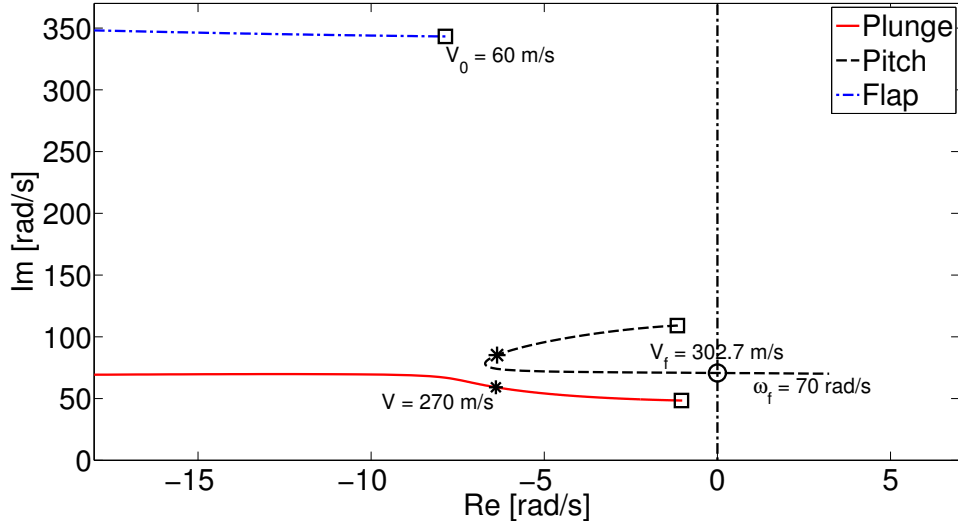


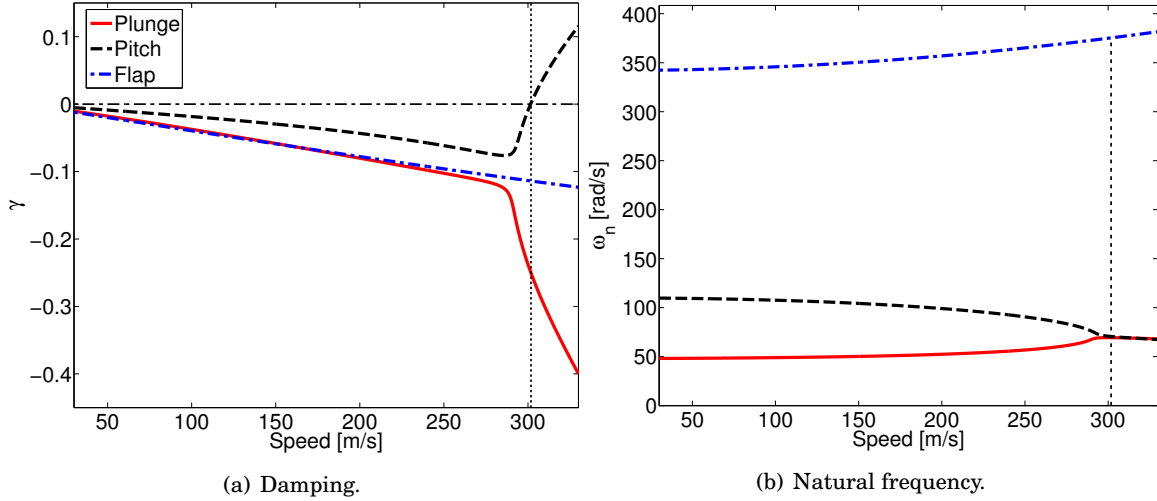
Figure 4.1: Poles location of the flap, pitch, and plunge modes as speed increases obtained with the  $p$  method.

In Fig. 4.2 the results obtained with the  $p$ - $k$  method are displayed by means of the frequency-damping-velocity diagram. Fig. 4.2(a) shows the rate of decay of the modes as speed increases, which clearly allows to detect the onset of flutter (recall from its definition in Eq. 4.3 that  $\gamma$  has the same sign of the real part of the eigenvalue). Flutter speed, highlighted with the vertical line, is distinguished by the pitch mode damping crossing the zero line. This calculation leads to a flutter speed of approximately  $302 \frac{m}{s}$  at a reduced frequency of 0.24 (corresponding to  $70.4 \frac{rad}{s}$ ). Fig. 4.2(b) shows the natural frequencies where the merging of the frequencies of plunge and pitch mode around flutter is visible.

### 4.1.3 Parametric study of body freedom flutter

The analyses shown in Sec. 4.1.2 give a prediction on the occurrence of flutter considering a restrained model, that is, assuming it unrelated to the rigid-body motion of the vehicle on which the aerodynamic body is mounted. In this section the so-called Body Freedom Flutter (BFF), originating from the strong coupling between rigid-body and elastic modes of the aircraft, will be investigated using the simplified aircraft model presented in Sec. 2.3.2.

First, the capability of the wing equivalence discussed in Sec. 2.3.2 to predict flutter onset


 Figure 4.2: Flutter analysis of the typical section with the *p-k* method.

of wing geometries of the type depicted in Fig. 2.4 is validated against the Goland wing, a well-known benchmark problem in the literature [93] (see Appendix A.2.2). This system consists of a uniform rectangular wing with constant structural and inertial properties along the span. In Table 4.2 a comparison of the results obtained in this work (applying the *p-k* method) with others from the literature is shown. There is a satisfactory matching with another 2D approximation of the straight wing model [32], while the discrepancies with an aeroelastic model comprising 3D effects [93] remain below 3% in terms of  $V_f$ . It is also important to remark here that, although the aspect ratio of the Goland wing is not very high (approximately 14), the employed model is still able to adequately capture its flutter behaviour. This can be ascribed to the simple geometry of the wing (null sweep angle, uniform geometrical properties) which reduces 3D aerodynamic effects.

Table 4.2: Comparison of flutter analysis of the Goland wing with literature results.

	Flutter velocity [ $\frac{m}{s}$ ]	Flutter frequency [ $\frac{rad}{s}$ ]
Present work	141.1	73.2
2D approximation [32]	141.2	72.5
Original reference [93]	137.2	70.7

The Goland wing case study is used to define the wing properties of the simplified aircraft model. Note that  $EI$  is assumed to represent an aeroelastic design variable reflecting the tendency towards a lightweight-oriented structural sizing and thus is given by  $EI = \sigma_s EI_G$  with  $EI_G$  set at the value for the Goland wing and  $\sigma_s$ , referred to as the bending stiffness factor, taking values

from 0.05 (maximum bending flexibility) to 1 (maximum bending rigidity). The other free design parameter is the distance from the nose to the tail leading edge  $D$ , assumed to vary in a range between 5m and 10m, complying with static stability requirements. The variability in the flight mechanics parameter  $D$  is used to reflect the trend towards highly manoeuvrable aircraft (with low static stability margins) that, together with the aforementioned increased flexibility of the wings, challenges the hypothesis of independence of rigid and elastic dynamics. Note also that low values of the tail volume  $V_{HT}$  have been shown to exacerbate the interaction between the rigid-body short period and the wing first bending mode [25]. This parameter is defined as:

$$V_{HT} = (\bar{X}_{AC}^t - \bar{X}_{CG}) \frac{S_t}{S}. \quad (4.6)$$

Recall that  $\bar{X}_{AC}^t$  and  $\bar{X}_{CG}$  are the dimensionless distances from the aircraft nose to the tail aerodynamic centre and the aircraft centre of gravity, respectively. Once the lifting surfaces sizes and inertial properties are fixed,  $V_{HT}$  is a function of  $D$ . In fact,  $D$  directly influences the value of  $\bar{X}_{AC}^t$  which is known to have great effect on the aerodynamic stability derivatives. All the other parameters defining the geometrical and inertial properties of the aircraft layout are obtained by scaling the values from [190], which examines a similar aircraft layout, through the Goland wing mass ratio and span as the reference mass and length (details are provided in Appendix A.2.2).

Following a parametric analysis approach, Fig. 4.3 shows the flutter speed  $V_f$  evaluated on a grid of values for the design parameters  $EI$  (equivalently  $\sigma_s$ ) and  $D$ . Three values of the bending stiffness factor  $\sigma_s$  (marked by vertical lines) are highlighted and will be discussed subsequently.

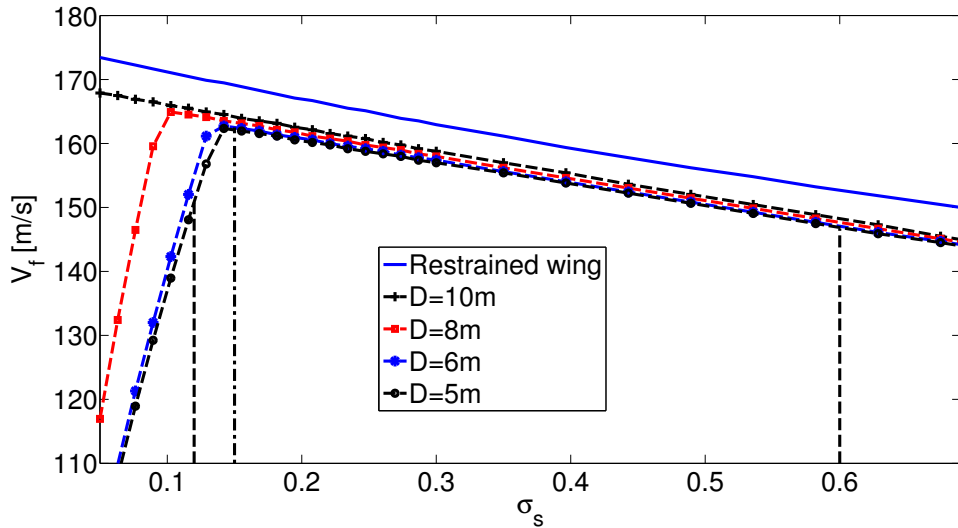


Figure 4.3: Parametric flutter analysis for discrete values of  $\sigma_s$  (i.e.  $EI$ ) and  $D$ .

The first apparent feature is that the tendency for instability is more pronounced as the bending  $\omega_h$  and torsional  $\omega_a$  frequencies get closer. This behaviour is familiar to aeroelasticians [111, 256], and is due to the fact that the two modes become more coupled. This is seen in

Fig. 4.3 from the slope of the restrained wing (solid line), which reveals an increase of  $V_f$  as  $\sigma_s$  (equivalently  $EI$ ) is reduced. Indeed, a decrease in  $EI$  implies an analogous trend in the bending frequency, as expressed by Eq. (2.13). Since the torsional stiffness is kept constant, a decrease in  $\sigma_s$  can hence be interpreted as a reduction in the ratio  $\frac{\omega_h}{\omega_a}$  between the first bending and torsional natural frequencies.

The flutter velocities obtained when rigid-elastic interactions are included (curves  $D=[5,6,8,10]$   $m$  in Fig. 4.3) maintain the above trend but only for as long as the tail volume of the vehicle does not become critical to the stability. In fact, there is a range of bending flexibility of the wing ( $0.15 < \sigma_s < 1$ ) where  $V_{HT}$  proves to have a negligible influence on flutter occurrence, and thus the BFF model predicts only a relatively small decrease in flutter speed with respect to the restrained model (up to 3%). As the bending flexibility increases ( $\sigma_s < 0.15$ ), the interaction between the short-period and the bending mode becomes significant, leading to an abrupt decrease of flutter speed. Therefore, tail volume is confirmed to play a crucial twofold role: it prompts rigid-elastic coupling (in that it changes the  $\sigma_s$  threshold at which the leap occurs) and it determines (for a fixed value of  $\sigma_s$ ) the magnitude of the change in the  $V_f$  value itself. In particular, Fig. 4.3 shows that a lower  $D$  (i.e. lower  $V_{HT}$ ) anticipates the transition to the BFF mechanism and determines a lower flutter speed than for the scenario with greater  $V_{HT}$ , confirming its role discussed earlier.

The behaviour detected in Fig. 4.3 can be better clarified observing the trend of the eigenvalues, obtained with the  $p$ - $k$  method and reproduced in Fig. 4.4, for two aircraft configurations. Tail distance  $D$  is for both cases equal to 5 m, while the bending stiffness parameter  $\sigma_s$  is equal to 0.6 for case A and to 0.12 for case B (these two cases are highlighted in Fig. 4.3 with vertical dashed lines). Therefore, they each belong to one of the two stability regions identified before.

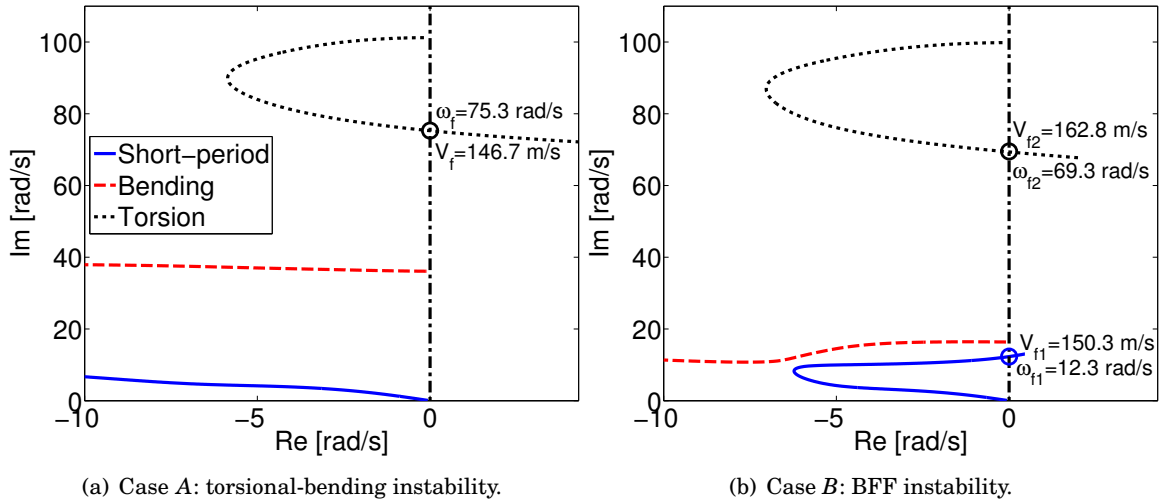


Figure 4.4: Poles location for two aircraft configurations.

In Fig. 4.4 the modes' branches are identified (and labeled) according to their genesis of pure

rigid-body or pure elastic modes. However, it is fair to remark that all the modes experience coupling due to the aerodynamics (*bending* and *torsion*) and to motion (*short period* and *bending*), and hence this labeling is only a naming convention for ease of explanation. For the first aircraft configuration, depicted in Fig. 4.4(a), the eigenvalues of the system exhibit a pattern qualitatively similar to the one shown in Fig. 4.1 for the typical section case study, indicating a restrained body flutter. In fact, the flutter mechanism does not involve coupling with rigid motion and it is the torsional mode which goes unstable at  $V_f=146.7 \frac{m}{s}$  and  $\omega_f=75.3 \frac{rad}{s}$  (high frequency instability). The short-period eigenvalue follows the pattern known for the pure rigid-body case (with a frequency increasing almost linearly with speed), and thus proves to be almost unperturbed by the wing deformation. However, when bending flexibility becomes more prominent (case *B* shown in Fig. 4.4b) two distinctive flutter mechanisms can be observed. The first imaginary axis crossing takes place at a speed  $V_{f1}=150.3 \frac{m}{s}$  and at a frequency  $\omega_{f1}=12.3 \frac{rad}{s}$ . This low-frequency instability is the result of the interaction between the short-period and the bending mode (that is, the Body Freedom Flutter). The second crossing takes place at  $V_{f2}=162.8 \frac{m}{s}$  at a higher frequency ( $\omega_{f2}=69.3 \frac{rad}{s}$ ), and is dominated by the torsion instability already encountered in the other configuration.

In conclusion, the trend depicted in Fig. 4.3 is motivated by a change in the mode first reaching the flutter condition, which for the curves  $D=[5,6,8] m$  (in the range of low bending stiffness, i.e. the left side of Fig. 4.3) is the rigid-elastic coupled mode, while in the other cases it is still the torsional mode (as clearly demonstrated in Fig. 4.4).

The above results confirm that the model presented in Sec. 2.3.2 is able to capture known physical effects of the BFF problem. Specifically, the use of standard nominal flutter methods can show the detrimental effect on stability of two important parameters and provides a characterisation of the multiple instabilities affecting the system by tracking the eigenvalues as the speed is varied (Fig. 4.4). The procedure implies a gridding of the parameter space and therefore it does not provide theoretical guarantees on the worst-case results, for example in terms of the lowest flutter speed among the possible combinations of  $D$  and  $EI$ . Moreover, when dealing with a larger number of variables, a parametric study such as the one performed here is expected to become difficult to interpret and computationally onerous. As the sizing required to ensure a flutter free behaviour of very flexible aircraft is inherently multidisciplinary, it is envisaged the opportunity to leverage the robustness modelling framework from Chapter 3 to propose analyses approaches that address some of the aforementioned issues.

## 4.2 Robust flutter analysis with $\mu$

In this section robust flutter analysis with  $\mu$ -LFT is applied to the two case studies analysed in the previous section. First, the typical section is considered and some of the modelling aspects discussed in Sec. 3.2.1 are demonstrated. Then, application to the simplified aircraft model

is investigated with the aim to showcase which additional insights can be provided by this framework.

### 4.2.1 Typical section

The nominal analyses in Sec. 4.1.2 have shown the occurrence of a binary flutter at approximately  $V_f = 303 \frac{m}{s}$  and  $\omega_f = 70.5 \frac{rad}{s}$ . A value of the speed  $V$  equal to  $270 \frac{m}{s}$ , for which the system was shown to be nominally stable (recall the asterisk in Fig. 4.1), is then selected for all the following analyses.

#### 4.2.1.1 Structural uncertainties only

First, the case with only uncertainties in the coefficients of the structural mass  $M_s$  and stiffness  $K_s$  matrices is considered. The uncertainty definition consists of a range of variation of 10% from the nominal value for  $M_{s,11}$ ,  $M_{s,22}$ ,  $K_{s,22}$  and of 5% for  $M_{s,12}$  and  $K_{s,11}$  (the numbers in the subscript denote the element of the matrix that is considered, e.g.  $K_{s,11} = K_h$  defined in Eq. 2.10). First, a multiplicative uncertainty description (3.4b) is applied to the five parameters, leading to the definition of the uncertainty levels  $\lambda_{M_{s,11}} = \lambda_{M_{s,22}} = \lambda_{K_{s,22}} = 0.1$  and  $\lambda_{M_{s,12}} = \lambda_{K_{s,11}} = 0.05$ . Then, the two LFT development paths discussed in Sec. 3.2.1 are applied, and in both cases the uncertainty set associated with the LFT results in:

$$\Delta_s^{6,R} = \text{diag}(\delta_{M_{s,11}}, \delta_{M_{s,12}} I_2, \delta_{M_{s,22}}, \delta_{K_{s,11}}, \delta_{K_{s,22}}). \quad (4.7)$$

where the size of the  $\Delta$  block and the type of uncertainties (here only real  $R$ ) is recalled in the superscript. Since only structural parameters affect the uncertainty blocks, no mismatch in principle is expected when adopting either the state-space (SS) or the frequency-domain (FD) LFT formulation. In Fig. 4.5 the upper (UB) and lower (LB)  $\mu$  bound results obtained with both approaches are shown. The observable matching can be considered a validation of the two model development paths detailed in Sec. 3.2.1.

The estimation of  $\mu$  given by the algorithms is also very accurate since the values of the bounds are in close agreement, meaning that the actual value of  $\mu$  is well predicted. In particular, it can be concluded from the peak in the plot ( $\approx 1.38$ ) that the system is flutter free for structural uncertainties up to approximately 73% ( $\approx \frac{1}{1.38}$ ) of the assumed range of variation. Robust analyses carried out with  $\mu$  gives also a frequency perspective on the results. This is an important feature enriching the content of the prediction with something more than a simple binomial-type of output (either the system is robustly stable or not within the defined uncertainty set). In particular it shows the peak frequency at which instability occurs, how much it is modified compared to the nominal case, and when multiple instabilities exist it also provides insight into the different mechanisms taking place. In this example, only one instability is detected and the peak frequency is at about  $72 \frac{rad}{s}$ . This frequency is slightly greater than the nominal flutter frequency  $\omega_f$  and the difference can probably be ascribed to the perturbed values in the structural parameters

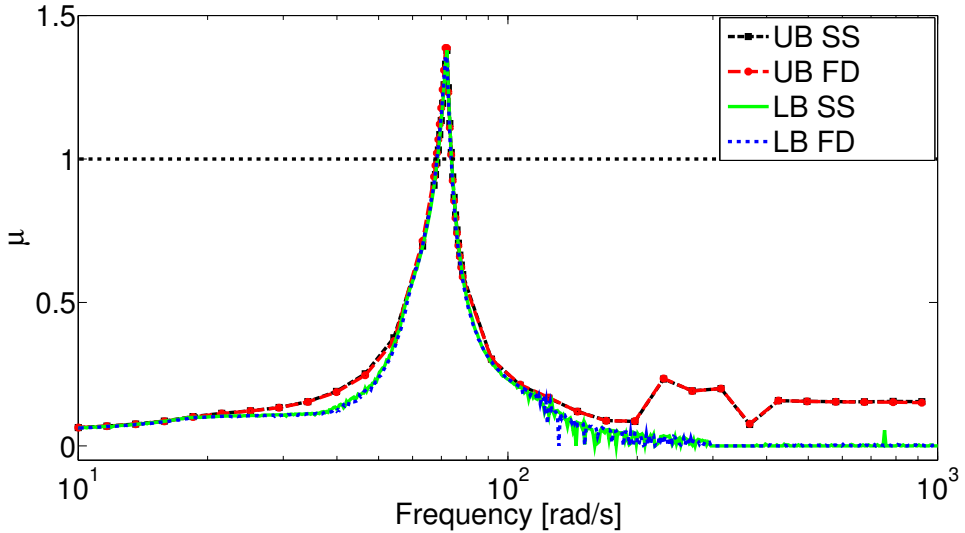


Figure 4.5: Comparison of the  $\mu$  analysis based on the state-space (SS) and frequency-domain (FD) formulations for the case of structural uncertainties.

and to a different wind speed ( $270 \frac{m}{s}$  instead of the flutter speed  $303 \frac{m}{s}$ ) which causes a different aerodynamic contribution to the system's frequencies. As can be observed in Figure 4.2(b), pitch frequency (responsible for the instability) is indeed higher at speeds lower than  $V_f$ .

The lower bound calculation also allows the worst-case perturbation matrix  $\Delta_s^{cr}$  corresponding to the peak in Fig. 4.5 to be extracted:

$$\begin{aligned} \Delta_s^{cr} &= \text{diag}\left(\delta_{M_{s,11}}^{cr}, \delta_{M_{s,12}}^{cr} I_2, \delta_{M_{s,22}}^{cr}, \delta_{K_{s,11}}^{cr}, \delta_{K_{s,22}}^{cr}\right), \\ &= \text{diag}(-0.7245, 0.7245 I_2, 0.711, 0.6460, -0.7213). \end{aligned} \quad (4.8)$$

Note that, due to the fact that upper and lower bounds almost perfectly overlap around the peak, this is *the* smallest matrix satisfying the determinant condition related to the ill-posedness of the LFT (3.12). To further highlight the insights  $\mu$  is able to provide when supported by an adequate system understanding, the worst parameter combination reported in (4.8) is further interpreted. From examining the signs and values of the above worst-case combination, it is noted that the structural parameters have opposite perturbations if grouped according to the affected degrees of freedom (matrix subscripts 11 for the plunge, and 22 for the pitch). Specifically, the plunge equilibrium sees a reduction in  $M_{s,11}$  and an increase in  $K_{s,11}$ , while the pitch equilibrium sees an increase in  $M_{s,22}$  and a reduction in  $K_{s,22}$ . From a free-vibration analysis point of view, this corresponds to getting the plunge and pitch natural frequencies closer, which is a trend known to be detrimental to flutter stability (also commented on in Sec. 4.1.3 with reference to the restrained wing flutter). Thus,  $\mu$  analysis predicts quantitatively the reduction of stability margin in the face of the uncertainties, and also points out the mechanism underlying the worst-case flutter onset. This kind of supplementary information may be in general of great utility to inform

passive design actions or sketch out active control strategies for flutter suppression.

Numerical aspects related to the usage of  $\mu$  analysis for robust flutter calculations are briefly discussed next. For the upper bound, the default option of the Robust Control Toolbox (RCT) is the Balanced form algorithm [78] which will be compared against the Linear Matrix Inequalities (LMI)-based solver [263] (employed in the results of Fig. 4.5). As for the lower bound calculation, default options depend on the nature of the problem. If at least one of the uncertainty blocks is complex, the default algorithm is based on the Standard Power Iteration (SPI) [182], which provides the highest accuracy but only for pure complex problems. In fact, convergence issues may be encountered for real-mixed problems and, in particular, for pure real uncertainties, such as the present one. In this case, the default is a recent algorithm [219] based on a worst-case gain calculation, namely the Gain-Based Algorithm (GBA), which was used also in Fig. 4.5.

In order to provide a measure of the performance of the aforementioned algorithms for this case study, Fig. 4.6 shows a comparison of the results obtained with the different options (reported in brackets in the legend) of the *mussv* routine of the RCT. These are all polynomial-time algorithms, with the Balanced and SPI generally providing faster calculations. In particular, for this case the  $\mu$  bounds were evaluated at one frequency point in about 0.1s with the Balanced and SPI methods, whereas GBA and LMI-based approach yielded approximately an order of magnitude slower calculations.

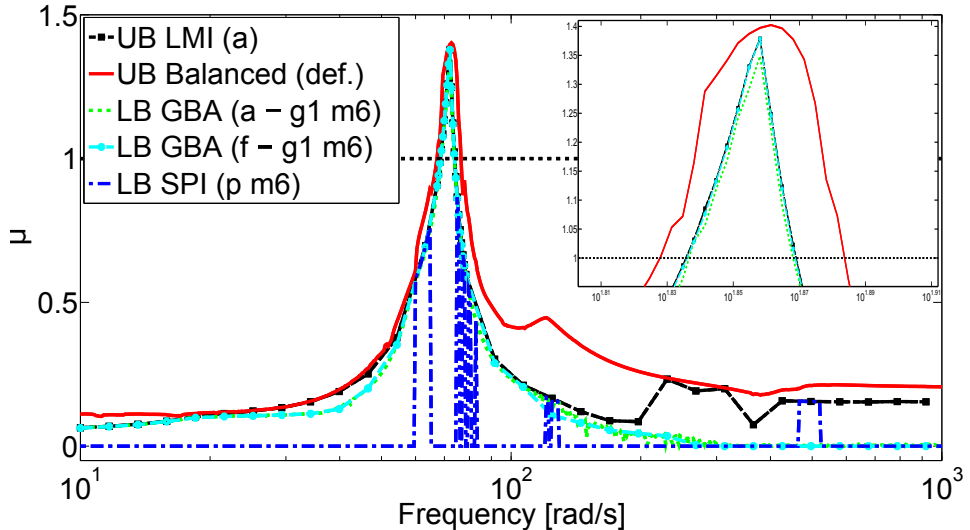


Figure 4.6: Comparison of  $\mu$  algorithms for the case of structural uncertainties.

A first observation inferred from Fig. 4.6 is that the LMI-based solver outperforms the default one in the calculation of the upper bound since it achieves lower predictions for all the frequencies. The plot also confirms that the SPI method has poor accuracy in providing a lower bound for this kind of problem, irrespective of the number of times the calculation is randomly reinitialised (defined by the integer following option  $m$ ). On the other hand, the GBA ensures a very accurate

prediction, which is barely affected by the maximum number of internal iterations (specified by the integer following  $g$  according to the rule  $10 + 10g$ ) or algorithm reinitialisations. Interestingly, the GBA makes use of the result of the upper bound calculation to update the search [219], and indeed a small sensitivity to the employed upper bound algorithm (specified by  $a$  or  $f$  in the brackets) can be noticed. From the enlargement it can be seen that employing GBA in conjunction with a faster upper bound calculation (option  $f$ ) leads to a lower bound perfectly matching the upper bound in the peak area. On the other hand when this is used with the more accurate upper bound (option  $a$ ), it provides slightly smaller bounds. This numerical aspect could be attributed to the fact that the use of a greater (i.e. faster) upper bound leads, at each GBA iteration, to a larger guess of  $\mu_{LB}$  and this may determine a greater final value of the lower bound when the iteration is stopped (see [219] for details on the iterations entailed by the GBA algorithm). This has been confirmed also when a higher number of iterations (e.g.  $a\text{-}g20$  or  $a\text{-}g6m3$ ) was employed. It is important to remark, however, that these discrepancies are very small and the option  $g$  guarantees a very accurate lower bound for this problem regardless of the selection of auxiliary options.

The numerical analysis shown in Fig. 4.6 considers only a benchmark case and thus it is not meant to be a detailed numerical assessment of the available algorithms (see for example [206]). The purpose is instead to highlight the influence of the nature of the parameters in  $\Delta$  (crucially, a real  $\mu$  problem is considered here) and to illustrate the rationale that informed the selection of the algorithms in the remainder of the chapter.

#### 4.2.1.2 Structural and aerodynamic uncertainties

Robustness of the system when the aerodynamics part is affected by uncertainties is addressed next. First, the state-space formulation is used and uncertainties in all the lag roots of the unsteady part of the approximate operators are considered. Two aeroelastic LFTs, built respectively with Roger and Minimum State methods (and indicated by subscripts  $Rg$  and  $MS$  respectively), are available and are defined by the following uncertainty sets:

$$\begin{aligned}\Delta_{Rg}^{12,R} &= \text{diag}(\delta_{\gamma_1} I_3, \delta_{\gamma_2} I_3, \delta_{\gamma_3} I_3, \delta_{\gamma_4} I_3), \\ \Delta_{MS}^{6,R} &= \text{diag}(\delta_{\gamma_1}, \delta_{\gamma_2}, \delta_{\gamma_3}, \delta_{\gamma_4}, \delta_{\gamma_5}, \delta_{\gamma_6}).\end{aligned}\quad (4.9)$$

The discussion in Sec. 3.2.2.1 pointed out that when the same range of variation holds for the lag terms of the two RFA operators, the frequency response families are markedly different and, in an attempt to reconcile the two maps, Algorithm 3.1 was proposed. It is thus expected to observe also a similar discrepancy in the robust stability margins. Fig. 4.7 shows the results for three different cases:  $Rg$  and  $MS$  where an uncertainty of 10% in the lag terms is considered for all the parameters listed in (4.9); and  $MS$  scaled where the uncertainty range  $\Lambda_{MS}$  of the lag roots for the Minimum State approximation is determined with Algorithm 3.1 by using  $\mathcal{F}_u(Q_{Rg}, \Delta_{Rg})$  as reference LFT. It is apparent that while the predictions associated with  $Rg$  and  $MS$  are far

apart, the difference in peak value between *MS scaled* and *Rg* falls below 30%. It is restated here that Algorithm 3.1 does not allow the two uncertainty definitions to be reconciled exactly, due to the inherent differences in the definition of  $\Gamma_{lag-Roger}$  and  $\Gamma_{lag-MS}$  (assessed in Sec. 2.2). However, it is deemed a useful tool to inform the definition of uncertainty levels in an LFT to map a reference LFT or data dispersion.

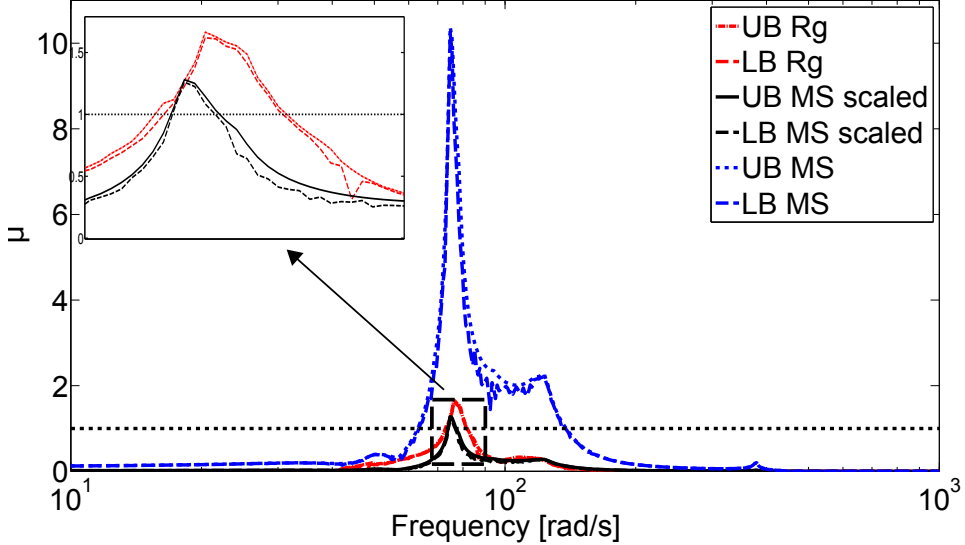


Figure 4.7: Comparison of  $\mu$  analysis for the case of uncertainties only in the lag roots of the two approximated aerodynamic operators.

Finally, as a validation of the unified approach presented in Sec. 3.2.3, the scenario with uncertainties in both the structural (mass and stiffness matrices) and aerodynamic operators is analysed. The uncertainty description consists of the set in (4.7) for the structural part and that discussed in (3.26a) for the aerodynamic one. Recall that the latter are complex uncertainties (referred to three transfer functions of the GAF  $Q_{hh}$ ) and range in the disc of the complex plane centred at the nominal values and have radii equal to 10% of their magnitudes. Starting from this parameter definition, two aeroelastic LFTs have been constructed: *FD* is based on the frequency-domain formulation (Sec. 3.2.1.1); while the LFT termed *uni* follows the rationale of the unified strategy, which works entirely with state-space models except for the aerodynamic perturbation terms (allowed to be referred to the original operator  $Q_{hh}$ ). The same mixed real ( $R$ )-complex ( $C$ ) uncertainty set is obtained for both the LFTs (regardless of the approach):

$$\begin{aligned} \Delta^{6,R-3,C} &= \text{diag}\left(\Delta_s^{6,R}, \Delta_{hh}^{3,C}\right), \\ &= \text{diag}\left(\delta_{M_{s,11}}, \delta_{M_{s,12}} I_2, \delta_{M_{s,22}}, \delta_{K_{s,11}}, \delta_{K_{s,22}}, \delta_{Q_{hh,12}}, \delta_{Q_{hh,21}}, \delta_{Q_{hh,22}}\right). \end{aligned} \quad (4.10)$$

Fig. 4.8 presents a comparison of the two  $\mu$  plots (for clarity only  $\mu_{UB}$  is reported since this is very close to  $\mu_{LB}$ ) which showcases an almost perfect match of the results. In making a comparison,

it should be considered that the nominal plant is defined by two different models and thus this could generate a slight mismatch in the predictions.

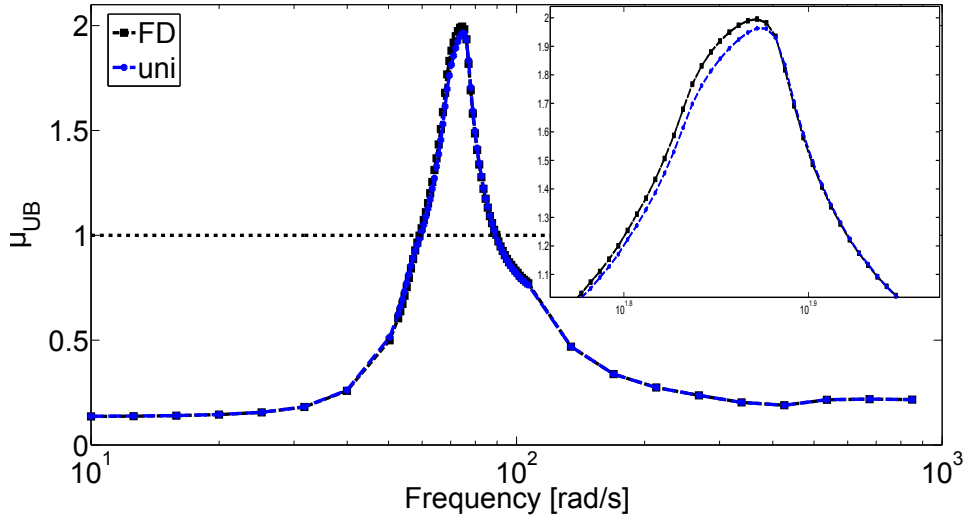


Figure 4.8: Comparison of the  $\mu$  analysis for the unified (*uni*) and frequency-domain (FD) formulations for the case of aerodynamics and structural uncertainties.

#### 4.2.2 Body freedom flutter

For the investigations of the body freedom flutter instability with robustness tools LFT models are built up using the frequency-domain approach –thus starting from (2.18). Based on the previous discussions, three important design variables are identified: wing bending stiffness  $EI$ , tail distance  $D$ , and wing mass ratio  $m_w$ . The first two parameters and their role in the BFF were addressed in the nominal analysis section. The wing mass is also a fundamental parameter of the flexible aircraft dynamics, since it significantly influences the rigid-body equilibrium: it alters the vehicle inertia properties (assumed to scale up with the wing weight) as well as the CG location (with important effects on the short-period properties). In addition, the restrained wing flutter itself is known to be highly dependent on the inertial contribution and thus an uncertainty affecting the structural mass matrix has substantial repercussions.

The reason to capture these parameters in an LFT fashion is therefore twofold. On the one hand, their values (especially  $EI$  and  $m_w$ ) are only known within a certain tolerance until the final design stage. On the other hand, they are key design variables selected during the conceptual design stage, typically characterised by different concurrent requirements, and hence additional insights are invaluable at that stage. In addition to these three parameters, perturbations in the same aerodynamic transfer functions captured in  $\Delta_{hh}$  (4.10) are considered to allow for inaccuracies in the aerodynamic model and potential violations of its underlying hypotheses (e.g.

the fact that 3D effects are not necessarily negligible). The radius of the disc in the complex plane where these uncertainties range is here 3% of their magnitude.

As a result of this discussion, 2 different LFT models (namely LFT-1 and LFT-2) defined by the following uncertainty sets are considered:

$$\Delta_1^{8,R-3,C} = \text{diag}(\delta_D I_7, \delta_{EI}, \delta_{Q_{hh,12}}, \delta_{Q_{hh,21}}, \delta_{Q_{hh,22}}), \quad (4.11a)$$

$$\Delta_2^{18,R-3,C} = \text{diag}(\delta_{m_w} I_{10}, \delta_D I_7, \delta_{EI}, \delta_{Q_{hh,12}}, \delta_{Q_{hh,21}}, \delta_{Q_{hh,22}}). \quad (4.11b)$$

Both LFTs capture the variability in aerodynamics, bending stiffness, and tail distance, but LFT-2 also that in the mass ratio  $\delta_{m_w}$ .

The nominal values for  $EI$  and  $D$  are  $EI = 0.15EI_G$  (i.e.  $\sigma_s = 0.15$ , marked with a vertical dashed-dotted line in Fig. 4.3) and  $D = 6\text{m}$ . It is worth noticing that the corresponding point in Fig. 4.3 is located close to the boundary between the two discussed stability regions. In particular, this configuration features (for the specified value of  $D$ ) one of the highest flutter speeds, lying at the same time close to the abrupt leap in the flutter curve. From a flutter design perspective, this layout can be regarded as optimal in that it attains the highest flutter speed given a prescribed margin from BFF occurrence, thus it is of interest to look at its robustness.

In order to further characterise the flutter behaviour of this nominal plant, Fig. 4.9 shows the poles root locus highlighting speeds and frequencies for the instabilities taking place. The system exhibits both the low frequency (Body Freedom Flutter at  $\omega_1$ ) and high frequency (restrained wing flutter at  $\omega_2$ ) instabilities. Note that in comparison to Fig. 4.4(b), the restrained wing flutter is the first to be encountered (i.e. corresponding to the lowest speed) at  $V_{f2} = 162 \frac{\text{m}}{\text{s}}$  and  $\omega_{f2} = 69.7 \frac{\text{rad}}{\text{s}}$ , while the BFF occurs at a speed  $V_{f1} = 175 \frac{\text{m}}{\text{s}}$  and a frequency  $\omega_{f1} = 14.7 \frac{\text{rad}}{\text{s}}$ . The sub-critical speed  $V = 150 \frac{\text{m}}{\text{s}}$  will then be considered in the following robust analyses.

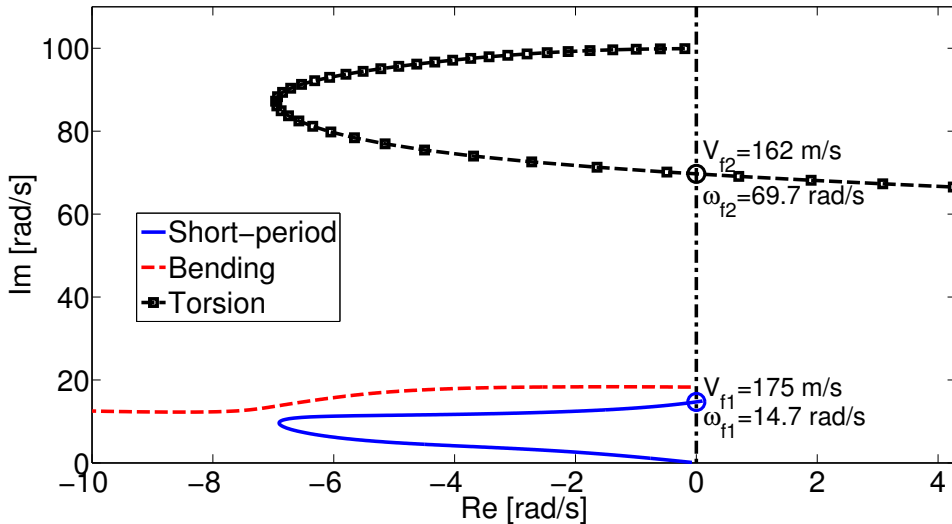


Figure 4.9: Poles location for the nominal aircraft model.

#### 4.2.2.1 Results for LFT Model 1

The first goal in using LFT-1 is to show the capability of  $\mu$  analysis to infer similar conclusions to those drawn via the standard parametric study. This is done by assessing the role played by  $EI$  and  $D$  in the robust stability calculation, i.e. a type of robust parametric sensitivity analysis performed within the  $\mu$  analysis framework. Once a condition is defined (for RS this is the determinant condition in 3.12 such that the LFT is ill-posed),  $\mu$  highlights the relevance of the parameters captured as uncertainties. Although more advanced  $\mu$  sensitivity analyses can be employed using the skew- $\mu$  concept [81, 161], this task is assessed here considering two different uncertainty levels for  $EI$  and  $D$ . The idea underlying this test is that, for each uncertainty, the increase of the peak value of the  $\mu$  plot as its range of variation is enlarged is directly related to the sensitivity of the instability to that parameter. Specifically, variations of 10% and 30% with respect to the parameters' nominal values will be considered here. This can be easily done by defining different values for the parameters  $\lambda_D$  and  $\lambda_{EI}$  used for the multiplicative uncertainty description (3.4b).

Fig. 4.10 shows the  $\mu$  results for the four different combinations (RC1-#) of the uncertainty levels  $\lambda_D$  and  $\lambda_{EI}$ . Since the upper and lower bounds are close in each case, for the sake of clarity only the upper bounds are reported. Before discussing the results, the significance of the four range cases (RC1-#) is assessed on the basis of the results of the parametric analysis (Fig. 4.3) and the nominal parameters used for these analyses ( $EI = \sigma_s EI_G$ , with  $\sigma_s = 0.15$ , and  $D = 6\text{m}$ ):

- RC1-A & RC1-B: the plant is expected to be robustly stable because when  $EI$  varies within 10% of its nominal value (i.e.,  $0.135 < \sigma_s < 0.165$ ) the flutter speed is always above  $150 \frac{\text{m}}{\text{s}}$ ;
- RC1-C & RC1-D: BFF is expected to occur at lower speeds than  $150 \frac{\text{m}}{\text{s}}$  because the rigid-elastic coupling could be magnified for certain allowed combinations of  $\sigma_s$  and  $D$ .

All the analyses show two distinct peaks in the  $\mu$  plot, one at a low frequency  $\omega_1 \approx 10 \frac{\text{rad}}{\text{s}}$  (related to the BFF mechanism) and another at a high frequency  $\omega_2 \approx 70 \frac{\text{rad}}{\text{s}}$  (related to the torsion-bending coupling). The values of these peaks for each case are also highlighted in a dedicated table inset in Fig. 4.10. When the first uncertainty level RC1-A is considered (solid line),  $\mu$  is smaller than 1 for the whole frequency range, indicating that the system is robustly stable in the face of the allowed uncertainties. The values of the peaks are respectively 0.58 at  $\omega_1$  and 0.62 at  $\omega_2$ . When the tail distance uncertainty level is tripled in RC1-B (red dashed line), there is a greater increase in the low frequency peak (0.74) than in the high-one (0.63). This suggests that the BFF instability is more sensitive to variations on  $D$ . When the wing bending stiffness is tripled in RC1-C (blue dotted line), the system RS undergoes a remarkable degradation. In particular the low frequency peak (1.37) is highly affected indicating that with the present uncertainty level the stability of the system is violated for the selected sub-critical speed of  $150 \frac{\text{m}}{\text{s}}$ . Recalling from Fig. 4.9 that the nominal tests indicated the torsional-bending ( $V_{f2} = 162.8 \frac{\text{m}}{\text{s}}$ ,  $\omega_{f2} = 69.7 \frac{\text{rad}}{\text{s}}$ ) to be the first to achieve instability with respect to the BFF ( $V_{f1}$

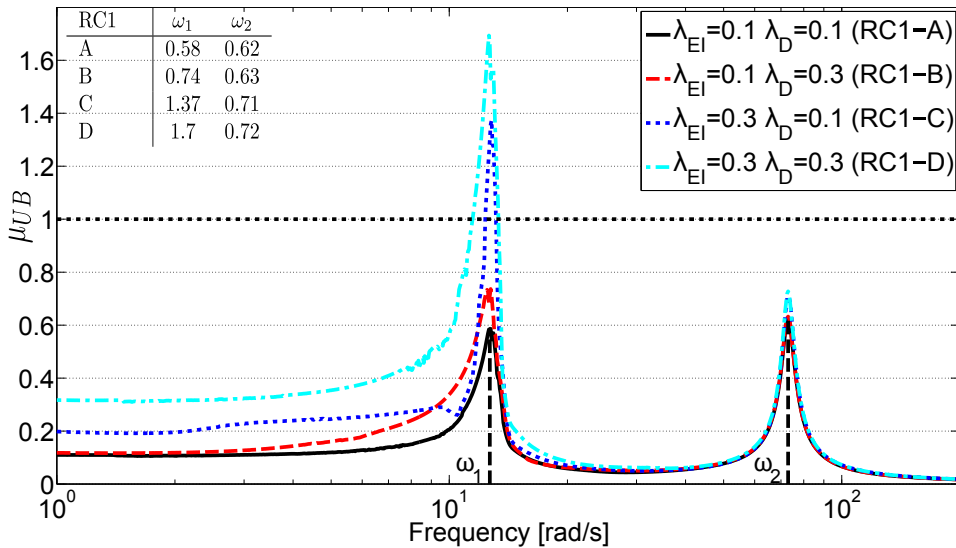


Figure 4.10:  $\mu$ -based sensitivity to EI and D using LFT-1.

$= 175 \frac{m}{s}$ ,  $\omega_f 1 = 14.7 \frac{rad}{s}$ ), now the reversal is seen in Fig. 4.11. That is, the instability predicted in the face of uncertainties is the one that was deemed less critical according to the nominal analyses in Fig. 4.9. Finally, the scenario when both the parameters vary with a triple uncertainty level in RC1-D (cyan dash-dot line) results in an even more critical robustness degradation for the BFF (1.7), whereas the high frequency instability is almost unchanged (0.72).

The observed trends provide another perspective on the discussion concerning Fig. 4.3, and point at similar conclusions. In particular, it is confirmed that both parameters are more critical for the BFF instability (than for the restrained one) and that in addition the tail distance  $D$  barely affects the torsional-bending coupling (high frequency instability) which reconciles with physical understanding. Another interesting aspect that can be deduced from these results is that the effect of  $D$  on BFF is not magnified when the stiffness uncertainty level is enlarged (given that the system is flexible enough to be susceptible to BFF). This is inferred from a comparison between the *relative* increase, almost the same, in the peaks between the uncertainty level cases (from 0.58 to 0.74 for RC1-A to RC1-B, and from 1.37 to 1.7 for RC1-C to RC1-D). In other words, the bending stiffness is highly detrimental, as often mentioned in the literature, but it does not further exacerbate the influence of  $D$  (which was not so obvious prior to the  $\mu$  analyses). This aspect is well connected with the curves for  $D = \{5, 6, 8\} m$  in Fig. 4.3, which have the same slope (i.e. they are parallel) in the BFF region –indicating that the relative drop in flutter speed (that is, from curve to curve) is irrespective of the value of  $EI$ .

In addition to the findings from Fig. 4.10, the  $\mu_{LB}$  calculation provides the smallest critical perturbation matrix able to determine flutter at the pre-fixed nominally stable speed  $V = 150 \frac{m}{s}$ . In Table 4.3 the values of  $\Delta_1^{cr}$  matrices obtained at the two peak frequencies for the case RC1-C

are reported. It is apparent that for the first peak the instability is triggered by a *reduction* of both  $EI$  and  $D$  (negative values for  $\delta_{EI}$  and  $\delta_D$ ), and this is in accordance with what happens in Fig. 4.3 within the region where BFF is prominent. The examination of the second peak ( $\Delta_1^{cr}|_{\omega_2}$ ) reveals that a positive perturbation  $\delta_{EI}$  is detrimental for the restrained flutter mechanism. This is in agreement with the previously commented fact that this type of instability is more pronounced as the bending stiffness is increased and thus bending and torsional frequencies become closer.

Table 4.3: Worst-case perturbations for LFT-1 (with uncertainty levels  $\lambda_{EI} = 0.3$ ,  $\lambda_D = 0.1$ ) at the two frequency peaks.

$\Delta_1^{cr}$	$\delta_D$	$\delta_{EI}$	$\delta_{Q_{hh,12}}$	$\delta_{Q_{hh,21}}$	$\delta_{Q_{hh,22}}$
$\Delta_1^{cr} _{\omega_1}$	-0.7622	-0.7622	-0.35-0.65i	$0.37 + 0.64i$	$-0.67 + 0.31i$
$\Delta_1^{cr} _{\omega_2}$	-1.4156	1.4156	$1.32 + 0.50i$	$1.1 - 0.9i$	$-0.72 + 1.21i$

#### 4.2.2.2 Results for LFT Model 2

This second LFT model augments the previous one with an additional uncertainty, namely the wing mass ratio  $m_w$  (4.11b). The sensitivity of the system's instabilities to this new parameter is studied following the same process as before. Fig. 4.11 shows the  $\mu$  analyses, now with three different uncertainty range combinations: RC2-A, RC2-B and RC2-C (see the inset in the figure).

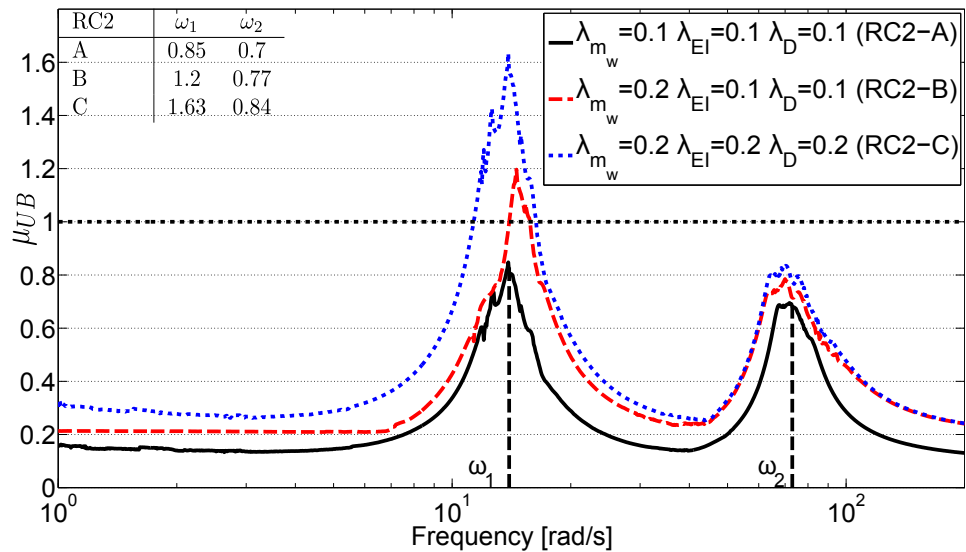


Figure 4.11:  $\mu$ -based sensitivity to  $EI$ ,  $D$ , and  $m_w$  using LFT-2.

As before, two frequency regions are observed each representing a different type of system instability. A comparison between the peak values for the case RC1-A in Fig. 4.10 and for the case RC2-A (solid line) here reveals that the variation in mass is detrimental, particularly for the low frequency instability. The peak corresponding to the high frequency is also affected, but less markedly. The other two uncertainty level cases analysed in Fig. 4.11 extend to the wing mass ratio the observations made before for the tail distance and the bending stiffness uncertain parameters. From further assessment of Fig. 4.11, it can be concluded that the  $m_w$  parameter is critical since the BFF mode (associated with  $\omega_1$ ) changes from stable to unstable between RC2-A and RC2-B (i.e. when  $\lambda_{m_w}$  varies from 0.1 to 0.2), while a similar result was not observed in Fig. 4.10 for the other parameters until their scaling level was three times higher. Note also that the closest instability mechanism to the nominal plant is also for LFT-2 the rigid-elastic one. As before, the critical perturbations are inspected and given in Table 4.4, where the results are relative to the uncertainty level combinations corresponding to the case RC2-B.

Table 4.4: Worst-case perturbations for LFT-2 (with uncertainty levels  $\lambda_{m_w} = 0.2$ ,  $\lambda_{EI} = 0.1$ ,  $\lambda_D = 0.1$ ) at the two frequency peaks.

$\Delta_2^{cr}$	$\delta_{m_w}$	$\delta_D$	$\delta_{EI}$	$\delta_{Q_{hh,12}}$	$\delta_{Q_{hh,21}}$	$\delta_{Q_{hh,22}}$
$\Delta_2^{cr} _{\omega_1}$	-0.87	-0.87	-0.87	-0.35 - 0.8i	0.33 + 0.8i	-0.83 + 0.25i
$\Delta_2^{cr} _{\omega_2}$	1.37	-1.37	1.37	1.20 + 0.65i	1.14 - 0.75i	-0.67 + 1.2i

For the BFF instability,  $\Delta_2^{cr}|_{\omega_1}$  confirms the trend in Table 4.3 for tail distance and bending stiffness, and indicates that this instability is exacerbated by a *decrease* in mass. As for the torsion-bending coupling instability,  $\Delta_2^{cr}|_{\omega_2}$  reveals that this is favoured by an increase in wing mass. While this last effect can be understood by focusing only on the interaction between the two elastic modes (similar to what was done in Table 4.3 for  $\Delta_1^{cr}|_{\omega_2}$ ), the interpretation of the negative mass perturbation for the BFF instability is more difficult. Nonetheless, the fact that a reduction in wing mass makes the aircraft more prone to BFF reconciles with known features in the literature, as it was the case before for  $D$  and  $EI$ . In fact, this was ascribed in [154] to the effect that a lower vehicle pitch inertia  $I_{yy}$  had in increasing the short period frequency  $\omega_{SP}$  and thus pushing it closer to the wing bending lowest frequency. The robust flutter framework presented in here allows this aspect to be ascertained from a worst-case perspective, and paves the way for analysis campaigns where additional relevant parameters can be included.

In the interest of compactness of presentation they are not reported here but further tests were performed, and published in [125], in order to gain a better understanding on the unstable mechanisms detected by Table 4.4. The main finding, aided by the use of the MAC indicator, was that the wing mass parameter is responsible for a coalescence between the first bending and short-period vibration modes. That is, a merging of the eigenmodes, in addition to that classically

expected of the frequencies, takes place at the onset of instability. This aspect is in accordance with previous works, such as that of reference [25], which stressed that the BFF instability is exacerbated by parameters which able to adversely modify the mode shapes of the aircraft.

### 4.3 Application of $\mu$ to uncertain high-order models

In this section an application of the strategies developed in Sec. 3.3 for studying uncertain high-order models is illustrated using the joined-wing aircraft system described in Sec. 2.3.3. Algorithm 3.2 is employed to build an LFT model capturing uncertainties in the physical stiffness and mass parameters defined in the FEM model. Then, Algorithm 3.3 is applied to compute the worst-case perturbation matrix determining flutter at a given (nominally stable) speed and thus to assess robustness.

#### 4.3.1 Nominal analysis of the joined-wing case study

The flutter behaviour of the *PrP250* configuration without uncertainties is investigated first. The analyses are carried out with the FSI solver CSHELL<sup>2</sup> (featuring a  $p$  method based on the Roger approximation of the  $Q_{hh}$  matrix), and then validated with the commercial software NASTRAN [203], considering only the first 10 structural modes ( $n_s=10$ ). Results of the flutter analysis are shown in Fig. 4.12 in terms of imaginary and real parts of the poles as speed is increased. It is seen on the right plot that mode I becomes unstable (indicated in the figure as flutter point) at approximately  $V_f = 297 \frac{m}{s}$  due to the coalescence of the frequencies of the first two bending modes (see left plot) before flutter occurs.

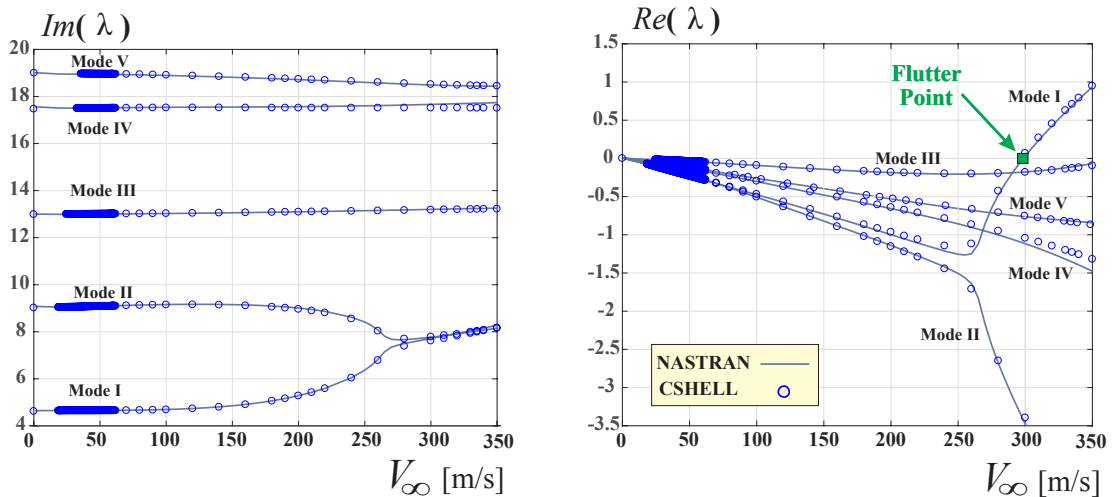


Figure 4.12: Flutter analysis of *PrP250* (real and imaginary part of the first 5 modes shown).

<sup>2</sup>CSHELL is a proprietary software developed by the authors of [40, 60].

Next, the wing model is connected with an elastic fuselage (clamped in the system centre of gravity –see Fig. 4.13). This new model aims at considering the effect of the fuselage elasticity (and so the mutual movement and pitching of the two wings roots) on the aeroelastic behaviour of the system and is an evolution of the one used in [40] where only concentrated inertial effects were retained. Lumped masses have been placed along its length to simulate distribute inertial effects of structures, systems, and payload. The fuselage is connected to the front wing root and the rudder with rigid links.

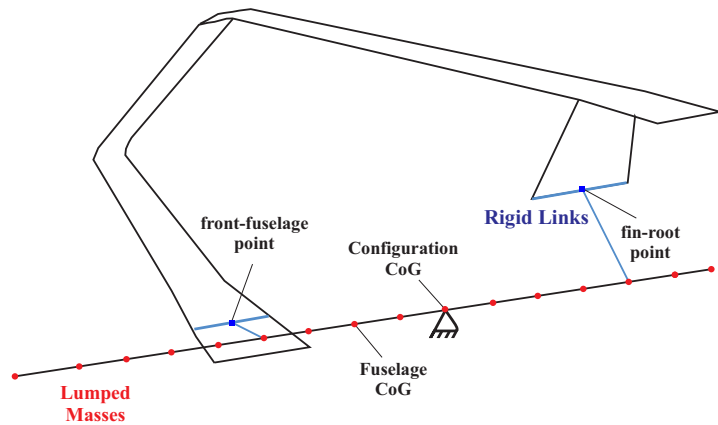


Figure 4.13: Layout of the *PrP250* featuring a clamped flexible fuselage.

Fig. 4.14 shows the results of flutter analysis. The coalescence of the first two elastic modes, observed already in Fig. 4.12, is still present, resulting in an instability of mode I at a similar speed as before. However, now flutter onset is caused by mode III which becomes unstable at approximately  $V_f = 270 \frac{m}{s}$ .

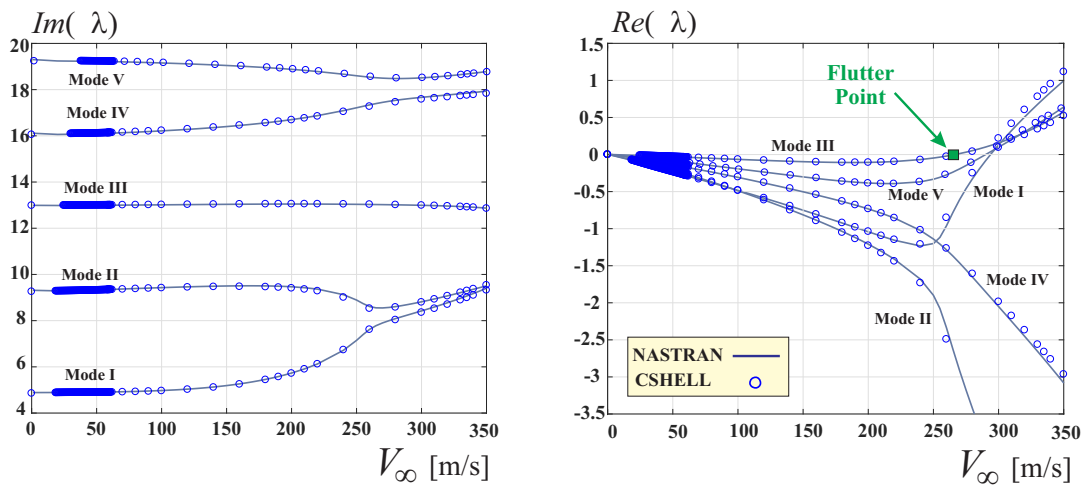


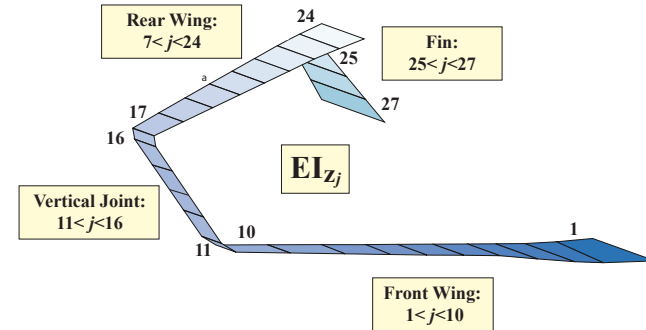
Figure 4.14: Flutter analysis of *PrP250* with elastic fuselage.

The robust flutter analysis will only consider the model without elastic fuselage (Fig. 4.12),

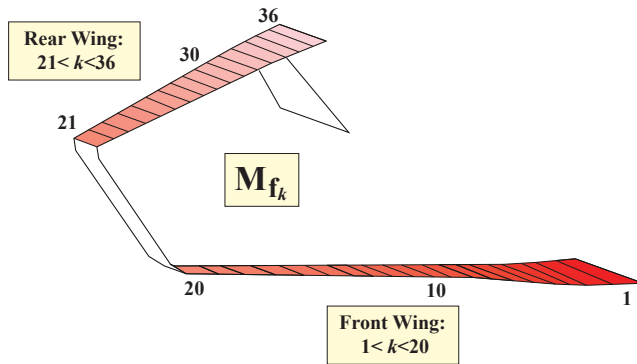
because results are available in the literature for this case study only. However, the effect of an elastic fuselage on the flutter of *PrP250* is preparatory for the discussion at the end of the next section.

### 4.3.2 Robust flutter analysis with the symbolic LFT-FSI approach

Uncertainties for the stiffness and mass distribution along the wing are selected following the rationale of uncertainty distribution sketched in Fig. 3.4. These are depicted in Fig. 4.15.



(a) Stiffness parameters.



(b) Mass parameters.

Figure 4.15: Uncertainty description for the joined-wing configuration.

The FEM model has 54 beam elements (Fig. 2.6). For each beam, the bending stiffness parameter  $EI_z$  is considered as an uncertain parameter. To allow for continuity among the elements, 27 reference stations (shown and numbered in Fig. 4.15a) are defined by pairing consecutive beams, and the uncertainties are perturbed in the same way if they belong to the same station. Therefore, the stiffness uncertainty description consists of 27 uncertainties (i.e.  $\delta_{EI_{z_j}}$  with  $j=1, \dots, 27$ ), each allowed to vary within 10% of its nominal value. As for the mass,

the 36 fuel masses  $m_f$  gathered in the model, and visualised in Fig. 4.15(b), are all assumed uncertain (i.e.  $\delta_{m_{f_k}}$  with  $k=1, \dots, 36$ ) and allowed to vary within 10% of their nominal values.

The symbolic LFT approach described in Algorithm 3.2 is then applied. Given the above uncertainty definitions (representing Step-S1), it is possible to obtain the symbolic physical matrices (Step-S2) and then assemble the symbolic modal matrices (Step-S3) using the nominal modal matrix  $\Phi_0$ . With the modal operators  $\bar{M}_s$  and  $\bar{K}_s$  expressed as a function of the uncertain parameters, it is now possible to build an aeroelastic LFT, characterised by the uncertainty block:

$$\Delta_{M-K}^{630,R} = \text{diag}(\delta_{EI_{z_1}} I_{10}, \dots, \delta_{EI_{z_{27}}} I_{10}, \delta_{m_{f_1}} I_{10}, \dots, \delta_{m_{f_{36}}} I_{10}). \quad (4.12)$$

Despite the adoption of LFT order reduction techniques [146], the size of the LFT in (4.12) is such that it cannot be used for  $\mu$  calculation at this stage. The very high dimension of 630 is ascribed to two main reasons: the large number of real parameters (63) captured in the LFT, and the presence of uncertainties in all the structural modes ( $n_s = 10$ ).

The large number of uncertain parameters initially considered was done deliberately to showcase the modelling capabilities (especially when compared to the numerical LFT approach). This also allows to demonstrate the ease of extracting reduced LFT models for specific analyses (such as focusing on fuel mass in certain areas of the wing or to independently analyse the effect of stiffness versus mass) once an initial large LFT has been built up.

In order to lower the size, firstly a reduced number of parameters is selected based on their contribution to the coefficients of the modal matrices (this can be done in Step-S4 because the modal matrices are available as polynomials in the uncertainties). As a result of this polynomial reduction process, the number of parameters in the LFTs decreases to 20 for the stiffness and 25 for the mass.

Afterwards, the selection of the number of modes  $n_{s,u}$  subject to uncertainties is considered. The nominal analyses pointed out that flutter is prompted by the coalescence of the first and second bending modes. Therefore a small number of modes  $n_{s,u} \leq n_s$  might be sufficient to capture the effect of the uncertainties on flutter. This assumption was confirmed by carrying out analyses for different values of  $n_{s,u}$  where a convergence of the predictions for  $n_{s,u} \geq 5$  was observed and hence  $n_{s,u} = 5$  is considered. It is stressed that this strategy for reducing the LFT size is distinctive of the modal-oriented modelling approach proposed here. A reduced-order LFT with a size of 225, and gathering in total 45 different real parameters, is finally obtained.

The analysis Algorithm 3.3 from Sec. 3.3.2.2 is then applied. This will detect a worst-case perturbation that makes the aeroelastic system flutter at the selected subcritical speed  $V_\mu$ . Specifically,  $V_\mu = 285 \frac{m}{s}$  is chosen considering the flutter behaviour of the nominal configuration ( $V_f = 297 \frac{m}{s}$  from Fig. 4.12). Fig. 4.16 shows in the main plot only the  $\mu$  upper (UB) and lower (LB) bounds corresponding to the first iteration (ITER1) of the algorithm, while in the inset the different iterations for the low frequency peak are given.

Note that two peaks are clearly observed, a lower frequency one, taking place at approximately  $\omega_1 = 7.2 \frac{rad}{s}$  and associated with the coalesced modes I-II, and a higher frequency one. As prescribed

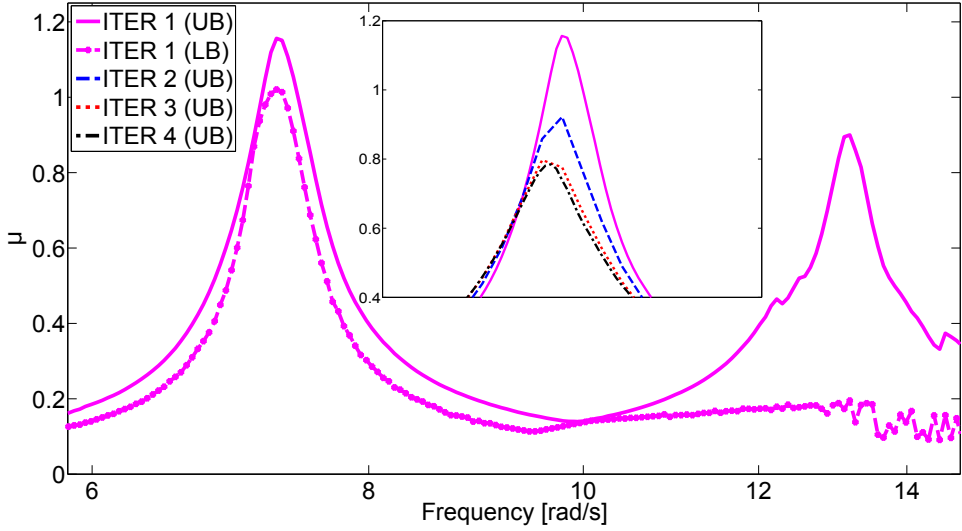


Figure 4.16: Results of the  $\mu$ -based iterative algorithm (convergence attained at the 4<sup>th</sup> iteration).

by the algorithm, the perturbation matrix extracted from the highest peak of the lower bound is used, and hence the instability related to modes I-II will be studied here. The same procedure could be applied to another point of the frequency grid by simply carrying out the iterations with respect to the corresponding perturbation matrix.

In the inset of Fig. 4.16 the upper bounds at all the other analysis algorithm's iterations (ITER#) are reported. For clarity, the lower bounds are not plotted since the relative gap between bounds for each iteration is similar to the one at ITER1. Table A.3 in Appendix A shows the entries of the perturbation matrices  $\Delta_{ITER\#}^{cr}$  and the corresponding flutter speed  $V_{f\mu}$  (calculated by CSHELL) at each iteration. For conciseness, Table 4.5 reports only the norm of the perturbation matrices and  $V_{f\mu}$  at each iteration.

Table 4.5: Flutter speed and corresponding perturbation matrix's norm at each iteration of Algorithm 3.3.

ITER	$V_{f\mu} \frac{m}{s}$	$\bar{\sigma}(\Delta^{cr})$
1	288.4	0.98
2	287.4	1.23
3	285.9	1.41
4	285.24	1.47

The algorithm achieves in 4 iterations a value of  $V_{f\mu}=285.2 \frac{m}{s}$  which is within 0.15% of the selected  $V_\mu=285 \frac{m}{s}$ . At each iteration #, the magnitude of  $\Delta_{ITER\#}^{cr}$  increases (this was already noticeable in Fig. 4.16 since smaller  $\mu_{UB}$  indicates larger norm of the perturbation matrix). The

change in magnitude of  $\Delta_{ITER\#}^{cr}$  can be explained by the importance of the perturbations in the modal base  $\Phi$ , not captured in the initial LFT representation (build up with the unperturbed base  $\Phi_0$ ) and taken into account with the iterative strategy (recall its interpretation given in Eq. 3.35). It is also important to observe (from Table A.3) that the perturbations show approximately the same directionality from one iteration to the other (e.g. positive/negative trends of the uncertain parameters). This qualitatively supports the accuracy of the predicted  $\hat{\Delta}^{cr}$ , and more generally indicates that worst-case regions are correctly detected (further comments on this will be given in the next section). When this pattern is observed, robustness properties such as robust flutter sensitivity (for example, the one carried out for the BFF case study in Sec. 4.2.2) can be inferred afterwards based on analyses which use the nominal modal matrix  $\Phi_0$ .

It is also important to consider the frequency content of the information provided by  $\mu$ , which in this case showed the presence of two distinct peaks. Recall indeed that the nominal flutter analyses only detected the presence of the modes I-II flutter (Fig. 4.12), while it was necessary to augment the model with an elastic fuselage (Fig. 4.14) to find that the mode III could become also critical for flutter. As seen in Fig. 4.16, robust analysis anticipates this for the analysed model (which does not include an elastic fuselage) when variations of particular stiffness and mass parameters are allowed in the system. Indeed, the higher frequency peak in Fig. 4.16 occurs at a frequency very close to that of mode III in Fig. 4.14 (approximately  $13 \frac{rad}{s}$ ). The insights provided by the frequency perspective on  $\mu$ , already highlighted in the robust BFF analyses earlier in this chapter, are deemed an important feature and an advantage of the proposed robust modelling analysis framework.

### 4.3.3 Optimality analysis of the worst-case perturbation

Uncertain parameters requiring subsequent detailed analysis were identified by looking, in the perturbation matrices  $\Delta_{ITER\#}^{cr}$  (Table A.3 in Appendix A), at changes in the direction of the perturbations within successive iterative steps. Specifically,  $EI_{z_5}$  and  $m_{f_{21}}$  were found to exhibit a non-uniform pattern. The former has an almost null perturbation in  $\Delta_{ITER1}^{cr}$  but then becomes positive for the other iterations, whereas  $m_{f_{21}}$  changes sign at the second iteration. By performing a  $\mu$  sensitivity analysis, it was concluded that the parameter  $EI_{z_5}$  has small importance for flutter, whereas  $m_{f_{21}}$  (a rear wing tip mass) proved to be relevant for the instability.

Algorithm 3.4 is applied to investigate the observed pattern of  $m_{f_{21}}$ , and in order to do so the tested perturbation matrices  $\Delta_i^t$  must be selected (Step-C1 of the algorithm). Table 4.6 reports the definition for the 5 tested LFTs, along with the resulting  $\mu_{UB}$ . The LFTs are centred at: the perturbation matrix  $\Delta_{ITER1}^{cr}$  found in the first iteration (i.e. first row in Table A.3), this LFT is termed 1-1; the opposite of  $\Delta_{ITER1}^{cr}$  (case 1-2);  $\Delta_{ITER2}^{cr}$  (case 2-1); the opposite of  $\Delta_{ITER2}^{cr}$  (case 2-2);  $\Delta_{ITER2}^{cr}$  but considering opposite perturbation in the tip mass  $m_{f_{21}}$  (i.e. positive instead of the negative predicted at this iteration) (case 2-3).

Fig. 4.17 shows the results which, for a better visualisation, feature reversed axes with

Table 4.6: Tested worst-case perturbations in the optimality check.

<i>case</i>	<i>ITER</i>	$\Delta_i^t$	$\mu_{UB}$
1-1	1	$\Delta_{ITER1}^{cr}$	4.4
1-2	1	$-\Delta_{ITER1}^{cr}$	0.53
2-1	2	$\Delta_{ITER2}^{cr}$	6.3
2-2	2	$-\Delta_{ITER2}^{cr}$	0.44
2-3	2	$\Delta_{ITER2}^{cr}, \delta_{m_f,21} = -\delta_{m_f,21}^{cr}$	9

respect to the usual convention, i.e.  $\mu_{UB}$  plotted on the *x*-axis and  $\omega$  on the *y*-axis. For comparison purposes, the curves from Fig. 4.16 for iteration 1 (ITER1) and iteration 2 (ITER2) are presented as solid lines with cross and square markers respectively.

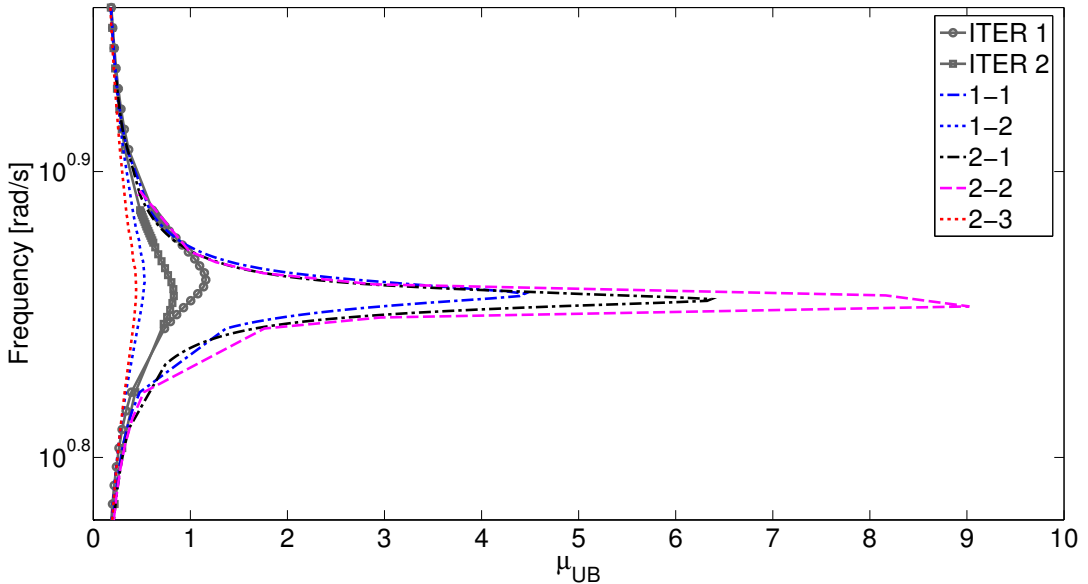


Figure 4.17:  $\mu$  analysis of LFTs featuring different nominal plants. The value of the peak is a measure of the proximity of the nominal plant to the actual worst-case.

Let us first consider the curves relative to the first iteration, that is 1-1 (blue dash-dot line) and 1-2 (blue dotted line). The dash-dot line has a higher peak than the one featured by *ITER 1*, whereas the dotted line has the smallest (among these 3). This, along with the noticeable sharp peak of the dash-dot curve, suggests that  $\Delta_{ITER1}^{cr}$  points at a worst-case direction for the system. It is stressed that Algorithm 3.4 builds each LFT based on the modal base  $\Phi$  associated with the tested worst-case perturbation (Step-C3). Therefore, even when an actual perturbation matrix predicted by  $\mu$  (e.g. 1-1) is tested, the corresponding nominal plant is not neutrally stable because that worst-case matrix was computed with respect to an LFT built up with a different modal base

$\Phi$ . Thus,  $\mu$  peak is not infinitely large and the procedure is numerically reliable, as confirmed next.

The analyses performed with respect to the results from the second iteration are then considered, i.e. 2-1 (black dash-dot line), 2-2 (red dotted line), and 2-3 (magenta dashed line). A first remark is that 2-1 exceeds 1-1, meaning that as the algorithm proceeds, it converges to the worst-case of the system (i.e.  $\Delta_{ITER2}^{cr}$  is a better estimation of  $\hat{\Delta}^{cr}$  than  $\Delta_{ITER1}^{cr}$ ). Another important aspect is inferred by comparing the magenta (2-3) and black (2-1) curves. The former has a greater peak than the latter, that is, the  $\mu_{UB}$  algorithm detects case 2-3 as a closer worst-case of the system than 2-1. In other words, the worst perturbation for  $m_{f_{21}}$  is the positive one (as initially predicted in the first iteration). Interestingly, the peak of  $\mu$  is not infinitely large for 2-1 (in fact, there exists another LFT with larger peak), which shows that the algorithm is numerically well-posed and is able to capture the effect of updating the modal base on the global optimum. Similar evidences on the role of parameter  $m_{f_{21}}$  were obtained by applying these analyses at ITER 3.

Prompted by these findings, the iterative cycle was restarted at ITER 2 with the perturbation matrix  $\Delta_{ITER2}^{cr}$  but enforcing a positive perturbation in  $m_{f_{21}}$ . Inspired by hybrid strategies common in applied optimisation [171], the idea is to initialise the (non-convex) algorithm with the best candidate in the population (represented by the three tested  $\Delta_i^t$ ) according to the cost function, which is here the peak of  $\mu$  in the plots of Fig. 4.17. The new iterative cycle only requires 3 iterations to converge, and Table A.4 reports the perturbation matrix  $\Delta_{ITER3-new}^{cr}$  and the corresponding flutter speed at the last iteration. It is noted that  $\bar{\sigma}(\Delta_{ITER3-new}^{cr}) \approx 1.34$ , whereas before it was  $\bar{\sigma}(\Delta_{ITER4}^{cr}) \approx 1.47$  (from Table 4.5), i.e. the perturbation identified thanks to Algorithm 3.4 has indeed a smaller norm. These analyses confirm that the proposed heuristics to check the correctness of the worst-case matrix can provide a helpful tool to monitor the accuracy of the results.

#### 4.3.4 Reconciliation with previous results

The connection of the results obtained by means of the  $\mu$ -LFT framework with other findings from the literature are discussed here. In [70] a detailed study of the flutter behaviour of the *PrP250* configuration was performed. In an attempt to increase the flutter speed, sensitivity of the instability of modes I-II was studied via standard parametric approach. Specifically, trend studies concerning bending stiffness (achieved by changing the skin thickness) and fuel masses at the tips of the wing were investigated. An important outcome of the study was that adding fuel tanks at the tip of the rear wing was highly detrimental for flutter, whereas placing masses at the tip of the front wing enhanced flutter performance. By looking at the worst-case perturbation in Table A.4, it can be noted that the latter aspect is confirmed by the analyses performed with  $\mu$ . A decrease in the front tip masses  $m_{f_{19}}$  and  $m_{f_{20}}$  can be observed, whereas the other masses (and in particular the rear tip ones  $m_{f_{22}}$ , and  $m_{f_{23}}$ ) have a positive perturbation. The worst-case direction

for the rear tip mass  $m_{f_{21}}$  was addressed by means of the global optimum check, confirming a detrimental effect when this is positive.

For what regards the stiffness parameters, the study in [70] found that increasing the skin thickness on both rear and front wings allowed to raise flutter velocity. To better assess this, a robust sensitivity analysis which follows the approach described in Sec. 4.2.2 is performed. As before, the task is addressed by considering two different uncertainty levels, namely 10% and 20%. For each uncertainty (in full generality, both stiffness and mass parameters will be considered), a  $\mu$  calculation is performed where the selected parameter has a 20% of variation, while all the others vary within 10% of their nominal values. The distance of the peak of each curve from that obtained with all parameters ranging within 10% is a measure of the sensitivity of the considered instability to that parameter. Fig. 4.18 shows all the curves involved in the sensitivity calculation. The solid red one ( $\lambda = 0.1$ ) corresponds to the analysis with all parameters' range set at 10% (this indeed coincides with the curve *ITER 1 (UB)* in Fig. 4.16). The dashed black curves are obtained by perturbing one by one the uncertainty level of the stiffness parameters, whereas the grey dotted ones consider the mass parameters. Note finally that this study is performed keeping the modal base fixed at the nominal value  $\Phi_0$ .

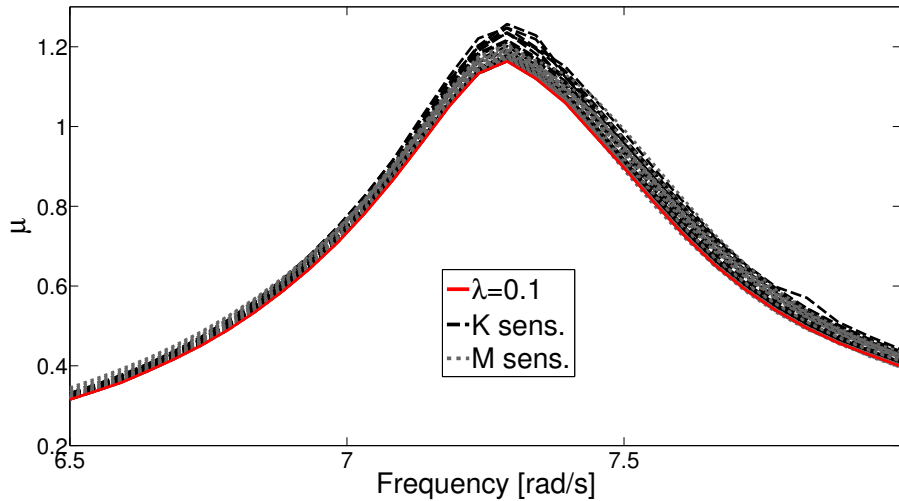


Figure 4.18:  $\mu$ -based sensitivity to the mass and stiffness parameters.

The stiffness parameters are then sorted according to the sensitivity revealed by Fig. 4.18. The ten most critical parameters belong to 4 distinct areas (see the numbering in Fig. 4.15(a)): front tip ( $EI_{z_9}$ - $EI_{z_{10}}$ ), rear root ( $EI_{z_{23}}$ - $EI_{z_{22}}$ - $EI_{z_{24}}$ ), rear tip ( $EI_{z_{18}}$ - $EI_{z_{17}}$ ), and front root ( $EI_{z_2}$ - $EI_{z_3}$ - $EI_{z_1}$ ). Note also that all these parameters feature a *negative* worst-case perturbation in Table A.4, in accordance with the findings in [70] where opposite trends were suggested in order to increase the flutter speed.

When the same analysis process was applied to the mass parameters, it was revealed that the most sensitive fuel masses are those located at the tip of the wings, which is the area considered

for the parametric analyses in [70]. The reconciliation with the results obtained in this section is indeed an important confirmation of the validity of the LFT approach presented in Sec. 3.3.2, and it shows that this methodology can be employed for assessments and investigations of complex aeroelastic systems.

## 4.4 Chapter summary

In this chapter linear flutter analysis have been applied to nominal and uncertain case studies featuring increasing complexity.

Two among the most established numerical methods ( $p$  and  $p$ - $k$ ) for nominal flutter analysis have been illustrated and then applied to the typical section and simplified aircraft systems. The former has been analysed keeping fixed all the parameters except the speed, which is increased until a condition of neutral stability, that is flutter, is reached. The tendency of the aircraft model to undergo BFF has been investigated instead via a parametric analysis applied to two relevant parameters (bending stiffness and tail volume). The results confirm that the proposed simplified model captures in a concise representation the basic features of the coupling between rigid and elastic modes and aids in understanding the fundamental mechanisms.

In order to address the study of flutter for systems subject to uncertainties, in a second stage the LFT modelling and  $\mu$  analysis are applied. It is first shown using the typical section how this framework can be employed to assess robustness at a fixed subcritical speed. An important point raised by the analyses is that the obtained prediction is something more than a binomial test on robust stability, as it also provides a wealth of information to the analyst. This message is further emphasised with the application to the simplified aircraft model, where the possibility to perform  $\mu$ -based sensitivity is exemplified. This allows results previously obtained with the parametric approach to be retrieved in a more systematic manner and with analytical guarantees, and enables further characteristics of the two observed instabilities (BFF and wing flutter) when the effect of additional parameters is sought to be inferred.

The robust framework is finally applied to study the effect of distributed mass and stiffness uncertainties on the flutter performance of an unconventional joined-wing configuration. The proposed LFT-FSI modelling and analysis paradigm developed in the previous chapter is successfully employed to determine worst-case perturbations that makes the system flutter at a given nominally stable speed. The predictions are validated in the high-fidelity FSI solver, and show good agreement with previous findings from the literature.

An important outcome of these investigations is that the study of complex systems, possibly experiencing different adverse interactions (e.g. between aeroelastic deformation of the restrained wing and rigid body motion of the aircraft in the BFF; among different modes of deformation and non-intuitive aerodynamics loads distributions in the Joined Wings) can greatly benefit from the joint use of conventional (nominal) strategies and robustness approaches. Indeed, the former

are fundamental in providing an overall understanding of the system and appropriate starting point for more systematic investigations over a larger parameter space. On the other hand, the information provided by an adequate modelling and robust analysis methodology is relevant for the design of modern flexible aircraft configurations, since this is inherently multidisciplinary. In a conceptual design stage, when typically a large number of concurrent requirements are taken into account, the  $\mu$ -LFT framework could supply invaluable understanding of the system. The analyses in this chapter, for example, have pointed out trade-offs in wing stiffness, mass and aircraft flight mechanics properties that could represent passive means to mitigate the onset of dynamic aeroelastic instabilities and as a result increase the flutter free envelope. In a more advanced stage, when the system layout is frozen, these tools can provide robustness stability certificates in an efficient way for the most critical operating conditions identified by the standard approaches. This complementarity between the different analyses approaches is highly desirable and one of the contributions of this study.



## WORST-CASE ANALYSIS OF FINITE HORIZON LINEAR TIME-VARYING SYSTEMS

The properties of an aeroelastic system are function of several parameters, as discussed in the previous two chapters. Among these, the flight speed  $V$  has a central importance, as testified by its adoption by industry and certification authorities to define the safe operating envelope of an aircraft. For manoeuvres involving a change of speed, the state-of-practice is to evaluate stability and performance with respect to linear time-invariant models corresponding to frozen time instances along the trajectory. This is a valid but not rigorous approach, and in some cases can lead to erroneous conclusions [137]. In the specific case of very flexible aircraft, where as shown in Chapter 4  $V$  is able to determine a strong coupling between aerodynamics, deformations, and flight mechanics, this simplifying hypothesis might be further challenged. As a result, the mathematical description of an aircraft manoeuvre is more accurately given as a Linear Time-Varying (LTV) system. Note that this reasoning holds true not only for speed but also for other properties of the system that might change during the manoeuvre (e.g. activation of feedback control only during specific parts of the mission). Moreover, capturing the presence of time-varying properties can be seen as a preliminary step to relax the linear assumption made so far. Indeed, a standard approach in aerospace applications [84, 162] is to linearise nonlinear models around different operating points each corresponding to an LTI system. The schematisation of this problem with an LTV representation gathering the family of linearised systems is then a possible approach to capture some nonlinear features of the original system.

Prompted by these considerations, this chapter proposes a method for analysing the performance of (nominal) Linear Time-Varying systems on a finite time horizon. Known facts from optimal control theory (Riccati differential equation, Hamiltonian dynamics, two-point boundary

value problem) represent the theoretical background for the technical result and are briefly reviewed in Section 5.1. The performance is defined by means of a generic quadratic cost function, from which commonly used metrics can be derived. The main technical contribution, covered in Section 5.2, consists of a numerical algorithm to compute the worst-case input signal verifying that a given performance objective is not achieved. To this end, an original solution to the well known issue connected to the simulation of Hamiltonian dynamics is proposed. The applicability of this novel approach is then shown in Section 5.3 with the aircraft demonstrator designed by the FLEXOP project consortium (Fig. 2.8).

The work presented in this Chapter was developed during a research collaboration with Prof. Pete Seiler from the University of Minnesota, who suggested the field of work. Specifically, the author: developed the novel technical contents (theoretical construction and numerical algorithms) in Sec. 5.2; devised the gust case study and performed all the analyses reported in Sec. 5.3.

**Publications<sup>1</sup>:** [130, 155] Section 5.2-Section 5.3.

## 5.1 Mathematical background

### 5.1.1 Generalities on LTV performance

Note first that, for a given a signal  $v : [0, T] \rightarrow \mathbb{R}^{n_v}$ , the finite-horizon  $\mathcal{L}_2^{n_v}[0, T]$  norm is defined as  $\|v\|_{2,[0,T]} := \sqrt{\int_0^T v(t)^\top v(t) dt}$ . If  $\|v\|_{2,[0,T]}$  is finite, then it is said that  $v \in \mathcal{L}_2^{n_v}[0, T]$ .

Consider an LTV system  $G$  defined on  $[0, T]$ , where it is assumed throughout that  $T < \infty$ :

$$\dot{x}(t) = A(t)x(t) + B(t)d(t), \quad (5.1a)$$

$$e(t) = C(t)x(t) + D(t)d(t). \quad (5.1b)$$

$x \in \mathbb{R}^{n_x}$  is the state,  $d \in \mathbb{R}^{n_d}$  is the input and  $e \in \mathbb{R}^{n_e}$  is the output. Note that the input vector  $d$  will also be referred to as disturbance throughout the chapter due to its meaning in this context. Similarly, the output vector is denoted by  $e$  because the focus here is performance, hence the output can be seen as an indicator of the error in achieving a certain objective (e.g. tracking a reference signal). The state matrices  $A : [0, T] \rightarrow \mathbb{R}^{n_x \times n_x}$ ,  $B : [0, T] \rightarrow \mathbb{R}^{n_x \times n_d}$ ,  $C : [0, T] \rightarrow \mathbb{R}^{n_e \times n_x}$  and  $D : [0, T] \rightarrow \mathbb{R}^{n_e \times n_d}$  are piecewise-continuous (bounded) functions of time. The dependence on  $t$  of these and other time-varying matrices will be omitted when it is clear from the context for ease of presentation. The state response due to an initial condition  $x(t_0) = x_0$  at  $t_0 \in [0, T]$  and a disturbance  $d \in \mathcal{L}_2^{n_d}[0, T]$  can be expressed using the state transition matrix  $\Psi$  as follows:

$$x(t) = \Psi(t, t_0)x_0 + \int_{t_0}^t \Psi(t, \tau)B(\tau)d(\tau)d\tau. \quad (5.2)$$

---

<sup>1</sup>Material published during the PhD which relates to the content of this chapter.

Since  $T < \infty$ ,  $x \in \mathcal{L}_2^{n_x}[0, T]$  for any  $x_0$  and  $d \in \mathcal{L}_2^{n_d}[0, T]$ . Moreover, there exists a constant  $M$  such that  $\|\Psi(t, \tau)\| \leq M$  for all  $t, \tau \in [0, T]$ , i.e.  $\Psi$  is uniformly bounded [36].

A generic quadratic cost is introduced next to unify different finite-horizon LTV performance metrics. Let  $Q : [0, T] \rightarrow \mathbb{S}^{n_x}$ ,  $R : [0, T] \rightarrow \mathbb{S}^{n_d}$ ,  $S : [0, T] \rightarrow \mathbb{R}^{n_x \times n_d}$  and  $F \in \mathbb{R}^{n_x \times n_x}$  be given.  $Q$ ,  $S$ , and  $R$  are assumed to be piecewise-continuous (bounded) functions. A quadratic cost function  $J : \mathcal{L}_2^{n_d}[0, T] \rightarrow \mathbb{R}$  is defined by  $(Q, S, R, F)$  as follows:

$$J(d) := x(T)^\top F x(T) + \int_0^T \begin{bmatrix} x(t) \\ d(t) \end{bmatrix}^\top \begin{bmatrix} Q(t) & S(t) \\ S(t)^\top & R(t) \end{bmatrix} \begin{bmatrix} x(t) \\ d(t) \end{bmatrix} dt, \quad (5.3a)$$

$$\text{subject to: Eq. (5.1a) with } x(0) = 0. \quad (5.3b)$$

The choice of  $(Q, S, R, F)$  defines the particular performance metric. The derivation of two well known performance metrics from the above general cost function is shown here. First, consider the *finite-horizon induced  $\mathcal{L}_2$ -gain of  $G$* :

$$\|G\|_{2,[0,T]} = \sup \left\{ \frac{\|e\|_{2,[0,T]}}{\|d\|_{2,[0,T]}} \mid x(0) = 0, 0 \neq d \in \mathcal{L}_{2,[0,T]}^{n_d} \right\}. \quad (5.4)$$

As noted above, the state matrices are assumed to be bounded and the state transition matrix is uniformly bounded. This can be used to show that the induced  $\mathcal{L}_2$  gain is bounded for any fixed horizon  $T < \infty$ . Consider now a given scalar  $\gamma > 0$  and select  $Q := C^\top C$ ,  $S := C^\top D$ ,  $R := D^\top D - \gamma^2 I_{n_d}$  and  $F := 0$ . These choices yield the following quadratic cost:

$$J_{2,\gamma}(d) = \|e\|_{2,[0,T]}^2 - \gamma^2 \|d\|_{2,[0,T]}^2. \quad (5.5)$$

Thus  $J_{2,\gamma}(d) \leq 0 \forall d \in \mathcal{L}_2^{n_d}[0, T]$  if and only if  $\|G\|_{2,[0,T]} \leq \gamma$ , which retrieves the performance metric from (5.4).

Next, assume  $D(T) = 0$ . Then the *finite-horizon induced  $\mathcal{L}_2$ -to-Euclidean gain of  $G$*  is:

$$\|G\|_{E,[0,T]} = \sup \left\{ \frac{\|e(T)\|_2}{\|d\|_{2,[0,T]}} \mid x(0) = 0, 0 \neq d \in \mathcal{L}_{2,[0,T]}^{n_d} \right\}. \quad (5.6)$$

The  $\mathcal{L}_2$ -to-Euclidean gain depends on the system output  $e$  only at the final time  $T$ , and can be used, for example, to bound the set of states  $x(T)$  reachable by disturbances of a given norm (reachability analysis). The assumption that  $D(T) = 0$  ensures this gain is well-defined. This performance metric can also be related to the quadratic cost  $J$  as follows. Let  $\gamma > 0$  be given and select  $Q := 0$ ,  $S := 0$ ,  $R := -\gamma^2 I_{n_d}$  and  $F := C(T)^\top C(T)$ . This yields the following cost function:

$$J_{E,\gamma}(d) = \|e(T)\|_2^2 - \gamma^2 \|d\|_{2,[0,T]}^2. \quad (5.7)$$

Thus  $J_{E,\gamma}(d) \leq 0 \forall d \in \mathcal{L}_2^{n_d}[0, T]$  if and only if  $\|G\|_{E,[0,T]} \leq \gamma$ , which retrieves the performance metric from (5.6).

The next theorem states an equivalence between a bound on the quadratic cost  $J$  and the existence of a solution to a Riccati Differential Equation (RDE).

**Theorem 5.1.** [98] Let  $(Q, S, R, F)$  be given with  $R(t) < 0$  for all  $t \in [0, T]$ . The following statements are equivalent:

1. There exists a constant  $\epsilon > 0$  such that  $J(d) \leq -\epsilon \|d\|_{2,[0,T]}^2 \forall d \in \mathcal{L}_2^{n_d}[0, T]$ .
2. There exists a differentiable function  $Y : [0, T] \rightarrow \mathbb{S}^n$  such that:

$$\dot{Y} + A^\top Y + YA + Q - (YB + S)R^{-1}(YB + S)^\top = 0, \quad (5.8a)$$

$$Y(T) = F. \quad (5.8b)$$

This result is given as Theorem 3.7.4 in [98] for the particular case of  $J$  corresponding to the induced  $\mathcal{L}_2$  gain. A statement and proof for general  $(Q, S, R, F)$  cost functions can be found in [218]. Theorem 5.1 allows to assess the performance of the finite-horizon LTV system in (5.1) using the RDE (5.8). Specifically, the performance  $J(d) \leq -\epsilon \|d\|_{2,[0,T]}^2$  is achieved if the associated RDE exists on  $[0, T]$  when integrated backward from  $Y(T) = F$ . Conversely, the performance is not achieved if the RDE solution fails to exist on the interval  $[0, T]$ . Note that the existence of a solution to (5.8) can be easily tested by numerically integrating the ordinary differential equation (5.8).

Bisection can be used in conjunction with this theorem to evaluate upper and lower bounds on the system performance [218]. For example, for the case of induced  $\mathcal{L}_2$  gain, it has been observed before that the quadratic cost  $J_{2,\gamma}$  depends on the choice of  $\gamma$ . If, for a given  $\gamma$ , the RDE solution exists on  $[0, T]$  then  $\|G\|_{2,[0,T]} < \gamma$ , i.e.  $\gamma$  is a valid upper bound ( $\gamma_{UB}$ ). Conversely, if  $\gamma$  is selected too small then the RDE solution will fail to exist on  $[0, T]$ . Moreover, if  $Y$  fails to exist then, by Theorem 5.1, for all  $\epsilon > 0$  there exists a non-trivial  $d_\epsilon$  such that:

$$J_{2,\gamma}(d_\epsilon) = \|e\|_{2,[0,T]}^2 - \gamma^2 \|d_\epsilon\|_{2,[0,T]}^2 > -\epsilon \|d_\epsilon\|_{2,[0,T]}^2. \quad (5.9)$$

This implies that  $\|G\|_{2,[0,T]} \geq \gamma$ , i.e.  $\gamma$  is a lower bound on the induced  $\mathcal{L}_2$  gain ( $\gamma_{LB}$ ). Moreover, the inputs  $d_\epsilon$  provide a validation that the gain is greater than or equal to  $\gamma$ . The objective of next section is to compute such a signal  $d_\epsilon$ .

An exemplification of the use of Theorem 5.1 in this context is given next.

**Example 5.1.** Consider the following LTI system

$$\begin{aligned} \dot{x} &= \begin{bmatrix} -11 & -2.5 \\ 4 & 0 \end{bmatrix} x + \begin{bmatrix} 2 \\ 0 \end{bmatrix} d, \\ e &= \begin{bmatrix} 0 & 1.25 \end{bmatrix} x. \end{aligned} \quad (5.10)$$

Bisection was used to compute an upper and lower bound on the induced  $\mathcal{L}_2$  gain on the horizon  $[0, T]$ , with  $T = 0.1$  s. This yielded the bounds  $\gamma_{UB} = 0.0156$  and  $\gamma_{LB} = 0.0155$ . As noted above (5.5), computing the induced  $\mathcal{L}_2$  gain entails applying a bisection where the RDE is integrated backward from  $Y(T) = 0$ . Fig. 5.1 shows the spectral radius of  $Y$  ( $\rho(Y)$ ) on  $[0, T]$  for the solutions

corresponding to  $\gamma_{LB}$  (red dashed) and  $\gamma_{UB}$  (blue solid). As expected, the solution for  $\gamma_{UB}$  exists on  $[0, T]$ . On the contrary the RDE solution associated with  $\gamma_{LB}$  fails to exist on the entire horizon. In fact, it grows unbounded at  $t_0 \approx 0.015$  when integrating backward from  $T$ .

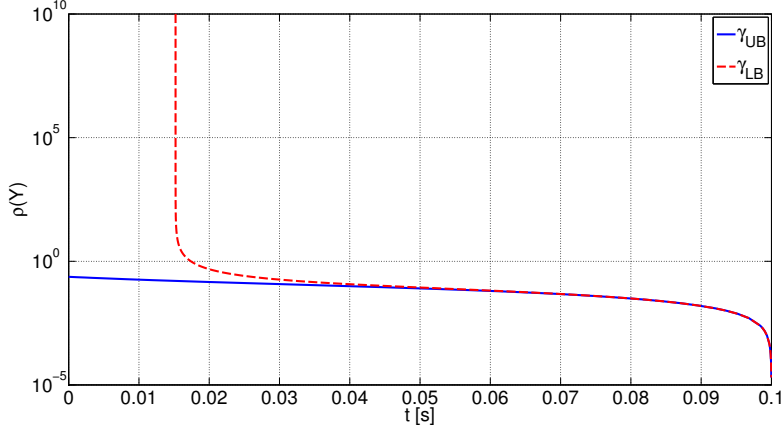


Figure 5.1: Spectral radius of  $Y$  for the upper and lower bound cases.

### 5.1.2 Hamiltonian dynamics

A two-point boundary value problem is used in the proof of Theorem 5.1, and this section briefly reviews a related useful result. First consider the following dynamics on  $[0, T]$ :

$$\begin{bmatrix} \dot{x}^*(t) \\ \dot{\lambda}(t) \end{bmatrix} = H(t) \begin{bmatrix} x^*(t) \\ \lambda(t) \end{bmatrix}, \quad (5.11a)$$

$$H := \begin{bmatrix} A & 0 \\ -Q & -A^\top \end{bmatrix} + \begin{bmatrix} -B \\ S \end{bmatrix} R^{-1} \begin{bmatrix} S^\top & B^\top \end{bmatrix}. \quad (5.11b)$$

The matrix  $H$  is the time-varying Hamiltonian associated with the RDE in (5.8). Denote with  $\Phi$  the associated state transition matrix. Then, given any final condition  $(x^*(T), \lambda(T))$ , the solution to (5.11) can be written as:

$$\begin{bmatrix} x^*(t) \\ \lambda(t) \end{bmatrix} = \Phi(t, T) \begin{bmatrix} x^*(T) \\ \lambda(T) \end{bmatrix}. \quad (5.12)$$

Next define a *generalised* quadratic cost function  $J^*(d, x_0, t_0)$  by:

$$J^*(d, x_0, t_0) := x(T)^\top F x(T) + \int_{t_0}^T \begin{bmatrix} \dot{x}(t) \\ d(t) \end{bmatrix}^\top \begin{bmatrix} Q(t) & S(t) \\ S(t)^\top & R(t) \end{bmatrix} \begin{bmatrix} \dot{x}(t) \\ d(t) \end{bmatrix} dt, \quad (5.13a)$$

$$\text{subject to: } \dot{x} = Ax + Bd \text{ with } x(t_0) = x_0. \quad (5.13b)$$

Note that the generalised cost  $J^*$  differs from the cost  $J$  defined in (5.3) in that it allows for a non-zero initial condition  $x_0$  at some time  $t_0 \in [0, T]$ . The next lemma provides a useful relationship between the generalised cost  $J^*(d, x_0, t_0)$  and the solution of the Hamiltonian dynamics.

**Lemma 5.1.** Let  $(Q, S, R, F)$  be given and let  $(x^*, \lambda)$  be a solution of (5.12) from any boundary condition satisfying  $\lambda(T) = Fx^*(T)$ . For  $t_0 \in [0, T]$ , define the signal:

$$\bar{d} := \begin{cases} 0. & t < t_0, \\ -R^{-1}(t)(S(t)^\top x^*(t) + B(t)^\top \lambda(t)). & t \geq t_0. \end{cases} \quad (5.14)$$

Then  $J^*(\bar{d}, x^*(t_0), t_0) = x^*(t_0)^\top \lambda(t_0)$ , where:

$$\begin{bmatrix} x^*(t_0) \\ \lambda(t_0) \end{bmatrix} = \Phi(t_0, T) \begin{bmatrix} x^*(T) \\ \lambda(T) \end{bmatrix}. \quad (5.15)$$

**Proof.** Note first that the Hamiltonian dynamics (5.11) can be re-written using the definition of  $\bar{d}$  from (5.14) as follows:

$$\begin{bmatrix} \dot{x}^* \\ \dot{\lambda} \end{bmatrix} = \begin{bmatrix} A & 0 \\ -Q & -A^\top \end{bmatrix} \begin{bmatrix} x^* \\ \lambda \end{bmatrix} - \begin{bmatrix} -B \\ S \end{bmatrix} \bar{d}. \quad (5.16)$$

Thus,  $x^*$  satisfies the LTV dynamics in (5.13b) with initial condition  $x^*(t_0)$ . Next, use the definition of  $\bar{d}$  and the Hamiltonian dynamics to show the following relation:

$$\begin{bmatrix} x^* \\ \bar{d} \end{bmatrix}^\top \begin{bmatrix} Q & S \\ S^\top & R \end{bmatrix} \begin{bmatrix} x^* \\ \bar{d} \end{bmatrix} = -x^{*\top}(\dot{\lambda} + A^\top \lambda) - (\dot{x}^* - Ax^*)^\top \lambda, \quad (5.17a)$$

$$= -\frac{d}{dt}(x^{*\top} \lambda). \quad (5.17b)$$

Use this relation to rewrite the generalised cost as:

$$J^*(\bar{d}, x^*(t_0), t_0) = x^*(T)^\top Fx^*(T) - \int_{t_0}^T \frac{d}{dt}(x^{*\top} \lambda) dt. \quad (5.18)$$

Integrate the last term and apply the boundary condition  $\lambda(T) = Fx^*(T)$  to yield  $J^*(\bar{d}, x^*(t_0), t_0) = x^*(t_0)^\top \lambda(t_0)$ .

■

## 5.2 An algorithm for constructing worst-case disturbances on finite horizons

According to Theorem 5.1, if there is no solution to the RDE in (5.8), then the performance associated with the quadratic cost  $J$  is not verified. The objective of this section is to derive an input signal which confirms that the defined performance is not achieved. First, an analytical expression of the worst-case signal is derived in Section 5.2.1 in terms of the Hamiltonian dynamics associated with the RDE. However, a straightforward implementation of this result features numerical issues commented on therein. This observation leads to a numerically reliable algorithm, presented in Section 5.2.2, which exploits the solution of the RDE.

### 5.2.1 Theoretical construction

Consider first the instances when a solution  $Y$  to the RDE does not exist. Note that the assumption  $R(t) < 0$  for all  $t \in [0, T]$  ensures  $R$  is always invertible and hence the RDE is well-defined. Therefore, the only reason for which there is no solution to the RDE is that  $Y$  becomes unbounded at a certain time inside the finite horizon. This was seen in Fig. 5.1 of Example 5.1, where the solution  $Y(t)$  associated with  $\gamma_{LB}$  became unbounded ( $\rho(Y) \rightarrow \infty$ ) as  $t \rightarrow t_0 > 0$  when integrating backward from  $Y(T) = 0$ . Prompted by this observation, the following lemma proposes an analytical expression for the worst-case disturbance.

**Lemma 5.2.** *Let  $(Q, S, R, F)$  be given with  $R(t) < 0$  for all  $t \in [0, T]$ . Assume the associated RDE in (5.8) has a solution only in the interval  $(t_0, T]$ , with  $t_0 > 0$ . Then, there exists a non-trivial input signal  $\bar{d} \in \mathcal{L}_2^{n_d}[0, T]$  such that  $J(\bar{d}) = 0$ .*

**Proof.** Consider the Hamiltonian dynamics (5.11) on the horizon  $[t_0, T]$  and the associated state transition matrix  $\Phi(t, T)$  (5.12). Next define the matrix functions  $X_1$  and  $X_2$  by:

$$\begin{bmatrix} X_1(t, T) \\ X_2(t, T) \end{bmatrix} := \Phi(t, T) \begin{bmatrix} I \\ F \end{bmatrix} = \begin{bmatrix} \Phi_{11}(t, T) & \Phi_{12}(t, T) \\ \Phi_{21}(t, T) & \Phi_{22}(t, T) \end{bmatrix} \begin{bmatrix} I \\ F \end{bmatrix}. \quad (5.19)$$

Here both  $X_1$  and  $X_2$  have  $n_x$  rows so that the partitioning is compatible with the states vector  $\begin{bmatrix} x^* \\ \lambda \end{bmatrix}$ . It can be shown that the RDE solution with boundary condition  $Y(T) = F$  satisfies  $Y(t) = X_2(t, T)X_1(t, T)^{-1}$  for values of  $t \in [0, T]$  where the RDE solution exists [218].

By hypothesis, the RDE cannot be integrated backward from  $Y(T) = F$  in the interval  $[0, T]$ . Specifically, it is assumed that  $Y$  only exists in the interval  $(t_0, T]$ . Note that  $\Phi(t, T)$  is uniformly bounded in  $t$  and this implies that  $X_2(t, T)$  is also uniformly bounded in  $t$ . Hence  $Y(t)$  becomes unbounded as  $t \rightarrow t_0$  if and only if  $X_1(t_0, T)$  is singular. Thus, there exists a non-trivial vector  $v$  such that  $X_1(t_0, T)v = 0$ . Setting  $x^*(T) = v$  and  $\lambda(T) = Fv$ , a solution of (5.12) can be determined as follows:

$$\begin{bmatrix} x^*(t) \\ \lambda(t) \end{bmatrix} = \Phi(t, T) \begin{bmatrix} v \\ Fv \end{bmatrix} = \begin{bmatrix} X_1(t, T) \\ X_2(t, T) \end{bmatrix} v. \quad (5.20)$$

Note that for this solution it holds  $x^*(t_0) = X_1(t_0, T)v = 0$ .

Construct  $\bar{d}$  based on (5.14) using the solution to the Hamiltonian dynamics given in (5.20). Apply Lemma 5.1 to show that  $J^*(\bar{d}, 0, t_0) = 0$ . Note finally from (5.16) that the response of the original LTV system (5.1) with input  $\bar{d}$  and initial condition  $x(0) = 0$  is given by  $x(t) = 0$  for  $t < t_0$  and  $x(t) = x^*(t)$  for  $t \geq t_0$ . As a consequence, it holds that  $J(\bar{d}) = J^*(\bar{d}, 0, t_0) = 0$ , which proves the statement. ■

The proof of Lemma 5.2 is constructive, in that it suggests a strategy to construct the worst-case disturbance  $\bar{d}$  based on the solution (5.20) of the Hamiltonian dynamics. Next, a pseudocode for a straightforward implementation of the proposed algorithm is provided.

**Algorithm 5.1.** *Construction of  $\bar{d}$  based on simulation of the Hamiltonian dynamics*

**Outputs:** worst-case signal  $\bar{d}$ .

**Inputs:**  $(Q, S, R, F)$  such that a solution  $Y(t)$  exists for  $t \in (t_0, T]$ ,  $t_0 > 0$ .

1. Step-1. Calculate the state transition matrix  $\Phi(t, T)$  of Eq. (5.11) and

compute  $X_1(t_0, T) = \Phi_{11}(t_0, T) + \Phi_{12}(t_0, T)F$ .

2. Step-2. Solve the eigenvalue problem for  $X_1(t_0, T)$  and determine the eigenvector  $v$  associated with the eigenvalue with the smallest magnitude.
3. Step-3. Use  $\Phi(t, T)$  from Step-1 and Eq. (5.20) to compute  $(x^*, \lambda)$ .
4. Step-4. Use Eq. (5.14) to build  $\bar{d}$ .

The main issue with Algorithm 5.1 arises from Step-1, which requires computing the state transition matrix of the Hamiltonian dynamics. This is achieved by simulating (5.11) for a set of linearly independent boundary conditions at  $t = T$  (single-point boundary conditions). However, it is known that for LTI systems and quadratic cost functions the eigenvalues of the constant matrix  $H$  are symmetric about the imaginary axis [269]. This will compromise the accuracy in predicting the worst-case signal, since the procedure relies on simulating a system with unstable dynamics.

**Example 5.2.** *The induced  $\mathcal{L}_2$  gain for the LTI system (5.10) introduced in Example 5.1 is studied. A generic finite horizon  $[0, T]$  is considered, and the bisection algorithm is first applied to determine guaranteed bounds on the performance objective for different  $T$ . Algorithm 5.1 can be used to compute the worst-case disturbance from the cost function matrices  $(Q, S, R, F)$  associated with the performance lower bound  $\gamma_{LB}$ . Fig. 5.2 shows a comparison between  $\gamma_{LB}$  (obtained via bisection using the RDE) and  $\gamma_d = \frac{\|\bar{e}\|_{2,[0,T]}}{\|\bar{d}\|_{2,[0,T]}}$ , where  $\bar{e}$  is the output of (5.10) corresponding to the input signal  $\bar{d}$  given by Algorithm 5.1.*

*It can be noted that when small finite horizons are considered ( $T \leq 2s$ ), the two values are practically the same, that is, Algorithm 5.1 accurately provides the worst-case signal  $\bar{d}$ . But as  $T$  increases, the gain  $\gamma_d$  is markedly different from the one obtained via bisection. Given that the latter provides a guaranteed lower bound on the metric, it is inferred that the calculation underlying  $\gamma_d$  is inaccurate.*

*This result can be understood by considering the Hamiltonian  $H$  associated with (5.10), which is time-invariant and whose spectrum, irrespective of the final time  $T$ , has always two eigenvalues on the imaginary axis and two on the real axis (symmetric about the imaginary axis). For example, for  $T = 10$ , the two pairs of eigenvalues are respectively  $\pm 0.29i \frac{rad}{s}$  and  $\pm 10.05 \frac{rad}{s}$ . As the finite horizon increases, the integration of the associated dynamics (Step-1 of Algorithm 5.1) is performed on a larger time window. Thus, the accuracy in computing the state transition matrix deteriorates*

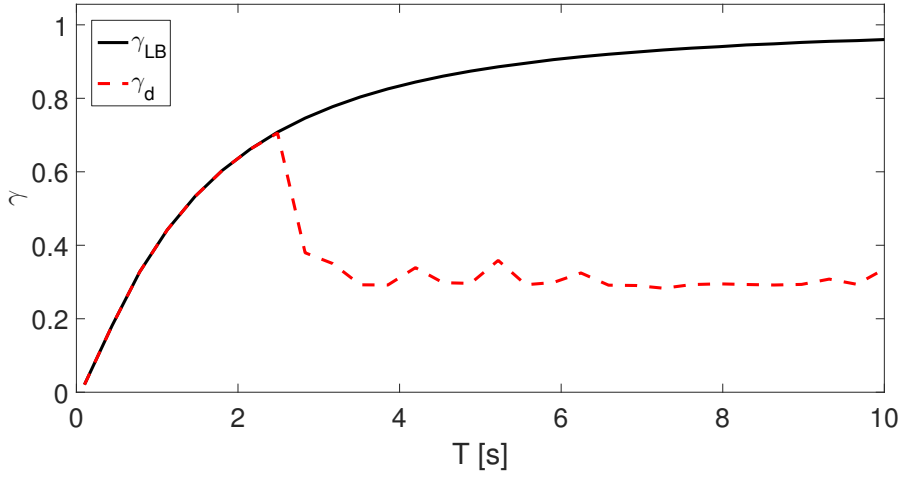


Figure 5.2: Worst-case  $\mathcal{L}_2$  gain from Algorithm 5.1 vs. guaranteed  $\gamma_{LB}$  for different horizons  $T$ .

due to the unstable dynamics. Consequently,  $X_1(t_0, T)$  and its eigenvector  $v$  (Step-2) are also poorly estimated, and this explains why the worst-case disturbance is not well captured.

### 5.2.2 A numerically robust construction of worst-case disturbance

The goal here is to propose an algorithm for the computation of  $\bar{d}$  which is robust to the numerical issues highlighted in Sec. 5.2.1. The driving idea is to exploit directly the knowledge of the solution  $Y$  of the RDE in the fraction of the finite horizon where it does exist. Let us first prove the following matrix algebra property which will be used later.

**Lemma 5.3.** *Let  $M \in \mathbb{S}^n$  and  $v, w \in \mathbb{R}^n$ . Then it holds:*

$$|v^\top M v - w^\top M w| \leq \bar{\sigma}(M) [||v|| + ||w||] ||v - w||. \quad (5.21)$$

**Proof.** The symmetry of  $M$  implies that  $w^\top M v = v^\top M w$ . This can be used to show the following relationship:

$$v^\top M v - w^\top M w = (v - w)^\top M (v + w). \quad (5.22)$$

This leads to the following bound:

$$\begin{aligned} |v^\top M v - w^\top M w| &= |(v - w)^\top M (v + w)|, \\ &\leq ||M(v + w)|| ||v - w||, \\ &\leq \bar{\sigma}(M) [||v|| + ||w||] ||v - w||. \end{aligned} \quad (5.23)$$

The first inequality follows (5.22) and Cauchy-Schwartz inequality. The second inequality follows from the definition of  $\bar{\sigma}(M)$ . The last inequality is an application of the triangle inequality. ■

The following lemma is central for the goal of the section. The statement bears similarities with the one of Lemma 5.2, but crucially the proof allows for an alternative construction of the disturbance that does not entail simulating  $H$ .

**Lemma 5.4.** Let  $(Q, S, R, F)$  be given with  $R(t) < 0$  for all  $t \in [0, T]$ . Assume the associated RDE in (5.8) has a solution only in the interval  $(t_0, T]$ , with  $t_0 > 0$ . Then for all  $\epsilon > 0$  there exists a non-trivial disturbance  $\bar{d}_\epsilon$  such that  $J(\bar{d}_\epsilon) > -\epsilon \|\bar{d}_\epsilon\|_{2,[0,T]}^2$ , i.e. condition 1 in Theorem 5.1 fails to hold.

**Proof.** By hypothesis, the solution  $Y(\hat{t}_0)$  to the RDE exists for any  $\hat{t}_0$  in  $(t_0, T]$ . Let  $(w, g)$  denote the eigenpair of  $Y(\hat{t}_0)$  associated with its largest eigenvalue in magnitude, i.e.  $Y(\hat{t}_0)w = gw$ ,  $g = \rho(Y(\hat{t}_0))$ , and  $\|w\| = 1$  without loss of generality. It holds that  $\rho(Y(\hat{t}_0)) \rightarrow \infty$  as  $\hat{t}_0 \rightarrow t_0$  (as discussed in the proof of Lemma 5.2 and observed in Example 5.1).

Next, recall the definition for  $(X_1, X_2)$  given in (5.19) and that  $Y(t) = X_2(t, T)X_1(t, T)^{-1}$  for values of  $t$  where  $Y$  exists. Let  $x^*$  and  $\lambda$  be the solution of the Hamiltonian dynamics with the following boundary condition:

$$\begin{bmatrix} x^*(T) \\ \lambda(T) \end{bmatrix} = \begin{bmatrix} I \\ F \end{bmatrix} z, \quad \text{where } z := X_1(\hat{t}_0, T)^{-1} \frac{w}{g}. \quad (5.24)$$

Then it is possible to construct  $\bar{d}$  as in (5.14) using the solution  $(x^*, \lambda)$  and  $t_0 = \hat{t}_0$ . Without loss of generality  $\bar{d}$  is scaled such that  $\|\bar{d}\|_{2,[0,T]}^2 = 1$ . Note that the signal  $\bar{d}$  depends on the choice of  $\hat{t}_0$  due to the boundary conditions in (5.24), i.e.  $\bar{d} = \bar{d}_{\hat{t}_0}$ . The subscript  $\hat{t}_0$  will be omitted in the sequel for clarity.

The solution of the Hamiltonian dynamics at  $t = \hat{t}_0$  is given by:

$$\begin{bmatrix} x^*(\hat{t}_0) \\ \lambda(\hat{t}_0) \end{bmatrix} = \begin{bmatrix} X_1(\hat{t}_0, T) \\ X_2(\hat{t}_0, T) \end{bmatrix} z = \begin{bmatrix} I \\ Y(\hat{t}_0) \end{bmatrix} \frac{w}{g} = \begin{bmatrix} \frac{w}{g} \\ w \end{bmatrix}. \quad (5.25)$$

It follows from Lemma 5.1 that  $J^*(\bar{d}, x^*(\hat{t}_0), \hat{t}_0) = \frac{w^\top w}{g}$ . It is important to note, however, that  $J^*(\bar{d}, x^*(\hat{t}_0), \hat{t}_0) \neq J(\bar{d})$  due to the non-zero initial conditions. To better appreciate this, note that the solution of the Hamiltonian dynamics satisfies the following on  $[\hat{t}_0, T]$ :

$$\dot{x}^* = Ax^* + B\bar{d}, \quad \text{with } x^*(\hat{t}_0) = \frac{w}{g}. \quad (5.26)$$

However, applying  $\bar{d}$  to the original LTV system (5.1a) from  $x(0) = 0$  yields  $x(t) = 0$  on  $[0, \hat{t}_0]$  and the following dynamics on  $[\hat{t}_0, T]$ :

$$\dot{x} = Ax + B\bar{d}, \quad \text{with } x(\hat{t}_0) = 0. \quad (5.27)$$

To address this aspect and hence complete the proof,  $J(\bar{d})$  is first rewritten as follows:

$$\begin{aligned} J(\bar{d}) &= x(T)^\top F x(T) + \int_{\hat{t}_0}^T \begin{bmatrix} \dot{x} \\ \bar{d} \end{bmatrix}^\top \begin{bmatrix} Q & S \\ S^\top & R \end{bmatrix} \begin{bmatrix} \dot{x} \\ \bar{d} \end{bmatrix} dt, \\ &= J^*(\bar{d}, x^*(\hat{t}_0), \hat{t}_0) + \chi, \\ &= \frac{w^\top w}{g} + \chi, \end{aligned} \quad (5.28)$$

---

## 5.2. AN ALGORITHM FOR CONSTRUCTING WORST-CASE DISTURBANCES ON FINITE HORIZONS

---

where the term  $\chi$  is given by:

$$\chi := x(T)^\top F x(T) + \int_{\hat{t}_0}^T \left[ \begin{array}{c} \dot{x} \\ \bar{d} \end{array} \right]^\top \left[ \begin{array}{cc} Q & S \\ S^\top & R \end{array} \right] \left[ \begin{array}{c} \dot{x} \\ \bar{d} \end{array} \right] dt - x^*(T)^\top F x^*(T) - \int_{\hat{t}_0}^T \left[ \begin{array}{c} x^* \\ \bar{d} \end{array} \right]^\top \left[ \begin{array}{cc} Q & S \\ S^\top & R \end{array} \right] \left[ \begin{array}{c} x^* \\ \bar{d} \end{array} \right] dt. \quad (5.29)$$

Using Lemma 5.3, this error term can be bounded as follows:

$$|\chi| \leq \left[ \bar{\sigma}(F) + (T - \hat{t}_0) \max_{t \in [\hat{t}_0, T]} \bar{\sigma}\left(\left[ \begin{array}{cc} Q(t) & S(t) \\ S(t)^\top & R(t) \end{array} \right]\right) \right] \left[ \|x\|_{\infty, [\hat{t}_0, T]} + \|x^*\|_{\infty, [\hat{t}_0, T]} \right] \|x - x^*\|_{\infty, [\hat{t}_0, T]}. \quad (5.30)$$

Both  $\|x\|_{\infty, [\hat{t}_0, T]}$  and  $\|x^*\|_{\infty, [\hat{t}_0, T]}$  are uniformly bounded as  $\hat{t}_0 \rightarrow t_0$  because  $\bar{d} (= \bar{d}_{\hat{t}_0})$  is selected to satisfy  $\|\bar{d}\|_{2, [0, T]}^2 = 1$ . Moreover,  $x(t) - x^*(t) = -\Psi(t, \hat{t}_0) \frac{w}{g}$  so that  $\|x - x^*\|_{\infty, [\hat{t}_0, T]} \rightarrow 0$  as  $\hat{t}_0 \rightarrow t_0$ . Therefore, it follows that  $|\chi| \rightarrow 0$  as  $\hat{t}_0 \rightarrow t_0$ .

Finally, it follows from (5.28) that  $|J(\bar{d})| \rightarrow 0$  as  $\hat{t}_0 \rightarrow t_0$ . Thus, for all  $\epsilon > 0$  there exists a  $\hat{t}_0 \in (t_0, T]$  such that  $\bar{d} (= \bar{d}_{\hat{t}_0})$  yields  $\|\bar{d}\|_{2, [0, T]} = 1$  and  $J(\bar{d}) > -\epsilon$ . ■

Lemma 5.4 is also constructive, because the worst-case disturbance can be obtained by computing  $x^*$  and  $\lambda$  with initial conditions (5.25). However, a straightforward implementation of this would still require the integration of the Hamiltonian  $H$ . The task of simulating the states of the Hamiltonian dynamics only without incurring numerical issues has been considered in the literature. For example in [38, 67] a Riccati transformation of the Hamiltonian is proposed (but note that this would have not applied to Algorithm 5.1, as the latter requires computing the state transition matrix of  $H$ ).

Another approach is taken here, prompted by the observation that if  $\begin{bmatrix} x^*(T) \\ \lambda(T) \end{bmatrix} = \begin{bmatrix} I \\ F \end{bmatrix} z$  then:

$$\begin{bmatrix} x^*(t) \\ \lambda(t) \end{bmatrix} = \begin{bmatrix} X_1(t, T) \\ X_2(t, T) \end{bmatrix} z = \begin{bmatrix} I \\ Y(t) \end{bmatrix} X_1(t, T) z. \quad (5.31)$$

This means that  $\lambda(t) = Y(t)x^*(t)$  for all  $t \in [\hat{t}_0, T]$ , which allows to express the disturbance  $\bar{d}$  equivalently in terms of  $(x^*, Y)$  rather than  $(x^*, \lambda)$ . Specifically, for  $t \in [\hat{t}_0, T]$  it holds:

$$\begin{aligned} \bar{d} &= -R^{-1}(S^\top x^* + B^\top \lambda), \\ &= -R^{-1}(S^\top + B^\top Y)x^*. \end{aligned} \quad (5.32)$$

The states  $x^*$  of the Hamiltonian dynamics are thus given by:

$$\dot{x}^* = [A - BR^{-1}(S^\top + B^\top Y)]x^*. \quad (5.33)$$

Eq. (5.33) can be used now to compute  $x^*$  without direct integration of  $H$ . Then, the states  $x^*$  and the RDE solution  $Y$  can be used to construct the disturbance according to (5.32). These formulae implicitly reconstruct also the co-states as  $\lambda(t) = Y(t)x^*(t)$ .

The following pseudocode recaps the main steps of the proposed algorithm to compute the worst-case disturbance without numerical integration of the Hamiltonian dynamics.

**Algorithm 5.2.** *Construction of  $\bar{d}$  exploiting the solution of the RDE*

**Outputs:** worst-case signal  $\bar{d}$ .

**Inputs:**  $(Q, S, R, F)$ , the associated RDE solution existing on  $(t_0, T]$ , and some time  $\hat{t}_0 \in (t_0, T]$ .

1. Step-1. Evaluate the eigenpair  $(g, w)$  associated with the largest (in magnitude) eigenvalue of  $Y(\hat{t}_0)$  to compute  $BC$ .
2. Step-2. Simulate  $x^*$  with Eq. (5.33) from the initial condition  $x^*(\hat{t}_0) = \frac{w}{g}$ .
3. Step-3. Use  $\Phi(t, T)$  from Step-1 and Eq. (5.20) to compute  $(x^*, \lambda)$ .
4. Step-4. Use  $x^*$  and  $Y$  to construct  $\bar{d}$  using Eq. (5.32).

Note that with this approach only  $n_x$  states are simulated (Step-2). This leads to a reduction in the run time compared to the calculation of the state transition matrix of  $H$  in Algorithm 5.1, since  $H$  has double size and it had to be computed there for  $2n_x$  linearly independent initial conditions. More importantly, Algorithm 5.2 is not subject to the aforementioned numerical issues because the states  $x^*$  are not obtained by simulation of the Hamiltonian, but rather by exploiting the knowledge of the solution  $Y$  of the RDE.

**Example 5.3.** The induced  $\mathcal{L}_2$  gain for the LTI system introduced in Example 5.1 is considered again. As done in Example 5.2, a comparison between  $\gamma_{LB}$  (obtained via bisection) and  $\gamma_d = \frac{\|\bar{e}\|_{2,[0,T]}}{\|\bar{d}\|_{2,[0,T]}}$  is considered. The difference is that  $\bar{e}$  corresponds now to the input signal  $\bar{d}$  given by Algorithm 5.2. Fig. 5.3 shows that Algorithm 5.2 is capable of accurately predicting the worst-case signal. Indeed  $\gamma_d$  matches the guaranteed lower bound  $\gamma_{LB}$  for all the finite horizons.

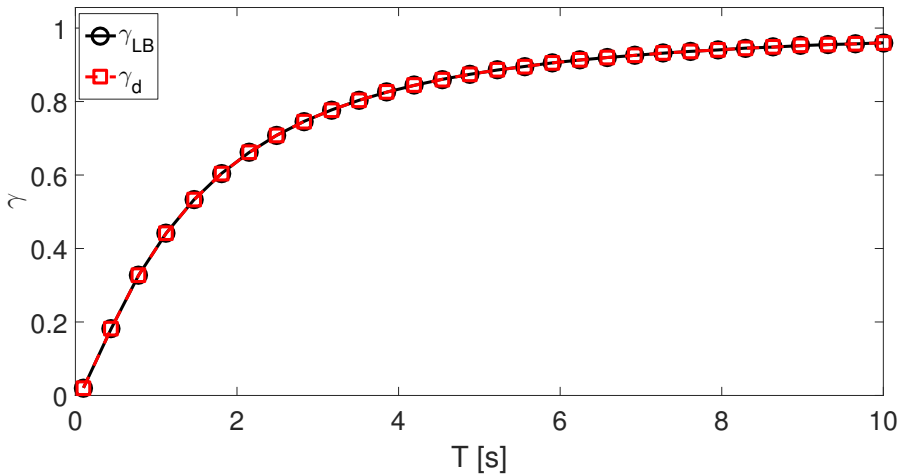


Figure 5.3: Worst-case  $\mathcal{L}_2$  gain from Algorithm 5.2 vs. guaranteed  $\gamma_{LB}$  for different horizons  $T$ .

## 5.3 Gust analysis of the FLEXOP demonstrator

This section shows an example of application of the finite horizon worst-case LTV analysis to investigate performance of the FLEXOP aircraft demonstrator (described in Section 2.3.4). Namely, the susceptibility to atmospheric gusts during a prototypical flight test manoeuvre is studied. After describing the problem in Section 5.3.1, the study will investigate the importance of capturing the time-varying nature of the problem (Section 5.3.2) and the difference between open and closed-loop performance (Section 5.3.3). Finally, a comparison of this approach with traditional gust analyses employed in aircraft design is performed in Section 5.3.4.

### 5.3.1 Manoeuvre definition

In Fig. 5.4 a schematic representation of the part of the flight test of interest for the analyses is reported. This consists of three sections: first a uniformly accelerated (AC) level flight manoeuvre (dashed) is performed to increase the speed from  $V_1$  to  $V_2$ , followed by a constant speed level flight (where the flutter controller is tested), and finally a uniformly decelerated (DC) manoeuvre (dash dot) where the speed of the aircraft is decreased. The scenario studied here is the leg AC, of which an enlargement is shown. The manoeuvre starts at  $t = 0$  with an initial speed  $V_1$  and is concluded when  $V = V_2$  at  $T = 2 \frac{L_{ac}}{V_1 + V_2}$ , where  $L_{ac}$  is the covered distance and  $V_m = \frac{V_1 + V_2}{2}$  the mean speed. The following values will be considered:  $V_1 = 45 \frac{m}{s}$ ,  $V_2 = 49 \frac{m}{s}$ , and  $L_{ac} = 250m$  (hence  $T = 5.3s$ ).

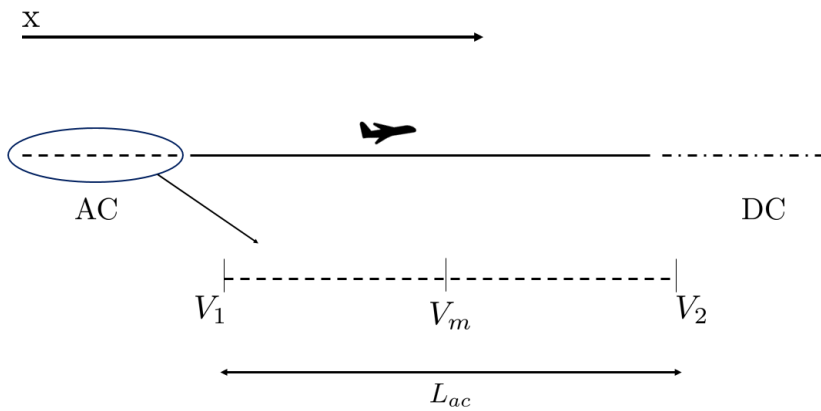


Figure 5.4: Detail of the analysed manoeuvre.

The modelling starting point is represented by the reduced order LTI models (38 states) [155] obtained linearising around the trajectory AC the original nonlinear model capturing the interaction between rigid body, elastic dynamics, and unsteady aerodynamic [257]. These models provide the state-matrices  $A$ ,  $B$ ,  $C$ , and  $D$  at fixed times, which are linearly interpolated with respect to time in the horizon  $[0, T]$ . This allows to finally build up the LTV model  $G_{LTV}$ , capturing the variability of the aircraft properties in the speed interval  $[V_1, V_2]$ . Consistently with

the generic LTV model defined in (5.1), the input and output vectors considered in the analyses will be denoted respectively by  $d$  and  $e$ . The disturbance  $d$  assumed here is a uniform vertical wind gust. Since the models do not have dedicated input channels for gust, this is accounted for by means of the control surface inputs  $\delta_{ail-L\bullet}$  and  $\delta_{ail-R\bullet}$ , with  $\bullet=1,2,3,4$  (the numbering of control effectors was indicated in Fig. 2.7). The premise for this is that, to a first approximation, the effect of a vertical gust is to change the local angle of attack of the wing, thus it can be captured as an equivalent rotation of the control surfaces (which modifies the curvature of the section, hence resulting in a similar effect to a change in the angle of attack). Therefore, the input  $d$  has units of speed (i.e.  $\frac{m}{s}$ ). Then, by means of first approximation formulae [212], this is scaled and will finally result in control surfaces rotation units (i.e.  $rad$ ). When a uniform symmetric gust is considered, the control surfaces have all the same rotation, i.e.  $\delta_{ail-L\bullet} = \delta_{ail-R\bullet} = d$ , which is the case studied here. This is done for exemplification, but variations of the wing's sections and gust properties along the span can easily be modelled. As for the outputs  $e$ , two different cases will be studied: vertical acceleration at the tip of the right wing  $a_{z-tR}$  (specifically, at the sensor R6 depicted in Fig. 2.7) and at the aircraft centre of gravity (CG)  $a_{z-CG}$ . In both cases,  $e$  is normalised with the gravitational acceleration  $g$ . For a better representation and comparison of the time-domain responses, the signals shown in the plots are adimensionalised and normalised such that  $\|d\|_{2,[0,T]} = 1$ .

### 5.3.2 Finite horizon LTI vs LTV

In this subsection the importance of considering the time-varying feature of the problem in the assessment of aircraft performance is investigated. The two performance metrics defined in Eqs. (5.4)-(5.6) (respectively induced  $\mathcal{L}_2$  and  $\mathcal{L}_2$ -to-Euclidean gains) are analysed, and the bisection algorithm proposed in Sec. 5.1.1 is applied. The RDE (5.8) is numerically integrated with the routine *ode45* from MATLAB®. Table 5.1 reports the results in terms of upper bounds on the performance  $\gamma_{UB}$ . In the first column the adopted model is defined:  $G_1$ ,  $G_m$ , and  $G_2$  are the LTI models at speeds  $V_1$ ,  $V_m$  (mid-speed), and  $V_2$  respectively; and  $G_{LTV}$  is the LTV model. In the second and third columns the two performance metrics for  $a_{z-tR}$  are listed, while for  $a_{z-CG}$  it is the fourth and fifth column. It is emphasised that for both LTI and LTV analyses a finite-horizon problem (of length  $T = 5.3s$ ) is considered.

It can be inferred from the results that analysing the aircraft manoeuvre with a frozen LTI approach leads to different results than with the LTV framework. A classic approach when adopting the former strategy is to consider the LTI plant corresponding to the mid-speed, on the basis that this sufficiently captures the effect of varying the speed. The results in Tab. 5.1 show that this is approximately true only for the induced  $\mathcal{L}_2$  gain (i.e. columns 2 and 4). In fact, by looking at columns 3 and 5 it can be noted that the predictions obtained with  $G_{LTV}$  are closer to the ones with  $G_2$  (i.e. the plant at the final speed).

By comparing the performance for the two outputs (tip and CG accelerations), it is also

Table 5.1: Comparison of finite horizons LTI and LTV performance based on  $\mathcal{L}_2$  and Euclidean gains.

	$e$	$a_{z-tR}$		$a_{z-CG}$		
		Metric	$\ G\ _2$	$\ G\ _E$	$\ G\ _2$	$\ G\ _E$
LTI	$G_1$	12.7	21.9	1.7	2.1	
	$G_m$	18.3	26.1	2.4	2.8	
	$G_2$	31.1	34.7	4.3	4.3	
LTV	$G_{LTV}$	20	32	2.7	3.8	
column		1	2	3	4	5

observed a substantial difference between the values, which can be interpreted as a measure of the flexibility of the wing. Complementing the quantitative information from Table 5.1, it is possible to identify the worst-case signals for both performance metrics. In particular, in Fig. 5.5 the worst-case signals for the induced  $\mathcal{L}_2$  gain of  $a_{z-CG}$  obtained with  $G_m$  and  $G_{LTV}$  are plotted, whereas Fig. 5.6 shows those corresponding to the Euclidean norm of  $a_{z-tR}$ . The cases for  $G_1$  and  $G_2$  are not shown here but have disturbance profiles similar to that of  $G_m$ .

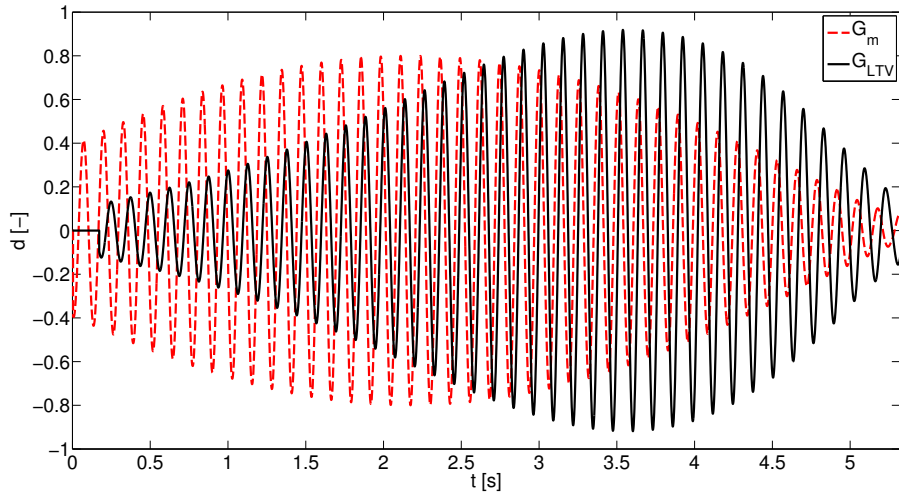


Figure 5.5:  $\mathcal{L}_2$  gain worst-case disturbances for  $a_{z-CG}$  (LTI vs. LTV).

From the figures it can be seen that the worst-case disturbance corresponding to the LTI system is different from the LTV case. This is more markedly noticeable from Fig. 5.5, but can also be appreciated in Fig. 5.6 where the discrepancies in the final part of the input signal have a large effect on the performance (recall that its value depends on the output  $e$  at time  $T$  only). Thus it is confirmed the importance of capturing the time variance of the system, anticipated by Table 5.1, in analysing the considered manoeuvre.

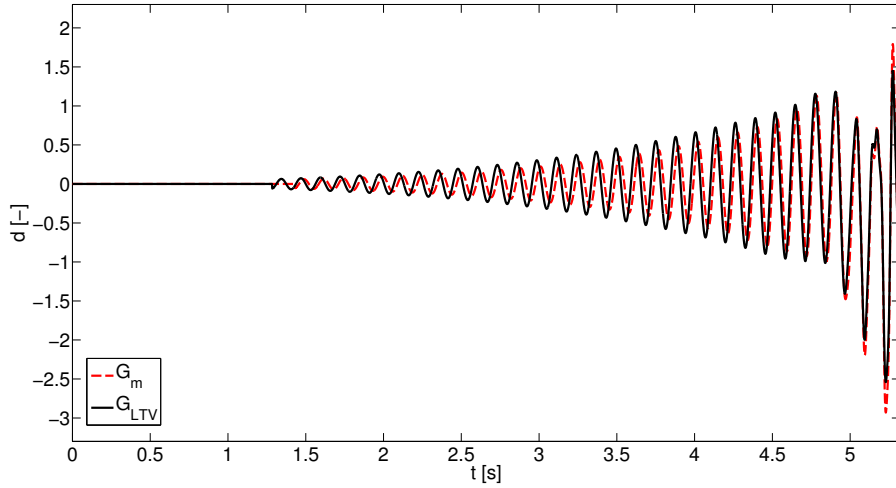


Figure 5.6:  $\mathcal{L}_2$ -to-Euclidean gain worst-case disturbances for  $a_{z-tR}$  (LTI vs. LTV).

### 5.3.3 Open-loop vs. Closed-loop manoeuvres

The open-loop model  $G_{LTV}$  is augmented with an  $\mathcal{H}_\infty$  controller designed to suppress the onset of flutter at the open-loop flutter speed  $V_{fl}$  and thus extend the FLEXOP demonstrator valid flight region<sup>2</sup>. A description of the synthesis strategy is provided in [155] (Section IV describes the University of Bristol team controller). Briefly, the control design process uses as performance channels the modal speeds for the first two flexible modes. The controller is a single LTI state-space system with 4 states, 4 inputs (pitch rate  $q$ ,  $a_{z-CG}$ ,  $a_{z-tR}$ ,  $a_{z-tL}$ ) and 2 outputs ( $\delta_{ail-L4}$  and  $\delta_{ail-R4}$ ).

For ease of comparison, the previous results from the open-loop (OL) LTV analysis are repeated in Table 5.2 together with the results from the application of the LTV analysis method to the closed-loop (CL) case. The associated worst-case signals will be displayed and discussed afterwards.

Table 5.2: Comparison of OL and CL performance of  $G_{LTV}$  based on  $\mathcal{L}_2$  and Euclidean gains.

e	$a_{z-tR}$		$a_{z-CG}$		
	Metric	$\ G\ _2$	$\ G\ _E$	$\ G\ _2$	$\ G\ _E$
OL	20	32	2.7	3.8	
CL	4.3	21.2	0.7	1.8	

A number of observations can be made with reference to the results in Table 5.2. It is first seen that the controller is able to significantly reduce all the gains. This is pronounced in the induced  $\mathcal{L}_2$  gain case (columns 2 and 4), for which it can be noticed also that the gap between

<sup>2</sup>The author is thankful to Sérgio Waitman for providing the controller used in the analyses.

$\|G\|_2^{tR}$  and  $\|G\|_2^{CG}$  is reduced. This was previously described as a measure of the flexibility of the system, and thus the analyses showcase the ability of the controller to tackle it. When looking at the Euclidean gain (columns 3 and 5), there is less improvement between OL and CL case, and the gap between  $\|G\|_E^{tR}$  and  $\|G\|_E^{CG}$  has actually increased. Note that this result can be motivated by considering the rationale behind the design technique employed for the investigated controller. It is based on the  $\mathcal{H}_\infty$  formalism, which aims at reducing the frequency response peak of the closed loop and thus is expected to enhance the performance for the induced  $\mathcal{L}_2$  gain, and not necessarily for others. In conclusion, the analyses are able to point out performance metrics for which the controller is less effective and can thus inform a redesign if these are deemed important in the tests.

Additional insights are provided by calculating the worst-case disturbance that maximises the energy of the selected output. Fig. 5.7 shows a comparison between the open-loop and closed-loop cases for the CG acceleration. A substantial difference is observed in the time-domain profile of the signals. Specifically, the CL case has a (dominant) lower frequency of approximatively  $10 \frac{\text{rad}}{\text{s}}$ , whereas the OL has a frequency of about  $50 \frac{\text{rad}}{\text{s}}$ , close to that of the first bending modes responsible for the onset of flutter [155]. This shows that the controller achieves the reduction in the closed-loop  $\mathcal{L}_2$  gain by reducing the energy associated with the first elastic modes (which was indeed the aim of the design process as mentioned before). Compared to the OL case, the worst-case gust associated with the CL excites lower frequency modes of the system, which have a lower energy content and thus results in the improved gain. It is also interesting to note that in the CL case the disturbance acts on a shorter time window ( $t_0 \approx 2\text{s}$ ).

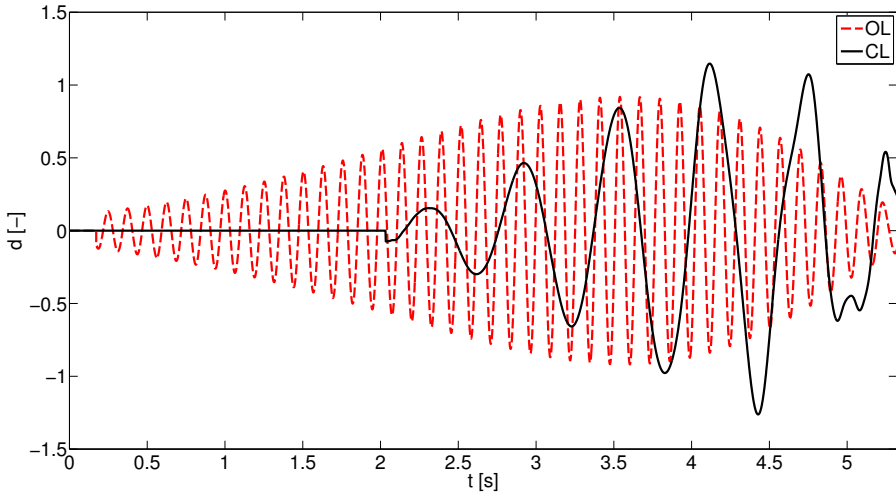


Figure 5.7:  $\mathcal{L}_2$  gain worst-case disturbances for  $\alpha_{z-CG}$  (OL vs CL).

This latter feature was also observed in other tests that were performed comparing the open and closed loops. It is interpreted here by observing that, from the point of view of maximising the energy of the output, it is more advantageous for the gust to act at later times since the

aircraft increases its speed and thus as time progresses it becomes more deformable. This is true in general, but in the *CL* case the advantage in acting at higher speeds is accentuated due to the effect of the controller of reducing flexibility. To support this explanation, Fig. 5.8 shows the same comparison displayed in Fig. 5.7, where now a deceleration is considered (*DC* in Fig. 5.4), that is the manoeuvre starts at  $V_2$  and finishes when  $V = V_1$ . Note that the signal  $\bar{d}$  for the *CL* case is now predicted to act from the first time steps of the horizon ( $t_0 \approx 0s$ ), and to converge (sooner than *OL*) to very small values as time increases. The tests in Figs. 5.7-5.8 thus points out that the activation time  $t_0$  of the worst-case signal (5.14), corresponding to the last time for which a solution to the RDE (5.8) exists, can indeed have a physical meaning in relation to the studied problem.

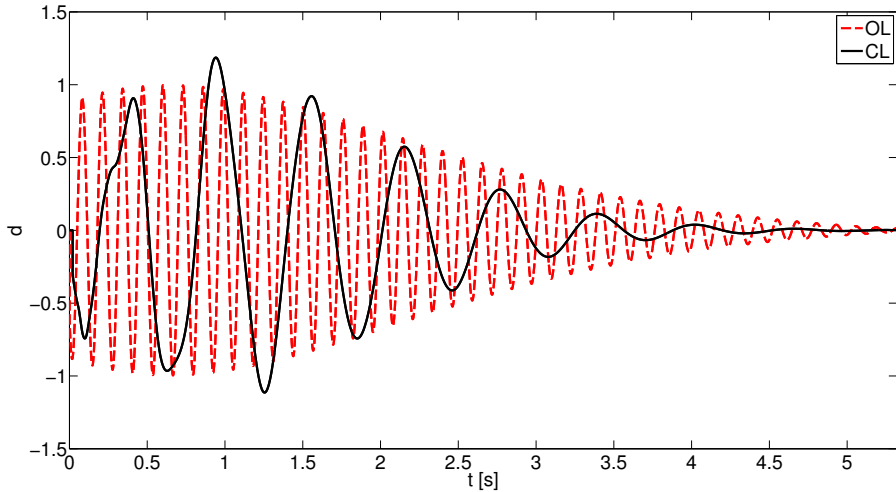


Figure 5.8:  $\mathcal{L}_2$  gain worst-case disturbances for  $a_{z-CG}$  (OL vs CL). Deceleration from  $V_2$  to  $V_1$ .

Finally, the sensitivity of the shape of the worst-case signal to the length of the finite horizon  $T$  is considered. Based on the nominal manoeuvre defined in Sec. 5.3.1, its value has been set to 5.3s so far. However, off-nominal conditions in the mission might result in a different value (e.g. because of a different acceleration, and thus covered distance  $L_{ac}$ , due to a difference performance of the engine). In order to investigate the effect on the results, the disturbances predicted for the closed loop case for larger horizons lengths (20%, 50%, and 100% larger than the nominal value  $T_0$ , respectively) are considered. The results are shown in Fig. 5.9, where also the case of nominal  $T_0$  (corresponding to the curve *CL* in Fig. 5.7) is reported. For a better comparison, the time  $t$  is adimensionalised for each curve with the corresponding horizon length (reported in the legend).

It can be observed that the disturbances are qualitatively very similar. In fact, they present the same dominant frequency and distinctive signal features (e.g. higher frequency component towards the end of the horizon). Moreover, the  $\mathcal{L}_2$  gains corresponding to each curve are within 1.5 % with respect to the performance metric associated with the nominal case (Table 5.2). It can then be concluded that, for this example, the algorithm is robust to changes in the horizon  $T$ .

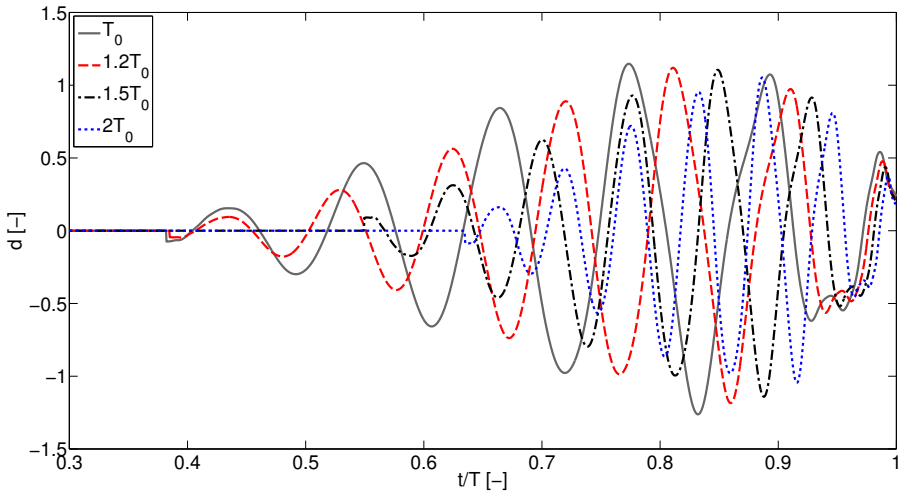


Figure 5.9: Effect of  $T$  on the  $\mathcal{L}_2$  gain worst-case disturbances for the CL system.

This property, also observed for other analysed scenarios, is advantageous because the gained insights (as those from Fig. 5.7) are not limited to specific cases but have a more general validity.

#### 5.3.4 Comparison with standard gust performance analysis

The results obtained with this framework are compared now with those from a standard approach widely used in the aerospace field for gust analysis. Atmospheric turbulence is typically considered for aircraft design purposes in one of the two idealised categories [110, 256]: discrete gusts, where the gust speed varies in a deterministic manner (provided in time domain); and continuous turbulence, where the gust velocity is assumed to vary randomly (provided in frequency domain). The former case is considered here, of which the most common example is the so called *1-cosine* gust. This provides the spatial variation of the vertical gust as:

$$w_g(x_g) = \frac{w_{g0}}{2} \left( 1 - \cos \left( \frac{2\pi x_g}{L_g} \right) \right) \quad 0 \leq x_g \leq L_g, \quad (5.34)$$

where  $w_{g0}$  is the value of the peak gust velocity and  $L_g$  is the gust length. For a given energy associated with the gust signal, Eq. (5.34) describes a set of gusts which vary depending on the gust length  $L_g$ . The comparison performed in this subsection is then between the performance achieved when the aircraft is subject to this set of gust profiles and that obtained under the worst-case signals computed with Algorithm 5.2.

Since the purpose is to simulate the effect of the idealised gust (5.34) on the LTV system  $G_{LTV}$  (described by means of its state-space representation), the gust velocity expression needs first to be transformed from a spatial into a temporal function (Fig. 5.10). This can be done recalling that the manoeuvre features a constant acceleration, and thus  $x_g$  is a quadratic function of time in the finite horizon  $[0, 5.3]$ s. The temporal signal will then be denoted by  $d_g$ . Moreover, since a comparison with the worst-case signals computed with Algorithm 5.2 is sought, the signal  $d_g$  is

normalised such that it is of unitary energy, i.e.  $\|d_g\|_{2,[0,T]}=1$ , and this fixes  $w_{g0}$ . Note that this practice is different from the usual convention in gust analysis [256] and is aimed at making a straightforward comparison in terms of the performance gains used in the previous sections (recall from the definitions (5.4)-(5.6) that the gains measure directly output quantities when the input has unitary energy). This is without loss of generality and other options could have been similarly pursued. A family of 15 gusts for  $\frac{L_{ac}}{15} \leq L_g \leq L_{ac}$  is computed and plotted in Fig. 5.10.

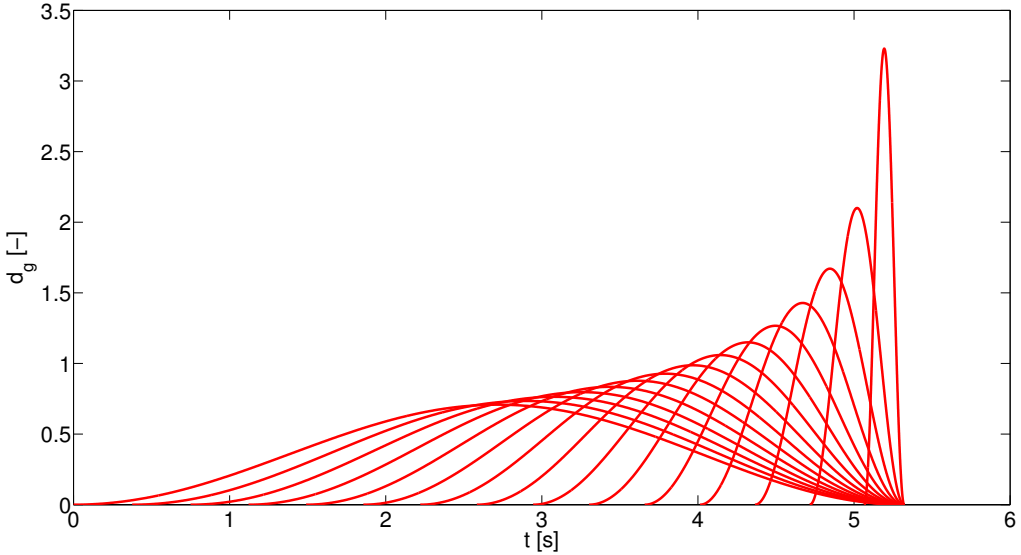


Figure 5.10: Set of 1-cosine gust signals for different gust length  $L_g$ .

This set of gusts is then simulated in the open-loop LTV plant  $G_{LTV}$  presented in Sec. 5.3.2. The two figures Fig. 5.11(a) and Fig. 5.11(b) report the two performance metrics  $\mathcal{L}_2$  and  $\mathcal{L}_2$ -to-Euclidean as a function of the gust length  $L_g$  for  $a_{z-tR}$  and  $a_{z-CG}$  respectively.

The performance gains read off from the y-axis in Fig. 5.11 are markedly different from those relative to the *OL* case in Table 5.1 (i.e. [20, 32, 2.7, 3.8]). These differences are not only quantitative, but also qualitative. For example, it can be noted that for the tip acceleration (Fig. 5.11b) these analyses point out a larger value for  $\|G\|_2$  than for  $\|G\|_E$ , whereas Table 5.1 indicated the opposite.

The motivation for this aspect is that a mathematically guaranteed *worst-case* signal is provided by the developed analysis method (i.e., Algorithm 5.2), thus the corresponding results are associated with the largest possible gain for the studied problem. Further, the computed disturbance is a function of the particular performance metric and output considered (examples of this were given in Sec. 5.3.2). In view of this, it is thus expected that the performance associated with the analytic worst-case gust  $\bar{d}$  will be worse than other idealised gusts which have a given shape independent of the particular performance problem studied. An example of the latter approach is the one proposed in [138], where genetic algorithm optimization was used to determine, for pre-defined ranges of flight conditions, the parameterised 1-cosine (i.e. with

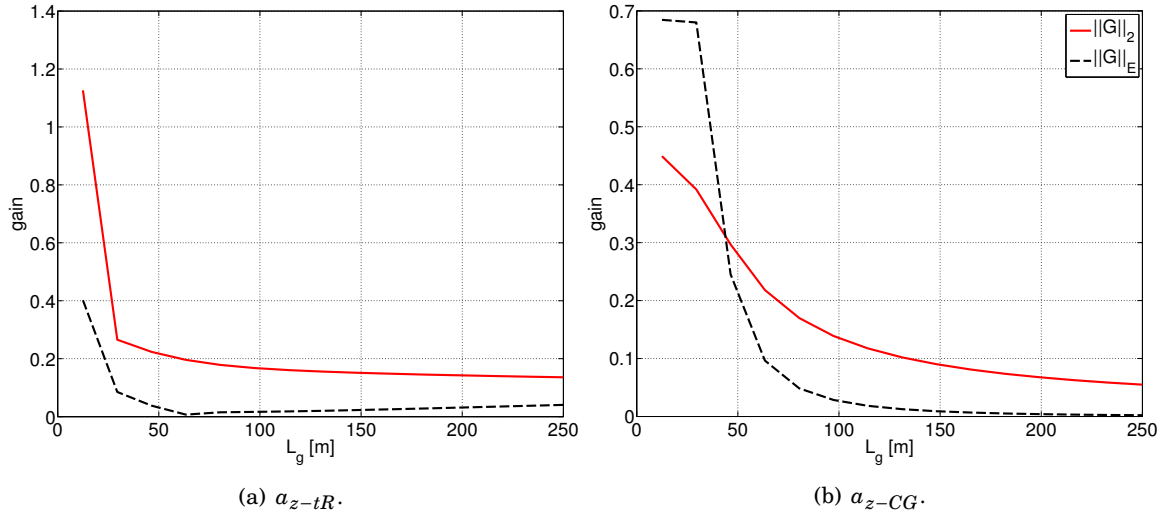


Figure 5.11:  $\mathcal{L}_2$  and  $\mathcal{L}_2$ -to-Euclidean gains as a function of the gust length.

fixed shape) gusts able to degrade the performance with respect to monitored quantities (e.g., bending moments, load factors). As intrinsic to these approaches, the *worst-case* (broadly speaking, because no globally optimum solution of the optimization is guaranteed to be found) character depends on the particular shape guessed for the gust. On the contrary, the approach presented here allows to construct the shape of the critical input signal (in this case exemplified by a gust) for a very generic definition of the performance (defined by means of the cost in Eq. 5.3, and which includes the classic monitored quantities [138] as particular cases). Moreover, a mathematical guarantee that the signal will attain the worst possible performance holds.

It is typical of worst-case analyses based on robust analytical methods that the computed signals do not usually have associated with them a probability of occurrence. Thus, the usual trade-off between analysing for cases that are very probable (but that yield *optimistic* results) versus analysing for a potentially very improbable case (but providing guaranteed worst-case answers) applies in here. In any case, once the gap between the predictions obtained with standard approaches and the actual worst-case is assessed, the proposed framework allows to construct the signal determining such a performance degradation. This knowledge can in turn drive additional investigations focused on specific objectives (e.g. determining the largest wing tip deflections).

Future research can look at more physical worst-case gust disturbances, and attempt to connect them with more elaborate gust models from the literature (e.g. Dryden wind turbulence model). In addition to the gust example proposed here, other applications to the analysis and design of very flexible aircraft are envisaged. For example, the active load alleviation problem, which has been drawing increasing interest in the community [258], can benefit from the developed analysis framework. This can indeed be used to identify worst-case manoeuvres which

prevent from achieving the performance targets and can in turn inform redesign of the feedback loop. It is finally noted that the shapes of the signals shown in this section (see for example Fig. 5.6) bear qualitative similarities to those investigated in the works [267, 268] where the concept of Matched Filter Theory was used for analysis of gust loads on aircraft. This can be ascribed to the fact that this theory, from the signal processing community, can provide a means to predict responses of the system maximising some prescribed metric under input (e.g. energy) constraints [186]. This observation also points out that the framework presented in this Chapter has in principle the potential to be applied in different contexts from the one in which it has been conceived, where a similar problem is of interest. An example is the design of input signals for system identification with the goal to maximise the information extracted from the experiments.

## 5.4 Chapter summary

This Chapter has investigated the computation of worst-case disturbances associated with the finite horizon performance of LTV systems.

A generalisation of the strict bounded real lemma stating an equivalence between a bound on a generic cost function, specifying the performance objective, and the existence of a solution to the associated Riccati Differential Equation is employed to provide an analytical expression for the disturbance. It is claimed and motivated with a simple example that a straightforward implementation of this result features numerical issues due to the need of simulating the Hamiltonian dynamics. This observation leads to the proposal of a numerically robust algorithm which exploits the structure of the worst-case signal and the properties of the solution of the RDE. It is noted that the approach taken here to overcome the problem of simulating the Hamiltonian is different from previous ones explored in the literature (e.g. based on a Riccati transformation).

A second contribution is the demonstration of the applicability of this finite horizon LTV analysis approach using a realistic aeronautic case study. The effect of atmospheric gusts on the performance of the FLEXOP aircraft demonstrator during a leg of the planned flight test manoeuvre is studied. The analyses allow, for example, to observe the effect of an  $\mathcal{H}_\infty$  controller designed to actively suppress flutter on the shape of the worst-case gust. Moreover, the provided results exemplify some of the insights that can be gained with this framework and include a comparison with the standard *1-cosine* approach used for gust analysis in aircraft design.



## LIMIT CYCLE OSCILLATIONS IN SYSTEMS WITH UNCERTAINTIES

The increase in flexibility of modern aeronautical structures and the demand for a more realistic physical description of the system needed to achieve higher performance compel to contemplate scenarios where the linear hypothesis no longer applies. This has been assumed so far in the study, with Chapter 5 partially allowing for nonlinear features to be captured with the introduction of time-varying properties. However, there exist inherently nonlinear behaviours that can be predicted only by studying the original (nonlinear) dynamics. This chapter is the first of three which aim at investigating analysis methodologies which are able to cope with these scenarios in the presence of uncertainties. In here focus is on the Limit Cycle Oscillation (LCO) phenomenon, which is of great concern for aeroelastic systems. In fact, while linear flutter is associated with an unstable diverging response, the presence of nonlinearities might lead to limited amplitude self-excited oscillations, generally named LCOs, whose investigation is of well-ascertained interest in accomplishing a satisfactory design. The contribution of the chapter is twofold. First, the combined application of Describing Functions and  $\mu$  is proposed to construct worst-case LCO curves and, based on this concept, to perform LCO tailoring (Section 6.2). Second, a strategy which allows Integral Quadratic Constraints to be employed for the study of the post-critical behaviour, instead of only for stability as it is typically done, is developed (Section 6.3). In both cases, application is demonstrated on a benchmark study, featuring freeplay, for which a wealth of analytical, numerical and experimental results from the literature are available.

**Publications<sup>1</sup>:** [119, 120] Section 6.2; [121, 126] Section 6.3.

---

<sup>1</sup>Material published during the PhD which relates to the content of this chapter.

## 6.1 Mathematical background

### 6.1.1 Describing Functions

The analysis and design of linear systems pivots on a complex-valued function, the frequency response. However, this function cannot be defined for nonlinear systems, hence frequency-domain techniques cannot be directly applied. The Describing Functions (DF) method [87] aims to overcome this obstacle by providing in these cases an alternative definition of frequency response. This method is mostly applied to systems which can be recast in the framework of Fig. 6.1, characterised by having separable linear and nonlinear parts connected in a feedback configuration. In the references [81, 136] the usage of DF for studying problems where  $G$  is uncertain was pioneered.

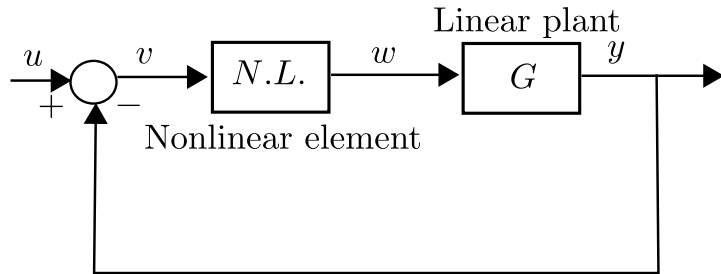


Figure 6.1: Feedback representation of a nonlinear system for DF analysis.

The concept of *quasi-linearisation* is the basis of the application of DF. By quasi-linearisation it is meant in this context that the approximation of the nonlinear operator is done through a linear one which depends on some properties of the input  $v$ . By doing so, the dependence of the response on the input, which is a basic nonlinear feature, is captured, and the advantages of a linear approximation are retained without the constraint of requiring small departures of the variables from the linear values. The application of the DF method requires for the quasi-linearisation process to specify the input signal form. In analogy to what is done in frequency-domain analysis, it is widely employed the concept of sinusoidal-input describing function, in the following simply abbreviated as DF. The interest in periodic signals here is mainly dictated by the aim to detect and analyse LCOs, but in general libraries of describing functions exist for different signal's forms [87].

Consider a sinusoidal signal  $v = A \sin(\omega t)$  at the nonlinear element. If the nonlinearity is single-valued (i.e. only one output is possible for any given value of the input, also called memoryless), the output  $w$  is a periodic function and thus can be expanded using Fourier series:

$$w(t) = \frac{a_0}{2} + \sum_{n=1}^{\infty} [a_n(A, \omega) \cos(n\omega t) + b_n(A, \omega) \sin(n\omega t)], \quad (6.1)$$

where  $a_n$  and  $b_n$  are the Fourier coefficients and are function of  $A$  and  $\omega$  (this dependence will be omitted when clear from the context). If an odd nonlinearity (i.e. the relation between the input

and output of the nonlinear block is symmetric about the origin) is considered, then  $a_0=0$ . This assumption is introduced to further simplify (6.1), without loss of generality.

The key hypothesis of the DF method is that only the fundamental component has to be retained in the periodic output  $w$ . This is an approximation because the output of a nonlinear element corresponding to a sinusoidal input usually contains higher harmonics. The rationale underpinning this assumption is that the higher harmonics in the output are filtered out by  $G$ , i.e. the linear element satisfies the low-pass filter condition (or *filter hypothesis*):

$$\|G(j\omega)\| \gg \|G(jn\omega)\| \quad \text{for } n \geq 2. \quad (6.2)$$

The DF of a nonlinear element is thus the complex fundamental-harmonic gain of a nonlinearity in the presence of a driving sinusoid of amplitude  $A$  and frequency  $\omega$ :

$$N(A, \omega) = \frac{M e^{j(\omega t + \theta)}}{A e^{j(\omega t)}} = \frac{M}{A} e^{j\theta} = \frac{b_1 + ja_1}{A},$$

with  $M(A, \omega) = \sqrt{a_1^2 + b_1^2}$ ;  $\theta(A, \omega) = \arctan\left(\frac{a_1}{b_1}\right)$ ,

(6.3)

where  $a_1$  and  $b_1$  are the first Fourier coefficients in (6.1) and both depend on  $(A, \omega)$ . This method hence consists of treating the nonlinear element of Fig. 6.1 in the presence of a sinusoidal input as if it were a linear element with a frequency response  $N(A, \omega)$ . Note that the complex gain in (6.3) can be interpreted as an operator which acts upon a sinusoidal input and gives the phased sinusoidal output (i.e. proportional plus derivative element), or in other words:

$$N(A, \omega) = \frac{b_1 + ja_1}{A} = n_p(A, \omega) + jn_q(A, \omega) = n_p + \frac{n_q}{\omega}s, \quad (6.4)$$

where the subscripts  $p$  and  $q$  are used to stress the in-phase and quadrature nature of the gains of the nonlinearity (and  $s$  is the Laplace variable). In [87] it is shown that Eq. (6.4) minimises the mean-squared error between the output of the approximation and that of the actual nonlinearity (this property holds also for the DF corresponding to other input signal forms and not only the sinusoid one).

Another important aspect of the application of DF is that, from a modelling perspective, the representation in Fig. 6.1 can be fitted into the LFT one (Fig. 3.1) by viewing the *N.L.* operator as the uncertainty block [81]. Therefore, application of DF to systems described in an LFT fashion is straightforward.

While the use of the DF method has been supported by theoretical arguments [26] and experimental evidences [52], it is important to stress the main assumptions underlying its application:

- the nonlinear element is time-invariant;
- the actual signal at the input of the nonlinearity has a form resembling the one used to derive the describing function (e.g. sinusoid);

- the output of the nonlinear element in response to a sinusoid is periodic (always true when the nonlinearity is single-valued);
- the linear part of the system acts as a low pass filter, i.e. condition (6.2) is satisfied.

In particular the last assumption is often regarded as critical for a profitable use of this method. With reference to aeroelastic applications, several works [19, 58, 234] have supported the adoption of the filter hypothesis with numerical and experimental validation, but this is highly case-dependent and hence a check on the fulfilment of condition (6.2) is always recommended. For example, in [151] it was discovered that a large number of harmonics was needed for the analysis of an aerofoil with nonlinear torsion spring undergoing secondary Hopf (or Neimark-Sacker) bifurcation, characterised by quasi-periodic response. In these cases, the Harmonic Balance (HB) method should be employed to correctly predict Limit Cycles. The main idea of the HB method [69] is to approximate the periodic motion as a Fourier series up to  $n$  components (where  $n$  defines the order of the method) and equate the coefficients of each harmonic component on the two sides of the ordinary differential equations describing the dynamics. This procedure leads to the resolution of a system of nonlinear equations in the fundamental frequency and the Fourier coefficients  $a_n$  and  $b_n$ , which scales in size with  $n$ . The (sinusoidal input) Describing Function method is for this reason also referred to as first-order Harmonic Balance.

Note finally that DF can in principle be used in the presence of more than one nonlinearity [168, 169]. In practice, its application is more tedious and relevant works where this instance was considered in the analysis of aeroelastic systems are [184, 198].

### 6.1.2 Integral Quadratic Constraints

Integral Quadratic Constraints (IQC) is a well established technique to deal with stability and performance analysis of an LTI system  $G$  in feedback connection with a nonlinear and uncertain system  $\Delta$  within a unified framework [170, 259].

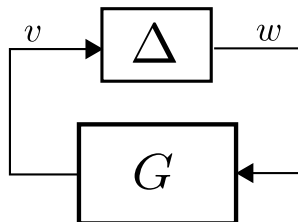


Figure 6.2: Feedback  $G - \Delta$  studied in IQC.

It is said that a vector signal  $v : [0, T] \rightarrow \mathbb{R}^{n_v}$  belongs to the space of square integrable functions  $\mathcal{L}_2^{n_v}[0, \infty)$  if  $\sqrt{\int_0^\infty v(t)^\top v(t) dt} < \infty$ . The idea then is to describe the operator  $\Delta : \mathcal{L}_2^{n_v}[0, \infty) \rightarrow \mathcal{L}_2^{n_w}[0, \infty)$  by means of an integral quadratic constraint on its input  $v$  and output  $w$ . Let

$\Pi : j\mathbb{R} \rightarrow \mathbb{C}^{(n_v+n_w) \times (n_v+n_w)}$  be a measurable Hermitian-valued function, commonly named multiplier and usually chosen among the rational functions bounded on the imaginary axis, i.e.  $\Pi \in \mathbb{RL}_\infty^{(n_v+n_w) \times (n_v+n_w)}$ . It is said that the two signals  $v \in \mathcal{L}_2^{n_v}[0, \infty)$  and  $w \in \mathcal{L}_2^{n_w}[0, \infty)$  satisfy the IQC defined by  $\Pi$  if:

$$\int_{-\infty}^{+\infty} \begin{bmatrix} \hat{v}(j\omega) \\ \hat{w}(j\omega) \end{bmatrix}^* \Pi(j\omega) \begin{bmatrix} \hat{v}(j\omega) \\ \hat{w}(j\omega) \end{bmatrix} d\omega \geq 0, \quad (6.5)$$

where  $\hat{v}$  and  $\hat{w}$  indicate the Fourier transforms of the corresponding signals. A bounded and causal operator  $\Delta$  is said to satisfy the frequency domain IQC defined by  $\Pi$  if the signals  $v$  and  $w = \Delta(v)$  satisfy Eq. (6.5) for all  $v \in \mathcal{L}_2^{n_v}[0, \infty)$ . This will be denoted here by writing  $\Delta \in \text{IQC}(\Pi)$ . The next theorem provides a stability condition for the interconnection of  $G$  and  $\Delta$ .

**Theorem 6.1.** [170] Let  $G \in \mathbb{RH}_\infty$  and  $\Delta$  be a causal bounded operator. Assume for all  $\tau \in [0, 1]$ :

1. the interconnection of  $G$  and  $\tau\Delta$  is well-posed.
2.  $\tau\Delta$  satisfies the IQC defined by  $\Pi$ .
3.  $\exists \epsilon$  such that

$$\begin{bmatrix} G(j\omega) \\ I \end{bmatrix}^* \Pi(j\omega) \begin{bmatrix} G(j\omega) \\ I \end{bmatrix} \leq -\epsilon I \quad \forall \omega \in \mathbb{R} \quad (6.6)$$

Then the feedback interconnection of  $G$  and  $\Delta$  is stable.

In order to numerically verify condition 3 of Theorem 6.1, it is common practice to factorise the multiplier as:

$$\Pi = \Psi^\sim M \Psi, \quad (6.7)$$

where  $M = M^\top \in \mathbb{R}^{n_z \times n_z}$  is a real matrix variable (typically sign indefinite) and  $\Psi \in \mathbb{RH}_\infty^{n_z \times (n_v+n_w)}$  is constructed from pre-selected basis transfer functions. Condition 3 in Theorem 6.1 can then be equivalently rewritten as:

$$\Phi(j\omega)^* M \Phi(j\omega) < 0 \quad \forall \omega \in \mathbb{R}, \quad (6.8)$$

with:

$$\Phi(j\omega) = \Psi(j\omega) \begin{bmatrix} G(j\omega) \\ I \end{bmatrix} = C_\Phi(j\omega - A_\Phi)^{-1} B_\Phi + D_\Phi, \quad (6.9)$$

where  $[A_\Phi, B_\Phi, C_\Phi, D_\Phi]$  are the state-matrices of  $\Phi$ . By exploiting the Kalman-Popov-Yakubovich (KYP) Lemma [199], it can be proved that (6.8) holds true if and only if there exists a matrix  $P = P^\top$  such that:

$$\begin{bmatrix} A_\Phi^\top P + PA_\Phi & PB_\Phi \\ B_\Phi^\top P & 0 \end{bmatrix} + \begin{bmatrix} C_\Phi^\top \\ D_\Phi^\top \end{bmatrix} M \begin{bmatrix} C_\Phi & D_\Phi \end{bmatrix} < 0. \quad (6.10)$$

The power of the KYP Lemma is to transform the infinite set of constraints in (6.8) into the Linear Matrix Inequality (6.10), which represents the standard way of solving IQC problems. In practice, this has the cost of introducing the optimisation matrix  $P$  whose size grows quadratically with

the order of  $G$  and the dynamics in  $\Psi$ . With the aim to mitigate the computational burden, an alternative solution has been recently proposed [61]. Briefly, the optimisation problem is solved directly using the frequency-domain inequalities (6.8) starting from an arbitrary frequency grid. A specific algorithm, based on LFT and  $\mu$ , is then applied in order to guarantee the validity of the solution on the frequency-domain continuum. This technique has thus the advantage of not relying on the (high-dimensional) optimisation matrix  $P$ , but in its current implementation, available with the SMAC toolbox [28], is restricted in terms of available parameterisations for  $\Pi$ . Due to this restriction, the IQC $\beta$  toolbox [133], which uses the standard LMI formulation in (6.10), will be employed in this thesis.

### 6.1.2.1 Time-domain interpretation of IQC

The core effort in IQC analysis is to find suitable multipliers  $\Pi$  that specify the properties of  $\Delta$  and thus allow less conservative results to be obtained. Libraries exist for various types of uncertainties and nonlinearities as summarised in [170, 251], many of them conveniently derived in the frequency-domain. Since the problem is actually solved with the LMI in (6.10), it has great importance the factorisation used for  $\Pi$  (6.7). Moreover, this factorisation provides a time-domain interpretation of (6.5) [215], which will be exploited in Chapter 7. For these reasons, a general discussion on it is given next.

By Parseval's theorem [269], after substituting the factorisation (6.7) in the frequency-domain constraint (6.5), it holds:

$$\int_0^\infty z(t)^\top Mz(t)dt \geq 0, \quad (6.11)$$

where  $z$  is the output of the LTI system  $\Psi$  with state matrices  $A_\Psi, B_\Psi = [B_{\Psi 1} B_{\Psi 2}], C_\Psi, D_\Psi = [D_{\Psi 1} D_{\Psi 2}]$ , and states  $x_\Psi$ :

$$\begin{aligned} \dot{x}_\Psi &= A_\Psi x_\Psi + B_{\Psi 1}v + B_{\Psi 2}w, \quad x_\Psi(0) = 0, \\ z &= C_\Psi x_\Psi + D_{\Psi 1}v + D_{\Psi 2}w. \end{aligned} \quad (6.12)$$

Fig. 6.3 aids in providing an interpretation of the new constraint (6.11). Indeed, the input and output of  $\Delta$  are filtered through  $\Psi$ , whose output  $z$  is constrained to satisfy the inequality in (6.11). In this new setting, conditions are given in terms of  $\Psi$  and  $M$ , which depend on  $\Pi$ , via the factorisation (6.7), and in turn on  $\Delta$ , via the original constraint (6.5).

It is stressed that an important distinction holds for time domain IQCs. Namely, a bounded causal operator  $\Delta : \mathcal{L}_2^{n_v}[0, \infty) \rightarrow \mathcal{L}_2^{n_w}[0, \infty)$  satisfies the time domain *soft* IQC defined by  $(\Psi, M)$  if the following inequality holds for all  $v \in \mathcal{L}_2^{n_v}[0, \infty)$  and  $w = \Delta(v)$ :

$$\int_0^\infty z(t)^\top Mz(t)dt \geq 0. \quad (6.13)$$

This will be denoted here by writing  $\Delta \in \text{SoftIQC}(\Psi, M)$ . On the other hand, a bounded causal operator  $\Delta : \mathcal{L}_2^{n_v}[0, \infty) \rightarrow \mathcal{L}_2^{n_w}[0, \infty)$  satisfies the time domain *hard* IQC defined by  $(\Psi, M)$  if the

following inequality holds for all  $v \in \mathcal{L}_2^{n_v}[0, T]$ ,  $w = \Delta(v)$  and for all  $T \geq 0$ :

$$\int_0^T z(t)^\top M z(t) dt \geq 0. \quad (6.14)$$

This will be denoted here by writing  $\Delta \in \text{HardIQC}(\Psi, M)$ . While by Parseval's theorem any time domain IQC yields a valid frequency domain IQC, i.e.  $\Delta \in \text{SoftIQC}(\Psi, M) \rightarrow \Delta \in \text{IQC}(\Pi)$  and  $\Delta \in \text{HardIQC}(\Psi, M) \rightarrow \Delta \in \text{IQC}(\Pi)$ , the converse is only true in the former case. In fact,  $\Delta \in \text{IQC}$  does not, in general, imply the existence of a factorisation  $(\Psi, M)$  for which  $\Delta \in \text{HardIQC}(\Psi, M)$ , the hard/soft property not being inherent to the multiplier  $\Pi$  but dependent on the (non-unique) factorisation  $(\Psi, M)$ .

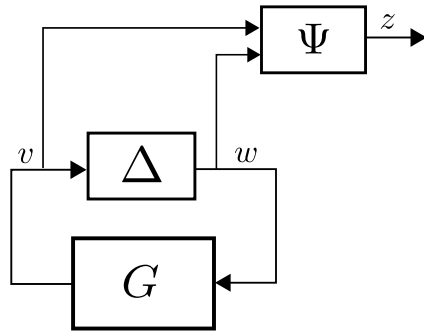


Figure 6.3: Augmented plant for the time-domain interpretation of IQC.

### 6.1.2.2 Example of hard/soft IQCs

To exemplify the difference between soft and hard IQCs and its implications for the analyses, let us consider a real constant uncertain parameter  $\delta \in \mathbb{R}$  satisfying  $|\delta| \leq k$ . A possible frequency domain multiplier  $\Pi_\delta$  is:

$$\Pi_\delta = \begin{bmatrix} k^2 X(j\omega) & Y(j\omega) \\ Y^*(j\omega) & -X(j\omega) \end{bmatrix}, \quad (6.15)$$

with  $X = X^* \geq 0$  and  $Y = -Y^*$  bounded functions of  $\omega$  [170]. A possible time domain factorisation for  $\Pi_{\delta_u}$  is [250]:

$$\Psi_\delta = \begin{bmatrix} kH_v & 0 \\ 0 & H_v \end{bmatrix}, \quad M_{DG} = \begin{bmatrix} M_{11} & M_{12} \\ M_{12}^\top & -M_{11} \end{bmatrix}, \quad (6.16)$$

where  $H_v \in \mathbb{RH}_\infty^{n_H}$  is a column vector of basis functions (typically chosen as low-pass filters, i.e.  $H_v := [1; \frac{1}{s+a_1}; \dots; \frac{1}{s+a_v}]$ ), and  $M_{11} = M_{11}^\top$ ,  $M_{12} = -M_{12}^\top$  are decision matrices constrained to satisfy  $H_v^\top(j\omega) M_{11} H_v(j\omega) \geq 0$ . This factorisation is a general expression for the so called *D-G scalings* [251, 269], and specifies that  $\delta$  is a constant and real parameter. It holds  $\delta \in \text{SoftIQC}(\Psi_\delta, M_{DG})$ .

The special case of (6.15) with  $Y \equiv 0$  corresponds to the frequency-domain IQC for a dynamic, norm-bounded LTI system, i.e.  $\delta \in \mathbb{RH}_\infty$  and  $\|\delta\|_\infty \leq k$ . For this case, a valid time-domain factorisation, known as *D scalings*, is given by  $(\Psi_\delta, M_D)$ , with  $M_D$  obtained from  $M_{DG}$  by setting

$M_{12} \equiv 0$ . It holds that  $\delta \in \text{HardIQC } (\Psi_\delta, M_D)$  [13]. It is important to note that, while  $(\Psi_\delta, M_D)$  holds the (stronger) hard property, it does not fully capture the nature of  $\delta$  as real uncertainty, thus it can possibly lead to more conservative results than those obtained with  $(\Psi_\delta, M_{DG})$ .

The IQC analyses in this Chapter use the standard frequency-domain interpretation (in conjunction with the KYP Lemma), and thus the influence of the adopted state-space factorisation is limited to the parameterisation of  $\Psi$  (this aspect will be investigated in Sec. 6.3.2). The distinction between soft and hard IQCs will instead play a crucial role in the Region of attraction (ROA) analysis approach developed in Chapter 7 which leverages the time-domain interpretation.

## 6.2 Robust LCO analysis with Describing Functions and $\mu$

This section proposes DF-based analysis methodologies to characterise properties of LCOs in nominal and uncertain systems. Section 6.2.1 considers the nominal case, and, despite being an application of known procedures in the field [83, 136], serves to highlight and reflect on the main features and capabilities of the technique. Moreover, in Section 6.2.1.2 a novel method for testing stability of the (nominal) LCO for models formulated in the frequency-domain, which generalises the one from [8], is proposed. Sec. 6.2.2 introduces the concept of worst-case LCO curve with the aim to provide a measure of the degradation of the LCO properties in the face of parametric uncertainties, whereas in Sec. 6.2.3 the idea of using  $\mu$  analysis in conjunction with DF to perform LCO tailoring is proposed. The approaches will be illustrated considering freeplay (due to the large amount of results available from literature), but are valid for any nonlinearity holding a Describing Function representation.

The combined use of DF and  $\mu$  was originally presented in [136], and an application to nonlinear aeroelastic systems shown in [16]. While in the former reference the theoretical foundation was established and the latter work demonstrated its applicability to nonlinear aeroelastic systems, the contribution of this section is to develop systematic approaches to study the effect of the uncertainties in terms of nonlinear response and to provide an interpretation of the results in terms of worst-case LCO curve.

### 6.2.1 Limit Cycle Oscillations in nominal systems

#### 6.2.1.1 Definition of $N$ and necessary conditions for LCO

The first step entailed by the application of DF is the definition of the describing function  $N$ , which depends on the nonlinearity. Due to the well established usage of the DF method in the control community, expressions can be found for the majority of nonlinearities commonly encountered in applications [87]. Among these freeplay, also called dead-zone or threshold, is characterised by the fact that the first part of the input is needed to overcome an initial opposition at the output,

as schematically depicted in Fig. 6.4. Its explicit mathematical definition is given by:

$$w = \begin{cases} 0, & |v| \leq \bar{\delta}, \\ k(v - \bar{\delta}), & |v| > \bar{\delta}, \end{cases} \quad (6.17)$$

where  $\bar{\delta}$  is the (positive) freeplay size and  $k$  is the linear constant. Freeplay (for example between the main wing and the control surface or the horizontal tail and the stabiliser) is relevant in aeroelasticity. Indeed, it is known to be a primary cause of LCO, as testified by the dedicated works in the literature [236, 237] (and other references therein).

It is worth noting some important properties of this nonlinearity, which determine simplifications of the associated describing function with respect to the generic definition in (6.4): it is odd (i.e. the relation is symmetric about the origin), memoryless (i.e. only one output is possible for any given value of the input, thus  $n_q=0$ ), and static (i.e. no dependence upon the input derivatives, thus  $n_p=n_p(A)$ ).

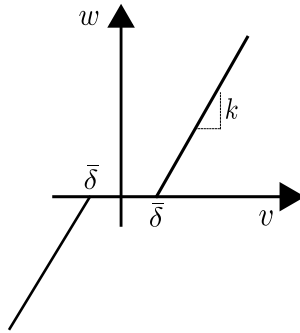


Figure 6.4: Freeplay nonlinearity.

The DF function  $N^F$  for freeplay can be obtained analytically [87] through Fourier integrals by applying the definition in (6.3) and assuming a sinusoidal input  $v = \beta_s \sin(\omega t)$ :

$$N^F = \begin{cases} 0, & |v| \leq \bar{\delta}, \\ \frac{k}{\pi} \left[ \pi - 2 \sin^{-1} \left( \frac{\bar{\delta}}{\beta_s} \right) - 2 \left( \frac{\bar{\delta}}{\beta_s} \right) \sqrt{1 - \left( \frac{\bar{\delta}}{\beta_s} \right)^2} \right], & |v| > \bar{\delta}, \end{cases} \quad (6.18)$$

The notation  $\beta_s$  is now adopted for the amplitude  $A$  since freeplay in the control surface rotation DOF  $\beta$  of the typical section will be considered in the numerical example. Consistently with the aforementioned properties,  $N^F$ , plotted in Fig. 6.5 for  $k=1$ , is a pure real gain not depending on frequency, but only on the amplitude of the input signal, in particular on its ratio with the freeplay size  $\bar{\delta}$ . Note also that  $N^F$  is monotonic increasing with respect to  $\frac{\beta_s}{\bar{\delta}}$ .

The methodology employed to study LCOs through DF takes the clue from the feedback representation of a nonlinear system in Fig. 6.1, specialised by specifying the signal circulating through the system as a sinusoid, and replacing the nonlinear element by its describing function

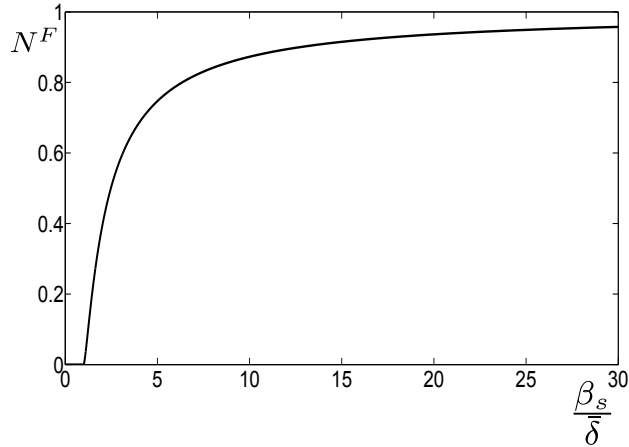


Figure 6.5: Freeplay describing function.

$N^F$ . Linear theory is then applied to the quasi-linearised system, searching for points of neutral stability which are interpreted as LCOs in the original (nonlinear) system. The well known feedback relations involve the frequency response of the signals and the transfer functions of the operators, and the resulting necessary condition for oscillations are:

$$\begin{aligned} \hat{v}(j\omega) &= -G(j\omega)\hat{w}(j\omega), \\ \hat{w}(j\omega) &= N^F(\beta_s)\hat{v}(j\omega), \\ [1 + G(j\omega)N^F(\beta_s)]\hat{v}(j\omega) &= 0. \end{aligned} \quad (6.19)$$

Solution of the characteristic equation gives amplitude  $\beta_s$  and frequency  $\omega$  of the self-sustained oscillations (or LCO) exhibited by the system.

### 6.2.1.2 Stability of the LCO

The characteristic equation in (6.19) gives a necessary condition for the occurrence of periodic oscillations in the system, because stability of the oscillations must still be verified. The stability of periodic orbits is generally posed in terms of the behaviour of perturbed trajectories. This can be formally addressed by looking at the eigenvalues of the monodromy matrix (also called Floquet multipliers) [145]. A drastic simplification holds when the problem can be studied with the DF approach. Specifically, the method from [8] allows to address this task analytically in the following manner.

Let us denote the eigenvalue of the quasi-linearised state-matrix  $\mathcal{A}$  associated with the occurrence of the LCO as  $\lambda_{LC} = \zeta + j\omega$ , with  $\zeta = 0$  when the necessary condition for oscillations is satisfied. This matrix is obtained by replacing the nonlinear element with the value of  $N^F$  (6.18) corresponding to the predicted amplitude  $\beta_s$  of the LCO. The idea is to study the variation of the real part  $\zeta$  following a perturbation in  $\beta_s$  (note that the frequency does not influence

$N^F$ , otherwise perturbations in  $\omega$  would have to be considered as well). The general spectral decomposition allows to express the state-matrix  $\mathcal{A}$  as:

$$\mathcal{A} = \sum_{k=1}^{n_x} \lambda_k u_k v_k^\top, \quad (6.20)$$

where  $u_k$  and  $v_k$  are the right and left eigenvectors corresponding to the eigenvalue  $\lambda_k$ . Starting from (6.20) and taking advantage of the orthogonal property of left and right eigenvectors, the following holds [8]:

$$\frac{\partial \zeta}{\partial \beta_s} = \Re \left( v_{LC}^\top \frac{\partial \mathcal{A}}{\partial \beta_s} u_{LC} \right). \quad (6.21)$$

By means of the DF, it is possible to express the nonlinear term in the state-matrix as a function of  $\beta_s$ , and thus the derivative can be analytically performed. The rationale is that if after amplitude perturbations the LCO returns to its original equilibrium state it is defined *stable*, whereas if its amplitude or frequency change in order to reach another equilibrium state, it is defined *unstable*. Therefore, a stable limit cycle requires  $\frac{\partial \zeta}{\partial \beta_s} < 0$ , since a positive perturbation in amplitude moves the trajectory outside the limit cycle and requires a decay in the response (negative real part) to move the trajectory back to the limit cycle, and conversely an unstable limit cycle will have  $\frac{\partial \zeta}{\partial \beta_s} > 0$ .

The application of this procedure is straightforward, and has been successfully employed in the analysis of aeroelastic systems [16]. However, it is limited to state-space representations. As highlighted in previous chapters, the frequency-domain is a common modelling option for flutter analysis, and thus an extension of this method for the study of stability in frequency-domain is proposed here. Let us define the aeroelastic frequency response matrix  $T$  based on the governing equation in (2.1):

$$T(s) = [s^2 \bar{M}_s + s \bar{C}_s + \bar{K}_s - q_\infty Q_{hh}(\bar{s})], \quad (6.22)$$

and its total derivative with respect to the LCO amplitude as:

$$\frac{\partial T}{\partial \beta_s} = \frac{\partial T}{\partial s} \frac{\partial s}{\partial \beta_s} + \frac{dT}{d\beta_s}. \quad (6.23)$$

Eq. (6.23) features the term  $\frac{\partial s}{\partial \beta_s}$ , which describes the variation of the considered eigenvalue when perturbing the LCO amplitude, and thus its real part is sought here to address the study of stability in frequency-domain. Assume that a flutter root  $s_T$  is given, that is for  $\eta \neq 0$  it holds:

$$T(s_T)\eta = 0. \quad (6.24)$$

This can be found, for example, by applying the *p-k* method (for a given value of  $\beta_s$ ). Then:

$$\begin{aligned} [\mathcal{A}_T - s_T I_{n_x}] \eta &= 0, \\ \text{with } \mathcal{A}_T &= T + s_T I_{n_x}. \end{aligned} \quad (6.25)$$

where  $\mathcal{A}_T$  can be interpreted as an *equivalent* state-matrix. In fact, let us define the right and left eigenvectors  $u_T$  and  $v_T$  of  $\mathcal{A}_T$  corresponding to its eigenvalue  $s_T$ . Then, the following property is satisfied:

$$v_T^\top T u_T = 0. \quad (6.26)$$

As a result of Eq. (6.26), and of known properties of eigenvectors, the following key relation is obtained:

$$\frac{\partial(v_T^\top T u_T)}{\partial \beta_s} = \frac{\partial v_T^\top}{\partial \beta_s} T u_T + v_T^\top \frac{\partial T}{\partial \beta_s} u_T + v_T^\top T \frac{\partial u_T}{\partial \beta_s} = v_T^\top \frac{\partial T}{\partial \beta_s} u_T = 0. \quad (6.27)$$

Eq. (6.27) enables the derivative of the root  $s$  associated with the LCO condition to be written out. By substituting (6.23) in (6.27), it is finally obtained:

$$\frac{\partial s_T}{\partial \beta_s} = - \frac{v_T^\top \frac{dT}{d\beta_s} u_T}{v_T^\top \frac{\partial T}{\partial s} u_T}. \quad (6.28)$$

Eq. (6.28) provides the variation of  $s_T$  when the LCO amplitude is perturbed. By specialising  $s_T$  to the LCO condition (i.e.  $s_T = \lambda_{LC} = j\omega$ ), an equivalent criterion to the one in (6.21) is obtained:

$$\Re\left(\frac{\partial s_T}{\partial \beta_s}\right)\Big|_{s_T=\lambda_{LC}} = - \Re\left(\frac{v_k^\top \frac{dT}{d\beta_s} u_k}{v_k^\top \frac{\partial T}{\partial s} u_k}\right)\Big|_{s_T=\lambda_{LC}}. \quad (6.29)$$

The calculation of the partial derivatives can be performed applying the definition of  $T$  (6.22). For the denominator it is:

$$\frac{\partial T}{\partial s} = 2s\bar{M}_s + s\bar{C}_s - q_\infty \frac{\partial Q_{hh}}{\partial s}. \quad (6.30)$$

Since the GAF matrix typically depends on the imaginary part of  $s$  only, it holds  $\frac{\partial Q_{hh}}{\partial s} = \frac{\partial Q_{hh}}{\partial \omega}$ . This can be evaluated for example by means of a finite difference scheme. However, the performed tests showed that this term is negligible compared to the other two in (6.30). As for the derivative in the numerator of (6.29), this can be evaluated once the operators in  $T$  (6.22) which are subject to the nonlinearity are replaced by the corresponding DF.

### 6.2.1.3 Application to a freeplay benchmark case study

The analyses in this Chapter will be applied to a benchmark case study consisting of a typical section model featuring freeplay in the control surface rotation. The reason is that results obtained by means of different approaches are available: experimental [52], analytical [234], harmonic-balance [152], numerical continuation [95], and DF- $\mu$  analysis [16]. Details of the model can be found in Appendix A.4.

Recalling the presentation of the typical section model in Sec. 2.3.1, the nonlinearity is in the diagonal term of the stiffness matrix  $K_s$  (2.10) corresponding to the DOF  $\beta$ . Based on the definition of freeplay in (6.17), the corresponding elastic moment  $M_\beta^E$  can be written as:

$$M_\beta^E = \begin{cases} 0. & |\beta| \leq \bar{\delta}, \\ K_\beta^L(\beta - \bar{\delta}). & |\beta| > \bar{\delta}, \end{cases} \quad (6.31)$$

where  $K_\beta^L$  is the flap stiffness in the linear case (i.e. for  $\bar{\delta} = 0$ ). By making use of the DF approximation, an expression for the nonlinear elastic moment  $M_\beta^E$  can be given as:

$$\begin{aligned} M_\beta^E &= K_\beta^{QL}(\beta_s)\beta, \\ K_\beta^{QL}(\beta_s) &= N^F(\beta_s)K_\beta^L, \end{aligned} \quad (6.32)$$

where  $K_\beta^{QL}$  can be seen as the quasi-linear flap stiffness and  $N^F$  is taken from (6.18) with  $k = 1$ . In other words, the nonlinear flap stiffness  $K_\beta$  is replaced by  $K_\beta^{QL}$ , which is a monotonic increasing function of the flap rotation amplitude  $\beta_s$  and ranges in the interval  $[0, K_\beta^L]$ .

The procedure to detect LCOs in the system can be applied now. A fundamental harmonic solution with fixed amplitude  $\beta_s$  is assumed, and from (6.18) the corresponding value of  $N^F$  is obtained. This enables to calculate the quasi-linear stiffness  $K_\beta^{QL}$  (6.32) and thus to quasi-linearise the system. At this stage standard (nominal linear) flutter analyses methods can be applied to evaluate the corresponding flutter speed  $V_f$  and flutter frequency  $\omega_f$ . Fig. 6.6 displays the results of these analyses. Specifically, on the  $x$  axis the values for  $K_\beta^{QL}$  are reported, while on the  $y$  axis there are  $V_f$  and  $\omega_f$ . The results are in good agreement with others from the literature [52, 234] (the latter reference providing also experimental results).

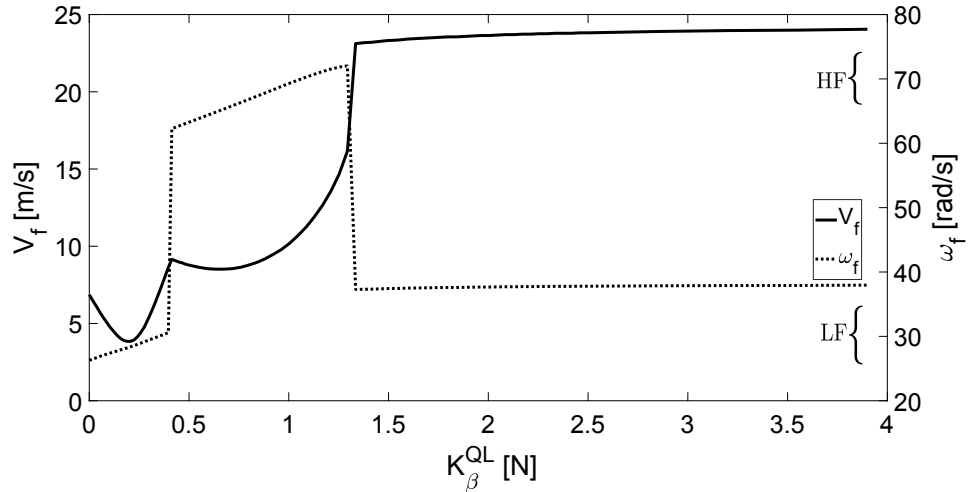


Figure 6.6: Flutter speed  $V_f$  and frequency  $\omega_f$  vs. quasi-linear flap stiffness  $K_\beta^{QL}$ .

The linear flutter speed of the system, which corresponds to  $K_\beta^{QL} = K_\beta^L = 3.9N$ , can be found to be equal to  $V_f \approx 24 \frac{m}{s}$ . An interesting feature also detectable in Fig. 6.6 is the existence, depending on the value of  $K_\beta^{QL}$ , of a low (LF) or high (HF) flutter frequency associated with the instability. The physical reason for this is that two distinct modes, respectively the plunge and pitch, go unstable as  $K_\beta^{QL}$  varies. This aspect will be further studied in Sec. 6.2.3.

The next step consists of associating the conditions of neutral stability for the quasi-linearised system with LCOs in the nonlinear system by using the key relation between  $K_\beta^{QL}$  and  $\beta_s$  in Eq. (6.32). The DF method is instrumental in guaranteeing the connection between these two

representations and enabling to transfer the information coming from multiple linear flutter analyses to an LCO curve characterisation. Fig. 6.7 presents the nondimensional LCO amplitude  $\frac{\beta_s}{\delta}$  against speed  $V$ . Note that an analogous plot with the LCO frequency on the  $y$  axis could also be built up by considering as basis the dashed curve in Fig. 6.6. Two curves are shown: the one labelled with *SS* (black curve) uses a state-space approach for flutter ( $p$  method) and LCO stability [8] analysis, whereas *FD* (red curve) is obtained using a frequency-domain approach for flutter ( $p - k$  method) and LCO stability (new method developed in Sec. 6.2.1.2). The two curves are in good agreement (indeed almost indistinguishable), and most importantly the same ranges of stable (solid line) and unstable (dashed line) oscillations are detected, therefore validating the proposed approach. It is worth stressing that the unstable branches are not physically meaningful because they represent a dynamic response not occurring in reality (the system will experience only the stable LCO branches).

The plot also allows to infer the onset of a subcritical Hopf bifurcation at  $V = V_H$ . Indeed for  $V < V_0 (= 3.8 \frac{m}{s})$  the equilibrium of the system is stable, whereas in the range  $V_0 < V < V_H (= 7 \frac{m}{s})$  the system can either settle down to the stable configuration (this branch is not reported in Fig. 6.7) or experience oscillations (on the upper stable branch), depending on the perturbation to the state trajectories. For  $V > V_H$  the only stable steady-state response is the LCO.

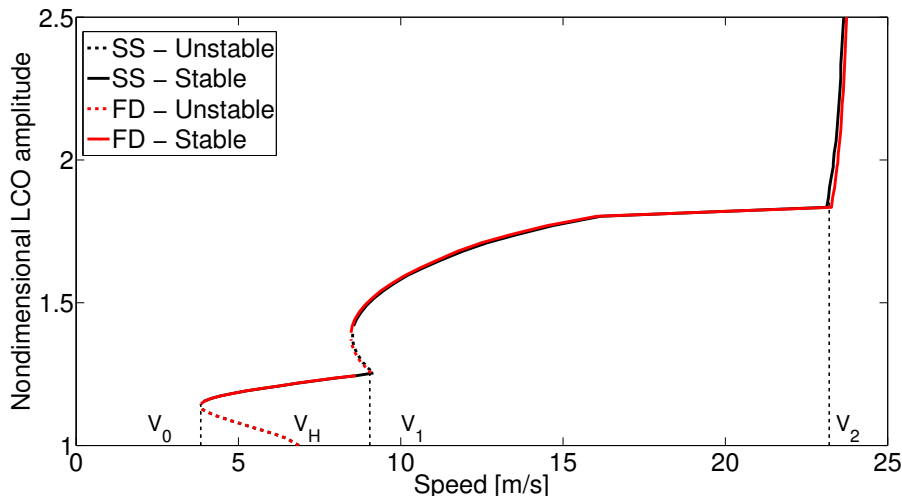


Figure 6.7: LCO amplitude  $\frac{\beta_s}{\delta}$  vs. speed  $V$ .

Additional features of the oscillations are displayed in Fig. 6.7, where three regions can be identified as the speed increases: (i)  $V_0 < V < V_1 (= 9 \frac{m}{s})$ , where the system undergoes LCOs associated with the plunge instability (recall from Fig. 6.6 that in this range a low frequency LCO is predicted); (ii)  $V_1 < V < V_2 (= 23.2 \frac{m}{s})$  where the LCO switches to the pitch instability (the frequency correspondingly changes, as in Fig. 6.6) and the amplitude visibly increases; and (iii)  $V > V_2$ , where there is an asymptote in the LCO amplitude corresponding to a dramatic growth of the oscillations. It is worth noting that the maximum speed for which the system does not

experience LCO (i.e.  $V_0$ ) is considerably smaller than the flutter speed evaluated with a linear model ( $V_f \approx 24 \frac{m}{s}$ ).

It is finally observed that equivalent results to those presented in this section could have been obtained by applying graphical methods, which closely resemble standard frequency-domain techniques based on Nyquist and Nichols plots [83]. Their application to this case study was detailed in [120], but it is not reported here in the interest of compactness of presentation.

### 6.2.2 Worst-case LCO curve with $\mu$

The interpretation of the plot in Fig. 6.7 is that at a given speed  $V$  the system will experience periodic oscillations as described by the stable curve. In particular, the oscillation amplitude  $\frac{\beta_s}{\delta}$  can be directly read off in the  $y$ -axis. If the nonlinear system is subject to modelling uncertainties (of the type discussed in Chapter 4), it is of practical interest to characterise how the stability properties (in terms of  $V_0$ ) and the features of the LCO change. To this end, the concept of *worst-case LCO curve* is proposed here. Conceptually, this is an analogous representation of Fig. 6.7 where a measure of the LCO amplitude and frequency degradation in the face of the uncertainties is provided. This is motivated by the fact that an accepted industry practice is to limit LCO accelerations in prescribed points of the airframe [19], and that these quantities can be estimated provided that a reliable characterisation of the response in terms of amplitude and frequency is available.

The task can be approached as follows. Consider a speed  $V$  and an amplitude  $\beta_s$  larger than the one associated with that speed in the nominal plot. Quasi-linearisation is performed via DF around the operating point  $(V, \frac{\beta_s}{\delta})$ , and the selected uncertainties are captured in an LFT fashion. Application of robust analysis with  $\mu$  will then allow to quantify how close the point is to become a Limit Cycle when uncertainties are considered. In other words, the  $\mu$  analysis will provide the minimum distance to the LCO curve by evaluating a robust stability margin of the quasi-linearised system. Exemplification of this idea is provided by considering the following uncertainty set consisting of 3 mass and 2 stiffness parameters of the typical section model (2.10):

$$\Delta^{7,R} = \text{diag}(\delta_{K_h}, \delta_{K_\alpha}, \delta_{r_\alpha}, \delta_{x_\alpha} I_2, \delta_{r_\beta} I_2). \quad (6.33)$$

All the parameters are allowed to vary within 10% of their nominal values.

The idea of using  $\mu$  to quantify the distance of an operating point from a possible LCO is illustrated first with Fig. 6.8. The plot shows the results of  $\mu$  for the quasi-linearised system associated with  $\frac{\beta_s}{\delta} = 1.9$  (corresponding to  $N^F = 0.367$  and  $K_\beta^{QL} = 1.43$  N) and  $V = 10.3 \frac{m}{s}$ . From Figs. 6.6-6.7 it is inferred that, in nominal conditions, an LCO with amplitude  $\frac{\beta_s}{\delta} = 1.9$  takes place at a speed  $V = 23.2 \frac{m}{s}$  and a frequency  $\omega = 37 \frac{rad}{s}$ , whereas at  $V = 10.3 \frac{m}{s}$  an LCO with amplitude  $\frac{\beta_s}{\delta} \approx 1.605$  (corresponding to  $K_\beta^{QL} = 1.02$  N) and frequency  $\omega = 70 \frac{rad}{s}$  is expected.

Upper and lower bounds are reported in the plot, featuring two distinct peaks. The smaller one takes place at a low frequency (close to the one of the nominal case), whereas the peak of

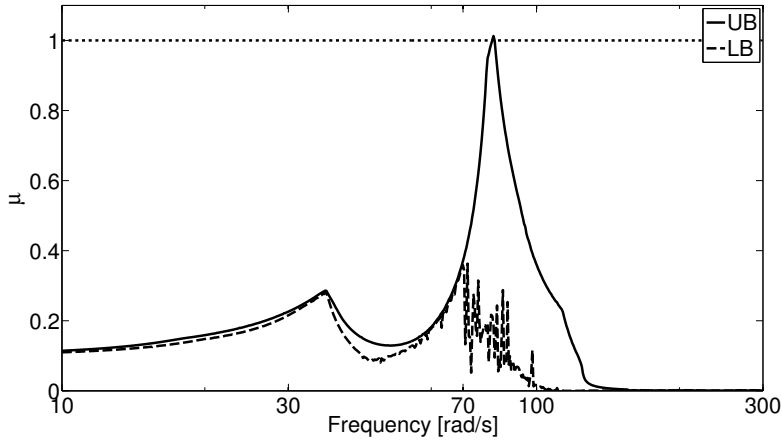


Figure 6.8:  $\mu$  analysis at  $V = 10.3 \frac{m}{s}$  and  $\frac{\beta_s}{\delta} = 1.9$ .

$\mu_{UB}$  (with a value around 1) has a higher frequency of approximately  $80 \frac{rad}{s}$ . The upper bound analysis thus suggests that an LCO with amplitude  $\frac{\beta_s}{\delta} = 1.9$  might occur at  $V = 10.3 \frac{m}{s}$ . This is a drastic change with respect to the nominal case in that this LCO would feature a considerably greater amplitude. Although no definitive conclusions can be drawn from Fig. 6.8, due to the gap in the bounds around the highest peak, this result suggests the need for further investigations.

The analysis strategy discussed above can be applied to scattered operating points (e.g. based on the planned mission of the system) and a possible representation of the results is proposed in Fig. 6.9. The solid curve is the nominal plot presented in Fig. 6.7, while the star markers represent four operating points where  $\mu$  analysis is applied (the corresponding upper bounds  $\mu_{UB}$  are shown in the smaller insets).

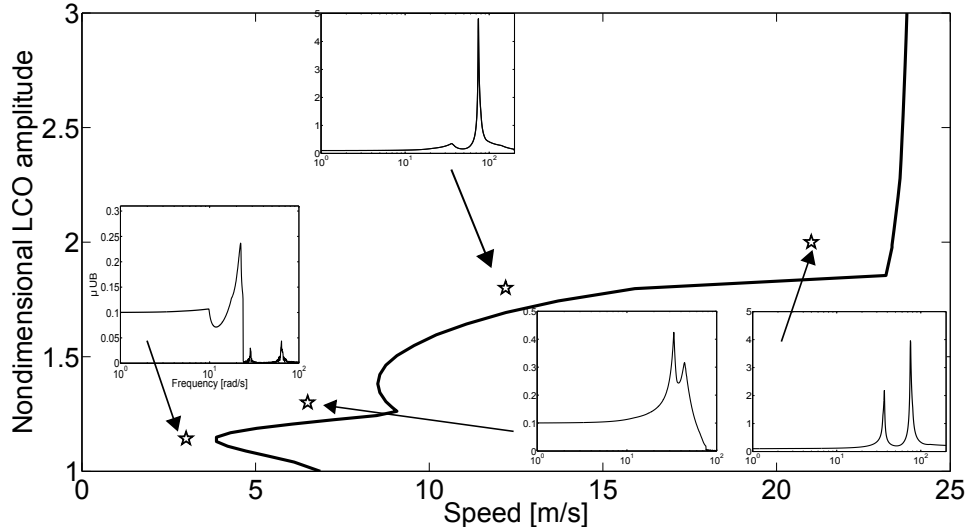


Figure 6.9: Robustness analysis of the LCO for scattered operating point.

According to the proposed interpretation of the results, when  $\mu < 1$  then it can be inferred that the LCO curve will lie below the considered point despite the uncertainties, that is, the worst-case amplitude of the LCO is smaller than the one associated with the star marker. Conversely, when  $\mu > 1$  then the LCO curve might lie above the point for an adverse (but within the considered range) combination of parameters, meaning in practice that the oscillatory response might feature greater amplitude than the one associated with that point.

These results predict robustness of the LCO at discrete operating points. Adding to this, a mismatch in the bounds was observed in Fig. 6.8, and predictions based only on  $\mu_{UB}$  can be too conservative. Prompted by these reasons, an improved methodology, leading to the calculation of the worst-case LCO curve, is proposed. This consists of evaluating a sufficiently fine grid of values of  $\beta_s$  and then implementing at each point a bisection-like algorithm searching for the two smallest speeds  $V$  attaining the conditions  $\mu_{UB} = 1$  and  $\mu_{LB} = 1$ , respectively. Note that, due to the fact that upper and lower bounds do not coincide in general, these two speeds might hold different values.

Results are shown in Fig. 6.10, which depicts the two distinct curves corresponding to the two bounds as well as that of the nominal for comparison purposes. The location of the four operating points at which  $\mu$  analysis was shown in Fig. 6.9 is reported for the benefit of the discussion. This plot can be interpreted as a worst-case analysis of the nonlinear flutter problem in terms of LCO onset and amplitude. In fact, it assesses how the properties discussed before (with reference to Fig. 6.7) degrade. The first information that can be inferred regards the smallest speed for which the system experiences an LCO. The assumed set of uncertainties slightly decreases this value from  $V_0 = 3.8 \frac{m}{s}$  to  $V_0^N = 3.6 \frac{m}{s}$ . A similar trend is observed for the Hopf bifurcation speed. As the speed is increased, the regions highlighted in Fig. 6.7 are still detectable but  $V_1$  and  $V_2$  are shifted towards smaller values ( $V_1^N$  and  $V_2^N$ ). Furthermore, the plot allows a significant deterioration in amplitude in the third region to be clearly appreciated. This trend was somehow foreseen in Fig. 6.8, but finds here a rigorous confirmation (note that the two dashed curves are very close meaning good agreement between the bounds). Although not reported in the plot, at each LCO point it is also possible to associate the oscillation frequency (corresponding to the peak value of  $\mu$ ). This information can provide physical insights into the problem. In this case, for example, Fig. 6.8 suggests that the drastic increase in amplitude caused by the uncertainties (highlighted by the gap nominal-robust becoming large) can be ascribed to the high frequency (pitch) LCO, which is also responsible for shifting towards left the asymptote (vertical branch).

It is finally remarked that the two points which in the insets of Fig. 6.9 yielded  $\mu_{UB} < 1$  (i.e. the two left-most points) lie above the worst-case LCO curves, whereas the two points resulting in  $\mu_{UB} > 1$  are located below it, as expected based on the proposed interpretation.

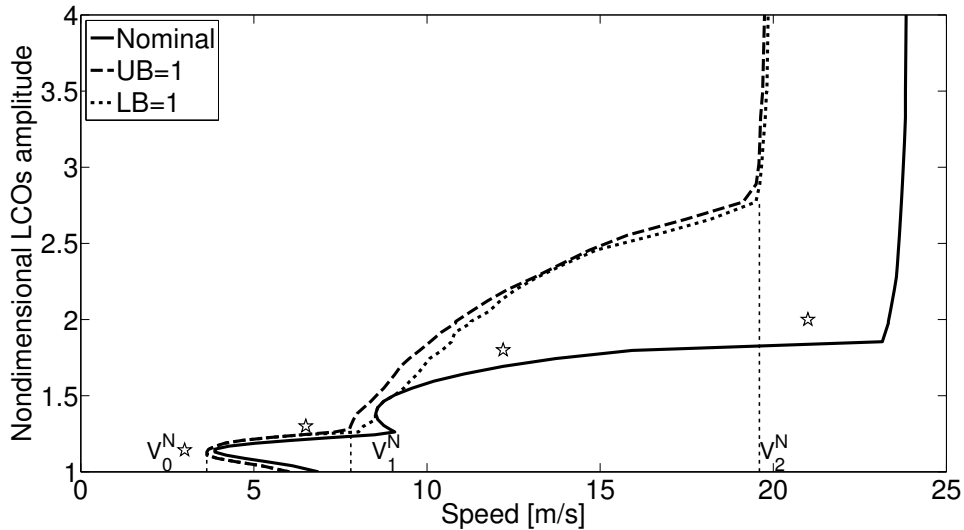


Figure 6.10: Worst-case LCO curve.

### 6.2.3 LCO amplitude tailoring

The objective of this section is to demonstrate how DF and  $\mu$  analysis can be advantageously employed to achieve a reduction in LCO amplitude *by design*. The rationale is to select tailoring variables and gather them in  $\Delta$ . Rather than an uncertainty set, this is now the variable design space made up of parameters which can be exploited in order to achieve a better nonlinear behaviour, here defined as an LCO curve featuring smaller amplitudes.

#### 6.2.3.1 Object definition

The connection between Fig. 6.6 and Fig. 6.7 represents the starting point for the formulation of the LCO tailoring problem. The solid curve in Fig. 6.6 indeed represents a parametric linear flutter analysis with respect to variation in the flap stiffness. Crucially, all the points lying on this curve feature a condition of neutral stability. This curve, together with Eqs. (6.18)-(6.32), provides in turn the LCO amplitude as a function of the speed (Fig. 6.7). It is thus apparent, recalling the monotonicity of  $N^F$  (Fig. 6.5), that a reduction in the LCO amplitude can be achieved by moving towards the left the flutter speed curve in Fig. 6.6.

The second important observation is that the standard application of  $\mu$  is to predict a measure (via the maximum singular value norm of the perturbation matrix) of the distance of a stable plant from the neutral stability condition. However, the algorithms can in principle be employed to obtain the same measure for an *unstable* plant, the meaning of it being distance to regain neutral stability. While this usage of  $\mu$  has to be considered exceptional and care should be put in interpreting the results (in fact, the classical  $\mu$  interpretation prescribes that the system is nominally stable), the idea here is to exploit it in order to understand how and which parameters should be modified to achieve the amplitude reduction goal.

Fig. 6.11 illustrates all the combinations of speed and quasi-linear flap stiffness for which the system has a pair of purely imaginary eigenvalues. The unstable eigenvalue is associated with its elastic mode via the Modal Assurance Criteria (Sec. 4.1.1). Compared to Fig. 6.6, where for each value of the stiffness only the smallest of such speeds  $V_f$  was indicated, it can be appreciated from Fig. 6.11 that for a large range of stiffness ( $0 < K_\beta^{QL} < 1.3$  N) both pitch (dashed) and plunge (solid) modes experience instability. Consider now the operating point denoted by the circle marker, which indicates that at  $V = 15 \frac{m}{s}$  the system will exhibit an LCO of amplitude  $\frac{\beta_s}{\delta} \approx 1.8$ . In order to achieve a reduction in the amplitude of oscillations at this speed, this point should lose the condition of neutral stability in favour of one lying on the horizontal line (dotted line in Fig. 6.11) at the left of the circle marker. For example, the point identified by the square marker (whose quasi-linearisation features an unstable eigenvalue associated with the pitch mode) would have a smaller LCO amplitude  $\frac{\beta_s}{\delta} \approx 1.45$ . From a  $\mu$  perspective, this problem can be solved by defining the nominal system as the one identified by the square marker, and by interpreting the largest peak found with  $\mu$  as the smallest perturbation in the design parameters space such that the nominal plant becomes the new LCO point. An important feature of this strategy is that it allows to specify the desired reduction in LCO amplitude at a certain speed  $V$  by selecting the value of  $K_\beta^{QL}$  at which the neutral stability condition is *regained* (roughly speaking, by defining the location of the square marker). Moreover, the worst-case scenario nature of  $\mu$  analysis has here a very practical consequence: the critical perturbation matrix  $\Delta^{cr}$  (provided by  $\mu_{LB}$ ) represents the smallest change from the nominal design necessary to achieve the stated objective, because it points out the combination of parameters with the overall minimum perturbation size. For this reason it is here referred to as an optimal design remedy.

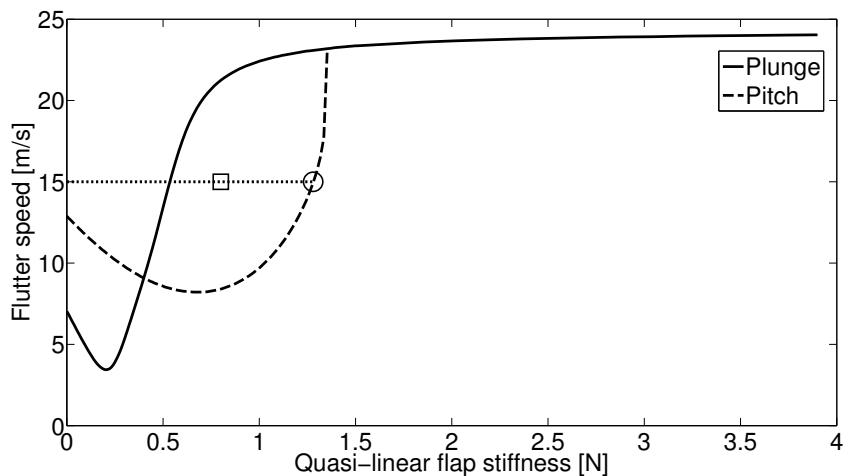


Figure 6.11: Objective definition for the DF and  $\mu$ -based tailoring.

A specific property of this case study complicates the tailoring process. In fact, Fig. 6.11 highlights that in the range of speed where there is a drastic increase in LCO amplitude (and thus mitigation strategies would be highly beneficial) the nominal plant lies in between the

pitch and plunge curves. As a result, if the tailoring is performed only with the objective of shifting towards the left the dashed curve, the change in the parameters might have an opposite (detrimental) effect on the solid curve, eventually leading towards only a partial or negligible achievement of the objective. To tackle this, a  $\mu$ -based sensitivity analysis can be performed in order to discern the effect of the parameters in the different frequency ranges, and thus make effective and efficient design changes.

### 6.2.3.2 Numerical example

As in standard  $\mu$  analysis, the procedure starts with the definition of the nominal plant and the block  $\Delta$ , which have now both a different meaning as stressed in the previous section. The variable design space gathers the same 5 parameters considered in the LCO robust analyses (6.33). For all of them a range of variation of 20% from the nominal value is assumed. As for the nominal plant, the one identified by the square marker in Fig. 6.11 is considered.

The next step consists of applying  $\mu$  analysis, and the results are shown in Fig. 6.12.

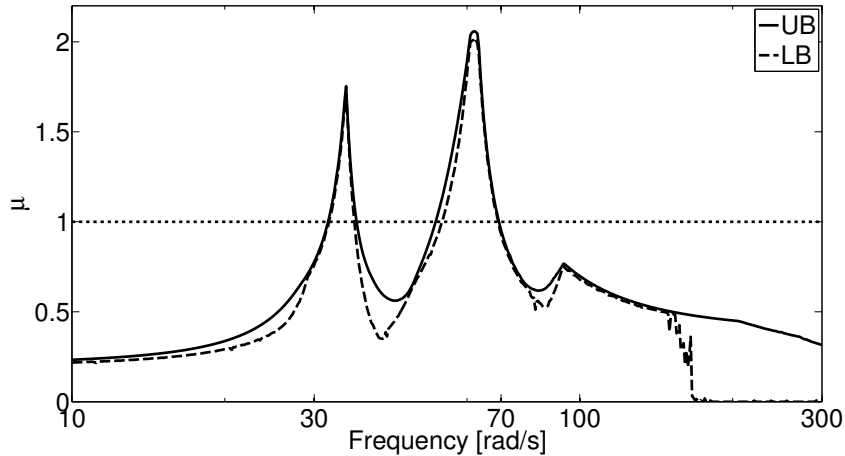


Figure 6.12:  $\mu$  analysis for the nominal plant identified by the square marker.

As expected, two peaks are predicted: a low frequency  $\omega_1 \cong 34 \frac{\text{rad}}{\text{s}}$  related to the plunge mode and a high frequency  $\omega_2 \cong 63 \frac{\text{rad}}{\text{s}}$  related to the pitch mode. Moreover, both peaks are greater than 1. The implication of this for the peak at  $\omega_2$  ( $\mu \cong 2.1$ ), which is associated with the dashed branch in Fig. 6.12, is that if all the parameters are perturbed within the allowed range of 20% a greater reduction than the one prescribed with the definition of the nominal plant will be achieved. In fact, it would be sufficient to perturb 45% ( $\approx \frac{1}{2.1}$ ) of that range to obtain the desired shift in the curve. Note also that the upper and lower bounds in both cases are close, especially around the peaks, thus the associated matrices  $\Delta_1^{cr}$  and  $\Delta_2^{cr}$  provide the smallest perturbations capable of determining a pair of purely imaginary eigenvalues in the nominal plant. Unfortunately,  $\Delta_2^{cr}$ , the critical worst-case combination for the tailoring, has similar values, for some parameters,

to those in  $\Delta_1^{cr}$ , thus the detrimental effect on the plunge branch envisaged before represents a concrete risk.

In order to minimise it, a  $\mu$ -based sensitivity analysis, as the one applied in Sec. 4.2.2 for the BFF instability, is performed to understand which parameters have a greater effect on the pitch instability. This basically consists of estimating the LCO amplitude sensitivity with respect to the parameters in  $\Delta$ . In an active control perspective, this study could drive the design of the feedback control law to actively reduce the LCO amplitudes and possibly eliminate LCOs [224]. The importance of this step is acknowledged in literature. In [223] for example the task of obtaining this sensitivity is tackled by differentiating the equations derived with the Harmonic Balance method and obtaining analytical sensitivities. The method proposed here is believed to be less affected by the complexity of the system since it does not rely on analytical formulations, and it can be straightforwardly applied once an LFT description of the system is available.

The conclusions of this sensitivity analysis step are:

- the dimensionless moments of inertia of the section and control surface have great effect on the pitch instability, but not on the plunge one. Hence, it can be advantageously modified according to  $\Delta_2^{cr}$ , i.e.  $\delta_{r_\alpha} = 1$  and  $\delta_{r_\beta} = -1$ ;
- the plunge stiffness parameter does not affect the pitch instability, but is relevant for the plunge one. Hence, it can be modified with opposite sign to that in  $\Delta_2^{cr}$  in order to push the plunge curve in Fig. 6.11 towards left and counteract potential undesired effect on it, i.e.  $\delta_{K_h} = -1$ ;
- the elastic axis location  $x_\alpha$  has in general a small influence and thus it is left unaltered since it would represent an ineffective design change, i.e.  $\delta_{x_\alpha} = 0$ ;
- the pitch stiffness parameter has great effect on both instabilities and its worst-case has the same perturbation sign ( $\delta_{K_\alpha} = -1$ ), thus it might have to be carefully considered.

With respect to the last point, it is observed that a sound tailoring strategy should not determine a decrease in  $V_0$  (hence worsening the stability of the system) or in  $V_2$  (where an asymptote in the LCO amplitude occurs). Since both speeds are associated with the plunge instability (this is visible in Fig. 6.11), it is foreseeable that  $K_\alpha$  will represent a trade-off between two different objectives: on the one hand maximising the reduction in the LCO amplitude, and on the other preserving the speed range where LCO occurs.

Based on the conclusions above, three different designs are defined in Table 6.1 in terms of percentage variations of the tailoring variables from the nominal values. The designs differ only in the pitch stiffness  $K_\alpha$ , in order to observe its global effect, and the corresponding LCO amplitude curves are plotted in Fig. 6.13 against the original case.

All the proposed designs achieve the main goal of reducing the LCO amplitude as well as fulfilling the requirement of maintaining the same lowest LCO occurrence speed  $V_0$ . Design 2

Table 6.1: Change in the tailoring variables to achieve the amplitude reduction goal.

	Design 1	Design 2	Design 3
$K_\alpha$	0%	-20%	+20%
$K_h$	-20%	-20%	-20%
$r_\alpha$	+20%	+20%	+20%
$r_\beta$	-20%	-20%	-20%
$x_\alpha$	0%	0%	0%

features the minimum LCO amplitude among the curves but presents, as side effect, a drastic reduction of the asymptotic speed  $V_2$ . Design 3 goes in the opposite direction for both objectives due to the role of  $K_\alpha$ . Finally Design 1, which does not alter the value of the pitch stiffness, represents a trade-off solution since it maintains similar values for  $V_0$  and  $V_2$  while achieving a noticeable amplitude reduction. Of course, other designs could be proposed which contemplate *absolute* variations of the parameters smaller than 20% and thus entail smaller changes in the design at the expense of lower amplitude reduction.

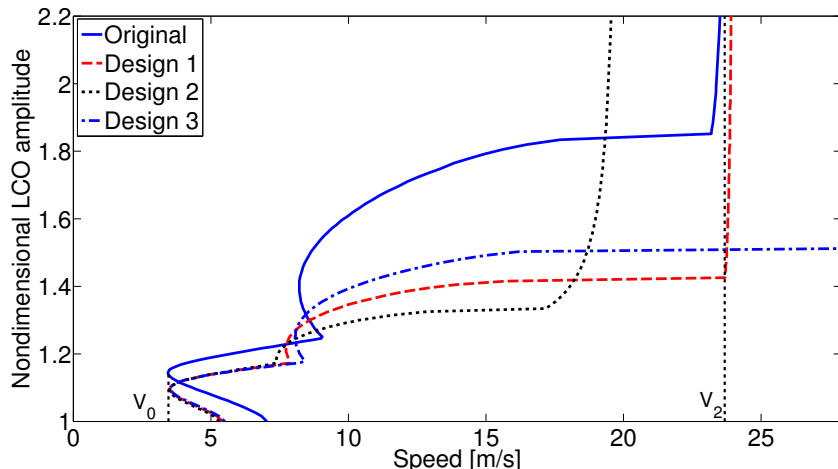


Figure 6.13: LCO amplitudes  $\frac{\beta_s}{\delta}$  obtained with the proposed tailoring strategy (3 possible designs are considered).

## 6.3 LCO analysis with IQC

In this section the use of IQC analysis to study the LCO problem is investigated. The power of this technique lies in the capability to handle uncertainties and nonlinearities in the same framework. However, it is acknowledged that a possible drawback lies in the conservatism associated with the results. This can be ascribed to various causes, and the focus has been here on two aspects: the selection of the multipliers (Section 6.3.2) and the local/global validity of the results (Section 6.3.3). The main outcome is a strategy to obtain worst-case predictions not only in terms of stability (as classically done in IQC analysis) but also on the post-critical response (here represented by LCO).

### 6.3.1 Posing of the problem

The starting point when applying IQC is the characterisation of the nonlinear uncertain operator  $\Delta$  via suitable multipliers. The IQC $\beta$  toolbox [133] allows to formulate the problem declaring the connections among the signals  $v$  and  $w$  through appropriate sub-functions which associate with them the constraint (6.5) given by the multipliers. Since the problem is solved via the KYP LMI (6.10), internally the toolbox implements the state-space factorisation of  $\Pi$ , typically parameterising the dynamic part  $\Psi$  with first or second order filters having user's selected frequencies and optimised gains.

In order to reduce the conservatism of the results, a collection of multipliers, reflecting different properties of freeplay, is adopted in the analyses [251]. For example, freeplay can be generically defined as a memoryless sector nonlinearity with bounds  $[\sigma, \eta]$ . The associated sector multiplier  $\Pi_S$  is:

$$\Pi_S = \lambda_S \begin{bmatrix} -2\sigma\eta & \sigma + \eta \\ \sigma + \eta & -2 \end{bmatrix}, \quad (6.34)$$

where  $\lambda_S$  is positive decision scalar. For the case of freeplay in the control surface, this property can be assigned by linking the signals  $\beta$  and  $M_\beta^E$  (6.31) with the sub-function `iqc_sector`. Since this is a static IQC (that is,  $\Pi_S$  does not depend on the frequency), no parameterisation is required and the only options to be specified are the sector bounds, discussed later.

The Popov IQC allows time-invariance of the nonlinearity to be captured:

$$\tilde{\Pi}_P = \lambda_P \begin{bmatrix} 0 & j\omega \\ -j\omega & 0 \end{bmatrix}, \quad (6.35)$$

where  $\lambda_P$  is a sign indefinite decision variable. Due to the unboundedness of  $\tilde{\Pi}_P$  on the imaginary axis, a loop transformation  $\Delta_1 = \Delta \frac{1}{s+1}$  is typically employed such that the new nonlinear operator  $\Delta_1$  satisfies the multiplier  $\Pi_P$ :

$$\Pi_P = \lambda_P \begin{bmatrix} 0 & \frac{j\omega}{1+j\omega} \\ -\frac{j\omega}{1-j\omega} & 0 \end{bmatrix}. \quad (6.36)$$

This multiplier can be assigned with the sub-function `iqc_popov_vect` and again it does not require any dynamic parameterisation. Precisely, the sub-function `iqc_popov` defines the combined sector and Popov IQC (which gives the classic Popov criterion), but in the analyses they will be reported separately for clarity. Note that, due to the loop transformation,  $\Pi_P$  can be employed only if the plant  $G$  is strictly proper [170].

A further refinement in the IQC description of this nonlinearity can be obtained observing that the freeplay is a monotonic and odd function, and thus a slope restriction in the sector  $[\sigma_1, \eta_1]$  holds. These properties lead to the Zames-Falb IQC [104, 266]:

$$\begin{aligned} \Pi_{ZF} &= \lambda_{ZF} \begin{bmatrix} \Pi_{ZF}^{11} & \Pi_{ZF}^{12} \\ \Pi_{ZF}^{21} & \Pi_{ZF}^{22} \end{bmatrix}, \\ \Pi_{ZF}^{11} &= -\sigma_1 \eta_1 (2 - H - H^\sim), & \Pi_{ZF}^{12} &= \sigma_1 (1 - H) + \eta_1 (1 - H^\sim), \\ \Pi_{ZF}^{21} &= \sigma_1 (1 - H^\sim) + \eta_1 (1 - H), & \Pi_{ZF}^{22} &= -2 + H + H^\sim, \end{aligned} \quad (6.37)$$

where  $\lambda_{ZF}$  is a positive decision scalar and  $H \in \mathbb{RL}_\infty$  is arbitrary except that the  $\mathcal{L}_1$ -norm of its impulse response must be smaller than 1. This multiplier can be selected in the  $\text{IQC}\beta$  toolbox with the sub-function `iqc_slope_odd`, which requires, in addition to the sector bounds, also the length  $N_H$  and the pole location  $a_H$  of the parameterisation:

$$H(s) \asymp \sum_{k=0}^{N_H} \frac{h_k}{(s + a_H)^{k+1}}, \quad (6.38)$$

where  $h_k$  are decision variables.

As for constant real uncertainties  $\delta \in \mathbb{R}$  satisfying  $|\delta| \leq k$ , a candidate is the frequency-domain multiplier  $\Pi_\delta$  introduced in (6.15), and repeated next for ease of readability:

$$\Pi_\delta = \begin{bmatrix} k^2 X(j\omega) & Y(j\omega) \\ Y^*(j\omega) & -X(j\omega) \end{bmatrix}. \quad (6.39)$$

This is parameterised in the  $\text{IQC}\beta$  toolbox with a standard conic combination of first and second order filters by invoking the sub-function `iqc_ltigain`. It is important to stress that this parameterisation is different from the state-space factorisation defined in Eq. (6.16) and originally proposed in [250], which will lead in general to less conservative results. The latter will be employed in Sec. 7.3, where the use of IQC to perform Region of Attraction analysis is presented and focus are given to the different parameterisations available for the case of scalar uncertainties.

It is well known that IQC analysis with  $D$ - $G$  scalings multipliers build on the same theoretical premises of  $\mu$ . An important difference is that thanks to the KYP lemma the LMI test (6.10) does not rely on a discretisation of the frequency range, which for numerical reasons is usually done in  $\mu$  implementation [14] (recall the evaluation of  $M_{11}$  on the frequency grid discussed in Chapter 3). Therefore, the stability certificate obtained with IQC is guaranteed on the whole frequency spectrum. However, this valuable property is penalised by the need to parameterise

$\Pi_\delta$  with a finite basis of rational functions  $\Psi_\delta$  and hence the feasibility of the LMI is only a sufficient condition on the stability of the system (i.e. nothing can be said if the test fails). These considerations apply also to the parameterisations of other multipliers (e.g. Eq. 6.38) and motivate some of the analyses performed in Sec. 6.3.2.

From the modelling point of view, the problem is formulated by building up an LFT  $\mathcal{F}_u(M, \Delta)$  where the linear nominal part is closed with the set  $\Delta$  gathering parametric uncertainties and the freeplay channel. While the former is standard, the latter needs a clarification for the normalisation. The (nonlinear) stiffness parameters  $K_\beta$  is treated (from an LFT viewpoint) as if it was an uncertain parameter. Once the sector bound  $[\sigma, \eta]$  is defined for  $\Pi_S$  (6.34), a range of variation for the stiffness is defined  $K_{\beta-1} < K_\beta < K_{\beta-2}$  (where  $K_{\beta-1} = 2\sigma - \eta$  and  $K_{\beta-2} = \eta$ ), with the corresponding block in  $\Delta$  normalised such that  $|\delta_{K_\beta}| \leq 1$ . This guarantees that  $K_\beta$  is in the sector  $[\sigma, \eta]$  when the normalised nonlinearity  $\delta_{K_\beta}$  is in the sector  $[0, 1]$ . That is, the sector  $[0, 1]$  will be assigned to the sub-function `iqc_sector` regardless of the true bounds (which are taken into account with the normalisation of the LFT). If  $\sigma \neq \sigma_1$  or  $\eta \neq \eta_1$ , the Zames-Falb sector for  $\delta_{K_\beta}$  will not be  $[0, 1]$ , but can be easily evaluated from the previous normalisation.

With this implementation, the sector bounds are defined with no ambiguity and can be easily modified in the course of the analyses (this will be particularly useful in the analyses of Sec. 6.3.3). Moreover, the fact that the analysis methodology pivots on LFT models is a strong point of the proposed approach. This indeed enables powerful techniques [20, 146, 156, 160] for the modelling of complex systems to be employed, and all the insights and methodologies developed in Chapter 3 and tailored to the aeroelastic case to be exploited. In addition, methods to derive LFT models of nonlinear systems have been recently proposed [113] (also specifically for aeroelastic applications [17]) and can be used for the present purpose.

### 6.3.2 Sensitivity of results to the multipliers

The analyses in this section are performed in an incremental way (in terms of number and type of uncertainty) with the goal of providing an overview of the application of IQC to the aeroelastic problem. Table 6.2 summarises the three LFTs adopted in this work by listing the captured parameters and total size of the operator  $\Delta$  (including repetitions). LFT 1 describes a nominal nonlinear problem, since only the freeplay is included; LFT 2 describes a linear robust problem with stiffness and mass uncertain parameters; and finally, LFT 3 considers the nonlinear robust problem featured by structural uncertainties and nonlinearity.

The first IQC tests, performed with LFT 1, aim to give a stability certificate for the nominal aerofoil affected by freeplay. The methodology consists of increasing the speed until the LMI problem in (6.10) becomes unfeasible (the first speed for which this happens is referred to as  $V_{unf}$ ). In this section the standard sector description adopted for the analysis of sector bounded nonlinearities is used, i.e.  $\sigma = \sigma_1 = 0$  and  $\eta = \eta_1 = K_\beta^L$ . This is shown in Fig. 6.14 where the shaded area identifies all the possible combinations of  $\beta$  and  $M_\beta^E$  fulfilling the IQC description.

Table 6.2: LFT models employed in the IQC analyses.

	Parameters $\in \Delta$		$\Delta$ size
LFT 1	$K_\beta$	—	1
LFT 2	—	$K_h, K_\alpha, x_\alpha, r_\alpha, r_\beta$	7
LFT 3	$K_\beta$	$K_h, K_\alpha, x_\alpha, r_\alpha, r_\beta$	8

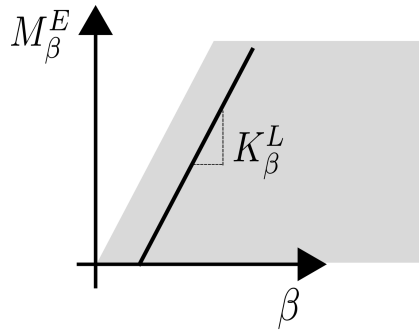


Figure 6.14: Standard sector constraint.

Table 6.3 reports for each test the multiplier (with corresponding options), the size of the LMI problem in terms of decision variables, the computation time, and the speed  $V_{unf}$ .

Table 6.3: IQC analysis of LFT 1 (only freeplay).

Case	Multiplier & Options	Size	Time	$V_{unf}$
1	$\Pi_S$	47	1 s	—
2	$\Pi_S, \Pi_P$	48	1.1 s	$3.81 \frac{m}{s}$
3	$\Pi_S, \Pi_P, \Pi_{ZF}(1 \frac{rad}{s})$	80	1.3 s	$3.82 \frac{m}{s}$

When only the memoryless sector bounded condition is enforced, no feasible solution is achieved (case 1). When the Popov multiplier  $\Pi_P$ , encompassing the time invariance of the freeplay, is added then it is possible to find  $V_{unf} = 3.8 \frac{m}{s}$ . This result is also recovered when using the  $\Pi_{ZF}$  multiplier (case 3). This value is the same as the speed  $V_0$  detected in Fig. 6.7 and it indicates that the approach of considering the entire sector provides the smallest speed such that the system experiences an LCO. The adoption of the entire sector can thus be interpreted as a search for global stability certificates. Note also that, due to the good agreement, this analysis may be seen as a validation of the stability result given by means of DF.

The analyses reported in Table 6.4 investigate the linear robust stability of LFT 2. In order to draw a parallel with the analyses in Fig. 6.8 (showing that  $\mu_{UB}=1$  at  $V = 10.3 \frac{m}{s}$ ), the nominal

LFT is obtained by fixing  $K_\beta^{QL}$  at the same value of  $1.43 N$  used in those analyses.

Table 6.4: IQC analysis of LFT 2 (only uncertainties).

Case	Multiplier & Options	Size	Time	$V_{unf}$
1	$\Pi_\delta (1 \frac{rad}{s})$	330	9 s	$8.6 \frac{m}{s}$
2	$\Pi_\delta (80 \frac{rad}{s})$	330	9 s	$8.9 \frac{m}{s}$
3	$\Pi_\delta (1 \frac{rad}{s}, 80 \frac{rad}{s})$	800	70 s	$10.3 \frac{m}{s}$

When only one filter is employed for the parameterisation (cases 1 and 2), the minimum speed at which the problem becomes unfeasible is still lower than what was obtained with  $\mu$  analysis. However, changing the pole from the default value (i.e.  $1 \frac{rad}{s}$ ) to one which is closer to the expected flutter frequency (about  $80 \frac{rad}{s}$  from the analyses in Fig. 6.8) increases the estimation of  $V_{unf}$ . The addition of another filter (case 3) aids to considerably improve the prediction, in particular it yields the same speed for which  $\mu_{UB} = 1$  in Fig. 6.8. This represents an important confirmation of what was shown in Fig. 6.8, since it holds on the frequency continuum.

This first set of tests concludes with a nonlinear robust analysis applied to LFT 3, reported in Table 6.5. It is clear from the results that when only one filter is used for  $\Pi_\delta$  (cases 1 and 2) the algorithm is not able to find a feasible solution (regardless of the description provided for the freeplay). In fact, it is decisive to increase the number of filters to 3 (cases 5 and 6) in order to match the largest stable speed  $V_{unf} = 3.6 \frac{m}{s}$  found in the analyses of Fig. 6.10. This IQC description for  $\Pi_\delta$  is reflected in an increase of the computation burden, but clearly improves the LMI feasibility problem solution.

Table 6.5: IQC analysis of LFT 3 (nonlinear uncertain).

Case	Multiplier & Options	Size	Time	$V_{unf}$
1	$\Pi_\delta (40 \frac{rad}{s}), \Pi_S, \Pi_P, \Pi_{ZF}(40 \frac{rad}{s})$	390	19 s	-
2	$\Pi_\delta (80 \frac{rad}{s}), \Pi_S, \Pi_P, \Pi_{ZF}(40 \frac{rad}{s}, 80 \frac{rad}{s})$	450	40 s	-
3	$\Pi_\delta (40 \frac{rad}{s}, 80 \frac{rad}{s}), \Pi_S, \Pi_P, \Pi_{ZF}(40 \frac{rad}{s})$	890	105 s	$3.1 \frac{m}{s}$
4	$\Pi_\delta (40 \frac{rad}{s}, 80 \frac{rad}{s}), \Pi_S, \Pi_P, \Pi_{ZF}(40 \frac{rad}{s}, 80 \frac{rad}{s})$	980	170 s	$3.1 \frac{m}{s}$
5	$\Pi_\delta (1 \frac{rad}{s}, 40 \frac{rad}{s}, 80 \frac{rad}{s}), \Pi_S, \Pi_P, \Pi_{ZF}(40 \frac{rad}{s})$	1590	530 s	$3.6 \frac{m}{s}$
6	$\Pi_\delta (1 \frac{rad}{s}, 40 \frac{rad}{s}, 80 \frac{rad}{s}), \Pi_S, \Pi_P, \Pi_{ZF}(40 \frac{rad}{s}, 80 \frac{rad}{s})$	1700	790 s	$3.6 \frac{m}{s}$

The results presented in this section confirm the well known dependence of IQC predictions on multipliers selection and parameterisation. However, in this study the importance of having reference results (here provided by the DF- $\mu$  approach, or in general also obtainable with

other tools) is stressed. Firstly, they provide a measure of the conservatism associated with the infeasibility of the LMI problem and therefore may point out the need to employ a more refined set of multipliers. While this is typically accomplished with a frequency sweep of the filter poles (time-consuming and not always successful), the availability of auxiliary reference results can also inform the improvement of the parameterisation for the multipliers: characterizing the sensitivity of the instability to certain sub-blocks of  $\Delta$  and hence allowing to focus only on the refinement of the associated multipliers; as well as highlighting critical frequencies of the systems. As for the latter aspect, the values of the filter poles are profitably selected here considering the expected unstable frequencies of the systems, obtained by DF-nominal analysis (Fig. 6.6) or DF- $\mu$  approach (Fig. 6.8).

### 6.3.3 Post-critical analysis with IQC

The certificates found in Sec. 6.3.2 with respect to LFT 3 guarantee global stability of the system. In fact, only the largest speed at which the system, in the face of parametric uncertainties, settles down to the original equilibrium when subject to any vanishing perturbation can be inferred from the results. This is ascribed to the selection of the standard sector for the freeplay nonlinearity (Fig. 6.14), here referred to as *global* because it covers the nonlinear relationship between  $\beta$  and  $M_\beta^E$  for all values of  $\beta$ . It is indeed well understood in the literature [141, 231] that results holding *locally* can enrich the contents of the analyses performed via IQC and reduce the conservatism. In this section an alternative definition of the sector condition, sketched in Fig. 6.15, is proposed, aimed at obtaining certificates concerning not only stability but also post-critical features.

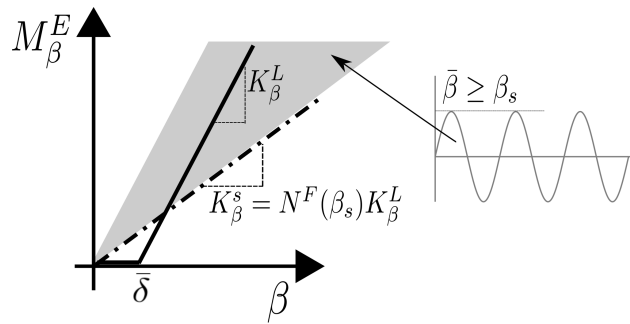


Figure 6.15: Local sector constraint for LCO analyses.

The premise of this relaxation is that the DF method provides, for a given freeplay size  $\bar{\delta}$ , a relation between the amplitude of the nonlinear response  $\beta_s$  and the equivalent stiffness  $K_\beta^{QL}$  (6.32). Assume that a (non-zero) oscillation level, quantified by  $\beta_s$ , can be withstood by the structure, and thus is tolerated as post-critical response. Then, the corresponding  $K_\beta^{QL}(\beta_s)$  can be computed from (6.32) and taken as the lower bound  $K_\beta^s$  of the sector (dashed-dotted line). The IQC analysis will in turn determine the largest speed  $V_{unf}$  such that the system is guaranteed to experience an oscillatory motion in the DOF  $\beta$  of amplitude smaller than  $\beta_s$ . Put it differently,

the shaded area covered by the local sector (Fig. 6.15) will only capture post-critical responses characterised by LCO amplitudes  $\bar{\beta}$  greater than  $\beta_s$ .

Note that from the limit on the nonlinear response of the DOF  $\beta$ , analogous information for the response of the other DOFs can be easily obtained by making use of the Describing Function method. This simple procedure was for example shown in [234] for the plunge and torsion DOFs of the typical section. The proposed local analysis allow therefore to detect operating conditions for which the system do not converge to the equilibrium but is attracted to self-sustained oscillatory responses featured by a given maximum level of amplitude.

It is remarked finally that the proposed relaxation applies in the exact same way to both the multipliers  $\Pi_S$  and  $\Pi_{ZF}$ .

### 6.3.3.1 Results

Table 6.6 shows the results obtained applying this approach to LFT 1 and 3. The upper sector limit  $\eta = \eta_1$  is fixed at  $K_\beta^L$  as in the previous analyses. A different lower limit for the sector  $\sigma = \sigma_1 = K_\beta^s$ , with an associated smallest amplitude  $\frac{\beta_s}{\delta}$ , is instead selected for each test and the smallest unfeasible speeds (namely  $V_{unf}^1$  for LFT 1 and  $V_{unf}^3$  for LFT 3) are reported. This analysis, repeated on a grid of values of  $K_\beta^s$ , can be interpreted as a nominal and robust characterisation of the nonlinear response of the system in that it provides the highest speed at which the system can be operated if oscillations below a certain threshold are tolerated. The parameterisation of the multipliers follows the rationale discussed in Sec. 6.3.2 so as to provide a reliable IQC description of the problem. It is remarked here that, especially for LFT 3, the multipliers had to be re-tuned in order to improve the accuracy as the value of  $K_\beta^s$  was increased. The LMI decision variables, tailored to each single case by making use of the heuristic strategy illustrated in the previous section, were always kept below 2000.

Table 6.6: Local IQC analysis of LFT 1 and LFT 3.

Cases	$K_\beta^s[N]$	$\frac{\beta_s}{\delta}$	$V_{unf}^1[\frac{m}{s}]$	$V_{unf}^3[\frac{m}{s}]$
1	0.01	1.02	3.8	3.6
2	0.18	1.13	3.8	3.6
3	0.32	1.21	5.9	4.3
4	0.86	1.5	9.0	8.45
5	1.15	1.69	12.2	9.2
6	1.39	1.9	23.05	10.3
7	1.72	2.2	23.5	12.3
8	2.00	2.5	23.6	15.7

From Table 6.6 it can be seen that the values of  $V_{unf}^1$  and  $V_{unf}^3$  for case 1 and 2 match with the predictions obtained using the global sector condition, reported in Tables 6.3-6.5 respectively. If Figs. 6.7-6.10 from Sec. 6.2 are examined, it can be observed that both the LCO amplitudes  $\frac{\beta_s}{\bar{\delta}} = 1.02$  and  $\frac{\beta_s}{\bar{\delta}} = 1.13$  are smaller than the one associated with the smallest LCO speed  $V_0$  and  $V_0^N$ . Indeed, at these two speeds the system will exhibit an LCO of amplitude  $\frac{\beta_s}{\bar{\delta}} \approx 1.16$ . Consistent with the given interpretation of the local sector condition, the analysis returns therefore the corresponding speed value (either  $V_0$  or  $V_0^N$ ). As  $\frac{\beta_s}{\bar{\delta}}$  is increased, it becomes evident the advantage of using the local sector since different unfeasible speeds are predicted for each lower sector bound. For  $\frac{\beta_s}{\bar{\delta}} \leq 1.5$  (a bold line is employed in Table 6.6 to emphasise the two regions), the degradation due to the uncertainties, measured by the difference between  $V_{unf}^1$  and  $V_{unf}^3$ , is not remarkable. As the amplitude is increased, it is evident a greater effect of the uncertainties in worsening the response (i.e. larger difference between the two speeds associated with the given amplitude  $\frac{\beta_s}{\bar{\delta}}$ ). For example, assume a nominal analysis cleared the system to operate at  $V=16\frac{m}{s}$  (because it was able to withstand an oscillation of amplitude  $1.9\bar{\delta}$ ). This amplitude corresponds to  $K_\beta^s=1.39N$  in Table 6.6 (case 6) and takes place indeed at  $V_{unf}^1=23.05\frac{m}{s}$  ( $> 16\frac{m}{s}$ ) in nominal conditions. The proposed analysis reveals however that in the face of uncertainties the system could exhibit an LCO greater than  $2.5\bar{\delta}$  (case 8) at  $V_{unf}^3 = 15.7\frac{m}{s}$ , and thus highlights possible risks in operating the system at  $V=16\frac{m}{s}$ .

The trend in Table 6.6 is in good agreement both qualitatively and quantitatively with the worst-case LCO curve proposed in Sec. 6.2.2. The intersections of horizontal lines (drawn for different values of the ordinate  $\frac{\beta_s}{\bar{\delta}}$ ) with the nominal and robust curves in Fig. 6.10 give points having as  $x$  coordinate approximately the corresponding values of  $V_{unf}^1$  and  $V_{unf}^3$ . Two curves were provided for the uncertain system, one for  $\mu_{UB} = 1$  and another for  $\mu_{LB} = 1$ . The values of  $V_{unf}^3$  are typically closer to the intersections with the curve  $\mu_{UB} = 1$ , which is expected since they both give only a sufficient condition for the stability violation. However, the two curves are very close as stressed before.

Finally, note that, for a given value of  $\frac{\beta_s}{\bar{\delta}}$ , the LCO amplitude  $\beta_s$  experienced by the system is a function of the freeplay size  $\bar{\delta}$ . Thus this methodology provides an outcome which depends also on this parameter (which is expected from a physical viewpoint). On the contrary, there was no influence of  $\bar{\delta}$  when the standard approach was employed.

### 6.3.3.2 Validation

The methods to study LCO in systems with uncertainties are validated here by means of time-marching simulations. In view of the close connections in the formulations of the worst-case LCO curve with the DF- $\mu$  approach (Sec. 6.2.2) and that just performed above with IQCs, the discussion and comparisons apply to both the approaches developed in this Chapter.

The library in [29], which enables to simulate LFR objects [156] in Simulink $\circledR$ , is employed to evaluate the response of the nonlinear system subject to uncertainties. In Fig. 6.16 a comparison

of the results in terms of the normalised oscillation amplitude  $\frac{\beta_s}{\delta}$  between the analytic approaches proposed here (*Analytic*) and the nonlinear simulations (*Simul.*) is presented for nominal (*Nom.*) and robust (*Rob.*) conditions. In the latter case, the largest amplitude of oscillation obtained with a vertex approach (*Vertex*), where all the possible combinations of the extreme values of the parameters are simulated, is reported. The 32 tested cases are deemed to provide a sufficiently good estimation of the worst-case amplitude because the uncertainty set is a polytope [269].

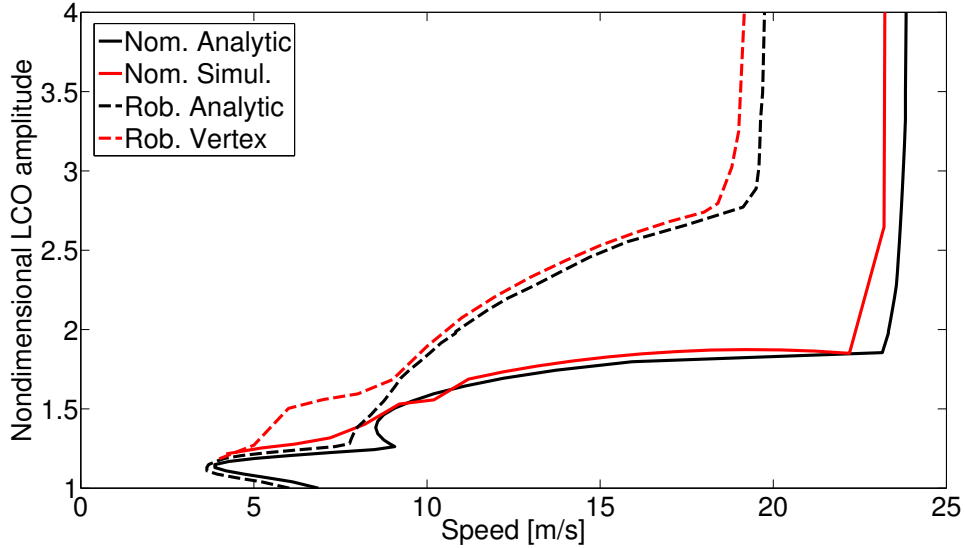


Figure 6.16: Validation via simulation of the worst-case LCO curve.

First, the nominal analyses are discussed. It is apparent a good agreement in terms of smallest LCO speed  $V_0$  and amplitudes (featuring a mismatch of less than 5%), except in a limited speed's interval (approximately  $7 \frac{m}{s} < V < 9 \frac{m}{s}$ ). The work in [52], which compared experimental and time-marching results, found that in the same range the system experiences complex behaviours such as quasiperiodicity and chaos.

As for the case with uncertainties, it is noted that all the conclusions drawn in the previous section by looking at the worst-case LCO curve (Fig. 6.10) are confirmed: little effect on  $V_0$ ; sizeable growth in amplitude for  $V > V_1$ ; drastic decrease in the asymptote speed  $V_2$ . The predictions are in good agreement also quantitatively, except for the branch in the speed range  $5.5 \frac{m}{s} < V < 9 \frac{m}{s}$ . To better interpret these results, the worst-case (i.e. featuring the maximum amplitude) time-domain responses at two different speeds are displayed in Fig. 6.17.

The plot in Fig. 6.17(a) shows the behaviour of the system at  $V = 6 \frac{m}{s}$  for different initial conditions (all the states are set to zero except  $\beta$ , whose initial value  $\beta_0$  is reported in the legend). The features apparent from the plot are nonperiodicity and sensitivity to the initial conditions, hinting at a chaotic behaviour of the system in this range, which was commented on before for the nominal case. It can be thus inferred that the adverse combination of the uncertainties are able to exacerbate these features (note that the speed range is increased when compared to the

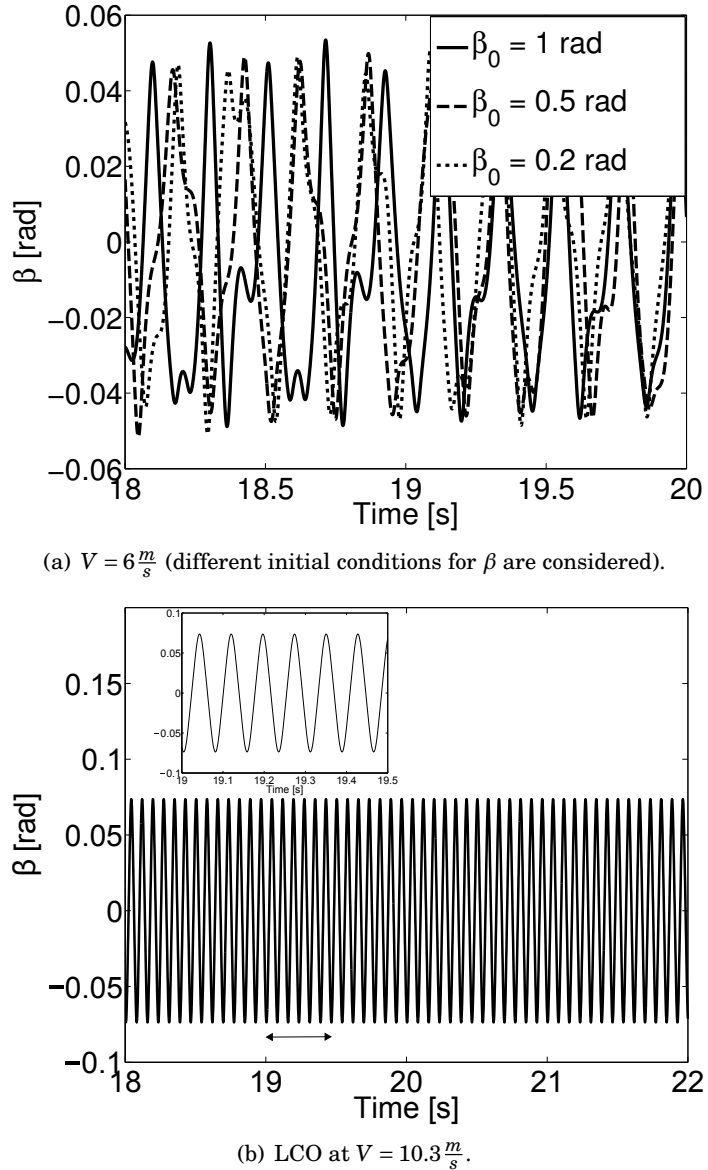


Figure 6.17: Simulated responses at two different speeds.

nominal case). The effect of uncertainties on chaotic behaviour can not clearly be captured by the approaches proposed here, because they assume periodic response of the system. In fact, the accuracy of the nonlinear simulations itself is not ascertained in these conditions when standard simulation algorithms are employed. Only refined time-marching methods [47], tailored to the simulation of piecewise linear systems, were able to reduce the discrepancies observed in [52] between experimental and numerical results. Fig. 6.17(b) shows the case at  $V = 10.3 \frac{m}{s}$ , where a limit cycle with amplitude  $\beta_s = 0.0735 \text{ rad}$  (i.e.  $\frac{\beta_s}{\delta} \approx 1.97$ ) and a period  $T = 0.077 \text{ s}$  can be clearly detected. The worst-case response at this speed was previously studied with the analytical

approaches. For example, a mismatch of less than 5% with the result in Table 6.6 (see the row with  $V_{unf}^3 = 10.3 \frac{m}{s}$ ) is registered. Moreover,  $\mu$  analysis in Fig. 6.8 captured the largest peak at a frequency of approximately  $80 \frac{rad}{s}$ , which corresponds to the LCO period detected from simulations.

The validation campaign shows that IQC can be efficiently used to guarantee global stability of the nonlinear aeroelastic system without requiring the same assumptions made by the DF- $\mu$  approach. When IQC is used to study the post-critical behaviour of the system, a criterion is needed to compute the reduced sector which allows for oscillations in the system. Here a lower bound on the sector is formulated by using the freeplay describing function  $N^F$ , thus its accuracy is inherently linked to the DF applicability. However, the core idea presented here of redefining the IQC multipliers based on some features of the system post-critical response can inspire other solutions which are not affected by this limitation.

## 6.4 Chapter summary

This Chapter proposes methodologies to study Limit Cycle Oscillations in aeroelastic systems with emphasis on the case when these are subject to uncertainties. Two approaches have been presented, the first featured by a combination of Describing Function and  $\mu$  analysis, and the second based on Integral Quadratic Constraints.

The main achievement of the first approach is the so-called worst-case LCO curve, quantifying the worst-case degradation in the response of the system (in terms of oscillation amplitude) due to the uncertainties. This is obtained by computing a robust stability margin of the quasi-linearised system with DF, and provides a guaranteed minimum distance of an operating point characterised by speed and oscillation amplitude to the LCO curve. Another point of view on the joint use of DF and  $\mu$  has led to the proposal of a tailoring strategy to inform passive design changes with the goal of reducing the LCO amplitude. Capabilities of  $\mu$  reviewed in the previous chapters (worst-case, sensitivity) are exploited to select which parameters should be perturbed, and how, in order to achieve the stated goal with the smallest departure from the nominal values.

The application of IQC to the aeroelastic problem is conducted in an incremental manner in order to achieve insights into the selection of the multipliers and their impact on the analyses. A major outcome of these investigations is a strategy allowing IQC to be used for the study of LCO. The core idea is to use relaxed integral quadratic constraints (not valid to prove global stability) that specify some properties of the post-critical response. An example is given by using an equivalent stiffness depending on the LCO amplitude as lower bound for the sector multiplier, but this interpretation can be followed to devise other solutions. In view of the importance of the LCO characterisation in the presence of uncertainties, this is believed to be a useful tool for nonlinear flutter analysis. Although IQC-based control synthesis is still an active area of research, this description of the freeplay nonlinearity could also be exploited for the design of

feedback control laws addressing active reduction of the LCO amplitudes.

A validation of the proposed frameworks, based on nonlinear time-marching simulations, was performed. This suggests that both approaches are able to cope with the nonlinear uncertain problem. Qualitative trends are well captured, and quantitative estimations are reliable except in limited cases when the hypotheses underpinning the approaches are violated.

## APPROACHES FOR THE ESTIMATION OF THE REGION OF ATTRACTION

The concept of stability of an equilibrium point  $x^*$  is fundamental in the study of dynamical systems. This property guarantees that, despite *small* departures from  $x^*$ , all the states trajectories will eventually converge to a *neighbourhood* of the equilibrium. For linear systems, stability guarantees that convergence to the equilibrium is a global asymptotic property. That is, regardless of the magnitude of the perturbation in their trajectory, the states of the system will converge to the equilibrium as time tends to infinity. On the contrary, for nonlinear systems stability guarantees might be valid only locally [137], and for this reason the notion of Region of attraction (ROA) has been proposed. The ROA of an equilibrium point  $x^*$  is the set of all the initial conditions from which the trajectories of the system converge to  $x^*$  as time goes to infinity, and its knowledge is of practical interest to guarantee the safe operation of nonlinear systems. A classic example where this aspect is relevant to aeroelastic systems is the onset of subcritical Hopf bifurcations. As discussed in Chapter 6, this determines the existence of stable Limit Cycle Oscillations at smaller speeds than the bifurcation one. Thus, there is a range of speeds for which perturbations of the trim condition (where the aircraft must be safely operated) are capable of driving the response into self-sustained oscillations. Therefore, a complete definition of flutter-free envelope in the nonlinear context should not only consider the variation with speed of stability properties, but also whether or not their validity is local and, in this case, evaluate the associated region of attraction.

The exact ROA is often difficult to compute either numerically or analytically [88], therefore algorithms have been proposed to calculate inner estimates of the ROA (recall Section 2.1.2.2 for a review of the existing methods). Prompted by the current limitations in the field, this work contributes to the state-of-the art by proposing two alternative approaches within the non-Lyapunov

class of methods. The first extends the application of a recent formulation based on invariant sets [246] to the case of uncertain systems (Section 7.2). The second allows generic nonlinearities to be studied and the nature of the uncertainties to be exploited by formulating the problem within the IQC framework (Section 7.3). The IQC-based approach was developed during a research collaboration with Prof. Pete Seiler from the University of Minnesota. Specifically, the author: formulated the ROA problem in the IQC framework and derived the theoretical guarantees for local stability (Theorem 7.3 and Theorem 7.4); devised the numerical SOS algorithms 7.7 and 7.8; performed all the analyses reported in Sec. 7.3.2.

**Publications<sup>1</sup>:** [123, 124, 127] Section 7.2; [129] Section 7.3.

## 7.1 Mathematical background

The notation used in the remainder of the section is regrouped here for the sake of clarity. The set of functions  $g : \mathbb{R}^n \rightarrow \mathbb{R}$  which are  $m$ -times continuously differentiable is denoted by  $\mathcal{C}^m$ .  $\mathbb{R}[x]$  indicates the set of all polynomials  $r : \mathbb{R}^n \rightarrow \mathbb{R}$  in  $n$  variables, and  $\partial(r)$  indicates the degree of  $r$ . Given a scalar  $c > 0$ , the level set of  $r$  is defined as  $\Omega_{r,c} = \{x \in \mathbb{R}^n : r(x) \leq c\}$  and  $\partial\Omega_{r,c} = \{x \in \mathbb{R}^n : r(x) = c\}$  denotes its boundary. A polynomial  $g$  is said to be a Sum of Squares if there exists a finite set of polynomials  $g_1, \dots, g_k$  such that  $g = \sum_{i=1}^k g_i^2$ . The set of Sum of Squares (SOS) polynomials in  $x$  will be denoted by  $\Sigma[x]$ .

### 7.1.1 Problem statement

Consider an autonomous nonlinear system of the form:

$$\dot{x} = f(x), \quad (7.1)$$

where  $f : \mathbb{R}^n \rightarrow \mathbb{R}^n$  is the vector field. The vector  $x^* \in \mathbb{R}^n$  is called a *fixed* or *equilibrium* point of (7.1) if  $f(x^*) = 0$ . Let  $\phi(t, x_0)$  denote the solution of (7.1) at time  $t$  with initial condition  $x(0) = x_0$ . The ROA associated with  $x^*$  is defined as:

$$\mathcal{R} := \left\{ x_0 \in \mathbb{R}^n : \lim_{t \rightarrow \infty} \phi(t, x_0) = x^* \right\}. \quad (7.2)$$

Thus  $\mathcal{R}$  is the set of all initial states that eventually converge to  $x^*$ . For nonlinear systems, it generally holds  $\mathcal{R} \subseteq \mathbb{R}^n$ .

Consider now the system governed by:

$$\dot{x} = f(x, \delta), \quad (7.3)$$

where  $\delta \in \Delta$  is the vector of unknown parameters,  $\Delta$  is a known bounded set, and  $f : \mathbb{R}^n \times \Delta \rightarrow \mathbb{R}^n$ . The robust Region of Attraction  $\mathcal{R}_\delta$  is defined as the intersection of the ROAs for all systems

---

<sup>1</sup>Material published during the PhD which relates to the content of this chapter.

governed by (7.3):

$$\mathcal{R}_\delta := \cap_{\delta \in \Delta} \{x_0 \in \mathbb{R}^n : \lim_{t \rightarrow \infty} \phi(t, x_0, \delta) = x^*(\delta)\}, \quad (7.4)$$

where  $\phi(t, x_0, \delta)$  denotes the solution of (7.3) at time  $t$  with initial condition  $x_0$  and subject to  $\delta$ . Note that, as explicitly reported in (7.4), the equilibrium point  $x^*$  can, in general, depend on the uncertainties. This chapter will provide certificates and develop algorithms for inner Estimates of the ROA (ERA) of nominal vector fields and Robust inner Estimates of the ROA (rERA) of uncertain vector fields.

### 7.1.2 State-of-practice in nominal ROA analysis

A standard approach to calculate ERA of  $\mathcal{R}$  consists of finding Lyapunov function level sets. The next result follows directly from Lyapunov's direct method:

**Lemma 7.1.** [137] Let  $\mathcal{D} \subset \mathbb{R}^n$  and let  $x^* \in \mathcal{D}$ . If there exists a 1-time continuously differentiable function  $V : \mathbb{R}^n \rightarrow \mathbb{R}$  such that:

$$V(x^*) = 0 \quad \text{and} \quad V(x) > 0 \quad \forall x \neq x^*, \quad (7.5a)$$

$$\nabla V(x) f(x) < 0 \quad \forall x \in \mathcal{D} \setminus x^*, \quad (7.5b)$$

$$\Omega_{V,\gamma} = \{x \in \mathbb{R}^n : V(x) \leq \gamma\} \quad \text{is bounded and} \quad \Omega_{V,\gamma} \subseteq \mathcal{D}, \quad (7.5c)$$

then  $\Omega_{V,\gamma} \in \mathcal{R}$ .

Lemma 7.1 prescribes that the function  $V$  defining the ROA fulfils *set containment constraints*. The problem of satisfying these constraints can be generically formulated as: given  $h, f_0, \dots, f_r \in \mathbb{R}[x]$ , does the following set containment holds?

$$\{x : h(x) = 0, f_1(x) \geq 0, \dots, f_r(x) \geq 0\} \subseteq \{x : f_0(x) \geq 0\}. \quad (7.6)$$

This problem is classically solved in control by applying the S-procedure [34, 259], which provides LMI constraints to ensure the validity of (7.6). This requires the polynomials in (7.6) to be quadratic, but it is possible to state a generalisation of the S-procedure to the case of polynomials with generic degree. First, note that (7.6) can be equivalently rewritten as a set emptiness condition:

$$\{x : h(x) = 0, f_1(x) \geq 0, \dots, f_r(x) \geq 0, -f_0(x) \leq 0, f_0(x) \neq 0\} = \emptyset. \quad (7.7)$$

This reformulation of the problem allows to use a result from real algebraic geometry. Namely, the Positivstellensatz (P-satz) Theorem states an equivalence between emptiness of an algebraic set and existence of polynomials with special properties and satisfying algebraic conditions [31]. An important result from [187] is that these conditions can be verified with convex tests by resorting to Sum of Squares optimisation. Starting from these premises, the lemma given next is central for the numerical recipes proposed in this chapter to compute ERA.

**Lemma 7.2.** (Generalised S-procedure) *If there exist polynomials  $p \in \mathbb{R}[x]$  and  $s_1, \dots, s_r \in \Sigma[x]$  such that:*

$$p(x)h(x) - \sum_{i=1}^r s_i(x)f_i(x) + f_0(x) \in \Sigma[x], \quad (7.8)$$

*than the set containment (7.6) holds.*

The problem of verifying the set containments in (7.5) has thus been recast as the search for an SOS decomposition of a polynomial (7.8).

The popularity of SOS optimisation in control [50, 107] is primarily motivated by their connection with convex optimisation. The idea is to express a given polynomial  $g$  with  $\partial(g)=2d$  as a quadratic form in all the monomials of degree less than or equal to  $d$ , i.e.  $g=z^\top Qz$  where  $z = [1, x_1, x_2, \dots, x_n, x_1x_2, \dots, x_n^d]$ . Since the variables in  $z$  are not algebraically independent, the matrix  $Q$ , named Gram matrix, is not unique. In fact, it can be shown that the set of matrices  $Q$  satisfying the previous relation is an affine subspace [188]. Most importantly,  $g$  belongs to the set of SOS polynomials in  $x$ , i.e.  $g \in \Sigma[x]$ , if and only if there exists  $Q = Q^\top \succeq 0$  such that  $g = z^\top Qz$ . Therefore, the search for an SOS decomposition of a polynomial amounts to determining if the intersection of the positive semidefinite matrix cone with an affine subspace is non-empty. This problem can be tackled by solving a Semidefinite Program (SDP), basically a convex optimisation problem with LMI constraints. There exist freely available software allowing to accomplish this in an efficient manner. In this work, the software SOSOPT from the suite of libraries in [15] is used in conjunction with the SDP solver Sedumi [229]. As for the computational aspects, note that if  $g$  is dense (or sparsity of the monomials is not exploited), the dimension of the Gram matrix is  $\binom{n+d}{d}$ . This means that the size of the SDP problem  $N_{SDP}$  grows polynomially with  $n$  if  $d$  is fixed (and vice versa), but it grows exponentially if both  $n$  and  $d$  increase.

Let us conclude this section with the formulation of an SOS program for the determination of Lyapunov Functions (LF) level sets. To this purpose, the conditions in (7.5) are expressed as a set containment condition of the type of (7.6).

$$\begin{aligned} V(x) &> 0 \quad \forall x \neq x^*, \\ \nabla V(x) f(x) &< 0 \quad \forall x \in \{x : V(x) \leq \gamma\}, \end{aligned} \quad (7.9)$$

where  $V$  is parameterised such that  $V(x^*) = 0$ .

The following SOS program represents then an application of the generalised S-procedure to (7.9) with the goal of computing the largest inner estimates of the ROA:

### Program 7.1.

$$\begin{aligned} \max_{s_1 \in \Sigma[x]; V \in \mathbb{R}[x]} \quad & \gamma, \\ V & \in \Sigma[x], \\ -\nabla V f - s_1(\gamma - V) & \in \Sigma[x]. \end{aligned} \quad (7.10)$$

In Program 7.1 there are bilinear terms featuring the multiplier  $s_1$ , the level set size  $\gamma$  and function  $V$ . When the objective function is one of the two terms in the bilinearity (this is the case of  $s_1\gamma$ ), it was demonstrated in [217] that the problem is quasi-convex, hence the global optimum can be computed via cost bisection. However, in general the shape  $V$  of the estimated ROA is part of the optimisation (except when verifying that a given level set is an ERA), and this makes the above program non-convex (because of the term  $s_1V$ ). This can be handled with Bilinear Matrix Inequality solvers [142] or by means of iterative schemes. A detailed study of the former approach was performed in [232], while in this research the latter strategy is considered and related aspects are investigated.

An example of iterative scheme proposed in the literature [43] to solve Program 7.1 is the so-called  $V-s$  iteration, which is presented next as it will serve as basis for new developments and comparisons in the next sections.

**Algorithm 7.1.** [43]  $V-s$  iteration

**Output:** the level sets  $\Omega_{V,\gamma}$  and  $\Omega_{p,\beta}$  (both inner estimates of the ROA).

**Input:** a polynomial  $V^0$  satisfying (7.5) for some  $\gamma$ .

1.  $\gamma$ -Step. Solve through bisection on  $\gamma$

$$\begin{aligned} & \max_{s_1 \in \Sigma[x]} \gamma, \\ & -(\nabla V^0 f + L_\epsilon) - s_1(\gamma - V_0) \in \Sigma[x], \end{aligned}$$

set  $\bar{\gamma} \leftarrow \gamma, \bar{s}_1 \leftarrow s_1$ .

2.  $\beta$ -Step. Maximise  $\beta$  such that  $\Omega_{p,\beta} \subseteq \Omega_{V,\gamma}$

$$\begin{aligned} & \max_{s_2 \in \Sigma[x]} \beta, \\ & (\bar{\gamma} - V^0) - s_2(\beta - p) \in \Sigma[x], \end{aligned}$$

set  $\bar{\beta} \leftarrow \beta, \bar{s}_2 \leftarrow s_2$ .

3.  $V$ -Step. Compute a new shape for the level set for a given  $\gamma$

$$\begin{aligned} & V - L_\epsilon \in \Sigma[x], \\ & -(\nabla V f + L_\epsilon) - \bar{s}_1(\bar{\gamma} - V) \in \Sigma[x], \\ & (\bar{\gamma} - V) - \bar{s}_2(\bar{\beta} - p) \in \Sigma[x], \end{aligned}$$

set  $V^0 \leftarrow V$  and go to  $\gamma$ -Step.

where  $L_\epsilon = \epsilon x^\top x$  with  $\epsilon$  on the order of  $10^{-6}$ . The idea of the  $V-s$  iteration is to employ a shape function  $p(x) = x^\top N x$ , where  $N \in \mathbb{S}^{n_x}$  (shape matrix) is chosen based on important directions in the state space, to enlarge the level set  $\Omega_{V,\gamma}$  throughout the iterations. In fact, the goal of the

$\beta$ -Step is to maximise the value of  $\beta$  for which  $\Omega_{p,\beta}$  is contained in  $\Omega_{V,\gamma}$ , and in the  $V$ -Step a new shape for  $\Omega_{V,\gamma}$  (with  $\gamma$  computed in the  $\gamma$ -Step) is optimised such that the new level set contains  $\Omega_{p,\beta}$ . Note that a candidate  $V$  is required to initialise the algorithm. A possible choice is any quadratic LF proving asymptotic stability of the linearised system (provided that the associated Jacobian is Hurwitz), denoted in the following as  $V_{lin}$ , or common functions (e.g. spheroid) for sufficiently small  $\gamma$ .

A final remark concerns the positive polynomial  $L_\epsilon$ . This term is adopted in other SOS-based iterative schemes [241, 243] because it provides at the end of every iteration a solution satisfying the constraints with some *margin*, increasing in this way the possibility of achieving feasibility in the subsequent iterative steps.

## 7.2 Invariant sets approach

The formulation of inner estimates of ROA as Lyapunov functions level sets is usually conservative due to the fact that contractiveness of the level set defining the ERA (that is, the condition in Eq. 7.5b) is unnecessary. In fact, LeSalle's theorem [137] points out that it suffices to consider compact positively invariant subsets of a domain  $\mathcal{D}$  where the function  $V$  satisfies the inequalities in Lemma 7.1. That is, a compact set  $\Omega \subseteq \mathcal{D}$  such that every trajectory starting in  $\Omega$  stays in there for all future times. Invariance of  $\Omega$  typically requires only conditions on its boundary to ensure that trajectories starting inside cannot leave.

Prompted by these observations, recently formalised in [246], this section proposes methods to study estimates of the Region of Attraction with invariant sets. In Sec. 7.2.1, which is dedicated to the nominal case, improved iterative schemes are presented and their performance is assessed. Sec. 7.2.2 extends the result in [246] to the case with uncertainties. It is highlighted that the hypothesis of polynomial vector field holds throughout this section.

Note also that only a subset of the numerical examples, deemed sufficient to provide an overview of the benefits of this contribution, is reported in this section to not clutter up the discussion. See [127] for a larger discussion on the results obtained with the proposed algorithms.

### 7.2.1 Computation of nominal ERAs using invariant sets

#### 7.2.1.1 Starting point

The formulation of an ERA (7.1) via invariant sets builds on the following result.

**Theorem 7.1.** ([246], Th. 1) *If there exist  $R, V_N : \mathbb{R}^n \rightarrow \mathbb{R}$ , with  $R, V_N \in \mathcal{C}^1$ , and a positive scalar  $\gamma$  satisfying:*

$$\nabla R(x)f(x) < 0 \quad \forall x \in \partial\Omega_{R,\gamma}, \quad (7.11a)$$

$$V_N(0) = 0 \quad \text{and} \quad V_N(x) > 0 \quad \forall x \in \Omega_{R,\gamma} \setminus \{0\}, \quad (7.11b)$$

$$\nabla V_N(x)f(x) < 0 \quad \forall x \in \Omega_{R,\gamma} \setminus \{0\}, \quad (7.11c)$$

$$\Omega_{R,\gamma} \text{ is compact and } 0 \in \Omega_{R,\gamma}, \quad (7.11d)$$

then  $\Omega_{R,\gamma}$  is an invariant set of  $\mathcal{R}$ .

The proof of this result can be found in [246]. The fundamental idea is that  $\Omega_{R,\gamma}$  is a positively invariant set, due to (7.11a)-(7.11d), and that all trajectories initiated from it converge to a level set of some LF, which is contractive and invariant because of (7.11b)-(7.11c), therefore guaranteeing such set to be an ERA. Note that the level set  $\Omega_{R,\gamma}$ , which is the positive invariant set generically denoted by  $\Omega$  in the previous discussion, is not contractive, because negativity of the gradient is only required on the boundary  $\partial\Omega_{R,\gamma}$ .

By means of the generalised S-procedure, the conditions in Theorem 7.1 can be certified via SOS optimisation.

**Lemma 7.3.** ([246] Let  $V_N$  and  $R$  be multivariable polynomials and  $\gamma$  a positive scalar. If there exist SOS polynomials  $s_1, s_2$  and a polynomial  $s_0$  such that:

$$-\nabla R f - s_0(\gamma - R) \in \Sigma[x], \quad (7.12a)$$

$$V_N - s_1(\gamma - R) \in \Sigma[x], \quad (7.12b)$$

$$-\nabla V_N f - s_2(\gamma - R) \in \Sigma[x], \quad (7.12c)$$

then the inequalities (7.11) are satisfied and  $\Omega_{R,\gamma}$  is an inner estimate of the ROA of the origin.

The following program can be employed to enlarge the provable ERA based on Lemma 7.3.

#### Program 7.2.

$$\max_{s_1, s_2 \in \Sigma[x]; s_0, V_N, R \in \mathbb{R}[x]} \gamma, \quad (7.13)$$

subject to conditions (7.12a-7.12b-7.12c).

It is observed that  $V_N$  and  $R$  are part of the optimisation, thus the same issue commented on in Sec. 7.1.2 concerning the presence of bilinearity arises. In [246] the following two-step (Invariant sets, IS) algorithm is proposed.

**Algorithm 7.2.** [246] IS - 2 Steps

**Output:** the level set  $\Omega_{R,\gamma}$  (inner estimate of the ROA).

**Input:** a polynomial  $R^0$  satisfying (7.12a) for some  $\gamma$ .

1. Step A1-1. Optimise  $V_N$  and multipliers through bisection on  $\gamma$

$$\begin{aligned} & \max_{s_1, s_2 \in \Sigma[x]; s_0, V_N \in \mathbb{R}[x]} \gamma, \\ & -\nabla R^0 f - s_0(\gamma - R^0) \in \Sigma[x], \\ & V_N - s_1(\gamma - R^0) \in \Sigma[x], \\ & -\nabla V_N f - s_2(\gamma - R^0) \in \Sigma[x], \end{aligned}$$

set  $\bar{\gamma} \leftarrow \gamma$ ,  $\bar{s}_\# \leftarrow s_\#$  ( $\# = 0, 1, 2$ ).

2. Step A1-2. Optimise  $V_N$  and  $R$  through bisection on  $\gamma$

$$\begin{aligned} & \max_{s_3 \in \Sigma[x]; V_N, R \in \mathbb{R}[x]} \gamma, \\ & -\nabla R f - \bar{s}_0(\gamma - R) \in \Sigma[x], \\ & V_N - \bar{s}_1(\gamma - R) \in \Sigma[x], \\ & -\nabla V_N f - \bar{s}_2(\gamma - R) \in \Sigma[x], \\ & (\gamma - R) - s_3(\gamma - R^0) \in \Sigma[x], \\ & \gamma - \bar{\gamma} \geq 0 \end{aligned}$$

set  $R^0 \leftarrow R$  and go to Step A1-1.

This iterative scheme consists of two steps. In Step 1 the multipliers  $s_\#$  and  $V_N$  are optimised, whereas Step 2 computes again  $V_N$  and the level set function  $R$ , which is updated ( $R^0 \leftarrow R$ ) before a new iteration is begun. The iterations terminate when one of the steps fails, i.e. the associated optimisation is found unfeasible, and the last optimised values for  $R$  and  $\gamma$  provide the output  $\Omega_{R,\gamma}$ . The last two constraints in Step 2 ensure that  $\Omega_{R^0, \bar{\gamma}} \subseteq \Omega_{R,\gamma}$ , i.e. the solution is a set that strictly contains the previous one. A candidate  $R$  is required to initialise the algorithm, and a possible choice is  $V_{lin}$ , i.e. the quadratic LF associated with the linearised system.

### 7.2.1.2 Improved algorithms

Alternative schemes to Algorithm 7.2 are proposed here to solve Program 7.2. The aim is on the one hand to improve the run time, and on the other to overcome numerical issues typically arising when employing SOS and commented throughout the section.

First, a modification of Algorithm 7.2 is discussed. The last two constraints in Step A1-2 (motivated before) make Step A1-2, in addition to Step A1-1, quasi-convex. To make it convex, the last two SOS constraints in Step A1-2 are replaced by:

$$(\gamma - R) - s_3(\bar{\gamma} - R^0) \in \Sigma[x]. \quad (7.14)$$

By direct application of Lemma 7.2, this constraint enforces  $\Omega_{R^0, \bar{\gamma}} \subseteq \Omega_{R, \gamma}$ . Thus, the estimated ROA increases at each step, but this is achieved now without introducing bilinearities. In the tested cases this modification led to a reduction in simulation and better accuracy in the results. Therefore, this is implemented in all the analyses shown here (i.e. Algorithm 7.2 represents already an improvement compared to the baseline proposed in [246]).

In addition to this, a new iteration strategy is devised which consists of splitting Step A1-1 into two steps, Step A2-1 and Step A2-2. The idea is to distribute the computational effort in order to ease the SDP calculations underpinning each step and in turn to enhance accuracy and efficiency of the estimations of the level set  $\Omega_{R, \gamma}$ . This is achieved with the three-step iteration scheme reported in the following.

**Algorithm 7.3. IS - 3 Steps**

**Output:** the level set  $\Omega_{R, \gamma}$  (inner estimate of the ROA).

**Input:** polynomials  $R^0, V_N^0$  satisfying (7.12) for some  $\gamma$ .

1. Step A2-1. Optimise the multipliers for fixed level sets shapes

$$\begin{aligned} & \max_{s_1, s_2 \in \Sigma[x]; s_0 \in \mathbb{R}[x]} \gamma, \\ & -\nabla R^0 f - s_0(\gamma - R^0) \in \Sigma[x], \\ & V_N^0 - s_1(\gamma - R^0) \in \Sigma[x], \\ & -\nabla V_N^0 f - s_2(\gamma - R^0) \in \Sigma[x], \end{aligned}$$

set  $\bar{\gamma} \leftarrow \gamma, \bar{s}_\# \leftarrow s_\# (\# = 0, 1, 2)$ .

2. Step A2-2. Optimise  $V_N$

$$\begin{aligned} & \max_{V_N \in \mathbb{R}[x]} \gamma, \\ & -\nabla R^0 f - \bar{s}_0(\gamma - R^0) \in \Sigma[x], \\ & V_N - \bar{s}_1(\gamma - R^0) \in \Sigma[x], \\ & -\nabla V_N f - \bar{s}_2(\gamma - R^0) \in \Sigma[x], \\ & \gamma \geq \bar{\gamma}, \end{aligned}$$

set  $\bar{V}_N \leftarrow V_N, \bar{\gamma} \leftarrow \gamma$ .

3. Step A2-3. Optimise  $R$

$$\begin{aligned} & \max_{s_3 \in \Sigma[x]; R \in \mathbb{R}[x]} \gamma, \\ & -\nabla R f - \bar{s}_0(\gamma - R) \in \Sigma[x], \\ & \bar{V}_N - \bar{s}_1(\gamma - R) \in \Sigma[x], \\ & -\nabla \bar{V}_N f - \bar{s}_2(\gamma - R) \in \Sigma[x], \\ & (\gamma - R) - s_3(\bar{\gamma} - R^0) \in \Sigma[x], \end{aligned}$$

set  $R^0 \leftarrow R, V_N^0 \leftarrow \bar{V}_N$  and go to Step A2-1.

The scheme consists of one quasi-convex step (Step A2-1) and two convex steps (Step A2-2 and Step A2-3). Each step has a specific task: Step A2-1 provides the multipliers for the next two steps; Step A2-2 calculates the function  $V_N$ ; and Step A2-3 (embedding the constraint proposed in Eq. 7.14) evaluates the sought level set  $\Omega_{R,\gamma}$  based on the iterates from the previous steps. The size  $\gamma$  of the ERA is maximised throughout each iteration, although Step A2-2 and Step A2-3 can also be solved as simple feasibility problems. In this regard, note that the optimality of the solution is already prevented by the non-convexity of (7.13), and that the algorithm ensures in any case that the ERA is non-decreasing. Therefore, resorting to just feasibility when maximisation fails is a viable solution.

Algorithm 7.3 requires initialisations for  $R$  and  $V_N$ . A first option is to choose for both  $V_{lin}$ , which automatically satisfies (7.12) for sufficiently small  $\gamma$ . Alternatively, the calculation can start with Algorithm 7.2 which in turn provides the initialisations  $R^0$  and  $V_N^0$  to Algorithm 7.3. It is stressed the importance of the fact that Algorithm 7.3 is initialised with both the functions  $R$  and  $V_N$ . This feature can be favourably used when preliminary estimations of the *shape* of the ERA are available in that the search can be seeded with them. In fact, while in Algorithm 7.2 this information would be partially lost because the function  $V_N$  is optimised anew with the multipliers in Step A1-1, Algorithm 7.3 optimises first the multipliers based on the provided estimations of  $R$  and  $V_N$ , and then adjusts  $V_N$  and  $R$  correspondingly in the next two steps. Even though the problem remains non-convex (and thus it cannot be guaranteed that the global optimum is found), the formulation of this iterative scheme privileges *local* searches, therefore can represent an important complement to Algorithm 7.2. This observation represents the premise for the hybrid algorithm described next.

The issues typically arising when computing ERA with SOS-based techniques are twofold: the SDP associated with each iteration can be computationally challenging, both in terms of run time and accuracy; the non-convexity due to the bilinear terms forces coordinate-wise search algorithms to be adopted, inevitably leading to local optima. While Algorithm 7.3 attempts to ameliorate the former behaviour, this is nonetheless affected by the same local optima pitfall. The issue of local optima is well known in the optimisation field and one of the proposed solutions is represented by so-called hybrid strategies [172]. In essence, global optimisers are crossed with problem-specific local search algorithms. In the currently investigated programs, the non-convexity is inherent to the adoption of SOS relaxations for the enforcement of set containments. Thus, hybrid schemes meant in the conventional sense do not look viable. However, the availability of the two distinct Algorithms 7.2 and 7.3 featuring the aforementioned properties is exploited to devise the following algorithm attempting to make the search of ERA more robust to numerical issues.

**Algorithm 7.4.** *IS - Hyb*

**Output:** the level set  $\Omega_{R,\gamma}$  (inner estimate of the ROA).

**Input:** a switching criterion  $sw_{cr}$ ; polynomials  $R^0, V_N^0$  satisfying (7.12) for some  $\gamma$ .

1. Stage 1. Execute Algorithm 7.2.

```
if Stage 1 converged then set  $R^0 \leftarrow R$  and  $V_N^0 \leftarrow V_N$ ,  
    if  $sw_{cr}$  is true then go to Stage 2,  
    else restart Stage 1,  
else go to Stage 2,
```

2. Stage 2. Execute Algorithm 7.3.

```
if Stage 2 converged then set  $R^0 \leftarrow R$  and  $V_N^0 \leftarrow V_N$ ,  
    if  $sw_{cr}$  is true then go to Stage 1,  
    else restart Stage 2,  
else set go to Stage 1,
```

The iterative scheme builds on the advantageous capability of switching from one algorithm to the other in case of failed solution or slow progress. The switching criterion  $sw_{cr}$  can be formulated based on the idea of associating with each stage a *reward* [171], that is, a figure of merit of the executed algorithm. If slow progress in the computation is considered as performance, the size of the level set  $\gamma$  can be employed. A possible metric to quantify the expansion rate of the ERA for a given algorithm is obtained comparing values of  $\gamma$  referred to the *same* shape function  $R$ . The cost bisections in the first steps of both the algorithms (Step A1-1 and Step A2-1) are performed keeping fixed  $R$  at the value of the previous iteration. Thus,  $sw_{cr}$  can be defined as a tolerance on the ratio between  $\gamma$  computed at the end of the first step and at the end of the previous iteration. Note that when Algorithm 7.3 is employed, another choice for  $sw_{cr}$  is the ratio between  $\gamma$  computed at Step A2-2 and Step A2-1, because the shape  $R$  is held *fixed* over the two steps. The number of failures in convergence experienced by the used algorithm can also be used to define the reward, because it reveals the suitability of adopting a certain search strategy for the considered problem.

The adoption of a switching criterion can reduce the run time by pointing at *faster* search directions, and can help taking advantage of the different features of the two algorithms. However, it should not be underestimated the utility of a scheme whose goal is simply to carry on the optimisation in case of failed solution of one algorithm. It is indeed often the case that infeasibility of one of the steps is not caused by the fact that the ERA is close to the actual ROA (and thus no further optimisation is possible), but by numerical issues of the SDP (exacerbated when the size of the program increases). This aspect motivates the choice made in this work of testing

Algorithm 7.4 with  $sw_{cr}$  defined such that the algorithm crosses the stages sequentially (i.e. the inner **if** condition is always true). The selection of  $sw_{cr}$  is deemed a problem-specific feature, and the study of alternative solutions is on itself an interesting research study that can be undertaken in future works focused on the study of ROA with hybrid approaches.

### 7.2.1.3 Numerical example

The invariant sets algorithms are applied here to a closed-loop nonlinear short-period (SP) model of an aircraft longitudinal dynamics [241]. It features 3 open-loop states (pitch rate  $z_1$ , angle of attack  $z_2$ , pitch angle  $z_3$ ) and 2 controller states  $\eta_1, \eta_2$ .

$$\begin{aligned} \dot{z} &= \begin{bmatrix} -3 & -1.35 & -0.56 \\ -0.91 & -0.64 & -0.02 \\ 1 & 0 & 0 \end{bmatrix} z + \begin{bmatrix} 1.35 - 0.04z_2 \\ 0.4 \\ 1 \end{bmatrix} u + \begin{bmatrix} 0.08z_1z_2 + 0.44z_2^2 + 0.01z_2z_3 + 0.22z_2^3 \\ -0.05z_2^2 + 0.11z_2z_3 - 0.05z_3^2 \\ 0 \end{bmatrix}, \\ y &= [z_1 \ z_3]^\top, \quad u = \eta_1 + 2.2\eta_2, \\ \dot{\eta} &= \begin{bmatrix} -0.6 & 0.09 \\ 0 & 0 \end{bmatrix} \eta + \begin{bmatrix} -0.06 & -0.02 \\ -0.75 & -0.28 \end{bmatrix} y. \end{aligned} \tag{7.15}$$

By defining  $x = [z; \eta]$ , the system is recast in the formalism of (7.1).

Fig. 7.1 shows different inner estimates of the ROA. *IS* and *LF* stand for invariant sets and Lyapunov functions level set approach, respectively. For the IS approach, Algorithms 7.2 (*IS - 2 Steps*), 7.3 (*IS - 3 Steps*) and 7.4 (*IS - Hyb*) are tested. The degree of the optimised polynomials ( $V, V_N, R$ ) is 4 in all cases. Since the system has more than 2 states, projections of the ERA onto particular planes have to be considered. In general, the analyst will focus on the states which are supposed to experience larger perturbations during the operation of the system.

The results confirm that the invariant set approach lead to a larger (i.e. less conservative) estimation of the ROA than the LF level set one, whose predictions obtained with an in-house implementation of the  $V - s$  algorithm (with the shape function  $p$  taken as the spheroid) are in good agreement with the results presented in [241]. The plot also allows to appreciate the effect of the adopted iteration scheme. Although no conclusive remarks can be stated, some trends, confirmed when changing the parameterisation of the multipliers and level set functions degrees, were observed. For example, the algorithms are sensitive to the initialisation, especially Algorithm 7.3 which requires a guess for both  $V_N$  and  $R$ . When initialised with the first iterate from Algorithm 7.2 (as it is the case in Fig. 7.1), the use of Algorithm 7.3 improves the accuracy of the ROA estimation and outperforms the results obtained with the invariant set baseline algorithm. When the two algorithms are used in conjunction, i.e. the hybrid algorithm is employed, the estimated ERA is usually larger.

Table 7.3 summarises the computational statistics of the employed algorithms. Recall that each algorithm is iterative and each iteration features two or three steps. Therefore, for each algorithm only the number of decision variables  $N_{var}$  and the size of the Gram matrix  $N_{SDP}$  for

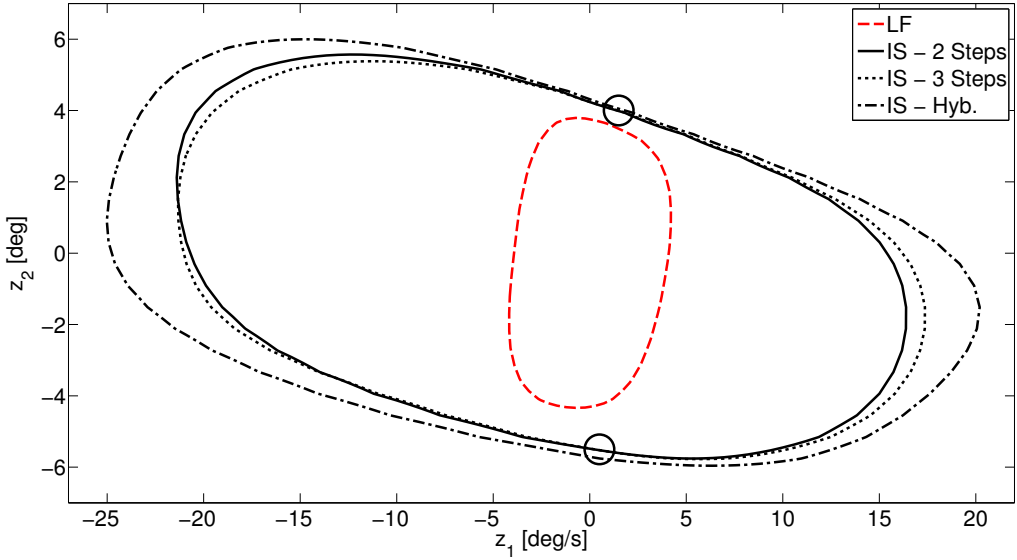


Figure 7.1: Comparison of the ERA of the short-period model with different algorithms.

the most demanding step are reported. In addition, the averaged processing time per iteration  $T_{iter}$  as well as the overall time  $T_{tot}$  required to determine the ERA are given.

Table 7.1: Computational statistics for the invariant sets ROA analyses.

Algorithm	$N_{var}$	$N_{SDP}$	$T_{iter}$ [s]	$T_{tot}$ [s]
LF (7.1)	120	3866	14	840
IS - 2 Steps (7.2)	246	12322	78	1872
IS - 3 Steps (7.3)	126	12322	70	1260
IS - Hyb (7.4)	246	12322	72	2742

Algorithm 7.3 has clearly a smaller  $T_{iter}$  than Algorithm 7.2. Even though the former consists of 3 steps (as opposed to Algorithm 7.2 which has only 2), this performance is a result of the redistribution of the computational effort driving the proposal of Algorithm 7.3 (and also benefiting Algorithm 7.4). Algorithm 7.3 also features the smallest  $T_{tot}$ . The high value observed for Algorithm 7.4 can be motivated observing that the associated ERA is markedly larger than the others and thus more iterations will be involved in its computation. This is an important aspect to keep in mind when using the metric  $T_{tot}$  to compare different algorithms.

Since the algorithms only provide a guaranteed region of stability (i.e. inner estimates, or lower bound, of the actual ROA) it is important to quantify the conservatism of the results. A useful aspect in this regard is that the availability of different ERA can enhance insight into the actual boundaries of the ROA. For example, from a closer inspection of Fig. 7.1, a dense presence of curves in some regions, marked with circles in the plot, can be identified. It can be speculated that these correspond to boundaries of the actual region of attraction of the system

on the basis of an approximate overlap of the estimations given by different algorithms. These observations can be of great help to inform extensive refined time-marching simulations as well as provide initialisations for further analyses (recall the importance of the initial guess and the possibility to exploit it in Algorithm 7.3 due to the required initialisation of two functions). In order to verify these inferences and quantify an upper bound on the size of the estimates, the following algorithm is proposed.

**Algorithm 7.5.** *Computation of upper bounds on the size of the estimated ROA*

**Output:** the value of  $\gamma_f$  such that  $\Omega_{R,\gamma_f} \not\subset \mathcal{R}$ ; a set of initial conditions which do not belong to  $\mathcal{R}$ .

**Input:**  $\partial\Omega_{R,\gamma}$ , integer  $N_s$ , and a small scalar  $\epsilon_\gamma$ .

1. Simulate the nonlinear system using as initial conditions  $N_s$  random points  $X_0$  on the boundary  $\partial\Omega_{R,\gamma}$  (time-marching campaign).
2. Define  $\mathcal{F} := \{X_0 \in \mathbb{R}^n : \lim_{t \rightarrow \infty} \phi(t, X_0) \neq x^*\}$ .
3. If  $\mathcal{F} = \emptyset$ , update the size  $\gamma = (1 + \epsilon_\gamma)\gamma$  and repeat from 1. Otherwise,  $\gamma_f = \gamma$  and  $\mathcal{F}$  gathers a set of initial conditions which do not belong to  $\mathcal{R}$ .

Algorithm 7.5 is applied to the level set  $\Omega_{R,\gamma}$  obtained with the hybrid iteration scheme, which gave  $\gamma=14.7$ . The algorithm, applied using  $N_s = 300$  and  $\epsilon_\gamma = 0.03$ , returns  $\gamma_f=15.6$ , i.e. there is a 6% gap between the lower bound  $\gamma$  obtained by the hybrid scheme and the upper bound  $\gamma_f$  from Algorithm 7.5. However, it is important to stress that Algorithm 7.5 gives an upper bound on the size of the ERA for a fixed shape  $R$ . This means that, even when  $\gamma$  and  $\gamma_f$  are close, the ERA might still not capture accurately the actual shape of the region of attraction. A heuristic method to assess this consists of checking the set  $\mathcal{F}$  returned by Algorithm 7.5. The more distributed around  $\partial\Omega_{R,\gamma}$  are the points in  $\mathcal{F}$ , the closer to the actual ROA the shape of the level set is.

Fig. 7.2 shows the results obtained applying this methodology to the SP case. Projections in two phase planes,  $z_1 - z_2$  (Fig. 7.2(a)) and  $z_2 - \eta_2$  (Fig. 7.2(b)), are considered. In each plot, the ERA is shown as well as cross markers corresponding to initial conditions whose trajectories do not converge to the equilibrium. Note that the markers are not confined in one area of the plane, but are distributed around distinct regions of the ERA. Specifically, the points certified to be outside of the ROA in Fig. 7.2(a) lie in the same regions highlighted in Fig. 7.1 by circle markers and discussed therein. This hints at the fact that the estimations capture also the actual shape of the ROA, and not only its size as inferred from the upper bound  $\gamma_f$ . By increasing the degree of  $V_N$  and  $R$ , an improvement of the ERA was observed along the directions where violations were not detected. Or, put it differently, where the curves in Fig. 7.1 were scattered.

Further results of the nominal invariant sets algorithms (obtained with this and another benchmark study from the literature) are discussed in [127].

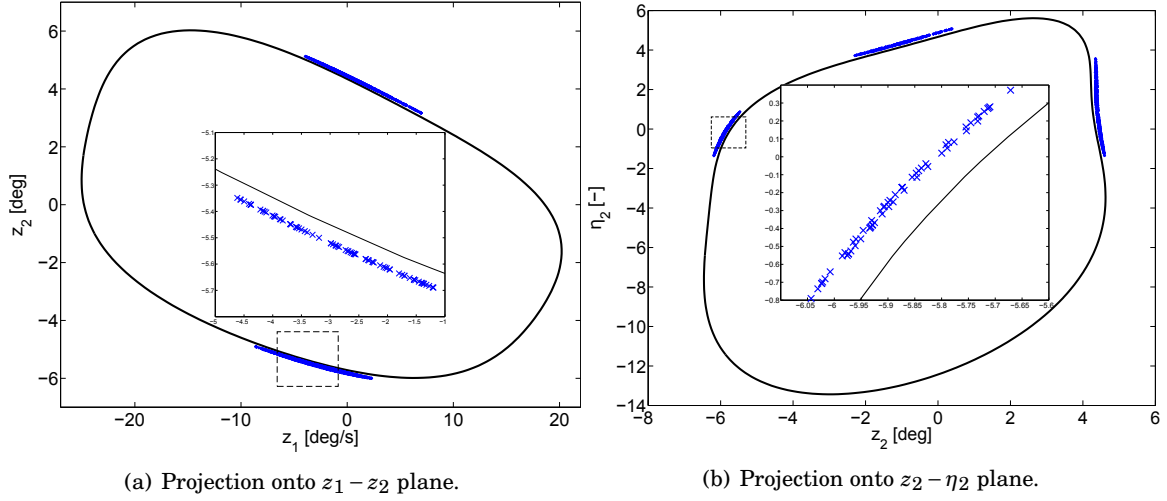


Figure 7.2: Upper bounds of the ERA.

### 7.2.2 Robust ROA with invariant sets

The case when the vector field is subject to parametric uncertainties is considered here. A first important aspect is that, as explicitly reported in the definition of  $\mathcal{R}_\delta$  (7.4), the equilibrium point  $x^*$  depend, in general, on the uncertainties. It is largely established in the literature [6, 49, 241] the assumption that  $f(0, \delta) = 0 \forall \delta \in \Delta$ , i.e. the equilibrium point (assumed without loss of generality to coincide with the origin) does not depend on the uncertainties. For the case of parametric uncertainties, i.e.  $\delta \in \Delta \subset \mathbb{R}^{n_\delta}$ , approaches are available to relax this assumption. In [12] an algorithm based on contraction metrics was proposed in the context of global stability and could be extended for local analysis purposes. An alternative approach, based on the idea of guaranteeing local stability without knowledge of the associated equilibrium, has been developed in this research (and published in [128]) and is detailed in Appendix B. In order to focus here on the new contribution to the invariant set framework, the aforementioned simplifying hypothesis is made and thus  $x^* = 0 \forall \delta \in \Delta$ . This is not a limitation because the approach described in Appendix B can be used to account for dependence of  $x^*$  on  $\Delta$ .

### 7.2.2.1 Local stability certificates with algebraic sets

The starting point to find robust inner estimate of the ROA, or rERA, with the invariant sets approach is represented by the following result.

**Theorem 7.2.** ([246], Th. 4) *Given  $R : \mathbb{R}^n \rightarrow \mathbb{R}$ ,  $V_N : \mathbb{R}^n \times \Delta \rightarrow \mathbb{R}$ ,  $R, V_N \in \mathcal{C}^1$  and a positive scalar  $\gamma$  satisfying:*

$$\nabla R(x)f(x, \delta) < 0 \quad \forall (x, \delta) \in \partial\Omega_{R, \gamma} \times \Delta, \quad (7.16a)$$

$$V_N(0, \cdot) = 0 \quad \text{and} \quad V_N(x, \delta) > 0 \quad \forall (x, \delta) \in \Omega_{R, \gamma} \setminus 0 \times \Delta, \quad (7.16b)$$

$$\nabla V_N(x, \delta)f(x) < 0 \quad \forall (x, \delta) \in \Omega_{R, \gamma} \setminus 0 \times \Delta, \quad (7.16c)$$

$$\Omega_{R, \gamma} \text{ is compact and } 0 \in \Omega_{R, \gamma}, \quad (7.16d)$$

then  $\Omega_{R, \gamma}$  is an invariant set of  $\mathcal{R}_\delta$ .

The proof is very similar to that for Theorem 7.1 (see the reference for details).

It is proposed here to describe  $\Delta$  as a semialgebraic set [6]:

$$\Delta = \{\delta \in \mathbb{R}^{n_\delta} : m_i(\delta) \geq 0, m_i \in \mathbb{R}[\delta], i = 1, \dots, n_\delta\}. \quad (7.17)$$

This strategy is quite general and allows both time-invariant and time-varying parametric uncertainties to be taken into account, as well as norm bounded operators. Moreover, no hypotheses on how the uncertainties enter the vector field are made. This is different from previous strategies, where, for example with reference to LF-based approaches,  $f$  is required to depend affinely on the uncertain parameters [241], or  $\Delta$  must be within a polytope [243]. A useful result is recalled next.

**Lemma 7.4.** [232] *For each  $y$  satisfying  $g_3(y) \leq 0$ ,*

$$\begin{aligned} \{x \mid g_1(x, y) \leq 0\} &\subseteq \{x \mid g_2(x, y) \leq 0\}, \\ \text{iff} \quad \{(x, y) \mid g_1(x, y) \leq 0, g_3(y) \leq 0\} &\subseteq \{(x, y) \mid g_2(x, y) \leq 0\}. \end{aligned} \quad (7.18)$$

The advantage of this result is that the last set-containment can be easily enforced with Lemma 7.2. Based on these preliminaries, the following Lemma allowing to study robust ERA within the framework of invariant sets is stated.

**Lemma 7.5.** *Given  $R \in \mathbb{R}[x]$ ,  $V_N \in \mathbb{R}[x, \delta]$  with  $V_N(0, \cdot) = 0$ , and a positive scalar  $\gamma$ , if there exist  $s_1, s_2, s_{0i}, s_{1i}, s_{2i} \in \Sigma[x, \delta]$  and  $s_0 \in \mathbb{R}[x, \delta]$  such that:*

$$-\nabla R f - s_0(\gamma - R) - \Gamma_{0j} \in \Sigma[x, \delta], \quad (7.19a)$$

$$V_N - s_1(\gamma - R) - \Gamma_{1j} \in \Sigma[x, \delta], \quad (7.19b)$$

$$-\nabla V_N f - s_2(\gamma - R) - \Gamma_{2j} \in \Sigma[x, \delta], \quad (7.19c)$$

$$\text{with } \Gamma_{\#j} = s_{\#1}m_1 + \dots + s_{\#i}m_i + \dots + s_{\#n_\delta}m_{n_\delta}, \quad \# = 0, 1, 2 \quad (7.19d)$$

then the conditions of Theorem 7.2 are satisfied and  $\Omega_{R, \gamma} \subseteq \mathcal{R}_\delta$ .

**Proof.** The proof of (7.19a)⇒(7.16a) is given here. By virtue of the uncertainty description in (7.17), condition (7.16a) can be stated as:

$$\begin{aligned} & \text{For each } \delta \text{ satisfying } m_i(\delta) \geq 0, (i = 1, \dots, n_\delta), \\ & \{x : \gamma - R(x) = 0\} \subseteq \{x : -\nabla R f(x, \delta) \geq 0\}. \end{aligned} \quad (7.20)$$

For Lemma 7.4, this holds if and only if

$$\{(x, \delta) : \gamma - R(x) = 0, m_i(\delta) \geq 0, i = 1, \dots, n_\delta\} \subseteq \{(x, \delta) : -\nabla R f(x, \delta) \geq 0\}. \quad (7.21)$$

This set containment constraint is in the form of (7.6). Indeed, it is enough to take  $h = \gamma - R(x)$ ,  $f_i = m_i$  and  $f_0 = -\nabla R f(x, \delta)$ . By applying the generalised S-procedure (Lemma 7.2) it is obtained the SOS constraint (7.19a), which hence provides a sufficient condition for (7.16a) to hold. A similar rationale applies to the other constraints in the Lemma. ■

Lemma 7.5 and provides a novel recipe for the determination of robustly invariant sets. The corresponding program to enlarge the provable rERA is:

### Program 7.3.

$$\begin{aligned} & \max_{s_1, s_2, s_{0i}, s_{1i}, s_{2i} \in \Sigma[x, \delta]; s_0, V_N \in \mathbb{R}[x, \delta]; R \in \mathbb{R}[x]} \gamma, \\ & \text{subject to conditions (7.19a-7.19b-7.19c).} \end{aligned} \quad (7.22)$$

Program 7.3 leads again to bilinearities and, to tackle this, adaptations of Algorithms 7.2, 7.3, and 7.4 can be employed. As an example, the extension of Algorithm 7.3 is reported next (the letter  $R$  in the name of the algorithm and of the steps stresses the fact that the algorithm allows the computation of robust ERA).

### Algorithm 7.6. $IS_R$ - 3 Steps

**Output:** the level set  $\Omega_{R, \gamma}$  (parameter-independent rERA).

**Input:** polynomials  $R^0, V_N^0$  satisfying (7.19) for some  $\gamma$ .

#### 1. Step A2R-1. Optimise the multipliers for fixed level sets shapes.

$$\begin{aligned} & \max_{s_1, s_2, s_{0i}, s_{1i}, s_{2i} \in \Sigma[x, \delta]; s_0 \in \mathbb{R}[x, \delta]} \gamma, \\ & -\nabla R^0 f - s_0(\gamma - R^0) - \Gamma_{0j} \in \Sigma[x, \delta], \\ & V_N^0 - s_1(\gamma - R^0) - \Gamma_{1j} \in \Sigma[x, \delta], \\ & -\nabla V_N^0 f - s_2(\gamma - R^0) - \Gamma_{2j} \in \Sigma[x, \delta], \end{aligned}$$

set  $\bar{s}_{\#i} \leftarrow s_{\#i}$  ( $\# = 0, 1, 2$ ,  $i = 1, \dots, n_\delta$ ).

2. Step A2R-2. Optimise  $V_N$ .

$$\begin{aligned} & \max_{V_N \in \mathbb{R}[x, \delta]} \gamma, \\ & -\nabla R^0 f - \bar{s}_0(\gamma - R^0) - \bar{\Gamma}_{0j} \in \Sigma[x, \delta], \\ & V_N - \bar{s}_1(\gamma - R^0) - \bar{\Gamma}_{1j} \in \Sigma[x, \delta], \\ & -\nabla V_N f - \bar{s}_2(\gamma - R^0) - \bar{\Gamma}_{2j} \in \Sigma[x, \delta], \end{aligned}$$

set  $\bar{V}_N \leftarrow V_N, \bar{\gamma} \leftarrow \gamma$ .

 3. Step A2R-3. Optimise  $R$ .

$$\begin{aligned} & \max_{s_3 \in \Sigma[x, \delta]; R \in \mathbb{R}[x]} \gamma, \\ & -\nabla R f - \bar{s}_0(\gamma - R) - \bar{\Gamma}_{0j} \in \Sigma[x, \delta], \\ & \bar{V}_N - \bar{s}_1(\gamma - R) - \bar{\Gamma}_{1j} \in \Sigma[x, \delta], \\ & -\nabla \bar{V}_N f - \bar{s}_2(\gamma - R) - \bar{\Gamma}_{2j} \in \Sigma[x, \delta], \\ & (\gamma - R) - s_3(\gamma - R^0) \in \Sigma[x, \delta], \end{aligned}$$

set  $R^0 \leftarrow R, V_N^0 \leftarrow \bar{V}_N$  and go to Step A2R-1.

$\Gamma_{\#j}$  is defined in Eq. (7.19d) and  $\bar{\Gamma}_{\#j} = \bar{s}_{\#1}m_1 + \dots + \bar{s}_{\#i}m_i + \dots + \bar{s}_{\#n_\delta}m_{n_\delta}$ . In addition to the options discussed previously for the nominal case, the initialisation of  $R$  and  $V_N$  can be done with the corresponding functions obtained with (nominal) ERA calculation. The independent variables of the optimisation now include the states of the system  $x$  and the uncertain parameters  $\delta$ . The polynomial multipliers  $s$  can thus potentially be function of both  $x$  and  $\delta$  (as reported in Algorithm 7.6), but in practice there is a trade-off between computational time and accuracy. One of the advantages of this formulation is that the level set function is  $R(x)$  (i.e. uncertain parameter-independent), whilst  $V_N(x, \delta)$  is parameter dependent. On the one hand, this is a less conservative approach than the one represented by parameter-independent level sets because  $V_N$  is allowed to be a function of  $\delta$ . On the other, the fact that the level set  $\Omega_{R, \gamma}$  is parameter-independent avoids the computation of the intersection of the parameterised estimates, resulting in a more accurate and easier to visualise outcome. Moreover,  $R$  is always multiplied by the SOS multipliers  $s_{\#}$  whereas  $V_N$  not, thus it is more computationally efficient to reduce the number of terms in the former polynomial. This favourable twofold behaviour is the result of using two distinct functions,  $R$  and  $V_N$ , which allows for greater flexibility in the optimisation.

The description of the set in (7.17) entails the definition of the polynomials  $m_i$ , which depend on the type of uncertainties featuring the system. This section focuses on parametric uncertainties, and thus possible definitions will be discussed for this case. Let us denote with  $\underline{\delta}_i$  and  $\bar{\delta}_i$  the minimum and maximum allowed values for each uncertain parameter  $\delta_i$ , respectively. Then, at

each parameter a polynomial  $m_i$  can be associated as follows:

$$\begin{aligned} m_i(\delta_i) &= -(\delta_i - \underline{\delta}_i)(\delta_i - \bar{\delta}_i), \\ \delta \in \Delta \iff m_i(\delta_i) &\geq 0, \\ \text{where } \delta &= [\delta_1; \dots; \delta_i; \dots; \delta_{n_\delta}]^\top. \end{aligned} \quad (7.23)$$

Recalling the definition of  $\Gamma_{\#j}$  in (7.19d), it is worth noting that for each employed  $m_i$  there are three multipliers  $s_{0i}, s_{1i}, s_{2i}$  (one for each constraint). Therefore, as the number of uncertain parameters increases, so does the size of the associated optimisation problem. An alternative solution is to define a single polynomial  $m_c$ :

$$\begin{aligned} m_c(\delta) &= -\sum_{i=1}^{n_\delta} (\delta_i - \underline{\delta}_i)(\delta_i - \bar{\delta}_i) = \sum_{i=1}^{n_\delta} m_i(\delta_i), \\ \delta \in \Delta \implies m_c(\delta) &\geq 0, \end{aligned} \quad (7.24)$$

which specialises  $\Gamma_{\#j}$  (7.19d) to  $\Gamma_{\#1} = s_{\#c} m_c$ . This definition gives only a sufficient condition (as opposed to the one in (7.23) which is also necessary), because there are values of  $\delta \notin \Delta$  for which the inequality  $m_c(\delta) \geq 0$  is satisfied. Therefore, the obtained rERA is valid for a larger range of uncertainties. However, the adoption of  $m_c$  has the advantage of adding only 3 multipliers  $s_{0c}, s_{1c}, s_{2c}$  regardless of the number of uncertainties.

### 7.2.2.2 Examples

The uncertain short-period was studied in [241, 242]. Compared to the nominal plant (7.15), two parametric uncertainties  $\delta_1$  and  $\delta_2$  affect the open loop dynamics:

$$\begin{aligned} \dot{z} &= \begin{bmatrix} -3 & -1.35 & -0.56 \\ -0.91 & -0.64 & -0.02 \\ 1 & 0 & 0 \end{bmatrix} z + \begin{bmatrix} 1.35 - 0.04z_2 \\ 0.4 \\ 1 \end{bmatrix} u + \\ &+ \begin{bmatrix} (1 + \delta_1)(0.08z_1z_2 + 0.44z_2^2 + 0.01z_2z_3 + 0.22z_2^3) \\ (1 + \delta_2)(-0.05z_2^2 + 0.11z_2z_3 - 0.05z_3^2) \\ 0 \end{bmatrix}, \\ \delta_1, \delta_2 &\in [-0.1, 0.1]. \end{aligned} \quad (7.25)$$

In [241, 242] LF level sets-based algorithms were adopted, featuring respectively: [241] a suboptimal strategy to avoid enforcing the V-s iteration at each vertex of the polytope; [242] a branch-and-bound refinement of the suboptimal algorithm consisting of partitioning the uncertainty set and determining a different parameter-independent LF for each cell. In both cases, the rERA was expressed in the form of  $\Omega_{p,\beta}$  because a unique LF  $V$  certifying the ROA over the entire uncertainty set was not computed by the algorithms.

The plot in Fig. 7.3 shows the analyses using  $\partial(R, V_N) = 2$  (the same nomenclature of Fig. 7.1 applies with  $IS_R$  instead of  $IS$ ). The largest estimate available in the published literature,

taken from [242] and obtained with quartic LFs employing the suboptimal (branch-and-bound refined) algorithm, corresponds to  $\beta = 11.1$  and  $p = x^\top x$  and is reported in here for comparison. Projections of the rERA onto the  $z_1 - z_2$  plane (Fig. 7.3(a)) and  $z_1 - z_3$  plane (Fig. 7.3(b)) are depicted. The results showcase that the three proposed algorithms based on invariant sets are close to each other and outperform the estimation given with the LF level set approach (which was obtained with a higher degree for the LF). The analyses in Fig. 7.3 were obtained describing the uncertainty set with a single polynomial  $m_c(\delta_1, \delta_2)$  following the idea in (7.24). In Table 7.2 the computational statistics are reported. Note that in [242] there is no reference to computational time or size of the problem. However, in [241] a smaller estimation (i.e. without branch-and-bound refinement) was achieved in approximately 2300 s (and this is taken as lower bound on the total processing time of algorithm *LF*). The same observations gathered for the nominal case can be made here.

Finally, an upper bound on the rERA of Fig. 7.3 is evaluated making use of an extension of Algorithm 7.5. Since now the system is subject to uncertainties, the evaluation of  $N_\delta$  random samples of the uncertainty vector  $\delta$  is performed first and, for each of them, Algorithm 7.5 is applied. Results, obtained with  $N_\delta = 100$ ,  $N_s = 300$ , and  $\epsilon_\gamma = 0.03$ , are visualised in Fig. 7.4 by means of projections of  $\Omega_{R,\gamma_f}$  and  $\Omega_{R,\gamma}$  onto the same planes used in Fig. 7.3.

Further results obtained with the nominal invariant sets algorithms (obtained with this and another benchmark study from the literature) are discussed in [127].

Table 7.2: Computational statistics for the invariant sets robust ROA analyses.

Algorithm	$N_{var}$	$N_{SDP}$	$T_{iter}$ [s]	$T_{tot}$ [s]
LF	-	-	-	> 2300
IS - 2 Steps	744	41772	220	2420
IS - 3 Steps	714	41772	210	1890
IS - Hyb	744	41772	203	2770

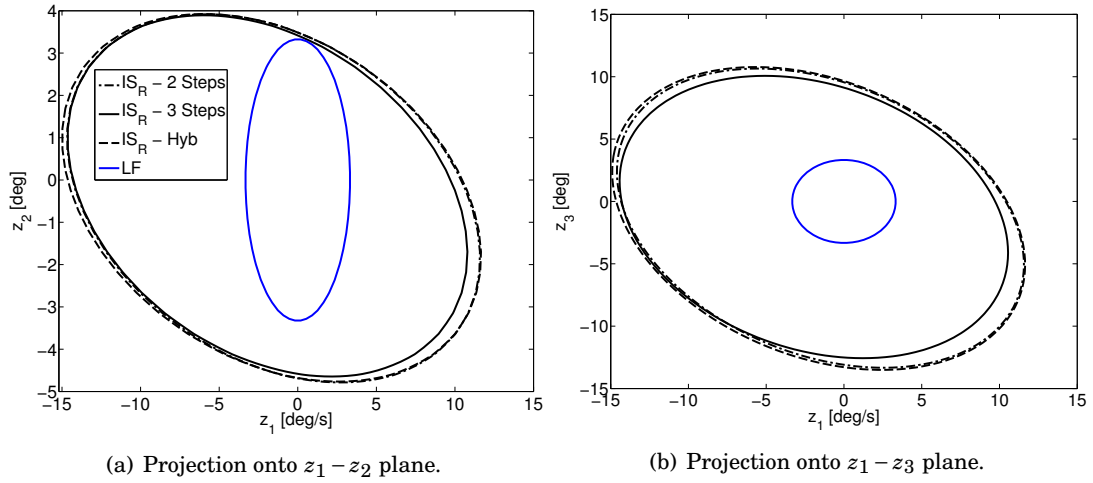


Figure 7.3: Comparison of the rERA of the short-period model with different algorithms.

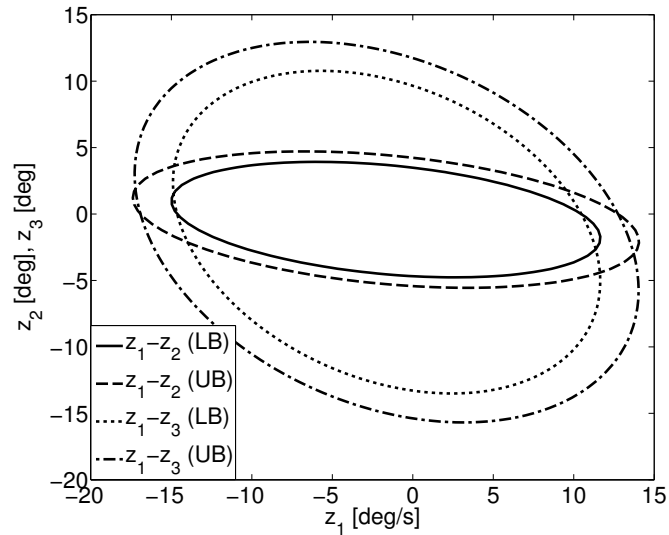


Figure 7.4: Upper bounds of the rERA.

## 7.3 IQC approach

A common feature of the available approaches for ERA [43, 108, 246], including the invariant set one discussed in the previous section, is that they require polynomial vector fields, thus a limitation holds on the types of nonlinearities that can be considered. In addition, the methods dealing with the case of uncertain systems [49, 243] do not typically allow to specify, and thus exploit, the nature of the uncertainty set (e.g. linear time-invariant, real constant, time-varying). This inherently leads to conservative outcomes because the results must hold for a larger set of uncertainties than the one actually affecting the system.

Based on these observations, a more general and flexible framework for local stability analysis of nonlinear uncertain systems is proposed. The problem is framed as the feedback interconnection of a system  $G$  with polynomial vector field and a bounded causal operator  $\Delta$  for which an Integral Quadratic Constraint description holds. The IQC paradigm (Sec. 6.1.2) is indeed particularly suited to address the desired task of reducing the conservatism, because it characterises a broad class of nonlinearities, and allows the description of the uncertainties to be refined by specifying their nature. The setup provided by the feedback interconnection  $G-\Delta$  is thus believed to be quite general and to adequately cover a large class of nonlinear systems encountered in engineering applications.

The time-domain interpretation of IQCs (Sec. 6.1.2.1) is instrumental to prove the main results. In particular, the connection between dissipation inequality and IQC is exploited to provide guarantees of local stability. Dissipation inequality arguments [210] classically require the IQC to be *hard* in the sense that the integral constraints must hold over all finite times [215]. This is not immediate because the frequency domain IQC only guarantees an equivalent counterpart in the time-domain as an infinite-horizon integral constraint (*soft* IQC) [170] (recall the example with the two alternative factorisations for the multiplier  $\Pi_\delta$  in Sec. 6.1.2.2). The main technical contribution is to establish certificates for the domain of attraction with both hard and soft factorisations (Sec. 7.3.1). Application to two benchmark studies from the ROA literature is then shown in Sec. 7.3.2.

### 7.3.1 Region of attraction certificates

The theoretical formulation of ROA analysis with IQC is presented here. First, the problem setup is detailed, and then local stability certificates for the cases of hard and soft IQCs are stated. Algorithms based on SOS are also provided to numerically solve the problem.

### 7.3.1.1 Problem statement

The proposed framework aims to analyse systems of the form:

$$\dot{x} = f(x, w), \quad (7.26a)$$

$$v = h(x, w), \quad (7.26b)$$

$$w = \Delta(v), \quad (7.26c)$$

where  $f$  and  $h$  are polynomial functions of  $x$  and  $w$  and define the nominal plant  $G$ , and  $\Delta$  is a bounded operator gathering nonlinearities and uncertainties for which an IQC description holds. The prototype of systems considered by this work thus consists of the standard interconnection  $G-\Delta$  (Fig. 2.2), where  $G$  now is polynomial and  $\Delta$  is a generic uncertainty. Thus, the combined system is in general non-polynomial. As already done for the invariant set approach, it will be assumed that  $x^*$  is not a function of  $\Delta$  (specifically  $x^* = 0$ ).

Starting from the generic description in (7.26), the first step consists of defining the augmented plant displayed in Fig. 7.5. Note that, compared to the similar interconnection described in Fig. 6.3, here  $G$  can have polynomial dynamics (whereas in standard IQC  $G$  is LTI). In particular, the feedback interconnection comprises the subsystems  $G$  (defined by (7.26a)-(7.26b)),  $\Delta$  (7.26c), and  $\Psi$ , derived from the time-domain representation of the IQCs (6.12).

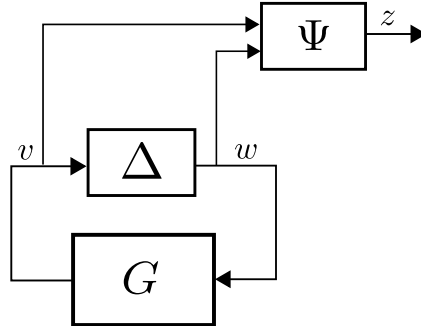


Figure 7.5: Augmented plant for IQC-based ROA analysis.

Introducing the vector  $\tilde{x} = [x; x_\Psi]$  gathering the states of  $G$  and of the LTI system  $\Psi$ , the plant can be reorganised eliminating any explicit dependence on  $\Delta$  as follows:

$$\begin{aligned} \dot{\tilde{x}} &= F(\tilde{x}, w), \\ z &= H(\tilde{x}, w), \end{aligned} \quad (7.27)$$

where  $F, H : \mathbb{R}^{n_{\tilde{x}}+n_w} \rightarrow \mathbb{R}^{n_{\tilde{x}}}$  are polynomial maps depending on both  $G$  and  $\Psi$ . It is stressed that this manipulation, leading from (7.26) to (7.27), does not make any assumption on  $\Delta$  except the existence of a factorisation  $\Psi$  for the associated multiplier  $\Pi$ .

**Remark 7.1.** Most IQCs require  $\Delta$  to map zero input to zero output, i.e.  $v = 0$  maps to  $w = \Delta(v) = 0$  ( $v = 0$  and  $w = 0$  mean here that the signals have zero  $\mathcal{L}_2$  norm). To see this, consider the case where  $v \equiv 0$ . Then, the frequency-domain IQC in (6.5) simplifies to:

$$\int_{-\infty}^{+\infty} \hat{w}(j\omega)^* \Pi_{22}(j\omega) \hat{w}(j\omega) d\omega \geq 0, \quad (7.28)$$

where the partition  $\Pi = \begin{bmatrix} \Pi_{11} & \Pi_{12} \\ \Pi_{12}^* & \Pi_{22} \end{bmatrix}$  is considered. It is typical that  $\Pi_{22}(j\omega) < 0$  for all  $\omega$  [170, 215] and hence, from Eq. (7.28), it must be  $w \equiv 0$ . This implies that, if  $\Delta$  has internal dynamics, e.g. LTI uncertainties, then it must have zero initial condition. This assumption, used in [13] in a similar context, is made here and can be interpreted as the absence of initial stored energy in  $\Delta$ . The instance of energy stored in the IQC has recently been addressed in [82, 193] and could allow to relax this assumption.

Having said that in principle this hypothesis could seem restrictive for analyses which allow for non-zero initial conditions in the plant  $G$ , there might be applications where this assumption is known *a priori* to be valid (from physical reasoning), or when there is no effect of the initial conditions of  $\Delta$  on the local stability (inferred from time-marching simulations). In fact, if the only detrimental effect on ROA is the input-output behaviour of the uncertain dynamics, this is correctly captured by the proposed framework.

For all these reasons, the results are stated here for a general  $\Delta$  and, in case of internal dynamics inside it, the aforementioned hypothesis is assumed to hold. This is done in order not to limit the application to static  $\Delta$ , which naturally fulfils this assumption and are indeed a particular class of the allowed set.

### 7.3.1.2 Case of Hard IQCs

The proposed estimation of invariant subsets of the ROA when  $\Delta$  has an hard IQC factorisation is based on the following theorem.

**Theorem 7.3.** Let  $F$  be the polynomial vector field defined in (7.27) and  $\Delta : \mathcal{L}_2^{n_v}[0, \infty) \rightarrow \mathcal{L}_2^{n_w}[0, \infty)$  be a bounded, causal operator. Further assume:

1.  $\Delta \in \text{HardIQC}(\Psi, M)$ ;
2. there exists a smooth function  $V : \mathbb{R}^{n_x} \rightarrow \mathbb{R}$  and positive scalars  $\epsilon_x$  and  $\epsilon_w$  such that:

$$V(0) = 0 \quad \text{and} \quad V(\tilde{x}) > 0 \quad \forall \tilde{x} \setminus \{0\}, \quad (7.29a)$$

$$\nabla V(\tilde{x}) F(\tilde{x}, w) + z^\top M z + \epsilon_x \tilde{x}^\top \tilde{x} + \epsilon_w w^\top w < 0 \quad \forall \tilde{x} \in \Omega_{V,\gamma} \setminus \{0\}, \quad \forall w \in \mathbb{R}^{n_w}. \quad (7.29b)$$

Then the intersection of  $\Omega_{V,\gamma}$  with the hyperplane  $x_\Psi = 0$  is an inner estimate of the ROA of (7.26).

**Proof.** The theorem assumes that Eq. (7.29b) holds only over the set  $\Omega_{V,\gamma}$ . Hence, the proof must ensure first that all the trajectories originating in  $\Omega_{V,\gamma}$  remain within for all finite time.

Assume there exists a  $T_1 > 0$  such that  $\tilde{x}(T_1) \notin \Omega_{V,\gamma}$ , and define  $T_2 := \inf_{\tilde{x}(T) \notin \Omega_{V,\gamma}} T$ . Since  $F$  and  $H$  are polynomial maps, solutions of Eq. (7.27) are continuous, thus  $\tilde{x}(T_2)$  is on the boundary of  $\Omega_{V,\gamma}$  and  $\tilde{x}(t) \in \Omega_{V,\gamma} \forall t \in [0, T_2]$ . Therefore, it is possible to integrate the inequality (7.29b) in this range:

$$V(\tilde{x}(T_2)) - V(\tilde{x}(0)) + \int_0^{T_2} z^\top M z + \epsilon_x \int_0^{T_2} \tilde{x}^\top \tilde{x} dt + \epsilon_w \int_0^{T_2} w^\top w dt < 0. \quad (7.30)$$

Since by hypothesis  $\Delta \in \text{HardIQC}(\Psi, M)$  and  $V(\tilde{x}(0)) \leq \gamma$ , it thus holds:

$$\gamma = V(\tilde{x}(T_2)) < \gamma. \quad (7.31)$$

This is contradictory and hence the assumption that  $\exists T_1 > 0$  such that  $\tilde{x}(T_1) \notin \Omega_{V,\gamma}$  can not hold. Thus  $\tilde{x}(0) \in \Omega_{V,\gamma}$  implies  $\tilde{x}(t) \in \Omega_{V,\gamma}$  for all finite time (invariance of the level set). Note that this proof by contradiction is needed otherwise there is no guarantee that the trajectories stay in the set (and thus that the inequality (7.29b), leveraged in the rest of the proof, holds).

Next, it is required to prove that the equilibrium point is attractive. Let us consider Eq. (7.30) with the integrals performed in a generic interval  $[0, T]$ . From  $\Delta \in \text{HardIQC}(\Psi, M)$  and  $V(\tilde{x}(T)) \geq 0$ , it follows that:

$$\epsilon_x \int_0^T \tilde{x}^\top \tilde{x} dt + \epsilon_w \int_0^T w^\top w dt < V(\tilde{x}(0)). \quad (7.32)$$

Let  $T \rightarrow \infty$  to see that  $\tilde{x} \in \mathcal{L}_2^{n_{\tilde{x}}}[0, \infty)$  and  $w \in \mathcal{L}_2^{n_w}[0, \infty)$ .

Let us now define  $y = [\tilde{x}; w]$  and  $\mathcal{D}_y = \{y(\tilde{x}, w) : \tilde{x} \in \Omega_{V,\gamma}, w \in \mathbb{R}^{n_w}\}$ . The vector field  $F$  is a polynomial function of  $\tilde{x}$  and  $w$ . Therefore,  $F$  is locally Lipschitz [137]:

$$\|F(y_2) - F(y_1)\| \leq L \|y_2 - y_1\| \quad \forall y_1, y_2 \in \mathcal{D}_y, \quad (7.33)$$

with  $L$  a real constant. In particular, for  $y_1 = [0; 0]$  and a generic  $y_2$ , it holds that:

$$\|F(y_2)\| \leq L \|y_2\|. \quad (7.34)$$

Eq. (7.34) is valid for any  $y_2$  in  $\mathcal{D}_y$ , hence the subscript will be omitted. It follows directly from Eq. (7.34) that:

$$\dot{\tilde{x}}^\top \dot{\tilde{x}} = \|F(y)\|^2 \leq L^2 \|y\|^2 = L^2 [\tilde{x}^\top \tilde{x} + w^\top w]. \quad (7.35)$$

By integrating both sides from 0 to  $\infty$ , it holds for any admissible trajectory:

$$\begin{aligned} \int_0^\infty \dot{\tilde{x}}^\top \dot{\tilde{x}} dt &\leq L^2 \int_0^\infty [\tilde{x}^\top \tilde{x} + w^\top w] dt, \\ \|\dot{\tilde{x}}\|_2^2 &\leq L^2 [\|\tilde{x}\|_2^2 + \|w\|_2^2]. \end{aligned} \quad (7.36)$$

Since  $\tilde{x} \in \mathcal{L}_2^{n_{\tilde{x}}}[0, \infty)$  and  $w \in \mathcal{L}_2^{n_w}[0, \infty)$ , it follows from (7.36) that  $\dot{\tilde{x}} \in \mathcal{L}_2^{n_{\dot{\tilde{x}}}}[0, \infty)$ . An identical argument applied to the map  $h$  from Eq. (7.26b) allows to conclude that  $v \in \mathcal{L}_2^{n_v}[0, \infty)$ , which guarantees that the signals in the loop belong to the space of signals requested from IQCs. Finally,  $(\dot{\tilde{x}}, \tilde{x}) \in \mathcal{L}_2^{n_{\dot{\tilde{x}}}}[0, \infty)$  implies that  $\tilde{x} \rightarrow 0$  as  $T \rightarrow \infty$  [64]. Therefore, all the trajectories originated by

initial conditions in  $\Omega_{V,\gamma}$  stay in the set and eventually converge to the equilibrium point. That is,  $\Omega_{V,\gamma}$  is a subset of the ROA of the system in Eq. (7.27).

Note finally that by definition of  $\Psi$  (6.12)  $x_\Psi(0)=0$ , i.e. the initial condition for the states  $x_\Psi$  always lies on the hyperplane  $x_\Psi=0$ . Thus its intersection with  $\Omega_{V,\gamma}$  provides an ERA for the original system (7.26). ■

**Remark 7.2.** Note that  $V$  is not a Lyapunov function of (7.27). In fact, it is possible for  $\dot{V}$  to be non-negative at some points in time. This is a consequence of the term  $z^\top Mz$  which in general only provides integral constraints. When the IQC defines a pointwise-in-time constraint (i.e.  $z^\top Mz \geq 0 \ \forall t$ ), then  $V$  is a Lyapunov function of the system. This can be the case sometimes for hard IQCs, e.g. the sector bound multiplier initially encountered in Sec. 6.3.1 and further used in Sec. 7.3.2.1.

**Remark 7.3.** It is common practice to tackle the nonlinear stability problem of systems subject to polynomial nonlinearities with Lyapunov techniques, whereas the study of systems subject to hard nonlinearities (and uncertainties) is addressed with multipliers-based techniques. The proposed result allows to consider the asymptotic stability problem [137] of systems generically described by (7.26) within a unified framework. To determine whether or not an equilibrium point  $x^*$  is asymptotically stable (without determining its ROA) it suffices indeed to satisfy Theorem 7.3 in any domain  $\mathcal{D} \subset \mathbb{R}^n$  containing  $x^*$ .

Theorem 7.3 is used here to compute inner estimates of the ROA of the original system (7.26). By restricting the attention to the class of polynomial functions  $V$ , SOS optimisation can be exploited to enforce the set containment constraints in Eq. (7.29). The following program is first proposed.

#### Program 7.4.

$$\max_{s_1 \in \Sigma[\tilde{x}, w]; V \in \mathbb{R}[\tilde{x}]} \gamma, \quad V \in \Sigma[\tilde{x}], \quad (7.37a)$$

$$-(\nabla V f + z^\top Mz + L_\epsilon) - s_1(\gamma - V) \in \Sigma[\tilde{x}, w]. \quad (7.37b)$$

where  $L_\epsilon = \epsilon[\tilde{x}; w]^\top [\tilde{x}; w]$  with  $\epsilon$  small real number on the order of  $10^{-6}$ . These constraints are sufficient conditions for (7.29). Indeed, (7.37a) ensures positivity of  $V$  (7.29a), whereas (7.37b) is, by direct application of Lemma 7.2, a sufficient condition for the set containment (7.29b).

As discussed for the SOS programs investigated in Sec. 7.2, bilinear terms arise as a consequence of the application of the generalised S-procedure. A three-step algorithm, inspired by Algorithm 7.1 (the  $V$ - $s$  iteration), is proposed with the aim to enlarge the inner estimates of the ROA via solution of a sequence of convex programs.

**Algorithm 7.7.** Hard-IQCs

**Outputs:** the level sets  $\Omega_{V,\gamma}$  and  $\Omega_{p,\beta}$  (both inner estimates of the ROA).

**Inputs:** a shape function  $p$ ; a polynomial  $V^0$  satisfying (7.5) for some  $\gamma$ .

1.  $\gamma$ -Step. Solve through bisection on  $\gamma$ .

$$\begin{aligned} & \max_{s_1 \in \Sigma[\tilde{x}, w], M} \gamma, \\ & -(\nabla V^0 F + z^\top M z + L_\epsilon) - s_1(\gamma - V^0) \in \Sigma[\tilde{x}, w], \end{aligned}$$

set  $\bar{\gamma} \leftarrow \gamma, \bar{s}_1 \leftarrow s_1$ .

2.  $\beta$ -Step Maximise the size of  $\Omega_{p,\beta}$  through bisection on  $\beta$  such that  $\Omega_{p,\beta} \subseteq \Omega_{V^0, \bar{\gamma}}$ .

$$\begin{aligned} & \max_{s_2 \in \Sigma[\tilde{x}]} \beta, \\ & (\bar{\gamma} - V^0) - s_2(\beta - p) \in \Sigma[\tilde{x}], \end{aligned}$$

set  $\bar{\beta} \leftarrow \beta, \bar{s}_2 \leftarrow s_2$ .

3.  $V$ -Step. Compute a new shape for the level set by solving over  $V, M$ .

$$\begin{aligned} & V - \epsilon \tilde{x}^\top \tilde{x} \in \Sigma[\tilde{x}, w], \\ & -(\nabla V F + z^\top M z + L_\epsilon) - \bar{s}_1(\bar{\gamma} - V) \in \Sigma[\tilde{x}, w], \\ & (\bar{\gamma} - V) - \bar{s}_2(\bar{\beta} - p) \in \Sigma[\tilde{x}], \end{aligned}$$

set  $V^0 \leftarrow V$  and go to  $\gamma$ -Step.

**Remark 7.4.** The positive polynomial  $L_\epsilon$  is required by the perturbation argument used in Theorem 7.3 (see Eq. 7.29b). In fact, this term is adopted in other SOS-based iterative schemes (this was already illustrated with regard to Algorithm 7.1) as a numerical trick to help achieving feasibility in the optimisations. With the same spirit it has been used here for the constraint on  $V$  (where there is no requirement in principle from Theorem 7.3). An important consequence of this is that the two  $\epsilon$ -terms in the dissipation inequality (7.29b) are costless, i.e. they are automatically taken into account by the proposed numerical recipes. This is an advantageous aspect of the proposed formulation, since the adoption of this perturbation argument allows to avoid other stronger assumptions (e.g. compactness of the level set  $\Omega_{V,\gamma}$ ).

The shape function  $p$  can be specified by the user based on important directions in the state space (its role was commented on when Algorithm 7.1 was presented). Since the selection of  $p$  has an influence on the results, if these information are not available to the analyst an alternative scheme which does not entail using  $p$  can be derived starting from Algorithm 7.7. This is omitted here since it does not present particular complexity and was presented in [129]. As for the initialisation of  $V$ , the same rationale followed in Sec. 7.2 can be followed here. Note

finally that  $M$  is a matrix of optimisation variables, as it is the case in standard IQC analysis. In general  $M$  will be subject to constraints in order to represent a valid IQC. These can be typically recast as SOS constraints and thus added to the optimisations. Examples of this instances will be evaluated in Sec. 7.3.1.3 and Sec. 7.3.2.2.

### 7.3.1.3 Region of Attraction certificates with Soft IQCs

Theorem 7.3 assumes that  $\Delta \in \text{HardIQC}(\Psi, M)$ . As discussed in the introductory section to IQC (Sec. 6.1.2.1), once a suitable multiplier  $\Pi$  is selected for the uncertainty  $\Delta$  (i.e.  $\Delta \in \text{IQC}(\Pi)$ ), its factorisation can, in general, hold only the *weaker* property  $\Delta \in \text{SoftIQC}(\Psi, M)$ . Indeed, it is often desirable to enrich the description of  $\Delta$  by using different multipliers  $\Pi$ , and for some of them only a soft factorisation might hold (e.g. the less conservative  $D$ - $G$  factorisation defined in Eq. 6.16 for real uncertainties). It is then deemed important to provide guarantees of local stability also for the cases that do not satisfy condition 1 of Theorem 7.3.

In order to make use of the key dissipation inequality argument (7.32), at least a bound on the finite-horizon integral is needed when no hard factorisation is available. To this end, a recent result is recalled next. Let us denote by  $\text{KYP}(A, B, C, D, M)$  the LMI constraint on a matrix  $Y = Y^\top$ :

$$\begin{bmatrix} A^\top Y + YA & YB \\ B^\top Y & 0 \end{bmatrix} + \begin{bmatrix} C^\top \\ D^\top \end{bmatrix} M \begin{bmatrix} C & D \end{bmatrix} < 0. \quad (7.38)$$

Let us also partition the frequency domain multiplier  $\Pi$  conformably with the dimensions of the input  $v$  and output  $w$  of  $\Delta$  as  $\Pi = \begin{bmatrix} \Pi_{11} & \Pi_{12} \\ \Pi_{21}^\top & \Pi_{22} \end{bmatrix}$ . Then, the result proposed in [82] (building on a previous finding from [215]) provides the desired bound.

**Lemma 7.6.** [82] Let  $\Psi \in \mathbb{RH}_\infty^{n_z \times (n_v + n_w)}$  and  $M = M^\top \in \mathbb{R}^{n_z \times n_z}$  be given and define  $\Pi = \Psi^\top M \Psi$ . If  $\Pi_{22} < 0 \ \forall \omega \in \mathbb{R} \cup \{\infty\}$  then:

- $D_{\Psi,2}^\top M D_{\Psi,2} < 0$  and there exists a solution  $Y_{22} = Y_{22}^\top$  to  $\text{KYP}(A_\Psi, B_{\Psi,2}, C_\Psi, D_{\Psi,2}, M)$ ;
- if  $\Delta \in \text{SoftIQC}(\Psi, M)$  then for all  $T \geq 0$ ,  $v \in \mathcal{L}_2^{n_v}[0, \infty)$  and  $w = \Delta(v)$ :

$$\int_0^T z(t)^\top M z(t) dt \geq -x_\Psi(T)^\top Y_{22} x_\Psi(T), \quad (7.39)$$

for any  $Y_{22}$  satisfying  $\text{KYP}(A_\Psi, B_{\Psi,2}, C_\Psi, D_{\Psi,2}, M)$ .

This result is particularly attractive because it relates the multiplier  $(\Psi, M)$  and the bound  $Y_{22}$  via a KYP constraint, which is a convex LMI on  $M$  and  $Y_{22}$ .

By making use of Lemma 7.6, Theorem 7.4 is proposed to address the estimation of ROA with soft IQCs.

**Theorem 7.4.** Let  $F$  be the polynomial vector field defined in (7.27) and  $\Delta : \mathcal{L}_2^{n_v}[0, \infty) \rightarrow \mathcal{L}_2^{n_w}[0, \infty)$  be a bounded, causal operator. Further assume:

1.  $\Delta \in \text{SoftIQC}(\Psi, M)$ ;
2. there exists a  $Y_{22} = Y_{22}^\top$  that satisfies  $\text{KYP}(A_\Psi, B_{\Psi 2}, C_\Psi, D_{\Psi 2}, M)$ ;
3. there exist smooth functions  $V: \mathbb{R}^{n_{\tilde{x}}} \rightarrow \mathbb{R}$  and  $\tilde{V} = V - x_\Psi^\top Y_{22} x_\Psi$ , and positive scalars  $\epsilon_x$  and  $\epsilon_w$  such that:

$$\tilde{V}(0) = 0 \quad \text{and} \quad \tilde{V}(\tilde{x}) > 0 \quad \forall \tilde{x} \setminus \{0\}, \quad (7.40a)$$

$$\nabla V(\tilde{x}) F(\tilde{x}, w) + z^\top M z + \epsilon_x \tilde{x}^\top \tilde{x} + \epsilon_w w^\top w < 0 \quad \forall \tilde{x} \in \Omega_{\tilde{V}, \gamma} \setminus \{0\}, \quad \forall w \in \mathbb{R}^{n_w}. \quad (7.40b)$$

Then the intersection of  $\Omega_{\tilde{V}, \gamma}$  with the hyperplane  $x_\Psi = 0$  is an inner estimate of the ROA of (7.26).

**Proof.** Integrating the inequality in Eq. (7.40b) in the interval  $[0, T]$ , it follows:

$$V(\tilde{x}(T)) - V(\tilde{x}(0)) + \int_0^T z^\top M z + \epsilon_x \int_0^T \tilde{x}^\top \tilde{x} dt + \epsilon_w \int_0^T w^\top w dt < 0. \quad (7.41)$$

Contrary to the case in the proof of Theorem 7.3, since  $\Delta \in \text{SoftIQC}(\Psi, M)$ , the finite-horizon integral involving the IQC term is not necessarily positive here. According to the result in Lemma 7.6, the following lower bound on the soft IQC  $(\Psi, M)$  is valid:

$$\int_0^T z^\top M z dt \geq -x_\Psi(T)^\top Y_{22} x_\Psi(T). \quad (7.42)$$

for any  $Y_{22}$  satisfying  $\text{KYP}(A_\Psi, B_{\Psi 2}, C_\Psi, D_{\Psi 2}, M)$ . Thus, by making use of this lower bound in Eq. (7.41), it holds:

$$V(\tilde{x}(T)) - V(\tilde{x}(0)) - x_\Psi(T)^\top Y_{22} x_\Psi(T) + \epsilon_x \int_0^T \tilde{x}^\top \tilde{x} dt + \epsilon_w \int_0^T w^\top w dt < 0. \quad (7.43)$$

Define  $\tilde{V}(\tilde{x}) = V(\tilde{x}) - x_\Psi^\top Y_{22} x_\Psi$ . Since  $x_\Psi(0) = 0$  (recall the definition of  $\Psi$  in Eq. (6.12)), the following holds directly from Eq. (7.43):

$$\tilde{V}(\tilde{x}(T)) - \tilde{V}(\tilde{x}(0)) + \epsilon_x \int_0^T \tilde{x}^\top \tilde{x} dt + \epsilon_w \int_0^T w^\top w dt \leq 0. \quad (7.44)$$

Note that (7.44) represents a formally equivalent expression of Eq. (7.30), with the crucial difference that  $\tilde{V}$  is now the level set function. Specifically, the same proof by contradiction of Theorem 7.3 can be used to prove the invariance of the set  $\Omega_{\tilde{V}, \gamma}$ . Moreover, due to the positivity of  $\tilde{V}$ , it holds again that  $\tilde{x} \in \mathcal{L}_2^{n_{\tilde{x}}}[0, \infty)$  and  $w \in \mathcal{L}_2^{n_w}[0, \infty)$ . Therefore, the same arguments apply to prove that the equilibrium point is attracting in the invariant set. It can then be concluded that the level set  $\Omega_{\tilde{V}, \gamma}$  is a subset of the ROA of the system in Eq. (7.27). Thus, the intersection of  $\Omega_{\tilde{V}, \gamma}$  with the hyperplane  $x_\Psi = 0$  (equivalently, the intersection of  $\Omega_{V, \gamma}$  with  $x_\Psi = 0$ ) provides an ERA for the original system (7.26). ■

**Remark 7.5.** *The key step in proving Theorem 7.4 is the finite-horizon bound on the soft IQC (7.42). In this case this is specified as an LMI constraint and thus can be easily incorporated in convex optimisation algorithms. However, as it has already been discussed throughout the Chapter, the numerical estimation of ROA via SOS inherently leads to bilinear terms. In view of this, other (less conservative) bounds involving non-convex bilinear matrix inequalities could be similarly considered. For example, in [216] an iterative scheme was presented to efficiently employ the tighter non-convex bound proposed in [215] and involving an Algebraic Riccati Equation. Theorem 7.4 can be adapted with small changes in the initial assumptions, and the bound from [215] can in turn be implemented in the SOS iterative schemes potentially determining less conservative results.*

In order to formulate an algorithm for the case of soft IQCs, a Lemma allowing condition 2 in Theorem 7.4 to be enforced as an SOS constraint is first presented.

**Lemma 7.7.** *The constraint  $KYP(A_\Psi, B_{\Psi 2}, C_\Psi, D_{\Psi 2}, M)$  on  $Y_{22}$  holds if and only if there exists a function  $V_\Psi = x_\Psi^\top Y_{22} x_\Psi: \mathbb{R}^{n_{x\Psi}} \rightarrow \mathbb{R}$  such that:*

$$\nabla V_\Psi(x_\Psi) f_\Psi(x_\Psi, w) + z^\top M z < 0, \quad (7.45)$$

$$\begin{aligned} \text{with } f_\Psi &= A_\Psi x_\Psi + B_{\Psi 2} w, \\ z &= C_\Psi x_\Psi + D_{\Psi 2} w. \end{aligned} \quad (7.46)$$

**Proof.** It immediately follows by left and right multiplying the LMI (7.38) by  $[x_\Psi; w]^\top$  and  $[x_\Psi; w]$  respectively. ■

It is important to note that enforcing (7.45) with an SOS constraint is lossless because it only features quadratic forms.

The SOS iterative scheme for the case of soft IQC is then stated.

#### Algorithm 7.8. Soft-IQCs

**Outputs:** the level sets  $\Omega_{\tilde{V}, \gamma}$  and  $\Omega_{p, \beta}$  (both inner estimates of the ROA).

**Inputs:** a shape function  $p$ ; a polynomial  $V^0$  satisfying (7.5) for some  $\gamma$ ;  $M^0; Y_{22}^0$ .

1.  $\gamma$ -Step. Set  $\tilde{V}^0 \leftarrow (V^0 - x_\Psi^\top Y_{22}^0 x_\Psi)$  and solve through bisection on  $\gamma$ .

$$\begin{aligned} \max_{s_1 \in \Sigma[\tilde{x}, w]} \gamma, \\ -(\nabla V^0 F + z^\top M^0 z + L_\epsilon) - s_1(\gamma - \tilde{V}^0) \in \Sigma[\tilde{x}, w]. \end{aligned}$$

set  $\bar{\gamma} \leftarrow \gamma$  and  $\bar{s}_1 \leftarrow s_1$ .

2.  $\beta$ -Step. Maximise the size of  $\Omega_{p, \beta}$  through bisection on  $\beta$  such that  $\Omega_{p, \beta} \subseteq \Omega_{\tilde{V}^0, \bar{\gamma}}$ .

$$\begin{aligned} \max_{s_2 \in \Sigma[\tilde{x}]} \beta, \\ (\bar{\gamma} - \tilde{V}^0) - s_2(\beta - p) \in \Sigma[\tilde{x}]. \end{aligned}$$

set  $\bar{\beta} \leftarrow \beta$  and  $\bar{s}_2 \leftarrow s_2$ .

3. V-Step. Compute a new shape for the level set by solving over  $V, M, Y_{22}$ .

$$\begin{aligned}\tilde{V} - \epsilon \tilde{x}^\top \tilde{x} &\in \Sigma[\tilde{x}, w], \\ -(\nabla V F + z^\top M z + L_e) - \bar{s}_1(\bar{\gamma} - \tilde{V}) &\in \Sigma[\tilde{x}, w], \\ (\bar{\gamma} - \tilde{V}) - \bar{s}_2(\bar{\beta} - p) &\in \Sigma[\tilde{x}], \\ -(\nabla V_\Psi f_\Psi + z^\top M z) + L_3 &\in \Sigma[\tilde{x}, w],\end{aligned}$$

set  $V^0 \leftarrow V$ ,  $M^0 \leftarrow M$ ,  $Y_{22}^0 \leftarrow Y_{22}$ , and go to  $\gamma$ -Step.

where  $V_\Psi, f_\Psi$  are defined in Lemma 7.7. It is worth remarking that in the proposed algorithm only the  $V$ -step is affected by the KYP constraint. In fact, in the  $\gamma$ -step only a maximisation of the size (given by the scalar  $\gamma$ ) of the level set is performed, but its shape (given by  $\tilde{V}$ ) is held fixed to a given value  $\tilde{V}^0$ . Therefore, by keeping in the  $\gamma$ -Step the multipliers  $M$  fixed to the value optimised at the previous iteration, the KYP constraint is automatically satisfied. In this regard, note that the algorithm needs an initialisation for  $M$  and  $Y_{22}$ . There are not formal guidelines for their selection, and here the  $\gamma$ -Step at the first iteration uses  $Y_{22}^0 = 0$  and optimises over  $M$  –that is, it is applied as in the case of hard IQCs (Algorithm 7.7). This potentially leads to an error on  $\bar{\gamma}$  which, however, only serves in the first iteration to perform the  $\beta$ -step and  $V$ -step. The latter then computes a level set  $\Omega_{\tilde{V}, \gamma}$  fulfilling all the prescribed constraints, and thus a valid ROA estimate of the system is achieved. This will in turn provide the sought initialisations for the next iteration and so forth.

This section is concluded with some remarks on the properties of the proposed framework for ROA analysis. The main advantage of this approach is that it allows to capture the effect of different kind of uncertainties on the local stability of the analysed system. It is indeed possible to refine the description of the uncertainty by adding different classes of multipliers (this property will be showcased in the example section). Different from other solutions proposed in the literature [6, 241, 243], this framework exploits the nature of the uncertainties (e.g. LTI, real constant, linear time varying) to reduce the conservatism by specializing the IQC description. In addition to that, a further refinement is allowed by the parameterisation of the dynamic multipliers (e.g. increasing the number of basis functions in the vector  $H_v$  of the D-G scalings (6.16)). In practice, a trade-off between computational time and accuracy will arise, and system-dependent investigations are required to assess the benefits of a more sophisticated description.

Another favourable feature is that the estimate of the ROA is given by means of parameter-independent level sets, i.e.  $V$  is a function of  $\tilde{x}$  only. The advantages of having a parameter-independent level set, together with the possible drawbacks, have already been discussed in Sec. 7.2.2, where a solution has been proposed by introducing in the formulation a second function which is allowed to depend on the uncertainties. The situation here is different, specifically the function  $V$  indirectly depends on the uncertainties via the IQC states  $x_\Psi$  (for dynamic IQCs).

This however has no effect on the interpretation of the results because it always holds  $x_\Psi(0) = 0$ , thus the analyst will only look at the intersection of  $\Omega_{V,\gamma}$  with the hyperplane  $x_\Psi = 0$ .

The main drawback of this approach is the presence of the states  $x_\Psi$  associated with dynamic multipliers, which determines an increase in the run time. Note however that there are a number of static multipliers which allow features of the operator  $\Delta$  (e.g. sector, norm bound, time varying real scalar) to be specified without affecting the size of  $\tilde{x}$ .

### 7.3.2 Numerical examples

This section illustrates the application of the proposed framework with two numerical examples. In the first case study (Section 7.3.2.1) hard IQCs are employed to describe input saturation of a closed-loop, nonlinear, short-period aircraft model, whereas in the second (Section 7.3.2.2) soft IQCs will be used for modelling parametric uncertainties affecting the Van der Pol oscillator.

#### 7.3.2.1 Closed-loop short period GTM aircraft

The closed-loop short period motion of the NASA's Generic Transport Model (GTM) can be approximated as a 2 states polynomial system [42]:

$$\begin{aligned}\dot{\alpha} &= -1.492\alpha^3 + 4.239\alpha^2 + 0.2402\alpha\delta_e + 0.003063\alpha q - 0.06491\delta_e^2 + \\ &\quad + 0.006226q^2 - 3.236\alpha - 0.3166\delta_e + 0.9227q, \\ \dot{q} &= -7.228\alpha^3 + 18.36\alpha^2 + 41.5\alpha\delta_e - 45.34\alpha - 59.99\delta_e - 4.372q + 1.103q^3, \\ \delta_{eCMD} &= Kq.\end{aligned}\tag{7.47}$$

where  $\alpha$  is the angle of attack,  $q$  is the pitch rate,  $\delta_e$  is the elevator deflection (all angles expressed in radians), and  $K = 4\frac{\pi}{180}$  is a constant gain. The GTM steady-state solution consists of a locally stable equilibrium point at the origin, i.e.  $x^* = 0$ . Previous studies focused on Region of Attraction analysis of the Open (OL) and Closed-Loop (CL) system [42], and worst-case  $\mathcal{L}_2$  gain analysis with saturated rate of  $\delta_e$  [44]. In this work, the elevator  $\delta_e$  is assumed to be subject to actuator magnitude saturation, that is:

$$\delta_e = \begin{cases} \delta_e^{sat}. & \delta_{eCMD} > \delta_e^{sat}, \\ \delta_{eCMD}. & |\delta_{eCMD}| \leq \delta_e^{sat}, \\ -\delta_e^{sat}. & \delta_{eCMD} < -\delta_e^{sat}, \end{cases}\tag{7.48}$$

where  $\delta_e^{sat}$  is a constant defining the saturation level. Note that there is a wealth of techniques which allows the ROA of a saturated system to be determined when the plant  $G$  is linear [114]. The novelty of the approach is that it allows to consider the more general case of polynomial, and potentially uncertain,  $G$ .

A characterisation of the saturation by means of IQC holding as finite-horizon time-domain constraints (i.e. hard IQCs) is discussed next. For example, the saturation is a memoryless and

bounded nonlinearity, thus satisfies the sector multiplier (6.34) introduced in Sec. (6.3.1) and used therein to model freeplay. This multiplier is static and a state-space factorisation is:

$$\Pi_S = \lambda_S \begin{bmatrix} -2\sigma\eta & \sigma + \eta \\ \sigma + \eta & -2 \end{bmatrix}, \quad \Psi_S = I_2, \quad M_S = \lambda_S \Pi_S, \quad (7.49)$$

Similarly to the case of the freeplay (Sec. 6.3.1), the slope of the saturation is also in the sector  $[\sigma_1, \eta_1]$  and thus the Zames-Falb multiplier  $\Pi_{ZF}$  can be used (6.37). In this example  $H$  will be parameterised by low pass filters, and a J-spectral factorisation  $J_{sf}(\Pi_{ZF})$  is obtained with the algorithm from [215], which provides an hard IQC factorisation  $(\Psi_{ZF}, M_{ZF})$ .

A common choice in IQC analysis of saturated systems is to consider the sector  $[0, 1]$  for both  $\Pi_S$  and  $\Pi_{ZF}$ . However, these IQCs include the OL system (i.e.  $\delta_e=0$ ) as a particular case and thus the estimated ROA cannot be larger than that. In order to address this aspect, two strategies have been developed, and presented in [129]. Here only one approach is illustrated in detail.

The idea is to devise a relaxation of the sector IQC by exploiting the fact that the ROA inherently provides a bound on the values of the states of the system. The premise is sketched in Fig. 7.6, which shows the relationship between commanded ( $\delta_{eCMD}$ ) and saturated ( $\delta_e$ ) input. On the horizontal axis it is highlighted  $\delta_{eCMD}^{max} = Kq_{max}$ , where  $q_{max}$  denotes the largest value for which  $q$  belongs to the region of attraction. It is then apparent that the lower bound  $\sigma$  of the sector multiplier has nonzero value, specifically it holds  $\sigma = \frac{\delta_e^{sat}}{K} \frac{1}{q_{max}}$ . It is worth noting that a similar relaxation does not hold for the sector slope multiplier  $\Pi_{ZF}$  because regardless of the bound on  $\delta_{eCMD}$ , the slope of the saturation stays always within the sector  $[0, 1]$ .

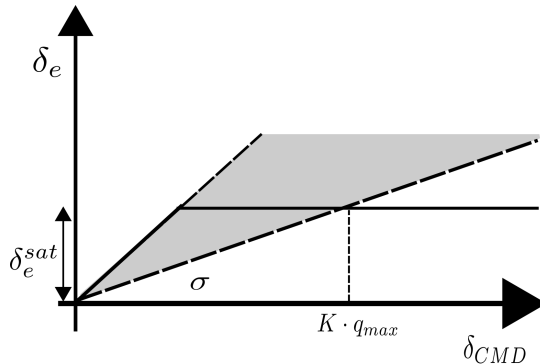


Figure 7.6: Relaxed sector constraint exploiting bounds on  $q_{max}$ .

In order to embed this relaxation in Algorithm 7.7 (a similar adaptation would hold for Algorithm 7.8),  $q_{max}$  is determined at the end of each iteration, and based on that the lower bound  $\sigma$  of the sector multiplier is updated. The expression of  $\Pi_S$  at iteration  $n+1$  is thus:

$$\Pi_S|^{n+1} = \Pi_S|_{\left[ \sigma = \frac{\delta_e^{sat}}{K} \frac{1}{q_{max}^{n+1}} ; \eta = 1 \right]}, \quad (7.50)$$

where the value  $q_{max}|^n$  can be computed at the end of iteration  $n$  with the following SOS program:

$$\begin{aligned} q_{max}|^n = \max_{s_{f_+}, s_{f_-} \in \Sigma[\tilde{x}]} q_{max}, \\ q + q_{max} - s_{f_+}(\gamma|^n - V|^n) \in \Sigma[\tilde{x}], \\ -q + q_{max} - s_{f_-}(\gamma|^n - V|^n) \in \Sigma[\tilde{x}]. \end{aligned} \quad (7.51)$$

This program is a direct application of Lemma 7.2 and guarantees that  $-q_{max}|^n \leq q|^n \leq q_{max}|^n$ . This strategy has the desired property that the sector employed at iteration  $n+1$  (function of  $q_{max}|^n$ ) is always consistent with the ROA computed at the same iteration. This results from the fact that the computed ROA is non-decreasing throughout the iterations, therefore  $q_{max}|^{n+1} \geq q_{max}|^n$ . The other strategy proposed in [129] consists of integrating in the program the lower bound of the sector  $\sigma$  as optimised variable.

The study here has formal similarities with that in Sec. 6.3.3 since both are concerned with less conservative IQC descriptions of hard-nonlinearities (of which freeplay and saturation are common examples). Despite the application to two different problems (in Chapter 6 LCO, while here inner estimates of the ROA), in both cases the adoption of the standard *global* approach would have been too restrictive, preventing in the former case to study the post-critical response and in here to quantify the effect of the controller on the local stability. These contributions thus aim at making IQC attractive for analyses where *local* descriptions are fundamental in order to obtain less conservative results.

Fig. 7.7 displays inner estimates of the ROA of the saturated GTM model obtained with Algorithm 7.7 and the discussed relaxation strategy. Three levels of saturation ( $\delta_e^{sat}=[0.05, 0.1, 0.2] \text{ rad}$ ) are considered, and the dynamic part of  $\Pi_{ZF}$  is parameterised with a low-pass filter with cross-over frequency  $1 \frac{\text{rad}}{\text{s}}$ . The open loop *OL* and unsaturated closed-loop *CL* cases are also reported for comparison. A quartic level set ( $\partial(V)=4$ ) is considered, and the shape matrix  $N=\text{diag}(8.16, 1.31)$  from [42] is employed to define the shape function  $p$ .

The first important observation is that the three curves obtained with the proposed approach are all larger than the *OL* one. It is also worth noting that the provided estimates of ROA depend on  $\delta_e^{sat}$ , which was not possible without the proposed relaxation. Specifically, as the value of  $\delta_e^{sat}$  is increased, the corresponding curves get closer to the unsaturated closed-loop, as expected.

A measure of the conservatism of the results is provided by means of extensive simulation campaigns. Fig. 7.7 shows three markers (asterisk for  $\delta_e^{sat}=0.05 \text{ rad}$ , cross for  $\delta_e^{sat}=0.1 \text{ rad}$ , and circle for  $\delta_e^{sat}=0.2 \text{ rad}$ ) corresponding to initial conditions for which the dynamics was found unstable, and the relative escaping trajectories in dashed-dotted lines. The inset allows to appreciate the small gap between markers and corresponding estimate of ROA, suggesting that the effect of saturation is well predicted by the proposed approach.

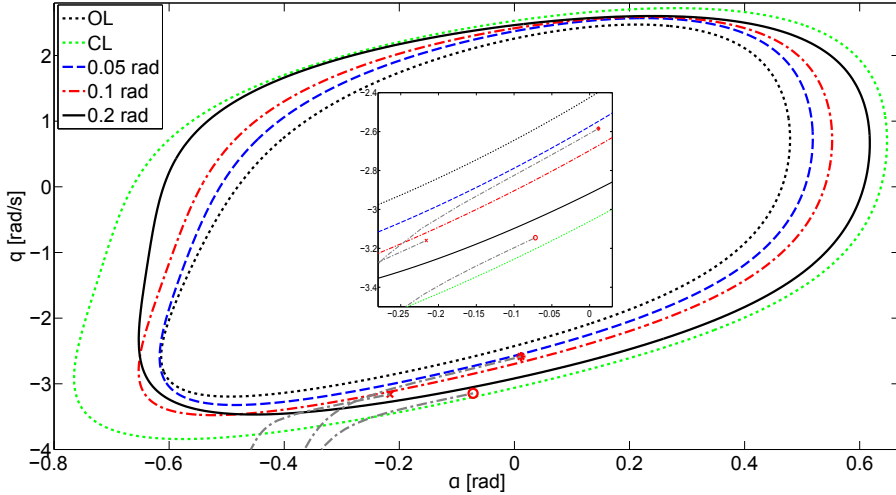


Figure 7.7: Estimates of the region of attraction for different saturation levels.

### 7.3.2.2 Uncertain Van der Pol oscillator

The Van der Pol oscillator is a polynomial nonlinear system with 2 states, often used as benchmark study in the ROA literature. The case with an uncertain scalar parameter  $\delta_1 \in [-1, 1]$  is taken from [241]:

$$\begin{aligned}\dot{x}_1 &= -x_2(1 + 0.2\delta_1), \\ \dot{x}_2 &= x_1 + (x_1^2 - 1)x_2.\end{aligned}\tag{7.52}$$

The steady-state solutions are characterised by an unstable limit cycle and a locally stable origin for the considered range of  $\delta_1$ . Note that the origin is an equilibrium point for all the values of the uncertainty, as it was assumed in the beginning. The ROA for this system is the region enclosed by the limit cycle and thus can be obtained from the numerical solution of (7.52) once the uncertain parameter is fixed.

The estimation of the ROA is performed exploiting the class of multipliers discussed in Sec. 6.1.2 for the case of real parametric uncertainties. The additional constraint  $H_v^\top M_{11} H_v > 0$  required from the factorisation (6.16) can be enforced without conservatism by means of KYP( $A_{H_v}, B_{H_v}, C_{H_v}, D_{H_v}, M_{11}$ ). This in turn can be expressed by Lemma 7.7 as an inequality involving the optimisation variables, and thus appended as an additional SOS constraint in the algorithms.

Fig. 7.8 shows the analyses with  $\partial(V) = 6$  and the shape function  $p = 0.378x_1^2 + 0.278x_2^2 - 0.274x_1x_2$  from [241]. Fig. 7.8(a) presents the results obtained with the *D-G* scalings multipliers (6.16), allowing to specify the nature of the uncertainty as real parameter but only providing soft IQCs, i.e. Algorithm 7.8 must be employed.  $H_v$  is parameterised as  $H_v = [1, \frac{1}{s+a_1}]$ , and the sensitivity of the results to the cross-over frequency  $a_1$  is investigated by showing two different curves, namely  $a_1=100$  (1 pole with frequency  $100 \frac{\text{rad}}{\text{s}}$ ) and  $a_1=1$  (1 pole with frequency  $1 \frac{\text{rad}}{\text{s}}$ ). For comparison purposes, the unstable limit cycles of the system corresponding to eight values of

$\delta_1$  across its range, labelled  $ROA(\delta_1)$ , are also reported. Fig. 7.8(b) shows the comparison between the estimates obtained with soft and hard IQCs. For the latter the hard factorisation  $(\Psi_\delta, M_D)$  is considered ( $D$  scalings), which captures  $\delta_1$  as an LTI uncertainty. This IQC description fulfils the assumption of Theorem 7.3 and thus allows to apply Algorithm 7.7.  $H_v$  is parameterised here with  $v = 1$  (and  $a_1 = 1 \frac{rad}{s}$ ).

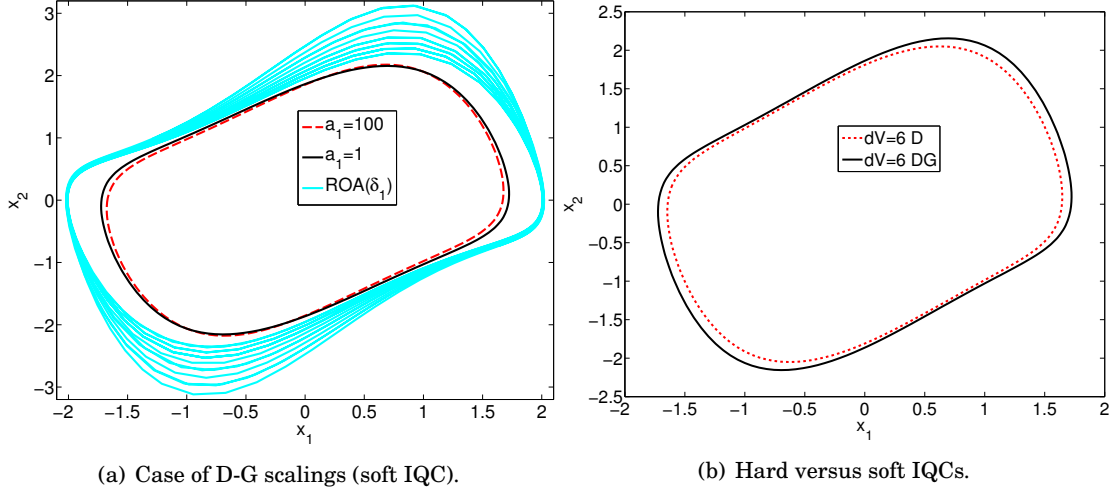


Figure 7.8: Estimates of the region of attraction for the uncertain Van der Pol oscillator.

In Fig. 7.8(a) the inner estimates of the ROA lie close to the smallest in size of the LCOs (which serve to provide upper bounds for the ROA of the uncertain system). Moreover, a sensitivity to the value of  $a_1$  can be detected. In fact, it was already shown in Sec. 6.3.2 that the parameterisation of the dynamic multipliers can be enhanced by placing the poles close to characteristic frequencies of the system. It is interesting to note that this is confirmed also in this case since the frequency of the unstable LCO is approximately  $1 \frac{rad}{s}$ , and the choice  $a_1 = 1 \frac{rad}{s}$  yields indeed an improvement in the estimation of the ROA.

As for Fig. 7.8(b), it can be noted that the estimation obtained with the  $D$ - $G$  scalings (specifying the nature of the uncertainty as real parameter) is the largest. This stresses once more the favourable effect of enriching the description of the uncertainties/nonlinearities with an appropriate selection of the IQCs. In addition, it motivates the importance of providing the main result also for the case of soft IQCs (Theorem 7.4). Finally, Table 7.3 reports a comparison in terms of computational statistics ( $N_{var}$  and  $N_{SDP}$  are respectively the number of decision variables and size of the Gram matrix for the most demanding steps of the two algorithms).

Since the variables optimised in the  $\gamma$ -Step of the two algorithms are the same, there is no difference for what concerns  $N_{var}$  and  $N_{SDP}$ . The soft IQC case features a small increment of variables in the  $V$ -Step, but this has barely an effect on the run time as noticeable from  $T_{iter}$ . Finally, a larger number of iterations was registered when using hard IQC. This is ascribed to a

Table 7.3: Computational statistics for the hard and soft IQCs

	$N_{var}$	$N_{SDP}$	$T_{iter}$ [s]	$N_{iter}$
Hard ( $D$ )	102	24025	31.6	50
Soft ( $DG$ )	102	24025	32.1	40

slow progress in the last iterations, which could be overcome adopting a stopping criterion (e.g. based on the increase of  $\beta$  during two successive iterations).

## 7.4 Chapter summary

This Chapter considers the problem of estimating the Region of Attraction of locally stable equilibria of nonlinear, and possibly uncertain, systems. Two distinct approaches are developed, which are connected with recent results in the literature.

First, a characterisation for nominal ROA analysis with positive invariant sets is adopted as the foundation for the proposal of improvements and extensions of this newly developed and less conservative framework. Two new iterative algorithms are devised to tackle the bilinearities arising when the set containments constraints are enforced as SOS conditions. The rationale underpinning the algorithmic choices is illustrated, and application to a numerical case study shows the advantages in terms of accuracy and computational time compared with the baseline algorithm. The other contribution of this section is the extension of the original result to the study of uncertain systems. The uncertainty set is described as a semialgebraic set and new stability certificates are derived based on the application of the generalised S-procedure. The dependence of the level set functions on the parameters, known to be a critical aspect, is addressed by exploiting the availability of two distinct functions. This solution is more numerically efficient than previous ones, and at the same time enhances the interpretation of the results by providing the region of stability as parameter-independent.

The goal considered next is the development of a framework able to deal with generic nonlinearities (i.e. not only polynomial) and to specify the class of uncertainty (in order to take into account in the estimation of the ROA only the actual perturbations affecting the system, and by doing so reduce conservatism). The proposed solution is to use IQC-based representations of nonlinear uncertain operators (well suited to enrich the description of the operator) in the dissipativity framework (allowing to include constraints for regional analysis), and for this the time-domain interpretation of IQC is leveraged. Since not every frequency-domain IQC has a hard factorisation (needed to use dissipativity arguments), certificates are provided for the distinct case of hard and soft IQC. In the latter case, a recent result providing a lower bound on the finite horizon integral is employed, and the possibility to use other (tighter) available results

is commented on. Iterative algorithms that allow to enlarge the provable invariant and attractive sets are then formulated and then applied to two case studies. The saturated closed-loop of a nonlinear short-period model is first considered, and a strategy to update the sector multiplier by combining it with the estimation of ROA is discussed. As done in Chapter 6 for the study of LCO, a local interpretation of IQC is suggested to obtain less conservative results and allow the study of a broader class of problems. In the second example, the effect of using  $D$  or  $D\text{-}G$  scalings multipliers to model real parametric uncertainties is investigated.

The relevance of ROA analysis to the nonlinear flutter problem has been motivated before, however no aeroelastic application, unlike in all the other Chapters, is shown here. The reason for that is twofold. A detailed presentation of the theoretical and algorithmic advances (e.g. properties of the invariant set and IQC approaches; rationale underlying the iterations; advantageous features of the formulations) has been privileged over an extended application section. In fact, only a restricted number of numerical examples to show the salient points of the approaches are discussed, and the overall quality of the work would have not been enhanced by the addition of analyses to simple case studies as the typical section. On the other hand, computational limitations of the available libraries for SOS optimisation must be acknowledged and would have prevented, at present, from applying the algorithms presented in the Chapter to more challenging aeroelastic problems. It is well known in the control community that an issue with the use of SOS is scalability, i.e. the significant growth in simulation time and corresponding decrease in computational efficiency as the size of the analysed system increases. This has stimulated the investigation of algorithmic strategies in Section 7.2, such as the adoption of different iteration schemes and the approximated polynomial descriptions of the uncertain semialgebraic sets. Indeed, providing alternative ways to solve the optimisation problem in case of failed solution is a possible way to prevent SOS related problems from hindering the estimation of the ROA. The research community is actively working on rigorous improvements to the well recognised issue of computational efficiency. For example, in [5] a method to decompose nonlinear dynamical systems into lower order ones and then compute the stability certificates on the latter is proposed. This method, suitable for systems which have a modular structure, can be further expedited if sparsity is imposed on the polynomials calculated for each subsystem. A survey on recent advances in SOS, covering also efficient ways to exploit sparsity, was recently presented in [1]. Another computationally promising strategy, also discussed in [1] and originally proposed in [2], is to relax the requirement that the Gram matrix  $Q$  is semidefinite with stronger but cheaper conditions, e.g. diagonally dominant and scaled diagonally dominant matrix. This has the benefit that the optimisation underpinning the determination of  $Q$  is a linear and a second order cone program respectively, in both cases more tractable than an SDP. These references (and those cited therein) show the potential for efficient advanced numerical tools which can make the SOS programs presented in this chapter more amenable for higher order systems, and thus aeroelastic applications, which are advised as possible future steps of the work.

## ROBUSTNESS FROM A DYNAMICAL SYSTEMS PERSPECTIVE

The two previous chapters have considered the problem of *quantitatively* assessing the detrimental effect of uncertainties on nonlinear phenomena. Examples are the increase of Limit Cycle Oscillation amplitude (Chapter 6) and the reduction of the size of the region of attraction (Chapter 7). A complementary approach, to which this chapter is devoted, consists of looking at whether uncertainties can determine *qualitative* changes in the response of the system (e.g. number and type of steady-state solutions).

Bifurcation theory is a well known tool to study the effect of parameters on the dynamics of nominal nonlinear systems. The typical approach is to select a few *bifurcation parameters*, equal in number to the codimension of the studied bifurcation (1 or 2 for the most common ones), based on their importance for the system. A classic example of bifurcation parameter for aeroelastic studies is the speed  $V$ . This analysis strategy, which uses numerical continuation to determine the type of equilibria and their stability as the parameters are varied, is beneficial since it allows complex dynamic behaviours to be characterised and an understanding of the system to be gained. However, it does not directly provide indications on the robustness of the results to uncertainties in the models. In fact, *uncertain parameters*, unlike the bifurcation parameters, in principle are not restricted in number, are allowed to vary simultaneously and their influence on the dynamics may not be known a priori. Examples of these parameters were discussed in the previous chapters and range from stiffness and mass parameters to aerodynamic coefficients. It is then important to predict whether, in the presence of uncertainties, bifurcations can occur at operating points cleared by nominal analyses.

The objective of this chapter is therefore to study robustness to qualitative changes in the steady-state solutions of an uncertain nonlinear system, and in this regard it provides an interpretation of robustness from a dynamical systems perspective. In particular, focus here is on

Hopf (or dynamic) bifurcations, where a stable branch of equilibria meets a branch of periodic solutions. This is the standard mechanism that leads to the onset of Limit Cycle Oscillations, a phenomenon amply discussed in Chapter 6 and closely related, in a nonlinear setting, to flutter.

To answer this question, the concept of robust bifurcation margins is proposed based on Linear Fractional Transformation (Chapter 3) and  $\mu$  analysis (Chapter 4). The core idea is to build an LFT model of the Jacobian of the uncertain vector field (which will generically depend on the states of the system and on the uncertainties) and to formulate the closest Hopf bifurcation as the worst-case perturbation matrix for which the LFT becomes singular. This bears similarities to the problem solved by  $\mu$ , but significant differences hold as will be stressed. The determination of the margins is posed as a nonlinear smooth optimisation problem, which also allows the type of Hopf bifurcation (subcritical or supercritical) to be specified. The issue of local minima, associated with the non-convexity of the optimisation, is discussed and different strategies are proposed to mitigate it. These include a continuation-based multi-start strategy based on the construction of a manifold of Hopf points connected to a given solution of the optimiser.

Section 8.1 provides a cursory overview of bifurcation and numerical continuation, whereas Section 8.2 addresses the technical contribution of the chapter. Section 8.3 finally demonstrates the application of the framework with the typical section system. Starting from the same (linear) case study analysed in Section 4.2, hardening plunge and pitch nonlinearities are added and the effect of different sets of uncertainties on the onset of supercritical and subcritical Hopf bifurcations are investigated. Interpretations of the results and an overview of the insights that can be gained by means of this analysis technique are also provided.

**Publications<sup>1</sup>:** [115].

## 8.1 Mathematical background

This section provides an introduction to the tools employed in the chapter, namely bifurcation theory (8.1.1) and numerical continuation (8.1.2). For a thorough description of these broad disciplines and their applications the reader is referred to the dedicated monographs [96, 99, 145]. The reader is referred to Section 3.1 for the background on LFT and  $\mu$ , which will also be central to the next section.

### 8.1.1 Bifurcation theory

Consider an autonomous nonlinear system of the form

$$\dot{x} = f(x, p), \quad (8.1)$$

where  $x \in \mathbb{R}^{n_x}$  and  $p \in \mathbb{R}^{n_p}$  are respectively the vectors of states and bifurcation parameters, and  $f : \mathbb{R}^{n_x} \times \mathbb{R}^{n_p} \rightarrow \mathbb{R}^{n_x}$  is the vector field. In this work  $f$  is assumed to gather smooth nonlinear

---

<sup>1</sup>Material published during the PhD which relates to the content of this chapter.

functions ( $f \in \mathcal{C}^\infty$ ), but bifurcation theory can also cope with the case of non-smooth vector fields [66, 68]. Therefore, the Jacobian matrix of the vector field  $\nabla_x f : \mathbb{R}^{n_x} \times \mathbb{R}^{n_p} \rightarrow \mathbb{R}^{n_x \times n_x}$ , denoted here by  $J$ , is always defined.

The vector  $x_0$  is called a fixed point or equilibrium of (8.1) corresponding to  $p_0$  if  $f(x_0, p_0) = 0$ . Let us denote with  $n_-$ ,  $n_0$ , and  $n_+$  the number of eigenvalues of  $J(x_0, p_0)$  with negative, zero, and positive real part, respectively. Then  $x_0$  is called a hyperbolic fixed point if  $n_0 = 0$ , otherwise it is called nonhyperbolic. Within the family of hyperbolic fixed points, if  $n_- = n_x$ , then  $x_0$  is a stable equilibrium (also called *sink*) whereas if  $n_- < n_x$  then  $x_0$  is an unstable equilibrium (also called *source*). Bifurcations of fixed points are concerned with the loss of hyperbolicity of the equilibrium as  $p$  is varied. Specifically, two scenarios can take place: static bifurcations and dynamic bifurcations [99, 145]. The former arise when  $J$  is singular at an equilibrium, i.e., it has a zero eigenvalue. The common feature of static bifurcations, which include saddle-node, pitchfork, and transcritical bifurcations, is that branches of fixed points meet at the bifurcation point. In the case of dynamic bifurcations, also referred to as Hopf bifurcation, branches of fixed points and periodic solutions meet. A bifurcation that requires at least  $c$  independent parameters to occur is called a codimension- $c$  bifurcation. The aforementioned bifurcations are all codimension-1.

The Hopf bifurcation is the focus of this chapter and is formally described by the following theorem.

**Theorem 8.1** ([99] Hopf bifurcation theorem). *Suppose that the system  $\dot{x} = f(x, p)$ ,  $x \in \mathbb{R}^{n_x}$  and  $p \in \mathbb{R}$  has an equilibrium  $(x_H, p_H)$  at which the following properties are satisfied:*

1.  *$J(x_H, p_H)$  has a simple pair of purely imaginary eigenvalues and no other eigenvalues with zero real parts. This implies, for the implicit function theorem, that there is a smooth curve of equilibria  $(x(p), p)$  with  $x(p_H) = x_H$ . The eigenvalues  $v(p)$ ,  $\bar{v}(p)$  of  $J(x(p))$ , with  $v(p_H) = i\omega_H$ , vary smoothly with  $p$ ;*
2. *and*

$$\frac{d}{dp} (\operatorname{Re} v(p))|_{p=p_H} = l_0 \neq 0. \quad (8.2)$$

*Then there is a unique three-dimensional centre manifold passing through  $(x_H, p_H)$  in  $\mathbb{R}^{n_x} \times \mathbb{R}$  and a smooth system of coordinates for which the Taylor expansion of degree 3 on the centre manifold is given in polar coordinates  $(\rho, \theta)$  by*

$$\begin{aligned} \dot{\rho} &= (l_0 p + l_1 \rho^2) \rho, \\ \dot{\theta} &= \omega + l_2 p + l_3 \rho^2, \end{aligned} \quad (8.3)$$

*where  $l_0$ ,  $l_1$ ,  $l_2$ , and  $l_3$  are real coefficients defining the manifold. If  $l_1 \neq 0$ , there is a surface of periodic solutions in the centre manifold which has quadratic tangency with the eigenspace of  $v(p)$ ,  $\bar{v}(p)$ . If  $l_1 < 0$ , then these periodic solutions are stable limit cycles, while if  $l_1 > 0$ , the periodic solutions are repelling.*

Note first that the theorem is stated considering a scalar  $p$  since the Hopf bifurcation is codimension-1. Condition 1 of Theorem 8.1 requires that the Jacobian of the vector field has a pair of purely imaginary eigenvalues (and no other eigenvalues on the imaginary axis). Condition 2, also known as the transversality condition, prescribes that these eigenvalues are not stationary with respect to  $p$  at the bifurcation. A fundamental parameter determining the dynamic behaviour in the neighbourhood of a Hopf point is  $l_1$ , also called the first Lyapunov coefficient. Its value determines whether the Hopf bifurcation is subcritical or supercritical, and its analytical expression is given by [145]:

$$l_1 = \frac{1}{2\omega_H} \operatorname{Re} \langle r, C(q, q, \bar{q}) - 2B(q, A^{-1}B(q, \bar{q})) + B(\bar{q}, (2i\omega_H I_n - A)^{-1}B(q, q)) \rangle. \quad (8.4)$$

Here the complex vectors  $r, q \in \mathbb{C}^{n_x}$  satisfy:

$$Jq = i\omega_H q, \quad J^\top r = -i\omega_H r, \quad \langle r, q \rangle = 1, \quad (8.5)$$

where  $\langle r, q \rangle$  is the scalar product in  $\mathbb{C}^{n_x}$ . The functions  $B : \mathbb{R}^{n_x} \times \mathbb{R}^{n_x} \rightarrow \mathbb{R}^{n_x}$  and  $C : \mathbb{R}^{n_x} \times \mathbb{R}^{n_x} \times \mathbb{R}^{n_x} \rightarrow \mathbb{R}^{n_x}$  are the tensors of second and third order derivatives evaluated at  $x_H$ , respectively. For example, for vectors  $\xi, \zeta, \chi \in \mathbb{R}^{n_x}$ ,  $B(\xi, \zeta)$  and  $C(\xi, \zeta, \chi)$  are in  $\mathbb{R}^{n_x}$  with components:

$$\begin{aligned} B_i(\xi, \zeta) &= \sum_{j,k=1}^{n_x} \left. \frac{\partial^2 f_i(x, p_0)}{\partial x_j \partial x_k} \right|_{x=x_H} \xi_j \zeta_k, \quad i = 1, 2, \dots, n_x, \\ C_i(\xi, \zeta, \chi) &= \sum_{j,k,l=1}^{n_x} \left. \frac{\partial^3 f_i(x, p_0)}{\partial x_j \partial x_k \partial x_l} \right|_{x=x_H} \xi_j \zeta_k \chi_l, \quad i = 1, 2, \dots, n_x. \end{aligned} \quad (8.6)$$

### 8.1.2 Numerical continuation

The computational tool of bifurcation analysis is numerical continuation [96], providing path-following algorithms allowing implicitly defined manifolds to be computed. These schemes are based on the implicit function theorem (IFT), which guarantees, under the condition that  $J$  is non-singular at an initial point  $(x_0, p_0)$ , that there exist neighbourhoods  $\mathcal{X}$  of  $x_0$  and  $\mathcal{P}$  of  $p_0$  and a function  $g : \mathcal{P} \rightarrow \mathcal{X}$  such that  $f(x, p) = 0$  has the unique solution  $x = g(p)$  in  $\mathcal{X}$ . In essence, the problem is to find:

$$x = g(p), \quad \text{such that } f(g(p), p) = 0, \quad (8.7)$$

with  $g : \mathcal{P} \rightarrow \mathcal{X}$ ,  $x_0 \in \mathcal{X}$ ,  $p_0 \in \mathcal{P}$ . Examples of numerical techniques to compute the implicit manifold  $g$  are Newton-Raphson, arclength, and pseudo-arclength continuation [96], efficiently implemented in freely available software, e.g., AUTO [72], MATCONT [65] and COCO [56].

Eq. (8.7) helps to clarify the substantial difference between the practice of linearising (8.1) around a fixed point  $(x_0, p_0)$ , common in various engineering applications, and the approach taken by bifurcation theory where linearisations along a curve  $g$  of fixed points are considered. In fact,  $g$  does not need to be computed explicitly, and is constructed numerically as  $p$  is continued, but it allows stability of the nonlinear system to be determined for finite ranges of  $p \in \mathcal{P}$ . In contrast,

the linearisation at a steady-state only gives information on the stability of the nonlinear system at the point where linearisation is performed (and, by continuity, in a neighbourhood of  $p_0$ ). It is also stressed that continuation applies not only to families of equilibria, but to steady-state solutions in general (e.g., branches of periodic solutions) and allows various types of codimension- $c$  bifurcations to be detected [27, 96].

A general continuation problem, so called *extended*, can be formulated as follows [56]:

$$F(u, \lambda) := \begin{pmatrix} \bar{\Phi}(u) \\ \bar{\Psi}(u) \end{pmatrix} - \begin{pmatrix} 0 \\ \lambda \end{pmatrix} = 0, \quad (8.8)$$

$$\bar{\Phi} : \mathbb{R}^{n_u} \rightarrow \mathbb{R}^m, \quad \bar{\Psi} : \mathbb{R}^{n_u} \rightarrow \mathbb{R}^{n_\lambda},$$

where  $\bar{\Phi}$  defines the zero problem in the vector  $u$  of continuation *variables*,  $\bar{\Psi}$  denotes a family of monitor functions and  $\lambda$  is a vector of continuation *parameters*. It is straightforward to see that the goal of tracking equilibria of the vector field  $f$  can be pursued by solving the zero problem only with  $\bar{\Phi} = f$ , and  $u = [x; p]$ . However, the extended continuation problem in (8.8) allows for a greater variety of problems to be solved, as the related concept of *restricted* continuation problem shows. Let  $\mathbb{I} \subseteq \{1, \dots, n_\lambda\}$  be an index set and  $\bar{\mathbb{I}}$  its complement in  $\{1, \dots, n_\lambda\}$ . Let  $\lambda_{\mathbb{I}} = \{\lambda_i | i \in \mathbb{I}\}$  and consider the restriction  $F(u, \lambda)|_{\lambda_{\mathbb{I}}=\lambda_{\mathbb{I}}^*}$  satisfying the IFT at some point  $(u^*, \lambda^* = \bar{\Psi}(u^*))$ . Then  $F(u, \lambda)|_{\lambda_{\mathbb{I}}=\lambda_{\mathbb{I}}^*}$  defines a continuation problem for a  $d$ -manifold with  $d = n_u - (m + |\mathbb{I}|)$ .  $\lambda_{\bar{\mathbb{I}}}$  and  $\lambda_{\mathbb{I}}$  are called the set of active and inactive continuation parameters respectively, since the former changes during continuation, while the latter remain constant. Analogously, equations corresponding to  $\lambda_{\bar{\mathbb{I}}}$  are inactive constraints, while equations corresponding to  $\lambda_{\mathbb{I}}$  are active constraints, because they impose an additional condition on the solutions to the set of zero problems. The formulation (8.8) is implemented in the software COCO, which is used for all the continuation analyses performed in this work.

Some of the previous works concerned with the application of bifurcation and continuation to aeroelastic problems are those from [69, 77, 95, 228].

## 8.2 Computation of robust bifurcation margins based on LFT and $\mu$

In this section the technical contribution of the chapter is presented. The addressed problem is formally defined in Section 8.2.1 and in Section 8.2.2 nonlinear optimisation programs are proposed to solve it. The step-by-step presentation, from Program 8.1, which calculates the *smallest* perturbations making the Jacobian unstable, to Program 8.4, which computes the closest subcritical and supercritical Hopf bifurcations, aims at clearly presenting the formulation of robust bifurcation margins. Finally, in Section 8.2.3 a novel multi-start strategy is developed, within the extended continuation paradigm, to mitigate the issue of local optima.

### 8.2.1 Problem statement

The objective of the work is to compute the margins of stable equilibria from the closest Hopf bifurcation for nonlinear systems affected by parametric uncertainties. The starting point is system (8.1) with  $n_p = 1$ . This is without loss of generality because the Hopf bifurcation is codimension-1 and thus 1 parameter is sufficient for its analysis (see Theorem 8.1). In fact, the case  $n_p > 1$  is typically handled by fixing  $n_p - 1$  parameters and continuing only 1.

Assume that the vector field  $f$  is subject to real parametric uncertainties gathered in the vector:

$$\delta = [\delta_1; \dots; \delta_i; \dots; \delta_{n_\delta}], \quad \delta \in \mathbb{R}^{n_\delta}. \quad (8.9)$$

This description allows the sources of uncertainty discussed in the previous chapters, e.g., lack of confidence on the values of model parameters or simplifying assumptions underlying the model, to be handled. The expression for the uncertain vector field  $\tilde{f}$  and associated Jacobian  $\tilde{J}$  is:

$$\dot{x} = \tilde{f}(x, p, \delta), \quad (8.10a)$$

$$\tilde{f} : \mathbb{R}^{n_x} \times \mathbb{R} \times \mathbb{R}^{n_\delta} \rightarrow \mathbb{R}^{n_x}, \quad \tilde{f} \in \mathcal{C}^\infty, \quad (8.10b)$$

$$\tilde{J} : \mathbb{R}^{n_x} \times \mathbb{R} \times \mathbb{R}^{n_\delta} \rightarrow \mathbb{R}^{n_x \times n_x}. \quad (8.10c)$$

Given a Hopf bifurcation point  $(x_H, p_H)$  for the nominal system  $f$ , and a value of the bifurcation parameter  $\bar{p}_0$  associated with a stable fixed point  $\bar{x}_0$  of  $f$ , the goal is to determine the *smallest* (or *worst-case*) perturbation  $\bar{\delta} \in \delta$  such that  $\tilde{f}$  undergoes a Hopf bifurcation at  $\bar{p}_0$ . In fact, it is relevant to distinguish between supercritical and subcritical Hopf bifurcations, hence two distinct worst-case perturbations will be considered. For the sake of readability, this distinction will be highlighted in the text when relevant but the notation used will be  $\bar{\delta}$  in both cases.

It is implied by the goal stated above the adoption of a metric for the magnitude of the perturbation, which allows the concept of worst-case to be formalised. Since the aim is to compute stability margins, the adopted metric should measure in some quantitative form (e.g. magnitude) the perturbation to which the system is subject. To this end, let us consider a generic uncertain parameter  $d$ , with  $\lambda_d$  indicating the uncertainty level with respect to a nominal value  $d_0$  and  $\delta_d \in [-1, 1]$  representing the normalised uncertain parameter. Note that  $d_0$  and  $\lambda_d$  are typically fixed by the analyst based on the knowledge of the nominal value and dispersion of the parameter  $d$  respectively. A multiplicative uncertain representation of  $d$  is thus obtained according to the definition provided in Eq. (3.4b) as:

$$d = (1 + \lambda_d \delta_d) d_0, \quad (8.11)$$

where  $\delta_d = 0$  corresponds to the nominal value of  $d$ , while  $\delta_d = \pm 1$  represents a perturbation at the extreme of the parameter range (e.g., a variation of  $\pm 20\%$  from  $d_0$  if  $\lambda_d = 0.2$ ). Once the normalisation (8.11) is applied to all the parameters in (8.9), a possible scalar metric (or norm) to quantify the magnitude of the perturbation is the largest of the absolute values of the elements

in  $\delta$ . This can be equivalently expressed as  $\bar{\sigma}(\text{diag}(\delta))$ , i.e., the maximum singular value of the diagonal matrix with elements of  $\delta$  on the diagonal. Such a metric quantifies the deviation of the uncertain parameters from their nominal values along the direction of the parameter space where this is largest. Specifically, the objective is to compute the perturbation vector with the smallest possible norm, providing therefore the distance from the closest Hopf bifurcation.

In fact,  $k_m = \bar{\sigma}(\text{diag}(\delta))$  can be regarded as a robust margin from bifurcation because  $k_m \leq 1$  means that a candidate (i.e., within the allowed range of the uncertainty set) perturbation exists which determines a Hopf bifurcation. Thus, the equilibrium  $\bar{x}_0$  of the nominal vector field is not robustly stable at  $\bar{p}_0$ . On the contrary, if  $k_m > 1$  then there is no perturbation inside the allowed set which is capable of prompting a Hopf bifurcation. This is pictorially represented in Figure 8.1, where on the x-axis is reported the bifurcation parameter and on the y-axis the margin  $k_m$  (note that the case  $\bar{p}_0 < p_H$  where a Hopf bifurcation is encountered by increasing  $p$  is assumed here without loss of generality). When the line  $k_m = 1$  is crossed, with  $p$  increasing, the system is operated in a region where Hopf bifurcations can occur in the face of the uncertainties accounted for in the system (shaded area).

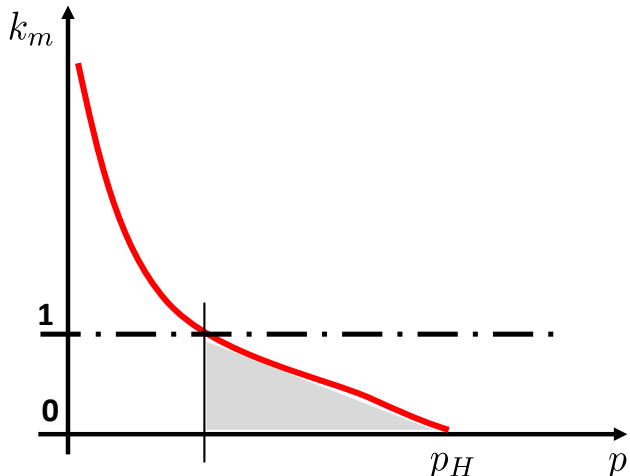


Figure 8.1: Concept of robust bifurcation margins.

### 8.2.2 Solution via nonlinear optimisation

The fundamental idea to address the stated objective is to exploit the interpretation of LFT as realisation technique discussed towards the end of Sec. 3.1.1 (see, for example, Fig. 3.2). Consider for a moment only Condition 1 of Theorem 8.1, which prescribes a pair of purely imaginary eigenvalues for the Jacobian. If  $\tilde{J}$  is interpreted as the uncertain state-matrix of the LTI case, an LFT model of the former with respect to the uncertain parameters in  $\delta$  can be built up (numerically or analytically [159]) and its singularity investigated. Recall then the connection

between singularity of an LFT and eigenvalues of the underlying system discussed with respect to Eq. (3.8) and Eq. (3.10) for the cases of nominal and uncertain LTI systems, respectively. The main difference from the linear case is that in general  $\tilde{J}$  is also a function of the states of the system  $x$ . This reflects the fact that in the nonlinear context uncertainties have a twofold effect on stability. They directly affect the matrix  $\tilde{J}$  as independent variables, but also indirectly by changing the location of the equilibrium (around which the vector field is linearised). The latter is a distinctive feature of the nonlinear setting, since in the linear case the location of the equilibrium does not have any effect on the spectrum of the state-matrix, and thus on stability.

The LFT of the Jacobian  $\mathcal{F}_u(M_{\tilde{J}}, \Delta)$  can then be written by making use of the generic definition of LFT given in Eq. (3.2) (the subscript of  $M$  emphasises that the uncertain Jacobian is considered here):

$$\mathcal{F}_u(M_{\tilde{J}}, \Delta) = \mathcal{F}_u(\mathcal{F}_u(M_{\tilde{J}}, \Delta_v), \Delta_x), \quad (8.12a)$$

$$\Delta = \text{diag}(\Delta_u, \Delta_x, \Delta_v), \quad M_{\tilde{J}} = [M_{\tilde{J}_{11}} M_{\tilde{J}_{12}}; M_{\tilde{J}_{21}} M_{\tilde{J}_{22}}], \quad (8.12b)$$

$$\Delta_u = \text{diag}(\delta_1 I_{d_1}, \dots, \delta_i I_{d_i}, \dots, \delta_{n_\delta} I_{d_{n_\delta}}), \quad (8.12c)$$

$$\Delta_x = \text{diag}(x_1 I_{x_1}, \dots, x_j I_{x_j}, \dots, x_{n_x} I_{x_{n_x}}), \quad (8.12d)$$

$$\Delta_v = \frac{1}{v} I_{n_x}, \quad v = i\omega, \quad (8.12e)$$

where (8.12a) exploits the property of interconnected LFTs, and  $\Delta_u$  is a particular instance of the structured uncertainty set defined in (3.3), where only real parameters are considered. Note that compared to the linear case (3.10),  $\Delta$  features now an additional block  $\Delta_x$ , which arises when performing the LFT modelling of  $\tilde{J}$  due to the discussed presence of the states, and for which a similar *structured* representation to the one adopted for  $\Delta_u$  is employed.  $\Delta_v$  finally restricts the attention to purely imaginary eigenvalues of  $\tilde{J}$  with frequency  $\omega$ .

Condition 1 of Theorem 8.1 can then be expressed as the singularity of the LFT (8.12a). This is the key step of the proposed extension from the linear context to the nonlinear one. Due to its centrality for the discussion, let us recall here a possible definition of  $\mu$  (previously given in Eq. (3.11)):

$$\mu_{\Delta}(M) = \left[ \min_{\Delta_u, \Delta_v} (\kappa : \mathcal{F}_u(\mathcal{F}_u(M, \Delta_v), \kappa \Delta_u) \text{ is singular; } \bar{\sigma}(\Delta_u) \leq 1) \right]^{-1}. \quad (8.13)$$

Note that  $\mu$  computes the worst-case (or smallest) perturbation matrix  $\Delta_u$  which makes the LFT ill-posed, and thus the associated LTI system neutrally stable. Moreover, in Eq. (8.13) the same metric as the one used to define the robust bifurcation margin  $k_m$  is employed. It follows indeed from the definitions and properties illustrated earlier that  $k_m = \bar{\sigma}(\text{diag}(\delta)) = \bar{\sigma}(\Delta_u)$ . Specifically,  $k_m$  is an *analogue* of the reciprocal of  $\mu$  and it has been adopted here because of its straightforward meaning of distance (or margin) to the onset of a bifurcation. Note in this regard that the symbol  $k_m$  was used in the early stages of robust control with the name of *excess stability margin* [208, 209].

The discussion above paves the way for the program presented next, which aims to compute the smallest perturbation for which  $\tilde{J}$  has a pair of purely imaginary eigenvalues.

**Program 8.1.**

$$\min_X k_m \quad \text{such that} \quad \begin{cases} \tilde{f}(x, \bar{p}_0, \delta) = 0, \\ \mathcal{F}_u(M_{\tilde{J}}, \Delta) \text{ is singular}, \end{cases} \quad (8.14a)$$

$$\bar{\sigma}(\Delta_u) \leq k_m, \quad (8.14b)$$

$$X = [x; \delta; \omega], \quad (8.14c)$$

$$X = [x; \delta; \omega],$$

where  $X$  is the vector of optimisation variables including: states  $x$ ; uncertain parameters  $\delta$ ; and frequency  $\omega$ .  $\hat{X}$  will indicate the solution vector gathering  $\hat{x}$ ,  $\hat{\delta}$ , and  $\hat{\omega}$  respectively. Let us examine the constraints of the program. Eq. (8.14a) guarantees that the solution  $(\hat{x}, \hat{\delta})$  corresponds to an equilibrium point for the system. Eq. (8.14b) ensures that  $\tilde{J}$  has a pair of complex eigenvalues  $\nu = \pm \hat{\omega}$ , and Eq. (8.14c) bounds the size of the perturbation matrix.

This is a similar optimisation problem to that in (8.13), with two crucial differences: constraint (8.14a), and the addition of  $\Delta_x$  in the block  $\Delta$  of  $\mathcal{F}_u(M_{\tilde{J}}, \Delta)$  (to which, notably, the constraint in Eq. (8.14c) does not apply). Due to these differences, available algorithms for  $\mu$  cannot be applied to compute solutions of (8.14), thus alternative ways should be pursued.

Let us examine closely (8.14b), and recall from Eq. (3.2) that a necessary and sufficient condition for the well-posedness of an LFT is the existence of the inverse of a matrix. Specifically,  $\mathcal{F}_u(M_{\tilde{J}}, \Delta)$  is singular if and only if  $\det(I - M_{\tilde{J}11}\Delta) = 0$ , which can be recast, once an LFT model of  $\tilde{J}$  is available, as a nonlinear constraint in the variables  $X$ .

As for (8.14c), this is a non-smooth constraint because of the maximum singular value operator, but it can be drastically simplified by exploiting the structure of  $\Delta_u$  (8.12c). Indeed, this constraint is equivalent to:

$$-k_m \leq \delta_i \leq k_m, \quad i = 1, \dots, n_\delta, \quad (8.15)$$

which is a set of linear inequalities in the optimisation variables and the objective function  $k_m$ . Note that a similar relaxation would hold also for complex scalar uncertainties, not considered in this work.

Based on the previous discussion, the following smooth nonlinear optimisation problem is proposed to solve Program 8.1.

**Program 8.2.**

$$\min_X k_m \quad \text{such that} \quad \begin{cases} \tilde{f}(x, \bar{p}_0, \delta) = 0, \end{cases} \quad (8.16a)$$

$$\det(I - M_{\tilde{J}11}\Delta) = 0, \quad (8.16b)$$

$$-k_m \leq \delta_i \leq k_m, \quad i = 1, \dots, n_\delta, \quad (8.16c)$$

$$X = [x; \delta; \omega].$$

The key idea behind Program 8.2 is to enforce singularity of the LFT (8.14b) by using directly the determinant condition represented by constraint (8.16b). In [206] this is listed among the methods for the computation of  $\mu_{LB}$ , and examples of related algorithms can be found in [103, 261]. The approaches presented in those works, however, are limited to the case of linear systems, i.e., they represent alternatives to well-established  $\mu$  lower bounds algorithms such as the power iteration [182] and the gain-based method [219]. To the best of the author's knowledge, this is indeed the first time that the concept of structured singular value is used in the context of worst-case bifurcations of a nonlinear vector field. Moreover, Program 8.2 recasts the optimisation so that the objective function and the constraints are smooth. This differs from the aforementioned works where the optimisation was performed by minimizing the nonsmooth function  $\bar{\sigma}(\Delta_u)$ . This is overcome here by considering the relaxation resulting in (8.15) and introducing the objective function  $k_m$  as an additional optimisation variable.

**Remark 8.1.** *Constraint (8.16b) consists of two (real and imaginary parts of the determinant) nonlinear equality constraints in the variables  $X$ . By using Laplace expansion of the determinant [11] and the fact that  $\Delta$  is structured, an analytical expression for the gradient of (8.16b) with respect to  $\delta$  and  $x$  can be obtained and provided to the optimiser. As for  $\omega$ , this is more tedious and therefore finite differences are employed.*

*Note also that, from a numerical continuation perspective, (8.16b) can be regarded as an analogue of the real scalar test functions commonly used to detect Hopf bifurcations [27]. The latter can be efficiently formulated by means of bordered matrices techniques and have the property that the test function has a zero at a bifurcation point. The main difference here is that (8.16b) is complex, thus consists of two real scalar equations. This is due to the fact that the frequency  $\omega$  of the purely imaginary eigenvalues appear explicitly in the constraint (and thus is an additional independent variable), which is different from the test functions formulation. This is an advantageous feature of the developed approach, and possible ways to exploit it are discussed later.*

### 8.2.2.1 Enforcing the transversality condition

Program 8.2 allows worst-case perturbations to be computed such that the Jacobian of  $\tilde{f}$  linearised around the perturbed equilibrium point has a pair of purely imaginary eigenvalues. This, however, does not mathematically guarantee that the perturbed system undergoes a Hopf bifurcation because transversality (Condition 2 of Theorem 8.1) is not automatically verified. Constraints guaranteeing that transversality is satisfied can be appended to (8.16) in different ways, including using test functions [27] or automatic differentiation [112]. Here an approach leveraging the versatility of the LFT paradigm is proposed. Consider a small fixed constant  $\epsilon_p$  which defines the perturbed bifurcation parameter  $\bar{p}_{\epsilon_p} = (1 + \epsilon_p)\bar{p}_0$ . The LFT  $\mathcal{F}_u(M_{\tilde{J}}^\epsilon, \Delta^\epsilon)$  of the Jacobian at  $\bar{p}_{\epsilon_p}$  can

be written, following Eq. (8.12), as:

$$\mathcal{F}_u \left( M_{\tilde{J}}^\epsilon, \Delta^\epsilon \right) = \mathcal{F}_u \left( \mathcal{F}_u \left( M_{\tilde{J}}^\epsilon, \Delta_v^\epsilon \right), \Delta_x^\epsilon \right), \quad (8.17a)$$

$$\Delta^\epsilon = \text{diag}(\Delta_u, \Delta_x^\epsilon, \Delta_v^\epsilon), \quad M_{\tilde{J}}^\epsilon = \begin{bmatrix} M_{\tilde{J}_{11}}^\epsilon & M_{\tilde{J}_{12}}^\epsilon \\ M_{\tilde{J}_{21}}^\epsilon & M_{\tilde{J}_{22}}^\epsilon \end{bmatrix}, \quad (8.17b)$$

$$\Delta_x^\epsilon = \text{diag}((1 + \epsilon_x)x_1 I_{x_1}, \dots, (1 + \epsilon_x)x_j I_{x_j}, \dots, (1 + \epsilon_x)x_{n_x} I_{k_{n_x}}), \quad (8.17c)$$

$$\Delta_v^\epsilon = \frac{1}{v^\epsilon} I_{n_x}, \quad v^\epsilon = \epsilon_v + (1 + \epsilon_\omega)\omega, \quad (8.17d)$$

where  $\epsilon_v$ ,  $\epsilon_x$ , and  $\epsilon_\omega$  are unknown scalars described later. The following optimisation problem is then proposed to determine the worst-case perturbation for which both conditions of the Hopf theorem are guaranteed to hold, that is, to rigorously calculate the margins to the closest Hopf bifurcation point.

### Program 8.3.

$$\min_X k_m \quad \text{such that} \quad \begin{cases} \tilde{f}(x, \bar{p}_0, \delta) = 0, & (8.18a) \\ \det(I - M_{\tilde{J}_{11}} \Delta) = 0, & (8.18b) \\ -k_m \leq \delta_i \leq k_m, & i = 1, \dots, n_\delta, \\ \tilde{f}((1 + \epsilon_x)x, \bar{p}_{\epsilon_p}, \delta) = 0, & (8.18d) \\ \det(I - M_{\tilde{J}_{11}}^\epsilon \Delta^\epsilon) = 0, & (8.18e) \end{cases} \quad (8.18c)$$

$$X = [x; \delta; \omega; \epsilon_v; \epsilon_x; \epsilon_\omega].$$

The first set of constraints (8.18a-8.18c) is identical to those in Program 8.2. The constraints (8.18d-8.18e) additionally ensure that the Jacobian linearised at  $\bar{p}_{\epsilon_p}$  has an eigenvalue  $v^\epsilon$  with real part  $\epsilon_v$  (8.17d). Making use of a finite difference approximation, it follows from the definition in (8.2) that  $l_0 = \frac{\epsilon_v}{\epsilon_p}$ . Therefore, existence of a solution to Program 8.3 with  $\hat{\epsilon}_v \neq 0$  guarantees a Hopf bifurcation for the system.

Underlying Program 8.3 there is a perturbation argument which builds on the application of the IFT to the states  $x$  and the eigenvalue  $v$  of the vector field  $\tilde{f}(x, p, \hat{\delta})$  for fixed  $\hat{\delta}$  and  $p$  in a neighbourhood of  $\bar{p}_0$ . Indeed, at  $p = \bar{p}_0$ , it holds  $x = \hat{x}$  and  $v = i\hat{\omega}$  for the constraints (8.18a-8.18c). When perturbing  $p$  by a small increment  $\epsilon_p$ , a first order approximation for  $x$  and  $v$  is assumed, and reflected in the choice of the scalars  $\epsilon_x$  (8.17c), as well as  $\epsilon_\omega$  and  $\epsilon_v$  (8.17d). A vector  $\epsilon_x$ , with an element for each component of  $x$ , could also be considered, by adding  $n_x - 1$  unknowns to Program 8.3.

**Remark 8.2.** *Program 8.2 does not guarantee the onset of a Hopf bifurcation because it does not take into account the transversality condition, and for this reason Program 8.3 is proposed. However, for engineering systems where  $p$  has a physical meaning (as it is the case for speed in aeroelasticity) the transversality condition is often automatically verified. In fact, the problem was stated in Sec. 8.2.1 assuming that the nominal system has a bifurcation at  $p_H$  whereas for  $p = \bar{p}_0$*

*the system has a stable equilibrium. It is thus implicit in the formulation of the problem that a change of  $p$  has an effect on the stability of the system. In particular, it is expected that the critical eigenvalues of the perturbed Jacobian will cross the imaginary axis as  $p$  is perturbed around  $\bar{p}_0$  (hence satisfying the transversality).*

*Even though Program 8.3 only barely increases the computational cost, a strong reason to resort to Program 8.2 whenever possible is related to the local optimality of the solutions of nonlinear programs. This issue will be further discussed in Sec. 8.2.3, but it is remarked here that the addition of the constraints (8.18d-8.18e) has a detrimental effect on it. Indeed, it is always advisable in nonlinear optimisation to avoid redundant constraints in order to reduce the likelihood of local optima [172]. Based on these considerations, the proposed strategy is to employ Program 8.2 to find robust bifurcation margins and, if continuation analysis of the perturbed system show that the transversality condition is not fulfilled, use Program 8.3. It is noted that none of the analyses done in this thesis required the adoption of Program 8.3 (which however was tested to verify its soundness). For this reason, and also for the sake of clarity, in the remainder of the work Program 8.2 will be considered as basis for discussion.*

### 8.2.2.2 Specifying the type of closest Hopf bifurcation

The robust bifurcation margin  $k_m$  has been associated so far with the occurrence of a generic Hopf bifurcation. Attention is now focused on the nature of the bifurcation, i.e., subcritical or supercritical. The idea is to add to the constraints of Program 8.2 a condition on the sign of the Lyapunov coefficient  $l_1$ . This can be done by using the definition of  $l_1$  (8.4), which requires the computation of left and right eigenvectors associated with the critical eigenvalue, and the tensors of second and third order derivative. By exploiting the fact that  $\omega$  is an optimisation variable, the eigenvectors can be computed without performing an eigenvalue analysis, but by direct computation as follows:

$$\begin{aligned} (\tilde{J} - i\omega I_{n_x})q &= 0; \quad q = [1; q_l], \\ (\tilde{J}^\top + i\omega I_{n_x})r &= 0; \quad r = [1; r_l], \\ \langle r, q \rangle &= 1, \end{aligned} \tag{8.19}$$

where without loss of generality the first element of the eigenvectors has been fixed to 1. As for the tensors, the derivatives in (8.6) can be computed analytically in simple cases and by automatic or symbolic differentiation for more complex ones. Alternatively, in [145] efficient strategies to avoid computing second and third order derivatives of the vector field are discussed. In any case, they are available as a function of the optimisation variables  $x$  and  $\delta$ , and thus there is no addition to the vector of unknowns  $X$ .

In conclusion, given a positive tolerance  $\epsilon_l$  on the value of the Lyapunov coefficient, and an integer  $s_l = \pm 1$  defining the sign of  $l_1$  ( $s_l = 1$  for subcritical and  $s_l = -1$  for supercritical), the following program allows the closest subcritical or supercritical Hopf bifurcation to be computed.

**Program 8.4.**

$$\min_X k_m \quad \text{such that} \quad \begin{cases} \tilde{f}(x, \bar{p}_0, \delta) = 0, \\ \det(I - M_{\tilde{J}11}\Delta) = 0, \\ -k_m \leq \delta_i \leq k_m, \quad i = 1, \dots, n_\delta, \\ s_l l_1 - \epsilon_l > 0, \end{cases} \quad \begin{aligned} (8.20a) \\ (8.20b) \\ (8.20c) \\ (8.20d) \end{aligned}$$

$$X = [x; \delta; \omega].$$

### 8.2.3 Continuation-based multi-start strategy

The programs discussed in Sec. 8.2.2 allow margins to Hopf bifurcation for a nominally stable equilibrium point in the face of uncertainties to be computed. The main issue with this approach is that, due to the fact that the optimisation is non-convex, there is no guarantee that the one found is the closest bifurcation, and thus only upper bounds on  $k_m$  are possibly computed. In other words, the global minimum might be missed and thus there could be a perturbation vector with a smaller norm than  $\hat{\delta}$  which causes a Hopf bifurcation. Local optima are a well known issue in nonlinear optimisation and, despite the large amount of research done on this topic, no standard solutions are available [91, 172].

#### 8.2.3.1 Local minima

Mitigation strategies depend on several aspects, including specific features of the program (constraints, objective functions) and adopted optimisation algorithms. For this problem the objective is to compute worst-case perturbations quantified by means of a scalar metric, thus a possible way to account for this issue is to estimate a guaranteed smallest magnitude of the perturbation for which the system is stable. This is the approach taken in  $\mu$  analysis, where the computation of  $\mu_{LB}$  is known to be prone to local minima and as a remedy upper bounds  $\mu_{UB}$  have been proposed. Lower bounds on  $k_m$  (nonlinear analogues of  $\mu_{UB}$ ) could then be a strategy, but this has not been pursued here and is a topic for future research. Note that a preliminary step in this direction could be the approach used in Sec. B.1.2 in the context of the equilibrium-independent ROA to define regions of the state space where the equilibria are guaranteed to satisfy certain properties (see Remark B.3).

As for the optimisation algorithms, the focus of this work is not on developing ad-hoc advanced optimisation strategies, hence off-the-shelf algorithms are employed, specifically the ones available in the MATLAB routine *fmincon* [165] for nonlinear constrained problems. These include: *interior point*, which solves the constrained problem using a sequence of unconstrained optimisations by using barrier or penalty functions to account for the constraints; *active set* and *sqp*, belonging to the class of sequential quadratic programming, which solve directly the constrained problem via a series of approximating quadratic programming based on the Karush-Kuhn-Tucker equations (necessary conditions for optimality of constrained optimisation problems). Leveraging

the availability of solvers based on different optimisation methods, a strategy employed in the work is to restart the programs using different solvers.

Another good practice to reduce the likelihood of local minima is to formulate the problem in the *simplest* way possible [172], e.g., using smooth objective functions and constraints and avoiding redundant constraints. These two principles have guided the idea of introducing the objective function  $k_m$  to relax the non-smooth bound on the uncertainty set involving  $\bar{\sigma}$ , which lead to the equivalent constraints (8.15). Moreover, the aim of simplifying the set of constraints as much as possible prompted the discussion in Remark 8.2, where it was proposed (based on a physically motivated assumption) to resort to Program 8.3 only if the solution does not satisfy the transversality condition.

A strategy which exploits a distinctive feature of this formulation is to run Program 8.2 at a given frequency, i.e.,  $\omega$  does not belong to  $X$  but is fixed a priori. The rationale behind this is twofold. From a mathematical point of view, the optimisation is simplified by the fact that constraint (8.16b) does not depend on the frequency and this enhances the accuracy of the result. From a bifurcation perspective, fixing the frequency restricts the mechanisms by which the system can undergo a Hopf bifurcation when subject to uncertainties, which reduces the number of feasible solutions in the first place, and as a result makes it also more likely to detect the optimal one. A value of  $k_m$  can be associated with each discrete frequency, and the smallest of these values is the most critical. A natural drawback of this approach is that critical frequencies can be missed, but this can be overcome by running subsequently Program 8.2 with  $\omega$  as optimisation variable and initializing it with values corresponding to the critical solution.

### 8.2.3.2 Application of the extended continuation paradigm

Despite these measures, the risk of falling into local minima is still present and particularly the programs' initialisation represents a critical aspect. For this reason, an original solution consisting of a continuation-based multi-start strategy is developed to allow multiple solution branches to be identified. Assume that the optimiser has found a solution  $\hat{X}$  to Program 8.2 (the same rationale would apply to Program 8.4). The goal is then to provide the optimiser with a set of initialisations, derived from  $\hat{X}$  but possibly not leading the optimiser to find the same solution, which allows an exhaustive optimisation campaign to be performed. The following extended continuation problem based on the constraints of Program 8.2 is first considered:

$$F(x, \delta, \omega, \lambda_d, \lambda_k) = \begin{pmatrix} \tilde{f}(x, \bar{p}_0, \delta) \\ \det(I - M_{\bar{J}_{11}} \Delta) \\ \bar{\sigma}(\Delta_u) \end{pmatrix} - \begin{pmatrix} 0 \\ \lambda_d \\ \lambda_k \end{pmatrix} = 0. \quad (8.21)$$

This can be recast in the formalism of (8.8) by setting:

$$\begin{aligned}
 u &= X = [x; \delta; \omega], \quad u \in \mathbb{R}^{n_u}, \quad n_u = n_x + n_\delta + 1, \\
 \lambda &= [\lambda_d; \lambda_k], \quad \lambda_d \in \mathbb{R}^2, \quad \lambda_k \in \mathbb{R}^1, \\
 \bar{\Phi} &= \tilde{f}(x, \bar{p}_0, \delta), \quad \bar{\Phi} : \mathbb{R}^{n_u} \rightarrow \mathbb{R}^{n_x}, \\
 \bar{\Psi} &= [\det(I - M_{\tilde{J}} \Delta); \bar{\sigma}(\Delta_u)], \quad \bar{\Psi} : \mathbb{R}^{n_u} \rightarrow \mathbb{R}^3, \\
 F &: \mathbb{R}^{n_x + n_\delta + 3} \rightarrow \mathbb{R}^{n_x + 3}.
 \end{aligned} \tag{8.22}$$

Let  $\mathbb{I} = \{1, 2\}$  and  $\bar{\mathbb{I}} = \{3\}$  be its complement, with  $\lambda_{\mathbb{I}} = \{\lambda_i | i \in \mathbb{I}\}$  and  $\lambda_{\bar{\mathbb{I}}} = \{\lambda_i | i \in \bar{\mathbb{I}}\}$ , and  $u^* = \hat{X}$ ,  $\lambda^* = \bar{\Psi}(u^*)$ . By construction, the restriction  $F(u^*, \lambda)|_{\lambda_{\mathbb{I}}=\lambda_{\mathbb{I}}^*} = 0$  and  $F(u, \lambda)|_{\lambda_{\mathbb{I}}=\lambda_{\mathbb{I}}^*}$  satisfies the IFT at  $(u^*, \lambda^*)$ . Therefore,  $F(u, \lambda)|_{\lambda_{\mathbb{I}}=\lambda_{\mathbb{I}}^*}$  defines a continuation problem for the  $d$ -manifold with  $d = n_x + n_\delta + 1 - (n_x + 2) = n_\delta - 1$ . Note that  $\lambda_{\mathbb{I}}$  (coinciding with  $\lambda_d$ ) are inactive continuation parameters (corresponding to active constraints) because they are kept constant during continuation and they ensure the singularity of the LFT  $\mathcal{F}_u(M_{\tilde{J}}, \Delta)$ . Since  $\lambda_d^* = 0$ , the corresponding active constraints could have been equivalently embedded in the zero function  $\bar{\Phi}$  but, for consistency with the parallel between  $f$  and  $\bar{\Phi}$  discussed in Sec. 8.1.2, this has been used for the vector field only. On the other hand,  $\lambda_{\bar{\mathbb{I}}}^*$  (i.e.,  $\lambda_k$ ) corresponds to an inactive monitor function bookkeeping the magnitude of the perturbation at each step of the continuation.

The manifold associated with (8.21), denoted here by  $\mathcal{H}$ , represents the set of Hopf bifurcation points *connected* to the solution  $\hat{X}$  in the uncertain parameter space. A first important observation is that the dimension of  $\mathcal{H}$  is  $n_\delta - 1$ . This is in agreement with the well known fact [27] that a branch (i.e., 1-dimensional manifold) of Hopf points can be obtained by continuing simultaneously two parameters starting from a known initial point. Indeed, in the case of two uncertainties ( $n_\delta = 2$ )  $\mathcal{H}$  is the branch of Hopf points connected to the initial solution  $\hat{X}$ .

### 8.2.3.3 Parameterisation of the manifold

In principle, the computation of  $\mathcal{H}$  could directly locate bifurcation points associated with perturbations featuring a smaller magnitude than  $\hat{\delta}$  by monitoring  $\lambda_k$  (note however that they could still be local optima since only the connected branches can be tracked). Moreover, exploring the *surroundings* of  $\hat{X}$  (using a continuation meaning of this terminology) can provide the sought initialisation points for a new optimisation campaign. Unfortunately,  $\mathcal{H}$  is generally multidimensional. In fact, it is reasonable to assume that even for a relatively small number of uncertainties computing  $\mathcal{H}$  is not viable. To overcome this, a 1-dimensional restriction of  $\mathcal{H}$  is constructed by considering a parameterisation of the uncertainty set  $\delta$  with a vector function  $g(z, y) : \mathbb{R}^2 \rightarrow \mathbb{R}^{n_\delta}$ , where the 2 independent variables  $z$  and  $y$  have been introduced. The definition of  $g$  is arbitrary and various strategies can be pursued. The approach taken here assumes that two solutions  $\hat{X}^1$  and  $\hat{X}^2$  from Program 8.2 are available (their selection will be assessed later).

Given the associated perturbation vectors  $\hat{\delta}^1$  and  $\hat{\delta}^2 \in \mathbb{R}^{n_\delta}$ , a possible choice for  $g$  is then:

$$g(z, y) : \mathbb{R}^2 \rightarrow \mathbb{R}^{n_\delta} \begin{cases} \hat{\delta}_1^1 z + \hat{\delta}_1^2 (1 - y), \\ \dots \\ \hat{\delta}_i^1 z + \hat{\delta}_i^2 (1 - y), \\ \dots \\ \hat{\delta}_{n_\delta}^1 z + \hat{\delta}_{n_\delta}^2 (1 - y). \end{cases} \quad (8.23)$$

Note that by construction  $g(1, 1) = \hat{\delta}^1$  and  $g(0, 0) = \hat{\delta}^2$ . Based on this, the following continuation problem is formulated:

$$F(x, \delta, \omega, z, y, \lambda_d, \lambda_k, \lambda_g) = \begin{pmatrix} \tilde{f}(x, \bar{p}_0, \delta) \\ \det(I - M_{\tilde{J}11}\Delta) \\ \bar{\sigma}(\Delta_u) \\ \delta - g(z, y) \end{pmatrix} - \begin{pmatrix} 0 \\ \lambda_d \\ \lambda_k \\ \lambda_g \end{pmatrix} = 0. \quad (8.24)$$

With respect to the definitions in (8.22),  $z$  and  $y$  have been added to the vector of continuation variables  $u$  (i.e.,  $u = [X; z; y]$ ), while the vector function  $\delta - g$  has been added to the family of monitor functions  $\bar{\Psi}$  (with associated continuation parameters  $\lambda_g \in \mathbb{R}^{n_\delta}$ ).

Let  $\mathbb{I} = \{1, 2, 4, \dots, 4 + n_\delta\}$ , and  $\bar{\mathbb{I}}$ ,  $\lambda_{\mathbb{I}}$ ,  $\lambda_{\bar{\mathbb{I}}}$  as before. Two starting points are available, respectively  $u^* = [\hat{X}^1; 1; 1]$  and  $u^* = [\hat{X}^2; 0; 0]$ , with  $\lambda^* = \bar{\Psi}(u^*)$ . Note that in both cases  $\lambda_g^* = \bar{\Psi}(u^*) = 0$  by construction. Therefore,  $\delta = g(z, y)$  at each step of the continuation, and  $\delta$  is expressed as a linear combination of  $\hat{\delta}^1$  and  $\hat{\delta}^2$ .

Since  $F(u, \lambda)|_{\lambda_{\mathbb{I}}=\lambda_{\mathbb{I}}^*} = 0$  and  $F(u, \lambda)|_{\lambda_{\bar{\mathbb{I}}}=\lambda_{\bar{\mathbb{I}}}} = 0$  satisfies the IFT at  $(u^*, \lambda^*)$ , then a manifold  $\mathcal{H}_g$  with dimension  $d = n_x + n_\delta + 3 - (n_x + 2 + n_\delta) = 1$  is defined. Crucially, the dimension is 1 irrespective of the number of uncertainties  $n_\delta$ , with the drawback that these are now constrained to vary according to (8.23).  $\mathcal{H}_g^1$  and  $\mathcal{H}_g^2$  indicate the manifold built starting from  $[\hat{X}^1; 1; 1]$  and  $[\hat{X}^2; 0; 0]$  respectively, with the subscript and the superscript highlighting the dependence on the parameterisation of the uncertainties  $g$  and the initial point.

The construction of  $\mathcal{H}_g$  requires two perturbation vectors  $\hat{\delta}^1$  and  $\hat{\delta}^2$ . This is not restrictive, since as a result of the local optimality typically more than one solution is available. In addition, the possibility of running the optimisation at a fixed frequency  $\omega$  can be advantageously exploited with the goal of obtaining different *modes* of perturbations. Indeed, as discussed before, Hopf bifurcations occurring at different frequencies could represent different mechanisms underlying the loss of stability, thus considering a linear combination of the perturbations as in (8.23) represent an efficient strategy to select points on  $\mathcal{H}_g$ .

To sum up the multi-start strategy approach, the starting point is Program 8.2 which provides a solution consisting of an equilibrium point  $\hat{x}$  of  $\tilde{f}$  perturbed by  $\hat{\delta}$  such that the associated Jacobian  $\tilde{J}$  has a pair of purely imaginary eigenvalues. This is not necessarily the closest bifurcation point to the nominal system due to the possibility of local minima. However,  $\hat{X}$  can be

used to compute the restricted manifold  $\mathcal{H}_g$  via a numerically *cheap* continuation problem once a parameterisation  $g$  for the uncertainty set is provided. Continuation of  $\mathcal{H}_g$  has two objectives. First, it could directly detect improved solutions of Program 8.2 (if  $\lambda_k < \hat{k}_m$ ). Second, points on  $\mathcal{H}_g$  can be used to run Program 8.2 with different initialisations.

If the manifold  $\mathcal{H}_g$  gathers a large number of points, and running the optimisation for each of them is not viable, criteria could be employed to select a subset of them only. Keeping in mind that the goal is to provide initialisations which possibly make the optimiser converge to different points from the initial solution  $\hat{X}$ , the premise of these criteria is to detect on  $\mathcal{H}_g$  perturbation vectors *qualitatively* different from  $\delta$ . Possible indicators are for example the frequency  $\omega$  and the changes in sign of the parameters in  $\delta$  (recall that these are normalised, thus a change in sign reveals a change in the direction of perturbation for the considered parameter).

### 8.3 Application to the typical section case study

The concept of robust bifurcation margins is applied to a nonlinear aeroelastic system with the goal of studying the influence of parametric uncertainties on qualitative changes in its steady-state behaviour. Following the notation in Sec. 8.2.1, let us denote with  $V_H$  the speed at which the nominal system undergoes a Hopf bifurcation. Given a subcritical speed  $\bar{V}_0$  such that  $\bar{V}_0 < V_H$  corresponds to a stable equilibrium and the definition of an uncertainty set, the distance in the parameter space of the equilibrium at  $\bar{V}_0$  from the closest Hopf bifurcation is computed by means of the margin  $k_m$ .

In order to emphasise the benefits of the newly proposed framework and the connections between the analyses allowed by it and those available with the standard LFT- $\mu$  approach, the same (linear) typical section study case considered in Chapter 4 is assumed as starting point. Specifically, Sec. 4.1.2 gathered the results of nominal (linear) analyses which predicted a flutter speed  $V_f = 302 \frac{m}{s}$  and a flutter frequency  $70.4 \frac{rad}{s}$  –see Table 4.1 and Fig. 4.1 for further details. In Sec. 4.2.1 the effect of perturbations in structural and aerodynamic parameters on flutter was assessed by building LFT models of the uncertain linear system and applying  $\mu$  analysis –see Fig. 4.5 and Fig. 4.8 for examples of robust (linear) flutter analyses.

In Section 8.3.1 nonlinearities in plunge and pitch DOF are introduced and standard bifurcation analysis is applied to study the nominal nonlinear flutter behaviour. Since the system has nonlinearities, robustness to parametric uncertainties can not be studied now with LFT- $\mu$  and thus the approach developed in Section 8.2 is applied. Results are presented in Section 8.3.2 and critically discussed therein. Finally, Section 8.3.3 reports on the effects of perturbations in the control surface dynamics and points out interesting connections with findings observed in the analyses performed in Chapter 6 with respect to freeplay-induced LCOs.

### 8.3.1 Nonlinear problem definition and bifurcation analysis

Recall first the mathematical description for a generic linear aeroelastic system in (2.7). This is written out here for the case where  $x_s = [\eta; \dot{\eta}]$  (with  $\eta = [\frac{h}{b}; \alpha; \beta]$ ) and  $x_a$  are the aerodynamic states from the Minimum State rational approximation:

$$\dot{x} = \begin{bmatrix} \dot{\eta} \\ \ddot{\eta} \\ \dot{x}_a \end{bmatrix} = \begin{bmatrix} 0 & I & 0 \\ -M^{-1}K & -M^{-1}B & M^{-1}D \\ 0 & \bar{E} & R \end{bmatrix} \begin{bmatrix} \eta \\ \dot{\eta} \\ x_a \end{bmatrix}, \quad (8.25)$$

where, with reference to Eqs. (2.8)-(2.9):  $M$ ,  $B$  and  $K$  are respectively the aeroelastic inertial, damping and stiffness matrices;  $D = q_\infty \bar{D}$ ;  $R = \chi_{aa-MS}$ ;  $\bar{D}$  and  $\bar{E}$  come from the unsteady part  $\Gamma_{lag-MS}$  of  $Q_{MS}$  (2.6).

Nonlinearities in the structural stiffness matrix  $K_s$  are considered in this work. Specifically, hardening cubic terms for the plunge and pitch degrees of freedom are assumed, and the expression of  $K_s$  (2.10) is specialised for this case as follows:

$$K_s = K_s^L + K_s^{NL} = \begin{bmatrix} K_h^L & 0 & 0 \\ 0 & K_\alpha^L & 0 \\ 0 & 0 & K_\beta \end{bmatrix} + \begin{bmatrix} K_h^{NL} K_h^L (\frac{h}{b})^2 & 0 & 0 \\ 0 & K_\alpha^{NL} K_\alpha^L \alpha^2 & 0 \\ 0 & 0 & 0 \end{bmatrix}, \quad (8.26)$$

where the linear  $K_s^L$  and nonlinear  $K_s^{NL}$  structural stiffness matrices have been introduced. As common practice [69], the nonlinear terms are assumed proportional to the corresponding linear ones through the coefficients  $K_h^{NL}$  and  $K_\alpha^{NL}$ . The hardening effect modelled in (8.26) takes into account the fact that the stiffness properties change when the system undergoes large deformations (as is the case for very flexible aircraft), and typically an increase in the stiffness is observed. Softening effects can also be exhibited in systems subject for example to compressive loads or heating at high Mach numbers [252], but, since these instances are less relevant to the study of flutter, they will not be considered here.

When the nonlinear stiffness matrix  $K_s$  (8.26) is used to define the aeroelastic matrix  $K$ , the dynamics (8.25) adopts the form of the generic vector field (8.1), and thus the following description holds:

$$\begin{aligned} \dot{x} &= f(x, V) = \mathcal{A}^L(V)x + f^{NL}(x, V), \\ J(x, V) &= \mathcal{A}^L(V) + \nabla_x f^{NL}(x, V), \end{aligned} \quad (8.27)$$

where  $\mathcal{A}^L : \mathbb{R} \rightarrow \mathbb{R}^{n_x \times n_x}$  is obtained from (8.25) by setting the nonlinear terms to zero (i.e.  $K_s^{NL} = 0$ ), and  $f^{NL} : \mathbb{R}^{n_x} \times \mathbb{R} \rightarrow \mathbb{R}^{n_x}$  is the nonlinear part of the vector field. For the case specified in (8.26), the following holds:

$$\mathcal{A}^L = \begin{bmatrix} 0 & I & 0 \\ -M^{-1}[K_s^L - \frac{1}{2}\rho_\infty V^2 A_0] & -M^{-1}B & M^{-1}D \\ 0 & \bar{E} & R \end{bmatrix}, \quad f^{NL} = \begin{bmatrix} 0 & 0 & 0 \\ -M^{-1}K_s^{NL} & 0 & 0 \\ 0 & 0 & 0 \end{bmatrix} x. \quad (8.28)$$

The bifurcation parameter  $p$  is typically the speed  $V$  in the context of flutter analysis, but other options could be considered as well.

Numerical continuation can thus be applied to (8.27) after having specified the value of the trim state  $x_t$ . A first important difference between linear and nonlinear flutter analysis is indeed the influence of  $x_t$  on the results. In the linear context, the presence of non-zero states has no effect on stability, since this can always be studied by considering the state-matrix only. This is not true in the nonlinear case, where results depend on  $x_t$ . Two trim conditions will be considered to exemplify this effect. The first corresponds to a zero trim state, i.e.,  $x_t = 0$ , whereas the second has a non-zero value  $\alpha_t = 1^\circ$  for the angle of attack of the section. This is physically motivated by the fact that the section is generating positive lift to counterbalance gravitational forces directed downwards. More refined descriptions for  $x_t$  could consider a dependence of  $\alpha_t$  on speed or the presence of a pre-deformed shape (with non-zero values for  $h$  and  $\beta$ ), but this is not done here since this description is sufficient to illustrate the role played by  $x_t$ .

In order to present an overview of the possible nonlinear responses of the system, 6 scenarios are considered. These arise from taking into account, for each trim state, the cases of plunge nonlinear stiffness only ( $K_h^{NL} = 0$ ), pitch nonlinear stiffness only ( $K_\alpha^{NL} = 0$ ), and both nonlinear stiffnesses. The results are presented in Table 8.1, where, for each scenario ( $s\#$ , with  $\# = 1, \dots, 6$ ), the speed  $V_H$  at which the Hopf bifurcation occurs, the frequency of the associated imaginary eigenvalues  $\omega_H$ , and the type of bifurcation (sub for subcritical and super for supercritical) are reported. Fig. 8.2 shows the corresponding bifurcation diagrams with  $V$  on the  $x$ -axis and the normalised plunge DOF  $\frac{h}{b}$  on the  $y$ -axis (in case of branches of LCO, this is the maximum value over a period). The usual convention of representing stable steady-states (equilibria and LCOs) with solid lines and unstable ones with dashed lines is adopted.

Table 8.1: Hopf bifurcations of the nominal system for different combinations of nonlinearities and trim states.

	$K_h^{NL}$	$K_\alpha^{NL}$	$x_t$	$V_H$	$\omega_H$	type
s1	100	0	0	$302.7 \frac{m}{s}$	$70 \frac{rad}{s}$	sub
s2	0	100	0	$302.7 \frac{m}{s}$	$70 \frac{rad}{s}$	super
s3	100	100	0	$302.7 \frac{m}{s}$	$70 \frac{rad}{s}$	super
s4	100	0	$\alpha_t = 1^\circ$	$288.2 \frac{m}{s}$	$75 \frac{rad}{s}$	sub
s5	0	100	$\alpha_t = 1^\circ$	$303.7 \frac{m}{s}$	$70 \frac{rad}{s}$	super
s6	100	100	$\alpha_t = 1^\circ$	$289 \frac{m}{s}$	$75 \frac{rad}{s}$	super

The first important observation from Fig. 8.2 is that when  $x_t = 0$  the branch of equilibria is  $x = 0$  regardless of  $V$ . This implies that  $J = \mathcal{A}^L$ , thus the occurrence of the Hopf bifurcation is independent of the nonlinear terms. This is in accordance with the results from Table 8.1, where

for  $s1$ ,  $s2$  and  $s3$  the results of the linear case are retrieved, i.e.  $V_H = V_f$  and  $\omega_H = \omega_f$  holds. Nonlinear terms however do have an effect on the type of bifurcation.

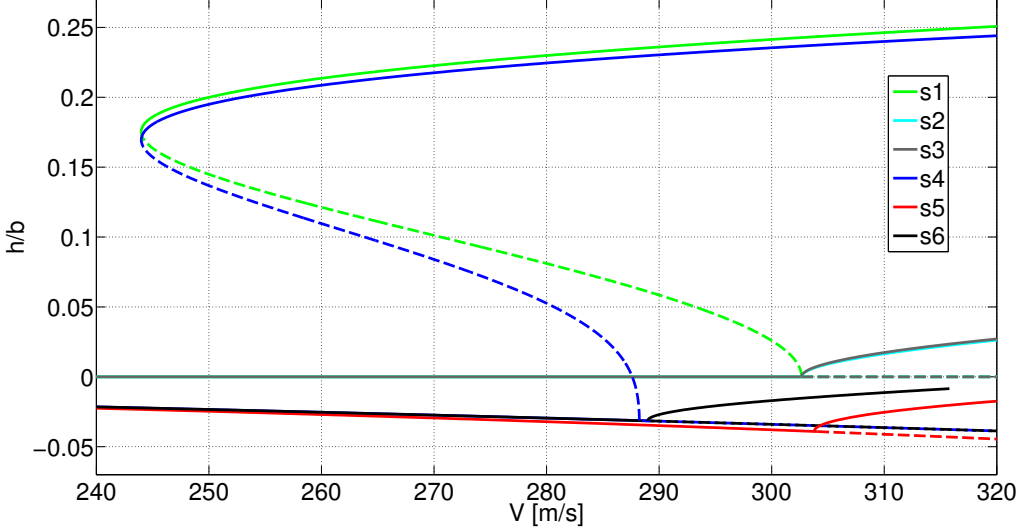


Figure 8.2: Bifurcation diagram of the nominal system for different combinations of nonlinearities and trim states.

When  $\alpha_t = 1^\circ$ , it can be seen that the branch of equilibria has a non-zero (speed dependent) value (note that  $s4$  and  $s6$  overlap). Moreover, different values of  $V_H$  and  $\omega_H$  are registered in the three cases depending on the nonlinearities affecting the system. This is due to the fact that the linearisation of the Jacobian is now affected by the nonlinear term of the vector field  $f^{NL}$ , thus there is an effect of the type of nonlinearity on the onset of the Hopf bifurcation. A consequence of the nonlinear terms is thus also that different values of  $\alpha_t$  (in general  $x_t$ ) will correspond to different  $V_H$ . This behaviour is not surprising since the dependence of flutter speed on the angle of attack is a known feature of nonlinear flutter [190].

Another important trend, also confirmed when  $x_t \neq 0$ , is that a subcritical bifurcation occurs for the cases of nonlinearity only in plunge ( $s1$  and  $s4$ ), whereas when there are nonlinearities in the pitch degree of freedom the bifurcation is always supercritical. This aspect is in agreement with the discussion in [69], where the concept of intermittent flutter based on the instantaneous natural frequencies of the underlying linear system is used to qualitatively explain the mechanisms prompting different LCOs. This is briefly discussed here with regard to  $s1$  and  $s2$  (similar arguments could be used for  $s4$  and  $s5$ ).

As a preamble, recall the trend of the plunge and pitch natural frequencies emphasised in Fig. 4.2(b). For the benefit of the discussion, a zoom of that plot is shown in Fig. 8.3. Consider a speed  $V_H^e$  slightly larger than  $V_H$ . Since the equilibrium is unstable, the system will start oscillating and the nonlinear terms will become important. In  $s2$  the pitch frequency  $\omega_\alpha$  will increase and, as the oscillations become larger, the plunge frequency  $\omega_h$  (which remains constant)

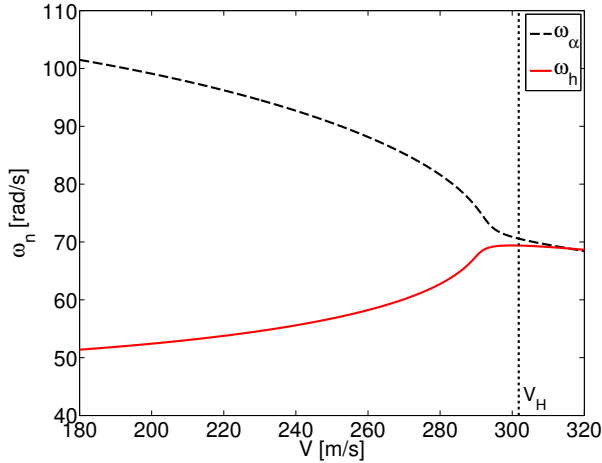


Figure 8.3: Zoom on the plunge (solid) and pitch (dashed) frequencies around the linear nominal flutter speed.

will be far from  $\omega_\alpha$  and thus the binary flutter mechanism prompting the instability will cease to exist. As a result, the oscillations will decay and reach a level which is compatible with the existence of a flutter mechanism. In essence, the amplitude of the LCO will stabilise at a cycle in which the system alternates between positive (when the frequencies get closer) and negative (when they are far away from each other) damping. Since  $\omega_\alpha > \omega_h$  at  $V_H^e$ , the growth in amplitude must be gradual and thus a supercritical LCO emanates from the Hopf point. The situation is different for  $s1$ . Indeed, the hardening plunge stiffness promotes an instantaneous higher value of  $\omega_h$  as the system starts oscillating, and, since  $\omega_\alpha > \omega_h$ , the existence of a flutter mechanism at larger amplitudes is possible. Moreover, if  $V$  is decreased below  $V_H$ , an LCO can still exist because oscillations in the system are compatible with coalescence of the natural frequencies. This qualitatively explains, at least for the case of binary flutter, the features of hysteresis and abrupt oscillations observed in an aeroelastic system undergoing a subcritical Hopf bifurcation.

In the case of  $s3$ , where both nonlinear terms are present, a supercritical bifurcation occurs. This is ascribed to the particular choice of  $K_h^{NL}$  and  $K_\alpha^{NL}$  in Table 8.1, which makes a mechanism qualitatively similar to the one described for  $s2$  prevail. By increasing the coefficient  $K_h^{NL}$  it is noted that a subcritical bifurcation would occur.

### 8.3.2 Robust margins to nonlinear flutter

This section investigates how uncertainties in the model can affect the results presented in the previous section. The first step to compute robust bifurcation margins is the definition of the nominal system and of the uncertainty set, which in turn will drive the construction of the underlying LFT. The former is described by the vector field (8.27) analysed in Sec. 8.3.1, while for the latter 5 structural parameters are initially considered, and then the set is incrementally augmented.

Including uncertainties in the nominal vector field of (8.27) yields the following expression:

$$\dot{x} = \tilde{f}(x, V, \delta) = \tilde{\mathcal{A}}^L(V, \delta)x + \tilde{f}^{NL}(x, V, \delta), \quad (8.29a)$$

$$\tilde{J}(x, V, \delta) = \tilde{\mathcal{A}}^L(V, \delta) + \nabla_x \tilde{f}^{NL}(x, V, \delta). \quad (8.29b)$$

The bifurcation parameter  $V$  will be fixed in the subsequent analyses to  $\bar{V}_0 = 270 \frac{m}{s}$  (the same used in the linear analysis with  $\mu$ ), which, recall Figure 8.2, is associated in both cases with stable equilibria –and hence, it is a valid choice according to the discussion in Sec. 8.2.1.

### 8.3.2.1 Structural uncertainties

The uncertainties considered here are those belonging to the set (4.7) originally studied in Sec. 4.2.1.1 and reported next:

$$\Delta_s = \text{diag}(\delta_{M_{s,11}}, \delta_{M_{s,12}}, \delta_{M_{s,22}}, \delta_{K_h^L}, \delta_{K_\alpha^L}). \quad (8.30)$$

All the cases considered in Table 8.1 are analysed with Program 8.2, with initialisation provided by the nominal values of the equilibrium point and of the uncertainties. Results are reported in Table 8.2 in terms of robust stability margin  $k_m$ , frequency  $\hat{\omega}$  of the imaginary eigenvalues at  $\bar{V}_0$ , and type of Hopf bifurcation. Note indeed that Program 8.2 calculates the closest Hopf bifurcation without constraining the value of  $l_1$ , and the type of predicted Hopf bifurcation is assessed a posteriori with numerical continuation of the perturbed system.

Table 8.2: Robust bifurcation margins at  $\bar{V}_0 = 270 \frac{m}{s}$  for different combinations of nonlinearities and trim states.

	$\hat{k}_m$	$\hat{\omega}$	type
s1	0.73	71.5 $\frac{\text{rad}}{\text{s}}$	sub
s2	0.73	71.5 $\frac{\text{rad}}{\text{s}}$	super
s3	0.73	71.5 $\frac{\text{rad}}{\text{s}}$	super
s4	0.47	75 $\frac{\text{rad}}{\text{s}}$	sub
s5	0.73	71.6 $\frac{\text{rad}}{\text{s}}$	super
s6	0.49	75.1 $\frac{\text{rad}}{\text{s}}$	super

Let us first comment on the results relative to s1-s2-s3 (having  $x_t = 0$ ), presenting the same robust margins and frequencies. Recall from the nominal analyses (Fig. 8.2) that the branch of equilibria  $x = 0$  was found for all these cases, and observe that  $\tilde{f}^{NL}(0, \cdot, \cdot) = 0$ . This implies that  $x = 0$  are equilibria of the uncertain vector field, too. Therefore,  $\nabla_x \tilde{f}^{NL} = 0$  and the determination of  $k_m$ , since this can not depend on the nonlinear terms, is equivalent to the problem solved by  $\mu$  in the linear case, i.e., finding the smallest perturbation matrix such that  $\tilde{\mathcal{A}}^L$  is neutrally stable.

This is an important result, which complements the discussion in Sec. 8.3.1 concerning the effect of  $x_t$  on nonlinear flutter. While the role played by  $x_t$  on (nominal) nonlinear flutter is better understood [190], that on robustness is relatively unexplored and should be considered when making the simplifying assumption of zero trim states [228].

An important observation is that the margin  $k_m$  computed for these cases is within less than 1% from the maximum singular value of the perturbation matrix found by  $\mu$  in the linear analyses of Sec. 4.2.1.1 (4.8). Moreover, the (normalised) uncertainty vector found by the optimiser is:

$$\begin{aligned}\hat{\delta} &= [\delta_{M_{s,11}}; \delta_{M_{s,12}}; \delta_{M_{s,22}}; \delta_{K_h^L}; \delta_{K_a^L}], \\ &= [-0.7328; 0.5027; 0.7328; 0.7328; -0.7328],\end{aligned}\quad (8.31)$$

which also features the same directions of perturbations as those detected in (4.8). This is very important, since  $\mu_{LB}$  and  $\mu_{UB}$  were shown to be close around the peak of Fig. 4.5, which indicates that, at least for this case, Program 8.2 is able to detect the global minimum of the optimisation. It is worth noting that Program 8.2 has the frequency  $\omega$  as decision variable, whereas  $\mu$  was applied at discrete frequencies (Fig. 4.5) because this is the available implementation for the standard algorithms [14].

Let us now turn the attention to the cases with  $x_t \neq 0$ . These cannot be analysed with  $\mu$  because  $\tilde{J}$  is now also a function of the nonlinear terms due to non zero values for the equilibria (which are in turn a function of the uncertainties). It is inferred that in all cases the Hopf bifurcation could be shifted to  $V = 270 \frac{m}{s}$  within the uncertainty range (note indeed that  $k_m < 1$ ). The values of  $k_m$  are consistent with the nominal analyses in Table 8.1, for which  $s4$  and  $s6$  presented a smaller  $V_H$  than  $s5$ . Thus,  $\bar{V} = 270 \frac{m}{s}$  being closer to the nominal bifurcation speeds for the former, they are also expected to have smaller margins.

Another insight available from Table 8.2 is that the closest Hopf bifurcations are of the same nature as the corresponding ones in nominal conditions. The case of subcritical LCOs is by far the most dangerous scenario, as amply commented in the thesis thus far and demonstrated by the attention received from many researchers [69, 77, 228]. Therefore, one of the goals of the rest of the analyses is to understand whether perturbations in the parameters can drive the Hopf bifurcation from supercritical to subcritical. Focus will therefore be on  $s5$  and  $s6$  only, which according to the intermittent flutter interpretation discussed before are prone to supercritical bifurcations.

### 8.3.2.2 Structural and aerodynamic uncertainties

Uncertainties in two aerodynamic parameters are added to the set of structural parameters. Specifically, the terms  $A_{0,12}$  and  $A_{0,22}$  of the steady aerodynamics matrix  $A_0$  (2.9) are allowed to vary within 20% from their nominal values. This choice is made in order to associate a physical meaning to the uncertain parameters, since  $A_{0,12}$  and  $A_{0,22}$  correspond respectively to the lift

and moment coefficients of the aerofoil. Other options could also be considered, e.g. lag terms of the unsteady part  $\gamma_i$  for which the indications provided in Sec. 3.2.2 could be followed.

Table 8.3 shows the solutions of Program 8.4, which allows the criticality of the closest Hopf bifurcation sought by the optimisation (a tolerance  $\epsilon_l = 1$  was used) to be specified. In the first and third columns the normalised perturbations leading to supercritical bifurcations are listed (in the brackets the percent variation from the nominal value), whereas second and fourth columns report the subcritical cases. The margin  $k_m$  and the frequency are also indicated.

Table 8.3: Worst-case perturbations and margins to the onset of supercritical and subcritical Hopf bifurcations for  $s5$  and  $s6$  (structural and aerodynamic uncertainties).

	$s5 \ l_1 < 0$	$s5 \ l_1 > 0$	$s6 \ l_1 < 0$	$s6 \ l_1 > 0$
$K_a^L$	-0.4062 (-4%)	-3.4169 (-34.2%)	-0.2493 (-2.5%)	-3.1358 (-31.3%)
$K_h^L$	0.4062 (+2%)	3.6470 (+17.1%)	0.2493 (+1.25%)	3.1358 (+15.7%)
$M_{s,11}$	-0.4062 (-4%)	-3.41690 (-34.2%)	-0.2493 (-2.5%)	-3.1358 (-31.3%)
$M_{s,12}$	0.4062 (+2%)	-3.4169 (-17.1%)	-0.2493 (-1.25%)	-3.1358 (-15.7%)
$M_{s,22}$	0.4062 (+4%)	3.4169 (+34.2%)	0.2493 (+2.5%)	3.1358 (+31.3%)
$A_{0,22}$	0.4062 (+8%)	3.4169 (+68.3%)	0.2493 (+5%)	3.1358 (+62.7%)
$A_{0,12}$	-0.4062(-8%)	1.9348 (+38.7%)	-0.2493 (-5 %)	1.83 (+36.5%)
$k_m$	0.4062	3.4169	0.25	3.13
$\hat{\omega}$	$72 \frac{rad}{s}$	$64 \frac{rad}{s}$	$76 \frac{rad}{s}$	$67 \frac{rad}{s}$

The execution time of Program 8.4 is larger than that of Program 8.2 (approximatively 6s against 3s for the case with 7 uncertainties). Most importantly, the addition of the constraint on  $l_1$  exacerbates the issue of local minima, especially when this is an active constraint (i.e., when  $l_1 > 0$  in this case). The results in Table 8.3 were thus obtained employing the set of strategies described in Sec. 8.2.3. Specifically, reinitializing the optimisation based on the solutions obtained with different solvers and using points on the auxiliary manifold  $\mathcal{H}_g$  lead to significant improvements on the solutions, which converged to the results in Table 8.3.

The supercritical cases are coherent with the results illustrated in Sec. 8.3.2.1. The margins approximatively halve in both cases as a result of additional uncertainty in the system, with the frequencies having similar values. By looking at the predicted variations in the parameters, it is noted that the structural ones have the same pattern with regard to the predictions obtained with  $\mu$  (4.8).  $M_{s,12}$  is the only one to change sign, and this can be explained by the small sensitivity of flutter to this parameter, as already discussed. As for the perturbations in  $A_{0,22}$  and  $A_{0,12}$ , they also have a physical interpretation. Due to the sign conventions, an increase in  $A_{0,22}$  and decrease in  $A_{0,12}$  (the predicted worst-case perturbations for these parameters) mean that a positive pitch rotation (Fig. 2.3) determines a larger clockwise pitching moment and upwards

vertical force respectively, making thus the system less stiff. It is thus intuitive that an increased flexibility under the action of the aerodynamic forces will amplify the coupling between elastic and aerodynamic terms, leading to earlier onset of instability. This has been confirmed by performing analyses with opposite perturbations for  $A_{0,22}$  and  $A_{0,12}$ , which all resulted in higher nonlinear flutter speeds.

Let us now consider the subcritical cases (second and fourth columns), which occur for higher perturbations in the system. While all parameters show the same trend as in the supercritical cases commented on above, this does not hold for  $A_{0,12}$ , which has an opposite perturbation and, in absolute value, smaller than the others. This is an interesting aspect, because according to the previous discussion a negative perturbation for  $A_{0,12}$  would be expected. The interpretation for this is that, in order for the subcritical Hopf bifurcation to take place, the natural frequencies of the system must substantially change (this aspect will be further investigated next) and this entails the large perturbations observed in Table 8.3 for the structural parameters. These have the same sign as for the supercritical cases, but are about one order of magnitude larger, thus they would cause the system instability at much smaller speeds. However, the bifurcation must occur at the pre-fixed speed  $\bar{V}_0 = 270 \frac{m}{s}$ , thus the perturbation in  $A_{0,12}$  is such that the bifurcation point is at  $\bar{V}_0$ . The scenario under consideration is distinctive of this problem, where different (possibly conflicting) constraints define the worst-case conditions. While robustness in the linear context focuses on the loss of stability only, from a dynamical systems perspective this becomes a multi-faceted concept characterised by concurrent conditions and thus non-intuitive results can be found.

With the aim to further investigate the mechanism behind the onset of subcritical LCOs, Fig. 8.4 shows bifurcation diagrams associated with worst-case perturbations predicted for  $s5$ . In addition to the branches relating to the first and second column from Table 8.3, additional subcritical LCOs obtained from Program 8.4 by increasing the tolerance parameter  $\epsilon_l$  are presented. The initialisation was provided this time by the values in the second column of Table 8.3 (corresponding to  $\epsilon_l = 1$ ). The solutions are qualitatively similar to the initial point but present slightly larger  $k_m$  (and consequently greater perturbations) as the parameter  $\epsilon_l$  is increased.

In the legend of Fig. 8.4, the value of the Lyapunov coefficient at the bifurcation point is indicated. Note first that in the supercritical case the constraint on  $l_1$  is not active and thus  $l_1$  has a large value irrespective of the tolerance  $\epsilon_l$ . On the contrary, in the subcritical cases this constraint is active, and as a result  $l_1 = \epsilon_l$  always holds. It is stressed that a quantitative interpretation of the absolute value of  $l_1$  depends on the arbitrary normalisation adopted for the eigenvector  $q$  in its definition (8.19). The point made here is qualitative, and specifically, that as the tolerance  $\epsilon_l$  (and thus  $l_1$ ) is increased, the subcritical Hopf bifurcation predicted by the optimiser is more pronounced (i.e. the range of speeds for which unstable and stable LCOs coexist with the branch of stable equilibria is larger). Even though this is not guaranteed by the Hopf bifurcation theorem, since  $l_1$  is defined on the centre manifold at the bifurcation point only, the

magnitude of the Lyapunov coefficient can be taken as a measure of the subcriticality of the LCO (when comparing different instances computed with the same normalisation of  $q$ ). This is well captured by the optimisation, as shown in the results in Figure 8.4.

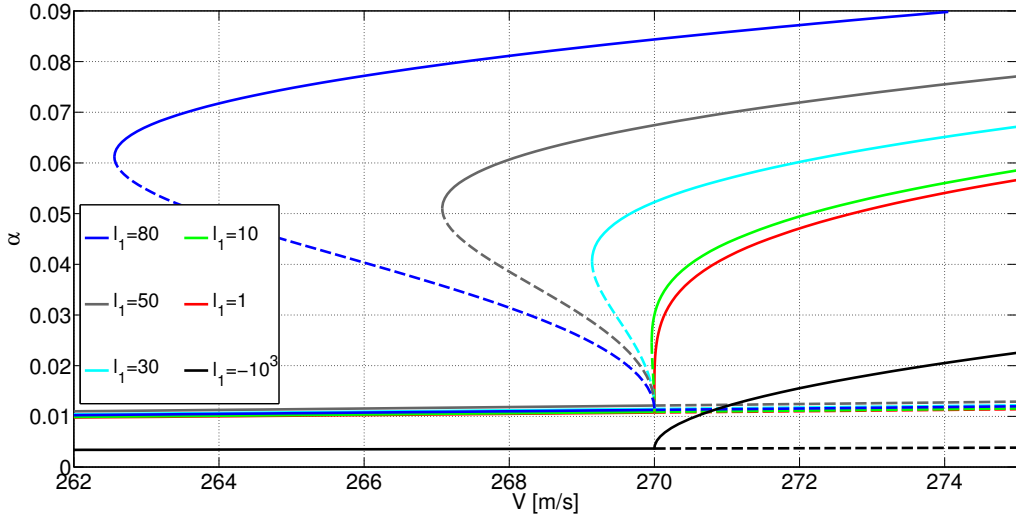


Figure 8.4: Bifurcation diagram of the perturbed system  $s5$ : supercritical and subcritical LCOs.

To conclude the analysis on subcritical bifurcations, plunge and pitch natural frequencies linearised around the branch of equilibria are computed as a function of  $V$  for all the cases analysed in Fig. 8.4. This is depicted in Fig. 8.5, where dashed and solid lines are used for  $\omega_a$  and  $\omega_h$  respectively. Fig. 8.5(b) shows an enlargement around the coalescence of the frequencies for the subcritical cases, and circle markers are used to indicate for each pair the point at which the two frequencies have the same values.

Two apparent differences between supercritical and subcritical cases can be appreciated from Fig. 8.5(a). The first concerns the coalescence between the natural frequencies. This takes place after the bifurcation for the supercritical case, and before for the subcritical one (see Fig. 8.5(a)). This is supported by the intermittent flutter interpretation of the LCO in [69], discussed for this case study in Sec. 8.3.1. Indeed, by having  $\omega_a < \omega_h$  at the bifurcation speed and a hardening pitch stiffness, large oscillations are compatible with the establishment of a flutter mechanism and thus a subcritical Hopf is expected. Secondly, Fig. 8.5(a) shows that the gap between the natural frequencies has decreased across all the speeds for the subcritical case. This results from the large perturbations reported in Table 8.3, which have the effect of amplifying the coupling between the modes. The role of the parameter  $A_{0,12}$  is thus, as discussed before, to ensure that despite the large adverse changes in parameters (whose effects are visible in Fig. 8.5(a)) the Hopf bifurcation will occur at  $\bar{V}_0$  (as verified by the continuation analyses in Fig. 8.4).

By looking at Fig. 8.5(b), it can also be noted that for the cases where the subcritical LCO is more pronounced (i.e., higher values for  $l_1$ ), the frequencies coalesce closer to the bifurcation

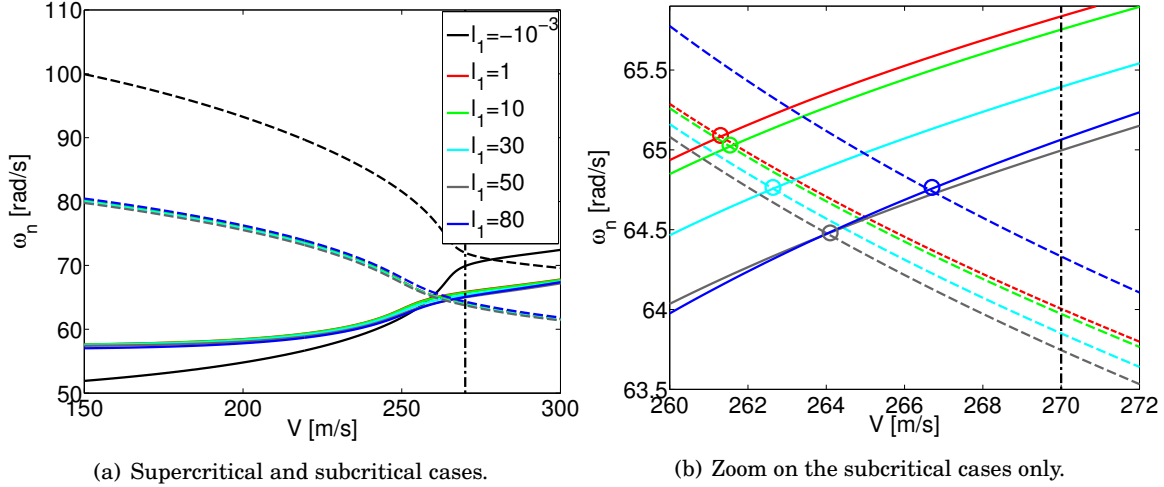


Figure 8.5: Linearised pitch (solid) and plunge (dashed) mode frequencies of the perturbed systems as  $V$  is increased.

point. An interpretation for this is that the coupling between the modes is in the latter case strong enough to allow stable oscillations on a larger interval of subcritical speeds, whereas, if the coalescence takes place further away, the interaction is weaker at subcritical speeds close to  $\bar{V}_0$  and the LCO can only take place over a smaller interval.

### 8.3.2.3 Effect of uncertainties in the nonlinear terms

The coefficients of the nonlinear plunge and pitch stiffnesses are given respectively by  $K_h^{NL}K_h^L$  and  $K_\alpha^{NL}K_\alpha^L$  (8.26). Thus, the uncertainty in the linear stiffness coefficients, considered so far, affect also the nonlinear stiffness matrix  $K_s^{NL}$ . However, the proportional coefficients  $K_h^{NL}$  and  $K_\alpha^{NL}$  have been assumed fixed (and equal to 100, see Table 8.1). Since their determination is far from being a consolidated practice, it is reasonable to account for a dispersion in their values. Specifically,  $K_h^{NL}$  and  $K_\alpha^{NL}$  will be allowed to vary within 20% from their nominal values. The uncertainty set is thus augmented with two new parameters and, as a result, each nonlinear coefficient is given by the multiplication of two independent uncertain parameters.

Table 8.4 gathers the worst-case perturbations and bifurcation margins in the face of the new set of uncertainties. The supercritical cases barely change with respect to the analyses in Table 8.3, and this is probably due to the fact that the predicted perturbations for  $K_h^{NL}$  and  $K_\alpha^{NL}$  are identical to the ones for the linear coefficients  $K_h^L$  and  $K_\alpha^L$ . Thus, the extra degree of freedom of perturbing individually the two terms defining the nonlinear stiffness coefficients is not exploited. This reasoning also applies to the subcritical case with only pitch nonlinearity ( $s5 l_1 > 0$ ), which also features a slightly smaller  $k_m$  than the corresponding case analysed in Table 8.3. The only detectable change concerns the last column, where the closest subcritical Hopf bifurcation for the

case with both plunge and pitch nonlinearity is reported. It is interesting to observe that, for this case, a positive perturbation for  $K_\alpha^{NL}$  is predicted by the optimisation, opposite to the one for the linear term  $K_\alpha^L$ . The perturbation to  $K_\alpha$  is thus now decoupled in the linear and nonlinear part, resulting in a lower bifurcation margin  $k_m$ .

Table 8.4: Worst-case perturbations and margins to the onset of supercritical and subcritical Hopf bifurcations for  $s5$  and  $s6$  (uncertainty also in the nonlinear coefficients).

	$s5 \ l_1 < 0$	$s5 \ l_1 > 0$	$s6 \ l_1 < 0$	$s6 \ l_1 > 0$
$K_\alpha^L$	-0.4054 (-4%)	-3.3595 (-33.6%)	-0.2432 (-2.5%)	-2.9641 (-31.3%)
$K_h^L$	0.4054 (+2%)	3.3595 (+16.8%)	0.2432 (+1.25%)	2.9641 (+15.7%)
$M_{s,11}$	-0.4054 (-4%)	-3.3595 (-33.6%)	-0.2432 (-2.5%)	-2.9641 (-31.3%)
$M_{s,12}$	0.4054 (+2%)	-3.3595 (-16.8%)	-0.2432 (-1.25%)	-2.9641 (-15.7%)
$M_{s,22}$	0.4054 (+4%)	3.3595 (+33.6%)	0.2432 (+2.5%)	2.9641 (+31.3%)
$A_{0,22}$	0.4054 (+8%)	3.3595 (+67.2%)	0.2432 (+5%)	2.9641 (+62.7%)
$A_{0,12}$	-0.4054(-8%)	1.9486 (+38.97%)	-0.2432 (-5 %)	1.77 (+36.5%)
$K_h^{NL}$	-	-	0.2432 (+5 %)	2.9641 (+36.5%)
$K_\alpha^{NL}$	-0.4054(-8%)	-3.3595 (-67.2%)	-0.2432 (-5 %)	2.65 (+36.5%)
$k_m$	0.4054	3.3595	0.24	2.9641
$\hat{\omega}$	$72 \frac{rad}{s}$	$63.5 \frac{rad}{s}$	$76 \frac{rad}{s}$	$69 \frac{rad}{s}$

To better ascertain this behaviour, a close investigation of the two subcritical bifurcations corresponding to the last columns of Table 8.3 (where no uncertainty in  $K_h^{NL}$  and  $K_\alpha^{NL}$  is captured, case *D1*) and Table 8.4 (case *D2*) is performed. The idea is to consider the stable LCO exhibited at  $\bar{V}_0 = 270 \frac{m}{s}$ , which is shown in Fig. 8.6(a) by plotting the response of  $\frac{h}{b}$  and  $\alpha$  over a period. By linearising the Jacobian around the trajectory of Fig. 8.6(a), it is possible to calculate the plunge and pitch natural frequencies at each time step. This is reported in Fig. 8.6(b), where for reference the natural frequencies linearised around the equilibrium at which the bifurcation occurs are reported as horizontal lines. From Fig. 8.6(a) it can be inferred that the LCO corresponding to *D1* features the largest amplitude. This could be motivated by the fact that the two natural frequencies are close over the period, as visible from Fig. 8.6(b), thus the flutter mechanism stabilises at higher amplitudes. The case *D2*, despite having a smaller LCO, exhibits a large excursion for  $\omega_\alpha$ , due to the fact that the positive perturbation for  $K_\alpha^{NL}$  determines a larger hardening term. The one observed for *D2* is thus a different LCO mechanism from that for *D1*, because stable oscillations exist even if the coupling between the modes seem weak over large parts of the period. This is an interesting aspect as it shows that, by enlarging the set of uncertainties, different scenarios can arise. Moreover, the bifurcation margin associated with *D2* is smaller which makes the characterisation of the associated bifurcation of practical importance.

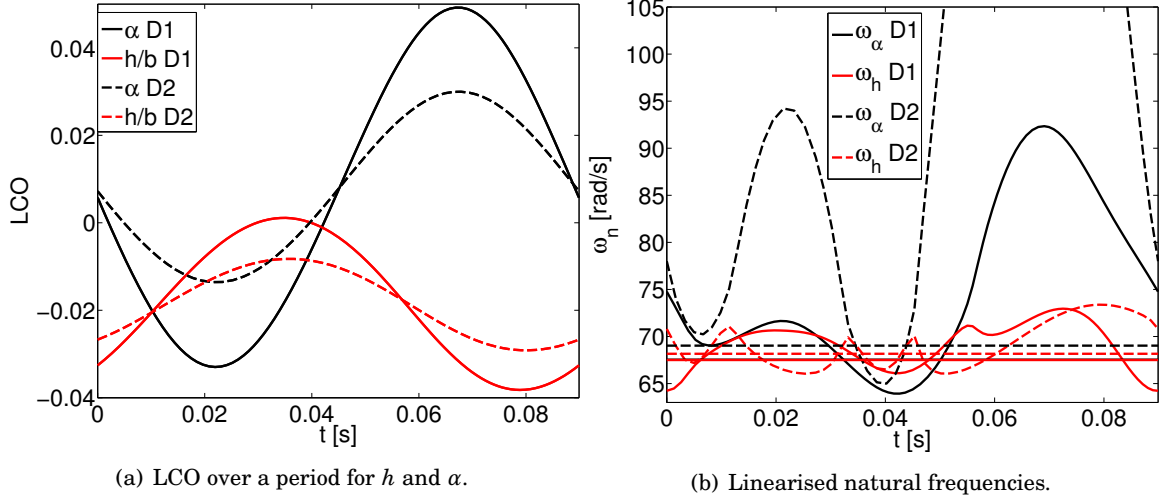


Figure 8.6: Effect of uncertainty in the nonlinear coefficients on the onset of a subcritical Hopf bifurcation.

As for the computational aspects, the availability of results from previous analyses (even if performed only on a subset of the uncertainty space, e.g. Table 8.4) greatly improves the required computational time and accuracy of the results, since these could be used to seed the optimisation (and the multi-start continuation-based search). Adding uncertainties incrementally, as done here, not only allows a deeper understanding of the physical mechanisms underlying the onset of Hopf bifurcations in the system, but represents an effective strategy to tackle the possible numerical issues associated with non-convex optimisation and discussed in Sec. 8.2.3.

A possible objection to this approach is that seeding the optimisation with previous results could bias the solution because new global minima, possibly appeared as an effect of the additional uncertainties in the system, might not be captured. For this reason, the possibility to run Program 8.4 at a fixed frequency  $\omega$  is exploited and the results are shown next. Fig. 8.7 shows the reciprocal of the robust bifurcation margin  $k_m$  for  $s6$ , subject to the set of uncertainties considered in this section, as a function of the frequency. The cases of supercritical and subcritical Hopf are respectively depicted in Fig. 8.7(a) and Fig. 8.7(b). Two different initialisations are considered: *Init. 1* uses zero for the uncertainties and the nominal equilibrium at  $\bar{V}_0$  for the states; *Init. 2* uses the solution corresponding to the maximum peak of *Init. 1*. The representations in Fig. 8.7 resemble those typically employed in linear robust analysis with  $\mu$  (recall for example Fig. 4.5). This points out once again the connection between the concept of  $k_m$  and the structured singular value  $\mu$ . In particular, when  $\frac{1}{k_m} \geq 1$ , a perturbation in the allowed range of uncertainties exist such that an Hopf bifurcation is experienced by the system when perturbed. In this regard, Fig. 8.7(a) features a pronounced peak of approximately 4, corresponding to a margin of 0.25

(which equals the result in the third column of Table 8.4). Fig. 8.7(a) shows also that there is no sensitivity of the solutions to the initial condition. This is primarily ascribed to the fact that the constraint on the Lyapunov coefficient is not active in this case and, as already highlighted, this makes the optimisation more robust to the issue of local minima. The results in Fig. 8.7(b) show on the other hand a sensitivity to the initialisation. However, the peak detected by the curve *Init. 2* (approximately 0.34), corresponds to the margin 2.95 reported in Table 8.4, which was obtained via the multi strategy outlined in Sec. 8.2.3.

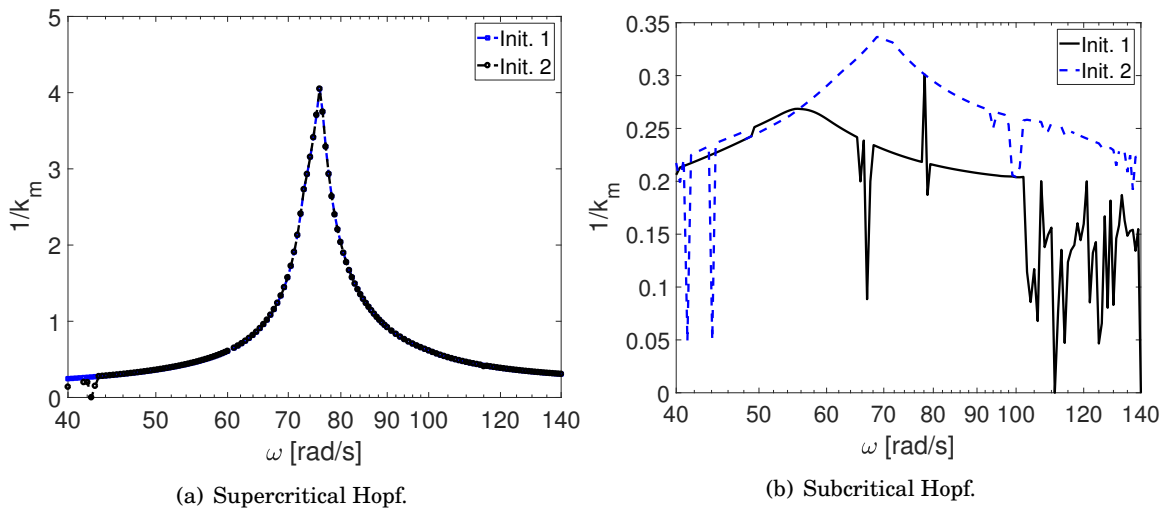


Figure 8.7: Frequency representation of the reciprocal of the robust bifurcation margin.

The analyses shown in Fig. 8.7 help not only in mitigating the issue of local minima, but provide additional insights into the instability. For example, the results here confirm that the closest supercritical and subcritical Hopf bifurcations take place in the range of frequencies where the pitch and plunge modes coalesce. This binary flutter mechanism was ascertained in nominal conditions with both linear (Sec. 4.1.2, e.g. Fig. 4.1) and nonlinear approaches (Table 8.1 and Fig. 8.2). Therefore, the presence of the uncertainties is able to prompt the onset of the Hopf bifurcation at lower speeds and to change the type (from supercritical to subcritical), but the underlying physical mechanism is unaltered. The next section shows that this analysis framework can also anticipate new mechanisms not observed in nominal conditions which, depending on the perturbations of the parameters, could become critical.

### 8.3.3 Effect of control surface stiffness uncertainty

The destabilising mechanism analysed so far is the result of a coupling between the two elastic states  $h$  and  $\alpha$ , while the third state  $\beta$  does not participate in it. This fact, supported by a wide frequency separation between the dynamics of  $\beta$  and the other two states, is often exploited to reduce the size of the problem by neglecting the flap motion [111]. However, this hypothesis might

be invalidated by a decrease in the stiffness of the control surface  $K_\beta$ . A possible cause for this, in addition to the lack of confidence on its exact value, could be the presence of nonlinear behaviours which typically affect control surfaces. For example, Chapter 6 has shown that freeplay can be an important driving force behind the onset of limit cycles, and notably of subcritical nature. The robust bifurcation margins framework assumes smooth vector fields, thus freeplay cannot be directly modelled, but its effect on the dynamics can be captured to a first approximation as a reduction in the value of  $K_\beta$ . For example, the Describing Function method, employed in Sec. 6.2, provides an equivalent value for  $K_\beta$  which lies in the interval  $[0, K_\beta^L]$  and depend on the amplitude of the LCO (6.32). In other words, freeplay has an *uncertain softening* effect on the associated stiffness, and thus the addition of  $K_\beta$  to the set of uncertainties is physically justified. A range of variation of 40% from its nominal value will be assumed.

The analyses reveal that the supercritical cases are practically unaltered because the magnitude of the worst-case perturbations associated with this instability (recall for example the small percent variations in Table 8.4) are not able to modify  $K_\beta$  in such a way that the flap motion dynamics participate in the instability. On the contrary, the subcritical cases feature a big sensitivity to this parameter. Fig. 8.8 shows the reciprocal of  $k_m$  as a function of the frequency and is built by using 4 different initialisations (derived from the multi-start strategy). For clarity, only the envelope curve of the maxima of these 4 tests (labelled *B1*) is reported. The curve *Init. 2* from Fig. 8.7(b) is also reported (labelled *B2*), which allows a comparison with the case where  $K_\beta$  holds a fixed nominal value.

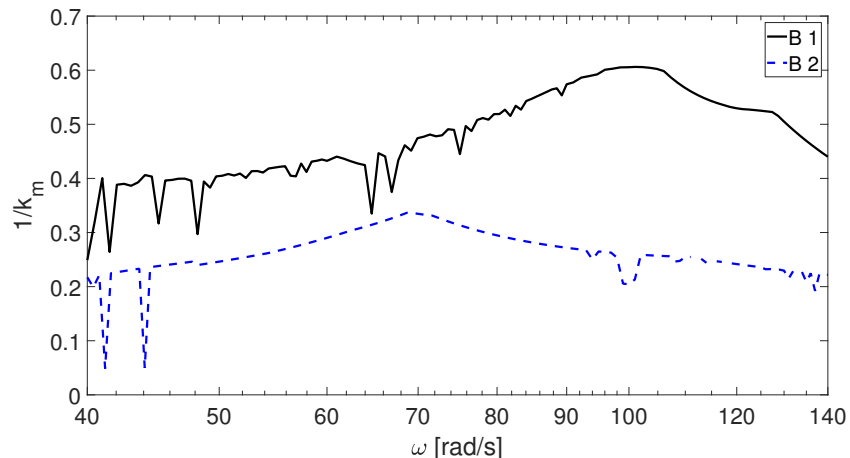


Figure 8.8: Comparison of  $k_m$  for the cases with and without uncertainty in  $K_\beta$ .

The results in Fig. 8.8 show that uncertainty in  $K_\beta$  has a strong impact on the potential onset of a subcritical LCO in the system. Note indeed that, even though the margin  $k_m$  is still above 1 (thus the predicted perturbation provoking the bifurcation lies outside the allowed set), this has drastically decreased compared to the previous analyses. Moreover, the peak of the

plot (corresponding to  $k_m \approx 1.65$ ) is in a different frequency interval, specifically around  $100 \frac{\text{rad}}{\text{s}}$ , which suggests a different physical mechanism prompting the Hopf bifurcation. The worst-case perturbations associated with the peak of curve  $B1$  are reported in Table 8.5.

Table 8.5: Worst-case perturbations for the onset of a subcritical Hopf bifurcation with uncertainty also in  $K_\beta$ .

$K_\alpha^L$	1.6587 (+16.59%)
$K_h^L$	-1.6587 (-8.29%)
$M_{s,11}$	0.2420 (+2.42%)
$M_{s,12}$	1.2101 (+6.05%)
$M_{s,22}$	-1.6587 (-16.59%)
$A_{0,22}$	-1.6587 (-33.17%)
$A_{0,12}$	-1.6587 (-32.97%)
$K_h^{NL}$	-1.6587 (-33.17%)
$K_\alpha^{NL}$	1.6587 (+33.17%)
$K_\beta$	-1.6587 (-66.35%)

The predicted variations for the structural parameters are markedly different from those encountered in all the previous analyses. The linear stiffness and mass parameters, for example, have opposite signs when compared to the results in Tables 8.3 and 8.4, and  $M_{s,11}$  is almost unperturbed. In fact, the perturbations do not bring the plunge and pitch modes closer in this case, but determine an increase in  $\omega_\alpha$  and a decrease in the flap frequency  $\omega_\beta$  (note the trends for  $K_\alpha^L$ ,  $M_{s,22}$ ,  $K_\alpha^{NL}$ , and  $K_\beta$ ).

Fig. 8.9 attempts to interpret this result by making use of the linear indicators commonly adopted in flutter analysis. At each speed  $V$  the Jacobian is linearised around the equilibria of the stable branch and an eigenvalue analysis is performed. This allows the natural frequencies of the three structural modes to be obtained as the speed is increased, which are reported in Fig. 8.9(a). In addition, Fig. 8.9(b) shows the Modal Assurance Criterion for the three modes. MAC was defined in (4.1) and can be advantageously employed to quantify the *similarity* (in a linear combination sense) between two mode shapes. Recall from Sec. 4.1.1 that MAC ranges between 0 and 1, where the extremes are achieved by two orthogonal or identical vectors respectively, while for values in between there is a certain degree of similarity between the reference and the tested modes. The idea is then to plot the MAC among the three structural modes in order to monitor how their coupling vary with speed. The labels  $MAC(\alpha, \beta)$  and  $MAC(\alpha, h)$  in Fig. 8.9(b) indicate the MAC between pitch mode and flap mode, and pitch mode and plunge mode respectively. In both figures, the indicators relative to the system with perturbations from Table 8.5 are compared with those for the nominal (i.e.,  $s6$  from Table 8.1).

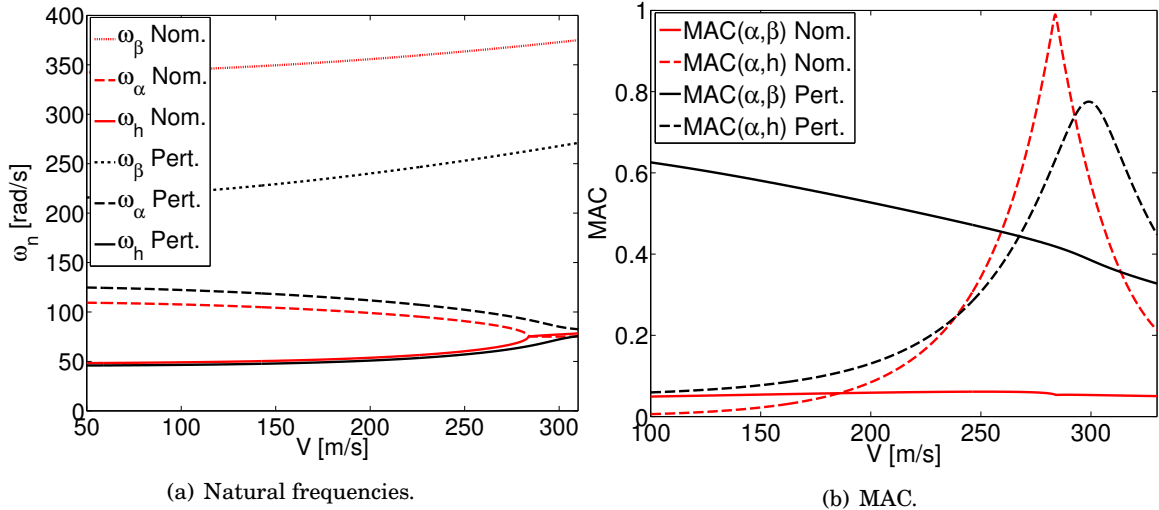


Figure 8.9: Linearised frequencies and MAC around the branch of equilibria for nominal (red) and perturbed (black) case *s6*.

The perturbed system shows in Fig. 8.9(a), as expected from the result of the optimisation gathered in Table 8.5, a significant reduction in  $\omega_\beta$  and increase in  $\omega_\alpha$  compared to the nominal system. However, there is still a considerable frequency gap between the pitch and flap modes, thus based on this plot only there seem to be no strong coupling between them. In fact, by recalling the intermittent flutter interpretation of LCO, the curves seem to suggest a supercritical Hopf bifurcation involving  $h$  and  $\alpha$  (indeed the trend of natural frequencies is similar to that in Fig. 8.3 which prompted a supercritical bifurcation). A different perspective is given by Fig. 8.9(b), where a marked increase in the coupling between  $\alpha$  and  $\beta$  is apparent for the perturbed system (observe the black solid line versus the red solid one), and a decrease in that for  $\alpha$  and  $h$  (dashed black and red lines). In particular, the black curves  $MAC(\alpha,\beta)$  and  $MAC(\alpha,h)$  have comparable values around  $\bar{V}_0$ , but their slope is opposite. This might suggest that at subcritical speeds there is opportunity for stable oscillations in the system, since the coupling between  $\alpha$  and  $\beta$  is amplified as the speed is decreased. In order to further support these claims, the Jacobian is linearised around the stable LCO at  $\bar{V}_0$  (depicted in Fig. 8.10(a)) and the variation of MAC over a period is plotted in Fig. 8.10(b), where the horizontal lines correspond to the values in Fig. 8.9(b) for  $V = \bar{V}_0$  (i.e., at the equilibrium point where the Hopf bifurcation occurs).

Fig. 8.10(b) shows that oscillations in the system allow a strong coupling between  $\beta$  and  $\alpha$  to take place. The MAC indeed has a value just below 0.9 for large parts of the period, which is much larger than the one corresponding to the equilibrium (the horizontal solid line). It is thus confirmed that the system has a stable (high amplitude) LCO at  $\bar{V}_0$  due to the interaction between  $\beta$  and  $\alpha$ . Note also from Fig. 8.10(a) that the frequency of the oscillations is about  $185 \frac{\text{rad}}{\text{s}}$ . This is markedly higher than the one observed for the plunge-pitch LCO in Fig. 8.6(a) and is in

agreement with the frequency interpretation of the margin  $k_m$  discussed in Fig. 8.8.

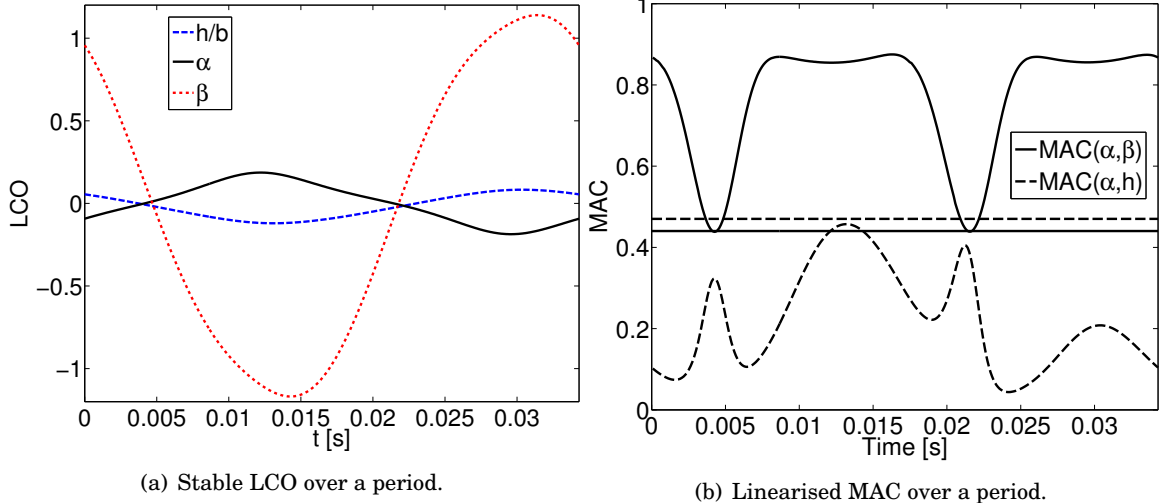


Figure 8.10: Periodic behaviour of the perturbed system  $s6$  at  $\bar{V}_0$ .

While the analyses so far has focused on the behaviour of the perturbed system around the speed  $\bar{V}_0$ , the response of the perturbed system from a *global* bifurcation analysis perspective is studied next. Numerical continuation is applied and the results are displayed by means of the bifurcation diagram in Fig. 8.11.

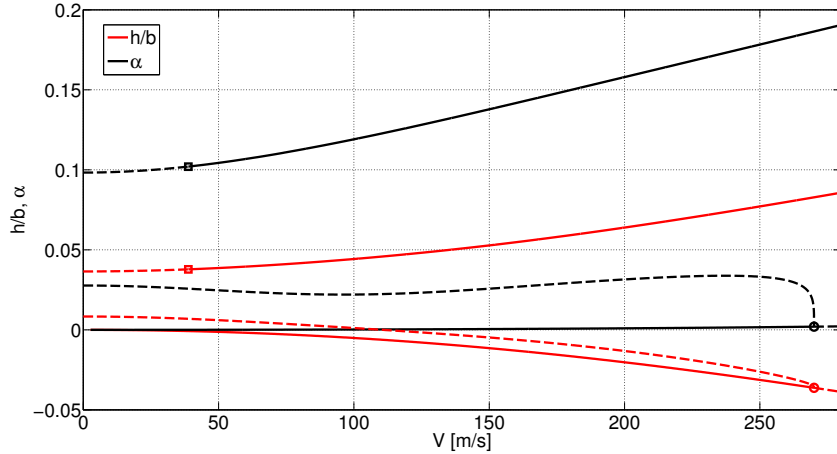


Figure 8.11: Bifurcation diagram of the perturbed  $s6$  for the DOFs  $\frac{h}{b}$  (red) and  $\alpha$  (black).

The plot features a branch of equilibria losing stability at  $\bar{V}_0$  where the subcritical Hopf bifurcation occurs (circle marker), and an unstable branch of LCO emanating from it. Note that this branch does not fold into a stable LCO as typically happens (recall for example the curves in Fig. 8.4). The stable LCO branch is constructed by initialising the continuation solver with

the periodic response obtained with time-marching simulations at  $\bar{V}_0$ . As the speed is decreased, this branch undergoes a supercritical Neimark-Sacker (NS), or torus, bifurcation [145] (square marker at  $V \approx 40 \frac{m}{s}$ ), with quasi-periodic solutions present in the system at smaller speeds.

These results show that the perturbations in Table 8.5 (predicted with respect to *local* bifurcations) are able to drive the system into a global complex scenario featuring bi-stability for very low values of  $V$ . This implies, for example, that the stable equilibrium branch is only locally stable at those speeds and thus ROA analyses as those investigated in Chapter 7 are required to guarantee a safe operation of the system. Moreover, for speeds greater than  $\bar{V}_0$  the system will jump into a stable LCO featuring very high amplitudes (compare the branch for  $\alpha$  in Fig. 8.11 with those in Fig. 8.4 which also emanated from a subcritical Hopf). This feature is even more critical considering that the  $k_m$  associated with the scenario in Fig. 8.11 is the smallest among all the subcritical cases detected in the analyses.

## 8.4 Chapter summary

In this chapter the problem of studying robustness of stable equilibria of nonlinear systems to the onset of Hopf bifurcations is considered.

The technical contribution is the proposal of a possible extension of the structured singular value  $\mu$  to the nonlinear context. A scalar metric quantifying a perturbation in the uncertainty set is first defined, and the magnitude of the smallest perturbation such that a stable equilibrium is driven into a Hopf bifurcation point is defined the robust bifurcation margin  $k_m$ . Its computation, which also allows the nature of the closest Hopf bifurcation (subcritical or supercritical) to be specified, is based on the idea of building a Linear Fractional Transformation model of the uncertain Jacobian and then studying its singularity. The problem of calculating  $k_m$  is then recast as a nonlinear smooth constrained optimisation problem, and as such it suffers in principle from the issue of local minima. Thus, the proposed numerical recipes technically provide only an upper bound on the margin. However, several mitigation strategies are described in order to tighten the gap with the actual margin, including a continuation-based multi-start strategy. The latter represents a novel solution to the problem of computing manifold of Hopf bifurcation points in the space of uncertain parameters.

The second part of the chapter shows an application of this approach to a typical section system featuring polynomial stiffness coefficients. A first important outcome is that, for a particular analysis case, the results are shown to correspond with those obtained with  $\mu$ , for the linear counterpart of the investigated case study, in Chapter 4. The uncertainty set is then incrementally augmented in order to assess the effect of perturbations on the nonlinear behaviour. The capability offered by the framework to specify the type of the closest Hopf bifurcation (subcritical or supercritical) is exploited to ascertain whether the uncertainties are able to change it with respect to what observed in the nominal system. One of the main findings is that uncertainty

in the control surface stiffness can drastically lower the margin to the onset of subcritical Hopf bifurcation even when the control surface dynamics does not participate in the destabilising mechanism in nominal conditions. Moreover, complex dynamics such as quasi-periodicity and bi-stability at low speeds are revealed suggesting the need to carefully consider the effect of uncertainties in bifurcation analysis. The detail devoted to the application section has a twofold aim: on the one hand it allows the various scenarios arising in the study of nonlinear flutter when uncertainties are accounted for to be investigated and discussed; on the other, it provides the reader with a complete example of application of the novel framework and interpretation of its results which could help its usage in future studies.

## CONCLUSIONS

This chapter draws general conclusions on the work described in the thesis, and discusses possible future direction.

### 9.1 Contributions

The three main objectives of the research work were outlined at the end of Section 1.1. Below, the contributions of the thesis towards achieving them are summarised.

#### **Linear robust flutter approaches for aeroelastic systems of increasing complexity**

The problem of addressing robustness of linear aeroelastic systems in the presence of uncertainties in the model has been addressed from the modelling and analysis perspectives.

A systematic and detailed investigation of two different Linear Fractional Transformation modelling paths was performed in Section 3.2. These two paths arose from the frequency-domain expression of the aerodynamic operator (non-rational in the Laplace variable  $s$ ) for flutter calculations. An important outcome of this was the presentation of a unifying formulation combining the respective advantages. This is believed to be an important step to facilitate a physical-based description of the aerodynamic uncertainties, which can have positive repercussions on both the analysis and robust control design tasks. The problem of providing a characterisation of the uncertainties capturing their physical meaning motivated also the approaches developed in Section 3.3. Their main benefit is that the LFT modelling step is performed embedded in the FSI solvers (which are typically employed in aeroelasticity), and in this way systems of moderate complexity can be efficiently obtained with the proposed framework.

On the analysis side, several applications of robust flutter analysis are performed in order to highlight the capability of  $\mu$  of providing a wealth of information in addition to its most common use as simple yes/no test on robust stability. This is showcased and compared with the previous works on the topic by application to body freedom flutter in Section 4.2.2 (for which a simplified model based on first principles has been developed here) and to the complex aeroelastic behaviour exhibited by an unconventional joined-wing configuration in Section 4.3.

The physics-oriented approach taken in this thesis to develop the modelling strategies and interpreting the analysis results is believed to help bridge the gap between the robust and aeroelastic communities.

### **Methods for investigating the effect of uncertainties on nonlinear phenomena**

The presence of nonlinearities prompts the onset of phenomena that must be carefully considered in the design of aeroelastic systems. Particularly relevant in this context are limit cycles, which might arise, instead of a diverging response, when the flutter speed is exceeded. Two distinct methods have been developed in Chapter 6 to predict the worst-case oscillation amplitude of LCOs as a function of speed. The approaches build respectively on Describing Functions and Integral Quadratic Constraints, and can be applied to different types of nonlinearities and uncertainties. A systematic application of these approaches to freeplay-induced LCOs for a system subject to parametric uncertainties has been illustrated, and the prowess of the predictions verified with time-marching simulations (showing very close results). The underlying hypotheses and associated limitations have been critically discussed in order to support the use of these methods for the study of LCOs.

Another important nonlinear effect is that stability of equilibrium points is in general only a local property, as exemplified in the case of subcritical LCO where for a certain range of speeds two (or potentially more) possible steady-states exist. In other words, depending on the perturbations of the states, the trajectories could converge to another attractor or even diverge instead of returning to the original equilibrium. This is for example the case when subcritical Hopf bifurcations occur, and it has motivated the study of region of attraction approaches. Specifically, the detrimental effect of the uncertainties on the size of the region where the system can be safely operated has been considered. The research carried out in Chapter 7 has contributed to the state-of-the-art in the field by focusing on two different aspects. The first concerns the investigation of non-Lyapunov approaches (known to be less conservative) within the framework of positively invariant sets, and resulted in the extension of an available approach to the uncertainty case and the proposal of alternative iterative algorithms (valid for polynomial systems) to improve the solution of the optimisation problems. The second proposes the use of IQC in order to capture generic nonlinearities (not necessarily polynomial) and exploit the properties of the uncertainties to reduce the conservatism of the estimations. Theoretical guarantees of local stability are given

for a generic factorisation of the IQC (hard or soft) and are based on recent results on the reconciliation between multiplier theory and dissipativity.

### **Interpretation of robustness from the bifurcation viewpoint**

The possibility of qualitative changes in the steady-state behaviour of uncertain systems has been characterised in Chapter 8 by means of the notion of the robust bifurcation margin  $k_m$ . While the underlying idea is general (i.e. applicable to different types of static bifurcations), the approach has been specialised here to Hopf bifurcations due to their importance in aeroelasticity (as justified throughout the second part of the thesis). The meaning of the results is recapped here: if  $k_m \leq 1$  then a perturbation within the allowed uncertainty range exists which causes the onset of bifurcation for a nominally stable fixed point, whereas if  $k_m > 1$  then the system has excess of stability, i.e. it is robustly stable to the uncertainties. This margin, which is a worst-case indicator, can be considered a possible nonlinear extension of the structured singular value  $\mu$ , and builds on a similar modelling framework. In fact, the computation of  $k_m$  requires the construction of an LFT representation of the Jacobian of the vector field and exploits the meaning associated with the singularity of this LFT. However, intrinsic differences hold with respect to the formulation of the problem in the linear context. One of them is the possibility to specify the type of the predicted closest Hopf bifurcation, namely subcritical or supercritical, which is a beneficial feature in view of the greater danger associated with the former. Moreover, an original solution to the known issue of local minima for non-convex programs is proposed, which consists of constructing a manifold of Hopf bifurcation points in the uncertain parameter space by leveraging the extended formulation of the numerical continuation problem.

A detailed application of this concept to a nonlinear aeroelastic case study is also proposed. The capabilities offered by the framework are exploited to investigate whether the uncertainties are able to prompt the onset of the Hopf bifurcation at lower speeds and to change its criticality with respect to what is obtained for the nominal system. Interesting patterns in the detected worst-case perturbations are revealed and reconciled with results from previous chapters. The level of detail devoted to the application part aims to: investigate the scenarios arising in the study of nonlinear flutter when uncertainties are accounted for in the model; and provide a complete example of application of the novel framework and interpretation of the results to support its usage in future studies.

In addition to the technical aspects, this contribution represents the culmination of the effort put in this PhD to reconcile robust control and dynamical systems techniques (recall Fig. 1.1). In fact, the dynamical systems point of view has been helpful in formulating the problem of uncertain LCO and ROA and in interpreting the results, but its interplay with robust control concepts has been instrumental for a novel interpretation of robustness in the nonlinear setting.

## 9.2 Recommendations for future research

This section discusses possible future works connected with technical aspects dealt with in the thesis.

### LFT-FSI co-modelling framework

The approaches described in Section 3.3 aim to provide strategies to perform Linear Fractional Transformation modeling embedded in fluid-structure interaction solvers. In order to foster the combined use of these tools in the aeroservoelastic community, three aspects can be further addressed. From a technical viewpoint, capturing the effect of variations in the structural parameters on the modal base is crucial in order to obtain accurate predictions, as confirmed by the analyses performed in this work. Additional strategies to the iterative cycle proposed with Algorithm 3.3 would hence be beneficial, and a possible novel starting point is the interpretation of the problem as a *nonlinear LFT* given in Eq. (3.34). On the application side, an opportunity is envisaged to analyse aircraft configurations other than the Joined Wings considered in Section 4.3. The reasoning behind that choice was to show the ability of the framework to cope with a known challenging case study, but other studies would be important to consolidate the framework. Finally, from the implementation perspective, the integration of an LFT library inside an FSI solver would allow for an efficient and reliable execution of Algorithms 3.2, 3.3 and 3.4 and could provide an off-the-shelf solution for robust aeroelastic analyses. In this regard, it would be interesting (and computationally advantageous) to investigate implementation of these tools inside low level programming languages (as is typically the case for high-fidelity aeroelastic solvers).

### Characterisation of LCO in the presence of uncertainties

The method presented in Section 6.3 to study Limit Cycle Oscillations by means of Integral Quadratic Constraints is to the best of the author's knowledge new. However, a possible connection holds with previous works where the study of limit cycles with dissipativity theory was proposed. Specifically, a *relaxed* version of the notion of passivity [137] is considered in [220, 227] by adding to the supply rate an activation term which allows the alternate mechanism of dissipation and storage of the energy, which intuitively characterises self sustained oscillations, to be described. In view of the existing parallel between IQC and dissipativity, and the qualitatively similar approach of relaxing the description of the input/output behaviour of the nonlinearities (by means of the multiplier description here and the supply rate in [220, 227]), it is of interest to further explore the connection between these studies. In particular, a formal extension of the passivity-based approach, valid for nominal systems, to the case of uncertainties is of potential interest. Indeed, no theoretical guarantee of the worst-case LCO analysis was given in Section 6.3, and the definition of the relaxed sector multiplier (Fig. 6.15) builds on the Describing Function approximation (with

the associated hypotheses). Toward this goal, previous studies that focused on the behaviour of periodic systems in the presence of uncertainties could be of interest [139, 221].

### Numerically efficient computation of ROA

The proposed recipes for calculating inner estimates of the Region of Attraction build on the solution of non-convex Sum of Squares programs. While the research here has studied different iterative schemes to tackle the bilinearities and has investigated their impact on the results, standard solvers have been employed for the solution of the Sum of Squares optimisation. The main issue is that SOS suffer from scalability and thus computational limitations might prevent the proposed analysis strategies from being applied to sufficiently accurate aeroelastic models (e.g. featuring a larger number of states and order of the nonlinearities). Research in the field of positive polynomials optimisation has been active in recent years, with two directions looking particularly promising: exploiting sparsity in the problem structure and underlying Semidefinite Program [1]; and formulating the certificates for positivity of the polynomials with stronger but cheaper conditions [2]. Both approaches have been recently implemented in MATLAB packages [79, 157] and thus their effectiveness in addressing ROA analysis with the new SOS-based algorithms developed in Chapter 7 could be investigated. Specifically, application to aeroelastic systems undergoing subcritical Hopf bifurcations is advised as a future activity of interest for nonlinear flutter problems.

### Tighter bounds on the robust bifurcation margins

The computation of the worst-case uncertainty combination prompting the onset of a Hopf bifurcation in a nominally stable system is recast as the solution of a smooth constrained optimisation problem. Specifically, the margin  $k_m$  is the objective function (to be minimised) of a non-convex program. One of the consequences of this formulation is that the computed  $k_m$  may be only an upper bound of the actual robust bifurcation margin. That is, there is no guarantee that the global minimum is computed, and thus a smaller perturbation leading to a Hopf bifurcation can exist. This issue is partially mitigated by the continuation-based multi-start strategy proposed in Section 8.2.3, but two aspects could further improve the framework. First, the application of advanced optimisation strategies to Programs 8.2-8.4. In this thesis the solvers available in the MATLAB routine *fmincon* have been used, but other options could be pursued, for example: employing existing global solvers, e.g. based on genetic algorithms or branch and bound methods; and developing more efficient optimisation strategies (e.g. in [230] an improved version of the standard sequential quadratic programming implemented in *fmincon* is presented based on its integration with a second-order cone program). Second, the proposal of a lower bound on  $k_m$  (in analogy to what is done in the structured singular value analysis with  $\mu_{UB}$ ). Starting points can be: the ideas presented in ([187], Section 7.4), where SOS are used to compute a *guaranteed smallest* distance to saddle-node bifurcations in the parameters space; or the approach used in

Section B.1.2 to compute regions of the state space (by means of the level set  $\Omega_{g_d, c_d}$ ) where the equilibria satisfy certain properties (see Remark B.3). Alternatively, extensions of established algorithms in  $\mu$  analysis can be investigated (e.g. power iteration, balanced form). With respect to Eq. (8.12), an expected difficulty here is represented by the block  $\Delta_x$ , which is subject to different constraints from  $\Delta_u$ , hence it must be handled differently in the optimisation problem. The concept of skew- $\mu$  [81] can be helpful in this regard.



## CASE STUDIES DATA

This Appendix gathers the data used for the case studies analysed in the manuscript. These are grouped according to the chapters where they were employed.

### A.1 Chapter 3

The geometry and aerodynamic properties used for the investigations of the aerodynamic LFTs in Sec. 3.2.2 are taken from the typical section model detailed in the next section.

### A.2 Chapter 4

#### A.2.1 Linear typical section

The properties of the typical section model used for the analyses in Sec. 4.1.2 and Sec. 4.2.1 are taken from [134]. With reference to the symbols defined in Sec. 2.3.1, the values of the geometry and structural parameters are reported in Table A.1. As for the aerodynamic model, the Theodorsen GAF matrix  $Q_{hh}$  was presented in (2.11) and recapped here:

$$Q_{hh} = \left( M_{nc} \bar{s}^2 + (B_{nc} + C(\bar{s})R_1 \cdot S_2) \bar{s} + K_{nc} + C(\bar{s})R_1 \cdot S_1 \right). \quad (\text{A.1})$$

Table A.1: Parameters of the linear typical section case study.

Parameter	Value	Parameter	Value
$b$	1 m	$r_\alpha$	0.497
$a$	-0.4	$K_h$	$3.85 \cdot 10^5 N$
$c$	0.6	$K_\alpha$	$3.85 \cdot 10^5 N$
$x_\alpha$	0.2	$K_\beta$	$8.66 \cdot 10^4 N$
$m_w$	$153.94 \frac{kg}{m}$	$c_h$	0 Ns
$r_\beta$	0.0791	$c_\alpha$	0 Ns
$S$	$2m^2$	$c_\beta$	0 Ns
$x_\beta$	-0.025	$\rho$	$1.225 \frac{kg}{m^3}$

The real coefficient matrices  $M_{nc}$ ,  $B_{nc}$ ,  $K_{nc}$ ,  $R_1$ ,  $S_1$  and  $S_2$ , depend on the dimensionless distances  $a$  and  $c$ , and their analytical expressions, taken from [134], are reported below.

$$M_{nc} = \begin{bmatrix} -\pi & \pi a & T_1 \\ \pi a & -\pi(a^2 + \frac{1}{8}) & -2T_{13} \\ T_1 & -2T_{13} & \frac{T_3}{\pi} \end{bmatrix}, \quad B_{nc} = \begin{bmatrix} 0 & -\pi & T_4 \\ 0 & \pi(a - 0.5) & -T_{16} \\ 0 & -T_{17} & -\frac{T_{19}}{\pi} \end{bmatrix},$$

$$K_{nc} = \begin{bmatrix} 0 & 0 & 0 \\ 0 & 0 & -T_{15} \\ 0 & 0 & -\frac{T_{18}}{\pi} \end{bmatrix}, \quad R_1 = \begin{bmatrix} -2\pi \\ 2\pi(a + 0.5) \\ -T_{12} \end{bmatrix}, \quad S_1 = \begin{bmatrix} 0 \\ 1 \\ \frac{T_{10}}{\pi} \end{bmatrix}^\top, \quad S_2 = \begin{bmatrix} 1 \\ 0.5 - a \\ \frac{T_{11}}{2\pi} \end{bmatrix}^\top,$$

where

$$T_1 = -\frac{1}{3}(2 + c^2)\sqrt{1 - c^2} + c \arccos(c),$$

$$T_3 = -\frac{1}{8}(1 - c^2)(5c^2 + 4) + \frac{1}{4}c(7 + 2c^2)\sqrt{1 - c^2} \arccos(c) - (c^2 + \frac{1}{8})(\arccos(c))^2,$$

$$T_4 = c\sqrt{1 - c^2} - \arccos(c), \quad T_5 = -(1 - c^2) - (\arccos(c))^2 + 2c\sqrt{1 - c^2} \arccos(c),$$

$$T_7 = \frac{1}{8}c(7 + 2c^2)\sqrt{1 - c^2} - (c^2 + \frac{1}{8})\arccos(c), \quad T_8 = -\frac{1}{3}(1 + 2c^2)\sqrt{1 - c^2} + c \arccos(c),$$

$$T_9 = \frac{1}{2}(\frac{1}{3}\frac{(1 - c^2)^3}{2} + aT_4), \quad T_{10} = \sqrt{1 - c^2} + \arccos(c),$$

$$T_{11} = (2 - c)\sqrt{1 - c^2} + (1 - 2c)\arccos(c), \quad T_{12} = \sqrt{1 - c^2}(2 + c) - (2c + 1)\arccos(c),$$

$$T_{13} = -0.5(T_7 + (c - a)T_1), \quad T_{15} = T_4 + T_{10},$$

$$T_{16} = T_1 - T_8 - (c - a)T_4 + 0.5T_{11}, \quad T_{17} = -2T_9 - T_1 + (a - 0.5)T_4,$$

$$T_{18} = T_5 - T_4T_{10}, \quad T_{19} = -0.5T_4T_{11}.$$

$C(\bar{s})$  is the Theodorsen function, which is a complex scalar defined as:

$$C(\bar{s}) = \frac{K_1(\bar{s})}{K_0(\bar{s}) + K_1(\bar{s})} = \frac{H_1(z)}{H_1(z) + iH_0(z)}, \quad z = -i\bar{s}, \quad (\text{A.2})$$

where  $K_n$  and  $H_n$  are respectively modified Bessel functions and Hankel functions of order  $n$ . The former can be obtained, for a given reduced frequency  $k$  and  $s = ik$ , with the MATLAB function *besselh*.

Finally, note that the equations of motion are all written in Newton ( $N$ ).

### A.2.2 Aircraft model

The parameter values for the BFF analyses performed in Sec. 4.1.3 and Sec. 4.2.2 are reported in Table A.2. The parameters defining the wing (upper part of the table) are taken from the Goland wing benchmark [93], whereas the geometry and inertial properties of the aircraft (lower part of the table) are obtained by scaling the values from [190] adopting the Goland wing mass ratio and span as the reference mass and length. As an example of the scaling procedure, the definition of the vehicle payload pitch inertia  $I_{yy_p}$  is:

$$I_{yy_p} = I_{yy_p}^0 \left( \frac{m_w}{m_w^0} \right) \left( \frac{L}{L^0} \right)^2, \quad (\text{A.3})$$

where the superscript 0 is used for values taken from [190], and  $\frac{m_w}{m_w^0}$  and  $\frac{L}{L^0}$  represent the mass and length scale factors respectively. The aircraft pitch inertia  $I_{yy}$  is then obtained summing up  $I_{yy_p}$  with the wing and tail contributions  $I_{yy_w}$  and  $I_{yy_t}$ .

The parameters  $EI = \sigma_s EI_G$  and  $D$  are varied in the nominal parametric analyses in Sec. 4.1.3 ( $0.15 < \sigma_s < 1$ ,  $5m < D < 10m$ ), and the values reported in the table are the nominal ones used to generate the LFTs used in Sec. 4.2.2.

Theodorsen theory (A.1) is used to model the aerodynamic forces acting on the wing in response to its deformation (see Sec. 2.3.2 for details on the modelling).

The evaluation of the aerodynamic stability derivatives, used to characterise the short period (2.14) and the coupling terms, employs a first-order approximation:

$$Z_\bullet^r = \frac{\partial Z^r}{\partial \bullet} = -q_\infty S C_{L\bullet}, \quad M_\bullet^r = \frac{\partial M^r}{\partial \bullet} = \bar{c} q_\infty S C_{M\bullet}, \quad (\text{A.4})$$

where  $\bullet = \{\bar{\alpha}, \bar{q}, \dot{\bar{\alpha}}\}$  and  $C_{L\bullet}$ ,  $C_{M\bullet}$  are functions of the aircraft's geometry [212]:

$$\begin{aligned} C_{L_{\bar{\alpha}}} &= C_{L_w} + C_{L_t} \frac{S_t}{S}, & C_{M_{\bar{\alpha}}} &= (\bar{X}_{CG} - \bar{X}_{AC}) C_{L_{\bar{\alpha}}}, \\ C_{L_{\bar{q}}} &= C_{L_t} \frac{S_t}{S} (\bar{X}_{CG} - \bar{X}_{AC}^t) \frac{\bar{c}}{V}, & C_{M_{\bar{q}}} &= -C_{L_t} \frac{S_t}{S} (\bar{X}_{CG} - \bar{X}_{AC}^t)^2 \frac{\bar{c}}{V}, \\ C_{L_{\dot{\bar{\alpha}}}} &= -(C_{L_t} \epsilon_{AR} (\bar{X}_{AC}^t - \bar{X}_{AC}^w) \frac{S_t}{S}) \frac{\bar{c}}{V} & C_{M_{\dot{\bar{\alpha}}}} &= -C_{L_{\dot{\bar{\alpha}}}} (\bar{X}_{AC}^t - \bar{X}_{AC}), \end{aligned}$$

Table A.2: Parameters for the aircraft model used in the BFF analyses.

Parameter	Value	Parameter	Value
$b$	0.9144 m	$a$	-0.333
$m_w$	35.7187 $\frac{kg}{m}$	$r_\alpha$	0.4998
$x_\alpha$	0.2	$\rho$	1.225 $\frac{kg}{m^3}$
$K_h$	1.493 $10^4 \frac{N}{m^2}$	$K_\alpha$	6.567 $10^4 N$
$EI_G$	9.77 $10^6 Nm^2$	$GJ$	9.89 $10^5 Nm^2$
$\bar{c}$	1.8288 m	$L$	12.192 m
$C_{L_\alpha}^w, C_{L_\alpha}^t$	$2\pi$	$\sigma_s$	0.15
$m$	1.351 $10^3 kg$	$I_{yy}$	1.39 $10^3 kg.m^2$
$D$	6 m		
$c_t$	0.3 m	$L_t$	2.2 m
$\bar{X}_{CG}$	0.266	$\bar{X}_{AC}^w$	0.25
$\bar{X}_{AC}^w$	3.3	$\bar{X}_{AC}$	0.3

with:

$$\begin{aligned}\bar{X}_{AC}^t &= \frac{D + 0.25c_t}{\bar{c}}, & \bar{X}_{AC} &= \frac{C_{L_w}\bar{X}_{AC}^w + C_{L_t}\bar{X}_{AC}^t \frac{S_t}{S}}{C_{L_w} + C_{L_t} \frac{S_t}{S}}, \\ C_{L_w} &= C_{L_\alpha}^w \frac{AR_w}{2 + \sqrt{AR_w^2 + 4}}, & C_{L_t} &= C_{L_\alpha}^t \frac{AR_t}{2 + \sqrt{AR_t^2 + 4}}, \\ AR_w &= L, & AR_w &= L_t, \\ \epsilon_{AR} &= 2 \frac{CL_w}{\pi AR_w}.\end{aligned}$$

### A.2.3 Joined Wings

A description of the *PrP250* aircraft model analysed in Sec. 4.3 can be found in the dedicated publications [55, 70]. Another relevant work where flutter analysis of this configuration was performed is [40].

In this section detailed aspects of the analyses performed with the iterative algorithm in Sec. 4.3.2 are presented. Table A.3 reports the normalised perturbations in the parameters as well as the corresponding flutter speed  $V_{f\mu}$  calculated by the FSI solver at each iteration. This table represents an extension of Table 4.5 where only  $V_{f\mu} \frac{m}{s}$  and  $\bar{\sigma}(\Delta^{cr})$  were listed. For the benefit

of readability, the columns are labelled with the symbol of the parameter (e.g.  $EI_{z_1}$ ), but the reported values are normalised perturbations (e.g.  $\delta_{EI_{z_1}}$ ).

Table A.4 reports the normalised perturbations in the parameters as well as the corresponding flutter speed  $V_{f\mu}$  at the final iteration (ITER=3) of the iterative cycle initialised based on the optimality check (Algorithm 3.4). See Sec. 4.3.3 for a discussion on it.

Table A.3: Perturbation matrix  $\Delta_{ITER\#}^{cr}$  and corresponding speed  $V_{f\mu}$  at each iteration.

ITER	$V_{f\mu} \frac{m}{s}$	$EI_{z_1}$	$EI_{z_2}$	$EI_{z_3}$	$EI_{z_4}$	$EI_{z_5}$	$EI_{z_6}$	$EI_{z_7}$	$EI_{z_8}$	$EI_{z_9}$	$EI_{z_{10}}$
1	288.4	-0.98	-0.98	-0.98	-0.98	0.082	0.98	0.98	-0.98	-0.98	-0.98
2	287.4	-1.23	-1.23	-1.23	-1.23	1.08	1.23	1.23	-1.23	-1.23	-1.23
3	285.9	-1.41	-1.41	-1.41	-1.41	1.37	1.41	1.41	-1.41	-1.41	-1.41
4	285.24	-1.47	-1.47	-1.47	-1.47	1.47	1.47	1.47	-1.47	-1.47	-1.47
$EI_{z_{13}}$	$EI_{z_{15}}$	$EI_{z_{17}}$	$EI_{z_{18}}$	$EI_{z_{19}}$	$EI_{z_{20}}$	$EI_{z_{21}}$	$EI_{z_{22}}$	$EI_{z_{23}}$	$EI_{z_{24}}$	$m_{f_7}$	$m_{f_8}$
-0.98	0.98	-0.98	-0.98	0.98	0.98	-0.98	-0.98	-0.98	-0.98	0.98	0.98
-1.23	1.23	-1.23	-1.23	1.23	1.23	-1.23	-1.23	-1.23	-1.23	1.23	1.23
-1.41	1.41	-1.41	-1.41	1.41	1.41	-1.41	-1.41	-1.41	-1.41	1.41	1.41
-1.47	1.47	-1.47	-1.47	1.47	1.47	-1.47	-1.47	-1.47	-1.47	1.47	1.47
$m_{f_9}$	$m_{f_{10}}$	$m_{f_{11}}$	$m_{f_{12}}$	$m_{f_{13}}$	$m_{f_{14}}$	$m_{f_{15}}$	$m_{f_{16}}$	$m_{f_{17}}$	$m_{f_{18}}$	$m_{f_{19}}$	$m_{f_{20}}$
0.98	0.98	0.98	0.98	0.98	0.98	0.98	0.98	0.98	0.98	-0.98	-0.98
1.23	1.23	1.23	1.23	1.23	1.23	1.23	1.23	1.23	1.23	-1.23	-1.23
1.41	1.41	1.41	1.41	1.41	1.41	1.41	1.41	1.41	1.41	-1.41	-1.41
1.47	1.47	1.47	1.47	1.47	1.47	1.47	1.47	1.47	1.47	-1.47	-1.47
$m_{f_{21}}$	$m_{f_{22}}$	$m_{f_{23}}$	$m_{f_{24}}$	$m_{f_{25}}$	$m_{f_{26}}$	$m_{f_{27}}$	$m_{f_{28}}$	$m_{f_{29}}$	$m_{f_{30}}$	$m_{f_{31}}$	$\bar{\sigma}(\Delta^{cr})$
0.82	0.98	0.92	0.98	0.98	0.98	0.98	0.98	0.98	0.98	0.98	0.98
-1.23	1.18	1.23	1.23	1.23	1.23	1.23	1.23	1.23	1.23	1.23	1.23
-1.3	1.39	1.41	1.41	1.41	1.41	1.41	1.41	1.41	1.41	1.41	1.41
-1.09	1.47	1.47	1.47	1.47	1.47	1.47	1.47	1.47	1.47	1.47	1.47

Table A.4: Perturbation matrix  $\Delta_{ITER3-new}^{cr}$  and corresponding  $V_{f\mu}$  at the final iteration of the re-initialised cycle.

$V_{f\mu} \frac{m}{s}$	$EI_{z_1}$	$EI_{z_2}$	$EI_{z_3}$	$EI_{z_4}$	$EI_{z_5}$	$EI_{z_6}$	$EI_{z_7}$	$EI_{z_8}$	$EI_{z_9}$	$EI_{z_{10}}$	$EI_{z_{13}}$
285.23	-1.34	-1.34	-1.34	-1.34	1.30	1.34	1.34	-1.34	-1.34	-1.34	-1.34
$EI_{z_{15}}$	$EI_{z_{17}}$	$EI_{z_{18}}$	$EI_{z_{19}}$	$EI_{z_{20}}$	$EI_{z_{21}}$	$EI_{z_{22}}$	$EI_{z_{23}}$	$EI_{z_{24}}$	$m_{f_7}$	$m_{f_8}$	$m_{f_9}$
1.34	-1.34	-1.34	1.29	1.34	-1.34	-1.34	-1.34	-1.34	1.34	1.34	1.34
$m_{f_{10}}$	$m_{f_{11}}$	$m_{f_{12}}$	$m_{f_{13}}$	$m_{f_{14}}$	$m_{f_{15}}$	$m_{f_{16}}$	$m_{f_{17}}$	$m_{f_{18}}$	$m_{f_{19}}$	$m_{f_{20}}$	$m_{f_{21}}$
1.34	1.34	1.34	1.34	1.34	1.34	1.34	1.34	1.34	-1.34	-1.34	1.34
$m_{f_{22}}$	$m_{f_{23}}$	$m_{f_{24}}$	$m_{f_{25}}$	$m_{f_{26}}$	$m_{f_{27}}$	$m_{f_{28}}$	$m_{f_{29}}$	$m_{f_{30}}$	$m_{f_{31}}$	$\bar{\sigma}(\Delta^{cr})$	
1.34	1.34	1.34	1.34	1.34	1.34	1.34	1.34	1.34	1.34	1.34	

### A.3 Chapter 5

The derivation of the reduced order LTI models used for analysis of the FLEXOP demonstrator was discussed in Sec. 2.3.4. A detailed description of the demonstrator [226], the nonlinear high-fidelity model [257], and the reduction procedure can be found in the references [155].

### A.4 Chapter 6

The parameters of the typical section benchmark with freeplay in the control surface are taken from [234] and are summarised in Table A.5.

Table A.5: Parameters of the nonlinear (with freeplay) typical section case study.

Parameter	Value	Parameter	Value
$b$	0.127 m	$r_\alpha$	0.4968
$a$	-0.5	$K_h$	$2818.8 \frac{N}{m^2}$
$c$	0.5	$K_\alpha$	37.3 N
$x_\alpha$	1.5731	$K_\beta^L$	3.9 N
$m_w$	$3.3843 \frac{kg}{m}$	$c_h$	0 Ns
$r_\beta$	0.0773	$c_\alpha$	0 Ns
$S$	$0.254 m^2$	$c_\beta$	0 Ns
$x_\beta$	0.0724	$\rho$	$1.225 \frac{kg}{m^3}$
$\bar{\delta}$	$2.12^\circ$		
$S_\alpha$	0.08587 Kg	$S_\beta$	0.00395 Kg
$I_\alpha$	0.01347 Kg m	$I_\beta$	0.0003264 Kg m

In [234] a slightly different notation from the one adopted in Sec. 2.3.1 to present the typical section model was adopted, and in particular two points are stressed next. First, in [234]  $S_\alpha$ ,  $S_\beta$ , and  $I_\alpha$  are used instead of the dimensionless counterparts  $x_\alpha$ ,  $x_\beta$ , and  $r_\alpha$ . Therefore, the expression for the latter reported in Table A.5 was obtained by normalising them with  $b$  and  $m_w$  (e.g.  $r_\alpha = \sqrt{\frac{I_\alpha}{m_w b^2}}$ ,  $x_\alpha = \frac{S_\alpha}{m_w b^2}$ ). Second, in [234] the plunge DOF is  $h$  and not  $\frac{h}{b}$  and the mass matrix  $M_s$  is thus written in a slightly different way. To avoid confusion, its expression using the convention in [234] is reported:

$$M_s = \begin{bmatrix} m_w & S_\alpha & S_\beta \\ S_\alpha & I_\alpha & I_\beta + S_\beta(c-a)b \\ S_\beta & I_\beta + S_\beta(c-a)b & I_\beta \end{bmatrix}. \quad (\text{A.5})$$

The terms of the aerodynamic matrix  $Q_{hh}$  should be consistently normalised such that in the end the equations of motion are expressed in  $\frac{N}{m}$  for the plunge equilibrium and in  $N$  for the moment equilibria.

## A.5 Chapter 7

Three different case studies are used for the Region of Attraction analysis, namely short-period model with dynamic controller (Sec. 7.2.1.3-7.2.2.2), short-period model (GTM) with static and saturated controller (Sec. 7.3.2.1), Van der Pol oscillator (Sec. 7.3.2.2). The definition of their vector fields can be found in the respective sections.

## A.6 Chapter 8

The typical section case study detailed in Sec. A.2.1 forms the basis for the model used to exemplify the computation of robust bifurcation margins. The linear benchmark is then augmented including cubic nonlinearities in the plunge and pitch DOF as described in Sec. 8.3.1.





## EQUILIBRIUM-INDEPENDENT ROA

The estimations of the robust Region of attraction in Chapter 7 assumed that the equilibrium point is independent of the uncertainty. This assumption, typically done in the literature [6, 49, 241], is primarily for the sake of simplicity and in most cases the uncertainty does alter the equilibrium point. In this Appendix an approach is proposed which allows to compute ROA of equilibrium points whose location is modified by the uncertainties (assumed here constant). Inner estimates of the ROA are formulated as invariant level set which does not explicitly depend on the equilibrium point or on the uncertainties. The result thus consists of an Equilibrium-Independent Region of attraction (EIR). Note that the formulation is given, for clarity and generality, in a Lyapunov setting, but it can be extended to both the invariant set (Sec. 7.2.2) and the IQC framework (Sec. 7.3.1).

The idea of guaranteeing a property of the system without knowledge of the equilibrium is inspired by the work in [109], where the notion of equilibrium-independent passivity was first introduced. This was then generalised in [10], where the concept of equilibrium-independent dissipativity for systems with unknown equilibria was formulated. However, the approach here considers an equilibrium-independent storage function, and, equally important, allows to study systems with multiple equilibria, relaxing the assumption in [109] that there exists a unique equilibrium for a given perturbation. This key feature is achieved by specifying the branch of equilibria considered in the analyses as the level set of a suitable function. If no a priori knowledge is available, a candidate function can be identified via Sum of Squares techniques, which is used to provide computational recipes for estimating subsets of the EIR.

A similar problem was studied in [53], where lower and upper estimates of the ROA were formulated based on viability theory. Specifically, that work considered convergence of the trajectories to a given set, whereas here the problem of asymptotic converge to an (unknown) equilibrium point is investigated. Another related work is [12], where an algorithm based on

contraction metrics was proposed to relax the uncertainty-independent equilibrium hypothesis. While that study focused on global stability certificates, the approach here is tailored to ROA analysis, even though it could be employed for certifying global stability of branches of fixed points as well.

This work was presented in [128] and has been developed in collaboration with Prof. Pete Seiler from the University of Minnesota.

## B.1 Equilibrium-independent region of attraction certificate

### B.1.1 Problem formulation

The problem of computing inner estimates of the robust ROA  $\mathcal{R}_\delta$  defined in Sec. 7.1.1 is considered. The analysed vector field is recalled next:

$$\dot{x} = f(x, \delta), \quad (\text{B.1})$$

where  $\delta \in \Delta \subset \mathbb{R}^{n_\delta}$  is a vector of constant unknown parameters,  $\Delta$  is a known bounded set, and  $f : \mathbb{R}^n \times \Delta \rightarrow \mathbb{R}^n$ . Crucially, the equilibrium point  $x^*(\delta)$  depend on the uncertainties as explicitly reported in the definition of  $\mathcal{R}_\delta$  (7.4). The proposed approach builds on the concept of equilibrium-independent passivity, introduced in [109]. The objective here is to find a storage function whose level set is attractive and invariant for any potential equilibrium point of the uncertain system. There are two main distinctions relative to [109]. First, the storage function does not explicitly reference the equilibrium point. This yields an equilibrium-independent ROA. Second, the proposed approach does not assume the existence of a unique equilibrium.

First, define  $\mathcal{E} := \{x^* : f(x^*, 0) = 0\}$ , i.e.  $\mathcal{E}$  is the set of equilibria of the *nominal* vector field (for the sake of notation, we assume without loss of generality that  $\delta = 0 \in \Delta$  corresponds to nominal conditions). We will assume that  $\mathcal{E}$  is non-empty, with  $|\mathcal{E}|$  indicating the cardinality of the set. In general,  $|\mathcal{E}| \geq 1$ , i.e. the nominal vector field has one or more fixed points  $x^*$ . Specifically, we will be concerned with the subset  $\mathcal{E}^a \subseteq \mathcal{E}$  gathering attractive equilibria.

Define the induced set  $\mathcal{D}_{x^*}^{\mathcal{E}} := \{\bar{x} : 0 = f(\bar{x}, \delta), \forall \delta \in \Delta\}$  which associates each element  $x^*$  of  $\mathcal{E}^a$  with the branch of equilibria resulting from varying  $\delta$  inside  $\Delta$ . Note that the definition of  $\mathcal{D}_{x^*}^{\mathcal{E}}$  only assumes that, as  $\delta$  takes values in the uncertainty set, the branch consists of attracting equilibria. Further discussions on this aspect are referred to Remark B.2 below. The objective is to compute an equilibrium independent region of attraction for the branch of fixed points  $\bar{x}$  associated with the selected nominal equilibrium point  $x^*$ .

The existing approach is to find a parameter-dependent Lyapunov function  $V(x, \delta)$ , but it is computationally demanding since the variables  $\delta$  need to be included in the SOS program. Moreover, it entails having a closed form expression for the dependence of the equilibria on the uncertainties in order to ensure that  $V(\bar{x}(\delta), \delta) = 0$ . To avoid this, consider the coordinate transformation  $y(x, \delta) = x - \bar{x}(\delta)$ . The new coordinate  $y$  can be interpreted as the deviation of the

state  $x$  relative to the equilibrium point  $\bar{x}(\delta)$  for uncertainty  $\delta \in \Delta$ . It is stressed that, since  $\delta$  is assumed constant, it holds  $\dot{y} = \dot{x}$ . Hence the vector field  $f(y + \bar{x}(\delta), \delta)$  governs the evolution of the state  $x$  relative to the equilibrium point  $\bar{x}(\delta)$  that occurs at  $\delta$ .

It is now possible to state the following result, which gives conditions to determine invariant and attractive regions associated with the equilibria of (7.3) via equilibrium-independent Lyapunov functions.

**Theorem B.1.** *Let  $x^*$  be an attractive equilibrium point of the nominal system, i.e.  $x^* \in \mathcal{E}^a$ . We denote with  $\mathcal{D}_{x^*}^{\mathcal{E}}$  the associated set and we apply to  $f$  the coordinate transformation  $x = y + \bar{x}$ , with  $\bar{x} \in \mathcal{D}_{x^*}^{\mathcal{E}}$ .*

*If there exists a smooth, continuously differentiable function  $\tilde{V}: \mathbb{R}^n \rightarrow \mathbb{R}$  and an associated level set  $\Omega_{\tilde{V}, \gamma} = \{y \in \mathbb{R}^n : \tilde{V}(y) \leq \gamma\}$  such that*

$$\tilde{V}(0) = 0 \quad \text{and} \quad \tilde{V}(y) > 0 \quad \forall y \setminus \{0\}, \quad (\text{B.2a})$$

$$\nabla \tilde{V}(y) \cdot f(y + \bar{x}(\delta), \delta) < 0 \quad \forall y \in \Omega_{\tilde{V}, \gamma} \setminus \{0\}, \quad \forall \delta \in \Delta, \forall \bar{x} \in \mathcal{D}_{x^*}^{\mathcal{E}}. \quad (\text{B.2b})$$

*Then  $\Omega_{\tilde{V}, \gamma}$  is an inner estimate of the EIR of the fixed points  $\bar{x} \in \mathcal{D}_{x^*}^{\mathcal{E}}$  when (B.1) is subject to perturbations in  $\Delta$ .*

**Proof.** The theorem assumes there exists a function  $\tilde{V}$  which is positive and decreasing inside a level set  $\Omega_{\tilde{V}, \gamma}$ , and its only zero is the origin. This implies, by application of the Lyapunov direct method [137], that this region is attractive and invariant, therefore it holds  $\Omega_{\tilde{V}, \gamma} \subseteq \mathcal{R}_\delta$ . Note the subtlety, compared to standard Lyapunov function level sets, that the function  $\tilde{V}$  decreases along trajectories  $y$  representing the deviation of the original state  $x$  from the equilibrium point  $\bar{x}$  as  $\delta$  take values in the uncertainty set. These trajectories will ultimately converge to  $y = 0$ , that is the state  $x$  will settle down to the equilibrium. ■

**Remark B.1.** *The robust Region of Attraction provided by Theorem B.1 is equilibrium independent, due to the fact that the level set is a function of  $y$  only. This choice privileges the interpretation of the results by making the domain of attraction only implicitly related to  $\bar{x}$ , which is in principle unknown (due to its dependence on the uncertainty). In view of this, an apparent practical benefit of the EIR formulation is that it is not required to fix a value of  $\bar{x}$  to represent the predicted region of local stability. In fact, this approach underlies the concept of family of ROA, consisting of a single region  $\Omega_{\tilde{V}, \gamma}$  which has embedded the information relative to multiple domains of attraction. Indeed if  $\tilde{V}$  satisfies the conditions of Theorem B.1, then  $V(x, \delta) = \tilde{V}(x - \bar{x}(\delta))$  provides a parameter-dependent Lyapunov function and  $\Omega_{V, \gamma} = \{x \in \mathbb{R}^n : V(x, \delta) \leq \gamma\}$  is a ROA relative to the equilibrium point  $\bar{x}(\delta)$ . For similar reasons, a parameter-dependent ROA of the type  $V(y, \delta)$  has not been pursued. This choice, despite being in principle a source of conservatism (because dependency on  $\delta$  is not exploited), aims to reduce the computational complexity of the ensuing numerical problem and favour a better interpretation of the results.*

**Remark B.2.** *The proposed framework can be applied to systems having multiple equilibria. This is achieved by introducing the set  $\mathcal{E}^a$  (where  $|\mathcal{E}^a| \geq 1$ ) and associating an EIR to each  $x^* \in \mathcal{E}^a$ . The induced set  $\mathcal{D}_{x^*}^{\mathcal{E}}$  is then instrumental in Theorem B.1 to ensure that the analyses are relative to a specific branch of solutions only (see the domain of  $\bar{x}$  where Eq. B.2b must hold). In practice, it is made the additional hypothesis that  $f(\bar{x}, \delta) = 0$  has a unique solution  $\bar{x}(\delta)$ , associated with a given  $x^*$ , for  $\delta \in \Delta$ . This assumption is not restrictive and, to show this, we consider the Implicit Function Theorem (IFT) [145]. Under the condition that the linearised Jacobian of  $f$  around the pair  $(x^*, 0)$  is not singular, it is guaranteed existence and uniqueness of a mapping  $F : \bar{x} = F(\delta)$  in neighbourhoods  $D$  and  $X$  of  $\delta = 0$  and  $x^*$  respectively. This condition is always satisfied if the steady-state solutions of  $f$  do not undergo qualitative changes (e.g. bifurcations) when the uncertainty vary inside the set  $\Delta$ . Having in mind that this framework is employed to study ROA of attractive fixed points, it can be assumed that  $D = \Delta$  holds, i.e., the additional assumption is natural in this context. Note that Theorem B.1 still holds when the IFT is not verified (e.g., pitchfork bifurcation, where it would suffice to consider one of the stable emanating branches), but the computational recipes proposed in the next sections do not apply.*

### B.1.2 Equilibria identification and computation of inner estimates of EIR

The computation of the EIR with Theorem B.1 involves finding a function that satisfies set containment conditions. Since interest is restricted to polynomial vector fields, the problem can be recast an SOS program by means of the generalised S-procedure (Lemma 7.2). In the following discussion  $\bar{x}$  and  $\delta$  are algebraic indeterminates satisfying particular conditions.

As proposed in Sec. 7.2.2, the bounded set  $\Delta$  is described as a semialgebraic set (7.17), and thus the condition  $\delta \in \Delta$  can be enforced by means of the multipliers  $m_i$  (7.23-7.24). Another set containment prescribed by (B.2b) is that the inequality must hold  $\forall \bar{x} \in \mathcal{D}_{x^*}^{\mathcal{E}}$ . In order to incorporate this condition into an SOS program, the idea is to find a function  $g$  such that  $\bar{x} \in \mathcal{D}_{x^*}^{\mathcal{E}} \implies g(\bar{x}) \geq 0$  and, similarly to what is done with the uncertainties, use this function to constrain the variables  $\bar{x}$ . If no a priori knowledge on the location of the branch is available to define  $g$ , the following strategy can be followed to compute it.

A function  $g_d$  with a prescribed shape is considered, and the smallest positive scalar  $c_d > 0$  such that  $\bar{x} \in \mathcal{D}_{x^*}^{\mathcal{E}} \implies \bar{x} \in \Omega_{g_d, c_d}$  is computed. Possible choices for  $g_d$  are the spheroid or ellipsoid centred at  $x^*$ . Then,  $g = c_d - g_d$  is a candidate function to enforce the constraint. This problem can be recast as an SOS optimisation. In order to specialise the search of the function  $g$  to the branch corresponding to  $x^*$  (in case  $|\mathcal{E}| > 1$ ), the auxiliary level set  $\Omega_{p_b, R_b}$  is introduced. The rationale behind the selection of  $p_b$  and  $R_b$  is that  $\Omega_{p_b, R_b}$  should include the branch of equilibria associated with  $\bar{x}$ , i.e.  $\mathcal{D}_{x^*}^{\mathcal{E}} \subseteq \Omega_{p_b, R_b}$ . The SOS program for computing  $c_d$  is presented next.

**Program B.1.**

$$\min_{s_b, s_{di} \in \Sigma[\bar{x}; \delta]; r_f \in \mathbb{R}[\bar{x}; \delta]} c_d, \\ r_f f - s_b (R_b - p_b) - \Gamma_d + (c_d - g_d) \in \Sigma[\bar{x}, \delta], \quad (\text{B.3a})$$

$$\Gamma_d = s_{d1} m_1(\delta_1) + \dots + s_{di} m_i(\delta_i) + \dots + s_{dj} m_j(\delta_j). \quad (\text{B.3b})$$

This program is a direct application of Lemma 7.2. The last term in (B.3a) is equivalent to  $f_0$  in (7.8) (i.e. the *including* set function), whereas the others are the *included* sets ( $h, f_i$ ) and relative multipliers. The first term provides the constraint that  $\bar{x}$  is a fixed point of the original vector field  $f$  as  $\delta$  varies within its range. Note however that, if  $|\mathcal{E}| > 1$  this information is not sufficient because there are multiple branches of solutions  $(\bar{x}, \delta)$  for which  $f(\bar{x}, \delta) = 0$ . For this reason, the aforementioned set  $\Omega_{p_b, R_b}$  is employed. Despite being seemingly similar,  $\Omega_{p_b, R_b}$  and  $\Omega_{g_d, c_d}$  have a substantially different meaning. The latter is indeed the smallest level set (for a given shape) to include the equilibria of the system, whereas  $\Omega_{p_b, R_b}$  has the purpose of selecting the branch of interest. Note that  $R_b$  has to be chosen such that  $\Omega_{p_b, R_b}$  does not include other branches of solutions. The optimisation over  $c_d$  guarantees then, even without a good initial guess for  $R_b$ , the sought estimation for  $\Omega_{g_d, c_d}$  is eventually obtained (e.g. iteratively).

Finally,  $\Gamma_d$  guarantees that the SOS constraint hold in the uncertainty set by applying the rationale discussed in (7.23). Note that a version of Program B.1 where the shape of the level set function  $g_d$  is optimised over can be also employed.

**Remark B.3.** *The aforementioned approach is proposed here with the aim to characterise the set  $\mathcal{D}_{\bar{x}^*}^\mathcal{E}$ . In other words, the level set  $\Omega_{g_d, c_d}$  allows regions of the state space where there is a branch of fixed points to be identified. It is common in the study of nonlinear dynamics to relate properties of the system (e.g. bifurcations in the steady-state solutions) to algebraic conditions fulfilled by the Jacobian of the vector field and its higher derivatives (see the case of Hopf bifurcation discussed in Sec. 8.1.1). These conditions can be easily appended to Program B.1, and thus this approach can be applied to investigate additional properties of uncertain systems described by the vector field in (7.3). An example could be the computation of guaranteed (lower) bounds on  $k_m$ .*

Based on the foregoing discussion, an SOS program to determine equilibrium independent regions of attraction based on Theorem B.1 is formulated. The independent variables of the optimisation are denoted by  $\tilde{y} = [y; \bar{x}; \delta]$ .

**Program B.2.**

$$\max_{s_D, s_{di}, s_1 \in \Sigma[\tilde{y}]; r_f \in \mathbb{R}[\tilde{y}]; \tilde{V} \in \mathbb{R}[y]} \gamma, \\ \tilde{V} - L_1 \in \Sigma[y], \\ r_f f - s_1 (\gamma - \tilde{V}) - s_D g - \Gamma_d - (\nabla \tilde{V} f + L_2) \in \Sigma[\tilde{y}], \quad (\text{B.4})$$

where  $\Gamma_d$  is defined as in (B.3b) and  $L_1$  and  $L_2$  are positive definite polynomials, specifically  $L_1 = \epsilon_1 y^T y$  and  $L_2 = \epsilon_2 \tilde{y}^T \tilde{y}$  with  $\epsilon_1$  and  $\epsilon_2$  small real numbers on the order of  $10^{-6}$  (the use of these terms was motivated in Remark 7.4 and has the aim to provide solutions satisfying the SOS constraints by some margin). Due to the presence of bilinear terms, an iterative scheme inspired by the V-s iteration (Algorithm 7.1), is proposed.

### Algorithm B.1.

**Output:** the level set  $\Omega_{\tilde{V}, \gamma}$  (inner estimate of the EIR).

**Input:** a polynomial  $\tilde{V}^0$  satisfying (B.2) for some  $\gamma$ .

1.  $\gamma$ -Step. Solve through bisection on  $\gamma$ .

$$\begin{aligned} & \max_{s_1, s_D, s_{di} \in \Sigma[\tilde{y}]; r_f \in \mathbb{R}[\tilde{y}]} \gamma, \\ & r_f f - s_1(\gamma - \tilde{V}^0) - s_D g - \Gamma_d - (\nabla \tilde{V}^0 f + L_2) \in \Sigma[\tilde{y}], \end{aligned}$$

set  $\bar{\gamma} \leftarrow \gamma, \bar{s}_1 \leftarrow s_1$ .

2.  $\beta$ -Step. Maximise  $\beta$  such that  $\varepsilon(p, \beta) \subseteq \varepsilon(V, \gamma)$ .

$$\begin{aligned} & \max_{s_2 \in \Sigma[y]} \beta, \\ & (\bar{\gamma} - \tilde{V}^0) - s_2(\beta - p) \in \Sigma[y], \end{aligned}$$

set  $\bar{\beta} \leftarrow \beta, \bar{s}_2 \leftarrow s_2$ .

3.  $V$ -Step. Compute a new shape for the level set for a given  $\gamma$ .

$$\begin{aligned} & \tilde{V} - L_1 \in \Sigma[y], \\ & (\bar{\gamma} - \tilde{V}) - \bar{s}_2(\bar{\beta} - p) \in \Sigma[y], \\ & r_f f - \bar{s}_1(\gamma - \tilde{V}) - s_D g - \Gamma_d - (\nabla \tilde{V} f + L_2) \in \Sigma[\tilde{y}], \end{aligned}$$

set  $\tilde{V}^0 \leftarrow \tilde{V}$  and go to  $\gamma$ -Step.

## B.2 Numerical example

### B.2.1 System description

The following nonlinear dynamics with an uncertain scalar parameter  $\delta$  is considered to demonstrate the application of the EIR framework.

$$\begin{aligned} \dot{\phi} &= -\psi - \frac{3}{2}\phi^2 - \frac{1}{2}\phi^3 + \delta, \\ \dot{\psi} &= 3\phi - \psi - \psi^2, \\ \delta &\in [0.9; 1.1]. \end{aligned} \tag{B.5}$$

The steady-state solutions of the system consist of two distinct branches of equilibria as  $\delta$  varies in the prescribed range. By linearising the Jacobian of (B.5) around the equilibria and evaluating the corresponding eigenvalues, it can be seen that one branch corresponds to sinks (i.e. stable fixed points), while the other corresponds to sources (i.e. unstable fixed points). This means that the cardinality of  $\mathcal{E}$  is 2 and thus the set of interest  $\mathcal{D}_{x^*}^{\mathcal{E}}$  (i.e. the one associated with sinks) must be specified. This characterisation can be performed by means of Program B.1, where the fixed shape function  $g_d$  is taken here as the circle centred at the nominal fixed point (i.e.  $\delta = 1$ ). Fig. B.1 displays the set of  $\mathcal{D}_{x^*}^{\mathcal{E}}$  (dotted curve *Equilibria*) and two boundaries  $g^1$  and  $g^2$ . The former (dashed curve) is relative to the level set  $\Omega_{g_d, c_d}$  where  $g_d$  is the circle discussed above and only the size  $c_d$  is optimised, whereas the latter (solid line) was obtained with Program B.1 by optimising both shape and size (i.e.  $g_d$  is not fixed a priori but is defined as a polynomial of degree 6). It can be noted that in both cases the level sets circumscribe the equilibria, and thus are both good candidates to characterise  $\mathcal{D}_{x^*}^{\mathcal{E}}$ . As expected, the case with optimised shape provides a tighter boundary for the set  $\mathcal{D}_{x^*}^{\mathcal{E}}$ , but this does not give advantages in this particular application.

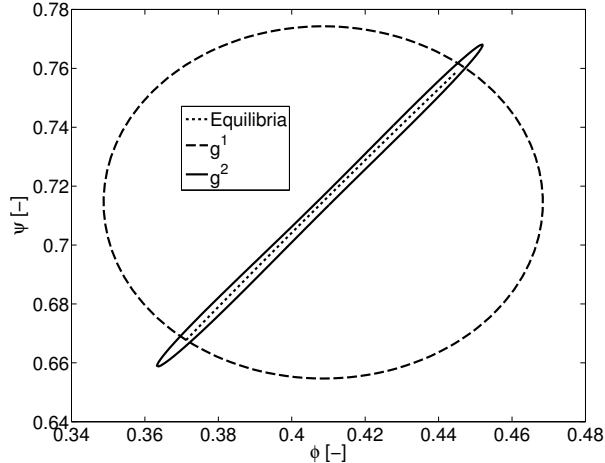


Figure B.1: Characterisation of the set of sinks via level sets.

Another important feature of the dynamics in (B.5) is that the sinks are only locally asymptotically stable. Therefore, the proposed approach can be used to determine the associated region of attraction. Note that, since the other branch of solutions is unstable, it is fundamental to specify that the analyses consider only the set of sinks, because otherwise no region of attraction could be estimated.

### B.2.2 EIR of the sinks

Equilibrium-independent estimations of the ROA of system (B.5) are computed in this section by means of Algorithm B.1. Fig. B.2 shows the results obtained with functions  $\tilde{V}$  of different degree, specifically  $\partial(\tilde{V}) = 2$  and  $\partial(\tilde{V}) = 4$ .

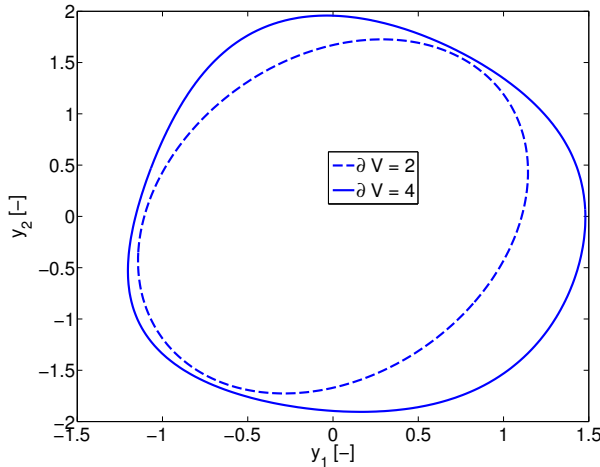


Figure B.2: EIR for  $\partial(\tilde{V}) = 2$  and  $\partial(\tilde{V}) = 4$ .

Note first that the shifted coordinates  $y_1 = \phi - \bar{\phi}$  and  $y_2 = \psi - \bar{\psi}$  are reported on the axes of the plots. This is consistent with the central idea of the approach of representing the domain of attraction as an equilibrium-independent level set. It can also be ascertained that by increasing the degree of  $\tilde{V}$ , the estimation of the ROA is improved. It is interesting to register an enlargement of the stability region in the lower right part of the plot. Further aspects associated with the concept of EIR are investigated next.

In Remark B.1 it was introduced the equilibrium-dependent level set  $\Omega_{V,\gamma}$  which is associated with  $\Omega_{\tilde{V},\gamma}$  via coordinates transformation. Once a value for the uncertainty is specified,  $\Omega_{V,\gamma}$  provides an estimate of the ROA for the associated equilibrium point  $\bar{x}(\delta)$ . Taking the cue from this, a Monte Carlo-based search to quantify the conservatism associated with the predictions reported in Fig. B.2 is employed. The goal is to compute the smallest  $\gamma_f > \gamma$  (and associated  $\delta$ ) such that there is an initial condition  $x_0$  on the boundary of  $\Omega_{V,\gamma_f}$  for which the system does not eventually converge to the equilibrium point.

Results are evaluated next with regard to the estimations shown in Fig. B.2 for the case of quartic  $V$  (serving as lower bound). The Monte Carlo search reveals that  $\delta = 0.9$  is the critical (i.e. leading to the smallest  $\gamma_f$ ) value for the uncertain parameter. Fig. B.3 shows lower (*LB*) and upper (*UB*) bounds of the ROA, as well as cross markers corresponding to initial conditions on  $\Omega_{V,\gamma_f}$  whose trajectories do not converge to the equilibrium (square marker).

It is interesting to notice that the cross markers in Fig. B.3 are all distributed in the region where Fig. B.2 featured the smaller gap between the curves  $\partial(V) = 2$  and  $\partial(V) = 4$  (note that

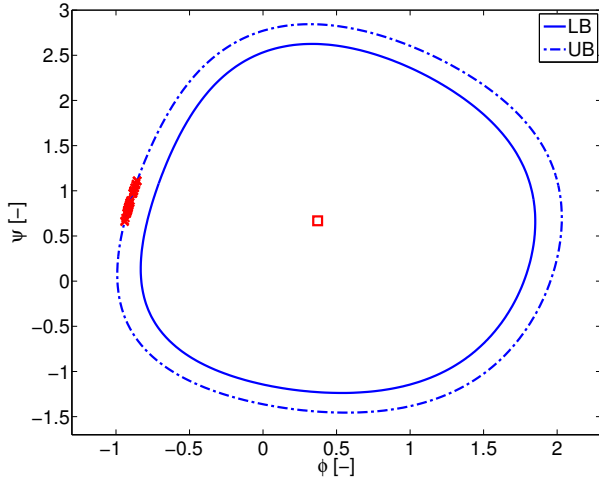


Figure B.3: Level sets  $\Omega_{V,\gamma}$  and  $\Omega_{V,\gamma_f}$  associated with  $\delta = 0.9$ .

the transformation  $y = x - \bar{x}$  is implied by the comparison). This is an important observation as it shows that Algorithm B.1 effectively exploits the higher degree of the level set function to enlarge the ROA in regions of the state space (e.g. lower right part) associated with converging trajectories.

The outcome in Fig. B.3 can be interpreted as a *worst-case* analysis, in that it detects the closest points to the estimated set which do not belong to the ROA of the system, and the associated combination of uncertain parameters (in this case the scalar  $\delta = 0.9$ ). One of the advantages of the equilibrium-independent framework proposed in this work is that also the *degradation* of local stability in the face of uncertainties can be efficiently visualised. This can be done by taking advantage of the concept of family of ROA underlying the formulation, which allows to represent the results compactly in the  $y$  space (or  $y_1-y_2$  plane, in the particular case  $n = 2$  considered here). The idea is to apply the Monte Carlo search discussed before repeatedly and so obtain  $\gamma_f$  as a function of the uncertainties. In the scalar case ( $n_\delta = 1$ ), this is straightforward, but the strategy can in principle be applied to the case  $n_\delta > 1$  by partitioning the uncertainty set  $\Delta$  and associating with each cell a value of  $\gamma_f$ .

Fig. B.4 shows an application of this approach, where the quartic level set  $\Omega_{V,\gamma}$  from Fig. B.2 is again used as basis for the analyses (LB). Based on the Monte Carlo campaign discussed above, a range of  $\delta$  is associated with a level set if, within that uncertainty interval, there are diverging trajectories with initial conditions on its boundary.

These analyses can be interpreted as an equilibrium-independent upper bound estimation of the ROA for different uncertainty ranges. In other words, the results give a measure of the robustness of the local stability. The key feature is that this information is unrelated to the specific equilibrium point, i.e. it allows to isolate the effect of  $\delta$  on the degradation of local stability from that on the equilibrium point. This is deemed an important feature, because it recovers the type

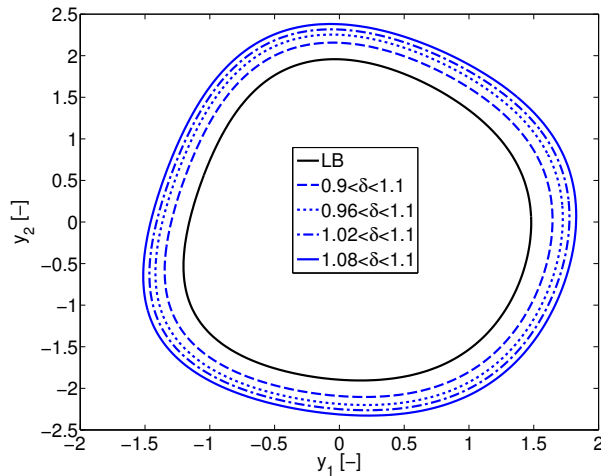


Figure B.4: Degradation of the local stability in the face of uncertainties.

of investigation commonly performed when the uncertainty-independent hypothesis is assumed for the equilibrium point. It is worth observing that, when the parameter-dependent level set  $\Omega_{V,\gamma}$  is considered, these types of analysis would not be possible because the representation of the ROA is inherently connected to a specific equilibrium  $\bar{x}$  (and thus to a specific  $\delta$ ).

Note finally that, to complement the stability degradation study displayed in Fig. B.4, an equilibrium-independent lower bound study can be performed by running Algorithm B.1 for different uncertainty ranges.

## BIBLIOGRAPHY

- [1] A. A. AHMADI, G. HALL, A. PAPACHRISTODOULOU, J. SAUNDERSON, AND Y. ZHENG, *Improving Efficiency and Scalability of Sum of Squares Optimization: Recent Advances and Limitations*, IEEE Conference on Decision and Control, December 2017.
- [2] A. A. AHMADI AND A. MAJUMDAR, *DSOS and SDSOS Optimization: More Tractable Alternatives to Sum of Squares and Semidefinite Optimization*, SIAM Journal on Applied Algebraic Geometry, 3 (2019), pp. 193–230.
- [3] E. ALBANO AND W. RODDEN, *A doublet lattice method for calculating lift distributions on oscillating surfaces in subsonic flows*, AIAA Journal, 7 (1969), pp. 279–285.
- [4] R. J. ALLEMANG AND D. L. BROWN, *A correlation coefficient for modal vector analysis*, International Modal Analysis Conference, October 1982.
- [5] J. ANDERSON AND A. PAPACHRISTODOULOU, *A Decomposition Technique for Nonlinear Dynamical System Analysis*, IEEE Transactions on Automatic Control, 57 (2012), pp. 1516–1521.
- [6] J. ANDERSON AND A. PAPACHRISTODOULOU, *Robust nonlinear stability and performance analysis of an F/A-18 aircraft model using sum of squares programming*, International Journal of Robust and Nonlinear Control, 23 (2013), pp. 1099–1114.
- [7] J. ANDERSON AND A. PAPACHRISTODOULOU, *Advances in computational Lyapunov analysis using sum-of-squares programming*, Discrete and Continuous Dynamical Systems - Series B, 20 (2015), pp. 2361–2381.
- [8] M. ANDERSON, *Pilot-induced oscillations involving multiple nonlinearities*, Journal of Guidance, Control, and Dynamics, 21 (1998), pp. 786–791.
- [9] P. APKARIAN, M. N. DAO, AND D. NOLL, *Parametric robust structured control design*, IEEE Transactions on Automatic Control, 60 (2015), pp. 1857–1869.
- [10] M. ARCAK, C. MEISSEN, AND A. PACKARD, *Networks of Dissipative Systems*, Springer International Publishing, 2016.

## BIBLIOGRAPHY

---

- [11] G. B. ARFKEN AND H. J. WEBER, *Mathematical methods for physicists*, Academic Press; 4th ed., San Diego, CA, 1995.
- [12] E. M. AYLWARD, P. A. PARRILO, AND J. E. SLOTINE, *Stability and robustness analysis of nonlinear systems via contraction metrics and SOS programming*, Automatica, 44 (2008), pp. 2163–2170.
- [13] V. BALAKRISHNAN, *Lyapunov functionals in complex  $\mu$  analysis*, IEEE Transactions on Automatic Control, 47 (2002), pp. 1466–1479.
- [14] G. BALAS, R. CHIANG, A. PACKARD, AND M. SAFONOV, *Robust Control Toolbox*, 2009.
- [15] G. J. BALAS, A. K. PACKARD, P. SEILER, AND U. TOPCU, *Robustness analysis of nonlinear systems*, available at <http://www.aem.umn.edu/~aerospacecontrol/>.
- [16] D. BALDELLI, R. LIND, AND M. BRENNER, *Robust Aerervoelastic Match-Point Solutions Using Describing Function Method*, Journal of Aircraft, 42 (2005), pp. 1597–1605.
- [17] D. H. BALDELLI, R. LIND, AND R. BRENNER, *Nonlinear aeroelastic/aerervoelastic modeling by block-oriented identification*, Journal of Guidance, Control, and Dynamics, 28 (2005), pp. 1056–1064.
- [18] J. BANERJEE, *Explicit frequency equation and mode shapes of a cantilever beam coupled in bending and torsion*, Journal of Sound and Vibration, 224 (1999), pp. 267–281.
- [19] P. BANSAL AND D. PITTS, *Uncertainties in control surface free-play and structural properties and their effect on flutter and LCO*, AIAA Scitech Conference, January 2014.
- [20] C. BELCASTRO, *On the numerical formulation of parametric linear fractional trasnformations (LFT) uncertainty models for multivariate matrix polynomial problems*, Technical Report NASA/TM-1998-206939, 1998.
- [21] T. BELYTSCHKO, W. LIU, AND B. MORAN, *Nonlinear finite elements for continua and structures*, Wiley, 2000.
- [22] S. BENNANI, B. BEUKER, J. VAN STAVEREN, AND J. MEIJER, *Flutter Analysis for the F-16A/B in Heavy Store Configuration*, Journal of Aircraft, 42 (2005), pp. 1566–1575.
- [23] P. BERAN, *Computation of Limit-Cycle Oscillation using a direct method*, AIAA Structures, Structural Dynamics, and Materials Conference, April 1999.
- [24] P. BERAN, C. PETTIT, AND D. MILLMAN, *Uncertainty quantification of limit cycle oscillations*, Journal of Computational Physics, 217 (2006), pp. 217–247.

- [25] J. BERANEK, L. NICOLAI, M. BUONANNO, E. BURNETT, C. ATKINSON, B. HOLM-HANSEN, AND P. FLICK, *Conceptual Design of a Multi-Utility Aeroelastic Demonstrator*, AIAA/ISSMO Multidisciplinary Analysis Optimization Conferences, September 2010.
- [26] A. BERGEN AND R. FRANKS, *Justification of the Describing Function method*, SIAM Journal on Control, 9 (1971), pp. 568–589.
- [27] W. BEYN, A. CHAMPNEYS, E. DOEDEL, W. GOVAERTS, Y. A. KUZNETSOV, AND B. SANDSTEDE, *Numerical continuation, and computation of normal forms*, in Handbook of Dynamical Systems, Vol 2 / Chapter 4., E. B. Fiedler (edit.), ed., 2002, pp. 149–219.
- [28] J.-M. BIANNIC, L. BURLION, F. DEMOURANT, G. FERRERES, G. HARDIER, T. LOQUEN, AND C. ROOS, *The SMAC Toolbox: a collection of libraries for Systems Modeling, Analysis and Control, available at <http://w3.onera.fr/smac/>*.
- [29] J. M. BIANNIC, C. DOLL, AND J. F. MAGNI, *SIMULINK-based tools for creating and simulating interconnected LFR objects*, IEEE Conference on Computer Aided Control System Design, October 2006.
- [30] R. L. BISPLINGHOFF AND H. ASHLEY, *Principles of Aeroelasticity*, Wiley, 1962.
- [31] J. BOCHNAK, M. COSTE, AND M.-F. ROY, *Real Algebraic Geometry*, Springer, 1998.
- [32] F. BORELLO, E. CESTINO, AND G. FRULLA, *Structural uncertainty effect on classical wing flutter characteristics*, Journal of Aerospace Engineering, 23 (2010), pp. 1217–1229.
- [33] D. BORGLUND, *The  $\mu$ -k Method for Robust Flutter Solutions*, Journal of Aircraft, 41 (2004), pp. 1209–1216.
- [34] S. BOYD, L. EL GHAOUI, E. FERON, AND V. BALAKRISHNAN, *Linear Matrix Inequalities in System and Control Theory*, Society for Industrial and Applied Mathematics (SIAM), 1994.
- [35] R. BRAATZ, P. YOUNG, J. DOYLE, AND M. MORARI, *Computational-complexity of  $\mu$ -calculation*, IEEE Transactions on Automatic Control, 39 (1994), pp. 1000–1002.
- [36] R. BROCKETT, *Finite dimensional linear systems*, Series in decision and control, Wiley, 1970.
- [37] C. A. CANIZARES, *Calculating optimal system parameters to maximize the distance to saddle-node bifurcations*, IEEE Transactions on Circuits and Systems, 45 (1998), pp. 225–237.
- [38] M. CANTONI AND H. SANDBERG, *Computing the  $l_2$  gain for linear periodic continuous-time systems*, Automatica, 45 (2009), pp. 783–789.

## BIBLIOGRAPHY

---

- [39] J. CARRASCO, W. P. HEATH, AND A. LANZON, *Factorization of multipliers in passivity and IQC analysis*, Automatica, 48 (2012), pp. 909–916.
- [40] R. CAVALLARO, R. BOMBARDIERI, L. DEMASI, AND A. IANNELLI, *Prandtlplane Joined Wing: Body freedom flutter, limit cycle oscillation and freeplay studies*, Journal of Fluids and Structures, 59 (2015), pp. 57–84.
- [41] R. CAVALLARO AND L. DEMASI, *Challenges, ideas, and innovations of joined-wing configurations: A concept from the past, an opportunity for the future*, Progress in Aerospace Sciences, 87 (2016), pp. 1–93.
- [42] A. CHAKRABORTY, P. SEILER, AND G. BALAS, *Nonlinear region of attraction analysis for flight control verification and validation*, Control Engineering Practice, 19 (2011), pp. 335–345.
- [43] ———, *Susceptibility of F/A-18 Flight Controllers to the Falling-Leaf Mode: Nonlinear Analysis*, Journal of Guidance, Control, and Dynamics, 34 (2011), pp. 73–85.
- [44] A. CHAKRABORTY, P. SEILER, AND G. J. BALAS, *Local Performance Analysis of Uncertain Polynomial Systems with Applications to Actuator Saturation*, IEEE Conference on Decision and Control, December 2010.
- [45] F. CHAVEZ AND D. SCHMIDT, *Systems approach to characterizing aircraft aeroelastic model variation for robust control applications*, AIAA Guidance, Navigation, and Control Conference, August 2001.
- [46] P. CHEN, *Damping perturbation method for flutter solution: The g-method*, AIAA Journal, 38 (2000), pp. 1519–1524.
- [47] P. C. CHEN AND E. SULAEAMAN, *Nonlinear response of aeroservoelastic systems using discrete state-space approach*, AIAA Journal, 41 (2003), pp. 1658–1666.
- [48] S. CHERNYSHENKO, P. J. GOULART, D. HUANG, AND A. PAPACHRISTODOULOU, *Polynomial sos in fluid dynamics: a review with a look ahead*, Philosophical Transactions of the Royal Society A, 372 (2014).
- [49] G. CHESI, *Estimating the domain of attraction for uncertain polynomial systems*, Automatica, 40 (2004), pp. 1981–1986.
- [50] ———, *Domain of Attraction: Analysis and Control via SOS Programming*, Springer, 2011.
- [51] G. CIRILLO, G. HABIB, G. KERSCHEN, AND R. SEPULCHRE, *Analysis and design of nonlinear resonances via singularity theory*, Journal of Sound and Vibration, 392 (2017), pp. 295–306.

- [52] M. CONNER, D. TANG, E. DOWELL, AND L. VIRGIN, *Nonlinear Behavior of a Typical Airfoil Section with Control Surface Freeplay. A Numerical and Experimental Study*, Journal of Fluids and Structures, 11 (1997), pp. 89–109.
- [53] E. CRUCK, R. MOITIE, AND N. SEUBE, *Estimation of basins of attraction for uncertain systems with affine and lipschitz dynamics*, Dynamics and Control, 11 (2001), pp. 211–227.
- [54] R. DAILEY, *A New Algorithm for the Real Structured Singular Value*, IEEE American Control Conference, May 1990.
- [55] D. DAL CANTO, A. FREDIANI, G. L. GHIRINGHELLI, AND M. TERRANEO, *The lifting system of a PrandtlPlane, part 1: Design and analysis of a light alloy structural solution*, in Variational Analysis and Aerospace Engineering: Mathematical Challenges for Aerospace Design, vol. 66 of Springer Optimization and Its Applications, 2012.
- [56] H. DANKOWICZ AND F. SCHILDER, *Recipes for Continuation*, Society for Industrial and Applied Mathematics, Philadelphia, PA, 2013.
- [57] B. DANOWSKY, C. THOMPSON, P.M. FARHAT, T. LIEU, C. HARRIS, AND J. LECHNIAK, *Dynamic stability of flexible forward swept wing aircraft*, Journal of Aircraft, 47 (2010), pp. 1274–1282.
- [58] B. DANOWSKY, P. THOMPSON, AND S. KUKREJA, *Nonlinear Analysis of Aeroservoelastic Models with Free Play Using Describing Functions*, Journal of Aircraft, 50 (2013), pp. 329–336.
- [59] M. DE C. HENSHAW, K. BADCOCK, G. VIO, C. ALLEN, J. CHAMBERLAIN, I. KAYNES, G. DIMITRIADIS, J. COOPER, M. WOODGATE, A. RAMPURAWALA, D. JONES, C. FENWICK, A. GAITONDE, N. TAYLOR, D. AMOR, T. ECCLES, AND C. DENLEY, *Non-linear aeroelastic prediction for aircraft applications*, Progress in Aerospace Sciences, 43 (2007), pp. 65–137.
- [60] L. DEMASI AND E. LIVNE, *Dynamic Aeroelasticity of Structurally Nonlinear Configurations Using Linear Modally Reduced Aerodynamic Generalized Forces*, AIAA Journal, 47 (2009), pp. 71–90.
- [61] F. DEMOURANT, *New algorithmic approach based on integral quadratic constraints for stability analysis of high order models*, IEEE European Control Conference, July 2013.
- [62] M. J. DESFORGES, J. E. COOPER, AND J. R. WRIGHT, *Mode tracking during flutter testing using the modal assurance criterion*, Proceedings of the Institution of Mechanical Engineers, Part G: Journal of Aerospace Engineering, 210 (1996), pp. 27–37.

## BIBLIOGRAPHY

---

- [63] R. DESMARAIS AND R. BENNETT, *An automated procedure for computing flutter eigenvalues*, Journal of Aircraft, 11 (1974), pp. 75–80.
- [64] C. DESOER AND M. VIDYASAGAR, *Feedback Systems: Input-Output Properties*, Academic Press: New York, 1975.
- [65] A. DHOOGHE, W. GOVAERTS, AND Y. A. KUZNETSOV, *Matcont: A matlab package for numerical bifurcation analysis of odes*, ACM Trans. Math. Softw., 29 (2003), pp. 141–164.
- [66] M. DI BERNARDO AND S. J. HOGAN, *Discontinuity-induced bifurcations of piecewise smooth dynamical systems*, Philosophical Transactions of the Royal Society A, 368 (2010), pp. 4915–4935.
- [67] L. DIECI, M. R. OSBORNE, AND R. D. RUSSELL, *A Riccati Transformation Method for Solving Linear BVPs. II: Computational Aspects*, SIAM Journal on Numerical Analysis, 25 (1988), pp. 1074–1092.
- [68] G. DIMITRIADIS, *Shooting-Based Complete Bifurcation Prediction for Aeroelastic Systems with Freeplay*, Journal of Aircraft, 48 (2011), pp. 1864–1877.
- [69] ———, *Introduction to Nonlinear Aeroelasticity*, Aerospace Series, Wiley, 2017.
- [70] N. DIVOUX AND A. FREDIANI, *The lifting system of a PrandtlPlane, part 2: Preliminary study on flutter characteristics*, in Variational Analysis and Aerospace Engineering: Mathematical Challenges for Aerospace Design, vol. 66 of Springer Optimization and Its Applications, 2012.
- [71] I. DOBSON, *Computing a closest bifurcation instability in multidimensional parameter space*, Journal of Nonlinear Science, 3 (1993), pp. 307–327.
- [72] E. J. DOEDEL, T. F. FAIRGRIEVE, B. SANDSTEDE, A. R. CHAMPNEYS, Y. A. KUZNETSOV, AND X. WANG, *Auto-07p: Continuation and bifurcation software for ordinary differential equations*, Technical Report, 2007.
- [73] P. DORATO, *A historical review of robust control*, IEEE Control Systems Magazine, 7 (1987), pp. 44–47.
- [74] E. DOWELL, J. EDWARDS, AND T. STRGANAC, *Nonlinear aeroelasticity*, Journal of Aircraft, Vol. 40 (2003), pp. 857–874.
- [75] J. DOYLE, *Analysis of feedback systems with structured uncertainties*, IEE Proceedings D, 129 (1982), pp. 242–250.

- [76] J. DOYLE AND G. STEIN, *Multivariable feedback design: Concepts for a classical / modern synthesis*, IEEE Transactions on Automatic Control, 26 (1981), pp. 4–16.
- [77] A. EATON, C. HOWCROFT, E. COETZEE, S. NEILD, M. LOWENBERG, AND J. COOPER, *Numerical continuation of limit cycle oscillations and bifurcations in high-aspect-ratio wings*, Aerospace, 5 (2018), pp. 1204–1213.
- [78] M. FAN, A. TITS, AND J. DOYLE, *Robustness in the Presence of Mixed Parametric Uncertainty and Unmodeled Dynamics*, IEEE Transactions on Automatic Control, 36 (1991), pp. 25–38.
- [79] G. FANTUZZI, *An open-source MATLAB ADMM solver for partially decomposable conic optimization programs, available at <https://github.com/OxfordControl/CDCS>*.
- [80] C. FARHAT, *CFD-Based Nonlinear Computational Aeroelasticity*, Encyclopedia of Computational Mechanics, 3 (2017), pp. 1–21.
- [81] G. FERRERES, *A practical approach to robustness analysis with aeronautical applications*, Kluwer Academic, New York, 1999.
- [82] M. FETZER, C. W. SCHERER, AND J. VEENMAN, *Invariance with dynamic multipliers*, IEEE Transactions on Automatic Control, 63 (2018), pp. 1929–1942.
- [83] C. FIELDING AND P. FLUX, *Non-linearities in flight control systems*, The Aeronautical Journal, 107 (2003), pp. 673–686.
- [84] C. FIELDING, A. VARGA, S. BENNANI, M. SELIER, AND EDS., *Advanced Techniques for Clearance of Flight Control Laws*, Springer-Verlag Berlin Heidelberg, 2002.
- [85] A. FREDIANI, V. CIOPOLLA, AND E. RIZZO, *The PrandtlPlane configuration: Overview on possible applications to civil aviation*, in Variational Analysis and Aerospace Engineering: Mathematical Challenges for Aerospace Design, vol. 66 of Springer Optimization and Its Applications, 2012, pp. 179–210.
- [86] M. FRISWELL, *Calculation of second and higher order eigenvector derivatives*, Journal of Guidance, Control, and Dynamics, 18 (1995), pp. 919–921.
- [87] A. GELB AND W. E. VANDER VELDE, *Multiple-Input Describing Functions and Nonlinear System Design*, McGraw-Hill, 1968.
- [88] R. GENESIO, M. TARTAGLIA, AND A. VICINO, *On the estimation of asymptotic stability regions: State of the art and new proposals*, IEEE Transactions on Automatic Control, 30 (1985), pp. 747–755.

## BIBLIOGRAPHY

---

- [89] J. GERHARD, W. MARQUARDT, AND M. MONNIGMANN, *Normal vectors on critical manifolds for robust design of transient processes in the presence of fast disturbances*, SIAM Journal on Applied Dynamical Systems, 7 (2008), pp. 461–490.
- [90] M. GHOMMEN, M. HAJJ, AND A. NAYFEH, *Uncertainty analysis near bifurcation of an aeroelastic system*, Journal of Sound and Vibration, 329 (2010), pp. 3335–3347.
- [91] P. GILL, W. MURRAY, AND M. WRIGHT, *Practical optimization*, Academic Press, 1981.
- [92] E. GILLEBAART AND R. DE BREUKER, *Reduced-Order Modeling of Continuous-Time State-Space Unsteady Aerodynamics*, AIAA Scitech Conference, January 2015.
- [93] M. GOLAND, *The flutter of a uniform cantilever wing*, Journal of Applied Mechanics, (1945), pp. 197–208.
- [94] M. GOLUBITSKY AND D. SCHAEFFER, *Singularities and Groups in Bifurcation Theory*, Applied Mathematical Sciences, Springer-Verlag New York, 1985.
- [95] J. GORDON, E. MEYER, AND R. MINOGUE, *Nonlinear Stability Analysis of Control Surface Flutter with Freeplay Effects*, Journal of Aircraft, 45 (2008), pp. 1904–1916.
- [96] W. GOVAERTS, *Numerical Methods for Bifurcations of Dynamical Equilibria*, Society for Industrial and Applied Mathematics, 2000.
- [97] R. GRAY, A. FRANCI, V. SRIVASTAVA, AND N. E. LEONARD, *Multiagent decision-making dynamics inspired by honeybees*, IEEE Transactions on Control of Network Systems, 5 (2018), pp. 793–806.
- [98] M. GREEN AND D. LIMEBEER, *Linear robust control*, Prentice Hall, 1995.
- [99] J. GUCKENHEIMER AND P. HOLMES, *Nonlinear Oscillations, Dynamical Systems, and Bifurcations of Vector Fields*, Applied Mathematical Sciences, Springer New York, 2002.
- [100] D. HAN, A. EL-GUINDY, AND M. ALTHOFF, *Estimating the Domain of Attraction Based on the Invariance Principle*, IEEE Conference on Decision and Control, December 2016.
- [101] A. HASSIBI, J. HOW, AND S. BOYD, *A path-following method for solving BMI problems in control*, IEEE American Control Conference, June 1999.
- [102] H. J. HASSIG, *An approximate true damping solution of the flutter equation by determinant iteration*, Journal of Aircraft, 33 (1971), pp. 885–889.
- [103] M. HAYES, D. BATES, AND I. POSTLETHWAITE, *New tools for computing tight bounds on the real structured singular value*, Journal of Guidance, Control, and Dynamics, 24 (2001), pp. 1204–1213.

- [104] W. P. HEATH AND A. G. WILLS, *Zames-Falb multipliers for quadratic programming*, IEEE Conference on Decision and Control, December 2005.
- [105] S. HECKER, A. VARGA, AND J.-F. MAGNI, *Enhanced lfr-toolbox for matlab*, Aerospace Science and Technology, 9 (2005), pp. 173–180.
- [106] S. HEINZE AND D. BORGLUND, *Robust Flutter Analysis Considering Mode Shape Variations*, Journal of Aircraft, 45 (2008), pp. 1070–1074.
- [107] D. HENRION AND A. GARULLI, *Positive Polynomials in Control*, Springer-Verlag Berlin Heidelberg, 2005.
- [108] D. HENRION AND M. KORDA, *Convex Computation of the Region of Attraction of Polynomial Control Systems*, IEEE Transactions on Automatic Control, 59 (2014), pp. 297–312.
- [109] G. H. HINES, M. ARCAK, AND A. PACKARD, *Equilibrium-independent passivity: A new definition and numerical certification*, Automatica, 47 (2011), pp. 1949–1956.
- [110] F. HOBLIT, *Gust Loads on Aircraft: Concepts and Applications*, AIAA education series, American Institute of Aeronautics & Astronautics, 1988.
- [111] D. H. HODGES AND G. A. PIERCE, *Introduction to Structural Dynamics and Aeroelasticity*, Cambridge University Press, 2011.
- [112] R. HORN AND C. JOHNSON, *Matrix Analysis*, Cambridge University Press, 1990.
- [113] K. HSU, K. POOLLA, AND T. L. VINCENT, *Identification of structured nonlinear systems*, IEEE Transactions on Automatic Control, 53 (2008), pp. 2497–2513.
- [114] T. HU AND Z. LIN, *Control Systems with Actuator Saturation*, Birkhauser Basel, 2001.
- [115] A. IANNELLI, M. LOWENBERG, AND A. MARCOS, *An extension of the structured singular value to nonlinear systems with application to robust flutter analysis*, CEAS Conference on Guidance, Navigation and Control, April 2019.
- [116] A. IANNELLI, A. MARCOS, R. BOMBARDIERI, AND R. CAVALLARO, *A symbolic LFT approach for robust flutter analysis of high-order models*, IEEE European Control Conference, June 2019.
- [117] A. IANNELLI, A. MARCOS, AND M. LOWENBERG, *Comparison of Aeroelastic Modeling and Robust Flutter Analysis of a Typical Section*, IFAC Symposium on Automatic Control in Aerospace, August 2016.
- [118] ———, *Modeling and Robust Body Freedom Flutter Analysis of Flexible Aircraft Configurations*, IEEE Multi-Conference on Systems and Control, September 2016.

## BIBLIOGRAPHY

---

- [119] ——, *Limit Cycle Oscillation amplitude tailoring based on Describing Functions and  $\mu$  Analysis*, in Advances in Aerospace Guidance, Navigation and Control, Springer-Verlag, ed., 2017.
- [120] ——, *Nonlinear flutter analysis with uncertainties based on Describing Function and Structured Singular Value with an IQC validation*, European Conference for Aeronautics and AeroSpace Sciences, July 2017.
- [121] ——, *Nonlinear stability and post-critical analysis of an uncertain plant with describing functions and integral quadratic constraints*, IEEE Conference on Decision and Control, December 2017.
- [122] ——, *Aeroelastic modeling and stability analysis: A robust approach to the flutter problem*, International Journal of Robust and Nonlinear Control, 28 (2018), pp. 342–364.
- [123] ——, *Algorithms for the estimation of the region of attraction with positively invariant sets*, International Conference on Systems and Control, October 2018.
- [124] ——, *Estimating the region of attraction of uncertain systems with invariant sets*, IFAC Symposium on Robust Control Design, September 2018.
- [125] ——, *Study of Flexible Aircraft Body Freedom Flutter with Robustness Tools*, Journal of Guidance, Control, and Dynamics, 41 (2018), pp. 1083–1094.
- [126] A. IANNELLI, A. MARCOS, AND M. LOWENBERG, *Nonlinear robust approaches to study stability and postcritical behavior of an aeroelastic plant*, IEEE Transactions on Control Systems Technology, 27 (2019), pp. 703–716.
- [127] A. IANNELLI, A. MARCOS, AND M. LOWENBERG, *Robust estimations of the region of attraction using invariant sets*, Journal of The Franklin Institute, 356 (2019), pp. 4622–4647.
- [128] A. IANNELLI, P. SEILER, AND A. MARCOS, *An equilibrium-independent region of attraction formulation for systems with uncertainty-dependent equilibria*, IEEE Conference on Decision and Control, December 2018.
- [129] ——, *Estimating the Region of Attraction of uncertain systems with Integral Quadratic Constraints*, IEEE Conference on Decision and Control, December 2018.
- [130] A. IANNELLI, P. SEILER, AND A. MARCOS, *Worst-case disturbances for Time-Varying systems with application to flexible aircraft*, Journal of Guidance, Control, and Dynamics (accepted), (2019).

- [131] M. IDAN, M. KARPEL, AND B. MOULIN, *Aeroservoelastic interaction between aircraft structural and control design schemes*, Journal of Guidance, Control, and Dynamics, 22 (1999), pp. 513–519.
- [132] P. IORDANOV AND M. HALTON, *Computation of the real structured singular value via pole migration*, International Journal of Robust and Nonlinear Control, 25 (2014), pp. 3163–3178.
- [133] U. JONSSON, C.-Y. KAO, A. MEGRETSKI, AND A. RANTZER, *A Guide to IQC  $\beta$ : A MATLAB Toolbox for Robust Stability and Performance Analysis*.
- [134] M. KARPEL, *Design for Active and Passive Flutter Suppression and Gust alleviation*, Nasa Report 3482, 1981.
- [135] M. KARPEL, B. MOULIN, AND M. IDAN, *Robust aeroservoelastic design with structural variations and modeling uncertainties*, Journal of Aircraft, 40 (2003), pp. 946–952.
- [136] M. KATEBI AND Y. ZHANG,  *$H_\infty$  control analysis and design for nonlinear systems*, International Journal of Control, 61 (1995), pp. 459–474.
- [137] H. K. KHALIL, *Nonlinear systems*, Prentice Hall, 1996.
- [138] H. H. KHODAPARAST AND J. E. COOPER, *Rapid prediction of worst-case gust loads following structural modification*, AIAA Journal, (2014), pp. 242–254.
- [139] J. KIM, D. G. BATES, AND I. POSTLETHWAITE, *Robustness analysis of linear periodic time-varying systems subject to structured uncertainty*, Systems & Control Letters, 55 (2006), pp. 719 – 725.
- [140] A. KNOBLACH, H. PFIFER, AND P. SEILER, *Worst case analysis of a saturated gust loads alleviation system*, AIAA Scitech Conference, January 2015.
- [141] A. KNOBLACH, H. PFIFER, AND P. SEILER, *Worst Case Analysis of a Saturated Gust Loads Alleviation System*, AIAA Scitech Conference, January 2015.
- [142] M. KOVARA AND M. STINGL, *PENBMI User's Guide (Version 2.1)*, 2006.
- [143] N. KRYLOV AND N. BOGOLIUBOV, *Introduction to Nonlinear Mechanics*, Princeton University Press, Princeton (N.J.), 1947.
- [144] A. KUMAR AND G. BALAS, *An approach to model validation in the  $\mu$  framework*, IEEE American Control Conference, June 1994.
- [145] Y. KUZNETSOV, *Elements of Applied Bifurcation Theory*, Springer-Verlag New York, 2004.

## BIBLIOGRAPHY

---

- [146] P. LAMBRECHTS, J. TERLOUW, S. BENNANI, AND M. STEINBUCH, *Parametric uncertainty modeling using LFTs*, IEEE American Control Conference, June 1993.
- [147] B. LEE, S. PRICE, AND Y. WONG, *Nonlinear aeroelastic analysis of airfoils: bifurcation and chaos*, Progress in Aerospace Sciences, 35 (1999), pp. 205–334.
- [148] R. LIND AND M. BRENNER, *Robust Flutter Margins of an F/A-18 Aircraft from Aeroelastic Flight Data*, Journal of Guidance, Control, and Dynamics, 20 (1997), pp. 597–604.
- [149] R. LIND AND M. BRENNER, *Flutterometer: An On-Line Tool to Predict Robust Flutter Margins*, Journal of Aircraft, 37 (2000), pp. 1105–1112.
- [150] LIND, R. AND BRENNER, M., *Robust Aerervoelastic Stability Analysis*, Advances in Industrial Control, Springer, 2012.
- [151] L. LIU AND E. H. DOWELL, *The secondary bifurcation of an aeroelastic airfoil motion: Effect of high harmonics*, Nonlinear Dynamics, 37 (2004), pp. 31–49.
- [152] LIU, L. AND DOWELL, E. H., *Harmonic Balance Approach for an Airfoil with a Freeplay Control Surface*, AIAA Journal, 43 (2005), pp. 802–815.
- [153] E. LIVNE, *Aircraft Active Flutter Suppression: State of the Art and Technology Maturation Needs*, Journal of Aircraft, 55 (2018), pp. 410–452.
- [154] M. LOVE, P. SCOTT ZINK, AND P. WIESELMANN, *Body Freedom Flutter of High Aspect Ratio Flying Wings*, AIAA/ASME/ASCE/AHS/ASC Conference, April 2005.
- [155] T. LUSPAY, D. OSSMANN, M. WUESTENHAGEN, D. TEUBL, T. BAAR, T. PENI, M. PUSCH, T. KIER, S. WAITMAN, A. IANNELLI, A. MARCOS, M. LOWENBERG, AND B. VANEK, *Flight control design for a highly flexible flutter demonstrator*, AIAA Scitech Conference, January 2019.
- [156] J. MAGNI, *Linear fractional representation toolbox modelling, order reduction, gain scheduling*, Technical Report TR 6/08162, DCSD, ONERA, Systems Control and Flight Dynamics Department, 2004.
- [157] A. MAJUMDAR, *Spotless software package, available at [https://github.com/anirudhamajumdar/spotless/tree/spotless\\_isos](https://github.com/anirudhamajumdar/spotless/tree/spotless_isos)*.
- [158] A. MARCOS AND G. BALAS, *Development of Linear Parameter Varying Models for Aircraft*, Journal of Guidance, Control, and Dynamics, 27 (2004), pp. 218–228.
- [159] A. MARCOS, D. BATES, AND I. POSTLETHWAITE, *Nonlinear symbolic LFT tools for modeling, analysis and design*, in Nonlinear Analysis and Synthesis Techniques in Aircraft Control, Springer-Verlag, ed., 2007.

- [160] A. MARCOS, D. BATES, AND I. POSTLETHWAITE, *A symbolic matrix decomposition algorithm for reduced order linear fractional transformation modelling*, Automatica, 43 (2007), pp. 1211–1218.
- [161] A. MARCOS, D. BATES, AND I. POSTLEWHITE, *Control oriented uncertainty modeling using  $\mu$  sensitivities and skewed  $\mu$  analysis tool*, IEEE Conference on Decision and Control, December 2005.
- [162] A. MARCOS, J. BIANNIC, M. JEANNEAU, D. BATES, AND I. POSTLETHWAITE, *Aircraft modeling for nonlinear and robust control design and analysis*, IFAC Symposium on Robust Control Design, July 2006.
- [163] A. MARCOS, J. VEENMAN, C. SCHERER, G. DE ZAIACOMO, D. MOSTAZA, M. KERR, H. KOROGLU, AND S. BENNANI, *Application of LPV Modeling, Design and Analysis Methods to a Re-entry Vehicle*, AIAA Guidance, Navigation, and Control Conference, August 2010.
- [164] MATHWORKS, *Symbolic Math Toolbox version 8.0.0*, Natick, Massachusetts, 2017.
- [165] MATLAB, *Optimization Toolbox User's Guide*, 2014.
- [166] A. MAZZOLENI AND I. DOBSON, *Closest bifurcation analysis and robust stability design of flexible satellites*, Journal of Guidance, Control, and Dynamics, 18 (1995), pp. 333–339.
- [167] Y. MEDDAIKAR, J. DILLINGER, T. KLIMMEK, W. KRUEGER, M. WUESTHENHAGEN, T. KIER, A. HERMANUTZ, M. HORNUNG, V. ROZOV, C. BREITSAMTER, J. ALDERMAN, B. TAKARICS, AND B. VANEK, *Aircraft Aeroseervoelastic Modelling of the FLEXOP Unmanned Flying Demonstrator*, AIAA Scitech Conference, January 2019.
- [168] A. MEES, *The describing function matrix*, IMA Journal of Applied Mathematics, 10 (1972), pp. 49–67.
- [169] ———, *Describing functions, circle criteria and multiple-loop feedback systems*, Proceedings of the Institution of Electrical Engineers, 120 (1973), pp. 126–130.
- [170] A. MEGRETSKI AND A. RANTZER, *System analysis via integral quadratic constraints*, IEEE Transactions on Automatic Control, 42 (1997), pp. 819–830.
- [171] P. P. MENON, J. KIM, D. G. BATES, AND I. POSTLEWHITE, *Clearance of Nonlinear Flight Control Laws Using Hybrid Evolutionary Optimization*, IEEE Transactions on Evolutionary Computation, 10 (2006), pp. 689–699.
- [172] Z. MICHALEWICZ AND D. FOGEL, *How to Solve It: Modern Heuristics*, Springer-Verlag, 2nd ed., 2004.

## BIBLIOGRAPHY

---

- [173] H. MITTELMANN, *An independent benchmarking of SDP and SOCP solvers*, Mathematical Programming, 95 (2003), pp. 407–430.
- [174] M. MONNIGMANN AND W. MARQUARDT, *Steady-state process optimization with guaranteed robust stability and feasibility*, AIChE Journal, 49 (2014), pp. 3110–3126.
- [175] B. MOULIN, M. IDAN, AND M. KARPEL, *Aeroservoelastic Structural and Control Optimization Using Robust Design Schemes*, Journal of Guidance, Control, and Dynamics, 25 (2002), pp. 152–159.
- [176] V. MUKHOPADHYAY, *Historical Perspective on Analysis and Control of Aeroelastic Responses*, Journal of Guidance, Control, and Dynamics, 26 (2003), pp. 673–684.
- [177] V. MUKHOPADHYAY AND E. LIVNE, *Aeroservoelasticity*, 2010.
- [178] A. NAYFEH AND B. BALACHANDRAN, *Applied Nonlinear Dynamics: Analytical, Computational and Experimental Methods*, Wiley Series in Nonlinear Science, Wiley, 2008.
- [179] A. PACKARD, G. BALAS, R. LIU, AND J. SHIN, *Results on worst-case performance assessment*, IEEE American Control Conference, June 2000.
- [180] A. PACKARD AND J. DOYLE, *The Complex Structured Singular Value*, Automatica, 29 (1993), pp. 71–109.
- [181] A. PACKARD, J. DOYLE, AND G. BALAS, *Linear, multivariable robust control with a  $\mu$  perspective*, Journal of Dynamic Systems, Measurement, and Control, 115 (1993), pp. 426–438.
- [182] A. PACKARD, M. FAN, AND J. DOYLE, *A power method for the structured singular value*, IEEE Conference on Decision and Control, December 1988.
- [183] A. PACKARD AND P. PANDEY, *Continuity properties of the real/complex structured singular value*, IEEE Transactions on Automatic Control, 38 (1993), pp. 415–428.
- [184] A. M. PADMANABHAN AND E. H. DOWELL, *Calculation of aeroelastic limit cycles due to localized nonlinearity and static preload*, AIAA Journal, 55 (2017), pp. 2762–2772.
- [185] A. PAPACHRISTODOULOU, J. ANDERSON, G. VALMORBIDA, S. PRAJNA, P. SEILER, AND P. A. PARRILO, *SOSTOOLS: Sum of squares optimization toolbox for MATLAB*, 2013.
- [186] A. PAPOULIS, *Maximum response with input energy constraints and the matched filter principle*, IEEE Transactions on Circuit Theory, 17 (1970), pp. 175–182.
- [187] P. PARRILO, *Structured Semidefinite Programs and Semialgebraic Geometry. Methods in Robustness and Optimization*, PhD thesis, California Institute of Technology, 2000.

- [188] P. PARRILO, *Semidefinite programming relaxations for semialgebraic problems*, Mathematical Programming, 96 (2003), pp. 293–320.
- [189] M. PATIL AND D. HODGES, *Limit cycle oscillations in high aspect ratio wings*, Journal of Fluids and Structures, 15 (2001), pp. 107–132.
- [190] M. J. PATIL, D. HODGES, AND C. CESNIK, *Nonlinear aeroelasticity and flight dynamics of high-altitude long-endurance aircraft*, Journal of Aircraft, 38 (2001), pp. 88–94.
- [191] D. PEAUCELLE, S. TARBOURIECH, M. GANET-SCHOELLER, AND S. BENNANI, *Evaluating regions of attraction of LTI systems with saturation in IQS framework*, IFAC Symposium on Robust Control Design, July 2012.
- [192] C. PETTIT, *Uncertainty Quantification in Aeroelasticity: Recent Results and Research Challenges*, Journal of Aircraft, 41 (2004), pp. 1217–1229.
- [193] H. PFIFER AND P. SEILER, *Less Conservative Robustness Analysis of Linear Parameter Varying Systems Using Integral Quadratic Constraints*, International Journal of Robust and Nonlinear Control, 26 (2015), pp. 3580–3594.
- [194] P. POLCZ, T. PENI, AND G. SZEDERKENYI, *Improved algorithm for computing the domain of attraction of rational nonlinear systems*, European Journal of Control, 39 (2017), pp. 53–67.
- [195] V. POPOV, *Absolute stability of nonlinear systems of automatic control*, Automation and Remote Control, 22 (1961), pp. 857–875.
- [196] I. POSTLETHWAITE, J. EDMUNDS, AND A. MACFARLANE, *Principal gains and principal phases in the analysis of linear multivariable feedback systems*, IEEE Transactions on Automatic Control, 26 (1981), pp. 32–46.
- [197] C. POUSSOT-VASSAL AND C. ROOS, *Generation of a reduced-order LPV/LFT model from a set of large-scale MIMO LTI flexible aircraft models*, Control Engineering Practice, 20 (2012), pp. 919–930.
- [198] S. PRICE, H. ALIGHANBARI, AND B. LEE, *The aeroelastic response of a two-dimensional airfoil with bilinear and cubic structural nonlinearities*, Journal of Fluids and Structures, 9 (1995), pp. 175–193.
- [199] A. RANTZER, *On the Kalman-Yakubovich-Popov lemma*, Systems & Control Letters, 28 (1996), pp. 7–10.
- [200] R. M. REDHEFFER, *On a certain linear fractional transformation*, Journal of Mathematics and Physics, 39 (1960), pp. 269–286.

## BIBLIOGRAPHY

---

- [201] U. T. RINGERTZ, *On structural optimization with aeroelasticity constraints*, Structural optimization, 8 (1994), pp. 16–23.
- [202] W. P. RODDEN, *Theoretical and Computational Aeroelasticity*, Crest Publishing, 2011.
- [203] W. P. RODDEN AND E. H. JOHNSON, *User Guide V 68 MSC/NASTRAN Aeroelastic Analysis*, MacNeal-Schwendler Corporation, 1994.
- [204] K. ROGER, *Airplane Math Modeling Methods for Active Control Design*, AGARD (CP228), (1977).
- [205] C. ROOS, *Systems modeling, analysis and control (SMAC) toolbox: An insight into the robustness analysis library*, IEEE Conference on Computer Aided Control System Design, August 2013.
- [206] C. ROOS AND J. BIANNIC, *A detailed comparative analysis of all practical algorithms to compute lower bounds on the structured singular value*, Control Engineering Practice, 44 (2015), pp. 219–230.
- [207] C. ROOS, G. HARDIER, AND J.-M. BIANNIC, *Polynomial and rational approximation with the APRICOT library of the SMAC toolbox*, IEEE Multiconference on Systems and Control, October 2014.
- [208] M. SAFONOV, *Origins of robust control: Early history and future speculations*, IFAC Symposium on Robust Control Design, June 2012.
- [209] M. SAFONOV AND M. ATHANS, *A multiloop generalization of the circle criterion for stability margin analysis*, IEEE Transactions on Automatic Control, 26 (1981), pp. 415–422.
- [210] C. SCHERER AND S. WEILAND, *Linear Matrix Inequalities in Control*, Lecture Notes, Dutch Institute for Systems and Control, 2000.
- [211] C. W. SCHERER AND J. VEENMAN, *Stability analysis by dynamic dissipation inequalities: On merging frequency-domain techniques with time-domain conditions*, Systems & Control Letters, 121 (2018), pp. 7 – 15.
- [212] D. SCHMIDT, *Modern flight dynamics*, McGraw-Hill, 2012.
- [213] D. SCHUSTER, D. LIU, AND J. LAWRENCE, *Computational aeroelasticity: Success, progress, challenge*, Journal of Aircraft, 40 (2003), pp. 843–856.
- [214] W. R. SEARS, *Operational Methods in the Theory of Airfoils in Non-Uniform motion*, Journal of The Franklin Institute, 230 (1940), pp. 95–111.
- [215] P. SEILER, *Stability Analysis with Dissipation Inequalities and Integral Quadratic Constraints*, IEEE Transactions on Automatic Control, 60 (2015), pp. 1704–1709.

- [216] ——, *An Iterative Algorithm to Estimate Invariant Sets for Uncertain Systems*, IEEE American Control Conference, June 2018.
- [217] P. SEILER AND G. BALAS, *Quasiconvex Sum-of-Squares Programming*, IEEE Conference on Decision and Control, December 2010.
- [218] P. SEILER, R. MOORE, C. MEISSEN, M. ARCAK, AND A. PACKARD, *Finite Horizon Robustness Analysis of LTV Systems Using Integral Quadratic Constraints*, Automatica, 100 (2019), pp. 135–143.
- [219] P. SEILER, A. PACKARD, AND G. J. BALAS, *A gain-based lower bound algorithm for real and mixed  $\mu$  problems*, Automatica, 46 (2010), pp. 493–500.
- [220] R. SEPULCHRE AND G.-B. STAN, *Feedback mechanisms for global oscillations in Lure systems*, Systems & Control Letters, 54 (2005), pp. 809 – 818.
- [221] S. Y. SHAFI, M. ARCAK, M. JOVANOVIC, AND A. K. PACKARD, *Synchronization of diffusively-coupled limit cycle oscillators*, Automatica, 49 (2013), pp. 3613 – 3622.
- [222] J. SHIN, G. BALAS, AND A. PACKARD, *Worst-Case Analysis of the X-38 Crew Return Vehicle Flight Control System*, Journal of Guidance, Control, and Dynamics, 24 (2001), pp. 261–269.
- [223] H. SHUKLA AND M. PATIL, *Control of Limit Cycle Oscillation Amplitudes in Nonlinear Aerelastic Systems using Nonlinear Normal Modes*, AIAA Scitech Conference, January 2016.
- [224] H. SHUKLA AND M. J. PATIL, *Nonlinear state feedback control design to eliminate subcritical limit cycle oscillations in aerelastic systems*, Nonlinear Dynamics, 88 (2017), pp. 1599–1614.
- [225] R. SMITH AND J. C. DOYLE, *Model validation: a connection between robust control and identification*, IEEE Transactions on Automatic Control, 37 (1992), pp. 942–952.
- [226] P. STAHL, F. SENDNER, A. HERMANUTZ, C. ROBLER, AND H. HORNUNG, *Mission and Aircraft Design of FLEXOP Unmanned Flying Demonstrator to Test Flutter Suppression within Visual Line of Sight*, AIAA Aviation Technology, Integration, and Operations Conference, June 2017.
- [227] G. STAN AND R. SEPULCHRE, *Analysis of interconnected oscillators by dissipativity theory*, IEEE Transactions on Automatic Control, 52 (2007), pp. 256–270.
- [228] B. STANFORD AND P. BERAN, *Direct flutter and limit cycle computations of highly flexible wings for efficient analysis and optimization*, Journal of Fluids and Structures, 36 (2013), pp. 1204–1213.

## BIBLIOGRAPHY

---

- [229] J. F. STURM, *Using SeDuMi 1.02, A Matlab toolbox for optimization over symmetric cones*, Optimization Methods and Software, 11 (1999), pp. 625–653.
- [230] Y. R. STÜRZ, M. MORARI, AND R. R. SMITH, *Sequential Quadratic Programming for the Control of an Architectural Cable Net Geometry*, IEEE American Control Conference, July 2016.
- [231] E. SUMMERS AND A. PACKARD, *L<sub>2</sub> gain verification for interconnections of locally stable systems using integral quadratic constraints*, IEEE Conference on Decision and Control, December 2010.
- [232] W. TAN, *Nonlinear Control Analysis and Synthesis using Sum-of-Squares Programming*, PhD thesis, University of California Berkeley, 2006.
- [233] W. TAN AND A. PACKARD, *Stability Region Analysis Using Polynomial and Composite Polynomial Lyapunov Functions and Sum-of-Squares Programming*, IEEE Transactions on Automatic Control, 53 (2008), pp. 565–571.
- [234] D. TANG, E. DOWELL, AND L. VIRGIN, *Limit Cycle Behavior of an Airfoil with a Control Surface*, Journal of Fluids and Structures, 12 (1998), pp. 839–858.
- [235] D. TANG AND E. H. DOWELL, *Experimental and theoretical study on aeroelastic response of high-aspect-ratio wings*, AIAA Journal, 39 (2001), pp. 1430–1441.
- [236] ——, *Aeroelastic Response Induced by Free Play, Part 1: Theory*, AIAA Journal, 49 (2011), pp. 2532–2542.
- [237] ——, *Aeroelastic Response Induced by Free Play, Part 2: Theoretical / Experimental Correlation Analysis*, AIAA Journal, 49 (2011), pp. 2543–2554.
- [238] J. THEIS, H. PFIFER, AND P. SEILER, *Robust Control Design for Active Flutter Suppression*, AIAA Scitech Conference, January 2016.
- [239] T. THEODORSEN, *General Theory of Aerodynamic Instability and the Mechanism of flutter*, Naca Report 496, (1935).
- [240] J. THOMAS, E. DOWELL, K. HALL, AND C. DENEGRI, *An Investigation of the Sensitivity of F-16 Fighter Flutter Onset and Limit Cycle Oscillations to Uncertainties*, AIAA Structures, Structural Dynamics, and Materials Conference, May 2006.
- [241] U. TOPCU AND A. PACKARD, *Local Stability Analysis for Uncertain Nonlinear Systems*, IEEE Transactions on Automatic Control, 54 (2009), pp. 1042–1047.

- [242] U. TOPCU, A. PACKARD, P. SEILER, AND G. BALAS, *Local stability analysis for uncertain nonlinear systems using a branch-and-bound algorithm*, IEEE American Control Conference, June 2008.
- [243] U. TOPCU, A. K. PACKARD, P. SEILER, AND G. J. BALAS, *Robust Region-of-Attraction Estimation*, IEEE Transactions on Automatic Control, 55 (2010), pp. 137–142.
- [244] J. TORRALBA, F. DEMOURANT, G. PUYOU, AND G. FERRERES, *A Method for Flexible Aircraft LFT Modelling*, IEEE European Control Conference, August 2009.
- [245] A. TROFINO AND T. J. M. DEZUO, *LMI stability conditions for uncertain rational nonlinear systems*, International Journal of Robust and Nonlinear Control, 24 (2013), pp. 3124–3169.
- [246] G. VALMORBIDA AND J. ANDERSON, *Region of attraction estimation using invariant sets and rational Lyapunov functions*, Automatica, 75 (2017), pp. 37–45.
- [247] G. VALMORBIDA, S. TARBOURIECH, AND G. GARCIA, *Region of attraction estimates for polynomial systems*, IEEE Conference on Decision and Control, December 2009.
- [248] A. VANNELLI AND M. VIDYASAGAR, *Maximal lyapunov functions and domains of attraction for autonomous nonlinear systems*, Automatica, 21 (1985), pp. 69–80.
- [249] A. VARGA AND G. LOOYE, *Symbolic and numerical software tools for lft-based low order uncertainty modeling*, IEEE International Symposium on Computed Aided Control System Design, August 1999.
- [250] J. VEENMAN AND C. SCHERER, *IQC-synthesis with general dynamic multipliers*, International Journal of Robust and Nonlinear Control, 23 (2014), pp. 3027–3056.
- [251] J. VEENMAN, C. W. SCHERER, AND H. KÖROĞLU, *Robust stability and performance analysis based on integral quadratic constraints*, European Journal of Control, 31 (2016), pp. 1–32.
- [252] X. WEI AND J. E. MOTTERSHEAD, *Aeroelastic systems with softening nonlinearity*, AIAA Journal, 52 (2014), pp. 1915–1927.
- [253] T. WEISSHAARM AND T. ZEILER, *Dynamic stability of flexible forward swept wing aircraft*, Journal of Aircraft, 20 (1983), pp. 1014–1020.
- [254] J. C. WILLEMS, *Dissipative dynamical systems part I: General theory*, Archive for Rational Mechanics and Analysis, 45 (1972), pp. 321–351.
- [255] M. WOODGATE AND K. J. BADCOCK, *Fast prediction of transonic aeroelastic stability and limit cycles*, AIAA Journal, 45 (2007), pp. 1370–1381.

## BIBLIOGRAPHY

---

- [256] J. WRIGHT AND J. COOPER, *Introduction to Aircraft Aeroelasticity and Loads*, AIAA education series, John Wiley & Sons, 2007.
- [257] M. WUESTENHAGEN, T. KIER, Y. MEDDAIKAR, M. PUSCH, D. OSSMANN, AND A. HERMANUTZ, *Aeroservoelastic Modeling and Analysis of a Highly Flexible Flutter Demonstrator*, AIAA Atmospheric Flight Mechanics Conference, June 2018.
- [258] J. XU AND I. KROO, *Aircraft design with active load alleviation and natural laminar flow*, Journal of Aircraft, 51 (2014), pp. 1532–1545.
- [259] V. YAKUBOVICH, *S-procedure in nonlinear control theory*, Vestnik Leningrad University, 1 (1971), pp. 62–77.
- [260] V. A. YAKUBOVICH, *A frequency theorem for the case in which the state and control spaces are hilbert spaces with an application to some problems of synthesis of optimal controls, parts i–ii*, Siberian Mathematical Journal, 15 (1974), pp. 639–668.
- [261] A. YAZICI, A. KARAMANCIOLU, AND R. KASIMBEYLI, *A nonlinear programming technique to compute a tight lower bound for the real structured singular value*, Optimization and Engineering, 12 (2011), pp. 445–458.
- [262] P. YOUNG AND J. C. DOYLE, *A lower bound for the mixed  $\mu$  problem*, IEEE Transactions on Automatic Control, 42 (1997), pp. 123–128.
- [263] P. YOUNG, M. NEWLIN, AND J. DOYLE, *Practical computation of the mixed  $\mu$  problem*, IEEE American Control Conference, June 1992.
- [264] G. ZAMES, *On the input-output stability of time-varying nonlinear feedback systems–part i: conditions derived using concepts of loop gain, conicity, and positivity*, IEEE Transactions on Automatic Control, 11 (1966), pp. 228–238.
- [265] ——, *On the input-output stability of time-varying nonlinear feedback systems–part ii: conditions involving circles in the frequency plane and sector nonlinearities*, IEEE Transactions on Automatic Control, 11 (1966), pp. 465–476.
- [266] G. ZAMES AND P. FALB, *Stability Conditions for Systems with Monotone and Slope-Restricted Nonlinearities*, SIAM Journal on Control, 6 (1968), pp. 89–108.
- [267] T. ZEILER, *Matched Filter Concept and Maximum Gust Loads*, Journal of Aircraft, 34 (1997), pp. 101–108.
- [268] T. ZEILER AND A. POTOTZKY, *On the relationship between matched filter theory as applied to gust loads and phased design loads analysis*, Nasa Report 181802, 1981.

---

## BIBLIOGRAPHY

- [269] K. ZHOU, J. C. DOYLE, AND K. GLOVER, *Robust and Optimal Control*, Prentice-Hall, Inc., 1996.
- [270] A. ZONA THECHNOLOGY INC., SCOTTSDALE, *ZAERO Version 5.2*, 2004.  
Theoretical Manual, Version 7.1.
- [271] V. ZUBOV, *Methods of A. M. Lyapunov and Their Application*, noordhoff, 1964.

